Università degli Studi di Napoli Federico II

Dottorato di Ricerca in

Ingegneria Strutturale, Geotecnica e Rischio Sismico

THESIS FOR THE DEGREE OF DOCTOR OF PHILOSOPHY

On the Performance of Lap-Shear Hot-Driven Riveted Connections:

Experimental and Numerical Study

by
Aldo Milone

Advisor: Prof. Raffaele Landolfo

Scuola Politecnica e delle Scienze di Base
Dipartimento di Strutture per l'Ingegneria e l'Architettura

*"Every machine is a smoke machine
if you operate it wrong enough"*

A realist Engineer,
yet
an optimistic SFX Director

On the Performance of Lap-Shear
Hot-Driven Riveted Connections:
Experimental and Numerical Study

Ph.D. Thesis presented

for the fulfilment of the Degree of Doctor of Philosophy

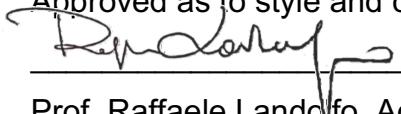in Ingegneria Strutturale, Geotecnica e Rischio Sismico

by

Aldo Milone

March 2023

Approved as to style and content by

_____

Prof. Raffaele Landolfo, Advisor

Università degli Studi di Napoli Federico II

Ph.D. Program in Ingegneria Strutturale, Geotecnica e Rischio Sismico

XXXV cycle - Chairman: Prof. Iunio Iervolino

Candidate's declaration

I hereby declare that this thesis submitted to obtain the academic degree of Philosophiæ Doctor (Ph.D.) in Ingegneria Strutturale, Geotecnica e Rischio Sismico is my own unaided work, that I have not used other than the sources indicated, and that all direct and indirect sources are acknowledged as references. Parts of this dissertation have been published in international journals and/or conference articles (see list of the author's publications at the end of the thesis).

Napoli, March, 10, 2023

Aldo Milone

Abstract

Hot-driven riveted connections are one of the most common structural details adopted for existing metal structures built prior to the '60s of the XXth Century.

Nowadays, several existing riveted constructions are still in service and usually exhibit structural deficiencies, owing to both *i*) a significant increase of acting loads with respect to erection time and/or *ii*) the lack of detailed provisions in earlier normative codes.

The present work is hence devoted to study the static and fatigue performance of lap-shear riveted connections accounting for their peculiarities.

After a initial state-of-the-art review dealing with *i*) manufacturing technology, *ii*) past significative applications, *iii*) peculiar issues, *iv*) normative provisions and *v*) previous literature studies related to hot-driven riveted connections, in this work some refined predictive models for the static and fatigue resistance of connections are proposed, calibrated and preliminarily validated.

To this end, advanced damage formulations and fatigue analysis techniques are adopted to account for peculiarities of riveted connections. For instance, both the effects of hot-driving process and stress concentrations nearby geometrical discontinuities are properly accounted as described in dedicated Sections.

Relevant model parameters have been calibrated against the results of three comprehensive experimental campaigns. The first set of tests, which was carried out in collaboration with Norwegian University of Science and Technology (NTNU), aimed at validating energetic approaches for fatigue assessment of blunt notched components made of mild steels.

The second set of trials, which was previously carried out by the Candidate's Research Group, was devoted to parametrically inspect the static behaviour of different lap-shear riveted connections accounting for the influence of *i*) hammering process and *ii*) specimens' geometrical features.

The most recent experimental campaign aimed at parametrically investigating the fatigue performance of a second set of identical hot-driven connections. Each experimental set-up and experimental outcomes are illustrated in detail in relevant Sections of the present work.

Based on a careful revision of obtained results, semi-empirical formulations are finally derived and compared with normative requirements reported in EN1993:1-8 & EN1993:1-9.

Finally, the effect of common constructional imperfections (i.e. the so called "camming" defects induced by plates misalignment) on the static performance of hot-driven riveted connections is preliminarily investigated and discussed.

Eventually, main conclusive remarks and possible further developments of the present research activity are summarized at the end of this work.

Keywords: Riveted Connections, Hot-Driving, Static Resistance, Fatigue Performance, Parametrical Study.

Sintesi in lingua italiana

I collegamenti chiodati a caldo sono uno dei dettagli strutturali più comuni nelle strutture metalliche esistenti realizzate prima degli Anni '60 del XX secolo.

Al giorno d'oggi, diverse costruzioni chiodate esistenti sono ancora in servizio e presentano solitamente inadeguatezze strutturali, dovute sia a *i*) un significativo aumento dei carichi agenti rispetto all'epoca di costruzione e/o *ii*) la mancanza di indicazioni dettagliate nei precedenti codici normativi.

Il presente lavoro è pertanto dedicato allo studio della performance statica e a fatica di connessioni a taglio chiodate in virtù delle peculiarità di queste ultime.

Dopo una disamina dello stato dell'arte riguardante *i*) la tecnologia esecutiva, *ii*) alcune rilevanti applicazioni passate, *iii*) le problematiche tipiche, *iv*) le indicazioni normative e *v*) i precedenti studi di letteratura relativi a connessioni chiodate a caldo, in questo lavoro vengono proposti, calibrati e preliminarmente validati dei modelli predittivi della resistenza statica e a fatica delle connessioni.

A tal fine, vengono adottate delle formulazioni di danno e delle tecniche di analisi a fatica avanzate per tener conto delle peculiarità delle connessioni chiodate. Per inciso, sia gli effetti del processo di battitura a caldo che le concentrazioni tensionali in prossimità delle discontinuità geometriche sono propriamente tenuti in conto come descritto nelle Sezioni dedicate.

I parametri rilevanti per tali modelli sono stati calibrati rispetto ai risultati di tre estese campagne sperimentali. La prima serie di test, che è stata condotta in collaborazione con la Norwegian University of Science and Technology (NTNU), mirava a validare l'uso di approcci energetici per l'assessment a fatica di componenti intagliati di acciaio dolce.

La seconda serie di test, precedentemente effettuata dal Gruppo di Ricerca del Candidato, ha riguardato lo studio parametrico del comportamento statico di diverse connessioni a taglio chiodate per indagare l'influenza *i*) del processo di battitura e *ii*) delle caratteristiche geometriche dei provini.

La più recente campagna sperimentale è stata rivolta a studiare parametricamente le prestazioni a fatica di connessioni chiodate a caldo aventi identica geometria. I set-up di prova ed i risultati sperimentali sono illustrati in dettaglio nelle Sezioni pertinenti di questo lavoro.
Sulla base di un'attenta revisione dei risultati ottenuti, delle formulazioni semi-empiriche vengono infine derivate e confrontate con i requisiti normativi riportati nelle norme EN1993:1-8 & EN1993:1-9.

Infine, viene preliminarmente studiato e discusso l'effetto di comuni imperfezioni costruttive (i cosiddetti difetti di "camming" indotti dal disallineamento delle piastre) sulle prestazioni statiche dei collegamenti chiodati a caldo. In ultimo, le principali conclusioni e i possibili futuri sviluppi della presente attività di ricerca sono riassunti al termine di questo lavoro di Tesi.

Parole Chiave: Connessioni Chiodate, Battitura a Caldo, Imperfezioni Costruttive, Resistenza Statica, Comportamento a Fatica, Studio Parametrico.

Acknowledgements

Contents

List of Figures

Chapter 2

Chapter 3

Chapter 4

Chapter 5

Chapter 6

Chapter 7

Chapter 8

List of Tables

Chapter 2

Chapter 3

Chapter 4

Chapter 5

Chapter 6

Chapter 8

Chapter 1

Introduction

1.1. Objectives of the work

Hot-driven riveted connections are one of the most common structural details adopted for existing metal structures built prior to the '60s of the XXth Century (*D'Aniello et al., 2011*).

Main structural applications of hot-driven rivets concerned railway bridges (e.g., the *Coalbrookdale Bridge* or the *Sydney Harbour Bridge*), monumental buildings (with the *Eiffel Tower* being the most iconic realization) and large span domes (notable is the example of the *Umberto I Gallery* in Naples).

Nowadays, several existing riveted constructions are still in service and usually exhibit structural deficiencies, owing to both *i*) a significant increase of acting loads with respect to erection time and/or *ii*) the lack of detailed provisions in earlier normative codes.

The primary objective of this work is hence to investigate the influence of relevant geometrical and mechanical parameters on the static and fatigue performance of lap-shear riveted connections accounting for their peculiarities.

To this end, it is worth emphasizing that current European normative provisions (*CEN, 2005a, 2005b*) only provide few indications with regard to both the static and fatigue assessment of riveted connections, e.g., mostly derived from bolted connections provisions in spite of some significant differences.

For this purpose, a comprehensive set of experimental activities is performed. Namely, a total of fifteen connection configurations are investigated, i.e., with varying *i*) splice arrangement (symmetric or unsymmetric), *ii*) rivet diameter (16, 19 or 22 mm), *iii*) rivets number (1 or 2), *iv*) plate thickness (10 or 12 mm) and *v*) plate width (70 or 90 mm).

Based on careful interpretation of obtained results, the influence of the hot-driven hammering process on both the monotonic and cyclic behaviour of such connections is deeply investigated. Indeed, as shown by earlier research works (*Hetchman, 1948; Munse et al., 1956)*, termo-mechanical alterations induced by hot-driving can drastically alter base material properties of rivets and, on a local extent, connected plates.

The effect of lateral compression among connected plates induced by shrinking of cooling rivets (that is, the so-called clamping force) is also parametrically investigated. Indeed, as opposed to high-strength bolted connections, the actual magnitude of clamping action is affected by a significant degree of uncertainty owing to the peculiar installation technique of hot-driven rivets (*Leonetti et al., 2020*).

Additionally, the effect of common constructional imperfections found in existing hot-driven riveted constructions (i.e., the so called "camming" defects induced by plates misalignment - *Sustainable Bridge, 2006*) is preliminarily investigated and discussed with reference to the lone static performance of connections.

The second aim of the present work is to inspect the validity of some advanced methods to assess the performance of lap-shear riveted connections. For instance, to properly inspect both static and fatigue response of splices, refined ductile damage models derived

from the pioneering work of *Rice & Tracey* (*1969*) are introduced and calibrated against experimental results. Moreover, advanced fatigue verification techniques are implemented alongside standard methods encoded in EN1993:1-9 (*CEN, 2005a*). In particular, the Strain Energy Density (SED) Method (*Lazzarin et al. 2001, Livieri & Lazzarin, 2005; Berto et al. 2009, 2014)* is initially applied and validated for blunt-V notched components made of mild steel and hence extended to lap-shear riveted connections. For this purpose, an additional set of experimental tests on both plain and notched mild steel coupons is appositely performed.

Both damage models and fatigue assessment methods are implemented with the aid of refined Finite Element Models (FEMs), which resemble specimens tested within the framework of relevant experimental activities.

The third and final objective of this thesis work is to provide some semi-empirical formulations to predict the static and fatigue response of investigated hot-driven connections based on the introduced theoretical background and observed results.

Whenever possible, such formulations are presented in a simplified form with the aim to give designers additional and straightforward tools for the assessment of riveted connections belonging to actual existing constructions. To this end, presented expressions are critically compared with relevant provisions encoded in normative documents in force (EN1993:1-8 – *CEN, 2005b*; EN1993:1-9 – *CEN, 2005a*). Finally, reliability of each formulation is statistically assessed within the framework of EN1990 (*CEN, 2002*) performance-based approach.

1.2. Outline of the work

The main body of the present work is divided in seven Chapters.

In *Chapter 2*, a comprehensive state-of-the-art review about hot-driven riveted connections is presented. Namely, key aspects concerning *i*) manufacturing technology, *ii*) past significative applications, *iii*) peculiar issues, *iv*) normative provisions and *v*) notable earlier literature studies are addressed in detail to provide a summary of the current scientific knowledge related to hot-driven riveted connections.

In *Chapter 3*, an overview about damage and fatigue modelling of structural steel elements is reported. For instance, a theoretical background about main damage models for ductile materials is first introduced; hence, most suitable models are applied to hot-driven riveted connections in order to account for their peculiarities.

An analogous logic is followed with reference to fatigue verification techniques. Indeed, standard fatigue assessment methods, both drawn from current normative provisions or established literature studies, are initially presented before quickly moving to advanced techniques. Namely, a strong emphasis is given to energetic approaches and especially to the Strain Energy Density (SED) method. Presented methods are hence applied to the relevant case of hot-driven riveted connections.

In *Chapter 4*, a detailed description of three experimental campaigns on mild steel components and aged hot-driven riveted connections is presented. In particular, the first set of tests, which was carried out in collaboration with *Norwegian University of Science and Technology* (NTNU), aims at validating energetic approaches for fatigue assessment of blunt V-notched components made of mild steels.

The second set of trials, which was previously carried out by the Candidate's Research Group, is devoted to parametrically inspect the static behaviour of different lap-shear riveted connections accounting for the influence of *i*) hammering process and *ii*) specimens' geometrical features.

The most recent experimental campaign aims at parametrically investigating the fatigue performance of assembled hot-driven connections having similar geometry to those tested by *D'Aniello et al.* (*2011*).

In *Chapter 5*, each of the peculiar aspects affecting the static performance of hot-driven riveted connections is addressed based on theoretical background and experimental activities presented in previous Chapters. For this purpose, refined FEMs resembling experimental specimens are developed in ABAQUS software (*Simulia, 2017*). Numerical analyses enable to quantify *i*) the impact of hot-driving process in terms of alteration of base material properties, *ii*) the effect and magnitude of clamping action and *iii*) the influence of geometrical features on the static performance of connections.

Additionally, the effect of some common constructional imperfections found in existing hot-driven riveted constructions ("camming" defects due to plates misalignment) is preliminarily investigated and discussed.

Each presented formulation is hence critically compared with current normative provisions reported in EN1993:1-8 (*CEN, 2005b*) and statistically assessed according to EN1990 (*CEN, 2002*) provisions.

In *Chapter 6*, the fatigue performance of mild steel components is preliminarily investigated before addressing the cyclic performance of assembled riveted connections. Namely, results of relevant experimental tests are interpreted through both standard and advanced verification techniques.

For this purpose, a second set of refined FEMs is properly developed. As a result, energetic fatigue approaches are validated for mild steels, allowing the extension of such methods to hot-driven riveted splices.

In *Chapter 7*, the fatigue performance of full-scale hot-driven riveted connections is eventually investigated by extending the same approaches adopted for single components. Namely, the SED method is employed to derive an equivalent master fatigue curve for hot-driven splices accounting for geometrical and mechanical peculiarities. Once again, each proposed formulation is critically compared against relevant literature formulations and encoded provisions reported in current and future version of EN1993:1-9 (*CEN, 2005a, 2020*).

In *Chapter 8*, main conclusions of the work are finally summarized, in conjunction with possible further research developments.

Chapter 2

Hot-Driven Riveted Connections: A State-of-the-Art Review

Hot-driven riveted connections had their heyday among the XIXth and the first half of the XXth century (*D'Aniello et al., 2011*). Indeed, as the advent of the industrial revolution resulted in major technological advances of the iron and steel industry, a strong popularity was rapidly gained by metallic constructions, in which rivets became massively adopted as the most common type of fastener (*Collette et al., 2011*).

The spreading of such kind of connection system led to established techniques for design and installation of rivets, although mostly based on empirical findings (*Marmo, 2011*).

As the use of high-strength bolts became more and more advocated starting from the 30s of XXth century (*Batho et al., 1934*), riveting gradually fell out of favour and therefore the required skilled labour became progressively unavailable. Nevertheless, a growing interest for this technology rekindled in recent times in the framework of *i*) preservation of the historical built heritage and *ii*) vulnerability mapping of older infrastructures still in service. For instance, the Italian railway network includes more than 3500 steel bridges in service, the majority of which was realized prior to the 1960s with hot-driven riveted connections (*Marmo, 2011*).

Also, in light of some calamitous events of the recent past, it has become really clear that assessing the vulnerability of such infrastructures is a crucial task in order to prevent unacceptable human and economic losses.

All the above considerations motivated the research study summarized in this thesis work. Before moving to the core of performed activities, in this Chapter a detailed state-of-the art review about hot-driven riveted connections is presented.

The following key related aspects are addressed in following Sections, namely: *i*) manufacturing technology (*Section 2.1*), *ii*) past significative applications (*Section 2.2*), *iii*) peculiar and recurring issues (*Section 2.3*), *iv*) normative provisions (*Section 2.4*) and *v*) notable past literature studies (*Section 2.5*).

2.1. Manufacturing technologies for hot-driven riveted connections

2.1.1 Generality about rivets

Rivets are a type of permanent mechanical fastener which can be used to join adjacent plates (usually also referred as "*plies*") or profiles by being installed in apposite holes. An undriven (i.e., still not installed) rivet consists of (Figure 2.1):

- a cylindrical shank having "undriven" diameter d_U and grip length h_S;
- an ending head having an enlarged diameter D and depth h_H;
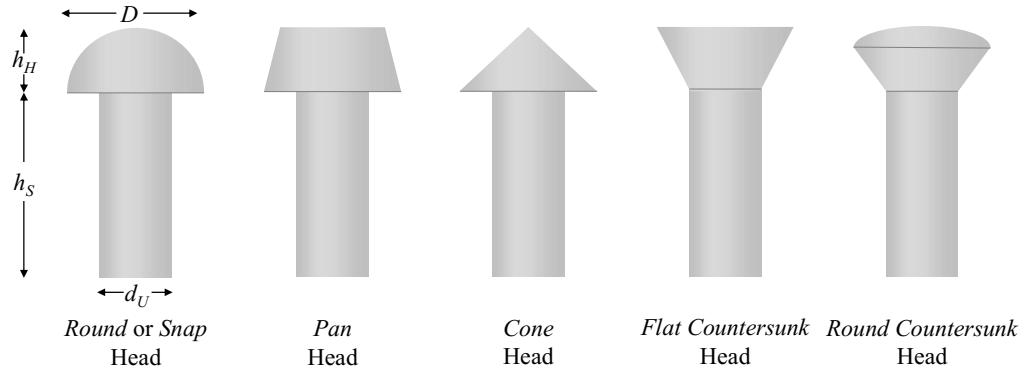
Figure 2.1 Most common typologies of rivets and relevant geometrical features (adapted from *Duggal, 2000; Marmo, 2011; Collette, 2014*).

To clearly distinguish it from the one manufactured by on-site hammering, the first head is usually referred as *shop head*, while the other one is referred as *field head* (*Duggal, 2000*).

Although several typologies of shop heads were developed during past centuries (i.e., round, pan, cone, flat or round countersunk), the round-shaped shop head became arguably the most popular owing to complex implementation of other solutions (pan or cone heads) or due to the undesirable loosening of rivets in time (countersunk heads) (*Collette, 2014*).

Regarding shop head-to-shank proportions, usually a D/d ratio among $1.60 \div 1.80$ was adopted to ensure a sufficient restraint action on connected plates (*Duggal, 2000*). Notably, typical shop head width-to-depth ratio D/h_H ranged between $2.00 \div 3.00$. As a matter of fact, hemispherical shop heads ($D/h_H = 2$) were not the most common solution, as button-shaped shop heads ($D/h_H > 2$) proved to be more popular instead, most likely for both aesthetic and technological reasons (*Kulak et al., 1987*).

As for the grip length h_S of the undriven rivet, an empirical formula was adopted to account for the required amount of material to form the field head (Equation 2.1):

$$h_S \approx 1.1 \sum_i t_i + 1.3 \, d_0 \qquad (2.1)$$

with t_i being the thickness of the i-th plate to be connected and $d_U < d_0 < D$ being the hole diameter (*Masi, 1996*).

2.1.2 Techniques for rivet driving

To install rivets and thus permanently tighten plies, two main techniques were available to form the field head, i.e., *cold-driving* and *hot-driving*. While the former technology was mostly adopted for soft metals (e.g., aluminium, brass) and/or in case of rather small diameters ($6 \div 10$ mm), hot-driving was the most popular solution to install ferrous rivets for civil engineering applications (*Kulak et al., 1987*).

Both technologies required the preliminary realization of accommodation holes in elements to be connected. Thus, both kinds of riveted connections configured themselves as intermittent joints, as opposed to welded (and hence, continuous) ones. Such need clearly introduced an additional source of structural weakness to be accounted.

This condition, in conjunction with the lack of redundancy of earlier metallic constructions (which were indeed realized with truss structural schemes, i.e., basically inherited by consolidated practice for timber structures) identified such joints as critical structural details from the very beginning of their technological development (*Guerrieri et al., 2005*).

Two alternative techniques were used to form holes in plies to be connected, i.e., *drilling* or *punching*. Drilling consists in removing fragments of base material from plates with the aid of an helicoidal drill (Figure 2.2a). As the resulting inner hole surface could be excessively rough, an additional finishing (*reaming*) was sometimes applied after the initial drilling (*Duggal, 2000*).

With respect to punching (Figure 2.2b), such technique involves an apposite device (cylindrical puncher) having an end with diameter equal (or, in some limiting cases, smaller) to d_0, which is pushed against the steel plate. In this way, holes are formed by removing a single cylindrical piece of base material.

a)	b)
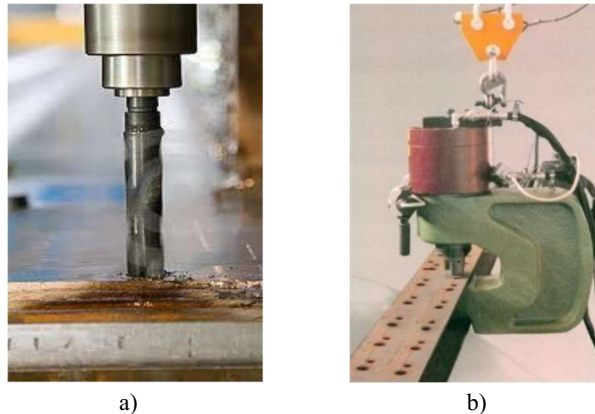
Figure 2.2 Example of hole (a) drilling and (b) punching (*Marmo, 2011*).

Punching holes with diameter directly equal to d_0 is allowed only for limited plate thicknesses (usually, for $t \leq 10$ mm). For thicker plates, holes having smaller diameter were usually punched and hence the required hole diameter was obtained by additional machining (*boring*). Once again, a reamed finishing was finally applied if required, although boring usually already ensured an excellent surface quality (*Duggal, 2000*).

As a matter of fact, the main drawback of punching technique lied in the strong local damage induced in perforated plates, which proved to have a detrimental effect on both the static and fatigue performance of riveted connections (*Iwankiw et al, 1982*). Moreover, hole punching was technologically unfeasible for very large holes (i.e., for $d_0 > t$), for which drilling was the only available option (*Marmo, 2011*).

As for the field head formation, both cold and hot riveting involved the use of a pneumatic or hydraulic hammer (see Figure 2.3a), which was used to realize the field head by applying a pressure (≈ 100 N/mm^2 in case of hot driving) on the protruding part of the undriven shank while the shop head was held firmly in place. This last operation was usually carried out with the aid of an appropriate device having a concave hemispherical end (i.e., the so-called "*bucking bar*", see Figure 2.3b).

Hand hammering was also sometimes performed when installing small diameter rivets directly on field. In this case, a mould was used to properly shape the field head of rivets, which were referred as *hand-driven rivets* (*Duggal, 2000; Marmo, 2011*).

The main difference between cold-driving and hot-driving obviously concerned the driving temperature of rivets.

For instance, cold riveting was directly performed at room temperature. On one hand, without the necessity of an apposite heat source, the process was arguably less energy and time consuming. On the other hand, hammering required a sensibly higher forming pressure.

| a) | b) |

Figure 2.3 a) Popular kind of pneumatic hammer ("*Chicago Boyer Long Stroke*" hammer – *Collette, 2014*) and b) example of a bucking bar (*Marmo, 2011*).

Moreover, clamping action between connected plies turned out to be lower and less controllable due to the absence of cooling-induced shrinking. Indeed, although a certain degree of proportionality was experimentally observed among forming pressure and residual clamping force in cold-driven rivets, no clear correlations were detected between such parameters (*Deng et al., 1998*).

Nevertheless, it is worth remarking that cold driving technology still finds its niche nowadays for connecting thin cold-formed steel (CFS) profiles (*Landolfo et al., 2022*).

For what concerns hot-driving process, installation of rivets was carried out after preemptively heating them in a special forge up to a temperature of ≈ 900 °C (*D'Aniello et al., 2011*), which was recognizable by the peculiar colour of heated rivets' surface (i.e., the so-called "*cherry red*", see Figure 2.4a).

Hot rivets were then held in place into holes with the bucking bar and thus the second field head was formed with the pneumatic or hydraulic hammer (Figure 2.4b). As opposed to cold-driven rivets, heated rivets reached a "plastic" (i.e., softened) consistency which allowed to use a lower forming pressure.

Hammering rivets while in this plastic state induced a strong lateral dilatation of the rivet shank, resulting in null final clearance between the driven rivet shank and the relative plate hole (Figure 2.4c). Therefore, for hot-driven riveted connections, the final shank diameter d occurred to be the same as the hole diameter d_0, thus differently from cold-driven riveted or bolted connections (*D'Aniello et al., 2011*).

Hot-hammering resulted in two positive effects on the performance of riveted connections, namely *i*) an increase of the yield strength of the rivets base material f_{yr0} (roughly estimated in $\approx 20\%$ of f_{yr0} - *Hetchman, 1948; Munse et al., 1956)* and *ii*) a stronger tightening of connected plates due to rivet shrinking as opposed to cold riveting.

| a) | b) |

c)
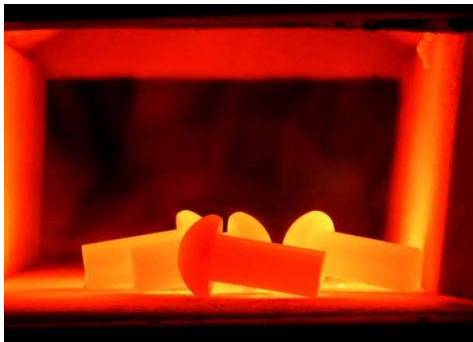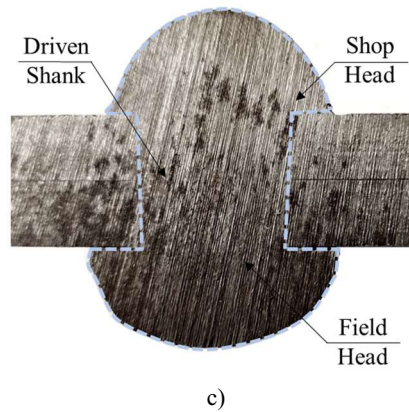
Figure 2.4 a) Rivets heating in a special forge up to the "cherry red" colour, b) on-site hot hammering of a rivet c) section of a hot-driven rivet showing no clearance between plate hole and rivet shank.

Nevertheless, it is worth remarking that both the increment of yield strength and the magnitude of clamping action strictly depended on the actual driving temperature and on-site cooling conditions, thus still resulting in a significant degree of uncertainty with regard to such key mechanical parameters (*Leonetti et al., 2020*)

2.1.3 Structural applications of hot-driven riveted connections

Within the framework of civil engineering constructions, hot-driven riveted connections mainly had their field of application in *i*) *coupling* iron or steel profiles and/or plates to obtain complex cross-section shapes (built-up sections) or *ii*) *connecting* structural members by means of shear or tensile joints (*Kulak et al., 1987; Duggal, 2000*).

With respect to built-up sections, a wide variety of open or hollow sections could be obtained by properly coupling straight plates, angle, and channel profiles (Figure 2.5a). A common solution involved the use of riveted battens to couple spaced profiles, especially when high bending moments and/or axial forces were expected in structural members (e.g., for bridge girders or main trusses, see Figure 2.5b).

A peculiar use of riveted battens also concerned the realization of built-up cruciform sections, in which connecting plates were alternatively placed in longitudinal and transversal direction to join two angle sections (e.g. for diagonal bracings, see Figure 2.5c). Nevertheless, use of rivets to directly connect two or multiple back-to-back profiles was also quite popular, e.g. for the realization of hollow columns (Figure 2.5d). It is worth noting that, in case of built-up sections, hot driving was entirely performed in shop, while only structural assemblage was performed on site (Collette, 2014).

a)
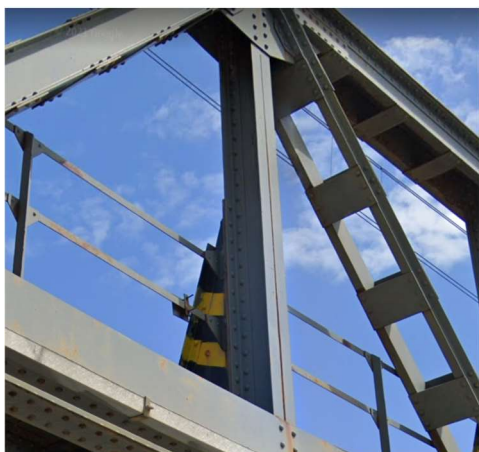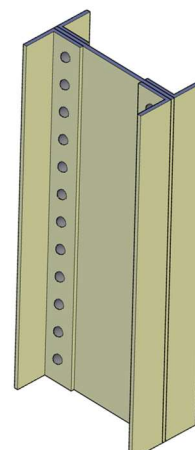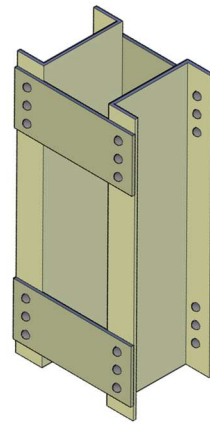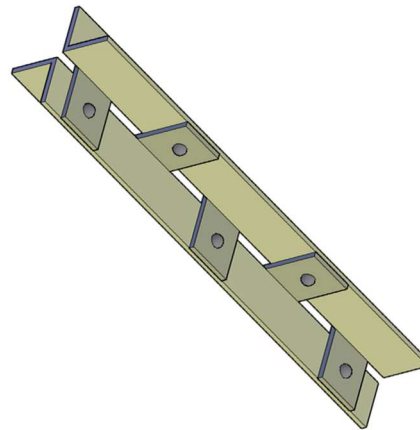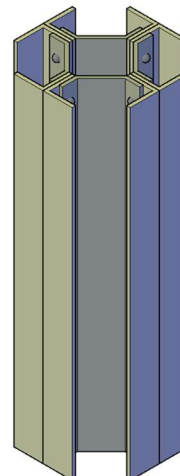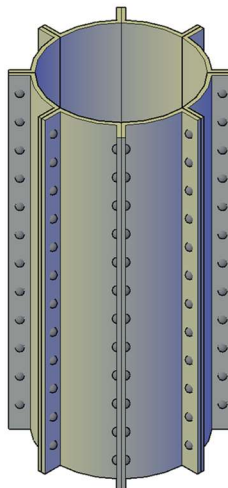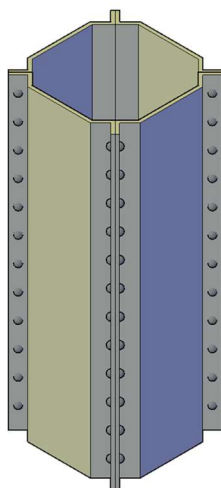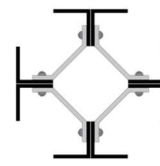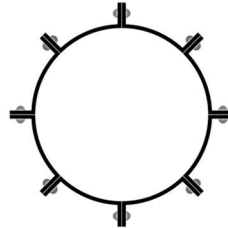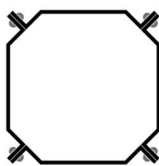
Figure 2.5 Examples riveted built-up sections: a) I-shaped compact section used as vertical strut (Bridge over Oliva torrent, Italy), b) battened box-shaped section employed as main diagonal truss (Bridge over Gesso River, Italy), c) cruciform battened section used as transverse bracing (Bridge over Oliva torrent, Italy), d) different kinds of hollow sections adopted for columns (adapted from *Freitag, 1904*).

It is worth remarking that, in case of built-up sections, hot driving was entirely performed in shop, and hence only the subsequent structural assemblage was performed on site (Collette, 2014).

The main advantage of riveted built-up sections was arguably represented by their intrinsic adaptability to various structural necessities.

Namely, rather deep and/or asymmetric cross-sections could be easily obtained (similarly to modern built-up welded sections). Moreover, U-shaped, Π-shaped, or box-shaped sections could be easily strengthened by means of additional back plates when needed. As a counterpoint, the adoption of complex built-up section often resulted in intricated joints involving a significant number of rivets and gusset plates (Figure 2.6).
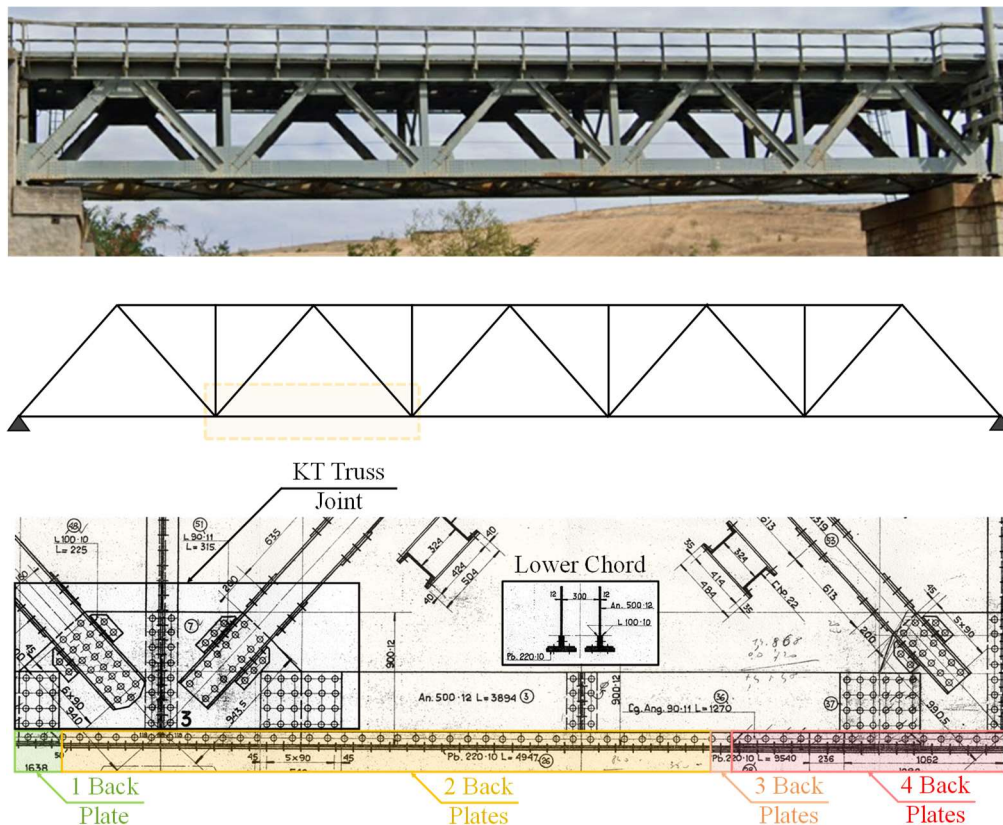
Figure 2.6 Structural details adopted in railway riveted bridge over Gesso River, in which *i*) a variable number of back plates (1 ÷ 4) is adopted for lower chords to resist increasing gravity effects towards mid-span and *ii*) rather complex KT truss joints are used to connect chords, struts and diagonals.
[Original design drawings are courtesy of Italian Railway Network (RFI)]

Nevertheless, even most complex riveted joints could be typologically reduced to a small class of "basic" connections (Kulak et al., 1987, Bresler et al., 1960):

- Shear connections, in which internal actions were (predominantly) transferred by rivet shearing. Depending on the arrangement of connected plates, *lap* or *butt* shear configurations could be obtained, both *symmetric* (S) or *unsymmetric* (U), and with one or multiple rivet rows (Figure 2.7a);
- Tension connections, in which internal actions were (predominantly) transferred by rivets in tension. *T-stub* configuration was arguably the most common arrangement (Figure 2.7b), although mild steel bolts were already preferred in past centuries when significant tensile actions were expected in fasteners (*Collette et al., 2011*);

Single Shear   Double Shear

Butt Splice

U

S

Lap Splice

U

S

a)

b)   c)
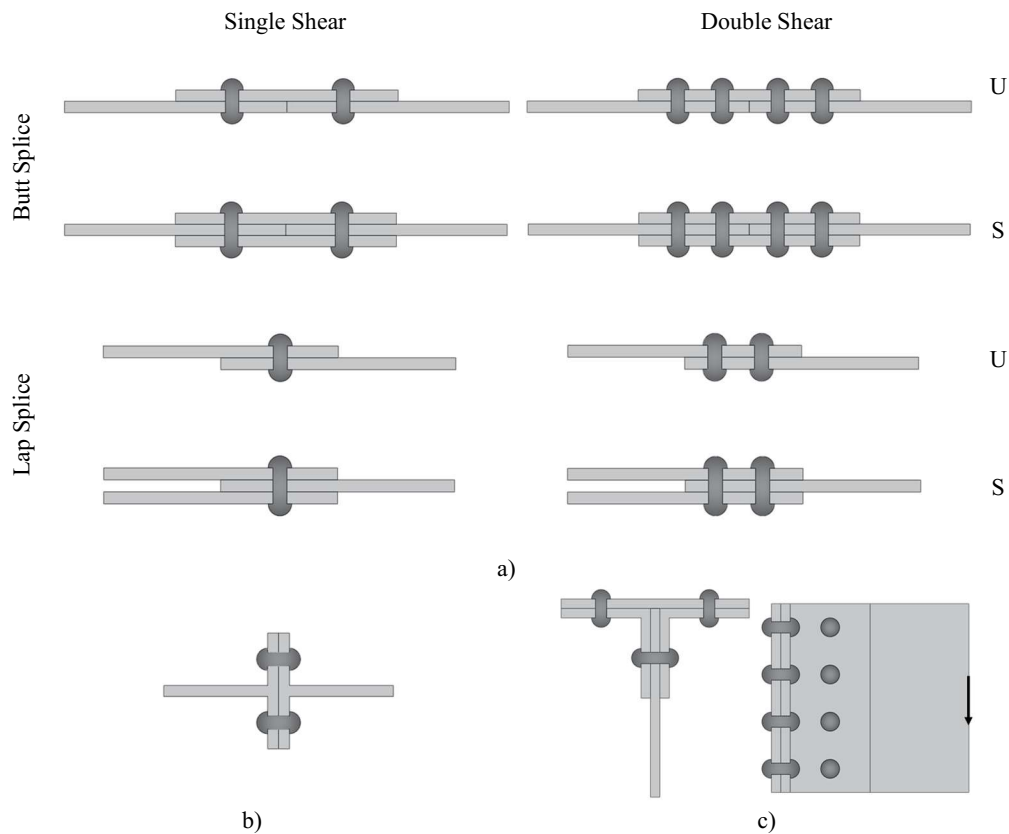
Figure 2.7 Examples of "basic" typologies of riveted connections: a) shear connections, b) T-stub tension connection, c) cleat angle hybrid connection.

- Hybrid shear-tension connections, in which internal actions were transferred by rivets under simultaneous shear and tension. Several configurations of hybrid connections were used, usually for framing (Figure 2.7c).

When multiple rivets had to be installed in lap or butt joints, two alternative configurations were usually adopted, i.e., *chain riveting*, with rivets being arranged in a regular grid of parallel rows, or *zig-zag riveting*, with adjacent rows being staggered instead (Figure 2.8a-b - *Kulak et al., 1987*).

In earlier manuals and handbooks, zig-zag configuration was regarded as stronger than an equivalent chain configuration having the same number of fasteners (*Collette, 2014*), as it was deemed able to spread shear forces more uniformly among the rivets.

Chain   *Zig-Zag*   *Convergent Zig-Zag*

a)   b)   c)
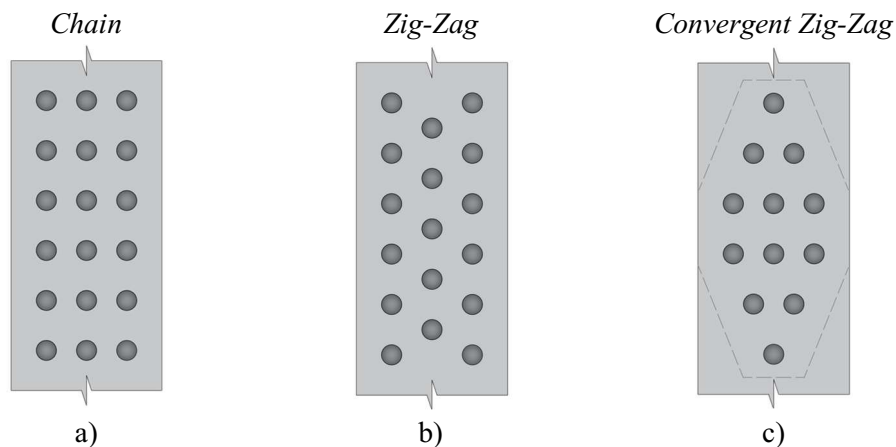
Figure 2.8 Adopted configurations for lap or butt splices with multiple rivet rows.

Such belief originated from the popular work of *Schwedler (1867)*, which proposed a handy design method for splices with multiple rivets in zig-zag configuration.

As zig-zag riveting became more and more widespread, a further development of such configuration gained popularity, i.e., the *convergent zig-zag* configuration (Figure 2.8c). In this arrangement, the number of rivets in outer rows was gradually reduced. For this purpose, diamond-shaped cover plates were appositely used, with the aim to minimize net-area stress concentrations on perforated plates.

However, convergent zig-zag riveting induced significant shear forces in lone end rivets; such detrimental effect was dangerously overlooked during past centuries owing to oversimplified design assumptions adopted at the time (*Collette, 2014*).

2.2. Past significative applications of hot-driven riveted connections

As the iron and steel industry quickly progressed during the Industrial Revolution, riveted constructions became widely popular within the framework of civil engineering. Main structural applications of hot-driven rivets concerned *i*) railway bridges, in which rivets were adopted both to couple plates and profiles through battens and to join structural members, *ii*) monumental buildings, in which the apparent lightness of riveted metallic structures was used to obtain sleek and elegant structures and *iii*) large span domes, with riveted frames being often coupled with glass panels to achieve remarkable aesthetic effects (*Masi, 1996; Ballio et al., 2020*).

In the present Section, a collection of some significative examples of riveted constructions is presented.

2.2.1 Coalbrookdale Bridge (1779)

The *Coalbrookdale Bridge* or *Iron Bridge* (Figure 2.9) was the first major cast-iron bridge erected in the world (*Duggal, 2000*). The bridge, which was designed by the architect Thomas Pritchard, resembled earlier masonry bridges with its arch structural scheme.

Figure 2.9 View of the Coalbrookdale Bridge.

This choice naturally descended from mechanical properties of cast-iron, which is rather strong in compression (up to $300 \div 350$ N/mm^2 – *Di Lorenzo et al., 2021*), but exhibits brittle and premature failure in tension owing to its high carbon content ($\geq 2.0\%$).

Construction of the bridge started in 1777 with masonry abutments and piles placed amidst the Severn riverbed, while cast-iron ribs belonging to the superstructure were realized in 1779 by assembling more than 1600 individual components with riveted connections (*Cossons et al., 2002*).

The bridge, which features a main span of 30.6 m and a rise of 20 m above the Severn River, was open to traffic in 1781. However, as the Ironbridge gorge showed dangerous tendency to landslides and owing to early cracks found in piles and abutments, several repairments were carried out in 1784, 1791 and 1792, e.g., local replacement of cracked rivets or installation of wrought iron and steel ties to confine masonry elements (*Cossons et al., 2002; Marmo, 2011*).

After several traffic limitations, the Coalbrookdale Bridge was permanently closed to traffic in 1934, and it is now included in UNESCO world heritage (since 1986) as one of the most prominent symbols of the industrial revolution (*Cossons et al., 2002*).

The success of this first cast-iron riveted bridge of considerable size strongly influenced the field of bridge engineering, leading the way for several subsequent applications with wider and wider span and rise (*Cossons et al., 2002; Marmo, 2011*).

2.2.2   Sydney Harbour Bridge (1932)

The *Sydney Harbour Bridge* (Figure 2.10) is a railway, highway, and pedestrian arch bridge crossing the Parrammatta estuary in the Sydney Harbour. Being opened to traffic in 1932, Sydney Harbour Bridge is still the tallest arch bridge in the world, with a rise of 134 m over the water level (*Spearritt, 2011*).

Conception and construction of Sydney Harbour Bridge took over nine years (1923-1932), with design being commissioned to the Australian engineer John Bradfield. The massive arch-through bridge was realized through a cantilever system, with the two halves being finally joined at midspan for a main span length of 503 m (*Marmo, 2011*).

Figure 2.10 View of the Sydney Harbour Bridge.

Over 52000 tonnes of structural steel were used for the bridge construction, including the two side (323 × 2 m long) approaching spans. Sydney Harbour Bridge is held together by over 6 millions hot-driven rivets, with the last one being installed on site in January, 1932 (*Mackaness, 2006; Marmo, 2011*).

After ninety years of service life, Sydney Harbour Bridge is still daily crossed by an average of 160435 vehicles, 204 trains and 1650 bicycles (*NSW Government, 2017*) and it is recognized as one of the main icons of Sydney, in conjunction with the nearby Sydney Opera House, and of Australia itself.

2.2.3 Golden Gate Bridge (1937)

The *Golden Gate Bridge* (Figure 2.11) is arguably the world's best-known suspended bridge in service. Conception and design of Golden Gate Bridge was first attempted in 1917 by Joseph Strauss, which initially proposed a massive double cantilever system with a central suspended segment (*Van der Zee, 2000*).

After local authorities expressed major concerns about this antiaesthetic and impractical solution, the idea of a suspended bridge was finally developed also in light of recent advances of metallurgy industry (*Marmo, 2011*).

The final design of Golden Gate Bridge implied an impressive 1282 m-long main span, two 345 m-long lateral spans and two 227 m-high towers. Each of the towers features more than 600000 hot-driven rivets.

250 pairs of vertical hangers, which are in turn connected to the two main cables, are devoted to carry the weight of the bridge deck, which is approximately hanged 67 m above the waterline. Each main cable is made of over 27500 wire strands, for a total outer diameter of 91 cm (*Van der Zee, 2000; Marmo, 2011*).

Golden Gate Bridge standed as the longest and tallest suspended bridge in the world until the Verrazzano-Narrows Bridge (1298 m-long) and the Mezcala Bridge (236 m-high) were opened to traffic in 1964 and 1993, respectively.

Nevertheless, after 85 years of service, the Golden Gate Bridge still experiences an average daily traffic of more than 112000 vehicles/day and it remains one of, if not the most renowned bridge in the world, being declared one of the Modern Wonders of the World by American Society of Civil Engineers (ASCE) in 1994 (*ASCE, 2010*).

Figure 2.11 View of the Golden Gate Bridge.

2.2.4 Eiffel Tower (1889)

Designed by the celebrated French engineer Gustave Eiffel, the *Eiffel Tower* (Figure 2.12) was constructed between 1887 and 1889 to act as the centrepiece of 1889 Paris Universal Exposition.

The iconic and elegant 330 m tower was conceived with a pyramidal lattice structure in light of its intended temporary destination and to minimize the wind effect on what is still the tallest construction in Paris nowadays (*Hanser, 2006*).

For the tower construction, more than 7300 tonnes of wrought iron were involved, and about 2 million and a half hot-driven rivets were used to couple and connect metallic profiles (*Billington, 1983*).

After taking six months to realize the concrete slabs serving as base foundations, metalwork started in July 1887 with the erection of the four legs, which were designed to self-stand as cantilevers before being joined at the first floor.

An exceptional precision was adopted in specifying locations of rivet holes and mutual positions of structural components to deal with the bold design of the tower, which traces a large, squared footprint at the base (124×124 m^2) while being only 10.4 m wide at the second floor (*Hanser, 2006*).

Notably, small segments of the tower were carried on the building site being held together by mild bolts, which were subsequently removed and replaced by hot-driven rivets during construction (*Billington, 1983*).

Eiffel planned to dismantle the tower 20 years after its opening to public. However, the increasing popularity of the monument, which featured 1'896'987 visitors only during the Universal Exposition, and the possibility of hosting radio telegraphy services lead the City of Paris to extend its standing permission (*Hanser, 2006*).

Figure 2.12 View of the Eiffel Tower.

Nowadays, Eiffel Tower stands as one of the most notable successes in the field of civil engineering, being the most-seen paid monument in the world, with over 250 million people having visited it since its completion in 1889 (*Hanser, 2006*).

2.2.5 Umberto I Gallery (1890)

The *Umberto I Gallery* (Figure 2.13) is a monumental shopping gallery located in Naples. Construction of the gallery started in 1887, after conspicuous funds were granted to rehabilitate the city with the approval of King Umberto I, to which the construction was entitled (*Carughi, 1996*).

Design of the gallery, which was carried out by Neapolitan engineer Emanuele Rocco, involved a cruciform plan with four entrances facing main streets of the historic city centre. The most recognizable detail of Umberto I Gallery, which immediately became the cornerstone of Neapolitan Rehabilitation ("*Risanamento*"), is arguably the huge iron-glass roof, which consists of four-barrel vault-wings and a central dome. For designing such impressive roof system, the aid of professor and engineer Francesco Paolo Boubée was asked (*Carughi, 1996*).

Lateral vaults are supported by reticular semi-circular arches having 15 m span and uniformly spaced 4.5 m away from each other. The dome, which is inscribed in an octagonal plan and covers a total surface of 1076.8 m^2, features sixteen wrought iron ribs ("meridians") and eleven wrought iron belts ("parallels") that were installed to carry the weight of glass and secondary elements (≈ 24 tonnes). The largest parallel, which stands on eight arches directly installed over masonry constructions, has an internal diameter of 36 m. Hot-driven rivets were used to connect and/or couple all structural elements (*Carughi, 1996*).

Figure 2.13 Interior view of the Umberto I Gallery.

Nowadays, Umberto I Gallery is one of the most popular attractions freely visitable in Naples, as well as one of the main pieces of evidence of neo-baroque and proto-liberty architectural style in Italy (*Carughi, 1996*).

2.3. Peculiar issues of hot-driven riveted connections

As shown in *Section 2.1*, hot-driven riveted connections are characterized by a distinctive manufacturing process which requires skilled labour and a proper equipment for on-field driving. Such a complex technology obviously implies a wide range of peculiar issues that should be properly accounted for while dealing with this kind of structural detail. In the present Section, an overview of such complexities and of their possible implications on the performance of connection is presented.

2.3.1 Disassembly, re-use or repairment of riveted constructions

The main feature that distinguishes riveted connections (both cold- and hot-driven) from bolted ones is clearly their permanent nature (*D'Aniello et al., 2011*). Indeed, once the field head is formed, the rivet acts as a unique piece tightening the connected plies. Moreover, the resulting clamping action and the possible permanent (i.e., plastic) deformation of hammered plates makes dismantling of connections even more complex. From a practical perspective, disassembly of hot-driven riveted connections can be only performed with the aid of a blowtorch or a chisel, thanks to which the heads can be burnt-out or fragmented, respectively (*Marmo, 2011*).

Consequently, only partial re-use of riveted constructions is viable, as lone connected members can be preserved while rivets are inevitably destroyed during dismantling. This issue represented one of the main reasons for high-strength bolts to gain popularity since the '30s of XXth century (*Batho et al., 1934; D'Aniello et al., 2011*).

Indeed, as *i*) high strength steels progressively became more affordable and reliable and *ii*) bolted connections proved to be leak- and slip-proof when sufficiently tightened, the use of hot-driven rivets quickly fell out of favour. Indeed, the possibility to quickly remove and/or replace even small portions of a metallic structure without the need of a specific labour and equipment strongly pushed bolted connections onto the market of metallic constructions up to present time (*Duggal, 2000*).

The issue of dismantling/replacing hot-driven riveted connections is often regarded as so critical that in recent times many operators preferred to replace rivets belonging to damaged metallic structures with same diameter high-strength bolts (Figure 2.14 – *Sustainable Bridge, 2006*) or injection bolts (*Pedrosa et al., 2017a, 2017b*).

Bolts replacing rivets
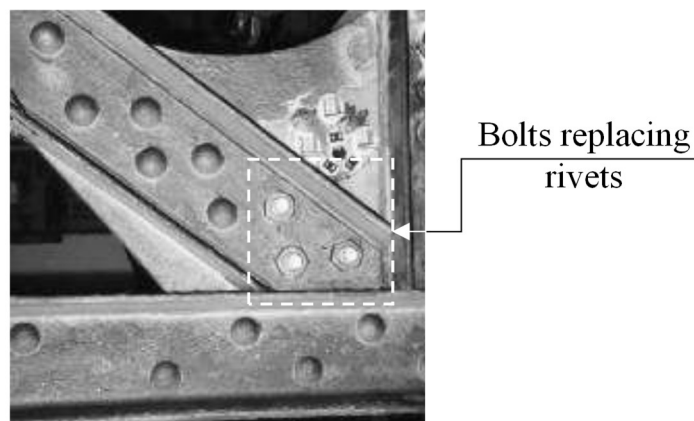
Figure 2.14 Replacement of rivets with bolts in an existing metallic bridge (*Sustainable Bridge, 2006*).

The latter technology has become especially popular in Portugal in recent times, where it was adopted to retrofit old metallic infrastructures such as the bridge in Figueira da Foz (*Pedrosa et al., 2017a*). Injection bolts involve the use of an epoxy resin to completely fill the bolt-hole gap, thus making these kind of connections slip-resistant. This condition, which is achieved by means of injection holes through the bolt heads, makes this kind of fasteners more similar to actual hot-driven riveted connections.

Nevertheless, it should be remarked that the practice of adopting modern fasteners for refurbishing old riveted connections is currently being discouraged, as not only it irremediably impairs the historical value of existing riveted constructions, but also owing to the different stiffness of high-strength bolts (especially if clamped) with respect to rivets. Namely, the actual behaviour of hot-driven joints featuring multiple rivets is already affected by a significant degree of uncertainty due to clamping variability (see *Section 2.3.2* for further details). This phenomenon locally affects the magnitude of plate pre-stress, resulting in an uneven repartition of actions on rivets. The introduction of pre-loaded high-strength bolts further exacerbates this effect, altering the structural performance of repaired joints in ways that can be difficult to predict (*Sustainable Bridge, 2006*).

2.3.2   Variability of clamping action and shear overstrength

One of the main concerns related to structural performance of hot-driven riveted connections is represented by the strong variability of both clamping action (*Leonetti et al., 2020*) and "effective" shear strength f_{yr} (*D'Aniello et al., 2011*). Indeed, the unique thermo-mechanical nature of hot-driving is responsible of strong local alterations of base material properties and it also controls the magnitude of clamping action.

With respect to mechanical properties, strong increments in terms of ultimate resistance of hot-driven connections failing due to rivet shearing have been reported in literature At the same time, a significant reduction of connections' ultimate ductility in static condition was observed (*Hrennikof, 1934; Hetchman, 1948; Munse et al., 1956; D'Aniello et al., 2011*).

Such outcomes, which are rather complex to quantify and are affected by a significant degree of uncertainty, have been plausibly justified in terms of *i*) increment of rivet shear strength and *ii*) ductility and toughness reduction of both rivets' and plates' base material (*D'Aniello et al., 2011*).

On one hand, tests performed by *Hechtman (1948)* showed that f_{yr} increases with increasing temperature. This effect could be recognized up to a temperature threshold of ≈ 900 °C. Contrariwise, no appreciable variations were found by varying the temperature within the range $900 \div 1200$ °C.

On the other hand, the experimental campaign carried out by *D'Aniello et al. (2011)* suggested how plates could be locally affected by a significant ductility reduction (up to $\approx 50 \div 55\%$ in terms of ultimate strain decrease). Moreover, earlier studies on ductility alteration of connected plies showed a strong dependence on the holes forming technique (that is, hole punching induces a stronger local damage on perforated plates with respect to drilling – *Iwankiw et al, 1982*).

Randomness associated to these phenomena mostly lead to empirical and sometimes overconservative approaches for designing riveted connections, which have been subsequently implemented in normative provisions (EN1993:1-8 and EN1993:1-9 for static and fatigue performance, respectively - *CEN, 2005a, 2005b*). Therefore, properly understanding the structural performance of hot-driven riveted connections has to be still

considered as an open and wide field of research (*D'Aniello et al., 2011; Collette, 2014; Milone et al., 2023*).

With respect to magnitude of clamping action, the significant variability encountered in hot-driven connections is shared with cold-driven ones, although owing to different motivations (*Deng et al., 1998; Leonetti et al., 2020*). Namely, while clamping action in cold-riveting loosely depends on rivet geometry, yield stress and on hammering pressure, in hot-riveting this phenomena is mainly governed by rivet shrinking due to on field cooling (*D'Aniello et al., 2011).*

Therefore, both forge's and ambient temperature play a key role in defining the real magnitude of clamping action, and their exact determination is obviously rather impractical, as rivets were deemed as ready to be hammered based on a qualitative criterion (that is, achievement of the "*cherry red*" colour, see *Section 2.1.2*).

Experimental measures carried out by *Leonetti et al. (2020)* indeed showed how clamping stresses in historical riveted connections are extremely variable, ranging from $0.1 \div 0.8\ f_{yr0}$. This condition, which may strongly affect both the static (especially if tensile) and fatigue performance (owing to unpredictable variations of the stress ratio R) of connections (*Milone et al., 2023*), is only indirectly accounted for by current normative provisions. Indeed, according to EN1993:1-8 recommendations, riveted connections cannot be regarded as slip-resistant ones, but only as bearing-type connections (*D'Aniello et al., 2011*)

These kinds of uncertainties are further worsened by the possible presence of constructional imperfections, which can alter the distribution of both shear/tensile and clamping stresses. To this end, an overview about common constructional imperfections found in existing riveted structures and their implications in terms of structural performance is reported in the following *Section 2.3.3*.

It is worth reporting that an attempt to carefully account for all the aforementioned phenomena is carried out in the present thesis work, namely in *Chapters 5* and *7*.

2.3.3 Common constructional imperfections

Owing to the peculiar installation process, hot-driven riveted are often affected by a multitude of constructional imperfections (Figure 2.15). Such imperfections can be either detectable by the naked eye or rather be invisible and hence only recognizable by means of destructive inspections (*Twelvetrees, 1900; Collette, 2014*).

With respect to visible defects, one of the most common imperfections is represented by rivets being loose (Figure 2.15a). This defect, which is caused by an improper tightening

a) Loose rivet

b) Rivet head lip

c) Rivet head eccentricity/distortion

d) Insufficient shank upset

e) Rivet hole deformation

f) Strain hardened plate edge

g) Camming defect
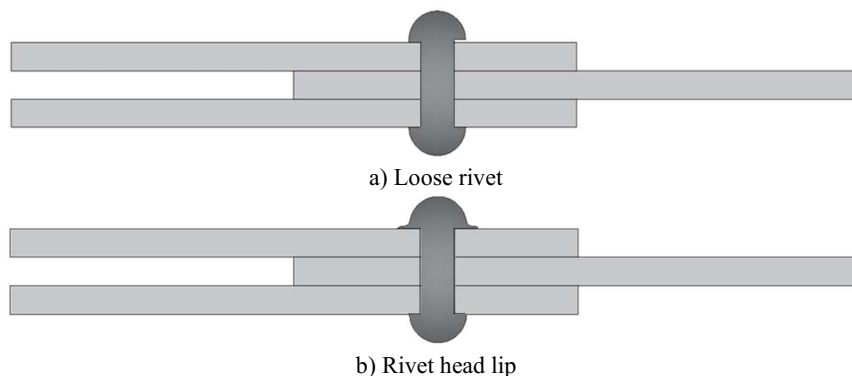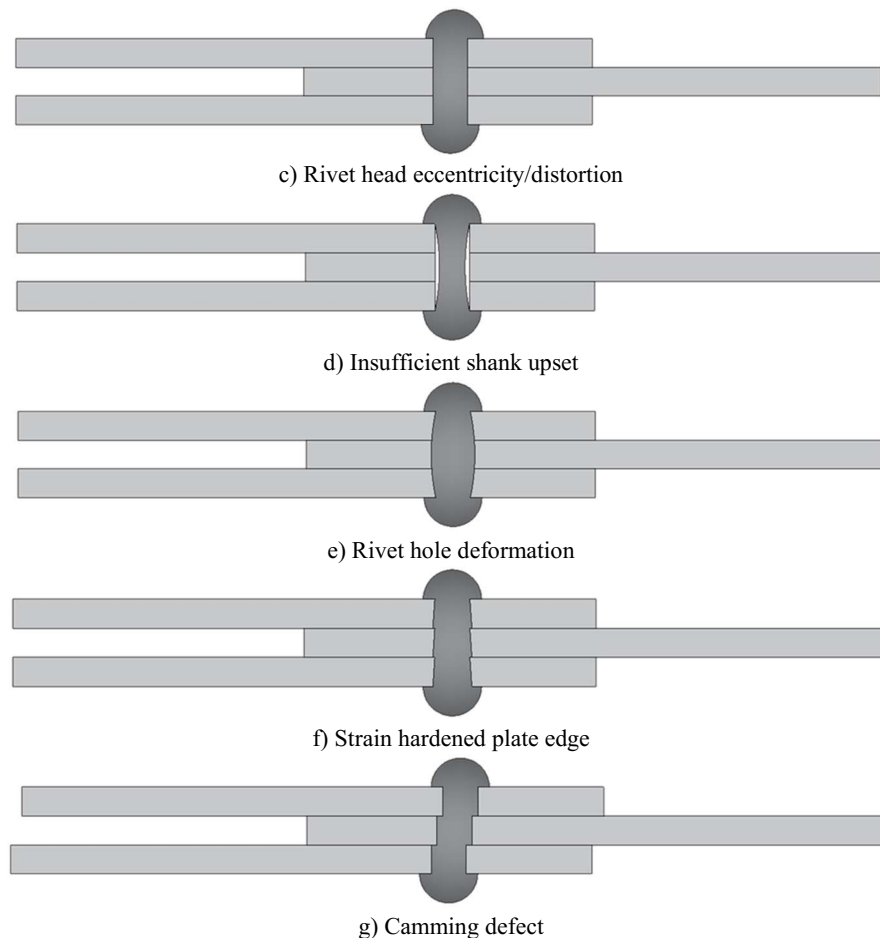
Figure 2.15 Common constructional imperfections found in existing hot-driven riveted connections (adapted from *Twelvetrees, 1900*).

of plies to be connected, can impair the development of clamping action and induce slight rivet movements under transient loads, although no significative effects are expected on the static performance of connections and only slight reductions of fatigue life may occur (*Collette, 2014*).

If the undriven rivet shank is not properly cut to match the thickness of stacked plates and/or a pneumatic hammer with excessively small snap is used, the field head can present a perimetral lip (Figure 2.15b). Although being often overlooked in visual inspections, head lips should be carefully considered, as wider lips may underlie an insufficient upset of the rivet shank (*Vermes, 2007*).

Another common visible imperfection found in existing riveted connections is the eccentricity/distortion of the rivets field head (Figure 2.15c). Indeed, if the pneumatic hammer is actioned while not being perfectly centred and/or perpendicular to the plies to be connected, a misaligned and/or distorted field head will be formed (*Twelvetrees, 1900; Vermes, 2007*). On one hand, severe head eccentricity or distortion can sometimes lead to fatigue collapse of hot-driven rivets due to premature head detachment (*Collette, 2014*). On the other hand, with respect to static conditions, head distortion slightly affects the tensile resistance of the rivets and the distribution of clamping stresses, owing to the alteration of restraints acting on the rivet shank.

With respect to invisible defects, one of the trickiest imperfections is represented by insufficient shank upset (Figure 2.15d). Several reasons can trigger this kind of defect, e.g., an insufficient driving temperature and/or pressure, the presence of multiple

(usually ≥ 4) plies to be connected or improper hand-driving (*Frémont, 1906*). In this case, owing to the reduction of the shank resisting area, a decrease of both bearing and especially shear resistance occurs in static conditions. Moreover, stress concentrations nearby the minimum cross-section can lead to unexpected shear fatigue failure of rivets, as opposed to net-area fatigue failure usually observed in pristine riveted connections (*Collette, 2014; Milone et al., 2022a*).

Contrariwise, if an excessive driving pressure is applied, lateral dilatation of the rivet shank can be so significant to induce a permanent rivet hole deformation (Figure 2.15e). Although this effect has no significant influence on the static resistance of rivets, it can *i*) make removal of rivets quite difficult and *ii*) detrimentally affect the fatigue performance of connections, as deep grooves may occur on the rivet shank owing to plate edge-to-rivet indentation (*Collette, 2014*).

Fatigue behaviour of connections can also be affected by strain hardening of hole edges (Figure 2.15f). This condition may occur if holes are perforated through the punching technique (see *Section 2.1.2*) without subsequent reaming. In this case, local damage on plates can result in unexpected brittleness and (micro)cracks that sensibly reduce the fatigue life of connections (*Twelvetrees, 1900; Collette, 2014*).

Finally, if plates to be connected are not properly aligned during the hammering process, the heat forging can result in a distorted shank with several geometric discontinuities nearby the shear planes (Figure 2.15g). This condition, which is known as "*camming defect*" (*Sustainable Bridge, 2006; Vermes, 2007; Collette, 2014*), can decrease both the static and fatigue strength of hot-driven riveted connections owing to *i*) a significant modification in terms of stress transmission along the shear planes (which may result in a reduction of the "effective" shear resisting cross-section), *ii*) a sharp rise of hot-spot stresses, which may promote crack propagation across the rivet shank and *iii*) an alteration of the clamping stresses distribution (*Milone et al., 2022a, 2023*). Moreover, in presence of cammed shanks, replacement of rivets can be more complex (*Twelvetrees, 1900; Collette 2014*).

Camming defect is arguably the most influent defect on the structural performance of hot-driven riveted connections. Therefore, in *Chapter 5*, an attempt to parametrically investigate its detrimental effect in static conditions is carried out.

2.4. Normative provisions for hot-driven riveted connections

2.4.1 Failure modes of hot-driven riveted connections

Failure modes of hot-driven riveted connections can be identified depending on the type of sustained action, namely:

- In case of shear connections (butt- or lap-splices, see Figure 2.7a), collapse may occur due to four different mechanisms, namely (*Bresler et al.,1960*): *i*) rivet shearing (Figure 2.16a), *ii*) plate bearing (Figure 2.16b), *iii*) plate net-area tensile failure (Figure 2.16c) or *iv*) plate shear-out (Figure 2.16d);
- In case of tensile connections (e.g., T-stubs, see Figure 2.7b), collapse may occur only due to rivet tensile failure (Figure 2.16e), while plate punching mechanism is considered to be prevented.

It is worth noting that these collapse mechanisms resemble the ones that may occur in bolted connections, although *i*) no frictional resistance is assumed for rivets owing to the

unreliability of clamping action (*D'Aniello et al., 2011*) and *ii*) plate punching resistance is assumed to be always greater than the corresponding rivet tensile resistance.

a) Rivet shearing

b) Plate bearing

c) Plate net-area tensile failure

d) Plate shear-out

e) Rivet tensile failure
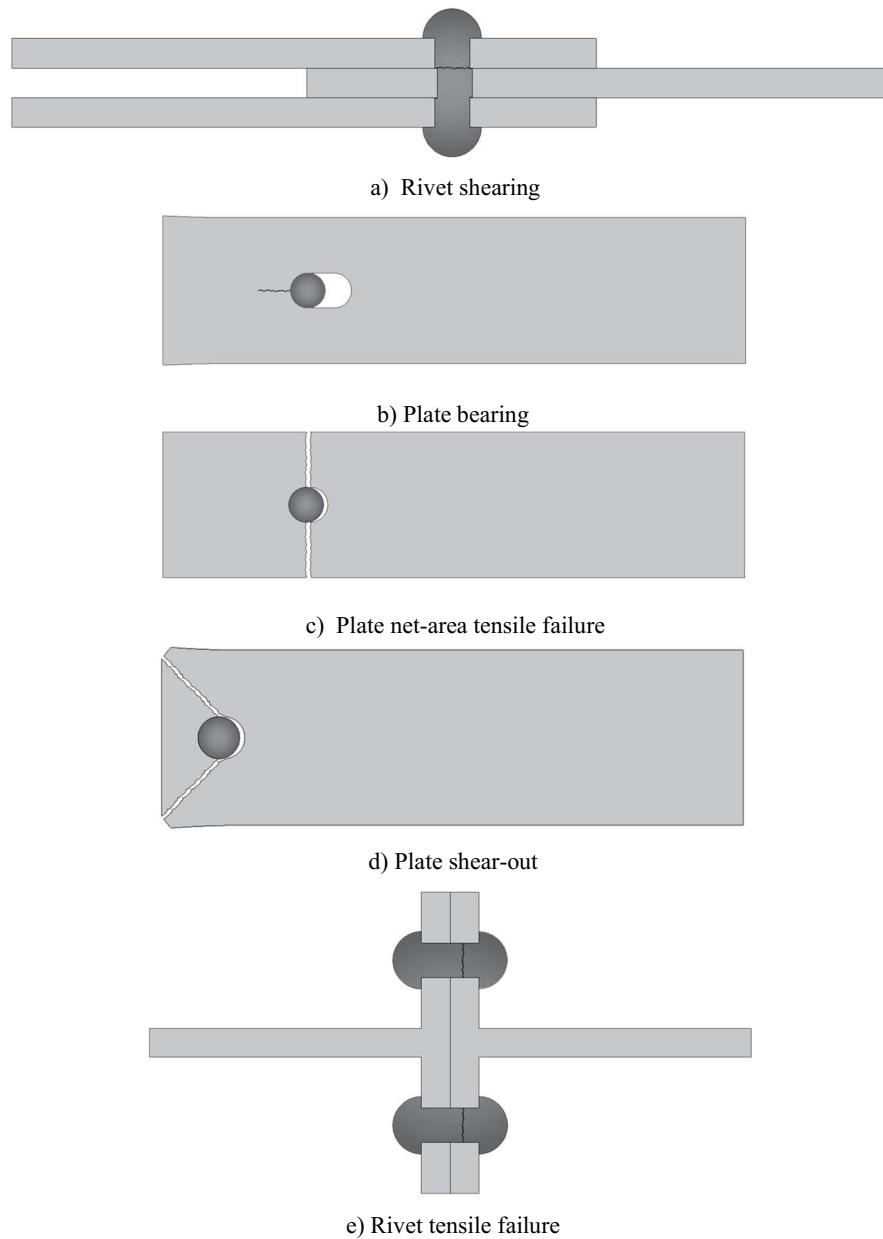
Figure 2.16 Possible collapse mechanisms for hot-driven riveted connections.

Several formulations were derived in the past to estimate the resistance of riveted connections failing due to all introduced mechanisms, mostly on the basis of experimental evidence. Remarkably, such formulations relied (and still rely in current normative provisions, e.g., EN1993:1-8 – *CEN, 2005b*) on a significant stress redistribution in ultimate conditions with respect to elastic response of connections (*Marmo, 2011*).

For example, failure due to rivet shearing is assumed to occur when shear plane(s) achieve an uniform stress equal to the shear strength of the rivet, while a simple application (yet approximate) of Jourawsky's formula (*Irgens, 2008*) rimmediately shows how shear stresses strongly vary along the shank cross-section in elastic conditions (Figure 2.17a).

Likewise, in case of plate bearing collapse, an uniform distribution of stresses (i.e., on the hole diametral plane) is nominally considered, while in elastic regime the "point bearing" condition implies a significantly higher stress on the hole tip in contact with the shank (Figure 2.17b). In case of plate bearing, uniform stresses are also assumed through the thickness; this hypothesis can be considered realistic only for inner plates, while, in reality, stresses considerably vary along the thickness of outer plates.

Stress inhomogeneity is further exacerbated by secondary bending, which occurs in case of unsymmetric joints, where forces transferred by plates form a couple which is resisted by an equal and opposite couple acting on the rivet heads (*Bresler et al., 1960*). Secondary bending, which becomes less influent only in case of rather long joints, also explains the inferior performance shown by countersunk rivets (*Marmo, 2011*).

Similarly, in case of net-area tensile failure of plates, the achievement of an uniform stress (that is, the plate ultimate tensile stress) on the net area is assumed at collapse, while linear elastic fracture mechanics (LEFM) suggests how the maximum elastic stress at hole's tip is about 3 times higher than the far field stress σ_0 acting on plates ends (Figure 2.17c – *Anderson, 2017*).

Contrariwise, stresses distribution in elastic conditions and at failure can be considered sufficiently similar for rivets in tension (*Bresler et al., 1960*).

It is really worth reporting that, while the above discrepancies may not play a significant role in static conditions, they have a key importance under fatigue conditions (especially in high-cycle fatigue, or *HCF*, regime – *Milone et al., 2022b*).

For instance, fatigue cracking of existing hot-driven riveted constructions was almost always found across net sections of connected elements (that is, due to near-hole stress amplifications and high tensile mean stress), although some cases of rivets head detachment have been also reported, e.g., in presence of relevant secondary bending and/or when constructional imperfections were detected (e.g., field head distortion or eccentricity – *Pipinato et al., 2009; Taras et al., 2010*).

a) Rivet shearing

b) Plate bearing

c) Plate net-area tensile failure
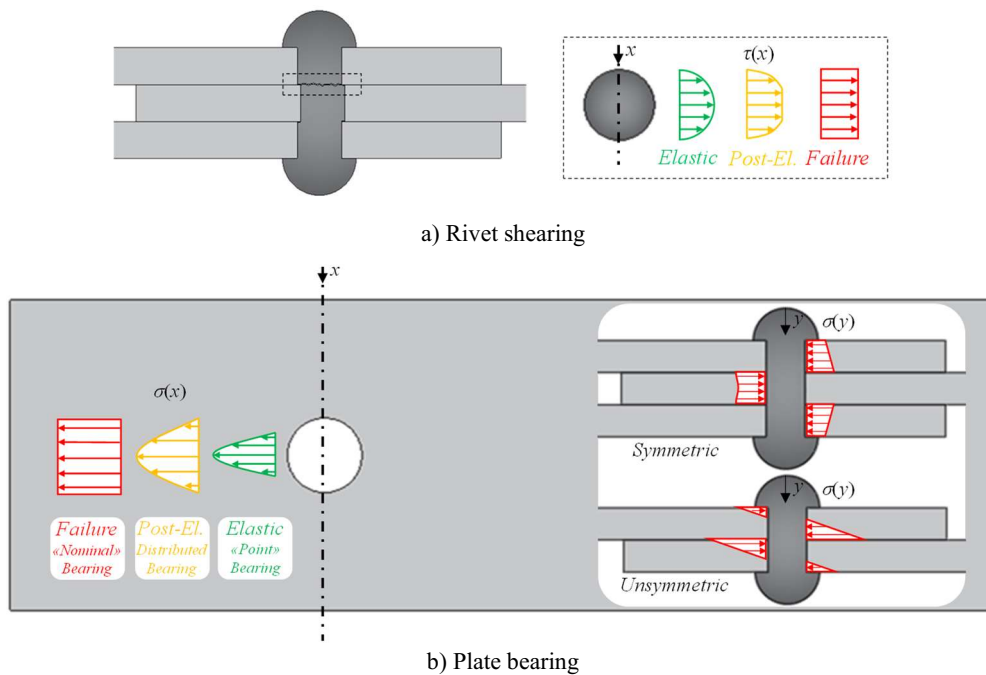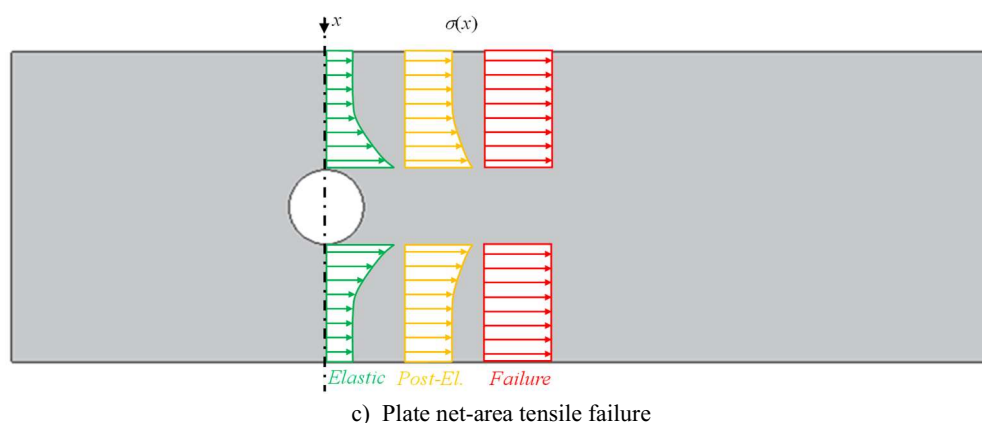
Figure 2.17 Stress redistribution from elastic to ultimate conditions for shear collapse mechanisms of hot-driven riveted connections (adapted from *Bresler et al., 1960*).

2.4.2 EN1993:1-8 prescriptions for hot-driven riveted connections

Relevant provisions for the estimation of design static resistance of riveted connections are reported in EN1993:1-8 (*CEN, 2005b*). Namely, for each of the introduced collapse mechanisms, a resistance model is provided, with the only notable exception of plate shear-out.

Indeed, as this kind of mechanism proves to be rather fragile and premature (*Ballio et al., 2020*), EN1993:1-8 implicitly avoids the occurrence of shear-out by means of geometrical limitations on edge-to-hole distance e_1 along the loaded direction. Additional prescriptions are also provided with regard to rivets pitch p_1 (for $n_r \geq 2$) and with respect to geometrical limitations in transverse direction. It should be remarked that these kind of restrictions are shared among all kinds of connections with mechanical fasteners (i.e., rivets, bolts, pins).

Geometrical prescriptions on riveted connections are summarized in Table 2.1, in which the symbology introduced in Figure 2.18 is used.

Table 2.1 Minimum and maximum spacing, end and edge distances for mechanically fastened connections (adapted from Table 3.3 of EN1993:1-8 – *CEN, 2005b*).

Distances and spacings	Minimum	Maximum[1) 2) 3)]		
		Structures made from steels conforming to EN 10025 except steels conforming to EN 10025-5		Structures made from steels conforming to EN 10025-5
		Steel exposed to the weather or other corrosive influences	Steel not exposed to the weather or other corrosive influences	Steel used unprotected
End distance e_1	1.2 d_0	$4t + 40$ mm		max $\{8t; 125 \text{ mm}\}$
Edge distance e_2	1.2 d_0	$4t + 40$ mm		max $\{8t; 125 \text{ mm}\}$
Distance e_3 in slotted holes	1.5 d_0 [4)]			
Distance e_4 in slotted holes	1.5 d_0 [4)]			

Spacing p_1	$2.2\ d_0$	min {14t; 200 mm}	min {14t; 200 mm}	min {14t; 175 mm}
Spacing $p_{1,o}$		min {14t; 200 mm}		
Spacing $p_{1,i}$		min {28t; 400 mm}		
Spacing p_2 [5)]	$2.4\ d_0$	min {14t; 200 mm}	min {14t; 200 mm}	min {14t; 175 mm}

[1)] Maximum values for spacings, edge and end distances are unlimited, except in the following cases:
  - for compression members in order to avoid local buckling and to prevent corrosion in exposed members (the limiting values are given in the table);
  - for exposed tension members to prevent corrosion (the limiting values are given in the table).

[2)] The local buckling resistance of the plate in compression between the fasteners should be calculated according to EN:1993-1-1 using 0.6 p_1 as buckling length. Local buckling between the fasteners need not to be checked if p_1/t is smaller than 9ε. The edge distance should not exceed the local buckling requirements for an outstand element in the compression members, see EN:1993-1-1. The end distance is not affected by this requirement.

[3)] t is the thickness of the thinner outer connected part.

[4)] The dimensional limits for slotted holes are given in 1.2.6 Reference Standards: Group 7.

[5)] For staggered rows of fasteners a minimum line spacing of $p_2 = 1.2\ d_0$ may be used, provided that the minimum distance L between any two fasteners is greater or equal than $2.4\ d_0$.

In addition, the British National Annex (*BSI, 2008*) provides further indications about rivets' grip length h_S. For instance, h_S should not exceed a limit value equal to 4.5 d or 6.5 d for hammer riveting or press riveting, respectively (*Marmo, 2011*).

Provided limitations grant that *i*) reported resistance models can reliably estimate the actual strength of fasteners (as they were calibrated on the basis of experimental outcomes) and *ii*) repartition of actions between multiple fasteners (if present) can be performed with simplified assumptions (*Ballio et al., 2020*), namely (*CEN, 2005b*):
- Resistance of joints should be estimated starting from resistances of its basic components;
- Linear-elastic or elastic-plastic analysis may be used to design and check joints;
- If elastic-plastic analysis is adopted, deformations descending from rigid body rotations and/or in-plane deformations should be physically possible;
- Assumed internal forces and moments should be in equilibrium with forces and moments acting on the joints;
- Each joint component should be able to resist relevant internal forces/moments;
- Deformations implied by the assumed forces distribution should not exceed the deformation capacity of fasteners and connected parts;
- Assumed distribution of internal forces should be realistic with respect to relative stiffness of joint components (e.g., in case of shear loads, it is recommended to distribute internal actions only among stiffer fasteners);
- In any case, adopted resistance models should comply with test results.
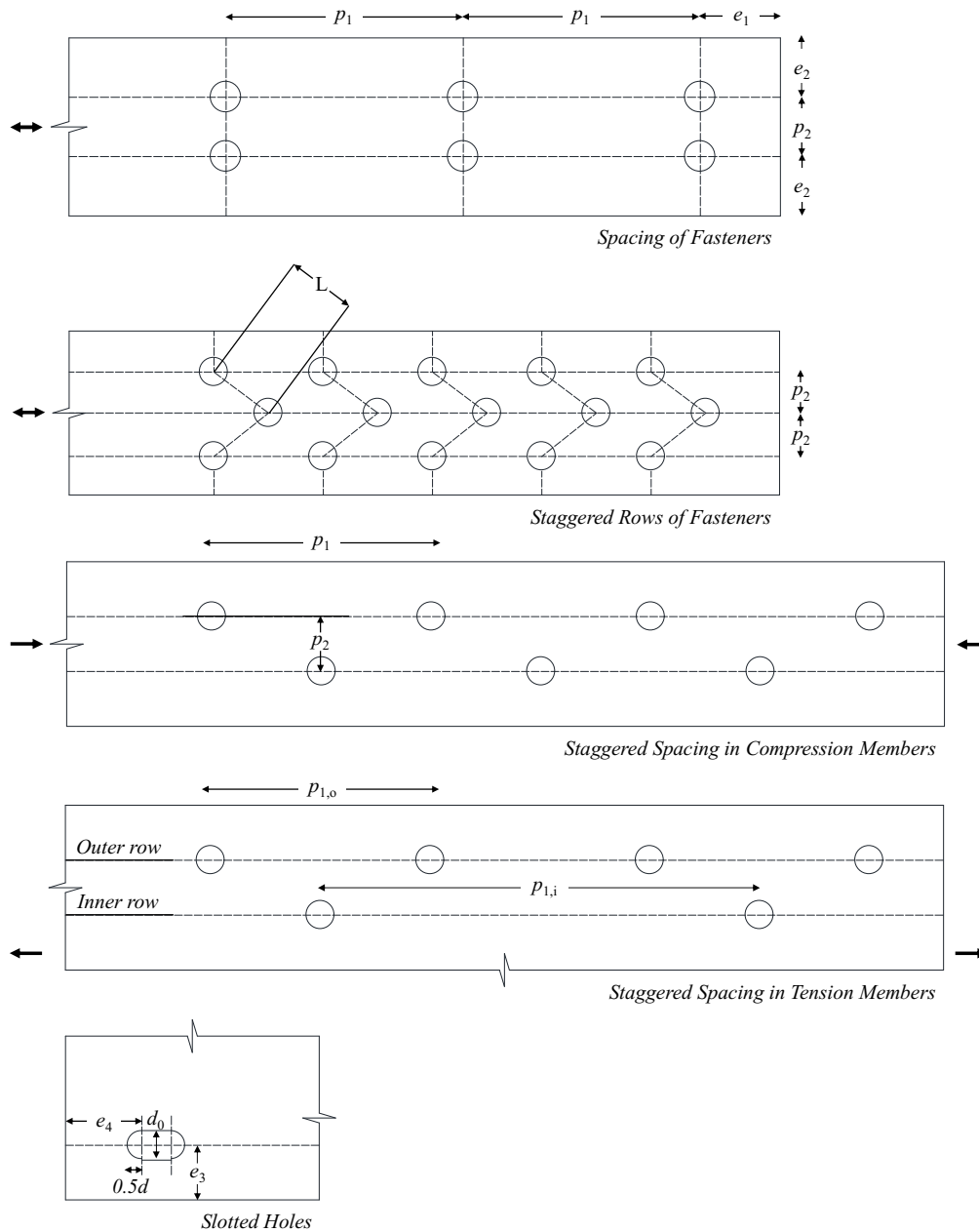
Figure 2.18 Symbols for end and edge distances and spacing of fasteners (adapted from Figure 3.1 of EN1993:1-8 – *CEN, 2005b*).

Although different methods complying with the above assumptions can be used to derive a realistic distribution of internal actions among fasteners, the most popular technique is arguably the so-called "*rigid plates-elastic fasteners*" (hence also referred as "RP-EF") method (*Duggal, 2000; Ballio et al., 2020*), in which connected plies are assumed to be infinitely rigid, while fasteners behave in a purely elastic manner. If this condition holds, repartition of actions can be carried out as follows:

- Shear loads can be equally spread among all the fasteners, provided that they share the same stiffness. Otherwise, loads can be equally spread among all stiffer fasteners (Figure 2.19a);
- Tensile loads can be spread among fasteners on account of their distance from the neutral axis, if present. In other terms, in case of pure tension acting on the joint, tensile loads can be equally spread among the fasteners (Figure 2.19b);

- If bending moments act on the joint, most centrifugated fasteners will carry the higher tensile loads. Under no circumstances, compressive forces equilibrating the tensile actions should be attributed to fasteners, as they will be transferred by plies in contact (Figure 2.19c);
- Torques are resisted by a couple given by shear forces acting on fasteners, which are proportional to the distance among a given fastener and the centroid of the assembly of fasteners (Figure 2.19d);
- Any composition of forces and moments acting on a joint can be addressed with the above rules using superimposition principle.

By using the RP-EF method, it can be easily recognized how the resistance of a riveted joint can be estimated by monotonically scaling apportioned internal actions F_i until the weakest element reaches its design resistance (limit conditions). Hence, the joint overall resistance will be equal to the resultant (force and/or moment) acting on the joint itself in limit conditions.

a) Shear force

b) Tension force

c) Bending moment

d) Torque
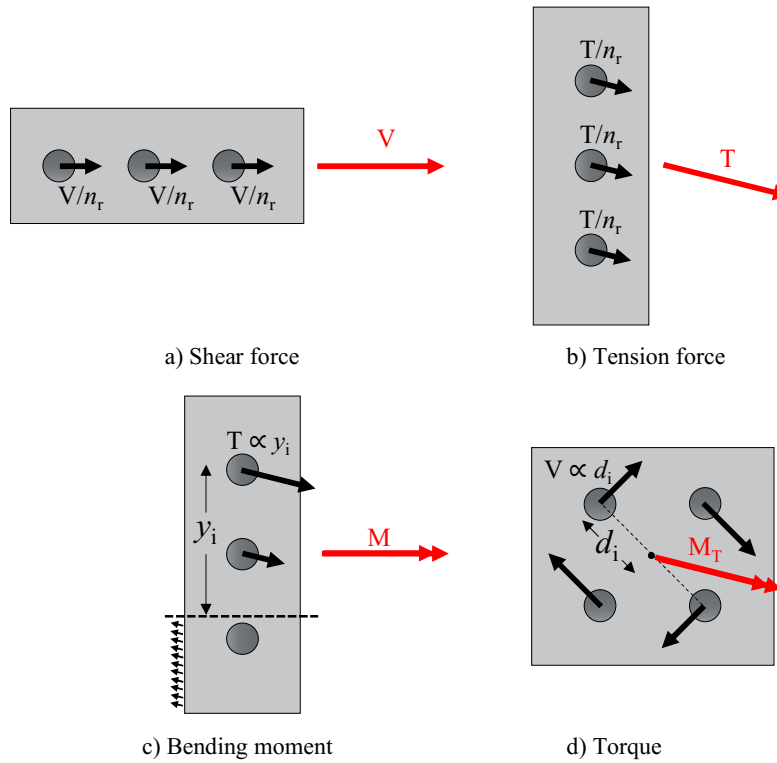
Figure 2.19 Repartition of internal actions according to the "rigid plates-elastic fasteners" method.

For example, in case of a lap-shear riveted joint involving n_r rivets, the overall shear resistance can be estimated as n_r times the shear resistance of the weakest fastener, which in turn is equal to the minimum between the rivet shear and the plate bearing resistance (that is, provided that the joint does not prematurely collapse due to net-area failure).

In light of the above, the resistance of any given hot-driven riveted connection can be estimated on the basis of four basic resistance models provided by EN1993:1-8, one for each of the collapse mechanisms shown in Figure 2.16 (besides plate shear-out):

- In case of rivet shear failure, the design shear resistance $F_{V,Rd}$ is given by Equation 2.2:

$$F_{V,Rd} = \frac{0.6 \, n_S \, A_0 \, f_{ur}}{\gamma_{M2}}$$

(2.2)

with:

0.6 being the shear-to-tensile strength ratio (empirical coefficient);

$n_S = n_P - 1$ being the number of shear planes per rivet;

$A_0 = \pi d_0^2/4$ being the rivet hole area;

f_{ur} being the rivet ultimate tensile strength;

$\gamma_{M2} = 1.25$ being the partial safety factor for connections resistance;

- In case of plate bearing failure, the design bearing resistance $F_{b,Rd}$ is given by Equation 2.3:

$$F_{b,Rd} = \frac{\alpha_b \, k_1 \, f_{up} \, d \, t_{min}}{\gamma_{M2}}$$

(2.3)

with:

α_b and k_1 being coefficients accounting for the stress diffusion along the longitudinal and transverse direction, respectively;

f_{up} being the plate ultimate tensile strength;

$d = d_0$ being the driven rivet diameter;

t_{min} being the minimum thickness among connected plies or, if multiple (≥ 3) plates are present, the minimum overall thickness of plates subjected to bearing pressure of the same sign;

$\gamma_{M2} = 1.25$ being the partial safety factor for connections resistance.

As for α_b and k_1, the following expressions are given (Equation 2.4a-d):

$$\alpha_b = \min\left\{\frac{e_1}{3\,d_0}; \frac{f_{ur}}{f_{up}}; 1\right\} \text{ for end bolts}$$

(2.4a)

$$\alpha_b = \min\left\{\frac{p_1}{3\,d_0} - \frac{1}{4}; \frac{f_{ur}}{f_{up}}; 1\right\} \text{ for inner bolts}$$

(2.4b)

$$k_1 = \min\left\{\frac{2.8\,e_2}{d_0} - 1.7; 2.5\right\} \text{ for edge bolts}$$

(2.4c)

$$k_1 = \min\left\{\frac{1.4\,p_2}{d_0} - 1.7; 2.5\right\} \text{ for inner bolts}$$

(2.4d)

- In case of plate net-area failure, the design tensile resistance $N_{U,Rd}$ is given by Equation 2.5:

$$N_{U,Rd} = \frac{0.9\,A_{net}\,f_{up}}{\gamma_{M2}}$$

(2.5)

with:

$A_{net} = A_p - d_0 t$ being the minimum net cross-section of the plate having gross cross-section equal to A_p;

f_{ub} being the plate ultimate tensile strength;

$\gamma_{M2} = 1.25$ being the partial safety factor for connections resistance;

- In case of rivet tensile failure, the design tensile resistance $F_{T,Rd}$ is given by Equation 2.6:

$$F_{T,Rd} = \frac{0.6\,A_0\,f_{ur}}{\gamma_{M2}}$$

(2.6)

with:

$A_0 = \pi d_0^2/4$ being the rivet hole area;

f_{ur} being the rivet ultimate tensile strength;

$\gamma_{M2} = 1.25$ being the partial safety factor for connections resistance;

Remarkably, a maximum work ratio of 60% is allowed for rivets in tension, as opposed to high-strength bolts, for which a maximum tensile work ratio of 90% is permitted. As a result, shear and tensile resistance of rivets basically share the same formulation for $n_S = 1$.

- In case of combined shear V_{Ed} and tensile T_{Ed} design actions, the following design resistance domain is provided for rivets (Equation 2.7):

$$\frac{V_{Ed}}{F_{V,Rd}} + \frac{T_{Ed}}{F_{T,Rd}} \leq 1 \qquad (2.7)$$

- In case of long joints (i.e., joints in which the distance L_f between the first and the last rivet measured along the direction of applied loads is higher than $15d$), assumptions of RP-EF method become less reliable, as plate deformations become non-negligible and thus outer rivets are more loaded than inner ones. In this case, the resistance of single fasteners should be properly reduced by means of a coefficient β_{Lf} (Equation 2.8):

$$\beta_{Lf} = 1 - \frac{L_f - 15\,d}{200\,d} \in [0.75 \div 1.0] \qquad (2.8)$$

In conclusion, mechanical and physical parameters governing static failure of hot-driven riveted connections according to EN1993:1-8 can be summarized as follows:
- Ultimate strength of rivets f_{ur} and plates f_{up};
- Rivets diameter d, number n_r, end/edge distances e_1/e_2 and pitch p_1/p_2;
- Plates width w, thickness t and number n_p.

2.4.3 EN1993:1-9 prescriptions for hot-driven riveted connections

EN1993:1-9 (*CEN, 2005a*) provides two alternative approaches to perform fatigue checks of structural steel components, i.e. the *Safe Life* (SL) approach and the *Damage Tolerant* (DT) approach:

- SL approach does not contemplate any fatigue damage in checked structures, and it is addressed by means of a punctual stress-based verification (i.e., it refers to the worst load conditions occurring in the service life);
- DT approach admits the development of controlled fatigue damage in verified structures. Expected damage D, which is estimated accounting for the entire service life, should not exceed a threshold value (D* = 1.0 in absence of more detailed provisions) associated with failure.

When dealing with existing steel structures such as historic riveted constructions, the DT approach is clearly the most suitable option, as it allows to account for the damage endured by steel elements during their past service life. Indeed, the amount of cumulated damage can be often significant for older structures, mainly owing to the inadequacy of the design requirements available at the erection time and/or to a progressive increase in cyclic loads over the years (*Milone et al., 2022b*).

Within the framework of DT approach, EN1993:1-9 provides fatigue resistance domain in the form of a limited range of Wohler (or S-N) curves. The selection of the S-N curve of concern depends on the nature of the structural detail to check, and each curve is identified by means of the so-called "detail class" $\Delta\sigma_C$, i.e., the applied stress range inducing fatigue collapse for a conventional number of cycles $N_C = 2 \cdot 10^6$.

Therefore, for a given value of applied stress range $\Delta\sigma_f$, the number of cycles at failure N can be estimated as follows (Equation 2.9a-b):

$$N \left(\gamma_{FF} \Delta\sigma_f \right)^{m_1} = N_C \left(\frac{\Delta\sigma_C}{\gamma_{MF}} \right)^{m_1} \quad \text{for } N \le 5 \cdot 10^6 \qquad (2.9a)$$

$$N \left(\gamma_{FF} \Delta\sigma_f \right)^{m_2} = N_D \left(\frac{\Delta\sigma_D}{\gamma_{MF}} \right)^{m_2} \quad \text{for } 5 \cdot 10^6 \le N \le 10^8 \qquad (2.9b)$$

with:

m_1 and m_2 being the inverse logarithmic slopes of the two branches of the design S-N curve, respectively ($m_1 = 3$ and $m_2 = 5$ unless otherwise stated);

$\gamma_{FF} = 1.0$ and $\gamma_{MF} = 1.0 \div 1.25$ being the partial safety factor for fatigue demand and strength, respectively;
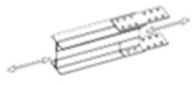
$\Delta\sigma_D$ being the constant amplitude fatigue limit (CAFL), i.e. the applied stress range inducing fatigue collapse for a conventional number of cycles $N_D = 5 \cdot 10^6$.

Further details concerning *i*) the proper value of γ_{MF}, *ii*) theoretical background and advantages/drawbacks of DT approach and *iii*) indications on how to deal with complex and aperiodic load histories within the framework of DT approach are reported in the relevant sections of *Chapter 3*.

Remarkably, no detail classes are reported in the current version of EN1993:1-9 for hot-driven riveted connections, thus leaving a critical normative vacuum when assessing the structural performance of riveted constructions subjected to relevant cyclic loads, such as railway bridges (*Pipinato et al., 2009; Taras et al., 2010; Milone et al., 2022a*).

Nevertheless, it is worth reporting that, in earlier drafts of EN1993:1-9, two separate detail classes were associated to riveted details, identified as "Category 2", i.e., unsymmetrical joints, and "Category 3", i.e., symmetrical joints (Table 2.2):

Table 2.2 Detail classes for hot-driven riveted details provided by earlier drafts of EN1993:1-9.

Detail Category	Detail Class $\Delta\sigma_C$	Detail	Description & Examples	Additional Remarks
Category 2	71 MPa $m_1 = m_2 = 5$		One-shear joint with gusset plates (unsymmetrical joint)	If the calculated shear force in the rivets is lower than the minimum value of slip resistance, $\Delta\sigma_C = 85$ MPa can be used
Category 3	90 MPa $m_1 = m_2 = 5$		Symmetrical joint with splice plates	Middle plates (having thickness t) in two-shear connections should be verified using $\Delta\sigma_C = 90$ MPa. Splice plates themselves (having thickness t_L) should be verified using $\Delta\sigma_C = 80$ MPa. no verification is required when $2t_L > 1.12\, t$. The ratio $\Delta\sigma_{bearing}$ to $\Delta\sigma_{net}$ should be smaller than 2. When rivets of steel grade St44 or higher were employed no corrosion protection coating must have been applied. If one of these conditions does not hold, $\Delta\sigma_C = 80$ MPa should be used instead.

2.5.   Notable previous literature studies on hot-driven riveted connections

As stated in previous Sections, peculiar issues related to technology and structural performance of hot-driven riveted connections represent a rather old question, in respect of which numerous research efforts have been made through the years, although several aspects still need to be properly addressed (*Collette, 2014; Leonetti et al., 2020; Milone et al., 2022a, 2023*). Hence, in the present Section an overview of notable previous literature studies concerning the static and fatigue performance of hot-driven riveted connections is presented.

2.5.1   Literature studies on the static performance of hot-driven riveted connections

Among the several contributions dealing with static performance of hot-driven riveted connections, it is worth mentioning pioneering studies carried out by Hrennikof (*"Work of Rivets in Riveted Joints", 1934*), Hetchman (*"A Study of the Effects of Heating and Driving Conditions on Hot-Driven Structural Steel Rivets", 1948*) and Munse & Cox ("*The Static Strength of Rivets Subjected to Combined Tension and Shear*", 1956).

Results of such and further studies have been hence collected by Kulak, Fisher & Struik, (*Guide to design criteria for bolted and riveted joints*, 1987).

In Munse & Cox (1956), round headed steel rivets were tested under different tension-to-shear ratios m, ranging from pure shear ($m = 0$) to pure tension ($m \to \infty$) by means of orientable pull plates drilled with 15° spacings (Figure 2.20). A wide parametrical study was carried out accounting for the variation of the following parameters, namely:

i) steel processing (rimmed, killed or semi-killed);
ii) rivet diameter ($^3/_4 \div 1$ inches, i.e., $19 \div 25$ mm);
iii) grip length ($1 \div 5$ inches, i.e., $25 \div 125$ mm);
iv) driving technique (hot- or cold-driving, machined or handmade);
v) forge temperature, when relevant ($1800 \div 1950$ F, i.e., $982 \div 1066$ °C);
iv) soaking time before driving, when relevant ($43 \div 138$ min).

Relevant variables for the parametric study were determined based on preliminary tests regarding common technical practices for rivets making and installation during the '50s. In compliance with experimental findings, the Authors concluded that *i*) no significant difference in terms of ultimate strength (< 5%) could be observed depending on steel processing for identical heating and driving conditions, *ii*) a slight dependence on forge temperature ($\approx$ 5% when decreasing T from 1850 to 1800 F) and driving technique could be observed instead, *iii)* clamping stress in rivets could be up to the yield point, although measures were made only for 2 inches long rivets and *iv*) a strong decrease of ultimate resistance could be observed for increasing soaking times ($\approx$ 10%, *Munse & Cox, 1956*). With regard to the actual set of 403 shear-tension tests, a notable decrease of peak strength ($\approx$ 8% for identical driving and test conditions) was noticed when increasing grip length from 1 inch to 5 inches.

This outcome probably derived from the shank upset becoming gradually insufficient for increasing grip length (Figure 2.21 – *Kulak et al., 1987*).

A moderate diminishing trend of ultimate strength with increasing rivet diameter was also observed for all tension-to-shear ratios m ($\approx$ 7% on average when ranging from $^3/_4 \div 1$ inch rivets).
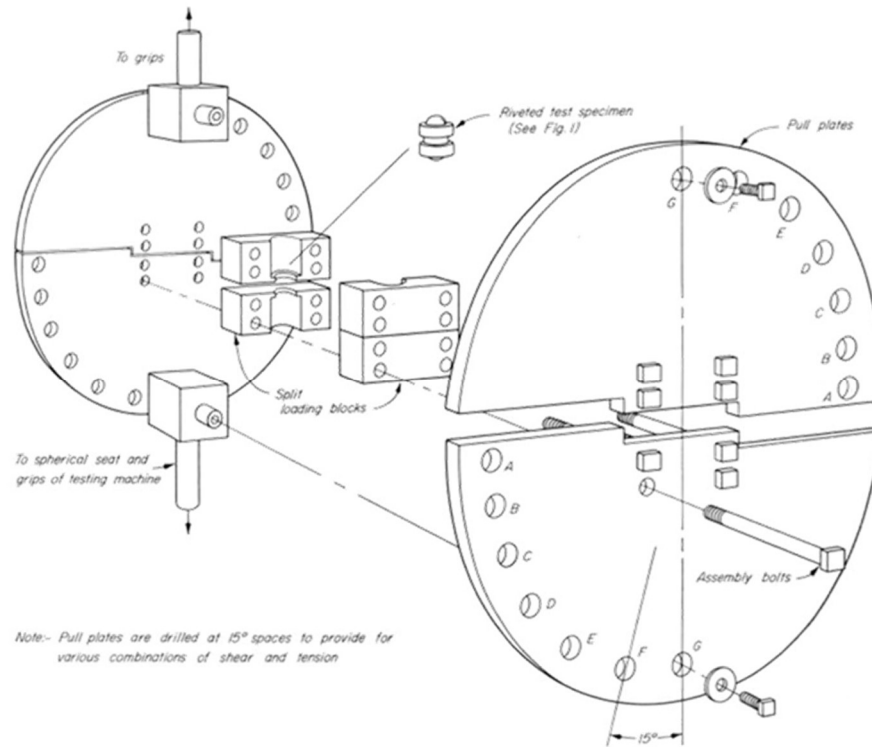
Figure 2.20 Experimental set-up designed by *Munse & Cox (1956)* to statically test hot-driven rivets under different tension-to-shear ratios.
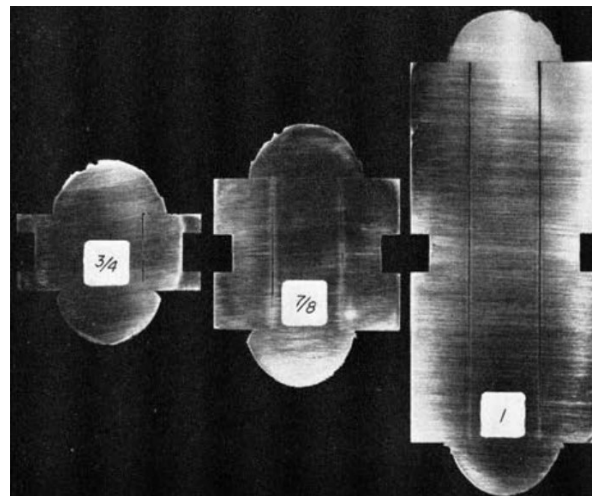
Figure 2.21 Sawed sections of hot-driven rivets with different grip length. An increasing clearance between rivet shank and holes can be observed for longer rivets *(Munse & Cox, 1956)*.

Notably, the parameter showing the larger range of variation for different values of m was the energy absorbing capacity (or, equivalently, the ultimate ductility) of rivets, which strongly reduced for decreasing values of m (Figure 2.22a).

Consistently, a stronger propension to necking at failure was observed for increasing m (Figure 2.22b). Specimens subjected to prevalent tension also showed a significant increase of nominal ultimate strength (up to 33%), although the worst conditions in terms of resistance and absorbed energy at failure proved to be for $m = 0.577$ rather than in pure shear (see Figure 2.22a, white circle markers).

a)

Tension-to-shear ratio *m*

− ∞ ────────────────────────── 1 ────────────────── 0 →
(pure tension)   (pure shear)

b)
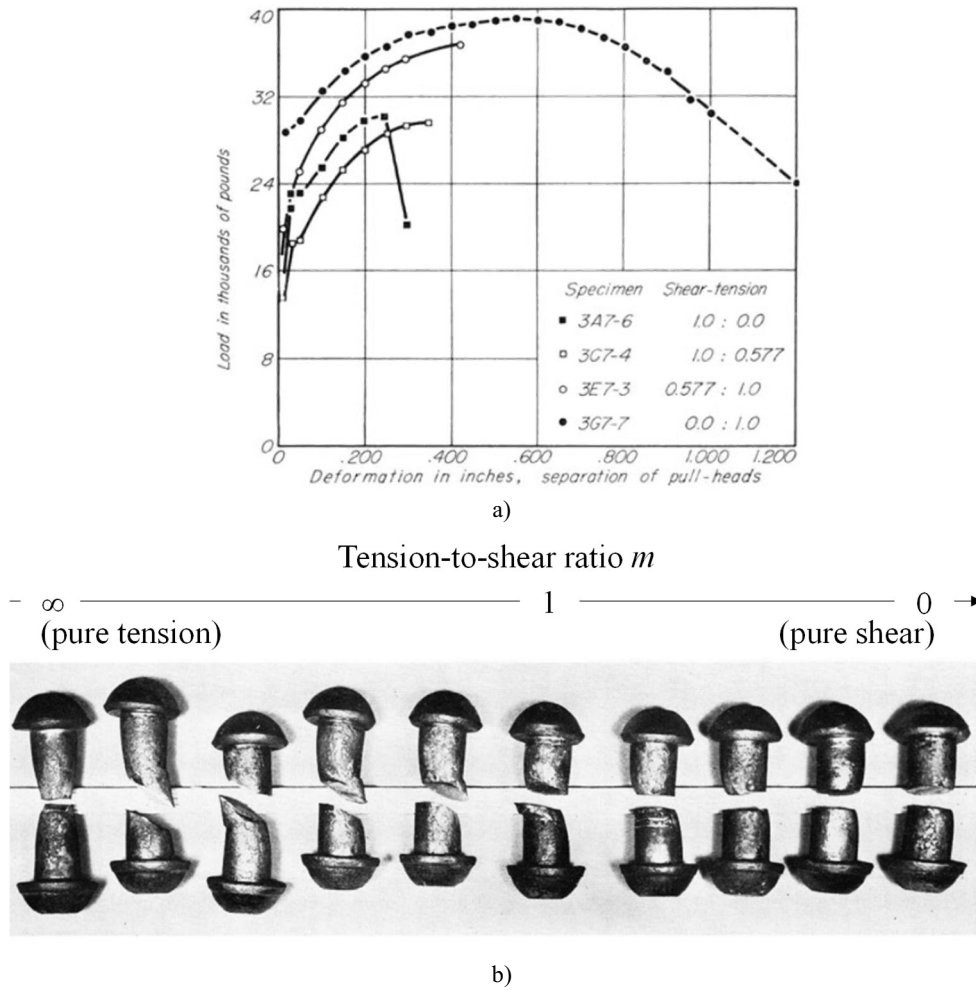
Figure 2.22 Typical a) force-displacement curves and b) fractures for rivets under different tension-to-shear ratios (adapted from *Munse & Cox, 1956*).

Based on test results, the Authors derived an ellipsoidal resistance domain for rivets subjected to contemporary tension and shear (Figure 2.23), which could be analytically expressed in terms of the lone rivets shear strength as follows (Equation 2.10, maximum error with respect to experimental results = ± 7% - *Munse & Cox, 1956*):

$$\left(\frac{y}{1.333}\right)^2 + \left(\frac{x}{1.000}\right)^2 \leq 1 \tag{2.10}$$

with *y* being the tension demand to shear capacity ratio and *x* being the shear demand to capacity ratio.

Almost identical findings are reported in *Kulak et al. (1987)*, in which further hybrid tests are drawn from literature resulting in the same equation for the resistance domain.

Almost identical findings are reported in *Kulak et al. (1987)*, in which further hybrid tests are drawn from literature resulting in the same equation for the resistance domain. To this end, it is worth remarking that the resistance model reported in current normative provisions (see Figure 2.23, red dashed line) is exceedingly conservative (Equation 2.7) with respect to experimental results.

Moreover, as test outcomes were normalized with respect to the average shear resistance of driven rivets rather than against base material properties, the beneficial effect of hot-driving was also implicitly neglected.
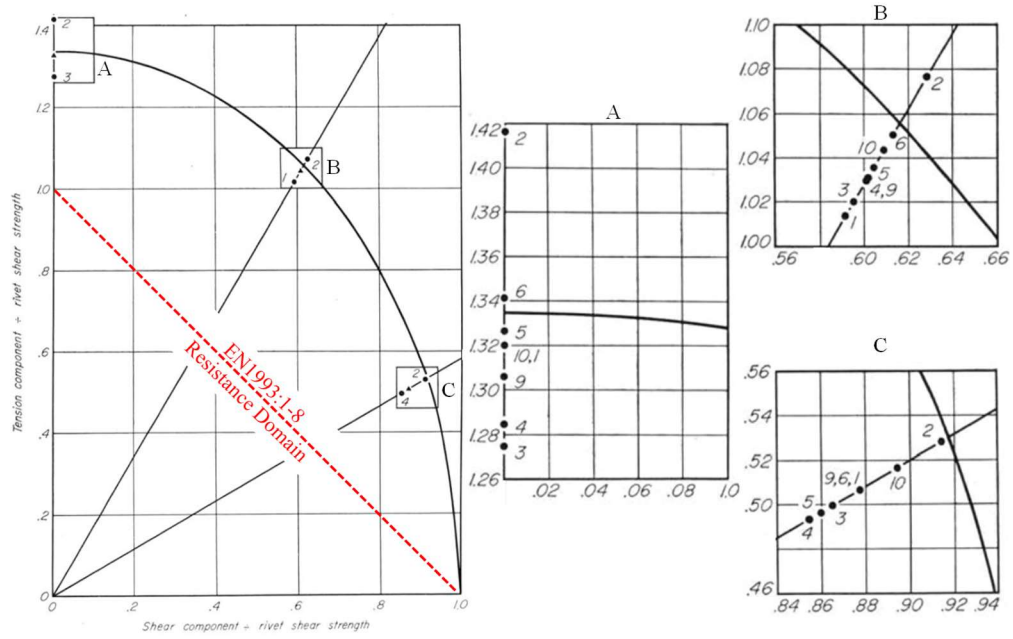
Figure 2.23 Experimental hybrid tension-shear domain for hot-driven rivets. Normative prescriptions for hybrid resistance are reported for the sake of comparison (adapted from *Munse & Cox, 1956*).

This effect, which is widely recognized in scientific literature (*Hrennikof, 1934; Hetchman, 1948; Kulak et al., 1987; Marmo, 2011; Collette, 2014*) and is completely disregarded by EN1993:1-8 (Equation 2.2), was experimentally investigated by the Candidate's Research Group (*D'Aniello et al., 2011)* for a wide group of connections configurations (that is, symmetric or unsymmetric, with one or multiple rivets having different diameter and connecting plies with varying thickness).

According to test outcomes, an average increase of ≈ 40% in terms of ultimate shear resistance was observed with respect to EN1993:1-8 predictions (Figure 2.24), which could be ascribed to *i*) the hot-driving induced overstrength Ω_1 of rivets being neglected and *ii*) the actual shear-to-tensile strength ratio Ω_2 being underestimated.

Namely, while current normative provisions set the shear to tensile strength ratio to 0.6, a ranging value of $\Omega_2 = 0.71 \div 0.84$ (average value = 0.76) was found by the Authors, thus confirming similar outcomes reported in earlier studies carried out by *Schenker et al. (1954)*.

With regard to rivets overstrength, the average value of Ω_1 was found to be equal to 1.25, while single ratios ranged from $1.14 \div 1.34$ for connections failing due to rivet shearing. Furthermore, in case of multiple shear planes (≥ 2), EN1993:1-8 often yielded wrong predictions in terms of collapse mechanism. Indeed, four (out of nine) specimens deemed to collapse due to plate net-area tension failure actually collapsed due to rivet shearing (see Figure 2.24, green square markers labelled with "V"). The Authors ascribed this effect to the "net-area efficiency" effect, i.e., an increase of the plies tensile strength (≈ 13%) due to constrained lateral deformations nearby holes. This condition, which was already pointed out by several researchers (*Koegler et al., 1943; Schutz, 1952; Schenker et al., 1954; Munse, 1970)*, descends from multiple factors, namely: *i*) the arise of a multi-axial stress state around the hole, *ii*) the beneficial effect of clamping action and *iii*) the local strain hardening of plates induced by perforation (*D'Aniello et al., 2011*).
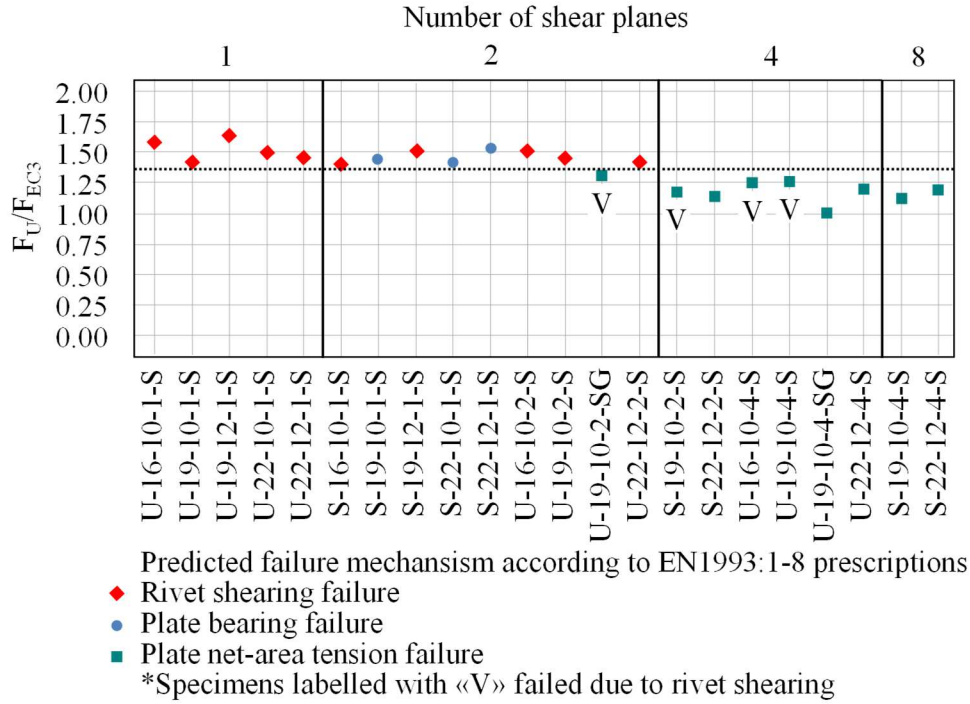
Figure 2.24 Experimental resistances and collapse mechanisms for hot-driven lap-shear connections against EN1993:1-8 predictions *(adapted from D'Aniello et al., 2011)*.

It should be remarked that average values of rivet overstrength and shear-to-tensile strength ratios were determined on the basis of a simple comparison with EN1993:1-8 prescriptions, hence only the product $\Omega_1\Omega_2$ was (to rigor) actually estimated. To properly distinguish these two phenomena (which are, in principle, always co-present in hot-driven riveted connections), Finite Element Analyses (FEAs) should be performed.

An attempt to do so is reported in this work (*Chapter 5*), in which plasticity and damage parameters for hot-driven connections tested by *D'Aniello et al.* (2011) have been estimated. Moreover, further details related to this earlier experimental investigation are reported in *Chapter 4*, as *i*) it served as a basis for subsequent parametrical FEAs and *ii*) specimens were nominally equal to the ones tested in fatigue conditions within the most recent campaign.

D'Aniello et al. (2011) also pointed out the high variability of clamping forces in hot-driven riveted connections, although no quantitative measures were carried out on tested specimens. To this end, a wide experimental and numerical study was carried out by *Leonetti et al.* (2020), which measured clamping forces in rivets extracted from a dismantled riveted roadway bridge (Botlek Bridge in Rotterdam).

Rivets, which were made of St44 mild steel (average yield stress $f_{yr0} = 277$ N/mm²), exhibited a large dispersion in terms of clamping stresses, although a clear increasing (and less scattered) trend was observed for increasing grip length/diameter ratios (Figure 2.25). Namely, for $h_S/d = 0.80$, an average clamping stress $\sigma_{C,av}$ of 102 N/mm² ($0.37\,f_{yr0}$, COV 0.59) was measured, while for $h_s/d = 4.76$, $\sigma_{C,av} = 241$ N/mm² ($0.87\,f_{yr0}$, COV 0.07). The Authors also pointed out that, for a given total grip length, connections with more plies (see Figure 2.25, red markers) usually show lower and strongly scattered clamping stresses, mainly due to constructional imperfections (e.g., camming defects) becoming more likely to occur. For instance, if only specimens with three plates are considered, $\sigma_{C,av}$ drops to 60 N/mm² ($0.22\,f_{yr0}$, COV > 2).
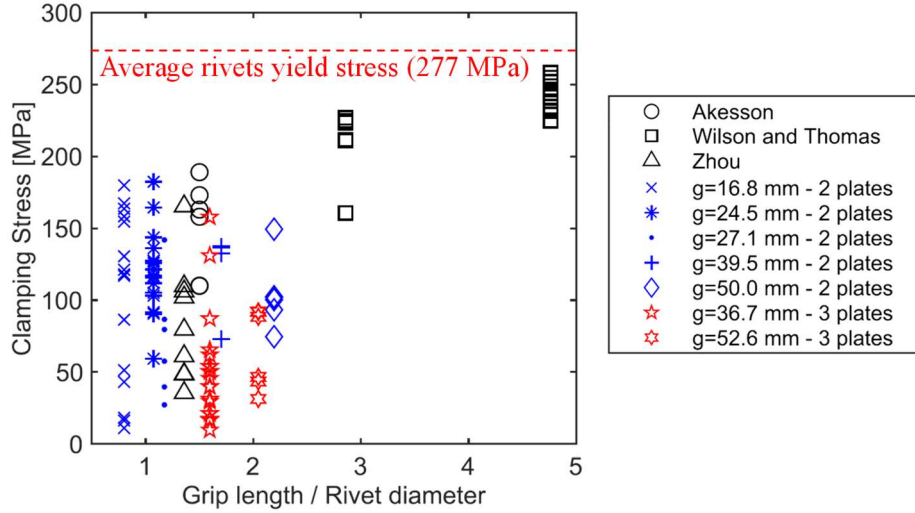
Figure 2.25 Experimental clamping stress vs. grip length/rivet diameter ratios for hot-driven rivets extracted from an existing roadway bridge *(*adapted from *Leonetti et al., 2020)*.

It should be remarked that, for most common structural application (that is, for $h_s/d = 0.8 \div 2.5$), a roughly average value of $\sigma_{C,av} \approx 0.5\ f_{yr0}$ can be assumed, although with a significant scatter. This outcome complies with preliminary remarks reported in *D'Aniello et al. (2011)*.

With regard to FE modelling of hot-driven riveted connections, it is worth mentioning the work of *Al-Bahkali (2011)* and *Kafie-Martinez et al. (2017)*. Namely, both authors aimed at investigating the effects of hot-driving process on the structural performance of lap-shear connections. For this purpose, coupled thermo-mechanical analyses were performed in order to *i*) reliably estimate clamping stresses in rivets (Figure 2.26b) and *ii*) investigate the effect of hot-driving on the static performance of such connections (Figure 2.26c). In both cases, rivets and plates were modelled by means of 8-node thermo-mechanical coupled bricks, with reduced integration (C3D8RHT). In order to properly capture phenomenology of clamping action, a very fine mesh was adopted nearby the rivet hole, while coarser elements were employed towards the plates' ends (Figure 2.26a – *Al-Bahkali, 2011*; *Kafie-Martinez et al. ,2017*). Cooling-induced clamping was modelled by assuming an initial temperature of the rivets equal to 1000 °C, and hence simulating on-site cooling up to ambient temperature (i.e., 20 °C).

Thermo-mechanical analyses basically confirmed experimental outcomes reported in earlier research (i.e., average clamping stress equal to $\approx 0.5\ f_{yr0}$ and beneficial effect of hot-driving on the static performance of connections, see Figure 2.26b, black dashed line).

a)

b)

c)
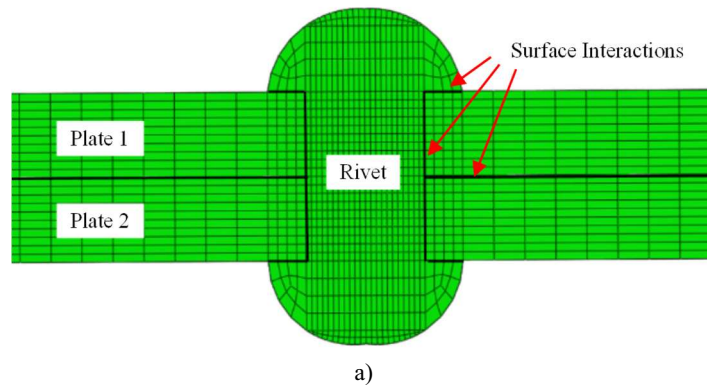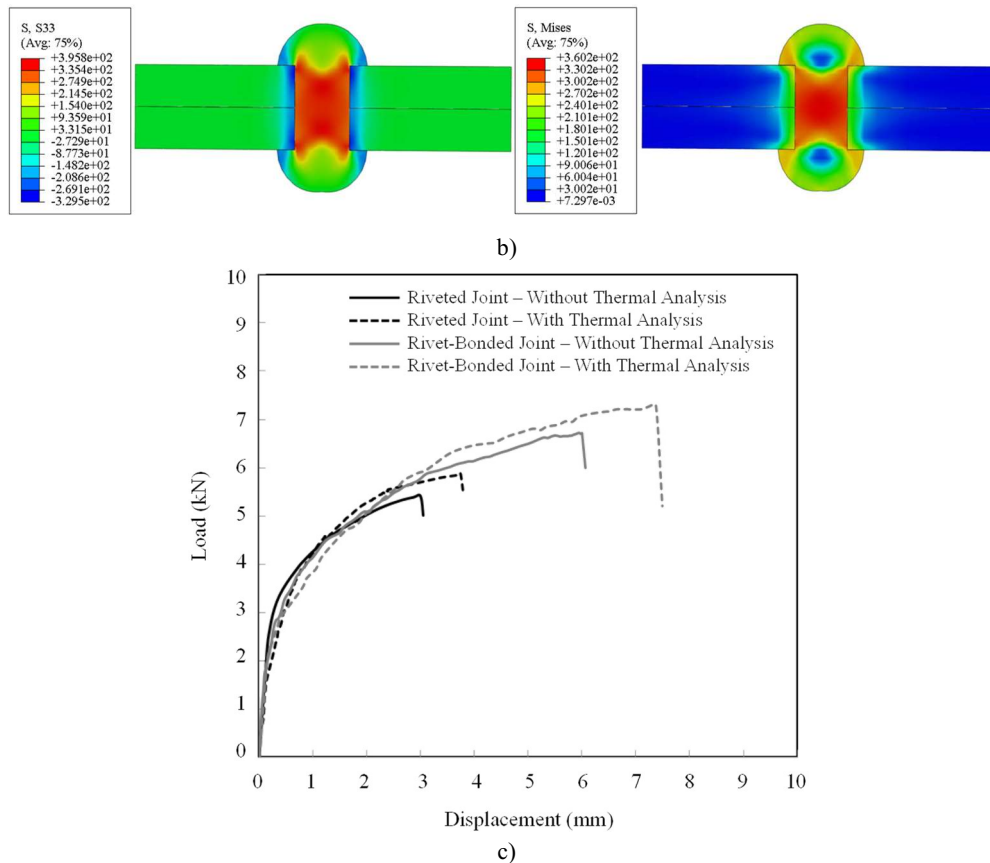
Figure 2.26 Coupled thermo-mechanical FEAs on riveted joints: a) adopted meshing and interactions for rivets and plates (*Al-Bahkali, 2011)*, b) resulting clamping stresses in rivets (adapted from *Kafie-Martinez et al., 2017*) and b) estimated effect of clamping action on the static performance of connections (*Al-Bahkali, 2011)*.

Works of *Al-Bahkali (2011)* and *Kafie-Martinez et al. (2017)* prove how advanced FEAs can be proficiently used to predict the structural performance of hot-driven riveted connections, provided that consistent and robust modelling assumptions are adopted. To this end, in *Chapters 5* to *7*, a particular focus on this aspect is given when presenting refined numerical analyses for connections subjected to both static and fatigue conditions.

2.5.2 Literature studies on the fatigue performance of hot-driven riveted connections

Owing to their peculiar fields of applications (e.g., railway steel bridges), several attempts to capture the fatigue performance of hot-driven riveted connections have been made in the past. Within this framework, it is worth mentioning the works of *Leahey et al. (1954)* and *Parola et al. (1964)*.

In *Leahey et al. (1954)*, the fatigue performance of both hot-driven riveted and bolted T-stub connections in direct tension was compared. As the study mainly aimed at investigating the effect of preloading on the fatigue performance of high-strength bolts, 18 bolted specimens were cyclically tested while only 3 riveted specimens were considered as a comparison.

Nevertheless, the Authors pointed out that, with regards to direct tension conditions, riveted connections always showed a worse fatigue strength with respect to nominally identical bolted ones, i.e., independently from connections geometrical features and applied stress ratio R (*Leahey et al., 1954*) For instance, bolted specimens showed an

almost 2 times higher fatigue strength (i.e., for $N^* = 2 \cdot 10^6$ cycles) with respect to riveted T-stubs. Moreover, while bolts rupture always occurred in shanks threaded sections, multiple riveted specimens collapsed due to field head detachment, i.e., proving the critical role played by this component in terms of fatigue performance of hot-driven rivets (Figure 2.27).
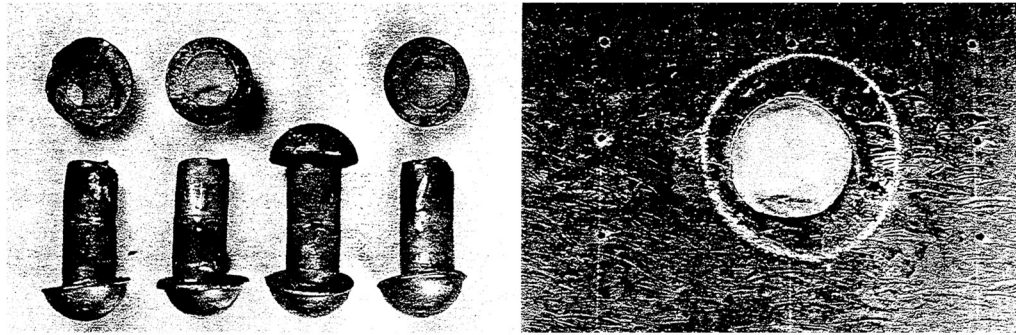
<div align="center">Specimen F5A   Specimen F5C</div>

Figure 2.27 Examples of hot-driven rivets failing under cyclic tension due to field head detachment (adapted from *Leahey et al., 1954*).

In *Parola et al. (1964)* fatigue performance of lap-shear riveted connections was addressed to investigate the influence of bearing ratio BR (that is, the ratio of the nominal bearing stress σ_{bear} on the rivet shanks over the average net section tensile stress σ_{net}, see Equation 2.11).

$$BR = \frac{\sigma_{bear}}{\sigma_{net}} = \frac{F_{Ed}}{d\,t}\frac{(w - n_{row}\,d)\,t}{F_{Ed}} = \frac{(w - n_{row}\,d)}{d} = \frac{w}{d} - n_{row} \qquad (2.11)$$

with F_{Ed} being the applied force and n_{row} being the number of rivets per row.

A total of 120 2 × 2 rivets lap-shear specimens were tested, considering four different bearing ratios (1.37, 1.83, 2.36, 2.74) and three increasing stress ratios R = -1, 0, 0.5 (Figure 2.28a-b). To achieve this purpose, $^7/_8$ inches (i.e., 22 mm) rivets were always used, while plates geometry was varied according to indications reported in Figure 2.28a.
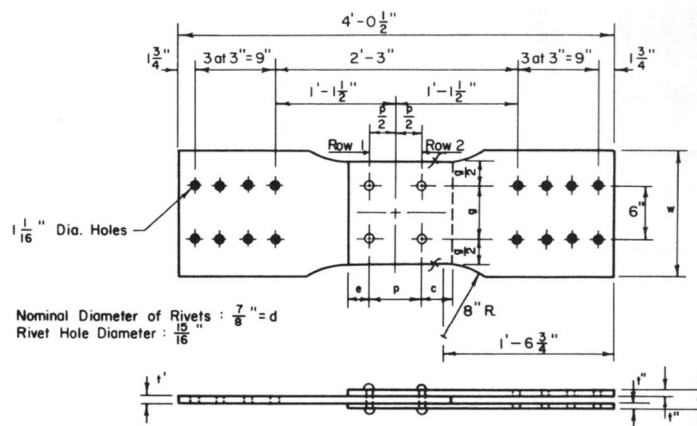
Spec. Type	Bearing Ratio	t'	t''	a	c	e	g	p	w	g/d
1 FR	2.74	$\frac{3}{8}$	$\frac{1}{4}$	$\frac{7}{8}$	3.25	2.50	5.74	5.74	1'-2"	6.55
2 FR	2.36	$\frac{7}{16}$	$\frac{5}{16}$	$1\frac{1}{16}$	2.84	1.96	5.08	5.08	1'-0"	5.81
3 FR	1.83	$\frac{9}{16}$	$\frac{3}{8}$	$1\frac{5}{16}$	2.30	1.68	4.14	4.14	0'-11"	4.73
4 FR	1.37	$\frac{3}{4}$	$\frac{1}{2}$	$1\frac{3}{4}$	1.58	1.58	3.34	3.34	0'-9"	3.82

<div align="center">a)</div>

| | b) | c) |
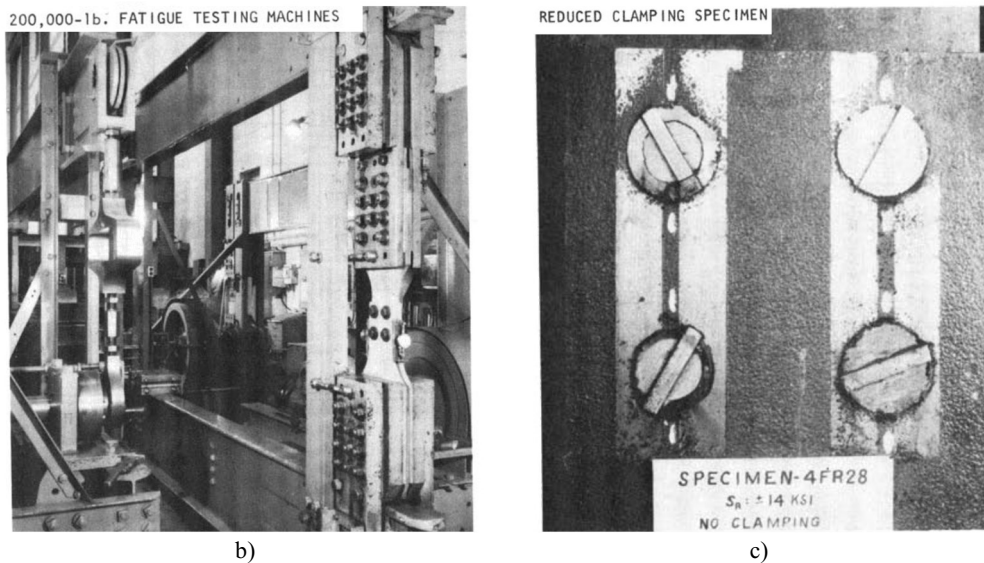
Figure 2.28 Experimental setup developed by *Parola et al. (1964)* for fatigue tests on lap-shear riveted connections: a) main setup geometrical features, b) adopted fatigue machine and c) example of reduced clamping specimen.

The Authors also investigated the influence of clamping action on the fatigue strength of specimens, i.e., by reducing clamping in some specimens by *i*) machining away most of the rivet heads and *ii*) pressing the rivet head in order to slightly detrude the shank (Figure 2.28c).

According to the Authors, results of performed fatigue tests could be summarized as follows (*Parola et al., 1964*):

i) independently from the considered stress ratio R, higher bearing ratios resulted in lower fatigue resistance of specimens. The only notable exception was represented by full-reversal tests (R = -1), in which connections having BR = 1.83 revealed a slightly higher fatigue strength with respect to BR = 1.37;

ii) decreasing plate thickness *t* and/or increasing transverse rivets spacing p_2 resulted in less uniform stress distribution on plates' net section, which reduced the fatigue strength;

ii) in most specimens, fracture initiated in the central plate, i.e., nearby the first row of rivet holes and hence the crack progressed outwards;

iii) as expected, reduced clamping specimens showed larger and premature slips. Although the tendency for the fatigue resistance to decrease with increasing slips per cycle was noticed, no clear relation among such entities was pointed out by the Authors owing to the large number of variables involved;

iv) uncertainty in terms of actual rivets clamping stress was the main reason behind observed scatter in results;

v) nevertheless, higher clamping stresses, which were obtained in case of longer rivets, resulted in longer fatigue life of specimens owing to the beneficial influence of plates precompression;

vi) apparently higher fatigue strengths were obtained for specimens subjected to increasing stress ratios R. However, results are reported in terms of maximum net stresses $\sigma_{net,max}$; hence, as R rises, lower stress ranges are actually applied on connections for given values of $\sigma_{net,max}$. Moreover, appreciably flatter S-N curves are derived for increasing stress ratios (Figure 2.29);

vii) fatigue design abaci were preliminary derived in the form of expressions depending on the material allowable stress σ_a and expected cycles at failure N* (Equation 2.12):
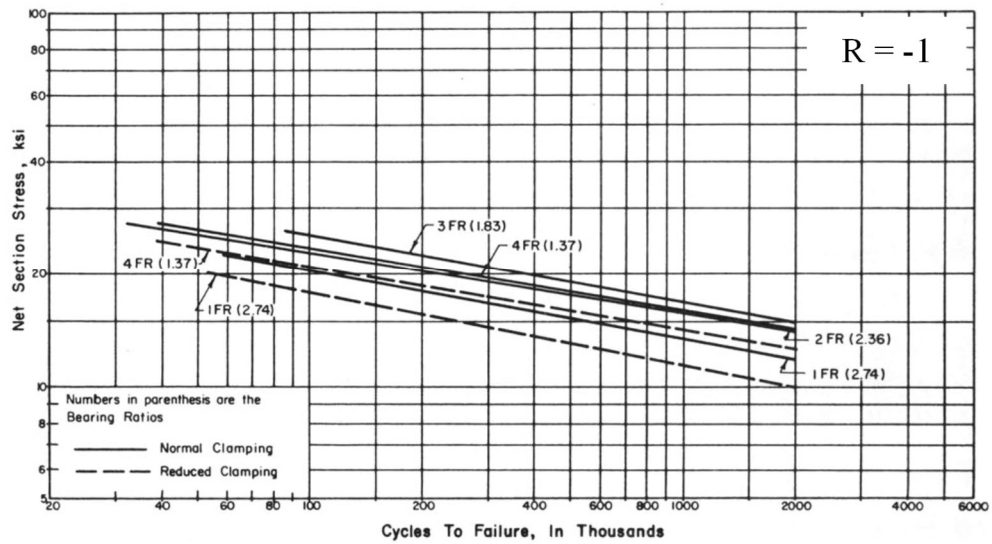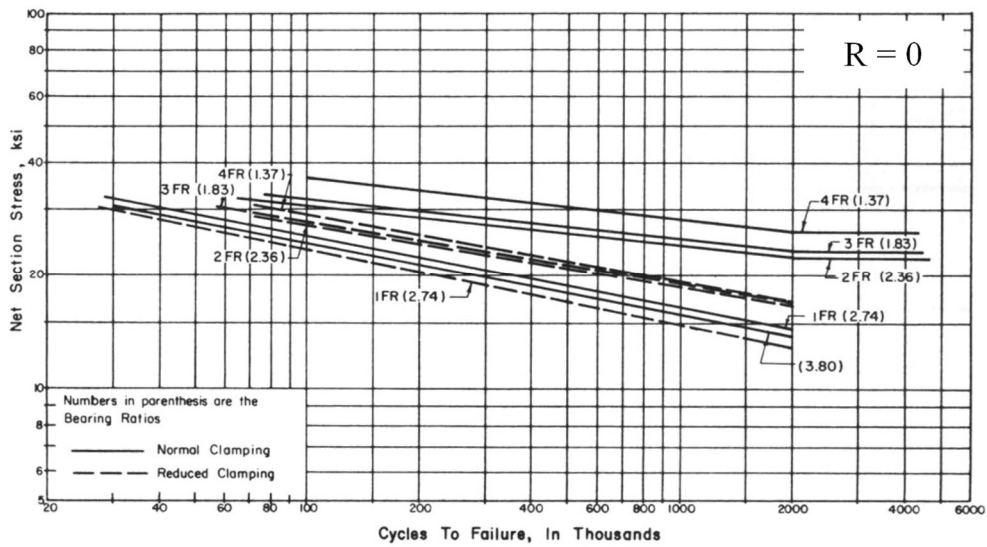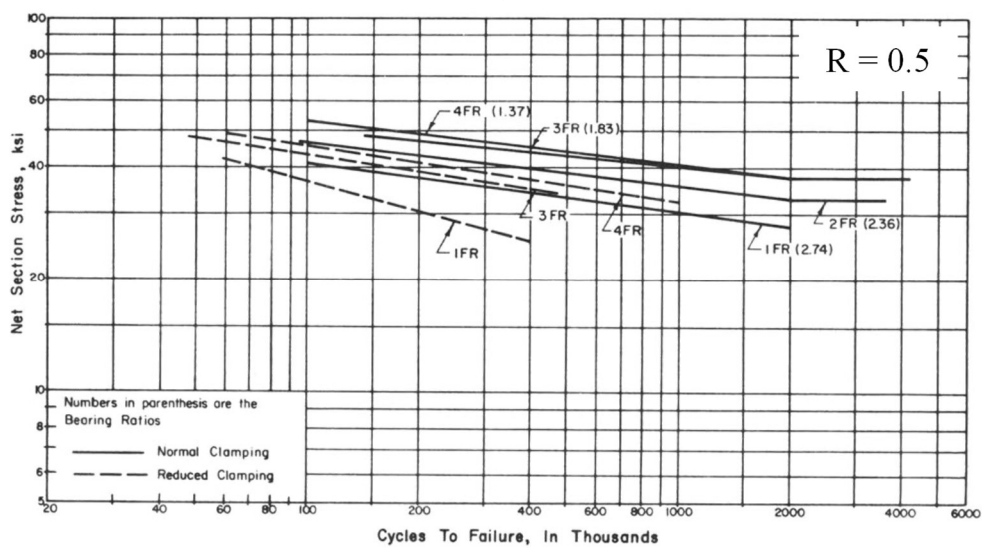
Figure 2.29 Experimental fatigue results derived by *Parola et al. (1964)*: a) fully-reversal tests (R = -1), b) zero-to-tension tests (R = 0), c) half-tension tests (R = 0.5).

$$\sigma_{net,max} = \frac{k_1 \, \sigma_a}{1 - k_2 \, R} \tag{2.12}$$

with $k_1 = 0.7 \div 1.0$, $k_2 = 0.50 \div 0.65$ depending on the expected value of N*. For instance, lower values of k_1 and higher values of k_2 should be assumed shifting from low-cycle (LCF) towards high-cycle fatigue (HCF) conditions, respectively (*Parola et al., 1964*). Similar remarks and further fatigue tests confirming outcomes pointed out by *Leahey et al. (1954)* and *Parola et al. (1964)* can be found in *Maarschalkerwaart (1982)*, *Out et al. (1984)*, *DiBattista et al., (1998)* and in *Kulak (2000)*.

More recently, *Taras et al. (2010)* attempted at defining a set of detail categories for most popular riveted connections and structural assemblies. Namely, five different categories were proposed (that is, symmetrical lap-/butt-shear joints, built-up girders, latticed members, bracings' gusset plates, cover plates – Figure 2.30).

Remarkably, for all considered categories, $m_1 = m_2 = 5$ and $\Delta\sigma_C$ ranged between $71 \div 90$ N/mm², i.e., consistently with provisions reported in the earlier drafts of EN1993:1-9 (*CEN, 2005a* – see also *Section 2.4.3*).

Reliability of derived categories was statistically checked accounting for EN1990 provisions (*CEN, 2002*) by means of the *maximum likelihood method* (MLE – *Pascual et al., 1996)*, which enabled the use of *run-outs* (that is, not failed for a given number of maximum cycles N_{max}) as valid inputs for data regression, as opposed to standard regression techniques (e.g. "direct" loglinear regression – *Taras et al., 2010*).

The Authors also investigated the influence of the material used for plates, profiles and rivets on the resulting fatigue performance of assemblies. Namely, a fatigue strength correction factor $f(R)$ depending on i) material properties and ii) stress ratio R was introduced (Equation 2.13):
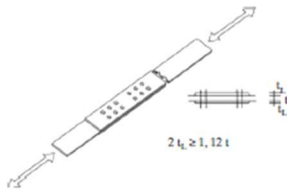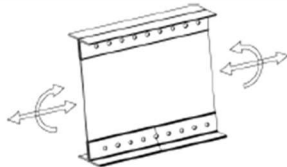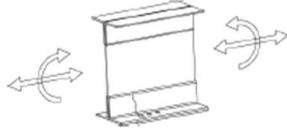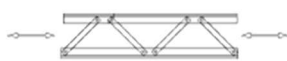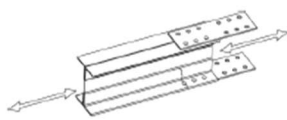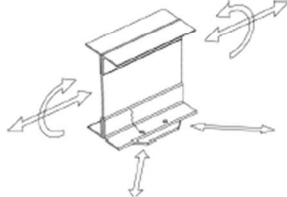
$$f(R) = \frac{1 - R}{1 - k(R; \, MP) \, R} \tag{2.13}$$

with recommended values for $k(R; MP)$ being summarized in Table 2.3.

It is worth remarking Equation 2.13 highly resembles the analytical expression proposed by *Parola et al. (1964)*. Moreover, i) for a given value of R, wrought iron and older mild steel (ante-1900) are associated with more severe correction factors. This condition clearly descends from the recognized brittleness of earlier metallic materials (*Di Lorenzo et al., 2021)*; ii) for a given material, tension-to-tension loads (R > 0) are penalized with respect to fully-reversal cycles (R = -1), owing to the detrimental effect of mean tensile stresses on crack propagation (*Anderson, 2017*).

a)
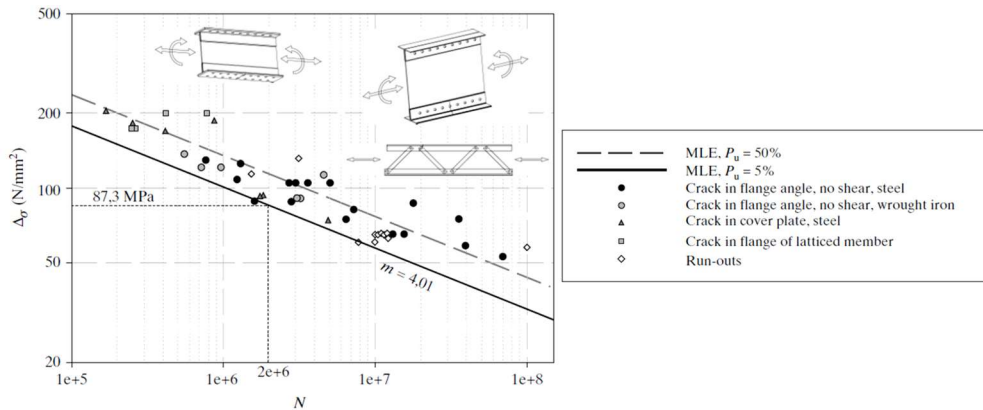
Fatigue strength (MPa)	Constructional detail	Description and examples	Remarks
$\Delta\sigma_c = 90$ (80) $m = 5$		Symmetrical joint with splice plates	The ratio $\sigma_{bearing}$ to σ_{net} must be smaller than 2
		– Middle plates in two-shear connections are to be verified with $\Delta\sigma_c = 90$	When rivets of steel grade St44 or higher were employed no corrosion protection coating must have been applied
		– $\Delta\sigma_c = 80$ applies for the splice plates themselves, so no verification is required when $2t_L > 1,12\,t$	If one of these conditions is not kept, $\Delta\sigma_c = 80$ applies (70 for the gusset plates)
$\Delta\sigma_c = 85, m = 5$		Continuous connection of flange angles and web plates in built-up girders $\Delta\sigma$ at the centre of the rivet	The calculated shear force per rivet and shearing area must not exceed the minimum value of slip resistance as indicated in *Table 3*
		Continuous connection between cover plates and flange angles in built-up girders	The calculated shear force per rivet and shearing area must not exceed the minimum value of slip resistance as indicated in *Table 3*
$\Delta\sigma_c = 85, m = 5$		Latticed members under tension or compression loads	The calculated shear force per rivet and shearing area must not exceed the minimum value of slip resistance as indicated in *Table 3*
$\Delta\sigma_c = 71, m = 5$		One-shear joint with gusset plates	If the calculated shear force in the rivets is lower than the minimum value of slip resistance, $\Delta\sigma_c = 85$ can be used
$\Delta\sigma_c = 71, m = 5$	—	All cases for which normally $\Delta\sigma_c = 85$ applies if the minimum value of slip resistance in the rivet is exceeded	The calculated shear force per rivet and shearing area exceeds the minimum value of slip resistance as indicated in *Table 3*
$\Delta\sigma_c = 71, m = 5$		Area of the connection of a lateral bracing element to the tension flange of a girder	If the restraining effect of the lateral bracing element is considered during the calculation of the applied stress range $\Delta\sigma_c = 85$ can be used
$\Delta\sigma_c = 71, m = 5$		Onset of a cover plate	If the calculated shear force in the rivets is lower than the minimum value of slip resistance $\Delta\sigma_c = 85$ can be used

b)

Figure 2.30 a) Statistical analysis and b) detail categories proposed by *Taras et al. (2010)* for riveted connections and assemblies.

Table 2.3 Values of k(R; MP) proposed by *Taras et al. (2010)* for the fatigue strength correction factor.

Stress Ratio R	Material Properties	k(R; MP)
-1.0 ÷ 0.0	Wrought iron Mild steel ante-1900	0.70
	Mild steel post-1900 St37, St48, St52, …	0.40
0.0 ÷ 1.0	Wrought iron Mild steel ante-1900	0.75
	Mild steel post-1900 St37, St48, St52, …	0.60

A further advance in fatigue assessment of hot-driven riveted connections was arguably represented by the use of refined, calibrated FEAs (*Da Silva, 2015*). Indeed, if base material properties are carefully estimated and peculiarities of hot-driving are accounted for, fatigue performance of riveted assemblies can be on principle reliably predicted.

However, the main drawback of such approach lies in the need of a wide set of experimental tests aimed at deriving (at least) *i*) cyclic constitutive behaviour, *ii*) crack initiation properties and *iii*) crack propagation properties for both rivets and plates (*Lesiuk et al., 2017; Correia et al., 2017*).

Moreover, as material fatigue properties should be derived using standardized specimens and test conditions (*Anderson, 2017*), effects of hot-driving and clamping action variability cannot be accounted directly, and should be hence assessed a-posteriori with the aid of further experimental tests.

Nevertheless, if robust statistical analyses for both assumed material parameters and numerical outputs are carried out, numerical fatigue life predictions can be surely considered as a viable option for hot-driven riveted connections. To this end, it is worth mentioning the recent contribution of *Da Silva et al. (2019)*.

The Authors addressed the numerical fatigue analysis of downscaled riveted joints resembling structural details adopted in a dismantled railway bridge located in Trezòi, Portugal. For this purpose, several samples of historic steel were extracted and tested to derive both flat and compact-tension (CT) specimens (Figure 2.31). Hence, the Authors derived Ramberg-Osgood parameters (hysteretic behavior – *Ramberg & Osgood, 1943*), Coffin-Manson parameters (crack initiation properties – *Manson, 1953*; *Coffin, 1954*) and Paris' law parameters (crack propagation properties – *Paris et al., 1961*) for the analysed historic steel (i.e., a low-carbon steel comparable with modern European S235 steel grade).

a)

b)

c)
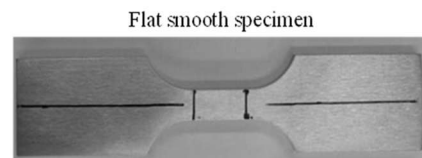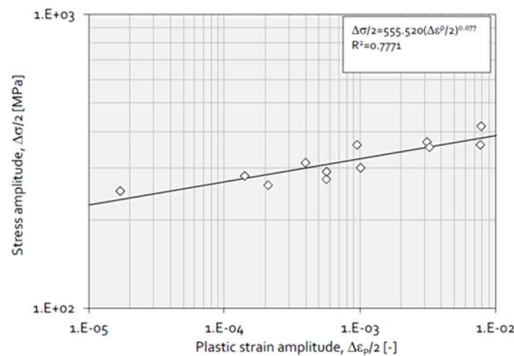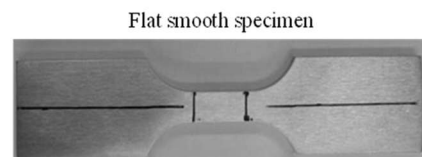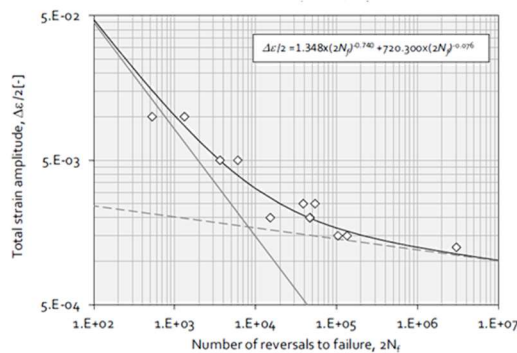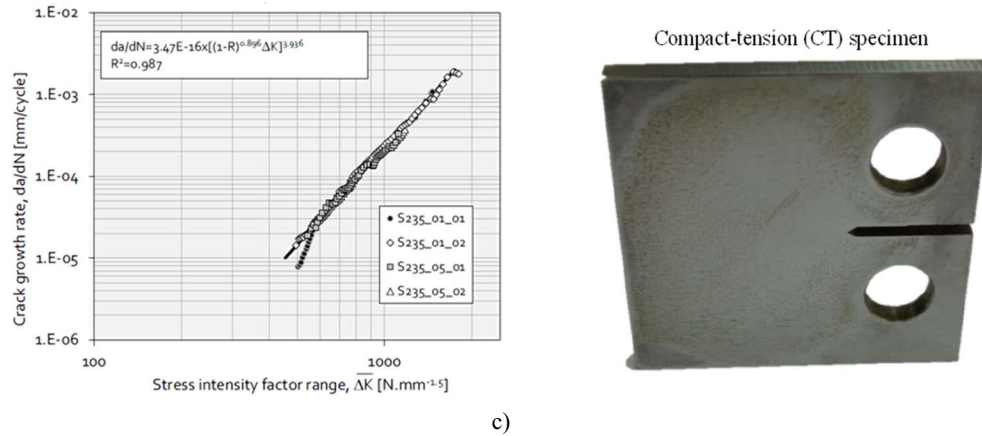
Figure 2.31 Plasticity and cracking properties for an historic mild steel adopted for a riveted bridge structure: a) cyclic plastic properties, b) crack initiation properties, c) crack propagation properties (adapted from *Da Silva, 2015* and *Da Silva et al.*, *2019*).

Based on derived properties, Authors performed experimental and numerical estimations of the fatigue live of downscaled joint belonging to Trezòi bridge (Figure 2.31). For this purpose, both standard and *extended* (or *enriched*) finite elements (XFEMs, *Moës et al., 1999*) able to capture crack growth without iterative model remeshing.

Total fatigue life N* for a given load condition was estimated by adding crack initiation life (N_i) estimated with damage-accounting FEAs to crack propagation life (N_p) calculated with the aid of XFEMs (*Da Silva, 2019*).

Experimental setup for one of the tested joints (R1 joint – shear tab joint in which a 2 m-long IPN220 beam is connected to an end-plate by means of five 19 mm hot-driven rivets passing through two 120 × 120 mm web angles) is depicted in Figure 2.32a.

In order to reliably estimate cyclic performance of assemblies, XFEM cracks were modelled starting from both the upper rivet hole and from the corner of the L profile (Figure 2.32b). Results were hence finally transposed into conventional S-N diagrams, in which stress ranges were properly corrected to account for tensile means stresses. Comparison between numerical and mean experimental outcomes confirmed the reliability of the proposed procedure (Figure 2.32c).

a)

b)

c)
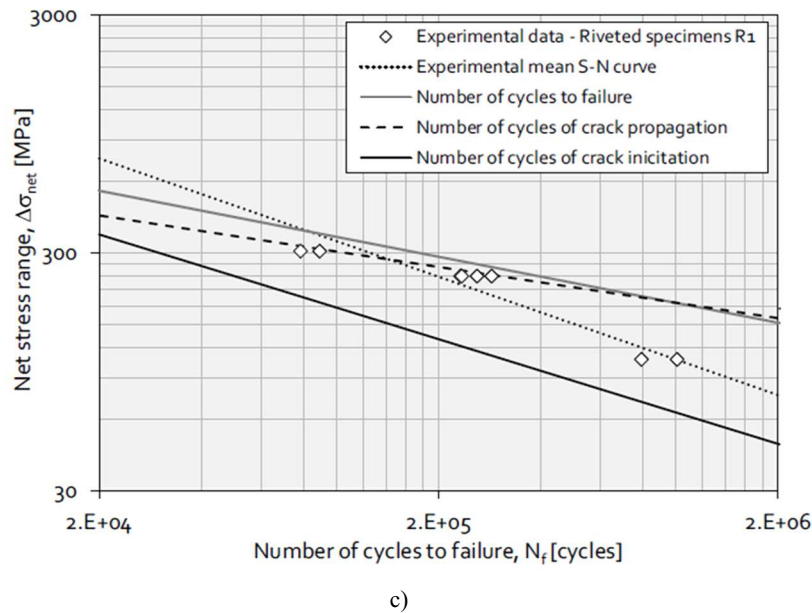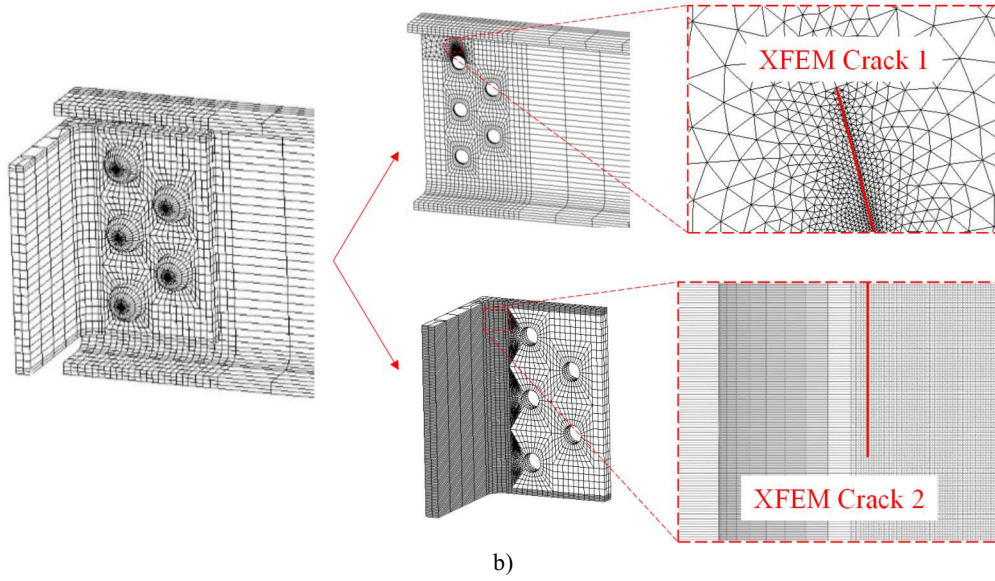
Figure 2.32 Fatigue life prediction for a riveted joint: a) experimental setup, b) FE modelling enriched with XFEM cracks, c) comparison of experimental and numerical results (adapted from *Da Silva, 2015* and *Da Silva et al.*, *2019*).

The work of *Da Silva et al. (2019)* prove how refined FEAs can be proficiently used to predict the fatigue performance of hot-driven riveted assemblies by means of local approaches. Moreover, derived experimental parameters could be used as a term of comparison for further investigations on fatigue properties of historic mild steels, although it should be remarked that this operation has to be carefully performed, as even nominally identical older metallic materials showed strong variability in terms of both chemical composition and mechanical properties (*Di Lorenzo et al., 2021*).

Damage and Fatigue Modelling of Hot-Driven Riveted Connections

As stated in previous Sections, in the present work both static and fatigue performance of hot-driven riveted connections will be addressed by means of refined local approaches, namely:

- With regard to the static response of connections, advanced damage models for ductile materials will be introduced and properly calibrated against experimental results;
- With regard to the cyclic performance of connections, advanced energetic fatigue approaches will be introduced, validated for mild steel components (see *Chapter 6* for further details) and hence properly calibrated against experimental results.

Therefore, in the present Chapter, an overview of main damage and fatigue models is provided. For instance, the following key topics are addressed in following Sections: *i*) damage models for ductile materials (*Section 3.1*), *ii*) application of damage models for hot-driven riveted connections (*Section 3.2*), *iii*) standard fatigue analysis techniques for structural components (*Section 3.3*), *iv*) advanced fatigue analysis techniques for structural components (*Section 3.4*) and *v*) application of presented fatigue analysis techniques for hot-driven riveted connections (*Section 3.5*).

3.1.   Main damage models for ductile materials

When dealing with the ductile fracture of metallic materials, it is widely recognized that two post-elastic behavioural stages can be identified before collapse, i.e., *plasticity-dominated stage* (hence also referred as "PDS") until the onset of necking and *damage-dominated stage* (hence also referred as "DDS") until fracture (*Voyiadjis et al., 1992*). However, it is worth remarking that this distinction is somewhat conventional, as *i*) on one hand, highly localized (i.e. at void scale) damage almost immediately occurs when the metallic component is experiencing PDS, while *ii*) on the other hand, damaged material still behaves plastically, albeit showing degradation, up to void coalescence and fracture (*Xin et al., 2021*).

Nevertheless, for engineering purposes, PDS and DDS can be conveniently separated and addressed by means of distinct models, which can be hence individually calibrated and hence coupled while analysing ductile fracture. This approach is known as "uncoupled (damage) analysis" in scientific literature (*Yang et al., 2019*).

In the following Subsections, after briefly dealing with the issue of post-necking behaviour of ductile materials, some of the main uncoupled damage models are introduced.

3.1.1   Post-necking behaviour of ductile materials

While performing uncoupled analysis, it is necessary to define a post-necking plastic behaviour for the considered materials, as "classic", constant-volume, relations linking

engineering and true stress-strain parameters are no longer valid after the onset of necking (Figure 3.1). When an uniaxial tensile test is performed, this condition can be easily recognized as the engineering stress-strain curve starts to decrease after reaching its maximum. In other words, necking manifests as an instability phenomenon occurring during tensile deformation, in which the specimen cross-section starts to decrease by a larger proportion than the material strain hardens.

Hence, the so-called *Considére criterion* (*Considére, 1885*) can be formulated in limit conditions, i.e., immediately before diffuse necking, when no net load increment dP (and thus, engineering stress $d\sigma_{eng}$) occurs for an infinitesimal increment of engineering strain $d\varepsilon_{eng}$ (Equation 3.1a-b – *Tu et al., 2019*):

$$d\sigma_{eng} = (d\sigma_{true} - \sigma_{true}\ d\varepsilon_{true})\ exp(-\varepsilon_{true}) = 0 \tag{3.1a}$$

$$d\sigma_{true} - \sigma_{true}\ d\varepsilon_{true} = 0 \rightarrow \frac{d\sigma_{true}}{d\varepsilon_{true}}\Big|_{necking} = \sigma_{true,neck} \tag{3.1b}$$

A second, obvious condition at the onset of necking descends from the so-called *continuity criterion*, according to which the true stress at the onset of necking is the last stress value that can be estimated with constant-volume relations (Equation 3.2):

$$\sigma_{true}|_{necking} = \sigma_{eng,max}\left(1 + \varepsilon_{eng,neck}\right) = \sigma_{true,neck} \tag{3.2}$$

Thus, every analytical model attempting at capturing post-necking behaviour of a ductile material should fulfil conditions reported in Equations 3.1-3.2. It should be remarked that *Considére* and *continuity* criteria (hence also referred as "CCC") do not provide sufficient information about the shape of the post-necking branch of the true stress-true strain curve, hence multiple formulations with increasing level of complexity can be adopted (*Tu et al., 2019*).

To this end, the simplest post-necking formulation is represented by the *linear hardening model* (hence also referred as "LHM"). Accordingly, the post-necking hardening branch of the true stress-strain curve can be modelled by means of a straight line (Equation 3.3):
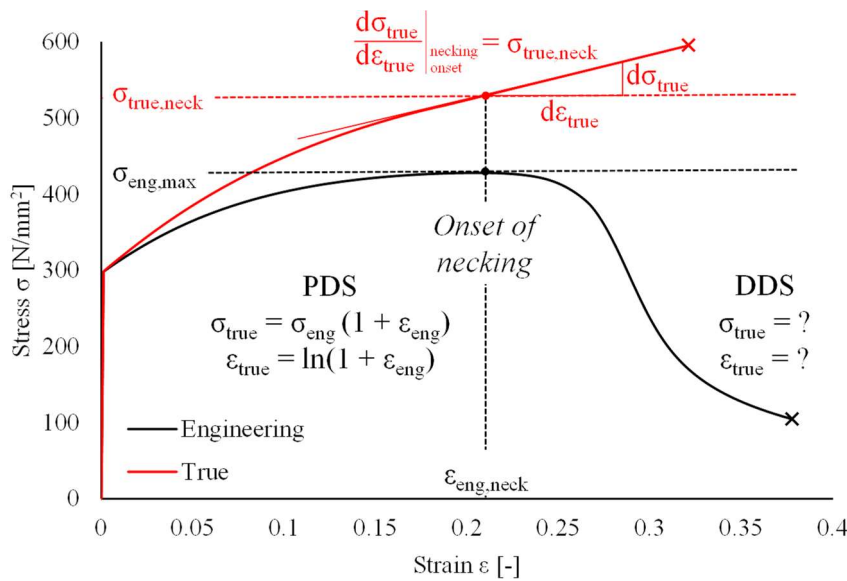
Figure 3.1 Typical constitutive law of a ductile material in plasticity-dominated and damage-dominated stages up to failure (for the sake of simplicity, it is assumed that $\varepsilon_{eng,neck} \approx \varepsilon_{true,neck}$).

$$\text{LHM: } \sigma_{true} = a_1\, \varepsilon_{true} + b_1 \tag{3.3}$$

in which coefficients a_1, b_1 should be derived to ensure fulfilment of CCC (Equation 3.4, *Tu et al., 2019*):

$$\text{LHM: } \begin{cases} a_1 = \sigma_{true,neck} \\ b_1 = \sigma_{true,neck}\, (1 - \varepsilon_{true,neck}) \end{cases} \tag{3.4}$$

It should be remarked that, although a_1 and b_1 are known when adopting LHM, the actual value of true strain at failure ($\varepsilon_{true,fail}$) is still unknown and should be calibrated according to tensile test results (*Tu et al., 2019*).

Another popular post-necking formulation is represented by the *power-law hardening model*, or *Hollomom hardening model* (hence also referred as "HHM" – *Hollomom, 1945*). Accordingly, a power law expression can be used to capture the post-necking branch of the true stress-strain curve (Equation 3.5):

$$\text{HHM: } \sigma_{true} = a_2\, (\varepsilon_{true})^{b_2} \tag{3.5}$$

in which coefficients a_2, b_2 should be derived to ensure fulfilment of CCC (Equation 3.6, *Tu et al., 2019*):

$$\text{HHM: } \begin{cases} a_2 = \dfrac{\sigma_{true,neck}}{\varepsilon_{true,neck}^{\varepsilon_{true,neck}}} \\ b_2 = \varepsilon_{true,neck} \end{cases} \tag{3.6}$$

Similarly to LHM, HHM yields known a_2, b_2 constants, while the actual value of $\varepsilon_{true,fail}$ should be properly calibrated.

With regard to b_2 (also known as "hardening exponent" in scientific literature – *Callister Jr., 2005*), it is worth remarking that it is strictly included within the range $0.0 \div 1.0$, with 0.0 representing an ideal perfectly plastic material, while for $b_2 = 1.0$ the LHM is obtained once again.

"Hybrid" LHM-HHM formulations (*line-power hardening models*, hence also referred as "LPHM") can be also found in scientific literature, in which a weighted average between the two models is assumed by means of a relative weight w (Equation 3.7 – *Ling, 1996*):

$$\text{LPHM: } \sigma_{true} = w\, (a_1\, \varepsilon_{true} + b_1) + (1 - w)\, [a_2\, (\varepsilon_{true})^{b_2}] \tag{3.7}$$

LPHM can, on principle, more accurately capture the post-necking behaviour of the considered material. However, a complex calibration procedure is required as both w and $\varepsilon_{true,fail}$ should be estimated based on experimental results (*Wang et al., 2016*).

Although LHM, HHM and LPHM are among the most popular post-necking hardening models adopted in literature, it is worth noting that even more complex, yet reliable formulations are currently available, e.g. the three-parameters *Misiolek exponential hardening model*, or analytical *shape-depending* models, which attempt at deriving the triaxial post-necking stress field accounting for the shape of the tensile specimen (cylindrical, flat, … – *Wang et al., 2016*; *Tu et al., 2019*).

The main common drawback for all above formulations lies in their intrinsic piecewise nature. Indeed, each of the presented models relate only on the post-necking branch of the true stress-strain curve, hence a separate formulation should be used for the PDS up

to the onset of necking. This issue can be overcome by adopting a continuous formulation which covers both PDS and DDS.

Among all the possible alternatives, the most popular formulation is arguably represented by the Ramberg-Osgood model (Equation 3.8 – *Ramberg & Osgood, 1943*):

$$\frac{\varepsilon_{true}}{\varepsilon_{true,y}} = \frac{\sigma_{true}}{\sigma_{true,y}} + \alpha_{RO}\left(\frac{\sigma_{true}}{\sigma_{true,y}}\right)^{n_{RO}} \tag{3.8}$$

with $\varepsilon_{true,y}$ and $\sigma_{true,y}$ being the true strain and true stress at yielding, respectively, and α_{RO} (also known as "*yield offset*") and n_{RO} (also known as "*hardening exponent*") being empirical parameters which can be obtained by fitting experimental results.

When adopting Ramberg-Osgood model, a careful effort has to be placed in calibrating actual values of α_{RO}, n_{RO} and $\varepsilon_{true,fail}$ in order to obtain reliable results. Indeed, as the latter addendum in Equation 3.8 is always non-null for $\sigma_{true} > 0$, plasticity is predicted to occur also in elastic range. The magnitude of this error, which represents the trade-off of adopting a continuous hardening model, can be controlled by appropriately manipulating yield offset and hardening exponent (*Callister Jr., 2005*).

3.1.2 Pioneering works related to damage of ductile materials

The next step in performing uncoupled analysis of ductile materials is represented by the selection of a proper damage model to capture DDS. To this end, it is worth recalling the phenomenology of ductile damage of metals before addressing the topic of predictive damage models.

Ductile fracture of metals occurs due to the nucleation and growth of microstructural voids, which are intrinsically present in metals as they surround inclusions and second-phase particles (*Anderson, 2017*). When subjected to multiaxial stress fields, such voids may get distorted and enlarged enough to cause local plastic deformations and necking (small-scale plasticity) up to *void coalescence*, which leads to macroscopical ductile fracture (Figure 3.2).
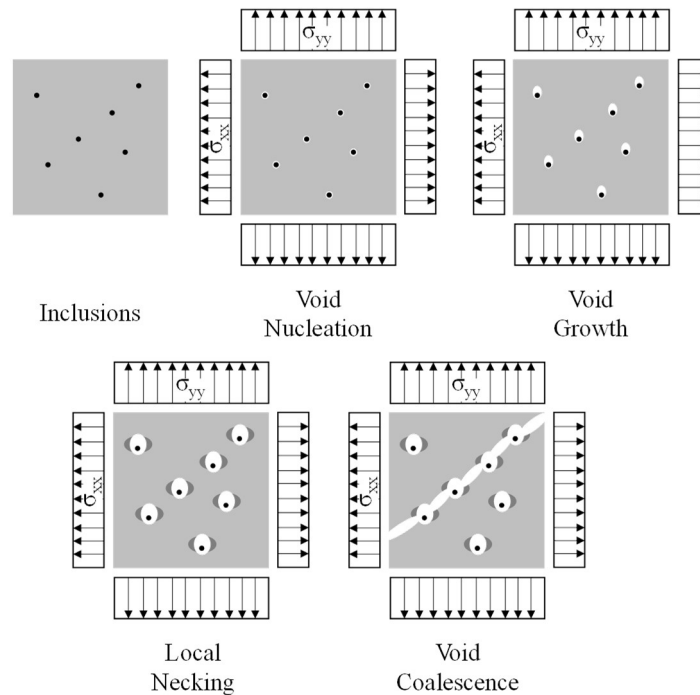
Figure 3.2 Phenomenology of ductile fracture of metals (adapted from *Anderson, 2017*).

In light of this peculiar phenomenology, it is clear that every attempt to analytically capture the nature of ductile fracture should account for void enlargement to some extent. To this end, pioneering contributions of *McClintock* (*1968*) and *Rice & Tracey* (1969) should be certainly mentioned. In both works, ductile voids enlargement in triaxial stress fields is addressed under some simplifying assumptions, namely:

i) the base material is isotropic and obeys the Hencky-Von Mises (*Von Mises, 1913*; *Hencky, 1924*) yield criterion;

ii) the considered void is isolated;

iii) an uniform stress field is remotely applied to the solid enclosing the void;

iv) the undeformed void has an a-priori known geometry (cylindrical or spherical according to *McClintock* (*1968*) or *Rice & Tracey* (1969), respectively).

Based on the following assumptions, an analytical expression for the void size increase in dependence from applied remote stresses was derived. With reference to the lone *Rice & Tracey* (1969) model, which met the highest popularity owing to a more realistic representation of voids, the following relation was derived (Equation 3.9 – *Rice & Tracey*, 1969):

$$\ln \frac{R}{R_0} = \frac{3}{2} e^{-\frac{5}{3}} \int_0^{\varepsilon_{pl,eq}} e^{\frac{3}{2}T} d\varepsilon_{pl,eq} \qquad (3.9)$$

with R being the deformed radius of the isolated void having initial radius equal to R_0, $\varepsilon_{pl,eq}$ being the equivalent plastic strain (PEEQ, Equation 3.10a) and T being the so-called triaxiality degree (Equation 3.10b):

$$\varepsilon_{pl,eq} = \sqrt{\frac{2}{3} \varepsilon_{pl,ij} : \varepsilon_{pl,ij}} \qquad (3.10a)$$

$$T = \frac{\sigma_m}{\sigma_{eq,VM}} \qquad (3.10b)$$

with $\varepsilon_{pl,ij}$ being the *ij*-th component of the plastic strain tensor $\boldsymbol{\varepsilon_{pl}}$ (":" denotes the scalar product operator), σ_m being the mean pressure, i.e., the arithmetic average of the three principal stresses $(\sigma_I + \sigma_{II} + \sigma_{III})/3$ and $\sigma_{eq,VM}$ being the the equivalent Von-Mises stress. It is worth remarking that, consistently with above formulations, PEEQ can be regarded as the direct "strain equivalent" of the Von Mises stress, while T allows to identify the nature of applied stress field (e.g., T = 1/3 for uniaxial tension or T = 0 for pure shear). Moreover, sign(T) allows to tell apart compressive (T < 0) from tensile (T > 0) stress fields, which result in shrinkage or enlargement of microstructural voids, respectively *Kanvinde et al., 2006*).

3.1.3   Void Growth Model (VGM)

Starting from the Rice & Tracey model, a failure criterion based on void coalescence can be immediately formulated, i.e., by postulating the occurrence of fracture for a critical value R* of the deformed void radius (Equation 3.11a-b – *Kanvinde et al., 2006*):

$$\ln R = \frac{3}{2} e^{-\frac{5}{3}} \ln R_0 \int_0^{\varepsilon_{pl,eq}} e^{\frac{3}{2}T} d\varepsilon_{pl,eq} = A \int_0^{\varepsilon_{pl,eq}} e^{\frac{3}{2}T} d\varepsilon_{pl,eq} = A \cdot VGI \qquad (3.11a)$$

$$R = R^* \rightarrow VGI = \int_0^{\varepsilon_{pl,eq}} e^{\frac{3}{2}T} d\varepsilon_{pl,eq} = VGI^* \rightarrow Failure \qquad (3.11b)$$

with A being a numerical coefficient recollecting all constant terms, VGI being the *Void Growth Index*, i.e., the integral on the right hand member which actually governs void

growth and VGI* being the critical value of VGI for which failure is predicted.

This failure model is known as Void Growth Model (VGM) in scientific literature, and it was first proposed by Rice & Tracey themselves as an extension of their void enlargement formulation (*Kanvinde et al., 2006*).

Critical Void Growth Index has to be intended as a material property, which should be calibrated on the basis of experimental results. According to *Kanvinde et al.* (*2006*), VGI* can be related to Charpy fracture energy for sharp-V notched specimen (CVN) as follows (Equation 3.12):

$$VGI^* \approx 0.018 \, CVN \, [J] - 1.30 \tag{3.12}$$

In order to actually predict failure due to void coalescence, fulfilment of VGM criterion (VGI $\geq$ VGI*) has to be achieved in a finite neighbourhood of the plasticized zone having size l^* (characteristic microstructural size).

Actual values of l^*, which are intended as an intrinsic material constant, are usually within the range $10 \div 200$ μm, and can be found in *Kanvinde et al.,* (*2006*) for several steel alloys.

3.1.4 Stress Modified Critical Strain (SMCS) Criterion

In numerous realistic situations of monotonic loadings, the entity of stress triaxiality T remains substantially constant during the load history (*Kanvinde et al., 2006*). Therefore, as first noticed by *Hancock et al.* (*1976*), this condition allows to directly calculate the critical equivalent plastic strain associated to failure $\varepsilon_{pl,eq}^*$ as a function of T, i.e., with higher triaxiality degrees leading to lower critical PEEQ and vice-versa.

This simplifying assumption underlies the so-called Stress Modified Critical Strain (SMCS) criterion, according to which $\varepsilon_{pl,eq}^*$ can be directly estimated as follows (Equation 3.13a-b – *Kanvinde et al., 2006*):

$$VGI^* = \int_0^{\varepsilon_{pl,eq}^*} e^{\frac{3}{2}T} \, d\varepsilon_{pl,eq} \rightarrow Failure \tag{3.13a}$$

$$Failure|_{T \approx const.} \rightarrow \varepsilon_{pl,eq}^* \approx \alpha \, e^{-\frac{3}{2}T} \tag{3.13b}$$

with α being an empirical material parameter (usually known as "toughness coefficient") with a similar meaning to VGI*. According to *Kanvinde et al.* (*2006*), α can be related to CVN as follows (Equation 3.14):

$$\alpha \approx 0.016 \, CVN \, [J] - 0.93 \tag{3.14}$$

In analogy with VGM, SMCS criterion predicts failure due to voids coalescence when $\varepsilon_{pl,eq} \geq \varepsilon_{pl,eq}^*$ in a finite volume having size l^*.

The SMCS criterion is arguably simpler with respect to VGM, as it does not require the integration of triaxiality and equivalent plastic strain along the load path. Indeed, only an "instantaneous" check of PEEQ demand against $\varepsilon_{pl,eq}^*$ is needed, with the latter parameter being a function of the relevant stress triaxiality.

Nevertheless, it should be remarked that, when T considerably changes during the loading history, the SMCS criterion may yield less accurate results with respect to the VGM (*Kanvinde et al., 2006*).

3.1.5 Cyclic Void Growth Model (CVGM)

Starting from the theoretical framework of VGM, *Kanvinde et al.* (*2007*) proposed an useful extension of ductile damage criteria with regard to cyclic loadings, i.e. load histories in which stress triaxiality changes sign multiple times. Accordingly, fracture initiation is monitored by means of a cyclic Void Growth Index (VGI_{cyc}) which can be estimated according to Equation 3.15 (*Kanvinde et al., 2007*):

$$VGI_{cyc} = \sum_{i\text{-th tensile cyc}} \int_{\varepsilon_{pl,eq,i}}^{\varepsilon_{pl,eq,i+1}} e^{\frac{3}{2}|T|} \, d\varepsilon_{pl,eq} - \sum_{j\text{-th compr. cyc}} \int_{\varepsilon_{pl,eq,j}}^{\varepsilon_{pl,eq,j+1}} e^{\frac{3}{2}|T|} \, d\varepsilon_{pl,eq} \qquad (3.15)$$

Differently from monotonic VGM, absolute value of stress triaxiality $|T|$ is considered for calculation, hence the integration over each *i*-th tensile and *j*-th compressive cycles has to be conducted separately, depending on the sign of the mean pressure σ_m.

According to the Authors, VGI_{cyc} should always remain non-negative. Therefore, when the index reaches zero (if it is the case) due to the contribution of a compressive cycle (in which the voids are shrinking, thus inhibiting coalescence), it stays null until the next tensile cycle (*Tartaglia et al., 2022*).

The fracture is predicted to occur when VGI_{cyc} reaches a critical value VGI^*_{cyc}, in a finite volume having characteristic size l^*. VGI^*_{cyc} can be expressed in function of fracture toughness parameter α (see *Section 3.1.4*) and accumulated PEEQ ($\varepsilon_{pl,eq,acc.}$) as follows (Equation 3.16 – *Kanvinde et al, 2007*):

$$VGI^*_{cyc,crit.} = \alpha \, e^{-\lambda \, \varepsilon_{pl,eq,acc.}} \qquad (3.16)$$

with λ being an experimental parameter which accounts for the material degradation under cyclic actions exceeding the elastic range. According to *Kanvinde et al.* (2007), recommended values for λ range between $0.4 \div 0.5$.

VGI^*_{cyc} has to be updated at the end of each compressive cycle and stays fixed during the following tensile excursion (Figure 3.3). In light of this, Equation 3.16 further clarifies how α represents the asymptotic value of material fracture toughness for elements subjected to monotonic tensile stress histories (that is, in absence of cyclic degradation phenomena – *Tartaglia et al., 2022*).
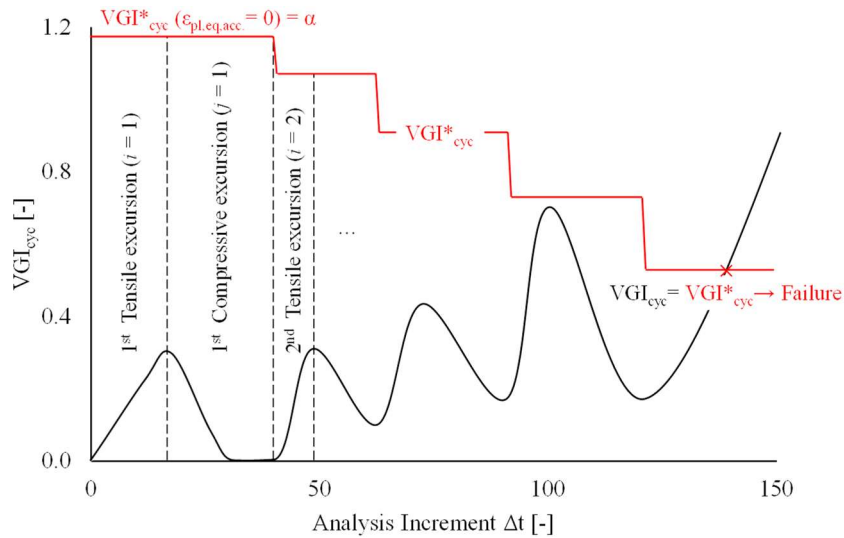
Figure 3.3 Graphical interpretation of failure according to CVGM (adapted from *Kanvinde et al., 2007*).

3.1.6 Generalized Ductile Damage Criteria

Each of the damage initiation criteria discussed earlier has the main drawback of requiring its fulfilment in a small, yet finite, neighbourhood of the plasticized zone having size equal to *l** (that is, few tens or hundreds of μm). Indeed, monitoring such a small volume can be really demanding, especially if this task is addressed by means of FEAs, as strongly refined meshes will be required (*Kanvinde et al., 2007*).

To overcome this issue, characteristic volume-independent ("generalized") ductile damage criteria (GDDC) can be introduced (*Jia et al., 2014*) by further extending Rice & Tracey void enlargement model. To this end, a damage state variable $\omega_D = 0.0 \div 1.0$ can be introduced according to Equation 3.17:

$$\omega_D = \int_{t_i}^{t_f} \frac{d\varepsilon_{pl,eq}(t)}{\varepsilon^*_{pl,eq}(t; \sigma_{ij}; \dots)} \qquad (3.17)$$

with t_i and t_f being the considered initial and final analysis steps, respectively and $\varepsilon^*_{pl,eq}$ being a generalized critical equivalent plastic strain, which can be, on principle, a function of the considered time step *t*, of the stress field (or appropriate combinations of stress variables) and, generally speaking, of other field variables such as temperature (*Johnson & Cook, 1985*).

In light of a peculiar choice of $\varepsilon^*_{pl,eq}$ trend, generalized ductile damage criteria can be "specialized" to model different materials. Nevertheless, when ω_D equals unity, punctual damage (i.e., generally speaking, *not* failure) is predicted to occur, and therefore the material locally starts to soften until fracture.

The most immediate choice for $\varepsilon^*_{pl,eq}$ is represented by the critical strain predicted by SCMS criterion (Equation 3.13b). Although this choice leads to a very similar failure model with respect to SMCS formulation, it should be remarked that, in this case, no assumptions are made on the control volume in which the failure criterion has to be fulfilled, as to each point is associated a distinct damage state variable.

It is worth remarking that, when selecting stress triaxiality T as the main parameter affecting the value of critical PEEQ, the use of an analytical expression to link these variables is not essential. Indeed, T- $\varepsilon^*_{pl,eq}$ relation can be conveniently expressed by the so-called *triaxiality curves* (*Bonora, 1997*). Triaxiality curves can also directly account for the material strain rate dependence, if relevant (*Callister Jr., 2005*).
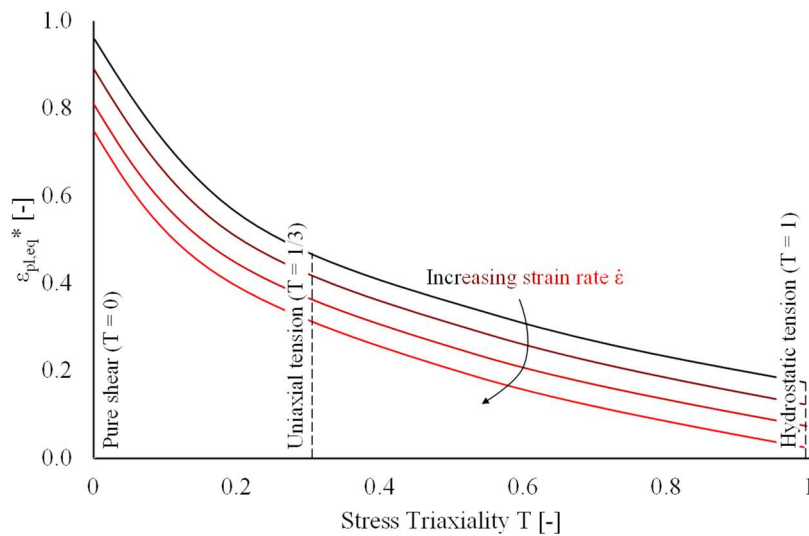
Figure 3.4 Typical triaxiality curves for ductile metals.

The typical shape of triaxiality curves for ductile metals is depicted in Figure 3.4. As a corollary of *Rice & Tracey* (*1969*) findings, triaxiality curves usually have a decreasing tendency for increasing values of T, with the worst condition represented by hydrostatic tension (T = 1).

However, it is worth noting that metallic materials may have a non-monotonic T- $\varepsilon^*_{pl,eq}$ trend when subjected to plane stress conditions (*Kõrgesaar, 2019*), with a maximum value of critical equivalent plastic strain achieved for T ≈ 1/3. Indeed, when plane stress conditions are achieved (e.g., in case of in plane-loaded thin shells and plates), a clear distinction can be between shear-failing specimens (T < 1/3) and necking-failing specimens (T ≥ 1/3). Nevertheless, generally speaking, the assumption of monotonically decreasing triaxiality curve can be considered sufficiently accurate for most practical purposes (*Yang et al., 2019*).

With regard to some metallic materials (e.g., Titanium or Nickel alloys – *Mirone et al., 2016*), a dependence of critical equivalent plastic strain on the so-called Lode angle $0 \leq \xi \leq \pi/3$ (Equation 3.18 – *Lode, 1926*) was also observed, i.e., the angle between the stress tensor projection on the deviatoric plane and the pure shear line (*Malcher et al., 2014*):

$$\xi = \frac{1}{3} \arccos \left(\frac{3\sqrt{3}}{2} \frac{J_3}{J_2^{3/2}} \right) \tag{3.18}$$

with J_2 and J_3 being the second and the third *main stress tensor invariant*, respectively (that is, stress invariants associated to the deviatoric stress tensor **S** – *Irgens, 2008*). In case of Lode angle-sensitive materials, *Lode curves* with analogous meaning to triaxiality curves can be conveniently defined (Figure 3.5 – *Erice et al., 2014*) based on interpretation of coupled axial-torsional experimental tests (*Mirone et al., 2016*).

Equivalently, shear fracture failure, when relevant, can be governed by means of the *shear stress ratio* $\theta_s = (k_s \sigma_m + \sigma_{eq,VM})/\tau_{max}$, with k_s being an experimental material parameter. A typical value of k_s for aluminium is $k_s = 0.3$ (*Hooputra et al., 2004*).

Finally, an explicit dependence on J_3 is also usually introduced in case of unsymmetric tensile-compressive fracture locus (e.g., in case of wrought and puddle iron, which show ductile compressive failure and brittle and premature tensile failure in light of the significant carbon content C > 2% – *Di Lorenzo et al., 2021*).
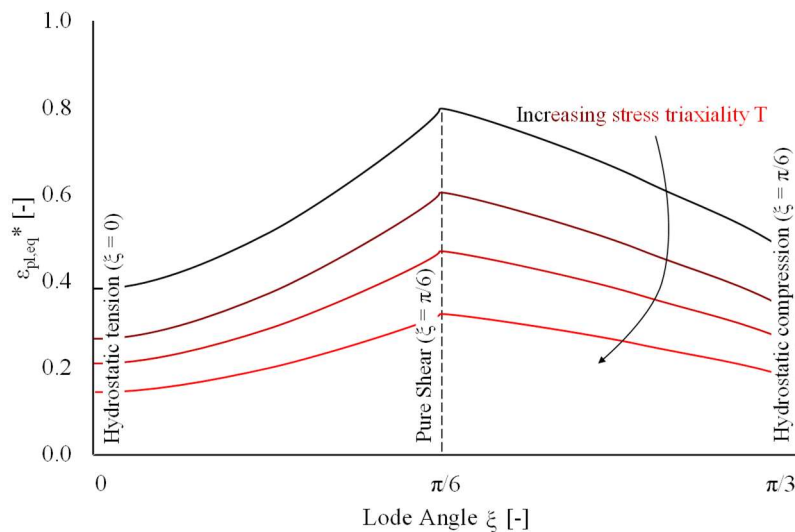
Figure 3.5 Typical Lode curves for some ductile metals, e.g. Titanium or Nickel alloys (adapted from *Erice et al., 2014)*.

Indeed, J_3 is the only main stress invariant parameter able to tell apart hydrostatic tension from hydrostatic compression, as J_2 is an even function and J_1 is identically null (*Irgens, 2008*).

3.1.7 Damage Evolution Criteria

When GDDC are adopted to capture ductile failure of metals, proper *damage evolution criteria* (DEC) could be also introduced to account for material damaged behaviour for $\varepsilon_{pl,eq} \geq \varepsilon^*_{pl,eq}$. Indeed, as opposed to VGM, SMCS and CVGM criteria, GDDC may account for a residual, post-cracked stiffness of materials before macroscopic fracture (*Hillerborg et al., 1976*).

DEC postulate the existence of a single damage evolution variable $D_e = 0.0 \div 1.0$ according to which the equivalent (Von-Mises) stress-strain constitutive law softens up to failure (Equation 3.19):

$$\sigma_{eq,VM,D} = (1 - D_e)\, \sigma_{eq,VM} \qquad (3.19)$$

with $\sigma_{eq,VM,D}$ being the "effective" Von-Mises equivalent stress for the damaged material. Consistently, extreme values of $D_e = 0.0$ and $D_e = 1.0$ are associated to a pristine and a completely failed material, respectively. It is worth remarking that, in the most general case of non-monotonic loadings, D_e both affects *i*) the material "effective" yield stress and *ii*) the re-loading residual stiffness $E_{res} = (1 - D_e)\, E$, with E being the pristine material Young Modulus (Figure 3.6 – *Hillerborg et al., 1976*).

Among the several literature proposals, two approaches linking the damage evolution variable with equivalent plastic strains gained the highest popularity, i.e. the *energy-based approach* and the *displacements-based approach*.

Accordingly, D_e monotonically increases depending on the fracture energy dissipation G_f or on the plastic displacement u_{pl} up to failure, respectively (Equation 3.20a-b):

$$G_f = \int_{\varepsilon^*_{pl,eq}}^{\bar{\varepsilon}_{pl,eq}} L_{char}\, \sigma_{eq,VM,D}\, d\varepsilon_{pl,eq} \qquad (3.20a)$$

$$u_{pl} = L_{char} \left(\bar{\varepsilon}_{pl,eq} - \varepsilon^*_{pl,eq} \right) \qquad (3.20b)$$
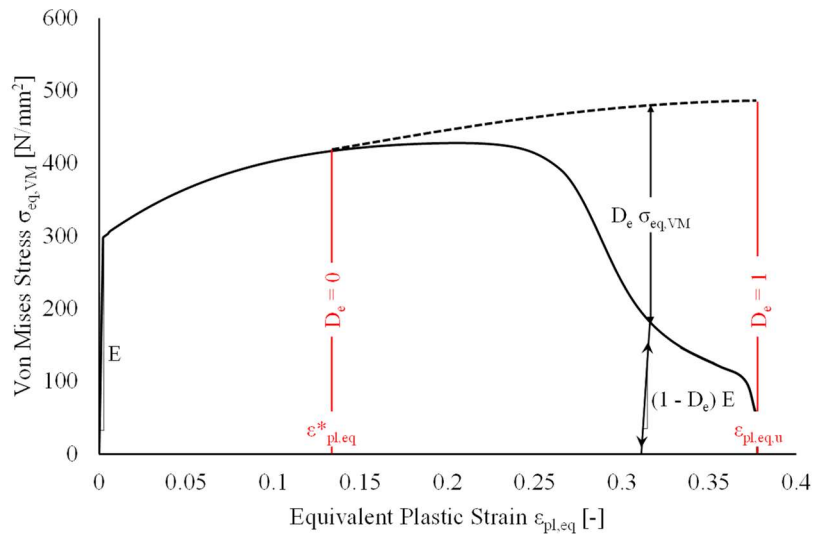
Figure 3.6 Typical softening behaviour of a damaged material according to DEC (adapted from *Hillerborg et al., 1976)*.

with $\bar{\varepsilon}_{pl,eq}$ being the PEEQ ($\geq \varepsilon^*_{pl,eq}$) for a given analysis step and L_{char} being a characteristic length parameter.

The introduction of L_{char} in both G_f and u_{pl} definitions is not a coincidence, as both quantities were conceived to be implemented in the framework of the Finite Element Method. Namely, by including a characteristic length in damage evolution monitoring, the strong mesh dependency exhibited by dissipated energy, yield stress and plastic strains for a damaged material can be effectively mitigated (*Hillerborg et al., 1976*).

In both cases, critical values of G^*_f and u^*_{pl} are assumed to be attained in correspondence of a (conventional) ultimate equivalent plastic strain $\varepsilon_{pl,eq,u}$ (that is, failure is predicted to occur when $\bar{\varepsilon}_{pl,eq} = \varepsilon_{pl,eq,u}$ in Equation 3.20a-b). Conventionality of $\varepsilon_{pl,eq,u}$ derives from the impracticability, in many real situations, of its explicit derivation on the basis of experimental outcomes. For practical purposes, direct estimation of G^*_f or u^*_{pl} is usually pursued with the aid of numerical tools to interpretate test results (*Yang et al., 2019*).

Although the energy-based formulation is sometimes used when dealing with some *Ti*, *Cu* or *Ni* alloys (*Qu et al., 2016*), it is worth noting that the displacement-based approach is arguably the most suitable for ductile metals. To this end, both linear (Equation 3.21a) and exponential (Equation 3.21b) trends have been proposed to describe the functional link among u_{pl} and D_e (*Ammar et al., 2022*):

$$\text{Linear DEC: } D_e = \frac{u_{pl}}{u^*_{pl}} \tag{3.21a}$$

$$\text{Exponential DEC: } D_e = \frac{1 - e^{\alpha_D \left(u_{pl}/u^*_{pl} \right)}}{1 - e^{\alpha_D}} \tag{3.21b}$$

with $\alpha_D \geq 0$ being an experimental parameter accounting for damage-displacement non-linearity. Notably, linear DEC can be considered as a particular case of exponential DEC for $\alpha_D \to 0$ (Figure 3.7). Moreover, when such analytical relations are used to link the damage state variable and the plastic displacement, equivalent energy-based formulations can be immediately deduced by observing that G_f is directly proportional to the underlying area in the $\sigma_{eq,VM}$ - u_{pl} plane for any given value of u_{pl}. For example, regarding to the simplest case of linear DEC, it can be easily derived that $G_f = u_{pl} \sigma_{eq,VM}/2$ (*Ammar et al., 2022*).
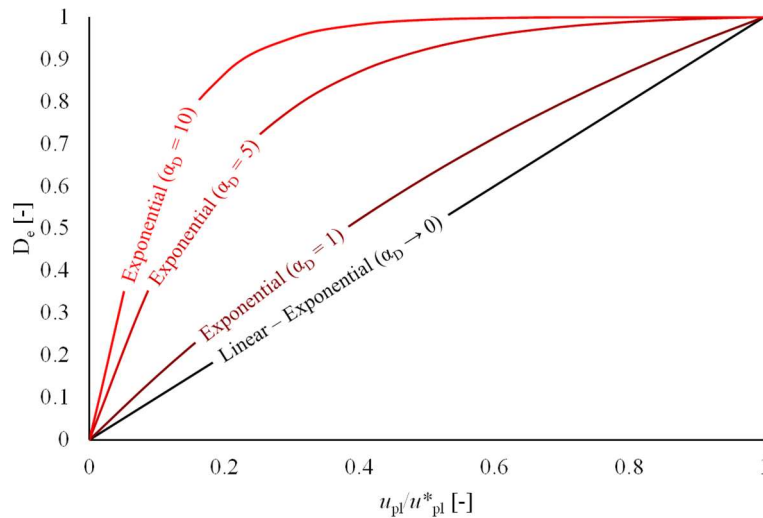
Figure 3.7 Graphical representation of linear and exponential displacement-based DEC.

3.2. Application of damage models for hot-driven riveted connections

As stated in *Section 2.3.2*, main peculiar issues affecting hot-driven riveted connections lie in the strong variability of *i*) rivets material overstrength, *ii*) rivets and plates material ductility reduction and *iii*) cooling-induced clamping action. Each of these effects may be regarded as a consequence of hot-driving process and, to a lesser extent, of holes perforation technique (*D'Aniello et al., 2011; Marmo, 2011; Collette, 2014*).

To this end, introduced post-necking and damage formulations can be suitably applied to quantitatively describe the influence of hammering process. In the present work, a two stages procedure is introduced to calibrate material parameters accounting for the effect of hot-driving (Figure 3.8).

In *Stage I*, calibration of base material properties for both plates and undriven rivets is addressed based on tensile coupon test results. Subsequently, hot-driving effects can be quantitatively estimated (*Stage II*) by interpretating static tests results on assembled hot-driven riveted connections. For this purpose, few non-dimensional parameters with a clear physical meaning are introduced and inversely calibrated. Finally, a statistical interpretation of derived values is carried out to emphasize the actual degree of variability of driving-induced effects.

Within *Stage II*, a peculiar and immediate attention is given to clamping actions effect, which can be parametrically investigated by simulating variable σ_{clamp} stress fields according to *D'Aniello et al.* (*2011*) and *Leonetti et al.* (*2020*) experimental findings.

In order to preserve the governability of investigated phenomena from the clearest and most quantitative possible point of view, the following assumptions are made, namely:

Within Stage I

i) the LHM is used to model post-necking behaviour of both pristine plates and undriven rivets (Equations 3.3-3.4). For PDS, constant-volume stress-strain formulation (Equations 3.1-3.2) is used until the onset of necking, i.e., until CCC are fulfilled;

ii) a stress triaxiality-dependent GDDC (Equation 3.17) is introduced to capture the onset of damage in DDS for both pristine plates and undriven rivets. Namely, an analytical, monotonically decreasing expression is assumed for triaxiality curves (Equation 3.22 – Figure 3.9a) according to *Yang et al., (2019)*:

$$\varepsilon^{*}_{pl,eq} (T) = \varepsilon^{*}_{pl,eq,uniax} \, e^{\left[-\frac{3}{2}\left(T - \frac{1}{3} \right) \right]} \tag{3.22}$$

with $\varepsilon^{*}_{pl,eq,uniax}$ being the critical equivalent plastic strain at the onset of damage for the simplest case of uniaxial tension (T = 1/3).

Accordingly, a single GDDC parameter can be conveniently calibrated with the aid of inverse method (*Tu et al., 2019*) based on tensile coupon tests. Triaxiality-dependent formulation is preferred to more shear-oriented damage models (*Section 3.1.6*) to account for diverse collapse mechanisms occurring in connections without loss of generality (see *Chapter 4* for further details). Besides, no J_3 dependence is assumed as tested rivets and plates were made of mild steels rather than wrought or puddle iron.

iii) a linear displacement-based DEC (Equations 3.20b-3.21a – Figure 3.9b) is assumed for both pristine plates and undriven rivets to provide a simple, yet reliable description of material failure. To this end, u^{*}_{pl} values are directly estimated in place of $\varepsilon_{pl,eq,u}$ with the aid of refined FEAs (*Tu et al., 2019*).
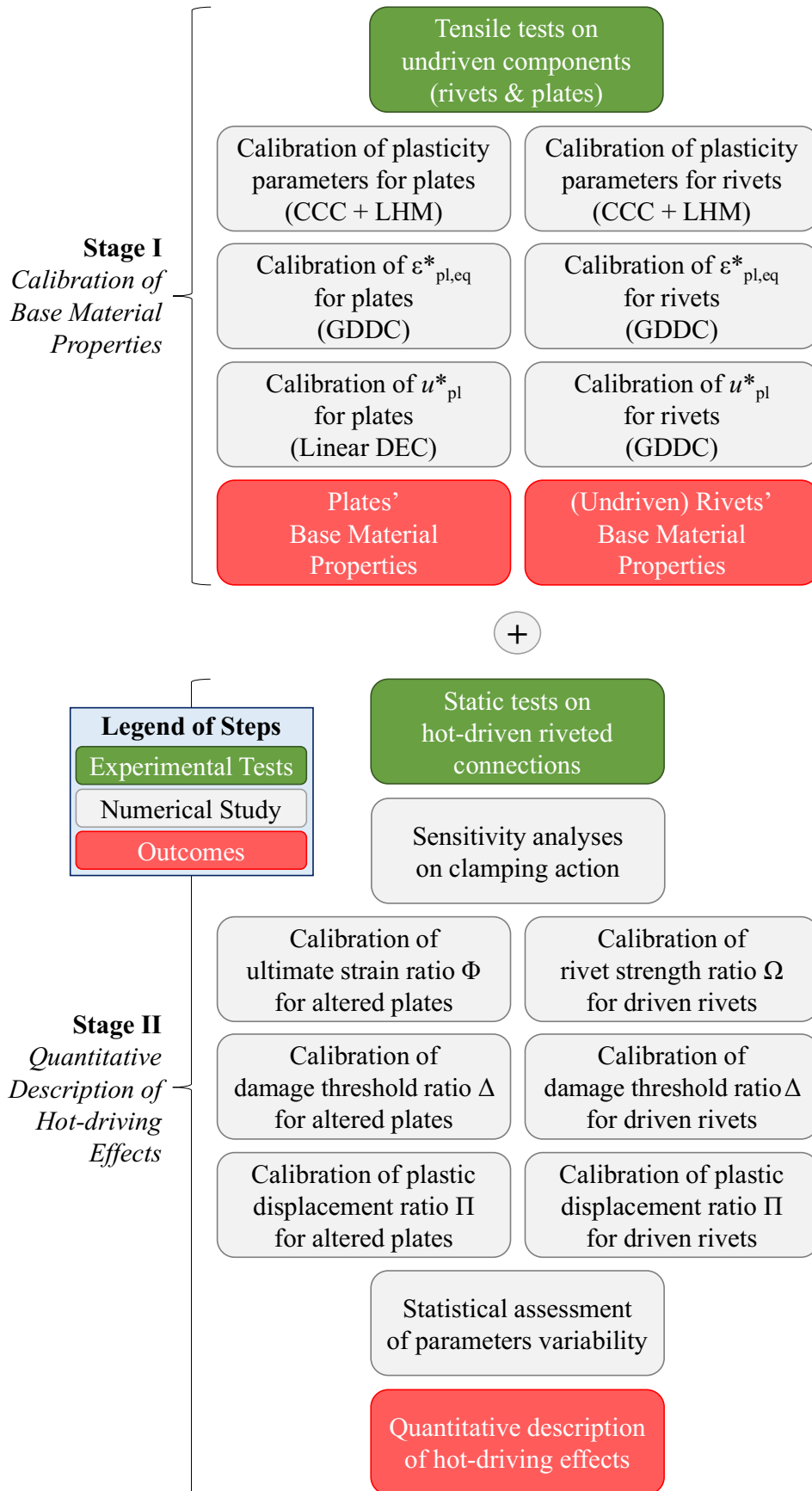
Figure 3.8 Adopted two stages procedure for the quantitative description of hot-driving effects on the structural performance of investigated riveted connections.
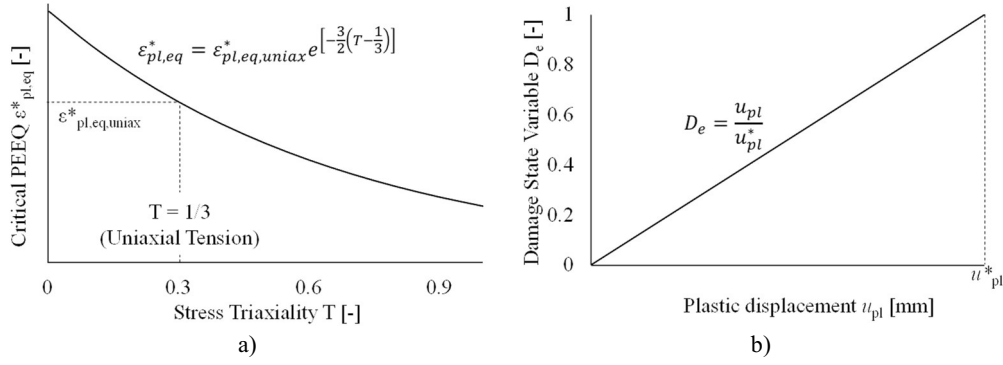
Figure 3.9 Adopted a) triaxiality curves (*Yang et al., 2019*) and b) linear DEC for pristine plates and undriven rivets.

Within Stage II

i) no coupled thermo-mechanical analysis is performed to assess the influence of hot-driving process, as it would result in a further source of uncertainty and a severe increment of computational effort. Indeed, as heating and cooling conditions are overly impractical to monitor in many real situations (*Section 2.1.2 – Kulak et al., 1987; Duggal, 2000; D'Aniello et al., 2011*), the definition of realistic (time-depending) temperature fields on investigated assemblies is not a viable option. Moreover, a coupled analysis would require the introduction of a proper, thermo-mechanically formulated, finite element (*Dassault, 2014*) and of a temperature-dependent GDDC (*Johnson & Cook, 1985*).

Therefore, purely mechanical FEAs are performed, based on which the effects of hot-driving are a-posteriori estimated;

ii) as a consequence, the parametrical study on clamping actions effect is carried out by imposing a clamping stress field on rivets, i.e., having variable amplitude within the ranges suggested by *D'Aniello et al.* (*2011*) and *Leonetti et al.* (*2020*).

iii) the same post-necking, damage onset and damage evolution formulations assumed for base components are used for hot-driven connections, thus providing a congruent comparison among the mechanical response of undriven and assembled parts. Effects of hot-driving are hence estimated by recalibrating relevant model parameters based on static tests results.

For this purpose, four non-dimensional parameters are appositely introduced. For the sake of clarity, in the following the subscript "*0*" is referred to undriven material properties, while no subscript is adopted for "real", post hot-driving material properties:

- The *rivet strength ratio* $\Omega = f_{yr}/f_{yr0} \geq 1$, which describes the beneficial effect of hot-driving on the yield and ultimate strength of rivets. Accordingly, Ω is used to homothetically scale the true stress-strain behaviour of pristine rivets (Figure 3.10a);

- The *ultimate strain ratio* $\Phi = \varepsilon_{true,fail,p}/\varepsilon_{true,fail,p0} \leq 1$, which describes the detrimental reduction of plates ultimate true strain due to holes perforation and hot-driving. Accordingly, Φ is used to reduce plates' plastic true strains with no corresponding alteration of true stresses (Figure 3.10b);

- The *damage threshold ratio* $\Delta = \varepsilon^*_{pl,eq,uniax} / \varepsilon^*_{pl,eq,uniax,0} \leq 1$, which describes the negative influence of hot-driving in terms of anticipation of damage onset on rivets and, to a local extent, plates. Accordingly, Δ is used to downscale triaxiality curves based on *Yang et al.* (*2019*) formulation (Figure 3.10c);

- The *plastic displacement ratio* $\Pi = u^*_{pl}/u^*_{pl0} \leq 1$, which describes the detrimental, hot-driving induced embrittlement of rivets and, on a local extent, plates. Accordingly, Π is used to downscale the critical plastic displacement within the framework of a linear DEC (Figure 3.10d).
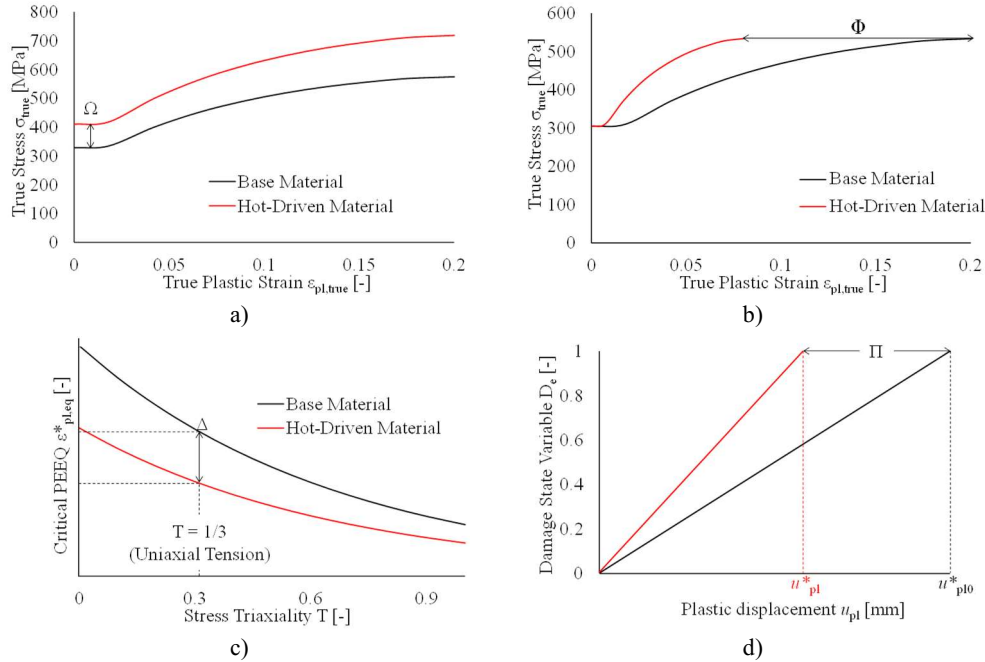
Figure 3.10 Graphical interpretation of non-dimensional parameters introduced to assess the effects of hot-driving: a) rivet strength ratio Ω, b) ultimate strain ratio Φ, c) damage threshold ratio Δ, d) plastic displacement ratio Π.

iv) statistical assessment of the above parameters is addressed by assuming that each quantity behaves as a random variably following either a normal or, when relevant, lognormal probability distribution, i.e., in compliance with EN1990 recommendations (*CEN, 2002*). Accordingly, mean values and standard deviations are derived for all parameters by means of consolidated data regression techniques (*Wakefield, 2013*).

3.3. Standard fatigue analysis techniques for structural components

Fatigue performance of steel structures and structural components has become a relevant topic for civil engineering since the first half of XXth century, mainly due to the occurrence of some relevant fatigue-related failures (*Anderson, 2017*). Sudden collapses indicated that steel constructions conceived to endure relevant cyclic actions during service life had to be preserved from fatigue failures due to their brittle nature, in order to avoid severe human and economic losses (*ECCS, 2018*).

Several advances in the understanding of fatigue phenomenology have been made up to recent times and, while the general topic of fatigue assessment of structural components still remains one of the most fruitful fields of research nowadays, "standard" techniques for the fatigue assessment of structural components in the framework of civil engineering can be now found in literature and normative provisions in force (*Milone et al., 2022b*). Two main families of standard methods are regarded as the most popular options for fatigue performance analysis, namely the *stress-life methods* (or *S-N methods*) and the *strain-life methods* (or *ε-N methods*), although only the former assessment philosophy is

currently encoded in European normative provisions (i.e., EN1993:1-9 for structural steel – *CEN, 2005a*).

3.3.1 Overview of Stress-Life Methods

The main concept behind the whole family of stress-life methods derives from the experimental observation that, when structural components are subjected to fluctuating stresses of constant (nominal) amplitude σ_a, a decreasing trend of fatigue life against increasing values of σ_a is obtained, albeit with a certain scatter of results. Contrariwise, for rather low values of σ_a, fatigue life proves to be basically unlimited, as tested specimens do not break even for an exceedingly large number of loading cycles.

Such phenomena can be noticed independently from the actual complexity of the considered structural detail (*ECCS, 2018*).

In light of the above, stress-life methods attempt to derive a functional link between fatigue life in terms of cycles to failure (N) and applied stresses (S), which are regarded as the main parameter influencing fatigue performance.

Comprehensive experimental campaigns dating back up to 150 years ago, starting from pioneering works of *Wohler (1860)* on rail car axes, revealed that fatigue cracks rarely occur and propagate in the base material remotely from any geometrical discontinuity or constructional detail, e.g., sharp corners, holes, mechanically fastened and welded connections. Such details remain critical spots for fatigue performance even if their static resistance is higher than assembled members, as they act as *stress raisers* (*ECCS, 2018*).

Within the framework of S-N methods, two alternative approaches can be followed to deal with such issue, namely (Figure 3.11 – *ECCS, 2018*):

- the definition of "*detail categories*", each one of them characterized by a given geometry, for which fatigue strength domains are defined in terms of nominal applied stresses and derived based on experimental tests;
- the characterization of base material fatigue properties (regarded as an intrinsic material parameter) and the subsequent estimation of fatigue life based on *actual maximum stresses* attained nearby a given constructional detail.

The former option is referred as "*Nominal Stress Method(s)*" (CEN, 2005a; *ECCS, 2018,* see *Section 3.3.2* for further details) and it arguably represents the simplest option for engineers addressing fatigue design, since the complex task of deriving the fatigue strength domain for a given detail is unrequired in many real situations, as it can be easily found within documents of sanctioned validity (i.e., normative codes and/or standards). Therefore, after global structural analysis is performed, elastic stresses in parent members nearby the detail can be easily calculated and used for fatigue verifications.

Currently, within the framework of steel structures, a wide list of 114 detail categories is encoded in EN1993:1-9 (*CEN, 2005a*), ranging from plain members to mechanically fastened joints, welded connections, stiffening details, tubular joints, orthotropic bridge decks, etc… Additionally, 5 fatigue categories are reported in EN1993:1-11 (*CEN, 2006*) for tension structural components (e.g., wires, strands, ropes, or prestressing bars).

The latter option is instead referred as "*Hot-Spot Stress Method(s)*" (CEN, 2005a; *ECCS, 2018,* see *Section 3.3.4* for further details), and it is usually adopted for critical structural details in which fatigue cracking is a-priori regarded as a design-governing phenomenon (e.g., load carrying welded joints). In this case, the aid of refined FEAs is allowed and fatigue checks are performed through few "master" fatigue strength domains. Notably, although a single domain should be sufficient for a given base material, multiple curves are usually available to account for the effect of different manufacturing processes.

STATIC SYSTEM

Road Bridge

TRANSVERSE CROSS-SECTION

Bridge Deck

Gusset Plate

Cross Girder

Main Girder

STRUCTURAL DETAIL

Web
Gusset

Flange

NOMINAL STRESS METHOD

Web
Gusset

$\sigma_{elastic}$

Flange

+

Detail category	Constructional detail	Description
100	④	4) Non-load carrying fillet welds.

HOT-SPOT STRESS METHOD

Fillet Weld

Gusset Plate

Crack
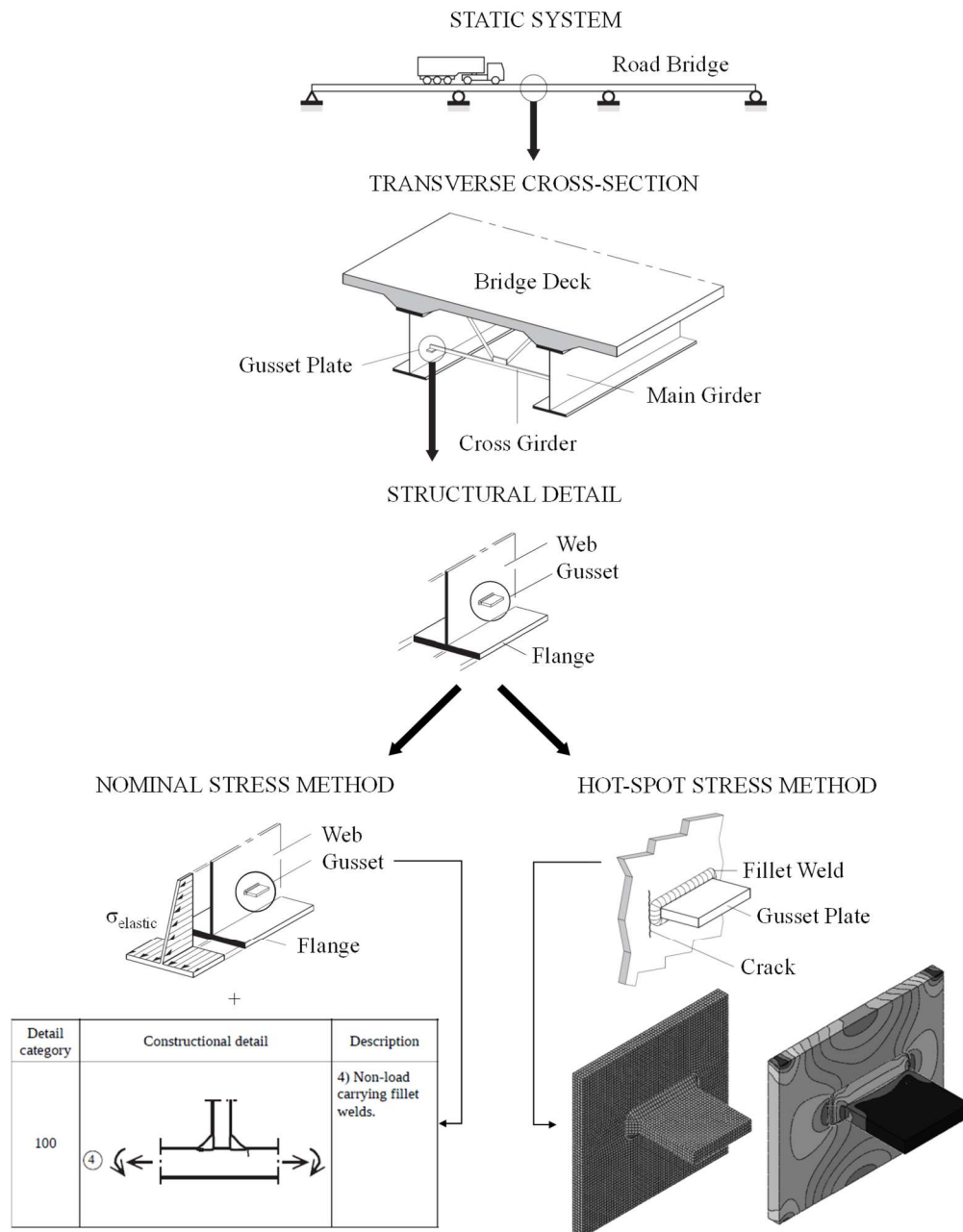
Figure 3.11 Stress-Life Methods for the fatigue analysis of a typical bridge constructional detail (adapted from *ECCS, 2018*).

3.3.2 Nominal Stress Methods

When applying Nominal Stress Methods, the main theoretical model describing the evolution of fluctuating stresses is represented by the *sinusoidal stress cycle* (Figure 3.12), i.e., an idealization of a real stress history shaped as a sine-wave. Such an approximation is a convenient choice as its mathematical description is provided by a periodic function of few and easily governable parameters, namely:

- The *maximum stress* σ_{max}, which is representative of the combined (additive) action of permanent loads (if any) and fluctuating stresses;
- The *minimum stress* σ_{min}, which is representative of the combined (subtractive) action of permanent loads (if any) and fluctuating stresses;

- The *mean stress* $\sigma_m = (\sigma_{max} + \sigma_{min})/2$, i.e. the average stress applied during the load cycle, which can detrimentally affect fatigue performance in some relevant cases (*Milone et al., 2022c*). Alternatively, the *stress ratio* $R = \sigma_{min}/\sigma_{max} \leq 1$ can be used to non-dimensionally describe the entity of mean stresses;
- The *stress range* $\Delta\sigma = \sigma_{max} - \sigma_{min}$, i.e. the "true" fatigue demand associated to the load cycle, depurated from static stress components. Alternatively, *stress amplitude* $\sigma_a = \Delta\sigma/2$ can be used to describe the fatigue demand.
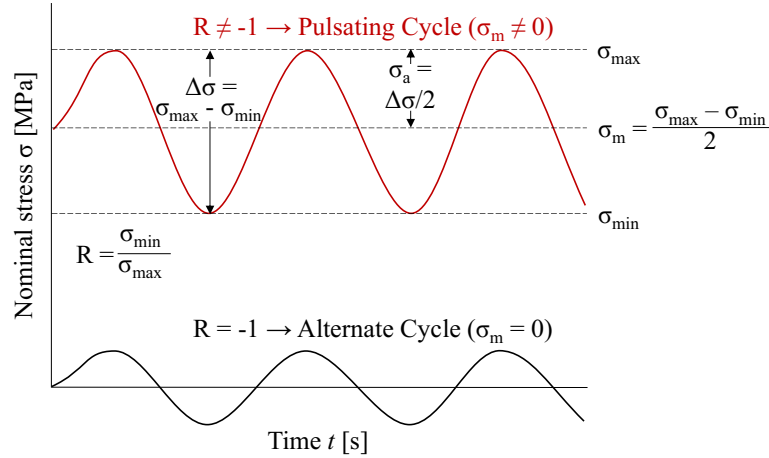
Figure 3.12 Representation and governing parameters for a sinusoidal stress cycle (*Anderson, 2017*).

It is worth remarking that only two independent parameters are needed to fully describe a sinusoidal stress cycle, as other quantities can easily derived from each other with arithmetical expressions (Equation 3.23a-c). Common choices are the following couples $(\sigma_{max}; \sigma_{min})$, (σ_a, σ_m) and $(\Delta\sigma, R)$:

$$\sigma_{max}; \sigma_{min} \qquad \Delta\sigma = 2\sigma_a = \sigma_{max} - \sigma_{min}; \sigma_m = \frac{\sigma_{max} + \sigma_{min}}{2}; R = \frac{\sigma_{max}}{\sigma_{min}} \qquad (3.23a)$$

$$\sigma_a; \sigma_m \qquad \Delta\sigma = 2\sigma_a; \sigma_{max}, \sigma_{min} = \sigma_m \pm \sigma_a; R = \frac{\sigma_m - \sigma_a}{\sigma_m + \sigma_a} \qquad (3.23b)$$

$$\Delta\sigma; R \qquad \sigma_a = \frac{\Delta\sigma}{2}; \sigma_{max} = \frac{\Delta\sigma}{1 - R}; \sigma_{min} = \frac{R\,\Delta\sigma}{1 - R}; \sigma_m = \frac{(1 + R)\,\Delta\sigma}{2\,(1 - R)} \qquad (3.23c)$$

For this simplest case of sinusoidal load histories, the fatigue strength of a given structural detail can be conveniently expressed in terms of *S-N* (or *Wohler*) *curves* linking the nominal stress range $\Delta\sigma$ to the observed number of cycles at failure N* (Figure 3.13 – *ECCS, 2018*).

S-N curves graphically summarize the outcomes of an experimental program for the detail of concern, which shall involve a sufficient amount of specimens in order to properly measure the results scatter. Indeed, even nominally identical test conditions for apparently identical test specimens systematically result in different values of N*. This occurs due to ineradicable small differences in the parameters which affect fatigue life (misalignments, tolerances, etc… – *ECCS, 2018*).

Remarkably, earlier experimental campaigns already proved how this scatter becomes larger for lower stress ranges (*Schijve, 2009*). Nevertheless, mean values of constant-amplitude fatigue tests results appear to order themselves on straight lines when plotted
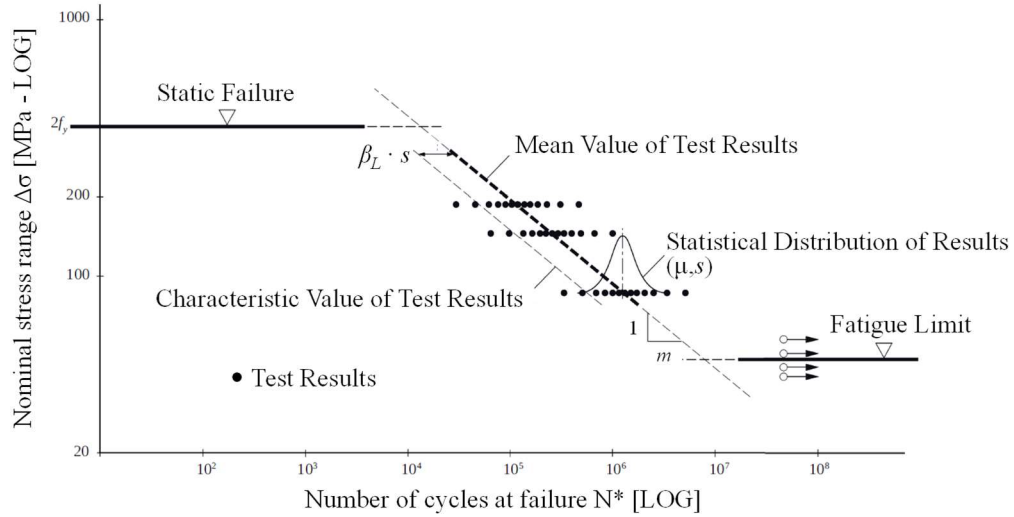
Figure 3.13 Fatigue resistance domain (S-N curve) for a structural steel detail tested under constant amplitude loading (adapted from *ECCS, 2018*).

on a double logarithmic scale (Figure 3.13 – bold dashed line). This property, which is not coincidental as it can be derived according to fracture mechanics considerations (*Anderson, 2017; ECCS, 2018*), is used to provide an handy analytical description of S-N curves (Equation 3.24):

$$N^* = C \, (\Delta\sigma)^{-m} \leftrightarrow \log N^* = \log C - m \log \Delta\sigma \qquad (3.24)$$

with C, *m* being logarithmic regression coefficients representing the influence of the structural detail (i.e., the fatigue strength of the detail for a conventional number of cycles at failure N_C) and the reciprocal (log-)slope of the mean results line, respectively. This expression is often referred as "*Basquin formula*", as it was first proposed by *Basquin* (1910), although in a slightly different form relating elastic strain reversals $\Delta\varepsilon_{el}/2$ to the number of reversal at failure 2N*. It is trivial that Equation 3.24 can be immediately deduced from Basquin original formulation by introducing the base material Young Modulus E.

In case of fully reverse (or "*alternate*") cycles, i.e. for R = -1, the upper limit of the S-N curve is represented by twice the ultimate material strength f_u.

Following the curve pattern, the region within $10^1 \leq N^* \leq 10^4$ is referred as Low-Cycle Fatigue range (LCF), i.e., a range in which significant cyclic plasticity is expected for ductile materials. For civil engineering purposes, LCF strength is considered relevant only in peculiar conditions, e.g., in case of earthquakes or pressure surges (*ECCS, 2018*). The subsequent region ($10^1 \leq N^* \leq 10^8$) is referred as High-Cycle Fatigue range (HCF), i.e., a range in which fatigue fracture occurs while the base material behaves elastically. The lower limit of the line is represented by the so-called *endurance limit*, or constant-amplitude fatigue limit (CAFL). Accordingly, lower values of $\Delta\sigma$ < CAFL (having constant amplitude) can be applied to the structural component without incurring in fatigue failure even for a very large number of cycles (> 10^8 – *ECCS, 2018*).

The emphasis on requiring a constant amplitude for test stress ranges is not coincidental, as aperiodic stress histories can lead to fatigue failure even if applied $\Delta\sigma$ are below the endurance limit (*Anderson, 2017*). Indeed, if earlier stress fluctuations are sufficiently high to induce crack opening, thus even small $\Delta\sigma$ can contribute to crack propagation and hence cause fatigue damage.

Moreover, in some relevant cases no fatigue limit can be clearly defined even under constant-amplitude loadings (e.g., for aluminium components or for pre-stressing high-strength steel strands – *ECCS, 2018; Milone et al, 2022c*).

This issue can be overcome by *i*) explicitly accounting for fatigue cracking development or, approximately, *ii*) assuming a finite, yet superior, fatigue strength for $\Delta\sigma < \text{CAFL}$. As proposed by *Haibach* (*1970*), this can be accomplished by adopting a broken line shaped S-N curve with increased reciprocal slope $m_2 = 2m - 1$ for $\Delta\sigma < \text{CAFL}$. A similar expedient was suggested by *ECCS* (*1985*), which recommended a value of $m_2 = m + 2$ (Figure 3.14a). Accordingly, identical values of m_2 are obtained for $m = 3$ ($\rightarrow m_2 = 5$), while for $m > 3$, ECCS correction results in more severe fatigue checks.

To this end, EN1993:1-9 (*CEN, 2005a*), EN1993:1-11 (*CEN, 2006*) and EN1999:1-3 (*CEN, 2007*) all follow ECCS suggestions for the relevant case of steel, high-strength steel (HSS) and aluminium details, respectively (Figure 3.14b).
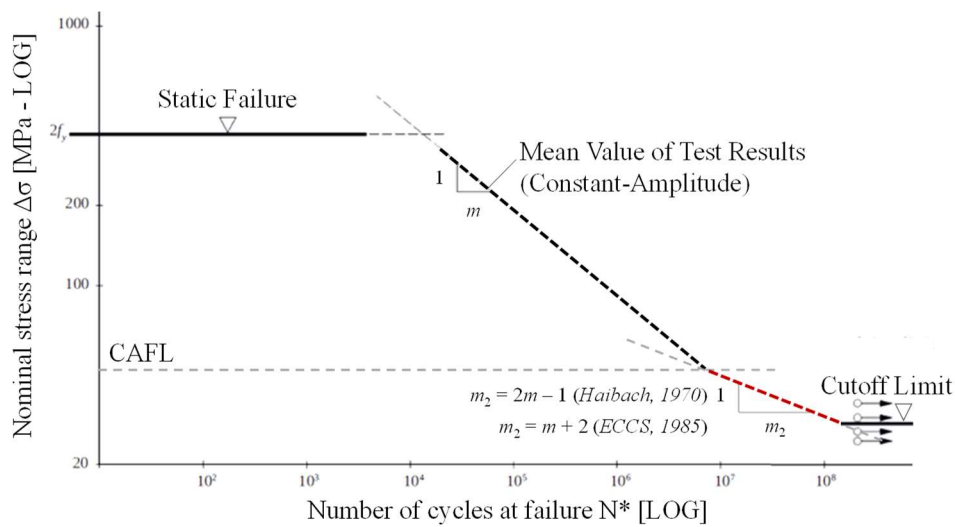
a)
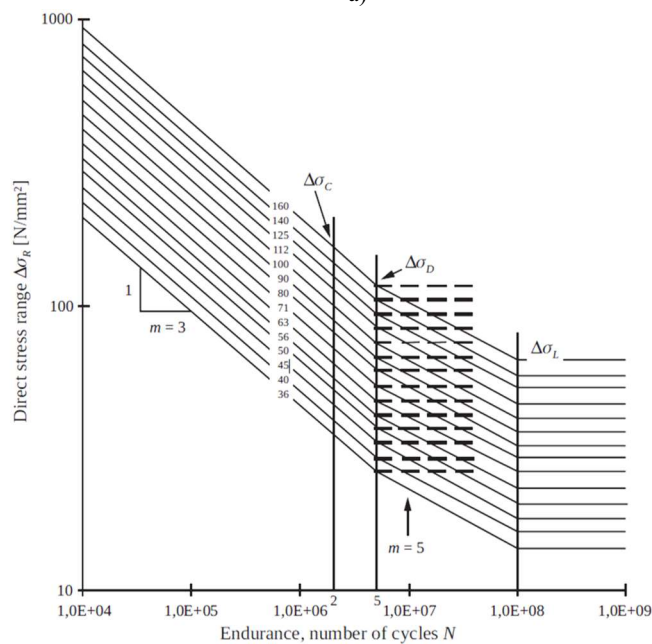
b)

Figure 3.14 a) Correction of the S-N curve accounting for variable-amplitude fatigue loadings (adapted from *ECCS, 2018*) and b) EN1993:1-9 S-N curves (*CEN, 2005a*).

The only differences refer to *i*) the adoption of different slopes *m* for the first branch of S-N curves (i.e., *m* = 3 for all steel structural details – *CEN, 2005a*, *m* = 4 for HSS details – *CEN, 2006* – while *m* = 3.4, 4.0, 4.3 or 7 for aluminium components depending on the considered detail – *CEN, 2007*) and *ii*) the presence of a *cut-off limit* (COL), i.e. a stress range limit below which no fatigue damage is assumed even under variable-amplitude loadings (that is, no COL is present for HSS and aluminium details according to experimental evidence – *ECCS, 2018*).

In all mentioned normative provisions, the influence of a given structural detail (see Equation 3.24, regression coefficient C) is conventionally addressed by introducing a *detail class* $\Delta\sigma_C$, i.e., the constant-amplitude stress range leading to fatigue failure for $N_C = 2 \cdot 10^6$ cycles. In EN1993:1-9, 14 different detail classes ($\Delta\sigma_C = 36 \div 160$ N/mm^2, see Figure 3.14b) are appropriately associated to each of the 114 detail categories as suggested in the relevant Chapter 8.

As for the CAFL (referred as $\Delta\sigma_D$ in structural Eurocodes), its definition is provided for a conventional number of cycles at failure $N_D = 5 \cdot 10^6$. Finally, the COL (referred as $\Delta\sigma_L$ in structural Eurocodes) is associated to a threshold value of $N_L = 10^8$ cycles.

Notably, as assumed reciprocal slopes are the same for all listed S-N curves, CAFL and COL can be directly estimated by downscaling $\Delta\sigma_C$ as follows, independently from the detail category of concern (Equation 3.25a-b):

$$\Delta\sigma_D = \left(\frac{N_C}{N_D}\right)^{1/m} \Delta\sigma_C = \left(\frac{2}{5}\right)^{1/3} \Delta\sigma_C = 0.737\ \Delta\sigma_C \tag{3.25a}$$

$$\Delta\sigma_L = \left(\frac{N_D}{N_L}\right)^{1/(m+2)} \Delta\sigma_L = \left(\frac{5}{100}\right)^{1/5} \Delta\sigma_D = 0.549\ \Delta\sigma_D = 0.405\ \Delta\sigma_C \tag{3.25b}$$

3.3.3 Fatigue Assessment for Variable-Amplitude Nominal Stresses

As clearly remarked in the previous Section, aperiodic stress histories represent a delicate topic when assessing the fatigue performance of structural components. Provided that an appropriate correction of S-N curves has been applied to account for the fatigue strength sensitivity to variable-amplitude nominal stresses (*Haibach, 1970; ECCS, 1985*), two further aspects need to be properly addressed when dealing with complex load histories, namely *i*) the reduction of such histories to a finite ensemble of stress ranges $\Delta\sigma_i$ that can be compared against S-N curves and *ii*) the cumulation of fatigue damages d_i associated to each extrapolated stress range $\Delta\sigma_i$.

With regard to the former aspect, several so-called *cycle-counting algorithms* can be found in both scientific literature and normative provisions, e.g., *peak count* methods, *level crossing count* methods, the *reservoir count* algorithm, the *rainflow count* algorithm. Among the others, the last two methods gained the highest popularity owing to their reliability and sound mathematical formulation (*ECCS, 2018*), and they are currently listed in normative provisions in force (*CEN, 2005a; CEN, 2006; CEN, 2007*).

Main steps of the reservoir count method can be summarized as follows (Figure 3.15):

i) rearrangement of the stress history, i.e., by cutting it at its absolute maximum and moving the left part so obtained at the end of the diagram, in such a way that the modified diagram is bounded by two absolute maxima;

ii) sort of the relative minima ("*valleys*") of the stress history in ascending order (1', 2', …, *i*', …, *n*');

iii) consideration of the modified stress history as *the bottom of a water reservoir*, virtually filled up to the absolute maxima (this operation give name to the algorithm);
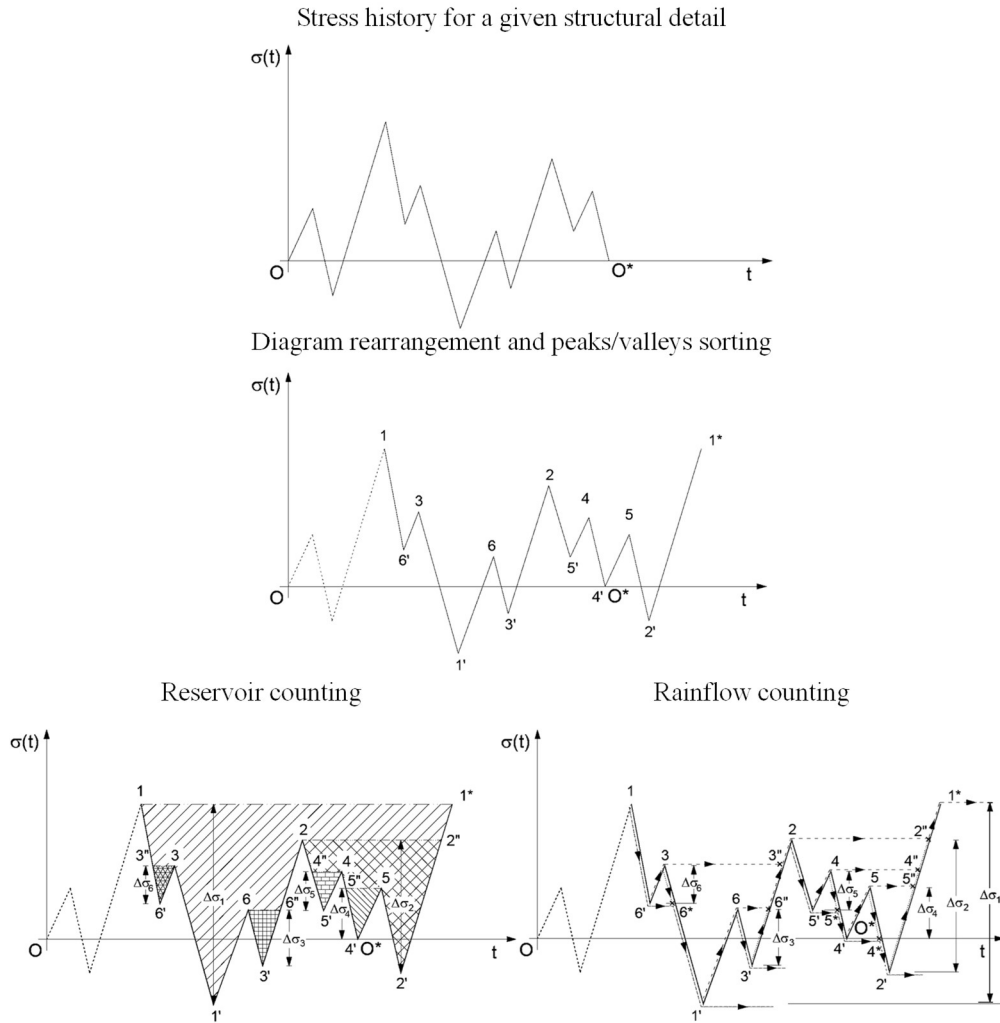
Figure 3.15 Main steps of the reservoir and rainflow counting methods (adapted from *CEN, 2020*).

iv) drainage of the reservoir from the valleys sorted in ascending order until it is completely empty. Accordingly, each discharging operation corresponds to one cycle having stress range $\Delta\sigma_i$ equal to the height of the discharged water.

v) coupling of cycles having the same stress range by adding up the relevant number of cycles.

The reservoir count method is sometimes preferred to the rainflow count method in light of its higher simplicity, as the two methods yield the exact same results, provided that they are applied correctly (*CEN, 2005a*). Nevertheless, the rainflow algorithm is recommended by EN1993:1-9 as it retains some (indirect) information about loading sequences owing to the adopted counting condition (*ECCS, 2018*).

Main steps of the rainflow count method, which was originally developed by the Japanese engineer Tatsuo Endo and his collaborator Masanora Matsuishi (*Matsuishi & Endo, 1968*), can be summarized as follows (Figure 3.15):

i) rearrangement of the stress history, i.e., by cutting it at its absolute maximum and moving the left part so obtained at the end of the diagram, in such a way that the modified diagram is bounded by two absolute maxima;

ii) virtual rotation of the stress history diagram by 90 degrees (clockwise), in such a way that the positive direction of the time axis is pointing downwards;

iii) sort of the relative maxima ("*peaks*") of the stress history in descending order (1, 2, …, *i*, …, *n*) and of the relative minima ("*valleys*") of the stress history in ascending order (1', 2', …, *i*', …, *n*').

iv) consideration of the rotated diagram as a guide for a sequence of raindrops falling from peaks and valleys due to the effect of gravity (this operation give name to the algorithm);

v) release of each drop from peaks in descending order and from valleys in increasing order of the stress history itself. Accordingly, the followed path by each drop on a dry part of the guide identifies a semi-cycle and its width measured along the ordinates represents the stress range of the semi-cycle $\Delta\sigma_i$. Each drop path ends when an already wet part or the end of the diagram is encountered;

vi) coupling of semi-cycles having the same stress range by adding up the relevant number of semi-cycles.

Rainflow method is regarded as the "gold standard" option for cycle counting, as it provides a better statistical reduction of load histories featuring numerous peaks and valleys with respect to other methods. Moreover, it allows an improved handling of both very large extreme values and small intermediate ranges, independently from the nature of the load history (narrow- or broad-band, flat or steep – *Schijve, 2009; ECCS, 2018*).

Soundness of rainflow method lies also in its correlation to the phenomenology of cyclic plasticity, when relevant. Indeed, as originally showed by *Matsuishi & Endo* (*1968*), each drop path uniquely relates to a closed hysteresis stress-strain (half-)loop.

This counting algorithm finally established its superiority during the '80s of XXth century, when *Rychlik* (*1987*) provided a closed-form mathematical definition for it, thus enabling its large-scale implementation in fatigue analysis software.

Independently from the adopted algorithm, the result of cycle counting operation is represented by the so-called *load spectrum*, i.e., a convenient description of the load history in terms of number n_i of equivalent, constant-amplitude, stress cycles having range $\Delta\sigma_i$. In many real applications, load spectra show a monotonically decreasing trend (Figure 3.16); that is, a given load history can be usually decomposed in few high-ranged stress cycles and in a significant number of small fluctuations.

Moreover, if the original stress history is represented by a continuous function, the resulting load spectrum is continuous as well. However, for practical purposes, the spectrum can be further reduced to a histogram, in which a convenient set of stress intervals can be assumed.
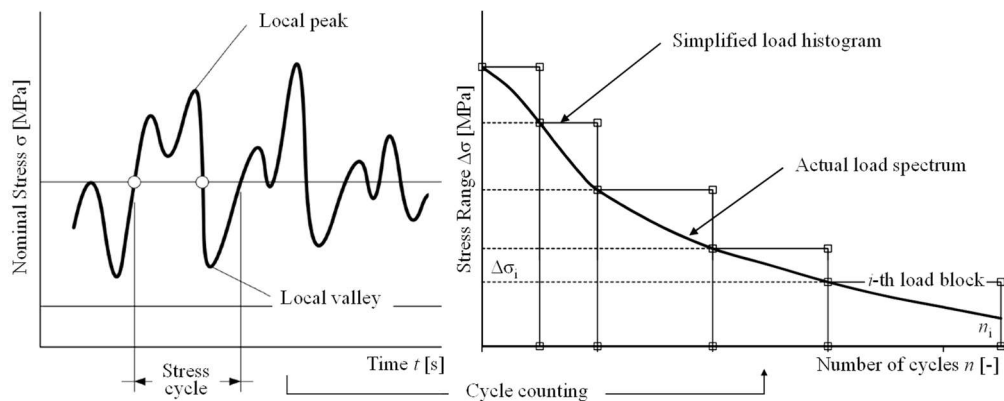
Figure 3.16 Example of derivation of the load spectrum for a given stress history and subsequent reduction to a load histogram (adapted from *ECCS, 2018*).

When doing so, the maximum stress range for each resulting block should be conservatively taken as a reference for the enveloped portion of the original load spectrum (*ECCS, 2018*).

With regard to damage cumulation, the simplest, yet most popular formulation is represented by the linear superposition of *i*-th elementary damage values d_i, one for each counted stress range $\Delta\sigma_i$ (Equation 3.26):

$$D_{TOT} = \sum_{i=1}^{n_{TOT}} d_i = \sum_{i=1}^{n_{TOT}} \frac{n_i}{N_i^*} = \int_{LS} \frac{dn}{N^*} \qquad (3.26)$$

with D_{TOT} being the total fatigue damage associated to a load history described by a load spectrum LS, which can be conveniently regarded as a number n_{TOT} of stress blocks.

Linear damage cumulation formula was first proposed by *Palmgren* (*1923*) and hence popularized by *Miner* (*1945*), thus it is usually referred as Palmgren-Miner's (PM) rule. According to PM rule, the *i*-th elementary damage is expressed as the ratio between the number of cycles n_i associated to the *i*-th stress range $\Delta\sigma_i$ and the expected number of cycles at failure N_i^* for the same stress range, with the latter being estimated using the relevant S-N curve.

When cumulating damage, stress ranges below the COL threshold may or may not be accounted for. The most conservative approach is clearly to disregard the COL and to further extend the previous branch of the S-N curve (Figure 3.17a – *ECCS, 2018*) Alternatively, to stress ranges $\Delta\sigma_i$ < COL an infinite fatigue life can be associated; that is, d_i ($\Delta\sigma_i$ < COL) = 0. However, as PM completely overlooks the actual sequence of applied loads, it is recommended to assume an infinite fatigue life only if the entire load spectrum in enclosed below the COL, in light of considerations reported in *Section 3.3.2* (Figure 3.17b – *ECCS, 2018*).

Fatigue failure is assumed to occur for a total damage threshold value $D^*_{TOT} = 1.0$. It is worth remarking that several experimental outcomes contradict this assumption, not least the ones derived by *Wohler* (*1860*) in its original work on fatigue of rail car axes. Indeed, as noticed by *Wirsching (*1987*)* when statistically assessing Wohler's results, the fatigue failure threshold for variable-amplitude loadings rather behaves as a lognormally distributed random variable with unitary mean and COV = 0.3 → $D^*_{TOT} \sim LN(1.0; 0.3)$. However, for practical engineering purposes, assuming $D^*_{TOT} = 1$ is often the only viable option, while uncertainties related to unavoidable constructional imperfections and to the influence of load sequences are overcome by means of proper partial safety factors.
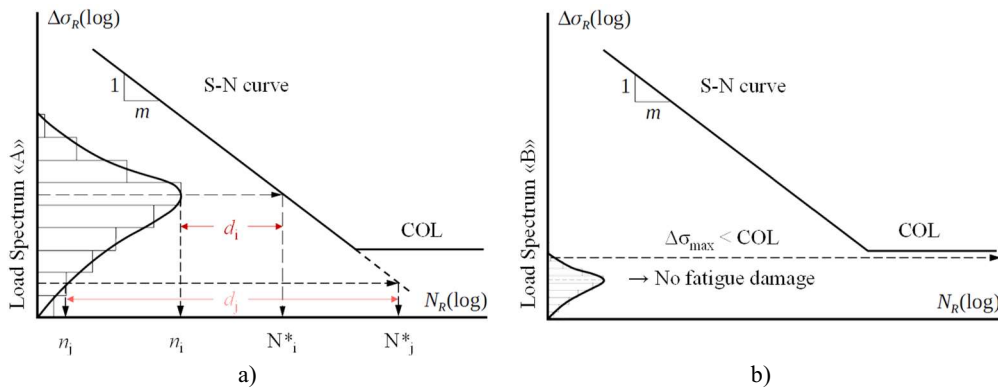
Figure 3.17 Linear damage cumulation (PM) rule for load spectra exceeding (a) or not exceeding (b) the COL (adapted from *ECCS, 2018*). For the sake of simplicity, a constant slope is assumed for $\Delta\sigma$ > COL.

For instance, this is the approach followed by EN1993:1-9, which encodes PM rule with unitary threshold for *Damage-Tolerant* (DT) fatigue checks. Accordingly, partial safety factors are applied to both fatigue demand (stress ranges) and fatigue strength (S-N curves), i.e., γ_{FF} and γ_{MF}, respectively (Table 3.1, first row). Fatigue damage is assumed to be tolerable provided that PM checks are fulfilled and that proper and periodic inspections are performed to detect macroscopic fatigue cracks (*CEN, 2005a*).

An alternative philosophy is represented by the *Safe-Life* (SL) approach, which requires to perform only a punctual check on the highest stress range $\Delta\sigma_{f,max}$, which should be compared with the relevant COL $\Delta\sigma_L$ (Equation 3.27 – *CEN, 2005a*):

$$\text{SL:} \quad \gamma_{FF}\,\Delta\sigma_{f,max} = \Delta\sigma_{Ed} \leq \Delta\sigma_{Rd} = \frac{\Delta\sigma_L}{\gamma_{MF}} \tag{3.27}$$

Uncoincidentally, this resembles the condition depicted in Figure 3.17b. Within the framework of SL approach, fatigue damage is assumed to be null for the entire reference structural life L_{ref}. Therefore, no inspections are required to detect fatigue damage (*CEN, 2005a*). However, considerably higher partial safety factors are needed as a trade-off for performing a simplified check and disregarding on-site fatigue damage detection (Table 3.1, second row).

Table 3.1 Partial safety factors recommended by EN1993:1-9 (*CEN, 2005a*) for fatigue checks.

Fatigue Demand	γ_{FF} = 1.0 in absence of more accurate evaluations	
Fatigue Strength		
Failure consequences *Selected approach* γ_{MF} =	Low consequences	High consequences
Damage-Tolerant (DT)	1.00	1.15
Safe-Life (SL)	1.15	1.35

3.3.4 Mean-Stress Effect in Nominal Stress Methods

Experimental tests on several structural components proved how the fatigue life can significantly reduce in presence of high tensile mean stresses $\sigma_m > 0$ (*Dowling, 2004*). Contrariwise, no decrease or even, in some cases, a slight improvement of fatigue performance was observed for $\sigma_m < 0$ (*Anderson, 2017*).

This phenomenon, which is referred as "*mean-stress effect*" in scientific literature, can be easily explained in terms of enhanced crack propagation for $\sigma_m > 0$, as tensile stresses promote crack opening, while propagation gets inhibited by compressive stress fields (Anderson, 2017). Moreover, as reported in *Section 3.1.2*, in case of ductile metals, tensile stress fields (especially if multiaxial) accelerate voids enlargement, leading to damage and premature voids coalescence (*Rice & Tracey, 1969*).

Mean-stress effect can be relevant in many civil engineering applications, e.g., bridge structures, owing to the presence of significant permanent loads and in light of adopted structural schemes (*Gimsing et al., 2012*). Nevertheless, while several literature models have been proposed to account for this effect (*Dowling, 2004*), it still remains only partially addressed in normative provisions in force (*CEN, 2005a*).

For instance, HSS wire ropes adopted for cable-stayed bridges usually endure fluctuating loads having stress ratio R ≈ 0.4 (*Milone et al., 2022c*) while, for riveted and bolted details adopted in truss bridges, common values of R are in the range 0.0 ÷ 0.5 in service conditions (*Parola et al., 1964*).

Therefore, unconservative fatigue predictions may be obtained by applying the nominal stress method if mean-stress effect is completely overlooked.

Within the framework of stress-life methods, several corrections to Basquin formula (Equation 3.24) have been proposed to account for the mean-stress effect (*Gerber, 1874; Goodman, 1899; Soderberg, 1930; Morrow, 1968; Walker, 1970; Smith, Watson & Topper, 1970*).

Gerber (*1874*) first proposed a fatigue strength domain according to which strength reduction is proportional to the mean-stress work rate, i.e. the ratio between σ_m and the material ultimate tensile strength (UTS) f_u. Notably, a quadratic dependence on σ_m/f_u ratio was suggested on the basis of experimental evidences on puddle-iron components (Equation 3.28):

$$\text{Gerber (1874):} \quad \frac{\sigma_a}{f_f} + \left(\frac{\sigma_m}{f_u}\right)^2 \leq 1 \tag{3.28}$$

with f_f being the fatigue strength for fully-reversal loadings (R = -1) estimated for the target number of cycles at failure N*. Accordingly, fatigue failure in presence of tensile mean stresses was predicted when exceeding the unitary threshold value.

Goodman (*1899*) cautiously suggested to linearly account for mean-stress work rate, proposing an equation that still finds common application in fatigue design nowadays (Equation 3.29):

$$\text{Goodman (1899):} \quad \frac{\sigma_a}{f_f} + \frac{\sigma_m}{f_u} \leq 1 \tag{3.29}$$

Moreover, Goodman also first introduced a graphical interpretation of fatigue strength domains in the $\sigma_a - \sigma_m$ plane bearing his name (*Goodman-Haigh diagram*, Figure 3.18a). In Goodman-Haigh diagram, all possible fatigue demands sharing a given stress ratio R lie on a pencil of straight lines, i.e., centred in the origin and sweeping the diagram clockwise for increasing values of R.

When adopting such representation, the Gerber criterion is represented by a parabolic segment having f_f and f_u as intersections with the σ_a- and σ_m-axis, respectively. Conversely, Goodman criterion acts as the linearization of the *Gerber's parabola*, with this operation being safe due to Gerber's domain convexity.

In both cases, fatigue strength corrections are assumed for the lone range of tensile mean stresses (R > -1), while the fatigue strength for $\sigma_m < 0$ should be always cautiously equal to f_f even if an higher resistance is predicted.

a)
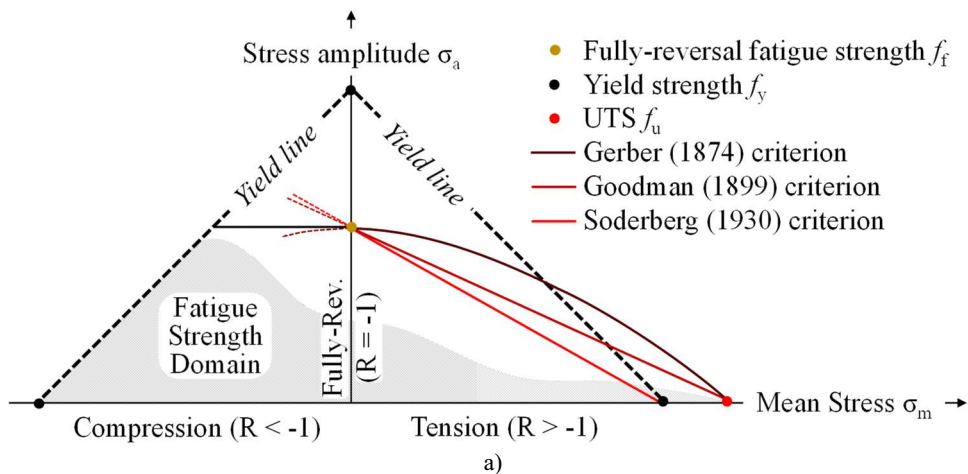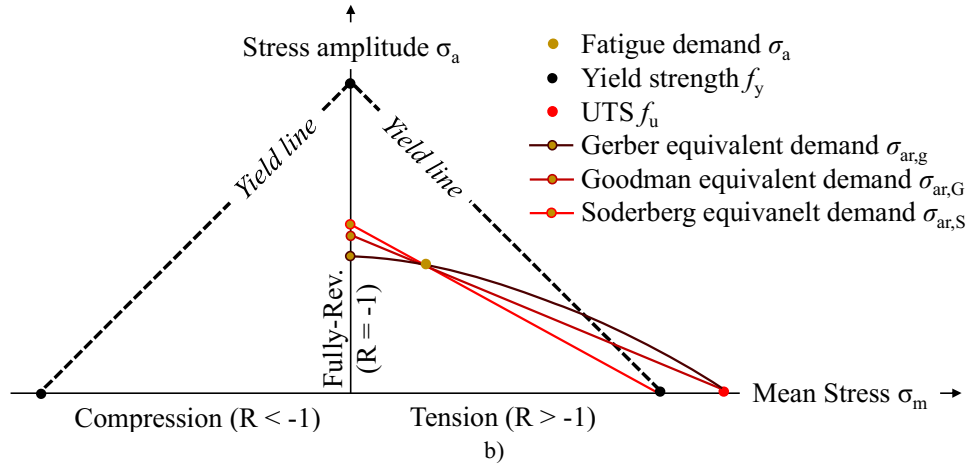
Figure 3.18 Graphical interpretation of *Gerber (1874), Goodman (1899) and Soderberg, (1930)* mean-stress corrections in the $\sigma_a - \sigma_m$ plane: a) fatigue strength domains and b) equivalent fully-reversal fatigue demands (adapted from *Milone et al., 2022c*).

For both Goodman and Gerber criteria, a slight incongruence can be graphically noticed with respect to yield lines, that is, the loci of points for which σ_{max} (for $R \geq -1$) or σ_{min} (for $R \leq -1$) equate the base material yield stress f_y, thus defining a threshold for LCF regime. Indeed, extreme portions of Gerber and Goodman domains both cross the tensile yield line (which is indeed inclined of -45 degrees with respect to coordinate axes). This is an obvious consequence of considering f_u in defining the mean-stress work rate.

This issue was overcome by *Soderberg (1930)*, which upgraded Goodman's formula by redefining the mean-stress work rate in function of f_y as follows (Equation 3.30):

$$\text{Soderberg (1930):} \quad \frac{\sigma_a}{f_f} + \frac{\sigma_m}{f_y} \leq 1 \tag{3.30}$$

Accordingly, Soderberg domain traces a second straight line in the Goodman-Haigh diagram, intersecting coordinate axes for $\sigma_a = f_f$ and $\sigma_m = f_y$, respectively, which can be conveniently truncated at f_f for $R \leq -1$. Therefore, this latter fatigue domain is coherently enclosed among the yield lines, and it represents the most severe option when compared with Gerber and Goodman criteria.

Still, Soderberg criterion did not encounter unanimous support among the scientific community, mainly because it leaded to overly conservative fatigue strength predictions in case of small, yet positive mean tensile stresses (*Milone et al, 2022c*). To this end, Goodman criterion gained the highest consent in light of its simplicity and ability to provide satisfactory strength estimations.

Nevertheless, as first highlighted by *Morrow (1968)*, Goodman criterion does not yield enough accurate results for very high stress ratios ($R \approx 0.7 \div 1.0$). Therefore, the Author suggested to shift the Goodman domain horizontal intercept towards the material true fracture strength $f_{u,true}$, resulting though in a loss of accuracy for small values of R.

Therefore, alternative approaches were followed both by *Smith, Watson & Topper (1970)*, hence also referred as "SWT", and by *Walker (1970)* to provide a more consistent description of mean-stress effect.

In both works, the effect of mean stresses was assumed to act on the *fatigue demand* side, rather than on the fatigue strength as suggested by earlier researchers. Accordingly, two similar formulations were proposed by the Authors (Equation 3.31a-b):

$$\text{SWT (1970):} \quad \sigma_{ar,SWT} = \sqrt{\sigma_a \, \sigma_{max}} = \sigma_a \sqrt{\frac{2}{1-R}} \quad \quad (3.31a)$$

$$\text{Walker (1970):} \quad \sigma_{ar,W} = \sigma_a^{\gamma} \, \sigma_{max}^{1-\gamma} = \sigma_a \left(\frac{2}{1-R}\right)^{1-\gamma} \quad \quad (3.31b)$$

with $\sigma_{ar,SWT}$ and $\sigma_{ar,W}$ being the equivalent fully-reversal fatigue demands that are expected to produce the same fatigue life as σ_a, respectively, and $\gamma = 0.0 \div 1.0$ being an empirical material parameter ("*Walker exponent*") quantifying the sensitivity to mean-stress effect.

Namely, for $\gamma = 0.0$ no influence of σ_m is assumed (that is, $\gamma = 0.0 \to \sigma_{ar} = \sigma_a$ for any value of σ_{max}). Contrariwise, for $\gamma = 1.0$ the mean-stress effect is totally governing fatigue failure, as any stress cycle will be regarded as a fully-reversal one with the same peak value (that is, $\gamma = 1.0 \to \sigma_{ar} = \sigma_{max}$ for any value of σ_a).

From Walker criterion perspective, SWT formulation can be clearly regarded as a particular case obtained by assuming $\gamma = 0.5$, i.e. considering a "balanced" sensitivity to mean-stress effect. The introduction of slightly different formulations descends from the considered sets of experimental observations (*Dowling, 2004*).

Indeed, while *SWT* (*1970*) investigated the fatigue performance of mild steel specimens (for which γ is actually rather close to 0.5), *Walker* (*1970*) focussed on aluminium components, proposing a calibrated value of $\gamma = 0.65$ (that is, aluminium is averagely more sensitive to mean-stress effect with respect to mild steel).

It is worth remarking that the above Gerber, Goodman and Soderberg criteria can all be equivalently expressed in terms of amplified fatigue demands, that is, by imposing the occurrence of fatigue failure in the right members of Equations 3.28-3.30 and thus solving for f_f (Equation 3.32a-c):

$$\text{Gerber (1874):} \quad \sigma_{ar,g} = \sigma_a \, \frac{1}{1 - \left(\frac{\sigma_m}{f_u}\right)^2} \quad \quad (3.32a)$$

$$\text{Goodman (1899):} \quad \sigma_{ar,G} = \sigma_a \, \frac{1}{1 - \frac{\sigma_m}{f_u}} \quad \quad (3.32b)$$

$$\text{Soderberg (1930):} \quad \sigma_{ar,S} = \sigma_a \, \frac{1}{1 - \frac{\sigma_m}{f_y}} \quad \quad (3.32c)$$

Notably, a graphical insight for equivalent fully-reversal fatigue demands according to *Gerber* (*1874*), *Goodman (*1899*)* and *Soderberg (*1930*)* formulations can be presented in the Goodman-Haigh diagram (Figure 3.18b). To this end, also *Walker* (*1970*) and *SWT* (*1970*) criteria could be represented in the $\sigma_a - \sigma_m$ plane, although neither of such criteria would result in a single trend on the plot, but rather they would form a family of curves (*Dowling, 2004*).

Addressing the mean-stress effect from the perspective of fatigue demand retains the undoubted advantage of using "standard" (i.e., encoded) S-N curves for fatigue checks. Accordingly, fatigue damage can be estimated based on equivalent fully-reversed stress ranges $\Delta\sigma_{eq} = 2 \, \sigma_{ar}$. In this regard, it is worth mentioning that both reservoir and rainflow count methods (see *Section 3.3.3*) easily allow to calculate mean stresses associated to each stress (half-)cycle.

Adopting the above formulations in presence of significant tensile stresses can be a suitable option when addressing normative-compliant fatigue design.

Indeed, EN1993:1-9 (*CEN, 2005a*) completely overlooks mean-stress effect for R > 0. This assumption can be considered sufficiently realistic for welded details (provided that they are non-stress relieved), as residual tensile stresses induced by welding process usually exceed tension fields in connected members. Therefore, experimental tests considered in the definition of welded detail categories intrinsically accounted for the mean-stress effect (*ECCS, 2018*).

Contrariwise, for the relevant case of stress-relieved or mechanically fastened details, a (favourable) mean-stress correction is only provided for R ≤ 0 (Figure 3.19). Indeed, if $\sigma_{min} < 0$, the compressive quota of the stress cycle can be reduced by 40%. Moreover, if the entire stress cycle is in compression, the whole stress range can be reduced by 40% (Equation 3.33a-c):

$$\sigma_{min} \geq 0 \rightarrow \Delta\sigma_{Ed} = \sigma_{max} - \sigma_{min} \tag{3.33a}$$

$$\sigma_{max} \geq 0, \sigma_{min} < 0 \rightarrow \Delta\sigma_{Ed,red} = \sigma_{max} - 0.6\,\sigma_{min} \tag{3.33b}$$

$$\sigma_{max} < 0 \rightarrow \Delta\sigma_{Ed,red} = 0.6\,(\sigma_{max} - \sigma_{min}) \tag{3.33c}$$
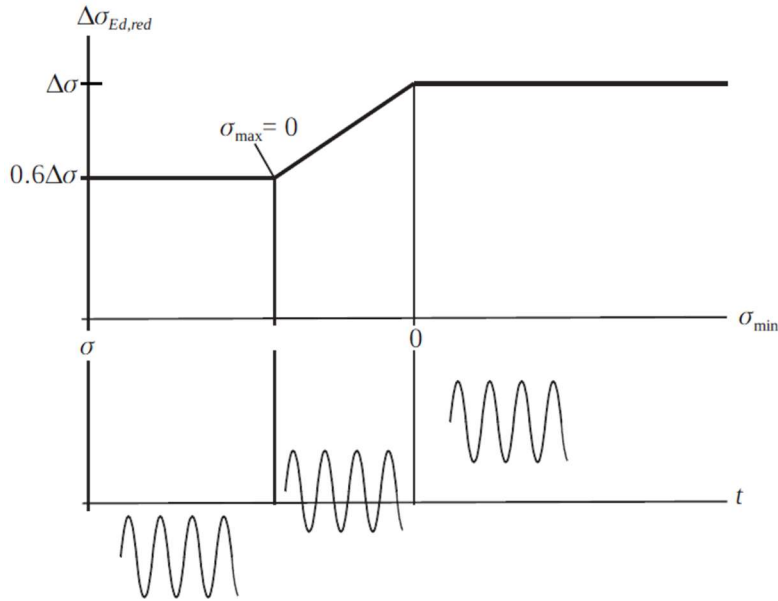
Figure 3.19 Graphical interpretation of mean-stress correction encoded in EN1993:1-9 (*ECCS, 2018*).

3.3.5 Hot-Spot Stress and Modified Stress Methods

As stated in *Section 3.3.1*, an alternative option to assess the fatigue performance of structural components within the framework of stress-life approaches is represented by the so-called *hot-spot stress method*. These methods aim at estimating the real stress acting on a potential crack spot, i.e. including all possible sources of stress rising associated to the structural detail of concern (*ECCS, 2018*).

Hot-spot stress method is particularly suitable for welded details in which the main principal stress is normal to the weld toe and thus fatigue cracking is expected to initiate from such spot (e.g., non-load carrying fillet welded details – *Niemi et al., 2006*).

To this end, standard procedures are available to extrapolate the hot-spot stress σ_{hs} at the weld toe starting from nearby locations, as a direct measure of weld-toe hot-spot stress

is unfeasible. Accordingly, local stress measures derived from testing or refined FEAs can be linearly projected up to the surface perpendicular to the weld toe (Figure 3.20a-b – *Schumacher, 2003*; *Niemi et al., 2006*; *ECCS, 2018*).

The extension of the extrapolation regions, within which the stresses to be projected should be estimated, is defined in documents of sanctioned validity for each relevant case (e.g., *IIW, 2000* for welds connecting plates and/or open profiles, *CIDECT, 2001* for hollow sections employed in tubular joints or *DNV, 2010* for FEM-based extrapolation).

It is worth remarking that, in both cases, microscopic effects (i.e., notch effects due to weld type and shape, flaws, etc…) cannot be directly accounted for even with highly refined measures. Therefore, a restricted, yet multiple set of hot-spot S-N curves should be used for fatigue checks to account for such effects (*ECCS, 2018*). To this end, 7 hot-spot welded detail categories are provided by EN1993:1-9, Annex B (*CEN, 2005a*), which are variously associated to 3 detail classes ($\Delta\sigma_{C,hs}$ = 90, 100 or 112 N/mm^2, respectively – Figure 3.21).

a)

b)
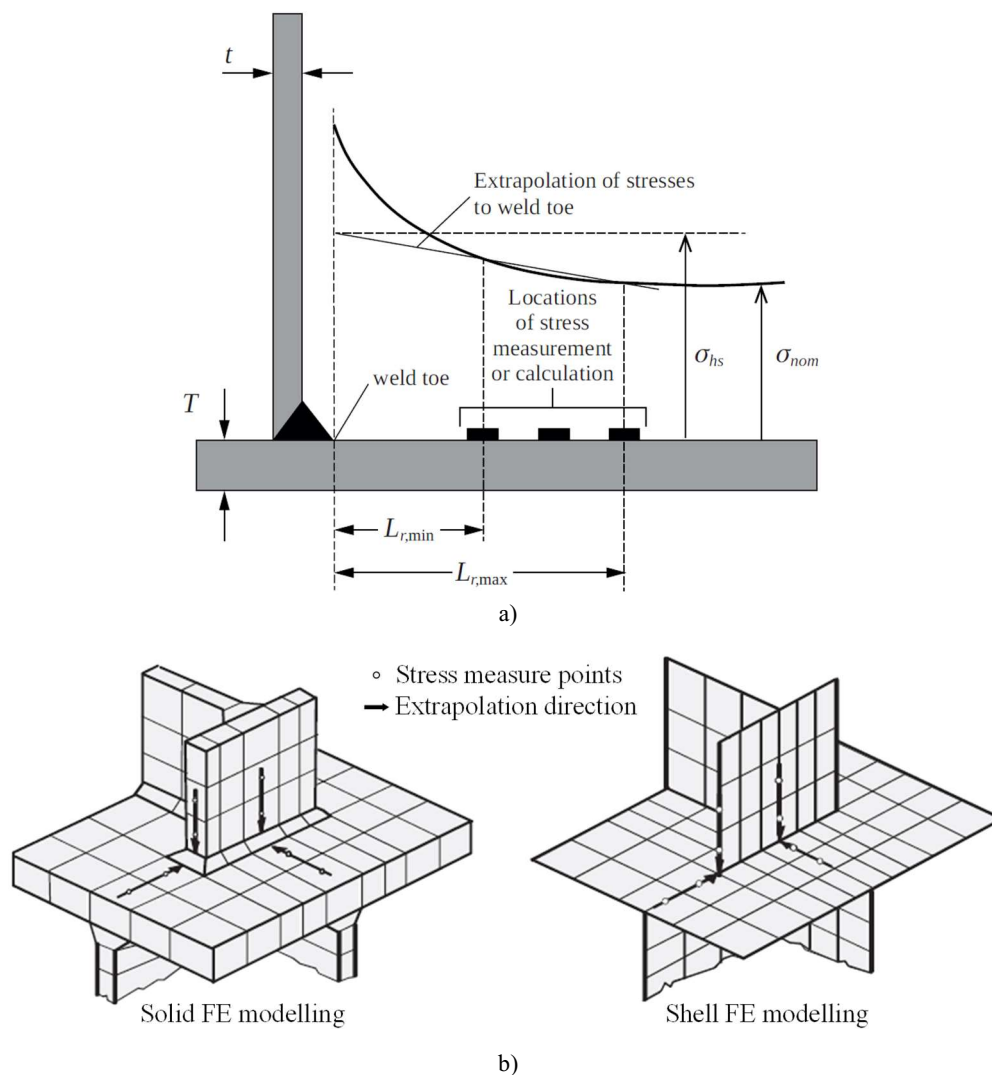
Figure 3.20 Extrapolation techniques of hot-spot stresses at the weld toe based on a) detail testing and b) advanced solid or shell FE modelling (adapted from *ECCS, 2018*).

Ff
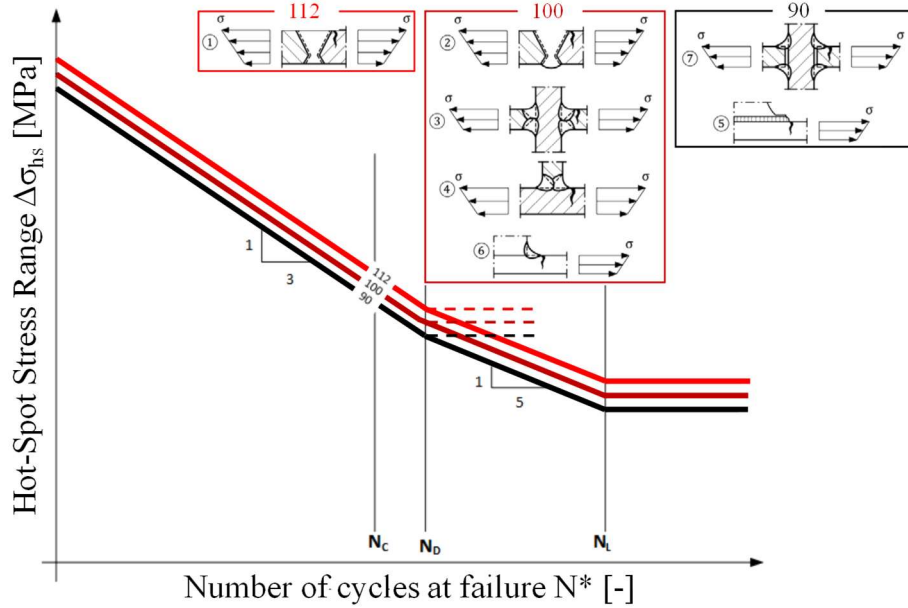
Figure 3.21 Hot-spot S-N curves for welded details encoded in EN1993:1-9 (adapted from *CEN, 2005a*).

Within the framework of normative provisions, the hot-spot stress method is only recommended for welded details that cannot be reduced to any of the standard detail categories or in case of complex stress fields expected at the weld toe. In other cases, *modified nominal stresses* should be used for fatigue checks (*CEN, 2005a*).

Modified nominal stress σ_{mod} is introduced for encoded structural details, yet subjected to stress raising sources not accounted for by normative S-N curves (e.g., macroscopic eccentricities, angular misalignments, re-entrant corners, complex shaped holes, etc...). The transformation of nominal stresses into modified ones is performed through non-dimensional *stress magnification* (or *concentration*) *factors* (SMFs – Equation 3.34), which should be borrowed from documents of sanctioned validity (e.g., *BS 7608, 2014*; *BS 7910, 2019*; *DNV, 2010*):

$$\prod_{i=1}^{\text{N stress raisers}} \text{SMF}_i = \frac{\sigma_{mod}}{\sigma_0} \tag{3.34}$$

Differently from the hot-spot stress method, modified nominal stress method finds its application also in the relevant case of riveted (and bolted) joints, that is, to account for the presence of holes (*ECCS, 2018*).

In this regard, SMFs for several configurations of perforated plates can be found in the renowned *Peterson's Handbook* (Figure 3.22 – *Peterson & Pilkey, 1997*). Namely, factors depending from geometrical properties of plates and rivets are there recollected in the form of charts (i.e., based on numerical analyses performed by several Authors). Consistently, presented abaci reduce to the well-known result of linear fracture mechanics (LFM), i.e. $\sigma_{mod,t} = 3\sigma_0$ for an thin, infinitely wide plate with a mid circular hole, with the maximum tensile stress being attained on both hole transverse quadrants (*Anderson, 2017*).

Conversely, the ideal LFM result in terms of maximum compressive stress (i.e., attained on the hole longitudinal quadrant closest to the plate edge) acts as a lower limit for plies in bearing, as Hertzian contact stresses (*Hertz, 1881*) superimpose to LFM solution.

Plate of finite width with a circular hole

$$\sigma_{max} = \sigma_A$$

$$K_{tg} = \frac{\sigma_{max}}{\sigma}$$

$$K_{tn} = K_{tg}\left(1 - \frac{d}{H}\right)$$

K_{tg}

K_{tn}

K_t

$$K_{tg} = 0.284 + \frac{2}{1 - \frac{d}{H}} - 0.600\left(1 - \frac{d}{H}\right) + 1.32\left(1 - \frac{d}{H}\right)^2$$

$$K_{tn} = 2 + 0.284\left(1 - \frac{d}{H}\right) - 0.600\left(1 - \frac{d}{H}\right)^2 + 1.32\left(1 - \frac{d}{H}\right)^3$$

For large H (infinite panel)
$\sigma_{max} = K_t \sigma_1$
$\sigma_A = 3\sigma_1$, $K_t = 3$
$\sigma_B = -\sigma_1$, $K_t = -1$

d/H
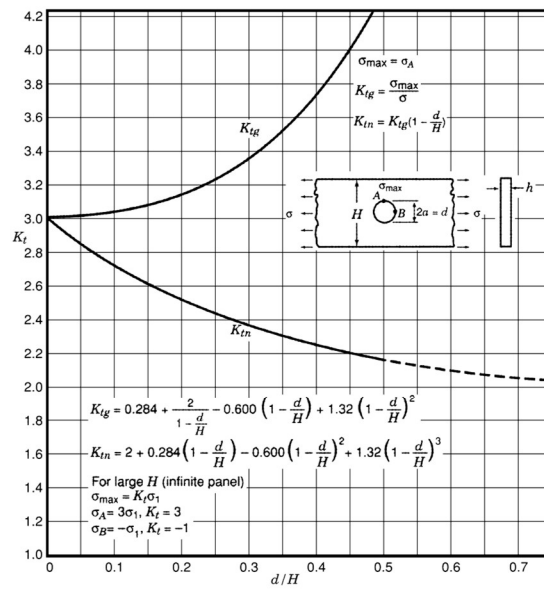
Plate of finite width with two circular holes

3.0

3.0 at ∞

K_t

$\frac{l}{d} = 0$ $\frac{l}{d} = 1$

$$K_t = \frac{\sigma_{max}}{\sigma}$$

for $0 \leq d/l \leq 1$

$$K_t = 3.000 - 0.712\left(\frac{d}{l}\right) + 0.271\left(\frac{d}{l}\right)^2$$

l/d
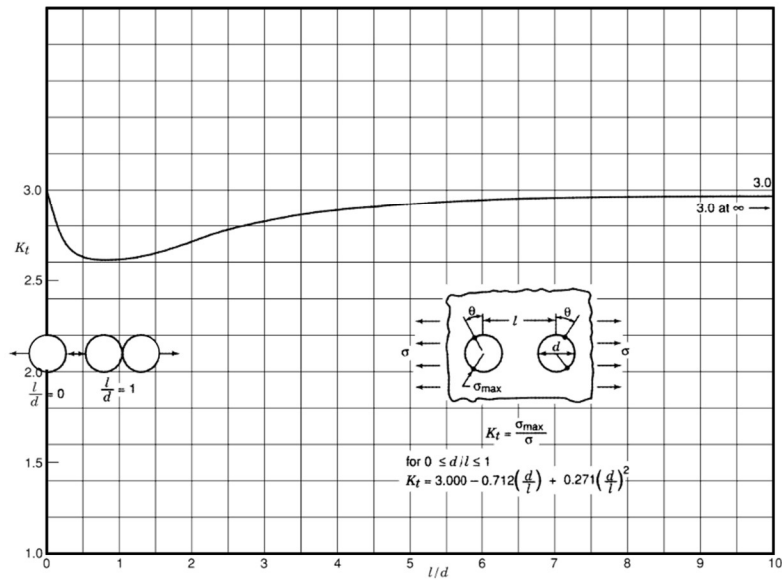
Square-ended plies with large rivets, bolts or pins (h/d < 0.5)

$K_{t0.2}$ = Stress concentration factor when the clearance e = 0.2%
K_{te} for e < 0.1

$\frac{e}{H}$
0.5
1.0
∞

$$K_t = \frac{\sigma_{max}}{\sigma_{nom}}$$

σ_{max} = Maximum tensile stress in lug around hole perimeters

$$\sigma_{nom} = \frac{P}{(H-d)h}$$

$e = \frac{\delta}{d}$ (Percentage), the pin to hole clearance

Approximate values for K_{te} for any e can be obtained by using

$$K_{te} = K_{t0.2} + f(K_{t100} - K_{t0.2})$$

where K_{t100} and f are taken from Chart 5.12

d/H

Clevis

H

d

Lug

Clevis ears

P
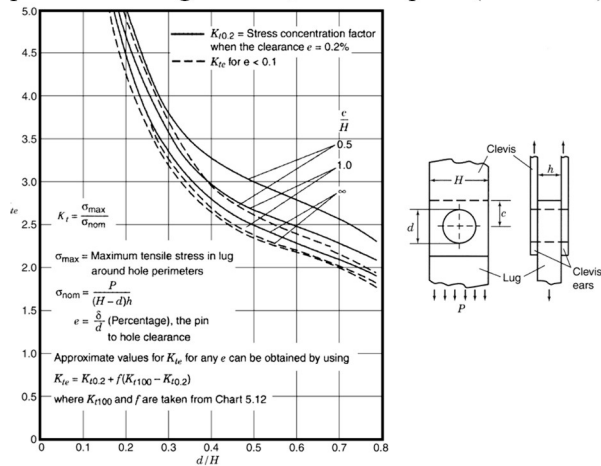
Figure 3.22 SMF charts suitable for riveted details (adapted from *Peterson & Pilkey, 1997*).

Clearly, for a widely spread contact ($d/w \to 1$), $\sigma_{mod,b} \to -\sigma_0$ as predicted by LFM (*Anderson, 2017*).

It is worth recalling that, while mean-stress effect can be neglected if the hot-spot stress method is used, $\sigma_m > 0$ should not be overlooked when applying the modified nominal stress method. Indeed, when adopting the latter approach, standard S-N curves should be used. Therefore, σ_m is not explicitly accounted for in fatigue checks, except for the sole stress range correction reported in Equation 3.33a-c for $R \leq 0$.

In this regard, mean stress can be conveniently accounted for by means of an equivalent stress magnification factor SMF_{ms} (*Milone et al., 2022c*) defined as σ_{ar}/σ_a, that is, according to one of the formulations reported in *Section 3.3.4* (Equation 3.35a-b):

$$ SMF_{ms,g} = \frac{1}{1 - \left(\dfrac{\sigma_m}{f_u}\right)^2} ; \quad SMF_{ms,G} = \frac{1}{1 - \dfrac{\sigma_m}{f_u}} ; \quad SMF_{ms,S} = \frac{1}{1 - \dfrac{\sigma_m}{f_y}} \tag{3.35a} $$

$$ SMF_{ms,SWT} = \sqrt{\frac{2}{1-R}} ; \quad SMF_{ms,W} = \left(\frac{2}{1-R}\right)^{1-\gamma} \tag{3.35b} $$

3.3.6 Overview of Strain-Life Methods

The main limit of all stress-life approaches is represented by the assumption of materials indefinitely behaving as linear elastic (*Osgood, 1982*). Indeed, even though some sources of non-linearity are (more or less explicitly) accounted for, e.g. contacts, friction, etc…, material plasticity is completely overlooked while performing fatigue analyses.

To partially overcome this issue, the range of validity for normative S-N curves is superiorly limited to $1.5\,f_y$ (*CEN, 2005a*). However, when dealing with details featuring sharp stress raisers, localized plasticity can occur even for rather small nominal stresses. For instance, the LFM solution for infinitely wide perforated plate (see Figure 3.21, first chart, $d/w \to 0$) already predicts localized plasticity around the hole for a nominal, far field stress $\sigma_0 = 0.33\,f_y$.

While it is true that this aspect is implicitly addressed by EN1993:1-9 with respect to encoded details (*ECCS, 2018*), it is worth mentioning that, in the general case, neglecting plasticity can lead to highly non-conservative fatigue life estimations, especially with low-tenacity metals (*Schijve, 2009*).

As mentioned is *Section 3.3.2*, the idea of addressing strain (half-)cycles to assess fatigue performance of components was first introduced by *Basquin* (*1910*). Further, crucial developments were provided independently by *Manson* (*1953*) and *Coffin* (*1954*). Namely, while Basquin attempted to relate fatigue life to elastic strain reversals $\Delta\varepsilon_e/2$, Coffin & Manson focussed on the influence of plastic reversals $\Delta\varepsilon_p/2$, and hence to total strain reversals (hence also referred as *strain amplitude* ε_a) (*Dowling, 2004*).

Accordingly, the strain-life *Basquin-Manson-Coffin* (BMC) model can be expressed according to Equation 3.36a-b:

$$ \varepsilon_a = \frac{\Delta\varepsilon_{tot}}{2} = \frac{\Delta\varepsilon_e}{2} + \frac{\Delta\varepsilon_p}{2} \tag{3.36a} $$

$$ BMC: \quad \varepsilon_a = \frac{\Delta\varepsilon_e}{2} + \frac{\Delta\varepsilon_p}{2} = \frac{\sigma_f'}{E}\left(2\,N^*\right)^b + \varepsilon_f'\left(2\,N^*\right)^c \tag{3.36b} $$

with σ'_f [F L^{-2}], ε'_f [-] being the so-called *fatigue strength coefficient* and *fatigue ductility coefficient*, respectively and b, c being the so-called *fatigue strength exponent* and *fatigue ductility exponent*, respectively. BMC coefficients are intended as intrinsic

material parameters that can be calibrated based on experimental, constant-amplitude, strain-control tests on round or flat smooth coupons (*Anderson, 2017*).

Usual values of c are in the range $-0.5 \div -0.7$ (the greater is $|c|$, the longer is fatigue life), while σ'_f ranges among $500 \div 1000$ N/mm² for mild steels (*Schijve, 2009*).

According to Equation 3.36b, it can be easily noticed that, while σ'_f and b govern HCF regime, ε'_f and c account for LCF material behaviour. A convenient graphical interpretation of this fact can be provided in the double-logarithmic *strain-life diagram* $\varepsilon_a - N^*$ (Figure 3.23), namely:

- for very high ε_a values, LCF failure points asymptotically follow a straight line *l* having a slope equal to $c < 0$ and passing through the point $L = (\varepsilon'_f, 1)$;
- for rather small ε_a values, HCF failure points asymptotically follow a second straight line *h* having a slope equal to $b < 0$ and passing through the point $H = (\sigma'_f/E, 1)$;
- for intermediate ε_a values, failure points follow a parabolic arc *m* gradually changing slope from c to b.

Accordingly, while estimating BMC parameters, it is recommended to account for at least five different strain amplitude levels, namely three for intermediate ε_a ranges and the remaining two identifying LCF and HCF asymptotes (*Da Silva et al., 2019*).

Nevertheless, it is worth reporting that some techniques for a rough estimation of BMC parameters based on static base material properties can be found in literature (*Schijve, 2009*). Among the different correlations proposed, *Boller-Seeger's formulas* (*Boller & Seeger, 1987*), based on interpretation of experimental tests for various metals, are quite commonly used (Equation 3.37a-b):

$$\text{Mild steels:} \quad \begin{cases} \sigma'_f = 1.5\,f_u \\ \varepsilon'_f = 0.59\min\left(1\,;\,1.375 - 125\,f_u/E\right) \\ b = -0.087 \\ c = -0.57 \end{cases} \tag{3.37a}$$

$$\text{Other metals:} \quad \begin{cases} \sigma'_f = 1.67\,f_u \\ \varepsilon'_f = 0.535 \\ b = -0.095 \\ c = -0.69 \end{cases} \tag{3.37b}$$
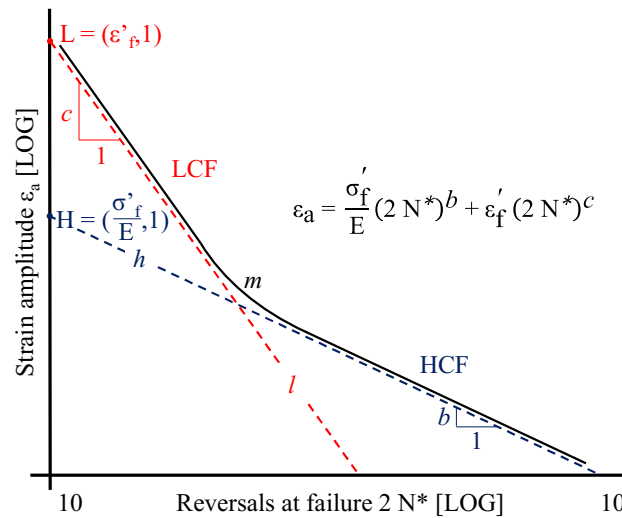
Figure 3.23 Graphical interpretation of the BCM fatigue life criterion (strain-life diagram).

It is worth recalling that, when using strain-life methods, an appropriate material cyclic constitutive law is required to deal with yielding and cyclic hardening. To this end, the already mentioned Ramberg-Osgood model (Equation 3.8 – *Ramberg & Osgood, 1943*) represents the most popular option. When addressing cyclic plasticity, Equation 3.8 is often used in an engineering, yet equivalent form involving the Ramberg-Osgood *strength coefficient* K_{RO} in place of the yield offset α_{RO} (Equation 3.38):

$$\varepsilon_{eng} = \frac{\sigma_{eng}}{E} + \left(\frac{\sigma_{eng}}{K_{RO}}\right)^{n_{RO}} \tag{3.38}$$

where K_{RO} and n_{RO} should be estimated with reference to the material stabilized cyclic response.

Uncoincidentally, *Boller & Seeger* (*1987*) provide handy empirical relations to roughly estimate K_{RO} and n_{RO} for various metals based on their UTS (Equation 3.39a-b):

$$\text{Mild steels:} \quad \begin{cases} K_{RO} = 1.65\,f_u \\ n_{RO} = 6.67 \end{cases} \tag{3.39a}$$

$$\text{Other metals:} \quad \begin{cases} K_{RO} = 1.61\,f_u \\ n_{RO} = 9.09 \end{cases} \tag{3.39b}$$

3.3.7 Mean-Stress Effect in Strain-Life Methods

Mean-stress effect can be conveniently accounted for in BMC equation by introducing appropriate corrections (*Schijve, 2009*). Notably, the same models introduced to account for σ_m in nominal stress methods (*Section 3.3.4*) can be easily placed in the framework of ε-N methods. As a matter of fact, many of the earlier described formulations were originally conceived for strain-life analysis and only later transposed to S-N methods. For instance, the *Morrow* (*1968*) model involving the mean-stress work rate was initially proposed to correct the elastic term of BMC formula as follows (Equation 3.40):

$$\text{Morrow:} \quad \varepsilon_a = \frac{\sigma_f' - \sigma_m}{E} \left(2\,N^*\right)^b + \varepsilon_f' \left(2\,N^*\right)^c \tag{3.40}$$

Accordingly, mean-stress effect is thought of having an appreciable influence only for the HCF regime. As this assumptions contrasts with experimental results, *Manson & Halford* (*1981*) proposed to extend Morrow's correction also to the plastic term of BMC formula (Equation 3.41):

$$\text{Manson \& Halford:} \quad \varepsilon_a = \frac{\sigma_f' - \sigma_m}{E} \left(2\,N^*\right)^b + \varepsilon_f' \left(\frac{\sigma_f' - \sigma_m}{\sigma_f'}\right)^{\frac{c}{b}} \left(2\,N^*\right)^c \tag{3.41}$$

The original work of *Smith, Watson & Topper* (*1970*) also concerned mean-stress effect within the framework of strain-life predictions. Indeed, the already mentioned dependence on σ_{max} was originally proposed to modify BMC formula as follows (Equation 3.42):

$$\text{SWT:} \quad \sigma_{max}\,\varepsilon_a = \frac{\left(\sigma_f'\right)^2}{E} \left(2\,N^*\right)^{2b} + \sigma_f'\,\varepsilon_f' \left(2\,N^*\right)^{b+c} \tag{3.42}$$

Dowling (*2004*) subsequently demonstrated how *Walker* (1970) model could be equivalently transposed into strain-life methods by substituting *b* with $(2 - 2\gamma)b$ in Equation 3.42, with γ being the aforementioned Walker exponent.

3.3.8 Hints about Crack Propagation and Stress Intensity Factors

All the above formulations presented in *Sections 3.3.1-3.3.7* address the topic of *total* fatigue life of structural components N*. More properly, fatigue life can be regarded as composed by two subsequent stages, namely *i*) the crack initiation life N^*_i and *ii*) the crack propagation life N^*_p.

The relative influence of crack initiation stage (CIS) and crack propagation stage (CPS) on the total fatigue life depends on many different factors (base material properties, manufacturing process, geometrical features, etc… – *Anderson, 2017*). For instance, in plain and narrow components $N^*_i \gg N^*_p$, while fatigue life of welded and/or severely notched elements is mainly governed by crack propagation (*ECCS, 2018*).

To separately deal with CIS and CPS when relevant, two aspects should be addressed, namely: *i*) clearly identifying the boundary between the two stages and *ii*) introducing a reliable crack propagation model (*Anderson, 2017*).

On one hand, t\he former aspect can be easily handled by performing constant-amplitude, displacement-control fatigue tests on plain narrow coupons. Indeed, provided that specimens have an appropriate *gauge segment* with length L_g, both S-N and ε-N diagrams for the sole CIS can be easily derived by assessing experimental results.

Indeed, the absence of stress raisers and the narrow cross section ensure a negligible value of N^*_p, which can be further filtered if the specimen stiffness is monitored through the test by means of a simple *strain gauge* (*Anderson, 2017*).

Moreover, as stresses and strains can be reasonably assumed to be uniform within the gauge segment, the endured ε_a can be directly estimated as δ_a/L_g, with δ_a being the imposed displacement amplitude, while σ_a is calculated as $F_a A_0/A_g$, with F_a being the force amplitude measured by the load cell, A_0 being the cross-section at grips and A_g being the minimum cross-section within the gauge segment.

To this end, it is worth mentioning that several standards in force regulate the shape and size of strain-life smooth specimens (Figure 3.24a), which is usually defined as a parametric function of its diameter *d* (round coupons) or thickness *t* (flat coupons), e.g. *ASTM E606* (*2012*).

On the other hand, crack propagation modelling is a rather complex topic which is still an open field of research nowadays, especially for two- or three-dimensional problems (*Anderson, 2017*). Therefore, only some related hints are summarized in this Section.

The basic formulation addressing CPS was introduced by Paul C. Paris (*Paris et al., 1961*; *Paris & Erdogan, 1963*), which proposed the homonymous crack growth equation (Equation 3.43 & Figure 3.25):

$$\text{Paris:} \quad \frac{d}{dN} a = C\,(\Delta K)^m \tag{3.43}$$

where *a* is the crack length, da/dN is the crack growth rate against the number of loading cycles N, $\Delta K = K_{max} - K_{min}$ is the *stress intensity factor range* and C, *m* are experimental regression parameters depending on *i*) material composition, *ii*) environmental conditions (temperature, corrosivity) and *iii*) applied stress ratio R. Further insights about ΔK and *stress intensity factors* (SIFs, usually also referred as "K") are provided at the end of the present Section.

Paris parameters for one-dimensional fracture propagation in tension (i.e., *Mode I*, crack opening – *Anderson, 2017*) are usually determined by means of compact-tension (CT) specimens with standard shape and size (Figure 3.24b – *ASTM E647, 2016*).
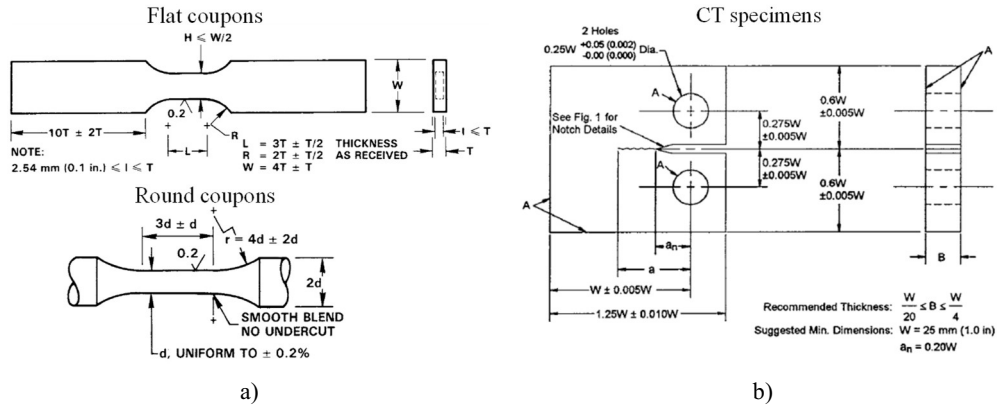
Figure 3.24 Standardized shapes and sizes for a) smooth and b) CT specimens according to ASTM E606 (2012) and *ASTM E647 (2016)* recommendations.

Paris law traces a straight line in the bi-logarithmic da/dN – ΔK plane, notably resembling Basquin's formula (Figure 3.25). The range of validity for Paris law is defined as *stable crack propagation region* (or *region II*), and it refers to intermediate ΔK values (*Anderson, 2017*).

For rather small values of ΔK, cracks do not propagate at all (that is, $da/dN = 0$). This condition occurs up to a threshold value ΔK_{th} which separates region II from the *inhibited crack propagation region* (or *region I*). Contrariwise, for large values of ΔK (i.e., larger than a critical value ΔK_c) crack propagation greatly accelerates until failure. This behaviour range is defined ad *instable crack propagation region* (or *region III* – *Anderson, 2017*). It is worth remarking that both ΔK_{th} and ΔK_c are functions of the same variables affecting C and *m* values.

Provided that Paris parameters have been accurately determined for the boundary conditions of concern, N^*_p can be easily estimated by integrating Equation 3.43 over a given load history LH (Equation 3.44):

$$N_p^* = \int_{LH} \frac{da}{C \, (\Delta K)^m} \tag{3.44}$$
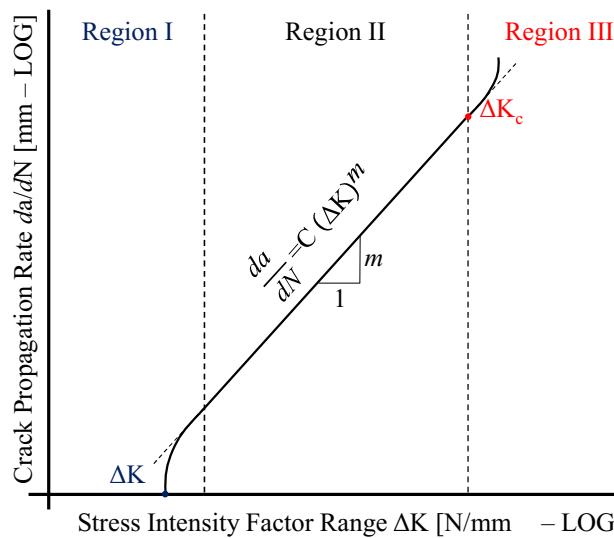
Figure 3.25 Crack propagation diagram and graphical interpretation of Paris law (*Anderson, 2017*).

Equation 3.44 provides an approximate estimation of N*$_p$ as it assumes a *region II* behaviour for the entire LH. A more accurate estimation of crack propagation life can be immediately performed by disregarding LH phases for which $\Delta K \leq \Delta K_{th}$ and arresting integration as soon as a value of $\Delta K \geq \Delta K_c$ (i.e., by conservatively assuming $m \rightarrow \infty$ for region III – Anderson, 2017). Nevertheless, several modifications of Paris Law attempting at capturing all the three behaviour regions can be found in scientific literature (e.g., *Klesnil & Lucas, 1972*; Donahue et al., 1972; *Forman & Mettu, 1992*), although neither of them gained the same popularity as the original formulation in light of their complexity.

The physical meaning of the stress intensity factor range ΔK relates to basic concepts of linear fracture mechanics (LFM). ΔK is defined as the difference between the extremal SIFs (usually also referred as "K") associated to a given load cycle $K_{max} - K_{min}$.

The concept of stress intensity factor was first introduced by *Irwin* (*1956*) while extending the pioneering work of *Griffith* (*1920*) on brittle fracture of materials featuring sharp cracks in tension (Mode I). Namely, it was well-known at the time that regarding a sharp crack as a limit case of elliptical hole in a wide plate ($w/2a \gg 0$), infinite tensile stresses $\sigma_A \rightarrow \infty$ at the crack tip would be predicted by the classic elasticity theory, as they inversely depend on the curvature radius $\rho \rightarrow 0$ (Figure 3.26a-b – *Anderson, 2017*). This outcome clearly contrasts with experimental observations, as ideally brittle materials (e.g. glass, PMMA, etc...) would instantaneously break for any small value of the far-field stress σ_0, while they exhibit a finite, yet reduced tensile resistance even in presence of sharp cracks.

While *Griffith* (*1920*) proposed an enlightening solution involving an energetic balance among potential and surface material energies, *Irwin* (*1956*) introduced a closed form expression for stresses in polar coordinates (r, θ) centred at the crack tip (Figure 3.26c). Accordingly, singular stresses σ_{ij} on a given director sweeping an angle θ with respect to the crack bisector can be expressed as a power series of the polar radius r (i.e., with first exponent $= -\,^1/_2$ and following ones > 0). Hence, for $r \rightarrow 0$, higher order terms can be conveniently neglected, leading to the following expression for σ_{ij} (Equation 3.45):

a)   b)
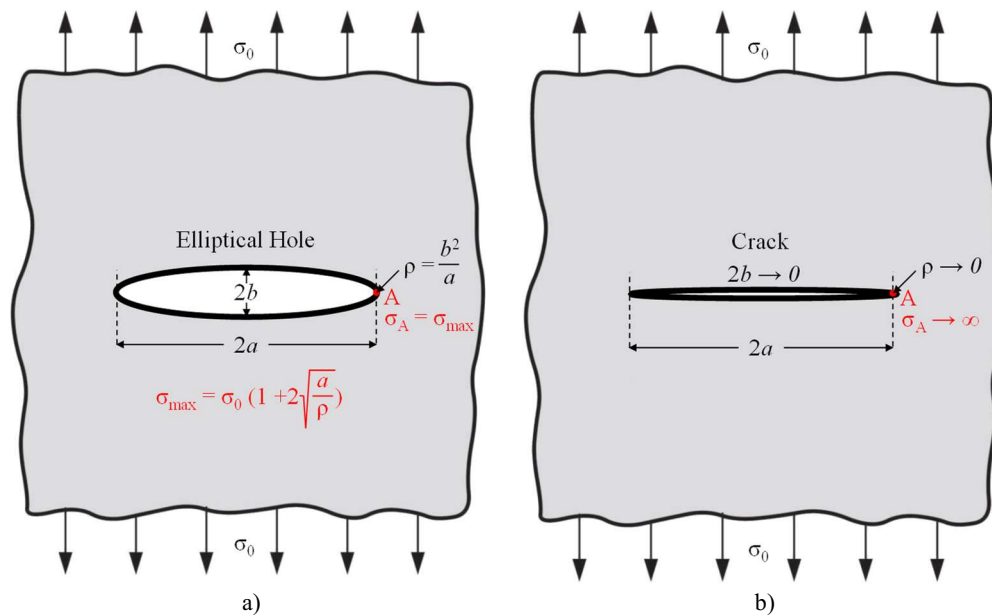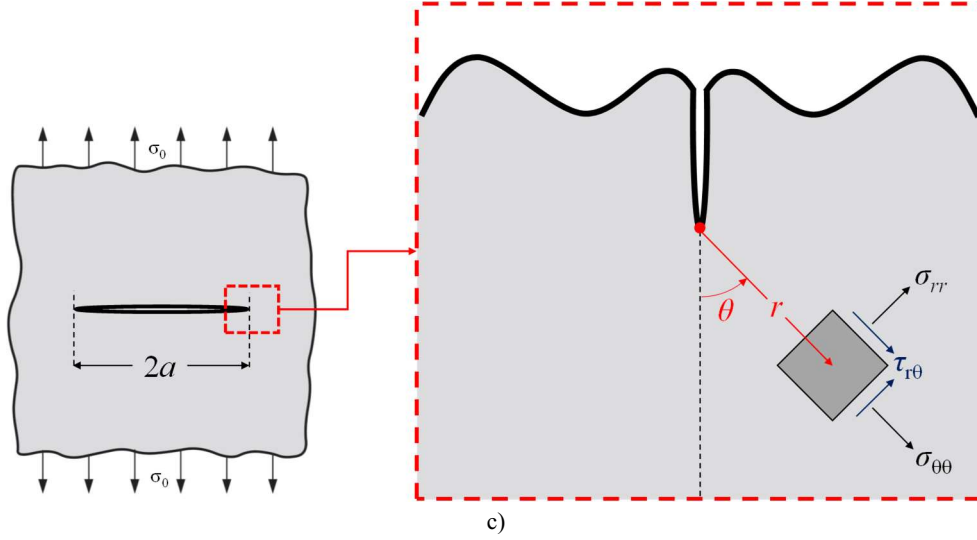
Figure 3.26 a, b) Sharp crack regarded as a limit case of elliptical hole and c) local stress field at the crack tip in polar coordinates (adapted from *Anderson, 2017*).

$$\sigma_{ij}(r, \theta) = \frac{K_I}{\sqrt{2\pi\, r}}\, f_{ij}^{(I)}(\theta) \rightarrow \lim_{r \to 0} \sigma_{ij} = \infty \qquad (3.45)$$

with K_I being a constant defined as the stress intensity factor for Mode I (hence also referred as SIF_I) and $f_{ij}^I(\theta)$ being an appropriate dimensionless, Mode I-related function of the angular coordinate θ.

Equivalent formulations can be derived for Mode II (in-plane shear) and Mode III (out-of-plane shear), with the superposition principle being valid for mixed-Mode fracture (*Anderson, 2017*).

SIF_I is hence defined as the (finite) limit of singular stresses multiplied by r- and θ-depending terms as follows (Equation 3.46):

$$K_I = \lim_{r,\, \theta \to 0} \frac{\sigma_{ij}(r, \theta)}{f_{ij}^{(I)}(\theta)}\, \sqrt{2\pi\, r} < \infty \qquad (3.46)$$

Existence and finiteness of limit featured in Equation 3.46 is granted by the $\sqrt{2\pi\, r}$ term, which eliminates stress singularity at crack tip $\propto r^{-1/2}$. Several closed forms for K_I exist for elastic isotropic bodies featuring variously shaped cracks (misaligned, edge, "penny-shaped" cracks, etc… – *Anderson, 2017*). As for the mentioned case of middle crack in an large, elastic isotropic plate subjected to Mode I, an elegant solution is obtained for K_I (Equation 3.47 – *Irwin, 1956*):

$$\text{Middle crack,}\ \frac{w}{2a} \gg 0: \quad K_I = \sigma_0\, \sqrt{\pi\, a} \qquad (3.47)$$

that is, $f_{ij}^I(0) = \sqrt{2}$.

Remarkably, SIF_I is linearly proportional to the far-field stress σ_0 and depends on the crack size a. These two "simple" findings serve as foundation of the entire linear elastic fracture mechanics (*Anderson, 2017*).

Equation 3.47 proves that K_I has rather "unusual" measure units, i.e., $[F / L^{3/2}]$. As it will be shown in *Section 3.4.1*, this is an intrinsic property of *sharp cracks*, while it is not true for *other components* featuring singular stresses (e.g., elements with re-entrant sharp corners – *Williams, 1952*).

The resulting difficulties in comparing the performance for varying geometries partly underlay the development of advanced techniques for fatigue and fracture analyses, e.g., the *Strain Energy Density* (SED) method (*Lazzarin & Zambardi, 2001*), which will be addressed in detail in *Section 3.4.2* before being suitably applied to the relevant case of hot-driven riveted connections.

The basic idea of LFM is that fracture of isotropic, linear elastic materials can be conveniently expressed in terms of SIFs, one for each of the three fracture Modes M. Namely, failure is predicted to occur when a critical value of $K_M = K_{MC}$ is attained.

K_{MC} is regarded as an intrinsic material property referred as *Mode M fracture toughness* (*Anderson, 2017*).

For practical purposes, standardized CT specimens (see Figure 3.24b) can be suitably used to estimate K_{IC}, provided that an initial sharp crack is formed at the corner, i.e., by means of cyclic pre-loading (*ASTM E1820, 2018*).

As discussed earlier in this section, the same concept was extended by Paris (*Paris et al., 1961*; *Paris & Erdogan, 1963*) to HCF by replacing K with ΔK to properly isolate fluctuating stresses from monotonic loadings.

Although based on rather complex ideas with respect to fatigue assessment techniques reported in previous Sections, SIFs and Paris law can be substantially regarded as "standard" fatigue analysis techniques, as they are widely used within the framework of mechanical engineering (*Anderson, 2017*) and, although for peculiar applications, civil engineering (e.g., *Jiang et al., 2018*; *Da Silva et al., 2019*).

Finally, it is really worth remarking that, although all the above concepts relate to linear elastic brittle materials, they have been successfully extended to fatigue performance of ductile materials, e.g., mild steels (*Radaj & Wormwald, 2013*).

Indeed, on one hand, material plasticity only occurs on a local scale nearby the crack tip in HCF regime (*small-scale yielding*). In this case, small or even no corrections are required to assess fatigue failure of ductile materials (*Radaj & Vormwald, 2013*; *Anderson, 2017*).

On the other hand, while it is true that *large-scale yielding* occurring in LCF regime can be addressed with alternative, yet more complex approaches (*elasto-plastic fracture mechanics* – EPFM – *Anderson, 2017*), it is also true that LCF is not particularly relevant for civil engineering structures, except in particular circumstances (*ECCS, 2018*).

3.3.9 Applied Statistics for Standard Fatigue Analysis Techniques

As constantly seen in previous Sections, logarithmic regression model finds a crucial field of application in "standard" fatigue analysis techniques, namely because either Basquin's formula, BMC model and Paris law feature power law expressions governed by experimental parameters.

However, it is well-known that the adoption of a logarithmic regression model underlies the assumption of constant data dispersion (*homoskedasticity – Wakefield, 2013*), which contrasts with observations reported in *Schijve* (*2009*) (e.g., the larger are the fluctuating stresses, the lower is the scatter shown by results and vice-versa).

Therefore, it may appear that some information about fatigue performance of structural components could be missed. This issue is practically overcome by *i*) performing a significant number of tests, whenever possible (at least ≥ 15, with ≥ 60 tests being the "gold standard"), *ii*) accounting for tests numerosity in the regression model and/or *iii*) providing additional information about the reliability of the model itself, usually by means of synthetic indicators (*Schijve, 2009*; *ECCS, 2018*).

To this end, *Liebermann beta coefficients* β_L (*Liebermann, 1957*) can be proficiently used to account for test numerosity within the framework of loglinear regression. According to EN1990 (*CEN, 2002*), the characteristic value R_k for any resistance model can be estimated by moving β standard deviations s away from the mean model results R_μ (provided that statistical significance tests for such model are successful).

β is defined as the *structural reliability*, which is a function of the assumed probability of failure P_f (Equation 3.48):

$$\beta = f(P_f) = \Phi^{-1}(P_f) \qquad (3.48)$$

with Φ^{-1} being the inverse cumulative distribution function (CDF) for a standard Normal random variable (i.e., with null mean μ and unitary standard deviation s) $N \sim (0; 1)$. Accordingly, the characteristic value (i.e., defined by a survival probability $P_S = 1 - P_F = 95\%$) can be estimated by assuming $\beta = 1.64$, while to design resistance value R_d ($P_F = 10^{-4}$) an higher value of $\beta = 3.00$ is usually associated (*CEN, 2002*).

However, when Equation 3.48 is used, only the failure probability for the *structural component* is explicitly accounted for, while no information explicitly concerning with the *model reliability* are provided. Contrariwise, by adopting Liebermann coefficients β_L in place of β, test numerosity N_{test} and model reliability (in the form of a required *confidence level* CL) can be explicitly accounted for (*Liebermann, 1957*).

In other words, while $\beta = f(P_f)$, $\beta_L = f(P_f; N_{test}; CL) \geq \beta$. As a limit case, for a sufficient number of tests ($\approx N_{test} \geq 30$) and the same confidence level (which EN1990 "implicitly" sets equal to 90% – *ECCS, 2018*), $\beta_L \rightarrow \beta$.

For instance, the practically relevant case of $P_F = 5\%$, CL = 90% and "intermediate" test numerosity ($15 \leq N_{test} \leq 30$) yields $\beta_L = 2.00 > 1.64$. Nevertheless, it is worth remarking that this finding is reported in technical background documents for structural Eurocodes, and this reliability gap is definitely overcome by means of partial safety factors γ_{MF} (*ECCS, 2018*),

In light of the above, when dealing with details encoded in European provisions, "soundness" and conservativity of fatigue predictions (that is, of listed S-N curves) is guaranteed within the framework of the semi-probabilistic *Limit States Method* (CEN, 2002; CEN, 2005a; *ECCS, 2018*). Contrariwise, when a particular detail category is missing (as for the relevant case of hot-driven riveted connections), a strong attention should be paid to the statistical assessment of results, even for the simplest approach of the *Nominal Stress Method*.

To this end, two summarizing indicators are mainly used to prove the reliability of interpreted results, namely the *coefficient of determination* $R^2 = 0.0 \div 1.0$ and the *scatter ratio* $T_v \geq 1$ for the variable v of concern (Equation 3.49a-b – *Wakefield, 2013*):

$$R^2 = 1 - \frac{s^2_{err}}{s^2_{tot}} \qquad (3.49a)$$

$$T_v = \frac{v_{sup}}{v_{inf}} = \frac{v_\mu + \beta_L \, s_{tot}}{v_\mu - \beta_L \, s_{tot}} \qquad (3.49b)$$

with s^2_{err} being the variance of the errors ε_i of the regression model, s^2_{tot} being the total variance of data for the variable v having mean equal to v_μ and v_{sup}/v_{inf} being the extreme values of the scatter band associated to relevant P_f, CL and N_{test} values (Figure 3.27).

s^2_{err} and s^2_{tot} can be conveniently estimated in terms of *i*) *i*-th experimental values v_i, *ii*) estimated regression coefficients a_i (= *m*), b_i according to the least-squares method and *iii*) the number n_{DOF} of degrees of freedom of the sample (*Wakefield, 2013*).

Notably, both R^2, $T_v \rightarrow 1$ for ideal (i.e., totally reliable) models. However, a loss of accuracy is hinted in opposite ways, as $R^2 \rightarrow 0$ for scarce prediction capability, while the scatter band will clearly widen (that is, $T_v \rightarrow \infty$).

Although they relate to similar quantities, it is worth recalling that R^2 and T_v provide different insights about the soundness of regression and results scatter. Indeed, while R^2 only accounts for *model reliability*, disregarding *structural reliability* as opposed to basic EN1990 recommendations (*CEN, 2002*), T_v both encloses model and structural reliability as it depends on β_L. However, as P_f and CL can be arbitrarily selected, more favourable values of T_v can be "artificially" obtained by assuming less strict predictability properties. In other words, a coherent reliability assessment for any given resistance model cannot exclude the estimation of either R^2 and T_v (*Wakefield, 2013*).

As a relevant example, in case of very large reciprocal slopes $1/m$, a logarithmic regression model would result in basically constant predictions $\bar{v}$, for which R^2 is identically null (that is, $s^2_{err} \rightarrow s^2_{tot}$ for $m \rightarrow 0$).

Hence this condition, e.g., that is rather common in case of fatigue failure for elevated stress ratios (*Schijve, 2009*), would result in no prediction capability at all according to R^2 index, while this result actually unveils the phenomenology of investigated phenomena. Contrariwise, by introducing the *scatter ratio* T_σ for stress ranges at failure, the reliability of results can be still proved if $T_\sigma \leq T_{\sigma,th}$, i.e., an upper threshold separating "clustered" and scattered results. For instance, a typical value of $T_{\sigma,th} \approx 1.50$ is commonly adopted for fatigue analyses (*Schijve, 2009*).
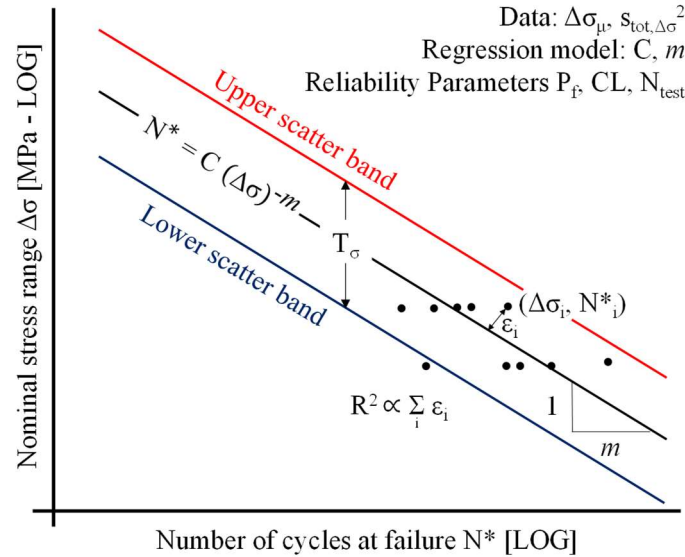
Figure 3.27 Reliability analysis of fatigue results with graphical interpretation of R^2 and T_σ indexes.

3.4. Advanced fatigue analysis techniques for structural components

In the previous Sections, standard fatigue assessment methods and their advantages/limitations have been briefly addressed. In the present Section, an overview of two advanced fatigue assessment techniques is presented, namely the Notch-Stress Intensity Factor (N-SIFs) approach and the Strain Energy Density (SED) method.

Within the present thesis work, only the latter approach will be conveniently applied to the relevant case of hot-driven riveted connections. To this end, the required theoretical background will be introduced in *Sections 3.4.2-3.5.2*, while its application with respect to performed experimental activities is the subject of both *Chapters 6* (mild steel components) and *7* (assembled connections).

Nevertheless, reporting some key hints about the N-SIF approach is deemed appropriate *i*) to fill some basic knowledge gaps concerning fatigue performance of weakened components and *ii*) for "historical" reasons, as the main concepts of the SED method were initially developed to overcome some issues related to fatigue and fracture analyses based on N-SIF approach (*Lazzarin & Zambardi, 2001*).

3.4.1 Hints about Notch-Stress Intensity Factors (N-SIF) Approach

As preliminarily remarked in *Section 3.3.8*, singular stresses arising at tip of a sharp crack embodied in an isotropic linear elastic materials can be conveniently described by means of SIFs related to the three basic fracture Modes (*Anderson, 2017*).

However, as first noticed by *Williams* (*1952*), sharp cracks are not the only source of singular stresses in weakened components. Indeed, using an appropriate Airy stress function for the case of a re-entrant corner under a remote stress field, Williams proved how polar coordinate-stresses are proportional to $r^{\lambda_M - 1}$, with λ_M being the so-called *Williams' eigenvalues*, one for each of the three fracture Modes (*Williams, 1952*).

λ_i were found to depend on the notch opening angle 2α, with λ_1, λ_3 being always ≤ 1 for re-entrant corners (that is, for $2\alpha = 0 \div \pi$), while $\lambda_2 \leq 1$ for $2\alpha = 0 \div 0.57\,\pi$, e.g., 102.6° (Figure 3.28 – *Lazzarin et al., 2004*). Therefore, all the three fracture modes are actually singular for re-entrant sharp notches (that is, $\lambda_i - 1 < 0$ and thus $\sigma_{ij} \to \infty$ for $r \to 0$), even though in-plane shear stresses can be non-singular for shallow corners ($2\alpha > 102.6°$).

In this regard, the condition of sharp crack can be regarded as a particular case of re-entrant corner having $2\alpha = 0$. Uncoincidentally, all Williams' eigenvalues approach 0.5 for null opening angle, returning the $\sigma_{ij} \propto r^{-1/2}$ proportionality already discovered by *Irwin* (*1956*). Contrariwise, for $2\alpha > 0$, stresses σ_{ij} at the notch tip still tend to an infinite value, although with a smaller degree of singularity ($\lambda_M - 1 > -0.5$).

Intuitively, as for the case of cracks, also stresses around a pointed V-notch can be expressed in polar coordinates in function of r, θ and a proper *notch-stress intensity factor* for the relevant fracture Mode (N-SIF or K^N_M – *Radaj & Vormwald, 2013*), i.e., as follows (Equation 3.50 & Figure 3.29):
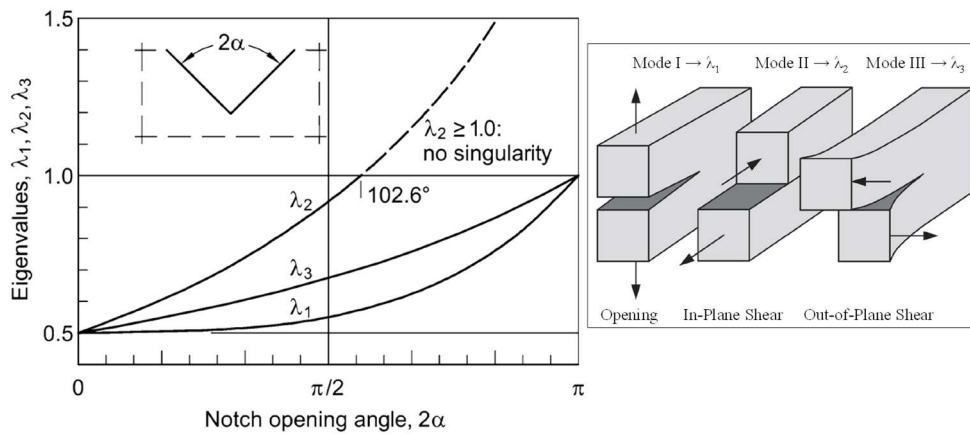
Figure 3.28 Williams' eigenvalues λ_i for re-entrant notches (*Lazzarin et al., 2004*; adapted from *Radaj & Vormwald, 2013* and *Anderson, 2017*).

$$\sigma_{ij}(r, \theta) = \frac{K_M^N}{\sqrt{2\pi}} \, r^{\lambda_M - 1} f_{ij}^{(M)}(\theta) \tag{3.50}$$

Therefore, the three N-SIFs K_M^N may be estimated based on the above stress components considering the limit values for $r \to 0$ (Equation 3.51 – *Gross & Mendelson, 1972*):

$$K_M^N = \lim_{r, \theta \to 0} \frac{\sigma_{ij}(r, \theta)}{f_{ij}^{(M)}(\theta)} \sqrt{2\pi} \, r^{1 - \lambda_M} \tag{3.51}$$

In analogy with assumptions made for sharp cracks, fracture behaviour of notched components can be addressed by considering *critical N-SIF* values K_{MC}^N associated to failure, with them being function not only of the base material but also of the notch geometry (*Anderson, 2017*).

As for the fatigue performance of notched components, a conceptual extension of Basquin's formula can be conveniently used to estimate N* depending on the relevant value of N-SIF (Equation 3.52). For example, this approach was successfully applied by *Lazzarin & Tovo (1998)* to fillet-welded transverse steel joints under tensile loading.

$$N^* = C \left(\Delta K_M^N \right)^{-m} \leftrightarrow \log N^* = \log C - m \log \Delta K_M^N \tag{3.52}$$

An equivalent option is represented by the definition of the *fatigue notch factor* K_f, i.e. the ratio among the COLs for a smooth and a notched specimen, respectively (*Radaj & Vormwald, 2013*). Considering the simplest case of uniaxial fatigue, K_f can be related to K_I^N by means of a material depending *notch sensitivity factor q > 0* (Equation 3.53):

$$K_f = \frac{\Delta\sigma_L}{\Delta\sigma_{L,notch}} = 1 + q \, (K_I^N - 1) \tag{3.53}$$

Accordingly, a given material has no sensitivity to notch effect for $q = 0$. Typically, for mild steels and aluminium alloys, q increases with UTS. Recommended values can be e.g. found in *Schijve (2009)*. Fatigue performance of notched components can be hence assessed by amplifying K_f times the nominal stress range $\Delta\sigma$ and using relevant S-N curves (*Radaj & Vormwald, 2013*).

Notably, as it descends from Equation 3.51, measure units for N-SIFs are not univocal, but they rather depend on the notch-stress degree of singularity; that is, $[F \, L^{-(1 + \lambda_M)}]$.
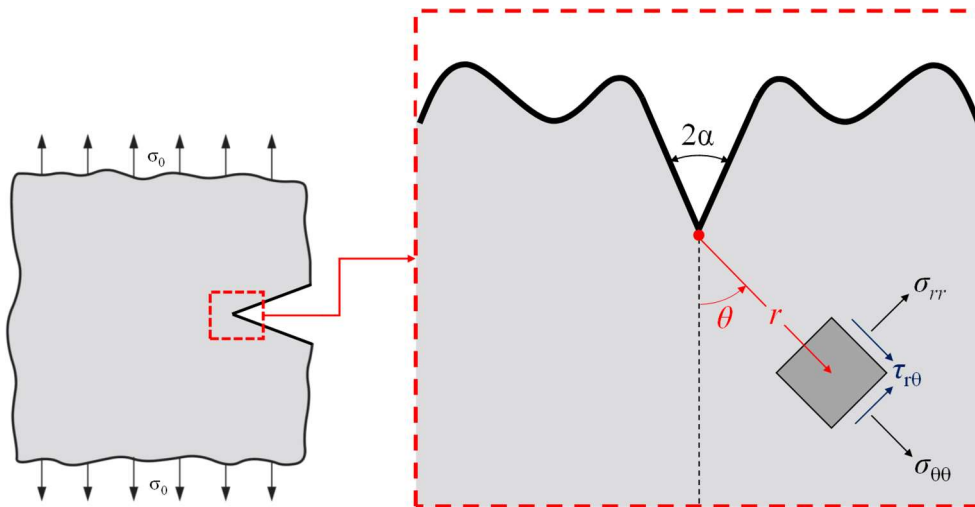
Figure 3.29 Local stress field at the notch tip in polar coordinates (adapted from *Anderson, 2017*).

Therefore, comparing the fatigue and fracture performance of notched specimens featuring different opening angles is somewhat difficult, as non-consistent measure units will be involved. This issue is usually overcome by normalizing N-SIFs with respect to $r^{1-\lambda_M}$ for a conventional value of r (*Anderson, 2017*).

Moreover, the introduction of mixed Modes fracture criteria become quite complex (*Radaj & Vormwald, 2013*). Indeed, even for the same specimen the N-SIFs related to each Mode are proportional to different William's eigenvalues (that is, generally speaking, $\lambda_1 \neq \lambda_2 \neq \lambda_3$ for a given value of 2α, see Figure 3.28).

As stated earlier, such incongruences related to *i*) experimental against theoretical values of K_f, *ii*) N-SIF comparability and *iii*) addressment of mixed Mode fracture notably lead to the development of the SED method, which elegantly overcomes these issues (*Lazzarin & Zambardi, 2001*).

Finally, it is worth remarking that N-SIF approach has been further extended to deal with different configurations of weakened components, namely *rounded* (or *blunt*) *V notches*, *U-notches* or *keyholes* (*Lazzarin & Tovo, 1998*).

Notch rounding substantially changes the stresses at the notch tip, as the stress singularity is removed for a notch radius $\rho > 0$ (*Radaj & Vormwald, 2013*). Nevertheless, similar stress field expressions as respect to Equation 3.50 can be analytically derived for blunt notches, with σ_{ij} being governed by *generalised N-SIFs* $K^N_{M\rho}$, which are in turn depending on ρ. Formulations for $K^N_{M\rho}$ can be found in literature with respect to many relevant cases, and they all reduce to "standard" N-SIFs for the limit case of $\rho = 0$ (*Lazzarin & Tovo, 1998*).

For the sake of brevity, stress analysis addressed through generalised N-SIFs is not reported in this Section. However, blunt notches will be addressed in detail within the framework of SED method, in order to provide the required theoretical background for *i*) the fatigue assessment of blunt-V notched specimens of mild steel (*Chapter 6*) and *ii*) the fatigue analyses of hot-driven riveted connections, which will be carried out based on SED method application to U-notches.

3.4.2 Strain Energy Density (SED) Method

Lazzarin & Zambardi (*2001*) first noticed that applying N-SIF approach to fatigue analysis would lead in many cases to the prediction of a higher fatigue strength than the value obtained by simply dividing the fatigue limit of a plain specimen by the theoretical value of K^N_M (that is, for $0 \leq q \leq 1$, see Equation 3.53).

This suggested that fatigue failure of notched components was not governed by the notch stress, but rather by a mean stress averaged over a finite neighbourhood centred at the notch tip (*Lazzarin & Zambardi*; *2001*). The Authors elegantly dealt with this aspect and with all the limitations of the N-SIF approach by means of an energetic formulation.

Accordingly, an energetic, stress-related parameter was introduced to describe fatigue and fracture behaviour of notched components, i.e., the *averaged strain energy density* (ASED, hence also referred as $\overline{W}$) over a control volume Ω_{SED} centred at (or nearby) the notch tip (Equation 3.54 & Figure 3.30 – *Lazzarin & Zambardi*; *2001*; *Berto & Lazzarin, 2009, 2014*; *Lazzarin et al., 2010*):

$$\overline{W} = \frac{1}{\Omega_{SED}} \int_0^{\varepsilon_{ij}} \sigma_{ij} \, d\varepsilon_{ij} = \frac{1}{2} \frac{\sigma_{ij} \, \varepsilon_{ij}}{\Omega_{SED}} = \frac{1}{2} \frac{(\sigma_{\theta\theta} \, \varepsilon_{\theta\theta} + \sigma_{rr} \, \varepsilon_{rr} + \sigma_{zz} \, \varepsilon_{zz} + \tau_{r\theta} \, \gamma_{r\theta})}{\Omega_{SED}} \qquad (3.54)$$

with ε_{ij} being the notch strain components.

Range of validity for Equation 3.54 includes linear elastic materials exhibiting brittle or quasi-brittle failure (*Berto & Lazzarin, 2014*). Shape and size of the control volume Ω_{SED} were determined based on theoretical considerations related to the stress distribution around the notch tip. Accordingly, for the relevant case of plain stresses and plain strains, Ω_{SED} is shaped as follows depending on the notch opening angle 2α and on the notch radius ρ (*Berto & Lazzarin, 2014*):

- In case of sharp V-notches and cracks, the control volume has a circular sector footprint centred at the notch tip, sweeping an angle $2\pi - 2\alpha$ and having radius R_0 (Figure 3.30a-b);
- In case of blunt V- or U-notches in Mode I loading, the control volume has a crescent moon footprint, aligned with the notch bisector and having maximum depth R_0. Ω_{SED} is given by the intersection between the component and a cylinder of radius $r + R_0$, where $r = \rho(\pi - 2\alpha)/(2\pi - 2\alpha)$ (Figure 3.30c-d);
- In case of blunt V- or U-notches in Mode II or mixed Mode loading, the control volume is identical to Mode I, yet aligned with a segment containing the notch centre N and the point S where the maximum principal stress is attained (Figure 3.30e-f).
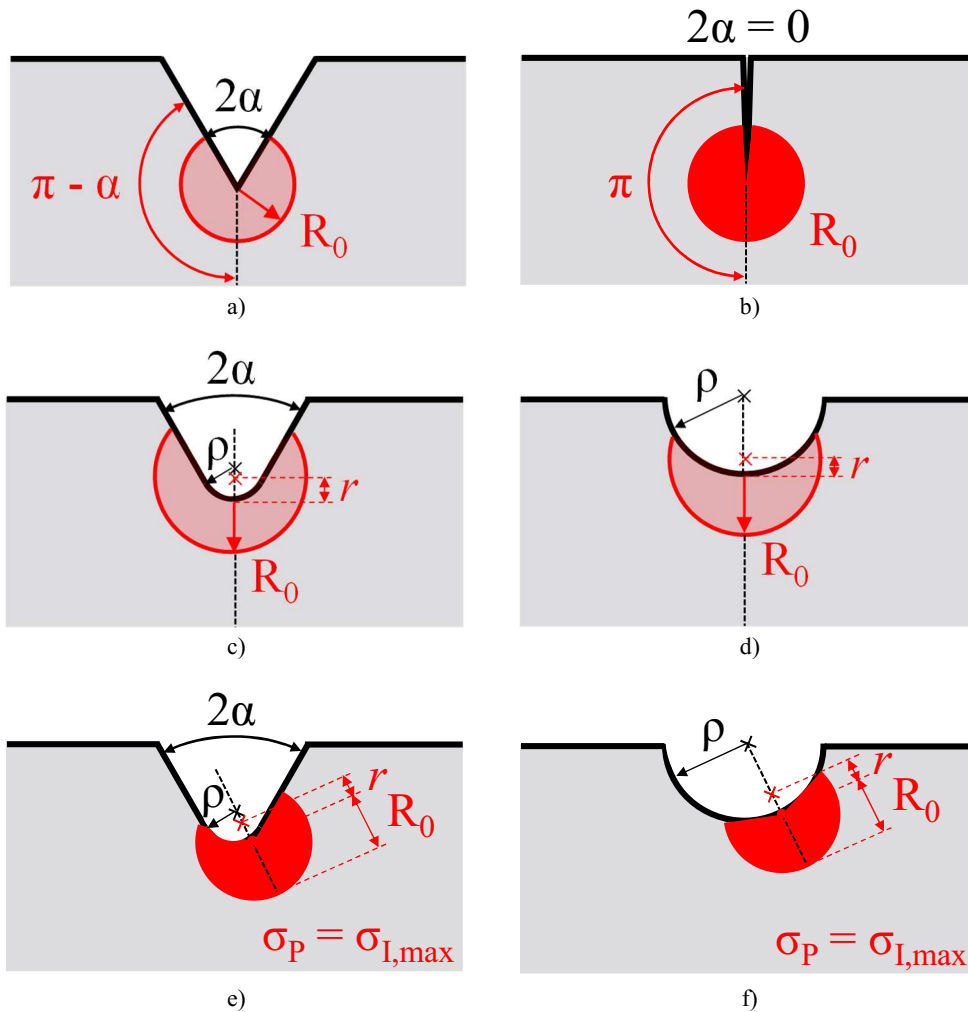
Figure 3.30 Shape and size of control volume Ω_{SED} for ASED calculations: sharp V-notches and cracks (a-b), blunt V- and U-notches under Mode I loading (c-d), blunt V- and U-notches under mixed Mode loading (e-f) (*Berto & Lazzarin, 2014*).

The control volume radius R_0 is intended as a material parameter independent on the notch geometry, although it is affected by the nature of applied stress field (e.g., plain stress or plain strain conditions – *Berto & Lazzarin, 2014*). Therefore, convenient limit conditions can be used to infer its value (e.g., sharp cracks for which $2\alpha = 0$).

Accordingly, for monotonic Mode I fracture, R_0 can be related to the material UTS and fracture toughness K_{IC} as follows (Equation 3.55 – *Lazzarin & Zambardi, 2001*):

$$R_0 = \frac{I_1(\gamma = \pi)}{\pi} \left(\frac{K_{IC}}{f_u}\right)^2 \tag{3.55}$$

where I_1 is the *opening-angle depending elastic integral* and $\gamma = \pi - \alpha$. I_1 values for varying γ were numerically derived by *Lazzarin & Zambardi* (*2001*), which proposed quadratic interpolating functions depending on 2α. However, for the relevant case of sharp cracks in plane stresses/strains conditions, elegant expressions for $I_1(\pi)$, and thus for R_0, have been derived by *Yoshibash* (*2004*) (Equation 3.56a-b):

$$\text{Plain stresses:} \quad R_0 = \frac{5 - 3\,v}{4\pi} \left(\frac{K_{IC}}{f_u}\right)^2 \tag{3.56a}$$

$$\text{Plain strains:} \quad R_0 = \frac{(1 + v)\,(5 - 8\,v)}{4\pi} \left(\frac{K_{IC}}{f_u}\right)^2 \tag{3.56b}$$

In monotonic conditions, fracture is predicted to occur when a *critical ASED* value $\overline{W}_C$ is attained. For an ideally elastic, isotropic and brittle material, critical ASED can be estimated directly as follows (Equation 3.57 – *Berto & Lazzarin, 2014*):

$$\overline{W} = \overline{W}_C = \frac{f_u^2}{2E} \rightarrow \text{Failure} \tag{3.57}$$

As for the relevant case of fatigue collapse, SED method can be successfully applied by introducing the *ASED range* $\Delta\overline{W} = \overline{W}_{max} - \overline{W}_{min}$ as a fracture indicator (*Radaj & Vormwald, 2013*). To this end, Basquin's formula can be conveniently expressed in terms of $\Delta\overline{W}$ as follows (Equation 3.58 – *Berto & Lazzarin, 2014*):

$$N^* = C\,(\Delta\overline{W})^{-m} \leftrightarrow \log N^* = \log C - m \log \Delta\overline{W} \tag{3.58}$$

In cyclic Mode I conditions, R_0 can be conveniently estimated by replacing K_{IC} with the endurable N-SIF range ΔK_E^N for a proper value of N^* (usually $N_C = 2 \cdot 10^6$) and the material UTS with the fatigue strength $\Delta\sigma_E$ of a smooth specimen for the same N^*, e.g., the detail class $\Delta\sigma_C$ if $N^* = N_C$ is assumed (Equation 3.59 – *Lazzarin & Zambardi, 2001*):

$$R_0 = \left[\frac{\Delta K_E^N}{f_1(2\alpha)\,\Delta\sigma_E}\right]^{\frac{1}{1-\lambda_1}} \tag{3.59}$$

with $f_1(2\alpha)$ being a dimensionless function of the notch opening angle. $f1$ values for varying 2α based on FEAs can be found in *Lazzarin & Zambardi* (*2001*).

Equation 3.59 suggests that the control volume size is, on principle, different for the same material under monotonic and cyclic conditions. However, as suggested by *Lazzarin et al.* (*2004*) when investigating welded steel joints, only minor differences in terms of fatigue predictions are obtained for different values of R_0, provided that Mode II stresses (if present) are non singular.

Therefore, a preliminary investigation of fatigue performance of components can be made by estimating the control volume radius R_0 according to Equation 3.56a-b. Fatigue analysis through $\Delta\overline{W}$ parameter was successfully applied to a bulk of more than 900 experimental tests on fillet welded cruciform joints, both made of steel and aluminium (Figure 3.31 – *Livieri & Lazzarin, 2005*).
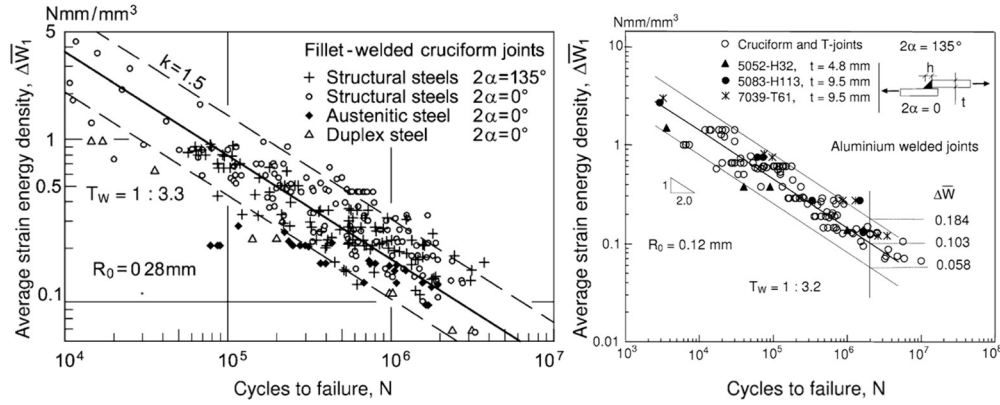
Figure 3.31 Validation of the SED method for the fatigue analysis of welded steel and aluminium joints (adapted from *Livieri & Lazzarin, 2005*).

It is worth mentioning that, differently from standard conditions for fatigue analyses (e.g., referring to fully-reversal loading, R = -1), ASED fatigue approach assumes zero-to-tension loading as a reference condition, i.e., R = 0 (*Radaj & Vormwald, 2013*). Nevertheless, mean-stress effect can be explicitly accounted for by means of a non-dimensional *prestress coefficient* c_w depending on the stress ratio as follows (Equation 3.60a-b – *Lazzarin et al., 2004*):

$$\Delta\overline{W}(R \neq 0) = c_w\, \Delta\overline{W}(R = 0) \tag{3.60a}$$

$$c_w = \frac{1 - \text{sign}(R)\, R^2}{(1 - R)^2} \tag{3.60b}$$

c_w can be graphically regarded as the ratio among the areas underlying stress-strain curves (that is, $\Delta\overline{W}$), bounded by the same stress range $\Delta\sigma$ but for $R \neq 0$ and R = 0, respectively (Figure 3.32 – *Lazzarin et al., 2004*)
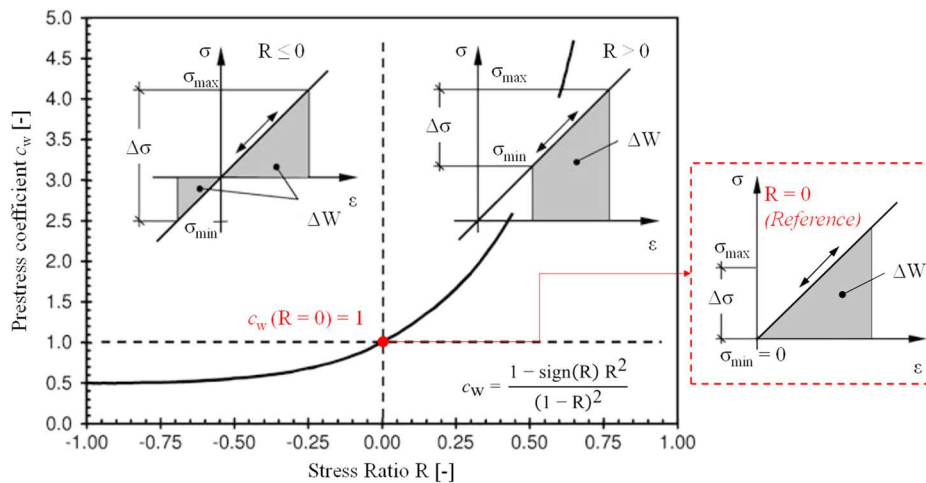
Figure 3.32 Graphical interpretation and relevant values of the prestress coefficient c_w against the stress ratio R (adapted from *Lazzarin et al., 2004*).

Notably, Equation 3.60b yields $c_w = 1$ for zero-to-tension loading (R = 0) and $c_w = 0.5$ for fully-reversal loading (R = –1).

Several closed forms for ASED estimations have been developed up to present time for both sharp and blunt notches. Some relevant expressions for plain stresses/strains Mode I conditions are reported in the following, as they can serve as an useful tool of comparison for more complex cases (Equation 3.61a-c – *Berto & Lazzarin, 2014*):

$$\text{Sharp notches } (\rho = 0, 2\alpha \geq 0): \quad \overline{W} = \frac{e_1(2\alpha)}{E}\left(K_I^N\, R_0^{\lambda_1 - 1}\right)^2 \tag{3.61a}$$

$$\text{Blunt V-notches } (\rho > 0, 2\alpha > 0): \quad \overline{W} = \frac{F(2\alpha)\, H\left(2\alpha, \dfrac{R_0}{\rho}, \nu\right)}{E}\, \sigma_{max}^2 \tag{3.61b}$$

$$\text{U-Notches } (\rho > 0, 2\alpha = 0): \quad \overline{W} = \frac{H\left(\dfrac{R_0}{\rho}, \nu\right)}{E}\, \frac{\pi\, \sigma_{max}^2}{4} \tag{3.61c}$$

with $e_1(2\alpha)$, $F(2\alpha)$, $H(2\alpha, R_0/\rho, \nu)$ being dimensionless functions of the notch opening angle and, as for H, the control volume radius, the notch radius and the material Poisson's ratio ν.

Remarkably, ASED for sharp notches has to be expressed in terms of the relevant N-SIF due to stress singularity, while for blunt notches $\overline{W}$ can be directly related to the maximum (finite) stress at the notch tip σ_{max}. Moreover, as U-notches can be regarded as a particular case of blunt V-notches having $2\alpha = 0$, the simplified expression reported in Equation 3.61c can be used, as $F(2\alpha = 0) = \pi/4$ and the dependence of H on 2α is removed (*Radaj & Vormwald, 2013*).

Values of the above functions are reported in Table 3.2 for the relevant case of steel, i.e., for $\nu = 0.3$ (*Berto & Lazzarin, 2014*).

Table 3.2 Values of $e_1(2\alpha)$, $F(2\alpha)$ and $H(2\alpha, R_0/\rho, \nu = 0.3)$ functions for different configurations of steel notches (*Berto & Lazzarin, 2014*).

2α [°]	e_1 [-]	F [-]	H ($\nu = 0.3$) [-]		
			$R_0/\rho = 0.01$	$R_0/\rho = 0.1$	$R_0/\rho = 1$
0	0.1330	0.7850	0.5638	0.4518	0.1314
45	0.1498	0.6692	0.6609	0.5264	0.1447
90	0.1449	0.7049	0.629	0.4955	0.1328
135	0.1182	1.0717	0.4114	0.3206	0.1037

3.5. Application of fatigue analysis techniques for hot-driven riveted connections

Presented formulations for the fatigue analysis of structural components can be suitably applied to the relevant case of hot-driven riveted connections.

In the present work, an appropriate procedure is introduced to provide design charts for the fatigue assessment of hot-driven riveted connections, namely based on both nominal stress method and SED method (Figure 3.33).

The control volume radius R_0 for the application of the SED method is conveniently estimated based on experimental activities and further results drawn from literature with reference to historic steels. Indeed, as stated in the previous Section, R_0 does not depend on the specimen geometry, but it is rather a base material parameter.
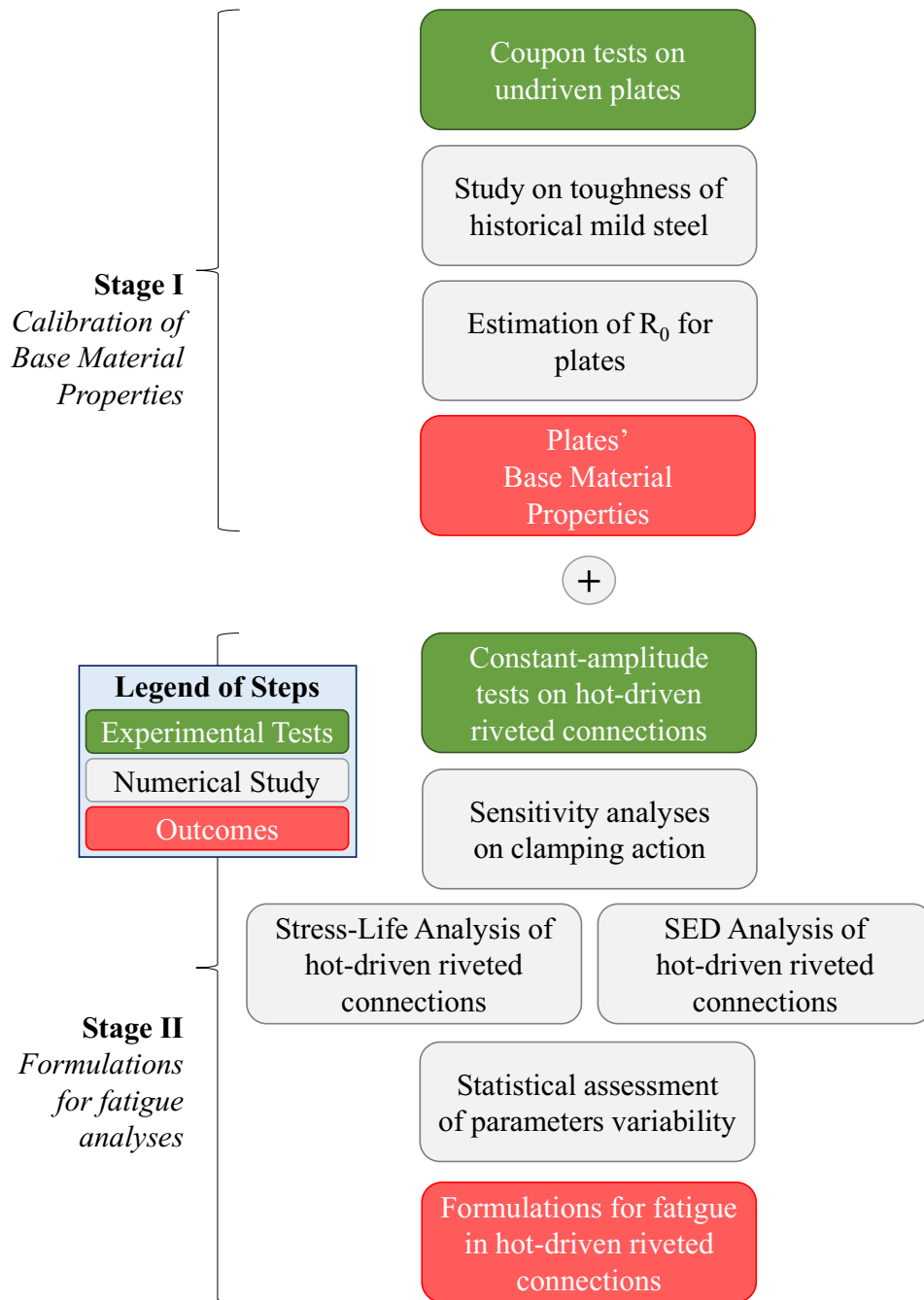
Figure 3.33 Adopted two stages procedure for the definition of design charts devoted to the fatigue analysis of hot-driven riveted connections.

The applicability of SED method with reference to blunt notched components made of mild steels is further investigated in *Chapter 6*. The influence of high stress ratios (R ≥ 0.7) is also investigated to ensure that randomness of clamping actions will not invalidate the reliability of results.

In Stage II, fatigue analysis of hot-driven riveted connections is performed. Mean stress effect is suitably accounted for by means of corrective models reported in *Section 3.3.4* (stress-life methods) and *Section 3.3.7* (strain-life methods).

For this purpose, a dedicated sensitivity analysis for clamping actions is preliminarily performed owing to their intrinsic variability (*Leonetti et al., 2020*).

Within the framework of modified nominal stress methods, a $\Delta\sigma$ correction proposed by *Maljaars & Euler* (*2021*) is also used as a comparing tool. Notably, this correction will be featured in the next version of European fatigue provisions, which is only available in form of an under review draft at present time (prEN1993:1-9-2020 – *CEN, 2020*). According to the Authors, $\Delta\sigma_{mod}$ should be estimated as follows (Equation 3.62a-b):

$$\Delta\sigma_{mod} = k_{mod}\,\Delta\sigma_{net} = k_{mod}\,\frac{w}{w - d_0}\,\Delta\sigma \tag{3.62a}$$

$$k_{mod} = a + \left(b - c\,\frac{d_0}{w}\right)^3 \tag{3.62b}$$

with *a*, *b*, *c* being calibrated non-dimensional parameters depending on the number of fasters rows. Suggested values are reported in Table 3.3.

Table 3.3 Suggested values of *a*, *b*, *c* for fatigue assessment of non-preloaded fitted bolted connections (*CEN, 2020*; *Maljaars & Euler, 2021*).

Number of rivet rows	*a* [-]	*b* [-]	*c* [-]
1	1.0	1.6	2.7
2	1.0	1.3	2.2
≥ 3	1.0	1.1	1.8

It is worth remarking that Equation 3.62a-b has not been originally formulated by *Maljaars & Euler* (*2021*) as respect to hot-driven assemblies. Indeed, the Authors derived the above formulation for *non-preloaded fitted bolts*, proposing a detail class $\Delta\sigma_C = 71$ N/mm². Nonetheless, geometries for hot-driven riveted and fitted bolted joints are quite similar due to hammering-induced shank dilatation (*D'Aniello et al., 2011*).

Moreover, as clamping action cannot be reliably controlled in hot-driven riveted connections (*Leonetti et al., 2020*), a further analogy can be established with non-preloaded bolts.

Comparison of experimental results with Equation 3.62a-b can provide an useful insight about the effect of hot-driving on the fatigue performance of riveted details, as the above detail class was derived with respect to connections unaffected by any thermo-mechanical manufacturing process.

As for the application of SED method to hot-driven assemblies, perforated plates can be conveniently addressed with the theory of U-notches (Figure 3.34).

Refined parametrical FEAs are performed to account for possible alterations of the control volume due to hot-driving. Indeed, realistic values of R_0 for mild steels are in the range $0.2 \div 1.0$ mm (*Radaj & Vormwald, 2013*), therefore Ω_{SED} is always included in the hot-driven affected zone (that is, the projection of the rivet field head on the perforated plate).

Finally, in order to provide handy design charts devoted to the fatigue assessment of hot-driven riveted connections, SED results can be also reduced to a stress-based formulation. Indeed, by manipulating Equations 3.60-3.61 an equivalent, SED-based stress magnification factor ($SMF_{eq,SED}$) can be introduced to account for connections geometry and mechanical features (Equation 3.63a-b):
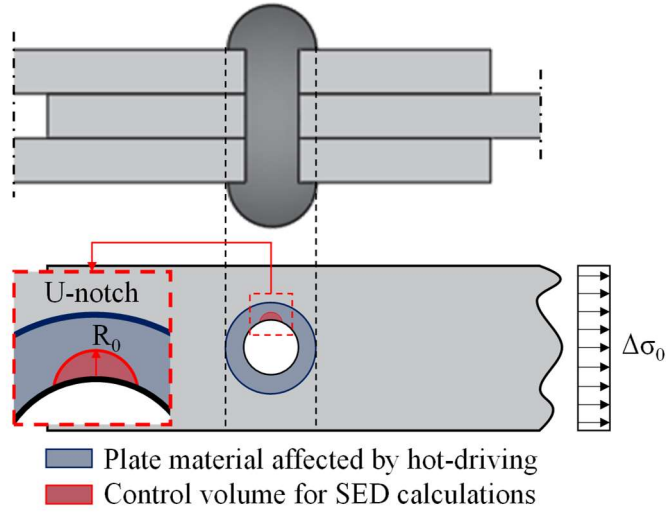
Figure 3.34 Application of SED method to hot-driven riveted connections.

$$\Delta \overline{W} = c_w \frac{H\left(\frac{R_0}{\rho}\right)}{E} \frac{\pi \, \Delta\sigma_{tip}^2}{4} \overset{def}{\cong} c_w \frac{(SMF_{eq,SED} \, \Delta\sigma)^2}{2E} \tag{3.63a}$$

$$SMF_{eq,SED} = \sqrt{\frac{2E}{c_w} \, \Delta\overline{W}} \, \frac{1}{\Delta\sigma} \tag{3.63b}$$

Values of $\Delta\overline{W}$ and $SMF_{eq,SED}$ can be conveniently estimated by means of *free mesh* FEAs. Indeed, as shown by *Lazzarin et al., 2010* and *Foti et al., 2020*, the Finite Element Method is a potent tool to perform ASED calculations.

Common finite elements (e.g. *solid bricks*, either *8-node linear* or *20-node quadratic* ones) feature displacement-based formulations (*Cook, 1995*). Therefore, calculated stresses (i.e., recollected in a stresses vector **σ**) are strongly mesh-sensitive, as they are estimated based on the following quantities, namely (Equation 3.64):

- the *vector of global nodal displacements **d***;
- the *displacement vector **u**(x)*, which collects interpolated displacements for any given point *x* within the element;
- the strain vector **ε**(x) which collects interpolated strains for any given point *x* within the element;
- the *constitutive matrix* **C**, that is, a square matrix describing the constitutive material behaviour. For the simplest and relevant case of elastic isotropic material, **C** only involves constant quantities expressed in terms of E and ν;
- the *strain-displacement matrix* **B**(x), that is, a square matrix containing space derivatives of shape functions $N_i(x)$, which are in turn recollected in the *shape functions interpolating matrix* **N**(x).

$$\boldsymbol{u}(x) = \mathbf{N}(x) \, \boldsymbol{d} \tag{3.64a}$$

$$\boldsymbol{\varepsilon}(x) = \frac{d\mathbf{u}(x)}{dx} = \frac{d\mathbf{N}(x)}{dx} \, \boldsymbol{d} = \mathbf{B}(x) \, \boldsymbol{d} \tag{3.64b}$$

$$\boldsymbol{\sigma}(x) = \mathbf{C} \, \boldsymbol{\varepsilon}(x) = \mathbf{C} \, \mathbf{B}(x) \, \boldsymbol{d} \tag{3.64c}$$

cxviii

Therefore, stress (and strain) estimation accuracy outside integration points ultimately depends on the nature of $\mathbf{N}(x)$, and hence on the ability of shape functions to simulate complex displacements, strains and stresses fields (*Cook, 1995*).

However, shape functions degree is bounded to be equal to the number of DOFs of the finite element in order to preserve $\mathbf{N}(x)$ invertibility, i.e., a condition required to provide a solution of the FE problem. Therefore, stress and strain estimation accuracy is intrinsically limited by the nature of the finite element and further penalized by the derivative introduced in Equation 3.64b, which lowers the degree of functions $d\mathrm{N}_i(x)/dx$ collected in the $\mathbf{B}(x)$ matrix (*Cook, 1995*).

Contrariwise, *Lazzarin et al.,* (*2010*) proved how averaged strain energy density is directly estimated based on the vector of nodal displacements. Indeed, if ASED definition is transposed in the framework of FEM, the following expressions hold true (Equation 3.65 – *Lazzarin et al., 2010*):

$$\mathrm{W}(\mathrm{x}) = \frac{1}{2}\boldsymbol{\varepsilon}^{\mathbf{T}}(x)\,\boldsymbol{\sigma}(x) = \frac{1}{2}\boldsymbol{d}^{\mathrm{T}}\mathbf{B}^{\mathrm{T}}(x)\,\mathbf{C}\,\mathbf{B}(x)\,\boldsymbol{d} \tag{3.65a}$$

$$\overline{\mathrm{W}} = \frac{1}{\Omega_{\mathrm{SED}}}\int_{\Omega_{\mathrm{SED}}}\mathrm{W}\,d\mathrm{V} = \frac{1}{2\Omega_{\mathrm{SED}}}\boldsymbol{d}^{\mathrm{T}}\mathbf{K}\,\boldsymbol{d} \tag{3.65b}$$

$$\boldsymbol{K} = \int_{\mathrm{FE}}\mathbf{B}^{\mathrm{T}}(x)\,\mathbf{C}\,\mathbf{B}(x)\,d\mathrm{V} \tag{3.65c}$$

where $\mathrm{W}(x)$ is the SED estimated on a given point x of the finite element and $\mathbf{K}$ is the so-called *stiffness matrix* of the FE (*Cook, 1995*).

Therefore, significantly coarser meshes can be used for ASED calculations with respect to stresses, as nodal displacement values are "exact" quantities (*Cook, 1995*).

Lazzarin et al. (*2010*) originally suggested a *control volume-based* FEM application of the SED method; that is, the Authors partitioned components in order to separate Ω_{SED} from the rest of the FE model. Accordingly, finite elements could be refined only within Ω_{SED}, while a very coarse mesh could be adopted elsewhere. The Authors successfully proved how this technique would result in negligible errors ($\leq 5\%$) with respect to theoretical ASED values.

However, this control volume-based FEM application reveals two major drawbacks when applied to blunt notched components, namely *i*) the necessity of performing two separate FEAs if the control volume centre is unknown (e.g., in case of mixed Mode loading) and *ii*) the difficulty in performing wide parametrical analyses, as the control volume needs to be partitioned and re-meshed several times. These issues were both overcome by developing and validating a *free mesh* FEM application of the SED method. As demonstrated by *Foti et al.* (*2020*), if free mesh (i.e., with no partitioned control volume) is adopted, accurate ASED estimations can be still achieved, provided that *i*) *quadratic* solid or shell elements are used and *ii*) the mesh size in the neighbourhood of the notch tip is smaller or equal than $R_0/4$.

If both conditions are met, the control volume can *a-posteriori* approximated with a *cylindric selection command* (*Dassault, 2014*), and $\overline{\mathrm{W}}$ can be estimated by considering the total strain energy and the volume of the sole *picked* elements, although the selection has jagged borders due to the lack of Ω_{SED} partition (Figure 3.35 – *Foti et al., 2020*).

This latter approach is followed in the present thesis work, in order to allow performing the aforementioned parametrical analyses on the value of R_0 for hot-driven plates. Accordingly, the minimum mesh size will be selected equal to $^1/_4$ of the minimum assumed control volume radius $R_{0,\mathrm{min}}$.
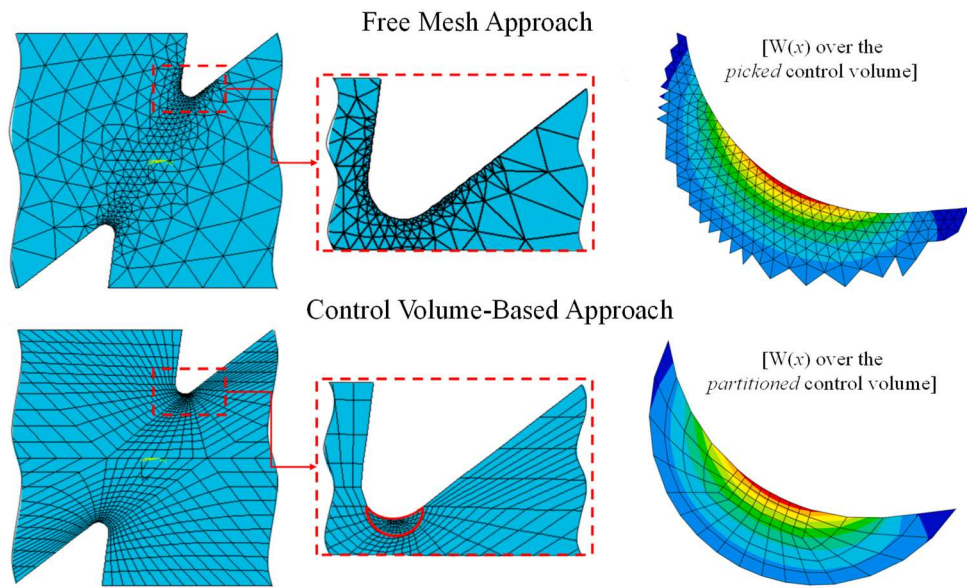
Figure 3.35 Comparison among control volume-based and free mesh FEM SED calculations for blunt notches under mixed Mode loading (adapted from *Foti et al., 2020*).

Chapter 4

Experimental Activities

The present Chapter provides a detailed description of performed experimental activities devoted to the static and fatigue performance of mild steel components and assembled hot-driven riveted connections.

For instance, the following test campaigns and relevant experimental results are presented in the following Sections: *i*) static and fatigue tests on mild steel blunt V-notched specimens (*Section 4.1*), *ii*) static tests on hot-driven riveted connections (*Section 4.2*) and *iii*) fatigue tests on hot-driven riveted connections (*Section 4.3*).

4.1. Experimental tests on mild steel blunt-V notched specimens

4.1.1 Generality

The present Section summarizes the experimental activities carried out on the characterization of the fatigue behavior of blunt V-notched cylinders made of mild steel grade C45 (*ISO 683-1, 2016*). Experimental tests were performed with the aid of the Candidate during his visiting period at *Norwegian University of Science and Technology* (NTNU, Trondheim, Norway).

In particular, the present experimental campaign aimed at *i*) investigating the validity of SED method for mild steel specimens and *ii*) assessing the cyclic behaviour of these specimens under high or very high stress ratios (R = 0.7 ÷ 0.9), in order to highlight the effect of these stress regimes on fatigue performance.

Two different configurations of notched cylindrical specimens were used for the fatigue characterization of C45 steel, for a total of 35 (18 + 17) specimens. In particular, the two geometries differ in terms of the diameter of the minimum section, as reported in Table 4.1. Geometrical features for investigated specimens are also depicted in Figure 4.1. parameters of these geometries.
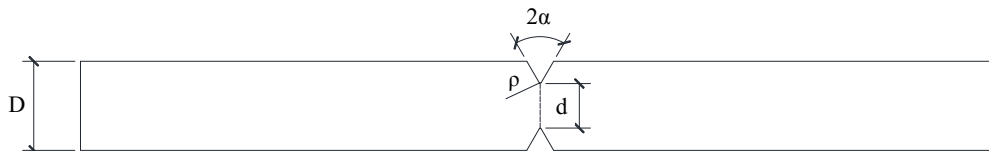
Figure 4.1 Geometrical features for the tested cylindrical notched specimens made of mild steel.

Table 4.1 Geometrical features for the tested cylindrical notched specimens made of mild steel.

	Configuration I	Configuration II
Outer diameter D [mm]	10.0	10.0
Inner (minimum) diameter d [mm]	5.0	7.5
Notch radius ρ [mm]	0.1	0.1
Notch opening angle 2α [°]	60	60

The specimens characterized by the same geometry were all nominally identical and made of C45 steel, the nominal physical and mechanical properties of which, as prescribed by *ISO 683-1* (*2016*), are summarized in Table 4.2.

Table 4.2 Nominal physical and mechanical parameters of C45 steel (*ISO 683-1, 2016*).

Steel	$d \leq 16$ mm				
	$R_{e,min}$	R_m	A_{min}	Z_{min}	KV^b_{min}
	[N/mm^2]	[N/mm^2]	[%]	[%]	[J]
	490	700 ÷ 850	14	35	-
	16 mm $\leq d \leq 40$ mm				
	$R_{e,min}$	R_m	A_{min}	Z_{min}	KV^b_{min}
C45	[N/mm^2]	[N/mm^2]	[%]	[%]	[J]
	430	650 ÷ 800	16	40	-
	40 mm $\leq d$				
	$R_{e,min}$	R_m	A_{min}	Z_{min}	KV^b_{min}
	[N/mm^2]	[N/mm^2]	[%]	[%]	[J]
	370	630 ÷ 780	17	45	-
$R_{e,min}$:	Minimum (granted) tensile resistance;				
R_m:	Mean tensile resistance;				
A_{min}:	Minimum elongation at failure;				
Z_{min}:	Minimum Z-quality (through thickness);				
KV^b_{min}:	Minimum impact energy.				

In the next Sections, the following key aspects related to performed experimental activities are addressed, namely:

- Experimental test plan;
- Summary of the results of the tests conducted;
- Issues encountered during the experimental campaign;
- Statistical characterization and preliminary interpretation of results.

4.1.1 Plan for Experimental Tests

Specimens were tested using the Universal Machine *Instron 8850 Axial-Torsion System*, which is located in the *NTNU Fatigue Lab* under the supervision of the Mechanical Engineering Department (MTP).

Instron 8850 features a servo-hydraulic dynamic test system and a combined axial/torsional actuator having a maximum capacity of ± 100 kN/ ± 1000 Nm (Figure 4.2). Compatibly with the characteristics of the base material, a constant test frequency f_{test} = 30 Hz was assumed for all fatigue tests.

The plan for the experimental campaign was defined in order to provide results as robust and distributed as possible in the ranges of cycles at failure N* of interest for engineering applications (that is, N* $\leq$ 100'000 cycles, 100'000 cycles < N* $\leq$ 1'000'000 cycles, N > 1'000'000 cycles – *Schijve, 2009*).

As mentioned, one of the key aims of this experimental campaign was to investigate the effect of very high stress ratios R on the fatigue performance of mild steels. For this purpose, three different values of R = 0.7, 0.8, 0.9 were therefore selected for the tests. Compatibly with base material UTS, identical stress ranges Δσ were assumed (whenever possible) for varying values of R, in order to properly isolate the influence of mean-stress effect.
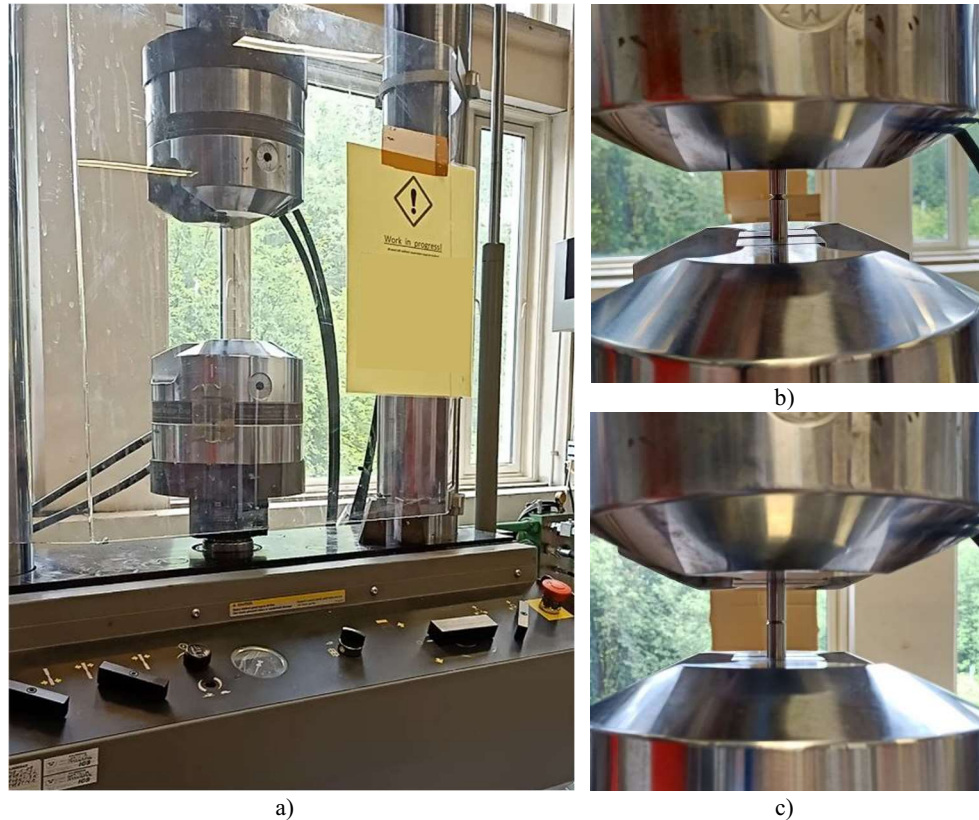
Figure 4.2 Experimental tests on mild steel blunt V-notched cylinders: a) Servo-hydraulic Universal Machine Instron 8850, b) specimen with $d = 5$ mm and c) specimen with $d = 10$ mm.

A large number of specimens $(18 + 17)$ was tested with the aim to (at least) double results for given values of R and $\Delta\sigma$, so as to allow a robust estimation of results scatter and thus to minimize statistical errors (*Schijve, 2009*).

The stress ranges $\Delta\sigma$ of concern were determined based on a preliminary characterization of the static properties of the specimens. Accordingly, subsequent fatigue tests were performed assuming aliquots of the ultimate load compliant with the desired number of cycles at failure N*.

It is worth remarking that the choice of stress ranges $\Delta\sigma$ was characterized by a certain degree of iteration, insofar as the preliminary results related to a small number of specimens were used to predict the outcomes of subsequent tests, thus optimizing the entire experimental campaign.

An appropriate labelling was also defined for all the performed tests, i.e., univocally summarizing the main test parameters for each specimen, namely:

Fatigue Tests
Labelling "FAABBCC" with:
F = Fatigue test (i.e., load-controlled, composed by an initial ramp up to the mean stress σ_m and by a superimposed constant-amplitude, sinusoidal wave with range $\Delta\sigma$);
AA = 50 or 75 in reference to the minimum diameter d of the notched section;
BB = 07, 08 or 09 with reference to the assumed stress ratio R;
CC = 01, 02, etc... with reference to order of performed tests, i.e., increasing for multiple tests having the same minimum diameter d and stress ratio R.

Static Tests

Labelling "TAACC" with:

T = Monotonic tensile test (i.e., displacement-controlled, with a constant displacement rate equal to 2 mm/min in order to avoid strain-rate related effects – *ASTM E8, 2010*);

AA = 50 or 75 in reference to the minimum diameter *d* of the notched section;

CC = 01, 02, etc... with reference to order of performed tests, i.e., increasing for multiple tests having the same minimum diameter *d*.

For the sake of clarity, the above nomenclature is hence always used within the present work to identify tested mild steel notched specimens.

Table 4.3 summarizes the tests carried out according to the above indications. For the sake of simplicity, the load protocols are hence expressed in terms of test settings required by the Instron 8850 Universal Machine, that is, the maximum and minimum applied forces (F_{max} and F_{min}, respectively) and force amplitudes $A = (F_{max} - F_{min})/2$.

Table 4.3 Summary of performed static and fatigue tests on C45 steel grade blunt notched cylinders.

Label	Test #	d	R	F_{max}	F_{min}	A	N* (expected)
[-]	[-]	[mm]	[-]	[kN]	[kN]	[kN]	[-]
T5001	1	5	Tensile Test				
T5002	2	5	Tensile Test				
F500701	1	5	0.7	20.0	14.0	3.0	< 100'000
F500702	2	5	0.7	13.3	9.3	2.0	1'000'000 ÷ 100'000
F500703	3	5	0.7	6.6	4.6	1.0	> 1'000'000
F500704	4	5	0.7	9.2	6.4	1.4	> 1'000'000
F500705	5	5	0.7	10.8	7.6	1.6	1'000'000 ÷ 100'000
F500706	6	5	0.7	13.3	9.3	2.0	1'000'000 ÷ 100'000
F500707	7	5	0.7	9.2	6.4	1.4	> 1'000'000
F500708	8	5	0.7	10.8	7.6	1.6	1'000'000 ÷ 100'000
F500801	1	5	0.8	20.0	16.0	2.0	1'000'000 ÷ 100'000
F500802	2	5	0.8	22.5	18.0	2.3	< 100'000
F500803	3	5	0.8	11.0	8.8	1.1	> 1'000'000
F500804	4	5	0.8	15.1	12.0	1.5	1'000'000 ÷ 100'000
F500901	1	5	0.9	21.1	19.0	1.1	> 1'000'000
F500902	2	5	0.9	23.0	20.7	1.2	1'000'000 ÷ 100'000
F500903	3	5	0.9	24.0	21.6	1.2	1'000'000 ÷ 100'000
F500904	4	5	0.9	18.8	16.9	0.9	> 1'000'000
T7501	1	7.5	Tensile Test				
T7502	2	7.5	Tensile Test				
F750701	1	7.5	0.7	40.0	28.0	6.0	< 100'000
F750702	2	7.5	0.7	32.8	23.0	4.9	1'000'000 ÷ 100'000
F750703	3	7.5	0.7	22.0	15.4	3.3	1'000'000 ÷ 100'000
F750704	4	7.5	0.7	40.0	28.0	6.0	< 100'000
F750705	5	7.5	0.7	32.8	23.0	4.9	1'000'000 ÷ 100'000

F750801	1	7.5	0.8	38.8	31.0	3.9	1'000'000 ÷ 100'000
F750802	2	7.5	0.8	40.0	32.0	4.0	1'000'000 ÷ 100'000
F750803	3	7.5	0.8	21.3	17.0	2.1	> 1'000'000
F750804	4	7.5	0.8	40.0	32.0	4.0	1'000'000 ÷ 100'000
F750805	5	7.5	0.8	38.8	31.0	3.9	1'000'000 ÷ 100'000
F750806	6	7.5	0.8	30.6	24.5	3.1	> 1'000'000
F750901	1	7.5	0.9	44.0	39.6	2.2	> 1'000'000
F750902	2	7.5	0.9	36.8	33.1	1.8	> 1'000'000
F750903	3	7.5	0.9	46.0	41.4	2.3	1'000'000 ÷ 100'000
F750904	4	7.5	0.9	45.0	40.5	2.3	1'000'000 ÷ 100'000

According to the above tests plan, 18 specimens with a minimum cross-section $d = 5$ mm were tested (2 static tests "T" + 16 fatigue tests "F"), while 17 specimens with a minimum cross-section $d = 7.5$ mm were tested instead (2 T + 15 F, Table 4.4).

It is worth remarking that the present campaign figures as part of a wider experimental investigations aiming at characterizing the fatigue performance of mild steel notched cylinders, namely with the aim to assess the influence of circumferential stresses ("*hoop stresses*" – *Irgens, 2008*) on fatigue life. Therefore, 12 F50BBCC specimens and 13 F75BBCC specimens are still being tested at present time as a complement for such investigation. To this end, preliminary numerical findings related to hoop stresses in blunt notched cylinders are reported in *Chapter 6*.

Table 4.4 Summary of tested and available blunt notched cylindrical specimens made of C45 steel.

Minimum diameter d [mm]	Tested specimens				Available specimens
5	T	F			12
		R = 0.7	R = 0.8	R = 0.9	
	2	8	4	4	
	Total	18			30
7.5	T	F			13
		R = 0.7	R = 0.8	R = 0.9	
	2	5	6	4	
	Total	17			30

4.1.2 Experimental Tests Results

As stated earlier, a total of 2 + 2 = 4 static tests were preliminarily performed on both configurations of notched specimens in order to provide an upper boundary to fatigue load protocols. Static tests results are summarized in Table 4.5 and Figure 4.3, respectively.

Table 4.5 Summary of static tests on notched specimens.

Minimum diameter d [mm]	Ultimate Load F_u [kN]			Ultimate Eng. Stress σ_u [N/mm^2]		
5	T1	T2	Avg.	T1	T2	Avg.
	24.9	26.1	25.5	1265.7	1330.5	1298.1
7.5	T1	T2	Avg.	T1	T2	Avg.
	47.7	48.8	48.1	1070.2	1105.6	1087.9
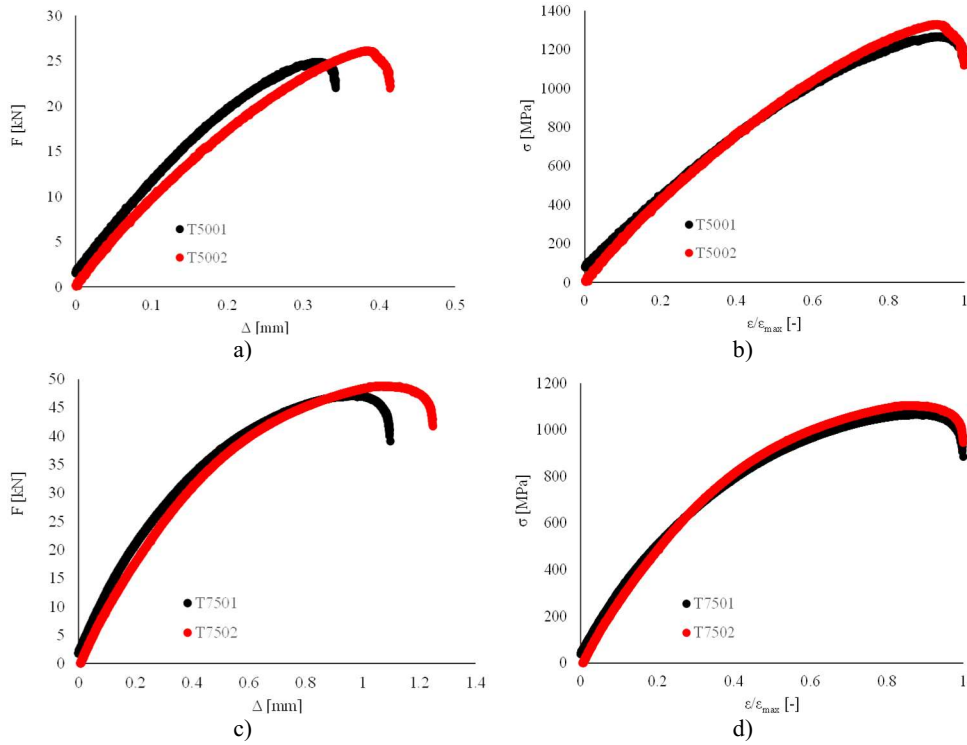
Figure 4.3 Static tests results: a) T50CC and b) T75CC.

For the sake of clarity, the monotonic response of specimens in expressed both in terms of Force-Displacement (F-Δ, Figure 4.3a-c) and Engineering stress-strain (σ-ε, Figure 4.3b-d) curves, with the latter parameter being normalized as respect to the engineering fracture strain ε_{max}.

It is worth noting that the ultimate engineering stresses σ_u are intended as nominal quantities referred to the minimum cross-section of the notched specimens (that is, $A_{min,T50CC} = 19.6$ mm^2 and $A_{min,T750CC} = 44.2$ mm^2, respectively). Accordingly, σ_u values were estimated as follows (Equation 4.1):

$$\sigma_u = \frac{4\,F_u}{\pi\,d^2} \tag{4.1}$$

As expected, both specimens show a significant notch effect (*Anderson, 2017*), which is stronger in the case of a smaller minimum cross-section. Namely, the maximum nominal stresses on the notched cross-section are equal, on average, to 1.66 (T500CC) and 1.40 (T750CC) times the ultimate tensile strength f_u for smooth specimens (779 N/mm^2). Additionally, a fictious "embrittlement" of specimens is observed owing to stress concentrations at the notch tip. Both effects are less pronounced in T750CC specimens as the notch depth (D – d)/2 is smaller (*Anderson, 2017*).

Nevertheless, an amount of ductility was preserved by both specimens, as noticeable both from engineering σ-ε curves and fracture surfaces, on which some traces of necking can be appreciated, i.e., mostly for specimens with $d = 7.5$ mm (Figure 4.4).

As for high stress ratio fatigue tests, relevant results are summarized in Table 4.6 and Figure 4.4a-b (Wohler diagrams), respectively.

For instance, nominal stress ranges $\Delta\sigma$ referred to the net cross-section (that is, estimated according to Equation 4.1 by replacing F_u with ΔF) are reported against the experimental number of cycles at failure N*. In this preliminary phase, no correction is applied to stress ranges to account for mean-stress effect.

<div align="center">a)   b)</div>

Figure 4.4 Macroscopical fracture surfaces for statically tested specimens: a) T5001 and b) T7501.

Therefore, mean Wohler curves for different values of *d* and R are separately depicted (*d* = 5 mm: Figure 4.5a, d = 7.5 mm: Figure 4.5b; R = 0.7: black points and dotted curves, R = 0.8, grey points and dotted curves, R = 0.9: red points and dotted curves).

Each nominal, mean S-N curve was derived adopting a logarithmic regression model corrected by means of Liebermann's beta coefficients β_L (see *Section 4.4.4* for further details – *Liebermann, 1957*).

In order to avoid overly time-consuming tests for specimens loaded below the CAFL (unknown), a runout value for the number of loading cycles $N_{max} = 2 \cdot 10^6$ was initially set. Nevertheless, in some cases specimens were tested for a number of cycles beyond N_{max} to attempt at identifying the CAFL within the experimental campaign. For the sake of clarity, specimens resulting in a runout are highlighted in grey in Table 4.6.

Table 4.6 Summary of fatigue tests on notched specimens.

Label	R	F_{max}	F_{min}	A	$\Delta\sigma$	σ_m	σ_{max}	N*	Remarks
[-]	[-]	[kN]	[kN]	[kN]	[N/mm²]	[N/mm²]	[N/mm²]	[-]	[-]
F500701	0.7	20.0	14.0	3.0	305.6	865.8	1018.6	39311	
F500702	0.7	13.3	9.3	2.0	203.2	575.8	677.4	149099	
F500703	0.7	6.6	4.6	1.0	100.8	285.7	336.1	2174000	Runout
F500704	0.7	9.2	6.4	1.4	140.0	396.5	466.5	2467119	
F500705	0.7	10.8	7.6	1.6	165.0	467.4	549.9	724228	
F500706	0.7	13.3	9.3	2.0	203.2	575.8	677.4	139981	
F500707	0.7	9.2	6.4	1.4	140.0	396.5	466.5	1475944	
F500708	0.7	10.8	7.6	1.6	165.0	467.5	550.0	385254	
F500801	0.8	20.0	16.0	2.0	203.7	916.7	1018.6	157354	
F500802	0.8	22.5	18.0	2.3	229.2	1031.3	1145.9	96466	
F500803	0.8	11.0	8.8	1.1	112.0	504.2	560.2	1.4E+07	
F500804	0.8	15.1	12.0	1.5	153.3	689.8	766.5	546636	
F500901	0.9	21.1	19.0	1.1	107.5	1020.9	1074.6	2761807	
F500902	0.9	23.0	20.7	1.2	117.1	1112.8	1171.4	632017	
F500903	0.9	24.0	21.6	1.2	122.2	1161.2	1222.3	248212	
F500904	0.9	18.8	16.9	0.9	95.6	908.6	956.5	2358780	Runout
F750701	0.7	40.0	28.0	6.0	271.6	769.6	905.4	61511	
F750702	0.7	32.8	23.0	4.9	223.0	631.8	743.3	120135	
F750703	0.7	22.0	15.4	3.3	149.4	423.3	498.0	492223	
F750704	0.7	40.0	28.0	6.0	271.6	769.6	905.4	40583	
F750705	0.7	32.8	23.0	4.9	223.0	631.8	743.3	120185	

F750801	0.8	38.8	31.0	3.9	175.7	790.4	878.3	234940	
F750802	0.8	40.0	32.0	4.0	181.1	814.9	905.4	175440	
F750803	0.8	21.3	17.0	2.1	96.4	433.9	482.1	2600000	Runout
F750804	0.8	40.0	32.0	4.0	181.1	814.9	905.4	146227	
F750805	0.8	38.8	31.0	3.9	175.7	790.4	878.3	185495	
F750806	0.8	30.6	24.5	3.1	138.5	623.4	692.6	514254	
F750901	0.9	44.0	39.6	2.2	99.6	946.2	996.0	1053000	
F750902	0.9	36.8	33.1	1.8	83.3	791.3	833.0	7470000	Runout
F750903	0.9	46.0	41.4	2.3	104.1	989.2	1041.2	632581	
F750904	0.9	45.0	40.5	2.3	101.9	967.7	1018.6	744442	

a)

b)
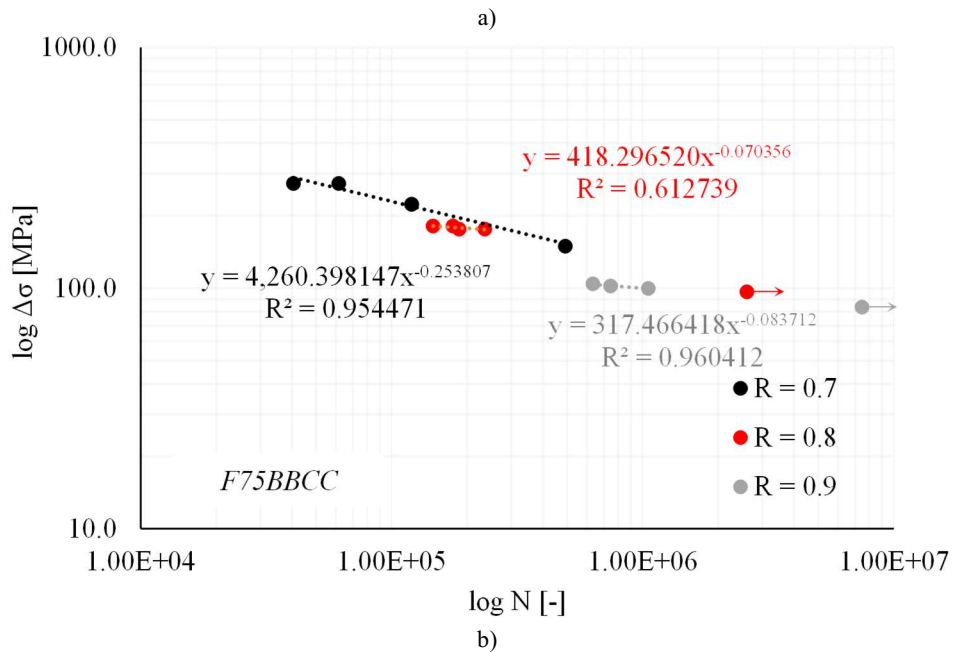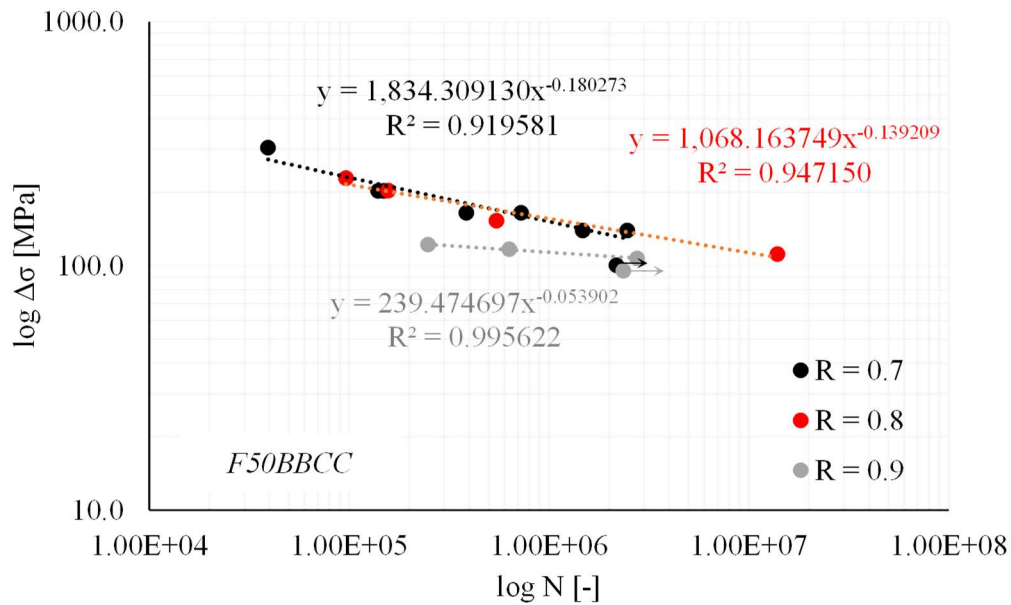
Figure 4.5 Mean nominal S-N curves for tested blunt notched components: a) F50BBCC and b) F75BBCC specimens. Stress ranges are nominally referred to the minimum cross-section, while runouts are labelled with an arrow.

On one hand, it can be clearly observed that the specimens failing for different stress ratio R are arranged on narrow, yet separate bands, namely characterized by decreasing slope m_R with increasing R. This result is consistent with observations reported in *Schijve* (*2009*) for mild steels. On the other hand, with R being the same, the behavior of the specimens having different geometry is rather similar.

4.1.3 Experimental Tests Issues

The performed experimental campaign revealed some critical issues when carrying out constant-amplitude fatigue tests.

On one hand, with reference to FAA09CC tests, the adoption of such high value of R = 0.9 leads to a premature achievement of the specimens tensile strength for rather low nominal stress ranges ($\Delta\sigma_{max,F5009CC} = 129.8$ N/mm^2 and $\Delta\sigma_{max,F7509CC} = 108.7$ N/mm^2, respectively).

This outcome, together with the observed significant flattening of the S-N curves for increasing R values (Figure 4.5a-b, red points and dotted curves), has determined in fact *i*) the impossibility of testing such specimens in the range of cycles N < 100'000 and *ii*) a poor governability of the results, as minimal variations of $\Delta\sigma$ have been accompanied by important variations in the observed number of cycles at failure N*.

On the other hand, in the preliminary design of the experimental campaign plan, the recommended value of clamping action for preloaded bolts according to EN1993:1-8 provisions (e.g., 0.7 times their tensile resistance $F_{T,Rd}$ – *CEN, 2005b*) was initially thought of as a reference value.

Indeed, the threaded shank of a preloaded bolt can be suitably assimilated to a blunt V-notched cylinder, and it will be subjected to a mean force close to 0.7 $F_{T,Rd}$ when subjected to cyclic axial loads (e.g. if it is part of a T-stub joint – *Tartaglia et al., 2020*). Therefore, a suitable load protocol for tested specimens could have involved the reference value $F_{ref} = 0.7$ F_u as F_{min}, F_{max} or $F_{mean} = (F_{max} + F_{min})/2$, respectively.

However, some of the obtained protocols (e.g., in case of R = 0.7) proved to be incompatible with the static resistance of notched specimens. As a matter of fact, this issue remains unsolved if R ≤ 0.7 and $F_{ref} = F_{min}$ are assumed as test parameters.

As reported in *Section 3.3.2*, fixing one of the above load parameters and the stress ratio R is sufficient to fully define a constant-amplitude fatigue protocol (Equation 3.23). Obtained protocols are reported in Table 4.7, with statically incompatible ones highlighted in red.

Table 4.7 Constant-amplitude fatigue protocols derived assuming F_{ref} as the minimum, mean or maximum applied force on notched specimens. Statically incompatible protocols are highlighted in red.

Minimum diameter d [mm]	Stress Ratio R [-]	F_{ref} [kN]		F_{min} [kN]	F_{mean} [kN]	F_{max} [kN]
5	0.7	17.9	= F_{min}	17.9	21.8	25.6
			= F_{mean}	14.7	17.9	21.1
			= F_{max}	12.5	15.2	17.9
	0.8		= F_{min}	17.9	20.2	22.4
			= F_{mean}	15.9	17.9	19.9
			= F_{max}	14.3	16.1	17.9
	0.9		= F_{min}	17.9	18.9	19.9
			= F_{mean}	17.0	17.9	18.8
			= F_{max}	16.1	17.0	17.9
7.5	0.7	33.7	= F_{min}	33.7	41.0	48.2
			= F_{mean}	27.7	33.7	39.7

		= F_{max}	23.5	28.6	33.7
		= F_{min}	33.7	38.0	42.2
0.8		= F_{mean}	29.9	33.7	37.5
		= F_{max}	26.9	30.3	33.7
		= F_{min}	33.7	35.6	37.5
0.7		= F_{mean}	32.0	33.7	35.4
		= F_{max}	30.3	32.0	33.7

4.1.4 Statistical Assessment and Preliminary Interpretation of Results

Table 4.8 summarizes the statistical characterization of fatigue tests results in terms of:

- Equivalent detail classes $\Delta\sigma_{C,PS}$ associated with a number of cycles at failure N = N_C = $2 \cdot 10^6$ for extreme and mean values of the considered confidence interval (that is, exceeding probability P_S = 10% – 50% – 90%);
- Inverse slopes m of logarithmic curves, assumed independent of the value of PS, compliantly with remarks reported in *Section 3.3.9*;
- Coefficient of determination R^2 for the mean curve;
- Scatter ratio $T_\sigma = \Delta\sigma_{C,10}/\Delta\sigma_{C,90}$.

Table 4.8 Statistical characterization of experimental fatigue results.

Minimum diameter d [mm]	Stress ratio R [-]	Upper v. $\Delta\sigma_{C,10}$ [N/mm²]	Mean v. $\Delta\sigma_{C,50}$ [N/mm²]	Lower v. $\Delta\sigma_{C,10}$ [N/mm²]	Inv. Slope m [-]	Coeff. of Det. R^2 [-]	Scatter Ratio T_σ [-]
	0.7	161.9	123.3	93.8	4.64	0.92	1.73
5	0.8	172.1	140.5	114.7	6.83	0.99	1.52
	0.9	112.6	109.5	106.5	18.71	0.95	1.06
	0.7	128.5	104.9	85.6	3.83	0.95	1.50
7.5	0.8	150.6	135.5	121.9	8.70	0.96	1.24
	0.9	97.1	93.8	90.7	11.50	0.61	1.07

As it can be noticed, fatigue data show a relatively low scatter within a given series of specimens sharing the same values of d and R (that is, $T_{\sigma,max}$ = 1.73 for F5007CC specimens), but they are arranged on significantly different bands when these parameters are varied.

The statistical interpretation confirms the flattening of the curves as R increases, with a more pronounced effect for specimens with a smaller minimum section. Flattening effect detrimentally influences the coefficients of determination R^2 for R = 0.9, as explained in *Section 3.3.9*. Indeed, while R^2 is still favorable for F5009CC specimens, it drops down to 0.61 for F7509CC ones, also in light of the few tests performed (4, with one of them resulting in a runout, see Table 4.6).

As for the performance for fixed stress ratios R, it can be noticed how the values of $\Delta\sigma_{C,50}$ are slightly higher in case for d = 5 mm. This outcome is plausibly an apparent effect descending from the increased notch sensitivity of F50BBCC specimens.

4.2. Experimental static tests on hot-driven riveted connections

4.3.1 Generalities

The present Section briefly summarizes the earlier experimental activities carried out by the Candidate Research Group to characterize the static behaviour of hot-driven riveted connections. Experimental tests were performed within the framework of European

PROHITECH Research Project – "Earthquake Protection of Historical Buildings by Reversible Mixed Technologies" (*Mazzolani, 2009*).

Relevant experimental results can be found in *D'Aniello et al.* (*2011*). Nevertheless, as they serve as a crucial background for refined FEAs described in *Chapter 5*, most relevant outcomes are summarized in this Section.

Specimens configurations and geometrical features were designed with the aid of the Steel Structure Division of Italian Railway Network RFI), i.e., in order to resemble connections typically used for railway riveted bridges (*D'Aniello et al., 2011*)

4.3.2 Experimental Tests on Base Materials

In order to preliminarily investigate the base material properties for undriven rivets and plates, *D'Aniello et al.* (*2011*) performed physical and mechanical tests on pristine components. Namely, tensile coupon tests, Brinell hardness (BH) tests, Charpy-V notch (CVN) tests and chemical analyses were carried out on multiple specimens.

Tensile tests were performed using the *Universal Machine MTS 500 with electro-mechanical system*, with both plates and rivets being equipped with strain gauges and LVDTs (Figure 4.6).

In particular, the rivet material was tested by means of cylindrical dog-bone coupons drawn from shanks of undriven rivets (Coupons "C16").

An impact CVN tester (*Zwick 5113*) was adopted to determine Charpy V-Notch toughness for both rivets and plates, while BH was assessed by means of the *ELBO TH-3000-OB* Universal Hardness Testing Machine.

<div align="center">a)   b)</div>
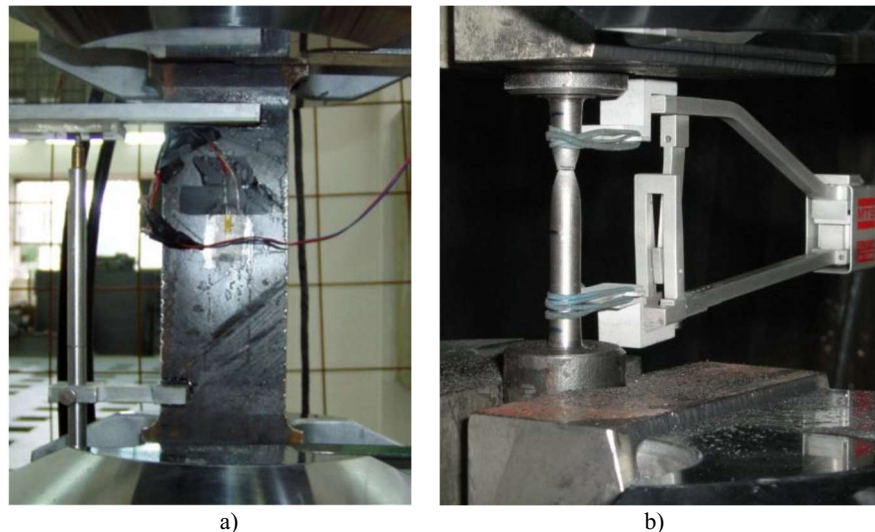
Figure 4.6 Experimental tests on base material for a) plates and b) rivets adopted in hot-driven riveted connections (*D'Aniello et al., 2011*).

As for the chemical composition of plates and rivets, a glow discharge atomic emission spectrometer (*LECO GDS850A*) was employed (*D'Aniello et al., 2011*).

Average material parameters for both rivets and plates are reported in Table 4.9.

Table 4.9 Experimental physical and mechanical parameters of plates and rivets adopted for hot-driven ri (average values – *D'Aniello et al., 2011*).

Steel	Mechanical parameters (Avg.)					
	BH	CVN	E_s	f_y	f_u	$\varepsilon_{eng,u}$
	[-]	[J]	[N/mm^2]	[N/mm^2]	[N/mm^2]	[-]
	121	31	206480	291	433	0.28
Historical, Mild, Adopted for Plates	Chemical composition					
	C	Si	Mn	P	S	Cu
	[%]	[%]	[%]	[%]	[%]	[%]
	0.08	0.17	0.54	0.01	0.06	0.37
	Cr	Ni	V	Mo	N	C_{eq}
	[%]	[%]	[%]	[%]	[%]	[%]
	0.07	0.11	0.00	0.02	0.01	0.22
Steel	Mechanical parameters (Avg.)					
	BH	CVN	E_s	f_y	f_u	$\varepsilon_{eng,u}$
	[-]	[J]	[N/mm^2]	[N/mm^2]	[N/mm^2]	[-]
	137	-	209412	315	412	0.16
Historical, Mild, Adopted for Rivets	Chemical composition					
	C	Si	Mn	P	S	Cu
	[%]	[%]	[%]	[%]	[%]	[%]
	0.39	0.02	0.22	0.05	0.07	0.07
	Cr	Ni	V	Mo	N	C_{eq}
	[%]	[%]	[%]	[%]	[%]	[%]
	0.09	0.22	-	-	0.02	0.47

BH: Brinell Hardness, 500 kgf load, 10 mm ball
CNV: Charpy V-Notch impact test energy
E_s: Young Modulus
f_y: Engineering yield stress
f_u: Engineering UTS
$\varepsilon_{eng,u}$: Engineering ultimate strain

An average yield stress of f_y = 291 N/mm^2 (COV = 0.02) was measured for plates (Coupons "S10"), while f_u = 433 (COV = 0.01) in correspondence of an average ultimate engineering strain $\varepsilon_{eng,u}$ = 0.28 (COV = 0.04). According to *D'Aniello et al.* (*2011*), plates material could be assimilated to a modern European S275 steel grade.

As for the undriven rivets, f_y = 315 N/mm^2 (COV = 0.08), f_u = 433 (COV = 0.04) and $\varepsilon_{eng,u}$ = 0.16 (COV = 0.36) were measured.

The scatter shown by rivets material properties reflected the lack of quality control in steel manufacturing process during the XXth century (*D'Aniello et al.*, *2011*). Also in light of its chemical composition (*Sustainable Bridge, 2006*), rivet material was deemed as produced with a Martin-Siemens process. Mean engineering stress-strain curves for both plates and undriven rivets are depicted in Figure 4.7 (*D'Aniello et al.*, *2011*).
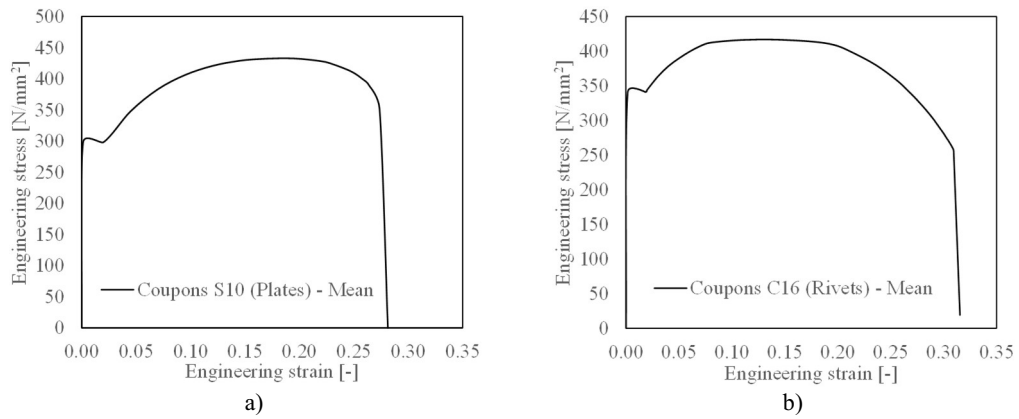
Figure 4.7 Mean engineering stress-strain curves for plates and undriven rivets (*D'Aniello et al., 2011*).

4.3.3 Experimental Tests on Hot-Driven Riveted Connections

Experimental tests on hot-driven riveted connections were performed by *D'Aniello et al.* (*2011*) by means of an *Universal Machine Zwick/Roell with electro-mechanical system* (Figure 4.8a). Specimens were equipped with two LVDTs, one on each side, assuming as reference measure points the cross-sections of plates being 30 mm away from the connected zone (Figure 4.8b). For the sake of clarity, ultimate displacement values Δ_u for all specimens were estimated accordingly. The displacement rate was fixed at 6 mm/min and an acquisition frequency of 10 Hz was assumed (*D'Aniello et al., 2011*).

An appropriate labelling was also defined for all the performed tests, i.e., univocally summarizing the main test parameters for each specimen, namely:

Labelling "C-D-T-N_S" with:
C = S or U with reference to the specimen configuration, i.e., symmetric or unsymmetric;
D = 16, 19 or 22 with reference to the rivet(s) diameter *d*;
T = 10 or 12 with reference to the plies thickness *t*;
N = 1 or 2 with reference to the number of rivets n_r;
S = A, B, C with reference to the specimen ID, i.e. increasing for multiple tests related to specimens with identical geometrical features.

Relevant geometrical features for tested hot-driven assemblies are reported in Table 4.10, namely adopting the symbology depicted in Figure 4.9 (*D'Aniello et al., 2011*).
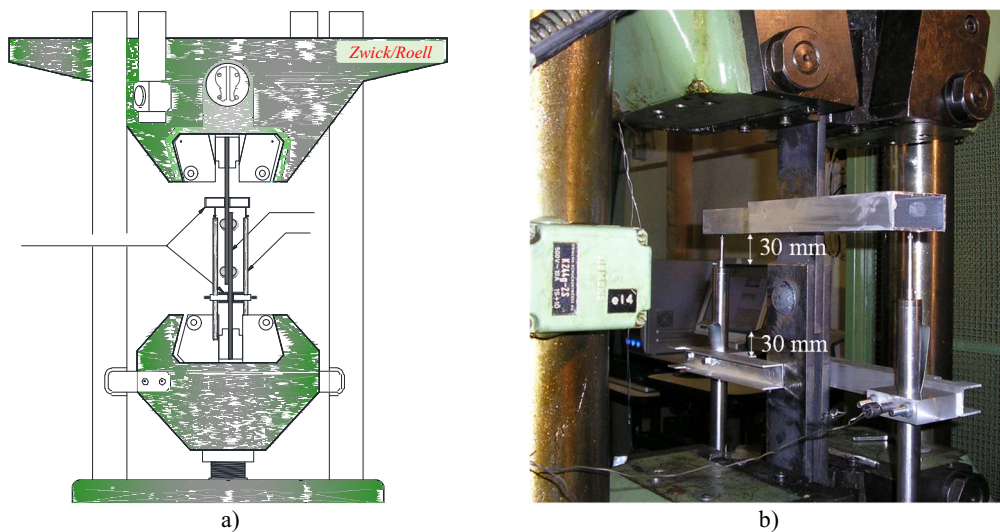
Figure 4.8 Static tests on hot-driven riveted connections: a) Zwick/Roell testing machine and b) example of specimen being instrumented with LVDTs (*D'Aniello et al., 2011*).
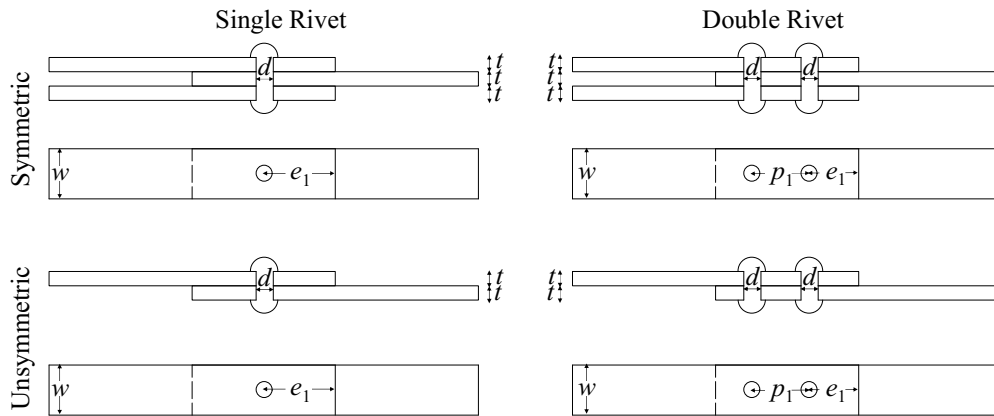
Figure 4.9 Main geometrical features of tested hot-driven riveted connections (*D'Aniello et al., 2011*).

Table 4.10 Main geometrical features of tested hot-driven riveted connections (*D'Aniello et al., 2011*).

Label [-]	Config. [-]	Rivet Diameter d [mm]	Plate Thickness t [mm]	Plate Width w [mm]	Edge Distance e_1 [mm]	Number of Rivets n_r [-]	Rivets Pitch p_1 [mm]
S-16-10-1	S	16	10	70	35	1	
S-19-10-1	S	19	10	90	45	1	
S-19-12-1	S	19	12	90	45	1	
S-22-10-1	S	22	10	70	35	1	
S-22-12-1	S	22	12	70	35	1	-
U-16-10-1	U	16	10	70	35	1	
U-19-10-1	U	19	10	90	45	1	
U-19-12-1	U	19	12	90	45	1	
U-22-10-1	U	22	10	70	35	1	
U-22-12-1	U	22	12	70	35	1	
S-19-10-2	S	19	10	90	45	2	118
S-22-12-2	S	22	12	70	35	2	118
U-16-10-2	U	16	10	70	35	2	140
U-19-10-2	U	19	10	90	45	2	118
U-22-12-2	U	22	12	70	35	2	90
S: Symmetric lap-shear specimen, three plies, two shear planes							
U: Unsymmetric lap-shear specimen, two plies, one shear plane							

The plate width to rivet diameter w/d ratios was appropriately set to investigate the "*net-area efficiency*" effect that could have influenced the tearing resistance of the connected plates (*Schenker et al., 1954*). Namely, the w/d ratio ranged among 3.16 ÷ 4.74. All investigated connections had edge-to-hole distance e_1 (measured along the direction of applied loads) equal to half of the relevant width of connected plates (i.e., $e_1 = 0.5\,w$).

The pitch-to-diameter ratio p/d in the lap shear connections equipped with two rivets ranged among 4.09 ÷ 8.75. Notable, geometric limits for each considered configuration are compliant with EN1993:1-8 (*CEN, 2005b*).

Three tests were performed for each specimen with nominally identical geometry. However, owing to some issues encountered with LVDTs, only two valid test results were retrieved for S-22-12-1_A/B and U-22-10-1_A/B specimens.

Experimental tests results are summarized in Tables 4.11-4.14 for all configurations.

Table 4.11 Static test results: ultimate resistance of single rivet specimens (*i*-th and mean values, COV, collapse mechanism) and comparisons with EN1993:1-8 provisions (*D'Aniello et al., 2011*).

Label	$F_{u,exp,i}$	$F_{u,exp,mean}$	COV	$F_{v,Rd}$	$F_{t,Rd}$	$F_{b,Rd}$	$F_{u,mean}/F_{EC3}$	Collapse Mechanism EC3/ Exp
[-]	[kN]	[kN]	[-]	[kN]	[kN]	[kN]	[-]	
S-16-10-1_A	146.1							V/V
S-16-10-1_B	148.0	141.8	0.06	99.3	233.6	126.2	1.43	V/V
S-16-10-1_C	131.4							V/V
U-16-10-1_A	80.0							V/V
U-16-10-1_B	83.9	80.2	0.05	49.7	233.6	126.2	1.62	V/V
U-16-10-1_C	76.7							V/V
S-19-10-1_A	180.5							V/V
S-19-10-1_B	232.4	206.6	0.13	140.0	307.2	162.3	1.48	V/V
S-19-10-1_C	207.1							V/B + V
U-19-10-1_A	87.0							V/V
U-19-10-1_B	108.9	101.5	0.12	70.0	307.2	162.3	1.45	V/V
U-19-10-1_C	108.5							V/V
S-19-12-1_A	225.2							V/B + V
S-19-12-1_B	207.2	216.5	0.04	140.0	368.6	194.7	1.55	V/B + V
S-19-12-1_C	217.2							V/B + V
U-19-12-1_A	100.6							V/V
U-19-12-1_B	145.3	117.6	0.21	70.0	368.6	194.7	1.68	V/V
U-19-12-1_C	106.8							V/V
S-22-10-1_A	173.6							B/B
S-22-10-1_B	184.6	183.0	0.05	187.8	207.7	126.2	1.45	B/B
S-22-10-1_C	190.9							B/B
U-22-10-1_A	143.1	144.8	0.02	93.9	207.7	126.2	1.54	V/V
U-22-10-1_B	146.4							V/V
S-22-12-1_A	236.2	237.2	0.01	187.8	249.2	151.4	1.57	B/B
S-22-12-1_B	238.2							B/B
U-22-12-1_A	143.4							V/V
U-22-12-1_B	128.7	140.2	0.07	93.9	249.2	151.4	1.49	V/V
U-22-12-1_C	148.6							V
	V: Rivet Shearing Failure							
	B: Plate Bearing Failure							
	T: Plate Net-Area Failure							

Table 4.12 Static test results: ultimate resistance of double rivet specimens (*i*-th and mean values, COV, collapse mechanism) and comparisons with EN1993:1-8 provisions (*D'Aniello et al., 2011*).

Label	$F_{u,exp,i}$	$F_{u,exp,mean}$	COV	$F_{v,Rd}$	$F_{t,Rd}$	$F_{b,Rd}$	$F_{u,mean}/F_{EC3}$	Collapse Mechanism EC3/Exp
[-]	[kN]	[kN]	[-]	[kN]	[kN]	[kN]	[-]	
U-16-10-2_A	141.9							V/V
U-16-10-2_B	162.2	155.2	0.07	99.3	233.6	252.4	1.56	V/V
U-16-10-2_C	161.4							V/V
S-19-10-2_A	336.6							V/T
S-19-10-2_B	346.0	338.4	0.02	280.1	307.2	324.5	1.21	V/T
S-19-10-2_C	332.6							V/T

U-19-10-2_A	201.6							V/V
U-19-10-2_B	196.2	210.0	0.09	140.0	307.2	324.5	1.50	V/V
U-19-10-2_C	232.4							V/V
S-22-12-2_A	278.9							V/T
S-22-12-2_B	298.4	291.4	0.04	357.5	249.2	302.9	1.17	V/T
S-22-12-2_C	296.9							V/T
U-22-12-2_A	279.1							V/V
U-22-12-2_B	255.2	271.7	0.05	187.8	249.2	302.9	1.45	V/V
U-22-12-2_C	280.8							V/V

V: Rivet Shearing Failure
B: Plate Bearing Failure
T: Plate Net-Area Failure

Table 4.13 Static test results: ultimate displacement of single rivet specimens (maximum, minimum, mean values, SD and COV – *D'Aniello et al., 2011*).

Label	$\Delta_{u,exp,i}$	$\Delta_{u,exp,max}$	$\Delta_{u,exp,min}$	$\Delta_{u,exp,mean}$	SD	COV
[-]	[mm]	[mm]	[mm]	[mm]	[mm]	[-]
S-16-10-1_A	7.4					
S-16-10-1_B	8.0	8.0	6.0	7.1	1.0	0.14
S-16-10-1_C	6.0					
U-16-10-1_A	3.8					
U-16-10-1_B	4.6	4.6	3.8	4.2	0.4	0.10
U-16-10-1_C	4.3					
S-19-10-1_A	11.9					
S-19-10-1_B	20.8	20.8	11.9	14.9	5.1	0.34
S-19-10-1_C	12.0					
U-19-10-1_A	4.4					
U-19-10-1_B	4.3	6.4	4.3	5.0	1.2	0.24
U-19-10-1_C	6.4					
S-19-12-1_A	8.2					
S-19-12-1_B	8.6	8.6	7.6	8.1	0.5	0.06
S-19-12-1_C	7.6					
U-19-12-1_A	4.4					
U-19-12-1_B	6.8	6.8	4.4	5.5	1.2	0.22
U-19-12-1_C	5.2					
S-22-10-1_A	10.2					
S-22-10-1_B	11.0	11.0	9.4	10.2	0.8	0.08
S-22-10-1_C	9.4					
U-22-10-1_A	10.5	11.5	10.5	11.0	0.7	0.06
U-22-10-1_B	11.5					
S-22-12-1_A	8.2	11.7	8.2	10.0	2.5	0.25
S-22-12-1_B	11.7					
U-22-12-1_A	4.8					
U-22-12-1_B	11.5	11.5	4.8	7.0	3.9	0.55
U-22-12-1_C	4.8					

Table 4.14 Static test results: ultimate displacement of single rivet specimens (maximum, minimum, mean values, SD and COV – *D'Aniello et al., 2011*).

Label	$\Delta_{u,exp,i}$	$\Delta_{u,exp,max}$	$\Delta_{u,exp,min}$	$\Delta_{u,exp,mean}$	SD	COV
[-]	[mm]	[mm]	[mm]	[mm]	[mm]	[-]
U-16-10-2_A	4.5					
U-16-10-2_B	4.9	4.9	3.9	4.4	0.5	0.11
U-16-10-2_C	3.9					
S-19-10-2_A	16.9					
S-19-10-2_B	20.5	20.5	14.0	17.1	3.3	0.19
S-19-10-2_C	14.0					
U-19-10-2_A	5.9					
U-19-10-2_B	5.8	6.7	5.8	6.1	0.5	0.08
U-19-10-2_C	6.7					
S-22-12-2_A	5.5					
S-22-12-2_B	10.0	10.7	5.5	8.7	2.8	0.32
S-22-12-2_C	10.7					
U-22-12-2_A	12.2					
U-22-12-2_B	4.0	12.2	4.0	9.2	4.5	0.49
U-22-12-2_C	11.5					

It can be easily noticed how experimental resistances $F_{u,exp,mean}$ were strongly underestimated when adopting EN1993:1-8 (*CEN, 2005b*) provisions. For consistency, normative calculations for $F_{u,EC3}$ were performed adopting mean values of material parameters and $\gamma_{M2} = 1.00$ (*D'Aniello et al., 2011*).

The average value of $F_{u,exp,mean}/F_{u,EC3}$ ratios resulted to be equal to 1.48 (COV = 0.09). Discrepancies could be ascribed to hot-driving effects being neglected (*D'Aniello et al., 2011*). Notably, this issue lead to mistaken EN1993:1-8 predictions for two specimen configurations in terms of occurring collapse mechanism, namely:

- Specimens S-19-12-1-A/B/C → EC3: rivet shearing "V" against EXP: mixed shearing + plate bearing "B + V");
- Specimens S-22-12-2-A/B/C → EC3: rivet shearing "V" against EXP: plate net area failure "T");

For thoroughness, mean force-displacement curves and experimental collapse mechanisms are reported in Figures 4.10-4.11 with reference to single rivet and double rivet specimens, respectively.
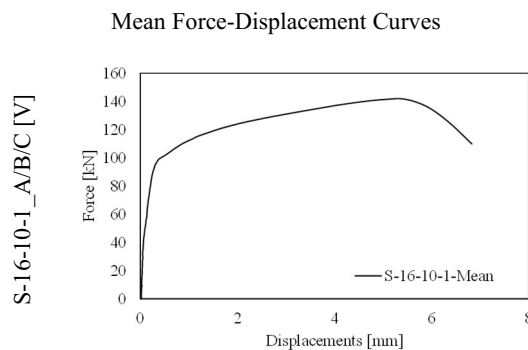
a)

b)

c)

d)

e)

f)

g)

h)

i)

j)

k)

l)

m)

n)

o)

p)

q)

r)

s)

t)
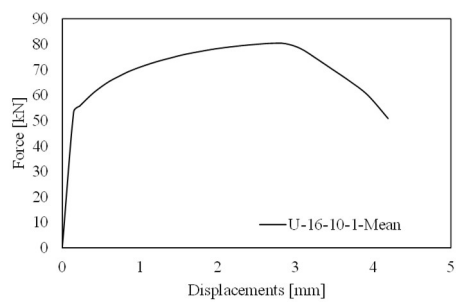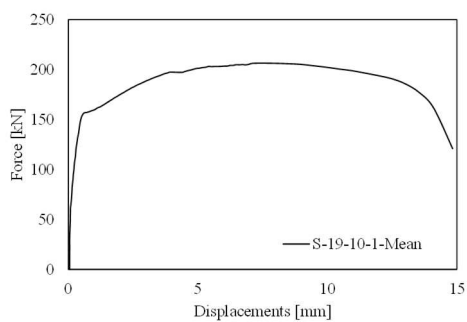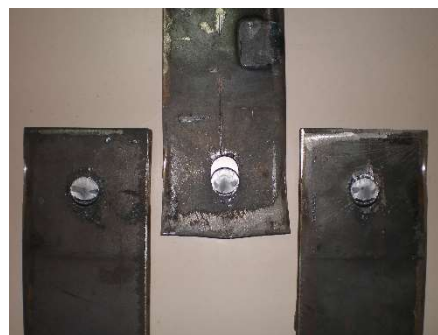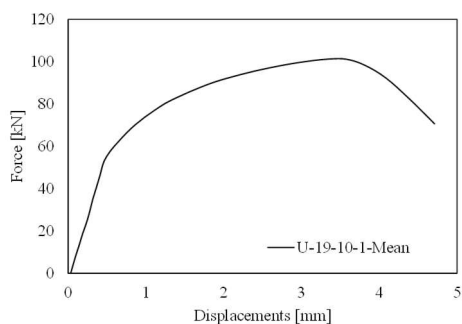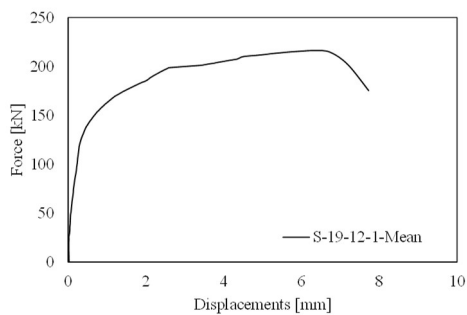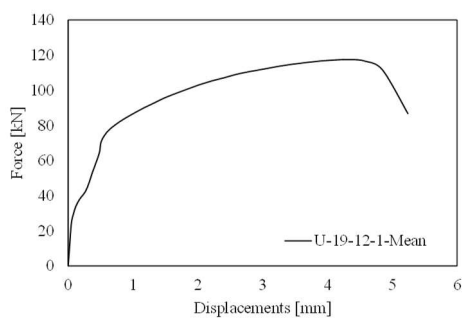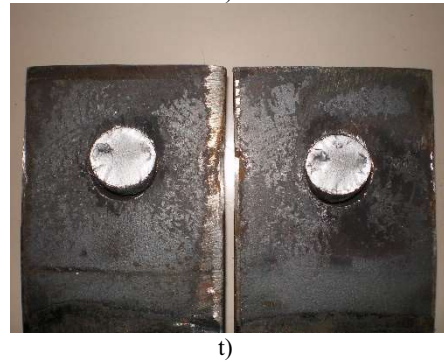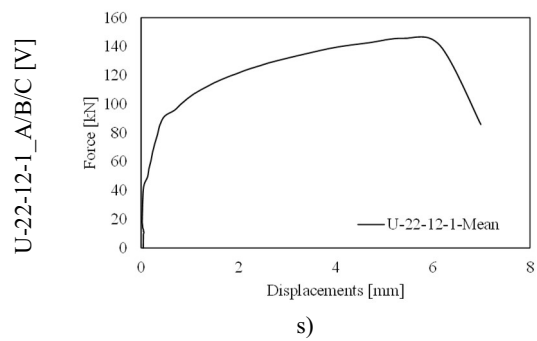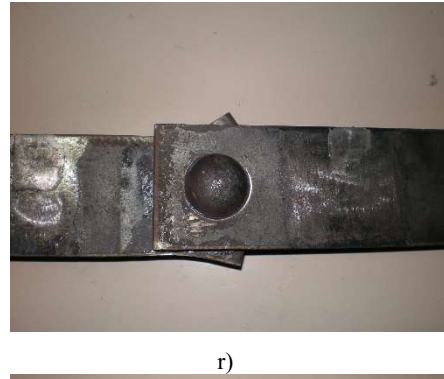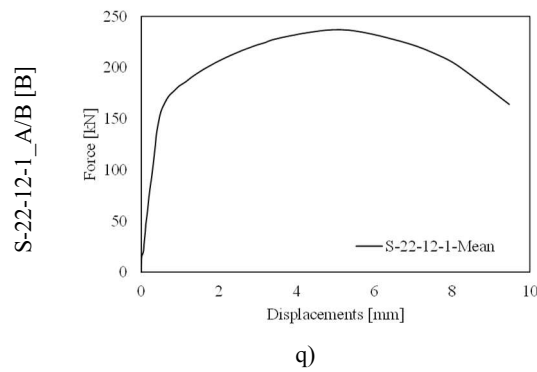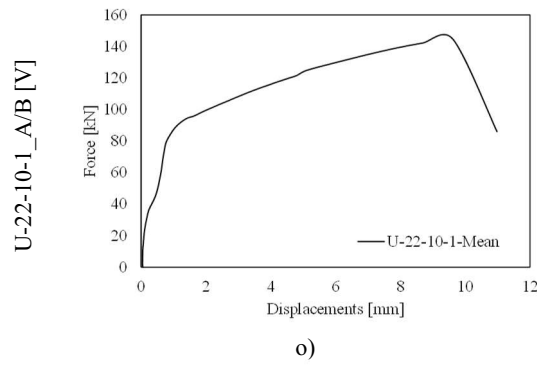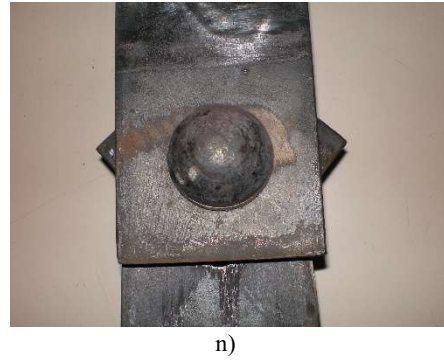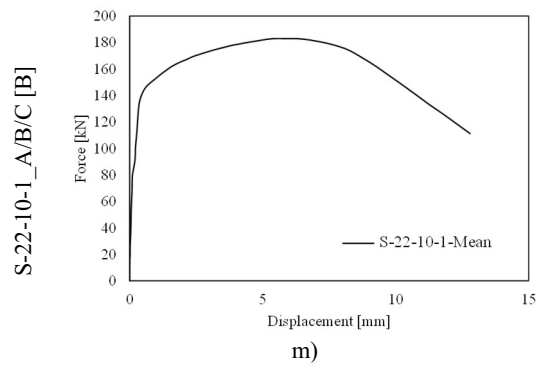
Figure 4.10 Static tests results for hot-driven riveted connections in terms of mean force-displacement curves and experimental collapse mechanisms: single rivet specimens (*D'Aniello et al., 2011*).
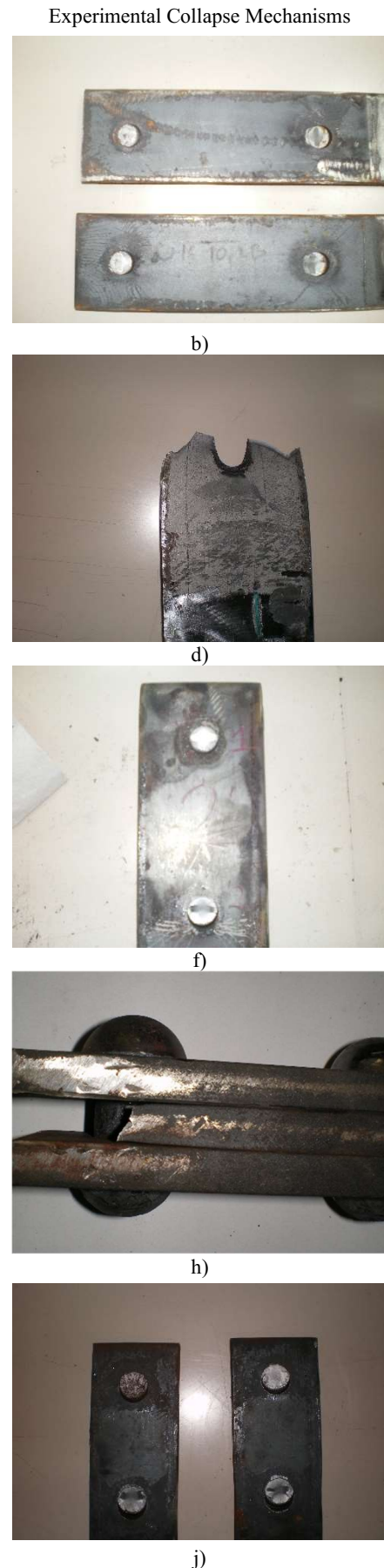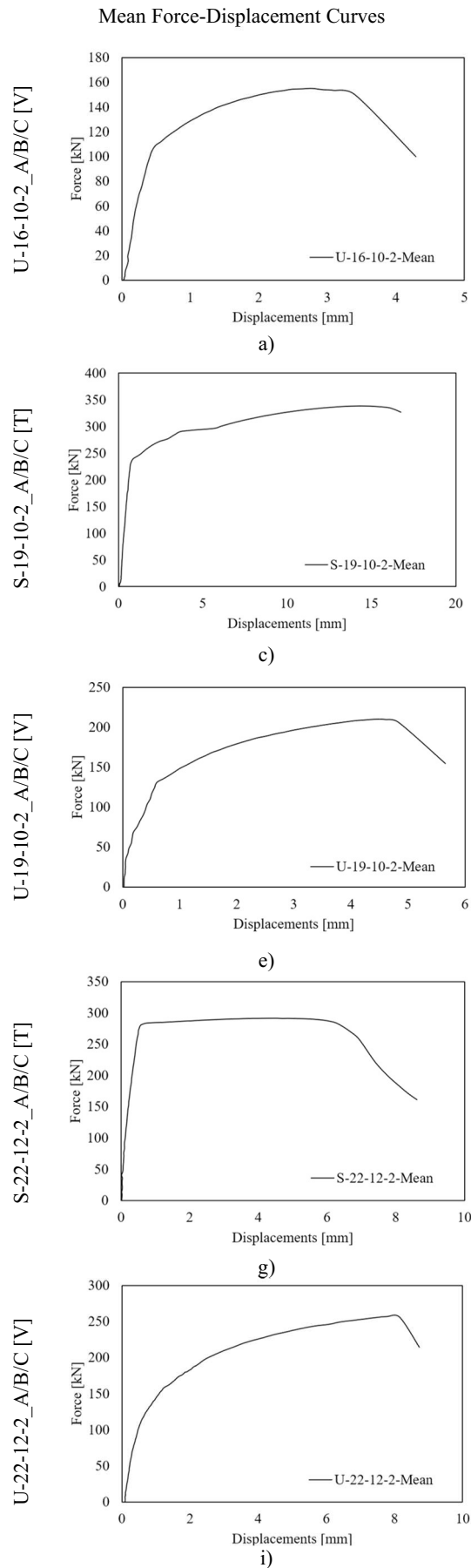
Figure 4.11 Static tests results for hot-driven riveted connections in terms of mean force-displacement curves and experimental collapse mechanisms: double rivet specimens (*D'Aniello et al., 2011*).

cxl

It is worth remarking that such curves and related damage patterns at failure have been used in the present Thesis work to calibrate plasticity and damage models for refined FEAs on hot-driven riveted connections.

Indeed, numerical models for refined FEAs are compliant with all the reported configurations of hot-driven assemblies experimentally tested by *D'Aniello et al.* (*2011*). Further details are reported in *Chapter 5*.

4.3. Experimental fatigue tests on hot-driven riveted connections

4.4.1 Generality

The present Section summarizes the experimental activities carried out on the characterization of the fatigue behavior of hot-driven riveted connections. Experimental tests were performed in collaboration with University of Salerno (UNISA), namely at the *Structural Engineering Test Hall* (StrEngTH) located in the UNISA university campus.

The present experimental campaign aimed at *i*) investigating the fatigue performance of hot-driven riveted connections accounting for their peculiarities and *ii*) compare the fatigue performance of hot-driven riveted and high-strength bolted connections having the same nominal geometry.

Within the framework of the present Thesis work, only results related to hot-driven riveted connections are considered, namely to provide a reliable experimental background for the advanced fatigue analysis of hot-driven assemblies through the SED method (*Lazzarin & Zambardi, 2001*; *Berto & Lazzarin, 2014*).

For consistency, the same geometries adopted for static trials performed by *D'Aniello et al.* (*2011*) were adopted for the fatigue tests described in this Section, i.e., compatibly with resources available at RFI warehouse. Accordingly, same base material properties derived by the Authors for undriven rivets and plates have been assumed within the present fatigue tests campaign.

In particular, six different configurations (S or U, n_r = 1, 2, for a total of 7 specimens) were tested at the UNISA StrEngTH Lab.

In the next Sections, the following key aspects related to performed experimental activities are addressed, namely:

- Experimental test plan;
- Summary of the results of the tests conducted;
- Issues encountered during experimental tests;
- Statistical characterization and preliminary interpretation of results.

4.4.2 Experimental Test Plan

Specimens were tested using the *Universal Machine MTS 250 with servo-hydraulic system* located at StrEngTh lab (UNISA), which features an axial actuator having maximum capacity equal to ± 250 kN.

Compatibly with the characteristics of the base material, a constant test frequency f_{test} = 5 Hz was assumed for all fatigue tests.

The plan for the experimental campaign was defined in order to provide results as robust and distributed as possible in the ranges of LCF and HCF (that is, N* ≤ 100'000 cycles

and 100'000 cycles < N* ≤ 1'000'000 cycles – Schijve, 2009). For all considered tests, zero-to-tension load protocols were adopted (R = 0).

The stress ranges Δσ of concern were determined based on their static properties assessed by *D'Aniello et al.* (*2011*). Accordingly, subsequent fatigue tests were performed assuming aliquots of the ultimate load compliant with the desired number of cycles at failure N*.

It is worth remarking that the choice of stress ranges Δσ was characterized by a certain degree of iteration, insofar as the preliminary results related to a small number of specimens were used to predict the outcomes of subsequent tests, thus optimizing the entire experimental campaign.

In order to univocally identify each specimen, a proper labelling was introduced, i.e. consistent with static tests performed by *D'Aniello et al. (2011)* and summarizing geometrical features and load protocols as follows:

Labelling "C-D-T-N-F-FR" with:
C = S or U with reference to the specimen configuration, i.e., symmetric or unsymmetric;
D = 16, 19 or 22 with reference to the rivet(s) diameter *d*;
T = 10 or 12 with reference to the plies thickness *t*;
N = 1 or 2 with reference to the number of rivets n_r;
SR = var. with reference to the applied force range ΔF on connected plies.

Geometrical features for investigated specimens are summarized in Table 4.15 and Figure 4.12, respectively.
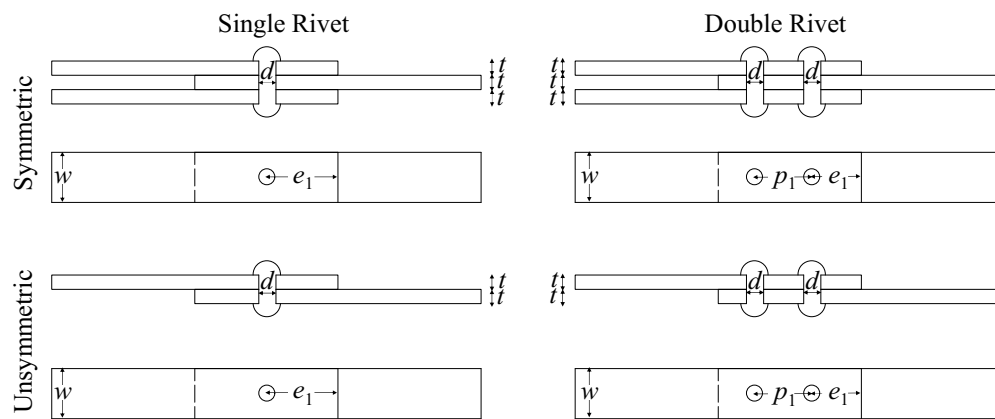
Figure 4.12 Main geometrical features for hot-driven riveted connections tested in fatigue conditions.

Table 4.15 Main geometrical features for hot-driven riveted connections tested in fatigue conditions.

Test Lab [-]	Label [-]	Config. [-]	Rivet Diameter *d* [mm]	Plate Thick. *t* [mm]	Plate Width *w* [mm]	Edge Distance e_1 [mm]	N. of Rivets n_r [-]	Riv. Pitch p_1 [mm]
UNISA	S-19-12-1-115	S	19	12	90	45	1	
UNISA	S-22-10-1-130	S	22	10	90	45	1	-
UNISA	S-22-12-1-60	S	22	12	70	35	1	
UNISA	S-22-12-2-160	S	22	12	70	35	2	118
UNISA	U-19-10-2-100	U	19	10	60	30	2	175

UNISA	U-22-12-2-160	U	22	12	70	35	2	90
UNISA	U-22-12-2-144	U	22	12	70	35	2	90
S:	Symmetric lap-shear specimen, three plies, two shear planes							
U:	Unsymmetric lap-shear specimen, two plies, one shear plane							

Test parameters designed according to the above indications are summarized in Table 4.16. Load protocols are conveniently expressed both in terms of test settings required by the MTS Universal Machine (that is, the lone maximum applied forces F_{max} in case of zero-to-tension load protocols) and relevant stress ranges. It is worth remarking that $\Delta\sigma$ are nominally referred to the gross cross-section of plates $A_{plate,gross} = t \times w$.

Table 4.16 Summary of performed fatigue tests on hot-driven riveted connections.

Label	F_{max}	$A_{plate,gross}$	$\Delta\sigma$	N* (expected)
[-]	[kN]	[mm^2]	[N/mm^2]	[-]
S-19-12-1-115	115	1080	106.5	1'000'000 ÷ 100'000
S-22-10-1-130	130	900	144.4	< 100'000
S-22-12-1-60	60	840	71.4	1'000'000 ÷ 100'000
S-22-12-2-160	160	840	190.5	1'000'000 ÷ 100'000
U-19-10-2-100	100	900	111.1	< 100'000
U-22-12-2-160	160	840	190.5	< 100'000
U-22-12-2-144	144	840	171.4	< 100'000

4.4.3 Experimental Tests Results

Fatigue tests results are summarized in Table 4.17. Fatigue failure points are hence transposed into the Wohler diagram reported in Figure 4.13, in which experimental collapse mechanisms are depicted as well.

It is worth remarking that results for specimen S-22-10-1-130 were not deemed as valid due to unexpected and premature rivet shear failure (see *Section 4.4.4* for further details) It can be immediately noticed how results are affected by a relevant degree of scatter. Moreover, the reciprocal slope determined according to a logarithmic regression model is significantly higher that the reference value suggested by EN1993:1-9 (that is, $m_{exp} = 1/0.09 = 11.2 \gg m_{EC3} = 5 - CEN, 2005a$). Nevertheless, all specimens failed due to cyclic net-area failure of plates as expected (*Kulak et al., 1987*).

Table 4.17 Summary of fatigue tests results for hot-driven riveted connections.

Label	F_{max}	$A_{plate,gross}$	$\Delta\sigma$	N*
[-]	[kN]	[mm^2]	[N/mm^2]	[-]
S-19-12-1-115	115	1080	106.5	602270
S-22-10-1-130	130	900	144.4	1706*
S-22-12-1-60	60	840	71.4	774056
S-22-12-2-160	160	840	190.5	497964
U-19-10-2-100	100	900	111.1	17436
U-22-12-2-160	160	840	190.5	26357
U-22-12-2-144	144	840	171.4	43963
*unexpected rivet shear collapse.				
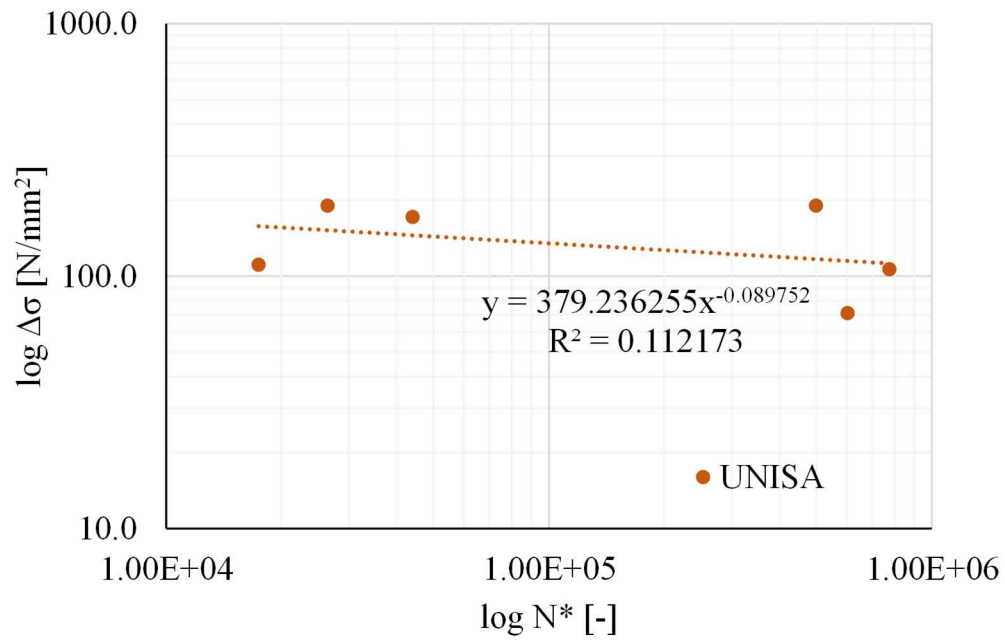
a)

b) S-19-12-1-115 N* = 602270
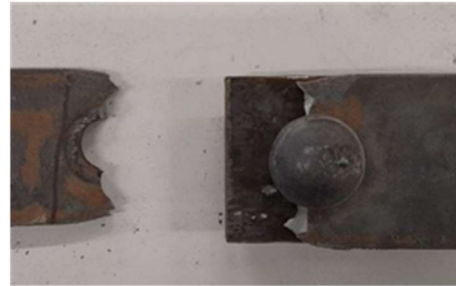
c) S-22-12-1-60 N* = 774056

d) S-22-12-2-160 N* = 497964

e) U-19-10-2-100 N* = 17436

f) U-22-12-2-160 N* = 26357

g) U-22-12-2-2-144

Figure 4.13 Summary of fatigue tests results for hot-driven riveted connections: a) Wohler diagram and b-g) experimental collapse mechanisms [*Courtesy of University of Salerno*].

It is worth emphasizing that all unsymmetric specimens, although being subjected to similar stress ranges, showed a significantly worse fatigue performance as respect to symmetric connections (that is, $N^*_U \approx 10^4$ is on average, one order of magnitude smaller than $N^*_S \approx 10^5$). This outcome plausibly descends from the detrimental effect of secondary bending moments (*Kulak et al., 1987*).

4.4.4 Experimental Tests Issues

The performed experimental campaign revealed some issues when carrying out constant-amplitude fatigue tests.

Indeed, an initial test on a symmetric specimen featuring a single 22 mm rivet and 10 mm plies was carried out, i.e. considering a zero-to-tension protocol (R = 0) with force range ΔF = 130 kN (S-22-10-1-130).

For such specimen, an average shear strength equal to 183.0 kN (out of three specimens) was derived from static tests (see Table 4.11, $F_{u,exp,min}$ = 173.6 kN), namely corresponding to plate bearing ("B") collapse. Moreover, according to experimental force-displacement curves, an average proportionality limit for S-22-10-1 of $\approx$ 145 kN was estimated. Therefore, the adopted load protocol was designed to achieve a failure collapse associated with $N^* \approx 80'000$, as confirmed by provisions of earlier drafts of EN1993:1-9 (e.g., assuming $\Delta\sigma_C$ = 71 N/mm^2, *m* = 5 – *CEN, 2005a*).

Nevertheless, the specimen exhibited a premature fatigue failure for N^* = 1706 cycles and, notably, due to rivet fatigue shear failure (Figure 4.14).

An *a-posteriori* analysis of cyclic tangential stresses in the rivet shank did not result in any significant expectation of fatigue collapse of the rivet ($N^*_r \gg 100'000$, also in light of the presence of two shear planes).

This outcome was plausibly caused by constructional imperfections inherent to the tested connection, e.g., an overlooked camming defect and/or rivet indentation due to inadequate surface finishing of rivet holes (*Twelvetrees, 1900*; *Kulak et al., 1987*).

Therefore, S-22-10-1-130 were not assumed as valid in subsequent fatigue analyses.

<center>a)   b)</center>
<center>S-22-10-1-130 N* = 1706</center>

Figure 4.14 Unexpected rivet shear fatigue failure for specimen S-22-10-1-130: a) rivet shear failure and b) particular of the fractured rivet shank [*Courtesy of University of Salerno*].

4.1.4 Statistical Assessment and Preliminary Interpretation of Results

Table 4.18 summarizes the statistical characterization of fatigue tests results in terms of:

- Equivalent detail class $\Delta\sigma_{C,PS}$ associated with a number of cycles at failure N = $N_C = 2 \cdot 10^6$ for the mean value of the considered confidence interval (that is, exceeding probability P_S = 10% – 50% – 90%); namely, $\Delta\sigma_{C,PS}$ is provided for symmetric specimens, unsymmetric ones and for the entire set of tests;

- Inverse slope m of logarithmic curves, assumed independent of the value of PS, compliantly with remarks reported in *Section 3.3.9*; namely, m is provided for symmetric specimens, unsymmetric ones and for the entire set of tests;
- Coefficient of determination R^2 for the mean curves;
- Scatter ratios T_σ.

Table 4.18 Statistical characterization of experimental fatigue results.

Upper v. $\Delta\sigma_{C,10}$ [N/mm^2]	Mean v. $\Delta\sigma_{C,50}$ [N/mm^2]	Lower v. $\Delta\sigma_{C,10}$ [N/mm^2]	Inv. Slope m [-]	Coeff. of Det. R^2 [-]	Scatter Ratio T_σ [-]
> 291.0	103.2	22.3	11.14	0.11	> 10.0

As it can be noticed, fatigue data show a strong scatter. The regression curve is very flattened ($m > 10$), resulting in a significant drop of $R^2 = 0.11$, also in light of the few tests performed (7, with one of them deemed as invalid, see Table 4.17).

As for the the values of $\Delta\sigma_{C,PS}$, it is worth remarking that, while $\Delta\sigma_{C,50} = 103.2$ N/mm^2 is compliant with earlier EN1993:1-9 provisions (*CEN, 2005a*), upper and lower bound of the scatter-band are rather distant ($T_\sigma > 10$).

This outcome recommends the application of more advanced fatigue analyses for the considered hot-driven riveted connections. This task is properly addressed in *Chapter 7*, where further details are reported.

Chapter 5

Static Performance of Hot-Driven Riveted Connections

The present Chapter deals with the static performance of hot-driven riveted connections, which is assessed by means of refined finite element analyses performed with ABAQUS 6.14 software (*Dassault, 2014*).

In particular, the results of a wide numerical study based on hot-driven riveted connections experimentally tested by D'Aniello et al. (*2011*) is presented in the following sections in order to *i*) parametrically investigate the influence of the main geometrical features on the response of shear connections, *ii*) examine the influence of the hot-driven process on the ultimate behaviour and *iii*) preliminarily investigate the influence of a common constructional imperfection on the ultimate response of the connections. The investigated FE models are representative of actual technological details adopted in existing railway riveted bridges located in Italy (*Landolfo et al., 2011*). The following aspects are addressed in detail in the following Sections, namely: *i*) the modelling assumptions adopted for FEAs, with a peculiar focus on the implementation of plasticity and damage models for ductile materials described in an earlier Chapter (*Section 5.1*), *ii*) the calibration of damage and plasticity parameters for base plate and rivet material based on coupon tests (*Section 5.2*), *iii*) a preliminary numerical investigation on the effect of clamping actions on the static performance of hot-driven riveted connections, in light of their significant randomness (*Section 5.3*), *iv*) a thorough description of the effects of hot-driving on material properties of rivets and plates (*Section 5.4*), *v*) an investigation on the effect of a common constructional imperfection (e.g. shank camming defect) on the performance of hot-driven assemblies, which is preliminarily addressed as respect to the sole static response of connections (*Section 5.5*), *vi*) a predictive model for the static resistance of connections accounting for the effects of hot-driving and camming defects (*Section 5.6*), the reliability of which is hence statistically assessed against EN1990 (*CEN, 2002*) recommendations (*Section 5.7*) and *vi*) a conclusive comparison against EN1993:1-8 (*CEN, 2005b*) recommendations in force for hot-driven riveted connections (*Section 5.8*).

5.1. Modelling Assumptions for Refined Static FEAs of hot-driven riveted connections

5.1.1 Coupon Tests on Base Materials

Finite Element models (FEMs) resembling coupon tests on plates (flat specimens) and rivets (dog-bone round specimens) were developed using ABAQUS 6.14 software (*Dassault, 2014*). The ultimate response of coupons was investigated by applying monotonic displacement histories at one end of the grip segment, with the other one being fixed, in order to mimic the test conditions reported in *D'Aniello et al. (2011)*. Adopted FEMs geometry and boundary conditions (BCs) are depicted in Figure 5.1a-b.

All elements were discretized using solid C3D8 elements (i.e., 8-node linear bricks). Preliminary sensitivity analyses were carried out with reference to the lone PDS to select the appropriate mesh density, which led to a mesh size equal to 1 mm for gauge lengths of both plate and rivet coupons, while a mesh size of 5 mm was kept for grip zones remaining in their elastic range (Figure 5.1c).

a)

b)

c)
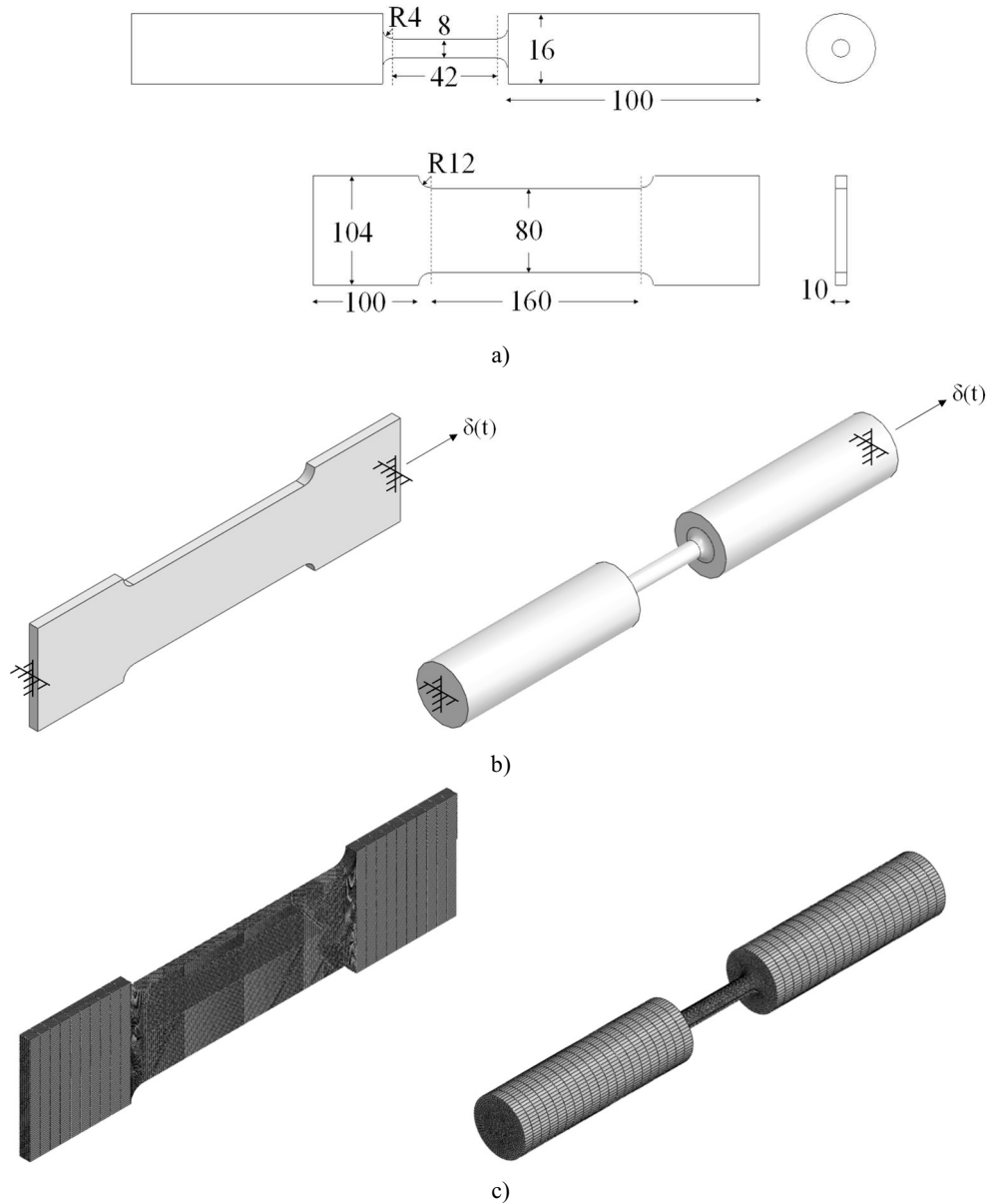
Figure 5.1 Refined FEAs on coupon tests for pristine plates and rivets: a) geometrical features, b) boundary conditions and c) adopted meshes.

Steel yielding was modelled using the Hencky-Von Mises criterion. The monotonic stress-strain curves of the materials of both rivets and plates were assumed as those experimentally derived in D'Aniello et al. (*2011*) up to the onset of necking. In particular, the yield and ultimate engineering stress of the steel plates were 291 MPa and 433 MPa, respectively, and the engineering strain corresponding to necking was 0.28. The yield and ultimate engineering stress of unheated rivets were 315 MPa and 412 MPa, respectively, and the engineering strain corresponding to necking was 0.16. Both kinematic and isotropic hardening were assumed according to *Dutta et al. (2010)*.

The "Ductile damage" module featured in ABAQUS 6.14 (*Dassault, 2014*) was used to simulate the material degradation for base material (*Stage I*, see *Section 3.2*). Namely, a GDDC was adopted, considering the influence of the sole stress triaxiality on the critical PEEQ $\varepsilon^*_{pl,eq}$ as suggested by *Kanvinde et al. (2007)* for mild steels.

As for the definition of triaxiality curves, the analytical expression proposed by *Yang et al. (2019)* was adopted, namely considering a monotonically decreasing T- $\varepsilon^*_{pl,eq}$ trend (see Equation 3.22 and relevant *Sections 3.1-3.2*). Moreover, a linear, displacement based DEC (see Equation 3.21 and relevant *Section 3.1*) was adopted as suitable for mild steels (*Ammar et al., 2022*).

Accordingly, the true strain at fracture $\varepsilon_{true,fail}$, the critical PEEQ for uniaxial tensile conditions $\varepsilon^*_{pl,eq,uniax}$ and the ultimate plastic displacement u^*_{pl} were properly calibrated for both plates and rivets, namely with the aid of the inverse method (*Tu et al., 2019*).

5.1.2 Static Tests on Hot-Driven Riveted Connections

FEMs resembling static tests performed by *D'Aniello et al.* (*2011*) on hot-driven riveted specimens were developed using ABAQUS 6.14 software (*Dassault, 2014*). In order to balance the accuracy and computational effort, the investigated riveted connections were modelled accounting for their geometrical and mechanical symmetry. The static response of connections was investigated by applying monotonic displacement histories at one end of the lap-shear riveted connections, with the other one(s) being fixed, in order to mimic the test conditions reported in *D'Aniello et al. (2011)*. Relevant BCs accounting for both symmetry and test conditions are depicted in Figure 5.2a-b.

a)

b)
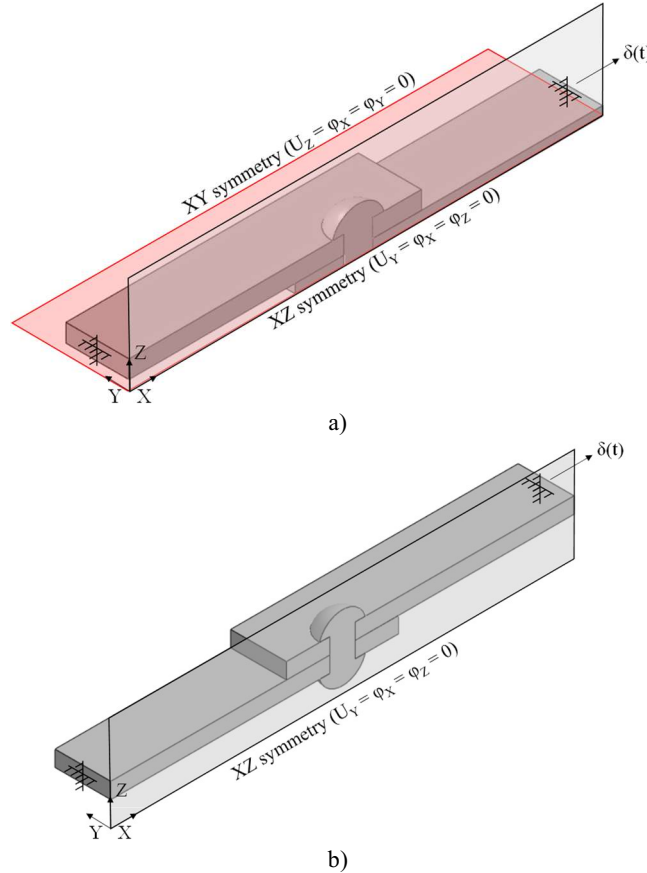
Figure 5.2 Refined static FEAs on hot-driven riveted connections: adopted boundary conditions for connections with a) two planes and b) one plane of symmetry.

Additionally, in order to preliminary investigate the influence of shank camming defect(s) on the static performance of connections, a parametric set of FEMs featuring such constructional imperfections was developed.

The camming imperfections were varied on the basis of the ratio among the shank eccentricity e and the rivet diameter d (Figure 5.3) in the range $0 \div 0.20$ (with increments of 0.05). This range of variation for e/d was assumed in accordance with the Sustainable Bridges report (*Sustainable Bridge, 2006*), where it is specified that camming defects can be considered tolerable for an existing riveted connection (i.e., connection repairment is not required) if the ratio among the shank eccentricity e (i.e., the distance between the centroids of the rivet heads measured along the longitudinal axis of the connection, as shown in Figure 5.3a) and the rivet diameter d does not exceed a threshold value equal to 0.15.

Nevertheless, in order to account for practical difficulties in on-field surveys that may result in inaccurate eccentricity measures (*Kulak et al., 1987*), a maximum value of e/d equal to 0.20 was also investigated. In addition, the influence of the orientation of the shank misalignment with respect to the applied shear force was numerically investigated by considering two separate sets of FE models, namely the first with camming defects directed as the applied loads (*"direct" shank eccentricity*, see Figure 5.3a), the second with the opposite configuration (*"reverse" shank eccentricity*, see Figure 5.3b).
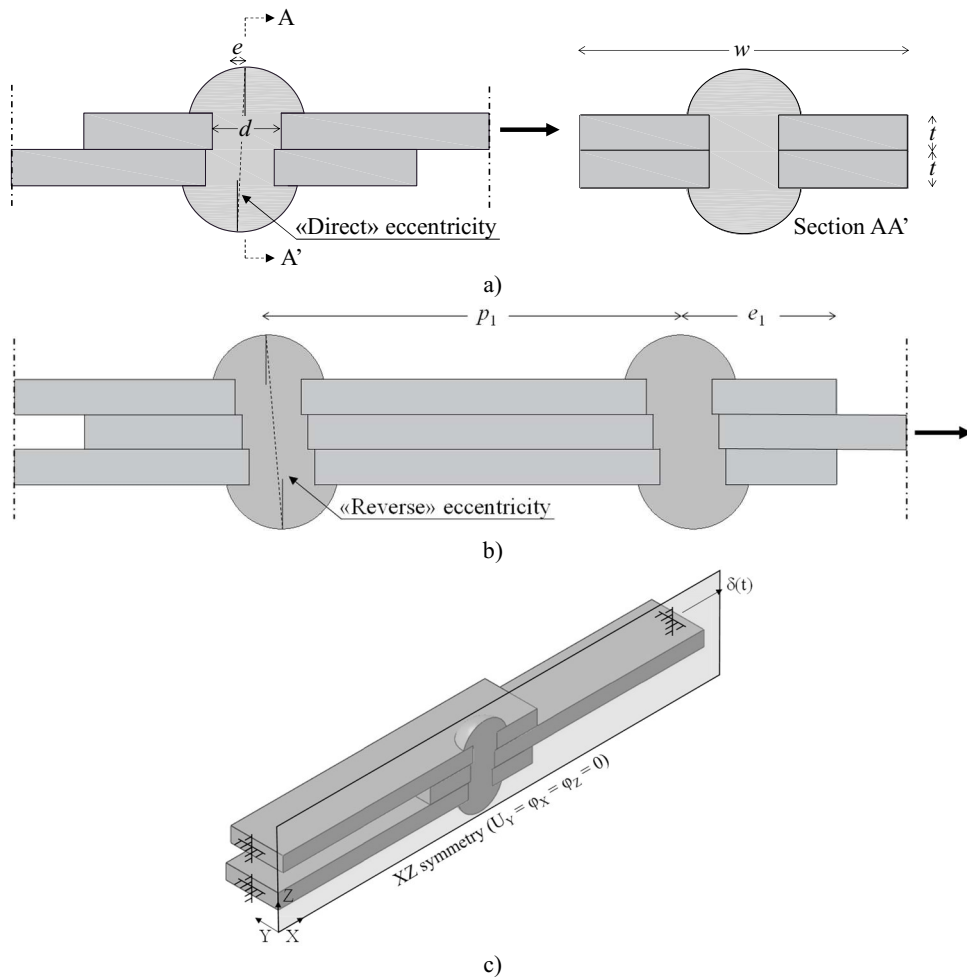
Figure 5.3 Main features for the investigated connections: a) single rivet specimens, b) double rivet specimens, c) modification of BCs for distorted symmetric specimens.

cl

Indeed, the orientation of the camming may affect the secondary bending effects, especially for unsymmetric connections.

Accordingly, BCs for lap-shear specimens with three plates were modified to account for the loss of longitudinal symmetry (Figure 5.3c).

With the aim to univocally identify each FEM, either corresponding to an undistorted or distorted connection, the labelling adopted in *Section 4.4* was modified as follows accounting for *e/d*, namely:

Labelling "C-D-T-N-E-O" with:

C = S or U with reference to the specimen configuration, i.e., symmetric or unsymmetric;

D = 16, 19 or 22 with reference to the rivet(s) diameter *d*;

T = 10 or 12 with reference to the plies thickness *t*;

N = 1 or 2 with reference to the number of rivets n_r;

E = 0.00 ÷ 0.20 with reference to the relative shank eccentricity *e/d*, with 0.00 being adopted for undistorted specimens;

O = D or R with reference to the camming orientation as respect to applied loads, i.e. direct or reverse eccentricity (when relevant).

A total of 15 × (1 + 4 + 4) = 135 refined FEAs were performed in accordance with model parameters summarized in Table 5.1.

All elements were discretized using solid C3D8 elements. Steel yielding was modelled using the Hencky-Von Mises criterion. The plasticity and damage parameters calibrated against coupon tests on plates and rivets were assumed as initial reference values with the aim to investigate the effect of hot-driving. Both kinematic and isotropic hardening were simulated as shown by *Dutta et al., (2010)*.

The "Ductile damage" module featured in ABAQUS 6.14 (*Dassault, 2014*) was used to simulate the material degradation (*Stage II*, see *Section 3.2*). Namely, the same damage formulations adopted for tensile coupon tests were employed for refined FEAs on connections.

Accordingly, the critical PEEQ for uniaxial tensile conditions $\varepsilon^*_{pl,eq,uniax}$ and the ultimate plastic displacement u^*_{pl} were properly recalibrated for rivets and, to a local extent, for plates, namely with the aid of the inverse method (see *Section 3.2*).

120 Preliminary sensitivity analyses were carried out with reference to the sole PDS to select the appropriate mesh density. Indeed, the influence of mesh size on the accuracy of FEAs is even more pronounced in case of connections as respect to coupon tests, mainly due to highly non-linear factors such as contacts and friction (*Milone et al., 2022a*). Therefore, a preliminary sensitivity analysis was carried out varying the mesh size from 5 mm to 0.5 mm (Figure 5.4) and comparing the experimental force-displacement curves against results from FEAs.

For the sake of brevity, solely the results of four undistorted connections (namely S-16-10-1, S-19-10-2, U-16-10-1 and U-19-10-2) are reported in Figure 5.4 in order to highlight possible variations owing to different configurations (i.e., symmetric or unsymmetric) or the number of rivets (1 or 2).

In these preliminary FEAs material damage was neglected, focusing only on plasticity, since the latter mainly governs the capacity of the connections, while material damage mainly influences the ultimate ductility. Moreover, the adopted linear DEC is almost mesh-insensitive due to the characteristic length parameter L_{char}, i.e., a function of finite element size (*Hillerborg et al., 1976*; *Dassault, 2014*).

Table 5.1 Main features for FEMs of hot-driven riveted connections.

Label	Conf.	Rivet Diameter d	Plate Thickness t	Plate Width w	Edge Distance e_1	N. of Rivets n_r	Rivets Pitch p_1	Relative Shank Ecc. e/d	Eccentricity Orientation O
[-]	[-]	[mm]	[mm]	[mm]	[mm]	[-]	[-]	[-]	[-]
S-16-10-1	S	16	10	70	35	1			
S-19-10-1	S	19	10	90	45	1			
S-19-12-1	S	19	12	90	45	1			
S-22-10-1	S	22	10	70	35	1			
S-22-12-1	S	22	12	70	35	1	-	From 0.00 (Undistorted connections) to 0.20 with an increase of 0.05	"Direct" or "Reverse"
U-16-10-1	U	16	10	70	35	1			
U-19-10-1	U	19	10	90	45	1			
U-19-12-1	U	19	12	90	45	1			
U-22-10-1	U	22	10	70	35	1			
U-22-12-1	U	22	12	70	35	1			
S-19-10-2	S	19	10	90	45	2	118		
S-22-12-2	S	22	12	70	35	2	118		
U-16-10-2	U	16	10	70	35	2	140		
U-19-10-2	U	19	10	90	45	2	118		
U-22-12-2	U	22	12	70	35	2	90		

In order to preliminarily account for the effects of the hot-driven process (HDP), in sensitivity analyses the yield strength of rivets was set 1.2 times greater than the value of the base material in accordance with *D'Aniello et al. (2011)*.

The results of sensitivity analyses are shown in Figure 5.4b-c-d-e, where it can be observed that using a coarse mesh leads to overestimating the resistance of the connections, while the elastic stiffness is less influenced. Nevertheless, for a mesh size equal to or smaller than 1 mm the differences between experimental and numerical force-displacement curves are negligible ($\leq 4\%$ at the onset of the degrading branch).

Moreover, the mesh size of the outermost parts of the plates does not modify the simulated response of the connections, since those portions behave in the elastic range. Therefore, a mesh size of 1 mm and 20 mm was selected for the connected zone and the ends of the plates, respectively.
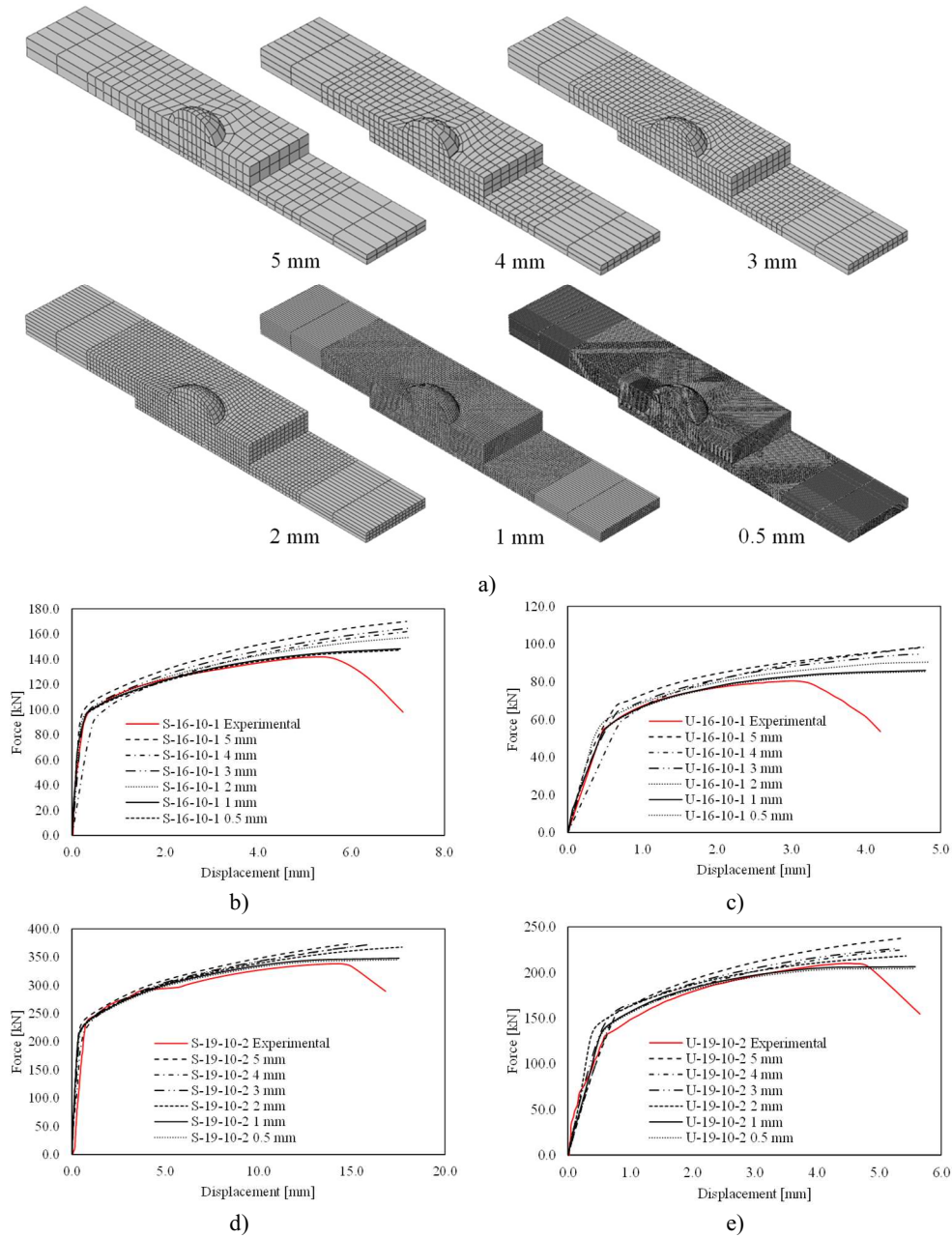
Figure 5.4 a) Details of different meshes adopted for the connections and results of mesh sensitivity analyses: b) S-16-10-1, c) U-16-10-1, d) S-19-10-2 and e) U-19-10-2.

5.2. Refined FEAs results for coupon tests

Results of refined FEAs for coupon tests on rivets (flat specimens "S10") and plates (dog-bone round specimens "C16") are depicted in Figure 5.5 in terms of calibrated engineering stress-strain curves and distribution of PEEQ and scalar damage (SDEG) at failure. For the sake of comparison, σ-ε curves derived by neglecting DDS (that is, by assuming a post-necking plasticity plateau and no damage) are also reported.
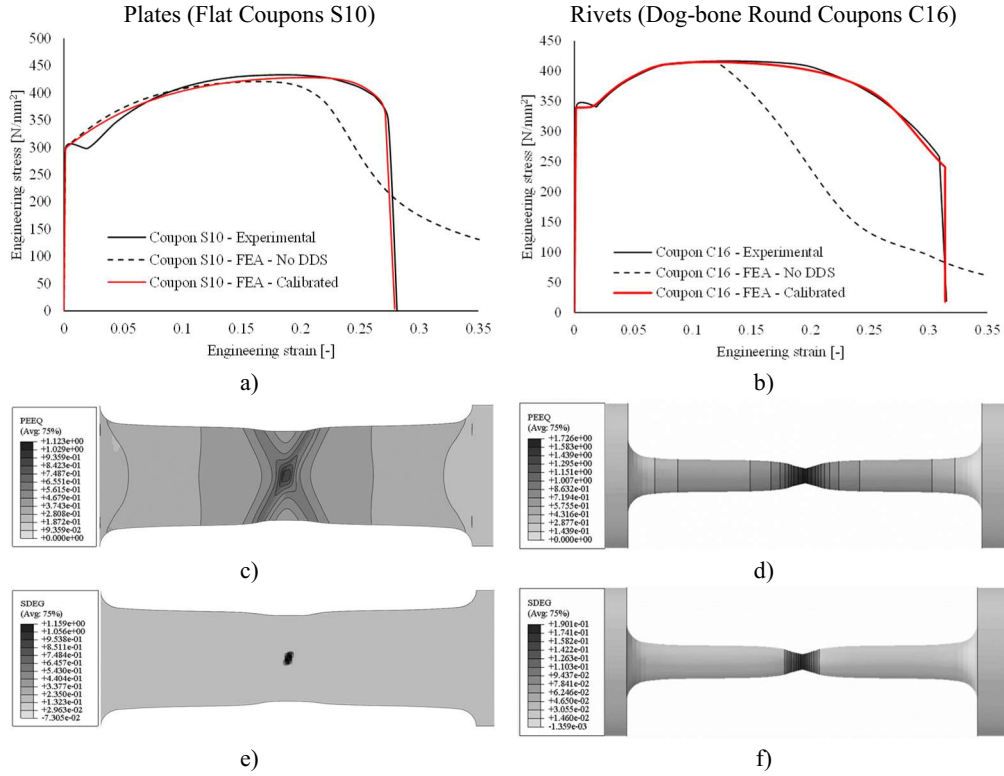
Figure 5.5 Refined FEAs on plates and rivets coupons: a-b) experimental, no DDS and calibrated engineering stress-strain curves, c-d) PEEQ distributions at failure and e-f) SDEG distributions at failure.

It can be easily noticed that both FEAs featuring no DDS formulation are still able to capture the post-necking degradation of coupons (Figure 5.5a-b, black dashed curves). Indeed, as shown by *Considére,* (*1885*), necking instability occurs as soon as the coupons cross-sections start to decrease of a larger amount than material hardening. Therefore, if geometric non-linearities are properly accounted for, necking will still occur even in absence of DDS modelling (*Yang et al., 2019*).

Calibrated FEAs (Figure 5.5a-b, red solid curves) are in very good agreement with experimental results, with negligible errors (< 1%) for f_y, f_u and $\varepsilon_{eng,u}$. Moreover, collapse mechanisms are properly captured. Indeed, while S10 features an inclined yield line due to plain strain conditions (*Kõrgesaar, 2019*), C16 shows diffuse necking.

Calibrated plasticity and damage parameters for both pristine plates and rivets are summarized in Table 5.2. Moreover, calibrated true stress-plastic strain curves, triaxiality curves and damage evolution curves are reported in Figure 5.6.

Table 5.2 Calibrated plasticity and damage parameters for pristine plates and rivets.

Coupon	f_y	f_u	$f_{u,true}$	ε_y	ε_u	$\varepsilon_{u,true}$	$\varepsilon^*_{pl,eq,uniax}$	u^*_{pl}
[-]	[N/mm²]	[N/mm²]	[N/mm²]	[-]	[-]	[-]	[-]	[mm]
Plates	291.0	433.0	620.0	0.00139	0.28	1.2840	1.04	0.4

Rivets	315.0	412.0	1240.0	0.00150	0.16	1.8755	1.02	1.1

a)

b)   c)
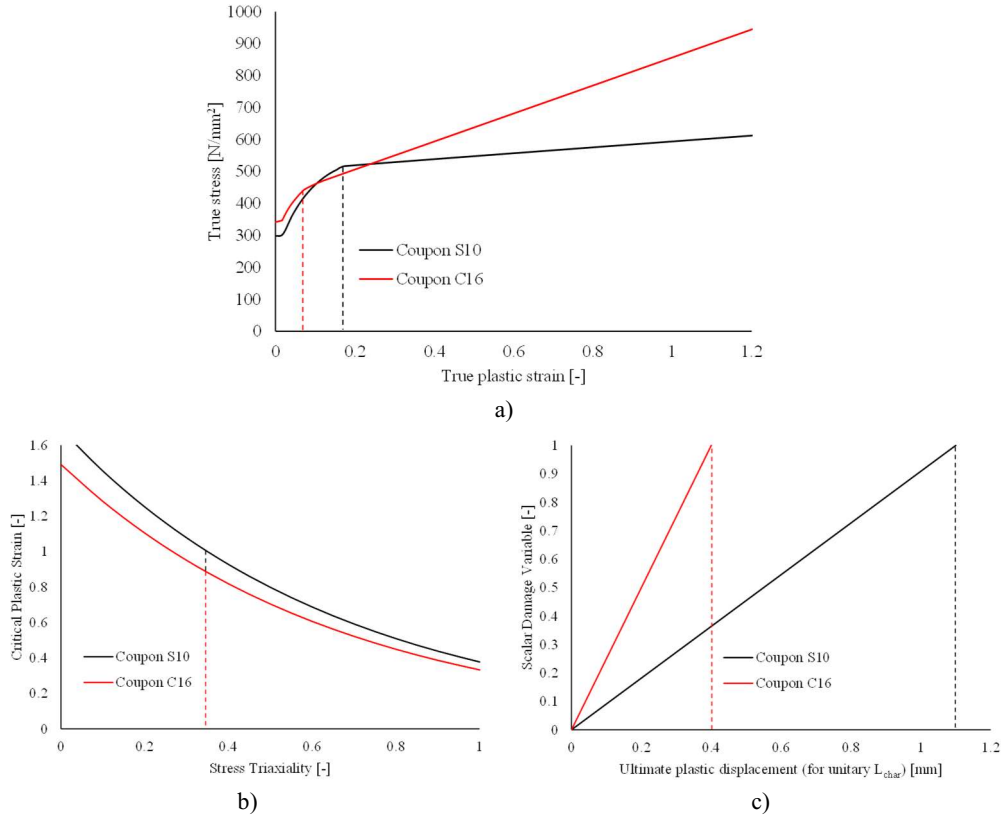
Figure 5.6 Calibrated damage and plasticity parameters for pristine rivets and plates: a) true stress-plastic strain curves, b) triaxiality curves, c) damage evolution curves.

It can be observed that undriven rivet steel is characterized by *i*) a stronger post-necking hardening and *ii*) a quicker damage development as respect to plate coupons. As suggested by *D'Aniello et al.* (*2011*), this outcome complies with its chemical composition (i.e., having a higher carbon content) and with the adopted Martin-Siemens productive process.

5.3. Magnitude and effect of clamping force on the performance of connections

Sensitivity analyses were carried out to highlight the influence of rivet pre-loading on the response of riveted connections. Indeed, as shown by *Leonetti et al.,* (*2020*), clamping stress in hot-driven rivets is highly variable, especially in case of short shanks ($h_s/d \leq 2$, see *Section 2.3.2* and Figure 2.25).

For this purpose, each connection was monotonically tested varying the preload stress in the range $0.1 \div 0.8\ f_{yr0}$, as shown in Figure 5.7. It is worth remarking that the clamping study was preliminarily performed accounting for no damage formulations, as DDS only affects the degrading branch of force-displacement curves, and it is thus only relevant as respect to connections ultimate ductility (*Milone et al., 2022a*).

For the sake of clarity, as no DDS FEAs cannot display a force drop, comparisons in terms of ultimate shear force for different values of σ_{clamp} were conventionally carried out at the onset of degrading branch of the experimental curves (Figure 5.7b-c-d-e, red solid lines).

$$\sigma_{clamp} = 0.1 \div 0.8 \; f_{yr0}$$

a)

b)

c)

d)

e)
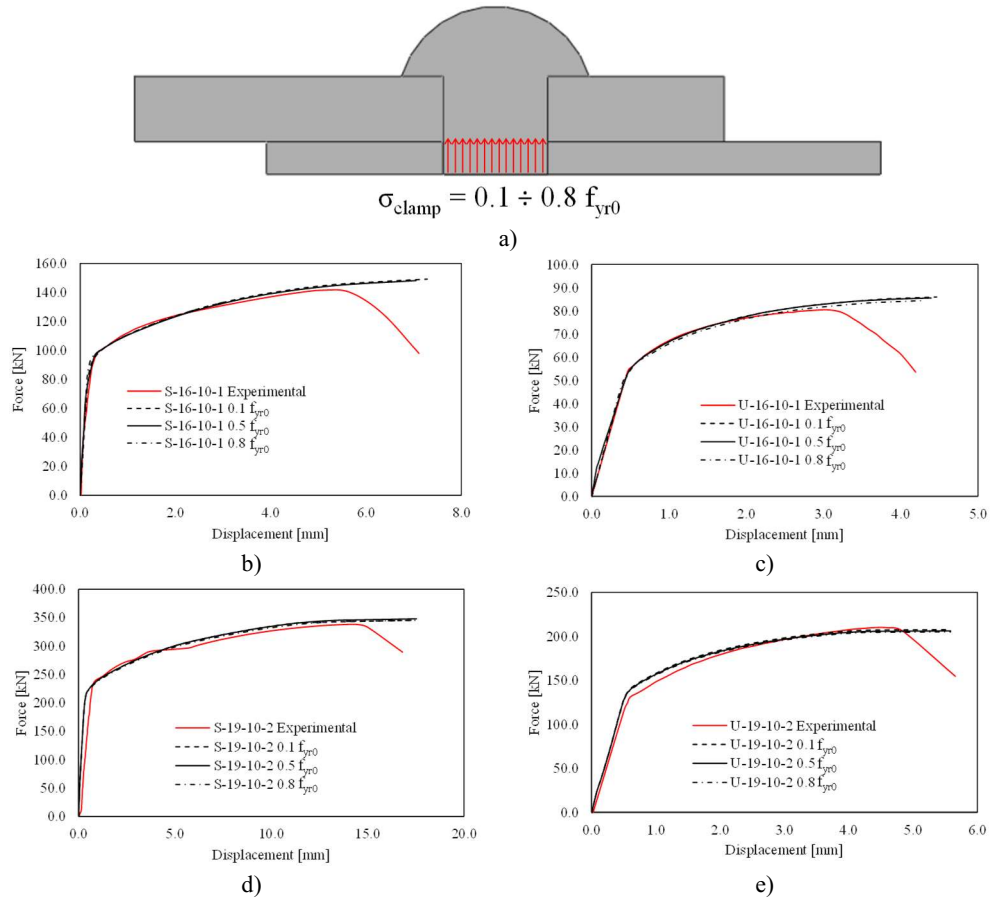
Figure 5.7 a) Details of different meshes adopted for the connections and results of mesh sensitivity analyses: b) S-16-10-1, c) U-16-10-1, d) S-19-10-2 and e) U-19-10-2.

For the sake of brevity, solely the results related to four connections (i.e., S-16-10-1, U-16-10-1, S-19-10-2 and U-19-10-2) are reported in Figure 5.7b-c-d-e. In all cases clamping stress does not appreciably influence the overall and local response of the connections (e.g., the maximum variation in terms of shear resistance is about 1%).

This outcome implies that constructional imperfections only affecting the clamping stresses distribution (e.g., head distortion) may be neglected when assessing the static performance of connections, consistently with observations reported in *Twelvetrees, 1900*; *Vermes, 2007*; *Collette, 2014*.

In light of the obtained results, a mean value of preload stress equal to 0.5 f_{yr0} was used for all static FEAs, that is, the mean value for hot-driven rivets with $h_s/d \leq 2$ as suggested by *D'Aniello et al.* (*2011*) and *Leonetti et al.* (*2020*).

Nevertheless, in light of its potential influence on the fatigue performance of connections (*Vermes, 2007*; *Kafie-Martinez et al., 2017*) a detailed parametric study concerning stresses transferred to connected plies and relative ASED values has been performed. Further details are reported in *Chapter 7*.

5.4. Effect of hot-driving on base material properties of rivets and plates

The hammering process deeply influences the behaviour of riveted connections, due to the combined effect of hammer pressure and abrupt change of temperature (*Hrennikof, 1934; Hetchman, 1948; Munse & Cox, 1956, D'Aniello et al, 2011*).

As highlighted by the above Authors, this phenomenon primarily induces a significant hardening of the rivet base material, resulting in a yield strength of the heat-treated rivet material f_{yr} which can be up to 1.5 times higher with respect to f_{yr0}. Moreover, this strength increase is accompanied by a significant reduction of material ductility.

Tests performed by *Hetchman* (*1948*) showed that f_{yr} increases with increasing temperature. This effect can be recognized up to a threshold of ~900 °C. Contrariwise, no appreciable variations were found by varying the temperature within the range $900 \div 1200$ °C.

As deeply described in *Section 3.2*, in the present work effects of hot-driven process on the rivet material were accounted by means of three non-dimensional coefficients, namely:

i) the *rivet strength ratio* $f_{yr}/f_{yr0} = \Omega \geq 1$;

ii) the *damage threshold ratio* $\varepsilon^*_{pl,eq,uniax}/\varepsilon^*_{pl,eq,uniax,0} = \Delta \leq 1$;

iii) the *plastic displacement ratio* $\Pi = u^*_{pl}/u^*_{pl0} \leq 1$.

In particular, HDP was simulated scaling the constitutive true stress-true strain relationship of rivet base material by a constant factor equal to Ω, while triaxiality curves were downscaled by reducing $\varepsilon^*_{pl,eq,uniax,0}$ preserving their shape according to the formulation proposed by *Yang et al., 2019*.

Values of Ω, Δ and Π calibrated against the experimental tests reported in *Chapter 4*, as well as their mean values and their corresponding coefficients of variation (COV) are summarized in Table 5.3 for all connections exhibiting rivet shearing.

For the sake of clarity, since u^*_{pl} is a mesh-size dependant parameter (*Hillerborg et al., 1976*), reported values are referred to a mesh size equal to 1 mm (i.e., the size adopted for parts which were expected to damage).

For the sake of comparison, the results of FEAs performed neglecting the effects of HDP are reported in Figure 5.8 for S-16-10-1-0.00 and U-16-10-1-0.00 in terms of PEEQ distribution and force-displacement curves.
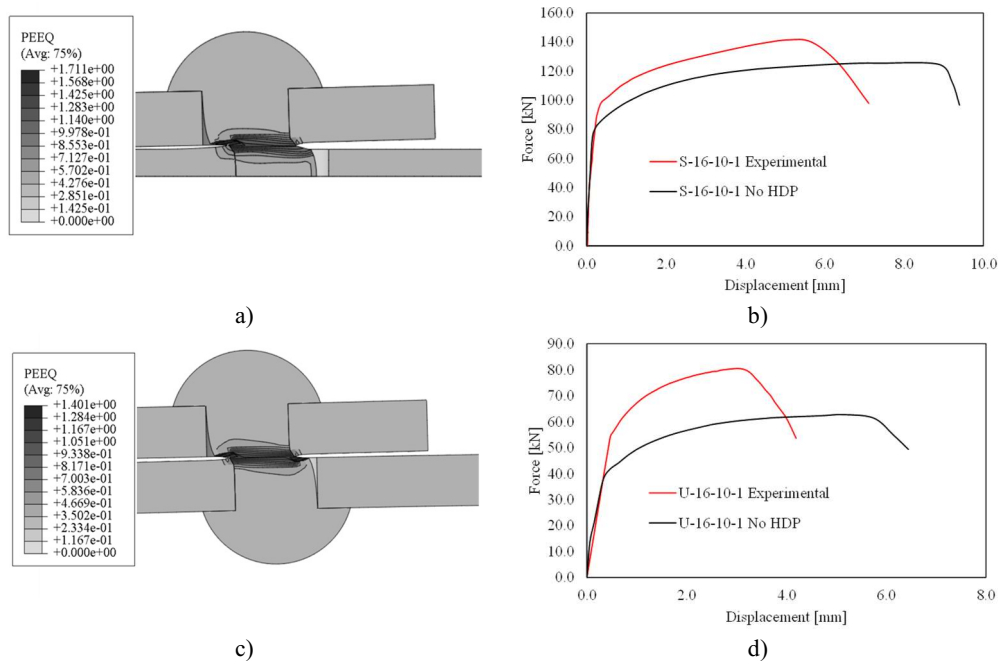
Figure 5.8 Results of FEAs performed neglecting the effects of the hot-driven process: PEEQ distribution and force-displacement curve for S-16-10-1-0.00 (a-b) and U-16-10-1-0.00 (c-d).

Table 5.3 Calibrated material parameters for connections exhibiting rivet shear failure.

Label [-]	f_{yr} [N/mm²]	$\Omega = f_{yr}/f_{yr0}$ [-]	$\varepsilon^*_{pl,eq,uniax}$ [-]	$\Delta = \varepsilon^*_{pl,eq,uniax}/\varepsilon^*_{pl,eq,uniax,0}$ [-]	u^*_{pl} [mm]	$\Pi = u^*_{pl}/u^*_{pl,0}$ [mm]
Coupon C16	315	-	1.02	-	1.1	-
S-16-10-1-0.00	365.4	1.16	0.54	0.53	1	0.91
S-19-10-1-0.00	368.6	1.17	0.98	0.96	1	1.00
S-19-12-1-0.00	393.8	1.25	0.6	0.59	1	1.00
U-16-10-1-0.00	447.3	1.42	0.28	0.27	0.7	0.70
U-19-10-1-0.00	378	1.2	0.32	0.31	0.5	0.71
U-19-12-1-0.00	447.3	1.42	0.48	0.47	0.7	1.40
U-22-10-1-0.00	378	1.20	0.88	0.86	0.6	0.86
U-22-12-1-0.00	444.2	1.41	0.24	0.24	0.7	1.17
S-19-10-2-0.00	318.1	1.01	1.65	1.61	0.4	0.57
U-16-10-2-0.00	441	1.40	0.23	0.23	0.8	2.00
U-19-10-2-0.00	390.6	1.24	0.46	0.45	0.6	0.75
U-22-12-2-0.00	393.8	1.25	0.21	0.21	0.6	1.00
Mean values	*397.6*	*1.26*	*0.58*	*0.57*	*0.73*	*1.01*
COV	*0.10*	*0.10*	*0.74*	*0.73*	*0.28*	*0.38*

It can be observed that, although the failure mechanism is correctly predicted in both cases (i.e., rivet shearing, see Figure 5.8a-c), the connection resistance is significantly underestimated (-11% and -24%, respectively).

Moreover, as remarked in *Section 3.2*, also connected plates are influenced by the hammering process. Indeed, the plates show a reduction of ductility nearby the holes, with an ultimate true strain $\varepsilon_{true,fail,p}$ which can be up to 0.4 times the ultimate true strain of the unaltered material $\varepsilon_{true,fail,p0}$. Contrariwise, no significant variation can be usually appreciated in terms of tensile strength. (*Hrennikof, 1934; Hetchman, 1948; Munse & Cox, 1956, D'Aniello et al, 2011*).

The localized alteration of the mechanical behaviour of plate base material was suitably simulated by assigning modified material properties only to the portion of plates included beneath the projection of rivet heads (Figure 5.9).
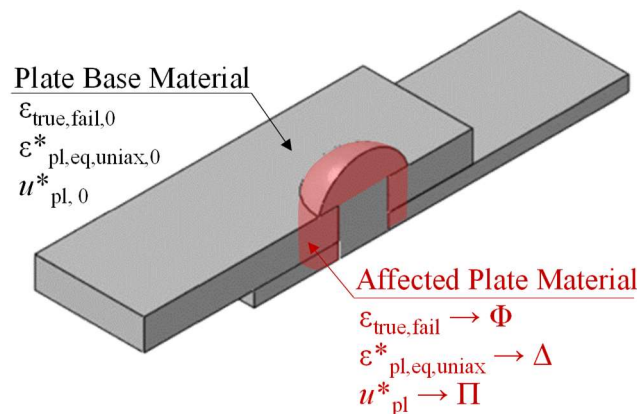
Figure 5.9 Assumed extension of the HDP affected zone for connected plates.

The effects of HDP on the response of connected plates in terms of ductility drop were accounted for by means of the *ultimate strain ratio* $\varepsilon_{true,fail,p}/\varepsilon_{true,fail,p0} = \Phi \leq 1$.

Material damage was also thoroughly accounted for by defining non-dimensional coefficient $\Delta \leq 1$, $\Pi \leq 1$ also for plates. Calibrated values of Φ, Δ and Π for connections exhibiting the failure of the plates are summarized in Table 5.4.

Table 5.4 Calibrated material parameters for connections exhibiting plate failure.

Label [-]	$\varepsilon_{true,fail,p}$ [-]	$\Phi =$ $\varepsilon_{true,fail,p}/\varepsilon_{true,fail,p0}$ [-]	$\varepsilon^*_{pl,eq,uniax}$ [-]	$\Delta =$ $\varepsilon^*_{pl,eq,uniax}/\varepsilon^*_{pl,eq,uniax,0}$ [-]	u^*_{pl} [mm]	$\Pi =$ $u^*_{pl}/u^*_{pl,0}$ [mm]
Coupon S10	1.28	-	1.04	-	0.4	-
S-22-10-1-0.00	0.92	0.72	0.2	0.19	0.4	1.00
S-22-12-1-0.00	0.35	0.27	0.13	0.13	0.2	0.50
S-22-12-2-0.00	0.82	0.64	0.33	0.32	0.2	1.00
Mean values	*0.70*	*0.54*	*0.22*	*0.21*	*0.26*	*0.83*
COV	*0.36*	*0.36*	*0.38*	*0.37*	*0.36*	*0.35*

As it can be observed, all damage parameters are significantly lower than unity ($\Phi_{mean} = 0.54$, $\Delta_{mean} = 0.21$, $\Pi_{mean} = 0.65$). It is worth remarking that, while plasticity and damage parameters for S-22-10-1-0.00 and S-22-12-1-0.00 were calibrated based on an observed plate bearing failure (B), relevant Φ, Δ and Π values for S-22-12-2-0.00 were derived interpretating the experimental net area tensile failure (T).

Further details about observed collapse mechanisms are reported in the next Section.

5.4.1 Observed Collapse Mechanisms

The failure modes of undistorted riveted connections are depicted in Figure 5.10 in terms of PEEQ at failure, scalar damage at failure and force-displacement curves.

For the sake of comparison, both calibrated (black dashed lines) and mean values (red solid lines) of plasticity and damage parameters were considered. Results of FEAs are also compared with collapse mechanisms observed experimentally.

For the sake of brevity, only results relative to six (out of fifteen) connections are reported (namely S-16-10-1-0.00, U-16-10-1-0.00, S-22-10-1-0.00, S-22-12-1-0.00, U-19-10-2-0.00 and S-22-12-2-0.00). Since most of the connections exhibited shear failure of the rivets (hence also referred to as "V"), only the three most representative configurations are shown hereinafter. Contrariwise, all results of specimens exhibiting the failure of the plates (both in bearing, also referred to as "B", or tearing of the net area, also referred to as "T") are reported in the following.

Rivet shear failure can be easily recognized for S-16-10-1-0.00 observing the PEEQ and the scalar damage distributions at failure (see Figure 5.10a). Moreover, a slight run-out of the middle hole can be noticed due to a secondary bearing mechanism (owing to the reduced thickness of the plates). This outcome is confirmed by the results of the experimental tests (see Figure 5.10b). A very good agreement between numerical and experimental results can be also noticed in terms of the force-displacement curve (see Figure 5.10c). S-16-10-1-0.00 exhibits a moderate overstrength due to the hot-driven process, with a calibrated value of $\Omega = 1.16$. On the contrary, the material ductility reduction is more significant ($\Delta = 0.54$).

Similar remarks can be drawn for the U-16-10-1-0.00. However, owing to the presence of a single shear plane, in this case the rivet shear resistance is significantly lower than the bearing resistance of connected plates (-38%). Therefore, no appreciable distortion

of the holes is present, as confirmed both by numerical and experimental results reported in Figure 5.10d-e-f. Notably, U-16-10-1-0.00 shows the highest HDP-induced overstrength (Ω = 1.42). Consistently with considerations reported in Section 4.1, the capacity increase is associated with a sharp reduction of ultimate ductility (Δ = 0.28).

PEEQ and Damage at Failure	Experimental Test	Force vs. Displacement Curves

a) b) c)

[V + B (sec.)] *Rivets: Ω = 1.16, Δ = 0.54*

d) e) f)

[V] *Rivets: Ω = 1.42, Δ = 0.28*

g) h) i)

[B] *Plates: Φ = 0.72, Δ = 0.20*

j) k) l)

[B] *Plates: Φ = 0.64, Δ = 0.33*
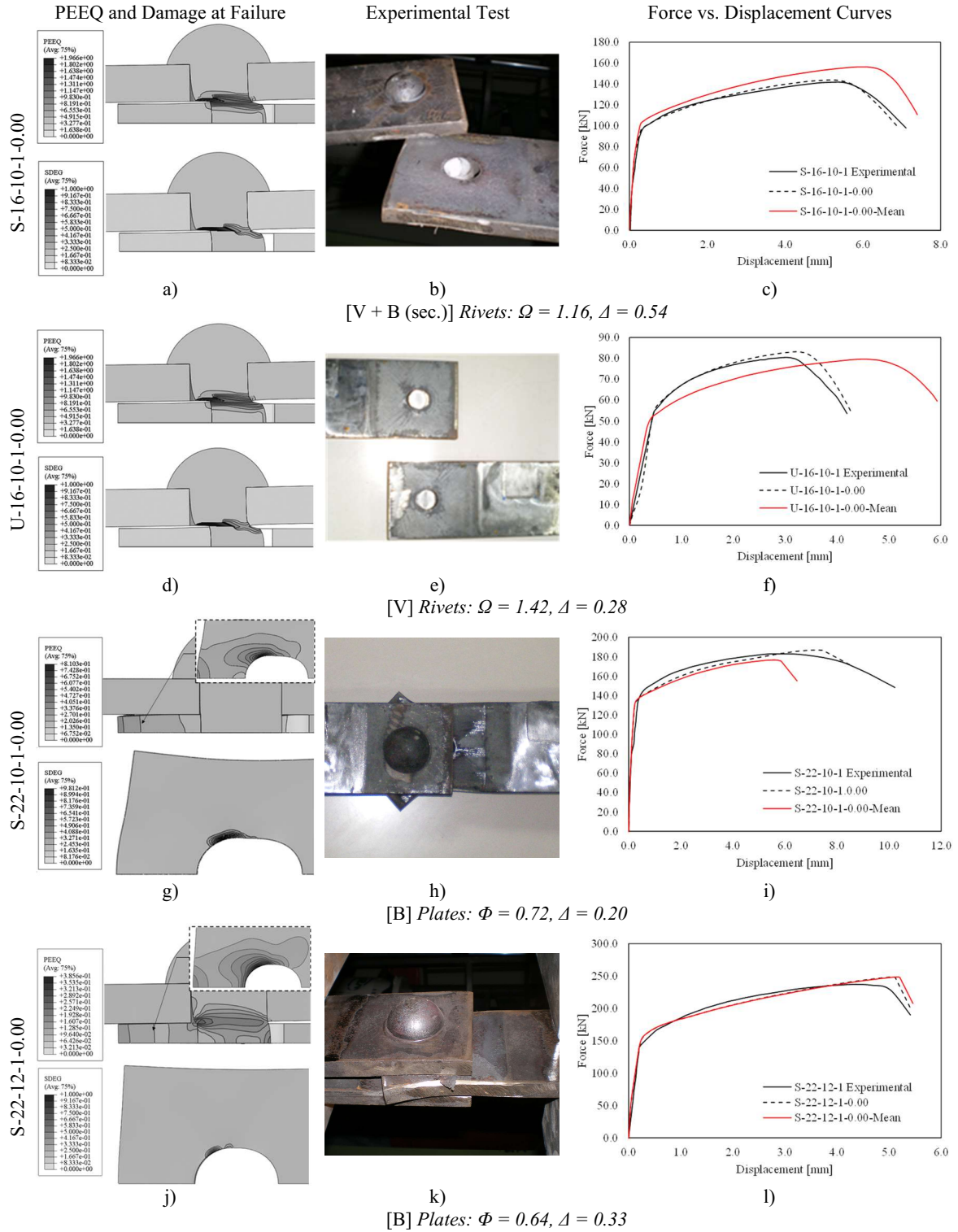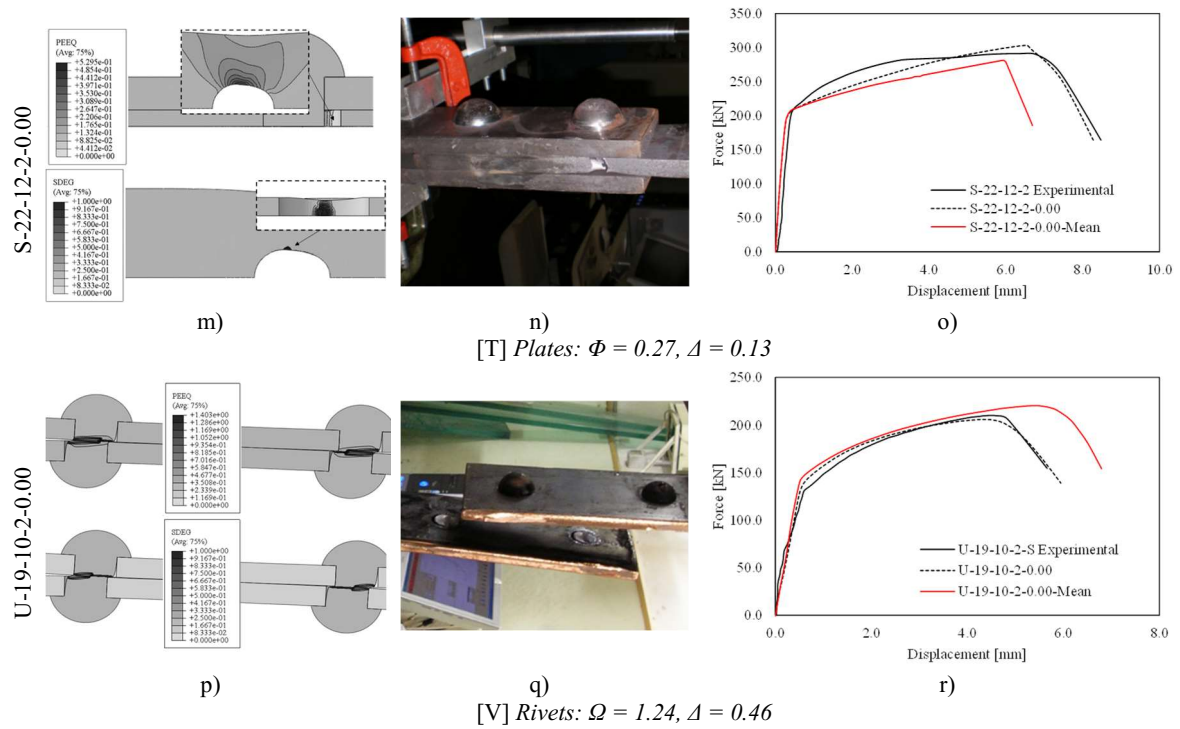
Figure 5.10: Comparison against experimental and numerical results for the investigated specimens in the undistorted configuration (C-T-D-N-0.00).

S-22-10-1-0.00 and S-22-12-1-0.00 are characterized by bearing failure (see Figure 5.10g-j). Notably, in the case of thicker plates (t = 12 mm) the simultaneous plasticization of rivets and plates can be observed. Nevertheless, as shown by scalar damage distributions reported in Figure 5.10g-j, plate bearing failure always governs the ultimate behaviour of both connections. FEAs are in good agreement with experimental results (see Figure 5.10i-l), confirming the occurrence of the predicted mechanism, as it can be observed in Figure 5.10h-k. Calibrated values of Φ highlight that the local ductility reduction of plates is significant (e.g., Φ = 0.27 for S-22-12-1-0.00).

S-22-12-2-0.00 is the unique specimen that exhibited net-area tensile failure of the plates. This outcome, which is confirmed by the experimental evidence (see Figure 5.10n), is highlighted by the distribution of PEEQ at failure, which are spread in the transverse direction, departing from the hole centre with an angle of ~30° (see Figure 5.10m – *Irgens, 2008*).

The ultimate behaviour of U-19-10-2-0.00 is governed by the shear failure of the rivet, as shown by the distribution of PEEQ and scalar damage at failure (see Figure 5.10p). A very good agreement can be noticed between numerical and experimental responses, see Figure 5.10r. Notably, a significant in-plane rotation can be observed owing to the arise of secondary bending moments.

As it can be observed, the force-displacement response curves of the FE models with the mean values of plasticity and damage parameters differ from those obtained using the calibrated values due to the variability of these mechanical properties. In fact, the damage parameters are characterised by a scatter (e.g., COV_Δ = 0.73, COV_Φ = 0.36, COV_{u*pl} = 0.36 in worst cases, see Tables 5.3-5.4) larger than the rivet strength ratio (e.g., COV_Ω = 0.10, see Table 5.3).

In light of these results, all FE models can be considered properly calibrated.

In the following, the behaviour of undistorted specimens is used as a benchmark to investigate the influence of constructional imperfections on the ultimate behaviour of hot-driven riveted connections. Further details are reported in the next *Section 5.5*.

5.5. Preliminary investigation on the effect of constructional imperfections on the static resistance of connections

The presence of constructional imperfections may detrimentally affect the ultimate behaviour of hot-driven riveted connections, both in terms of resistance and ductility. The influence of imperfections on the mechanical response strictly depends on the geometrical features of the connections, the type of failure mode and the shape and magnitude of the imperfections (*Twelvetrees, 1900*; *Sustainable Bridge, 2006*; *Vermes, 2007*; *Collette et al., 2011, 2015*; *Collette, 2014*).

In the present Section, an investigation on the effect of one of the most common constructional imperfections, i.e., shank camming defect, is preliminarily addressed with reference to the lone static performance of assemblies. Further developments concerning the influence of camming on the fatigue performance and, generally speaking, the effect of other constructional imperfections are planned and are beyond the scope of the present Thesis work.

In the case of camming defects, the degradation of the connections' performance is mainly due to:

- the reduction of the cross-section of the rivet shank, which is caused by local discontinuities on the shear plane(s), see Figure 5.11a);
- the secondary internal actions caused by distorted configurations, which modify *i*) the distribution of tensile principal stresses at the onset of plasticity and *ii*) the damage pattern failure, thus causing a reduction of the ultimate ductility (see Figure 5.11b). This phenomenon is particularly pronounced for unsymmetric connections, where the effects of imperfections magnify the secondary stresses already caused by the bending of the connected plates.

It should be remarked that shank distortion also modifies the distribution of the clamping stresses (see Figure 5.11c) although this effect is of minor importance in static conditions, since pre-loading does not have a significant influence on the ultimate performance of the connections, as highlighted in *Section 5.3*.

Residual
Cross-Section

a)

Undistorted Specimen   Distorted Specimen

b)

Undistorted Specimen   Distorted Specimen

c)
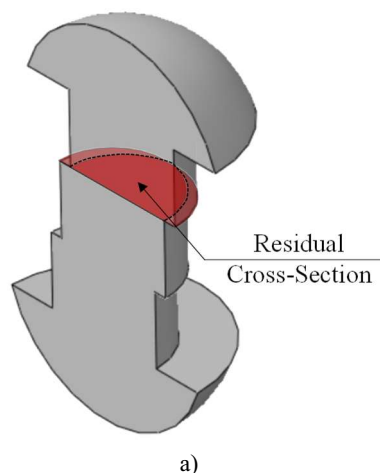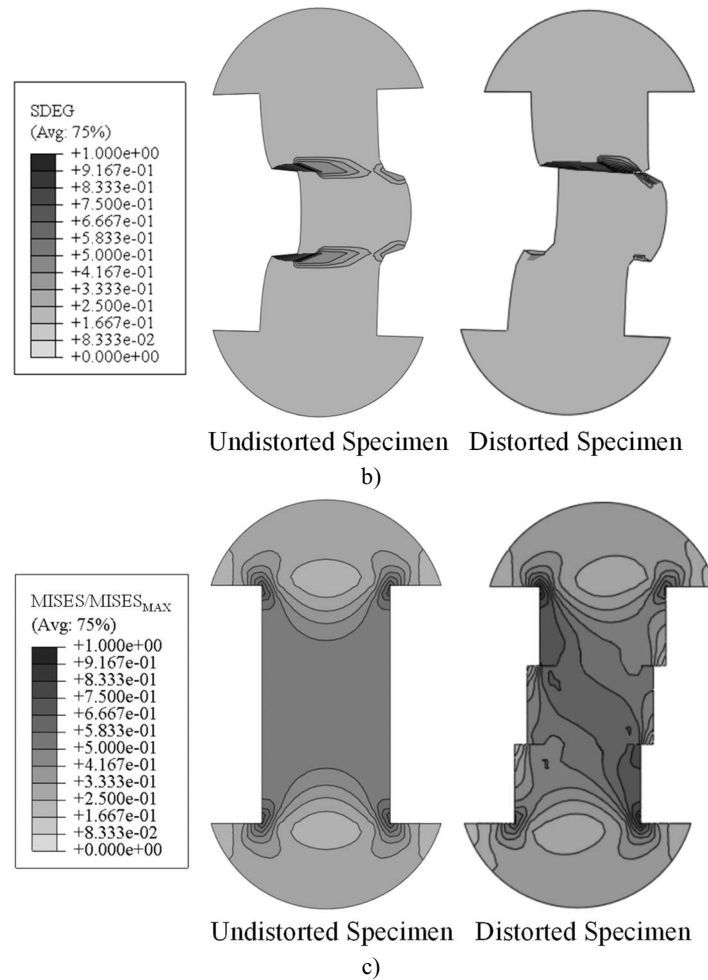
Figure 5.11 Effects of shank distortion on the connections response: a) reduction of the shear resisting cross-section, b) alteration of damage pattern at failure and c) alteration of clamping stress distribution.

5.5.1 Ultimate Behaviour of Distorted Symmetric Connections

The ultimate behaviour of symmetric riveted connections with camming is shown in Figures 5.12-5.13 in terms of force-displacement curves and distribution of PEEQ and scalar damage at failure. For the sake of clarity, distorted connections with three plates are still referred as "symmetric" in order to preserve a consistent labelling through this Chapter, although longitudinal symmetry is clearly lost due to imperfections. Moreover, it is worth noting that values of plasticity and damage parameters representative of each connection (see Tables 5.3-5.4) have been used to perform refined FEAs.

For the sake of brevity, only deformed configurations for the upper value of $e/d = 0.20$ are depicted. Ultimate values of resistance and displacement for symmetric distorted connections are also reported in Table 5.5.

In all cases, the shank misalignment does not appreciably influence the capacity of symmetric connections. For instance, the maximum resistance degradation is exhibited by S-19-10-1-0.20-D/R, i.e., about 4% with respect to the corresponding undistorted connection (see Figure 5.12f).

Nevertheless, the effects of shank distortion can be clearly observed for connections exhibiting shear failure of the rivets, which show a damage concentration into a single shear plane, which is the closest to the applied loads (i.e., the upper shear plane in case of "direct" eccentricity and the lower shear plane for "reverse" eccentricity).
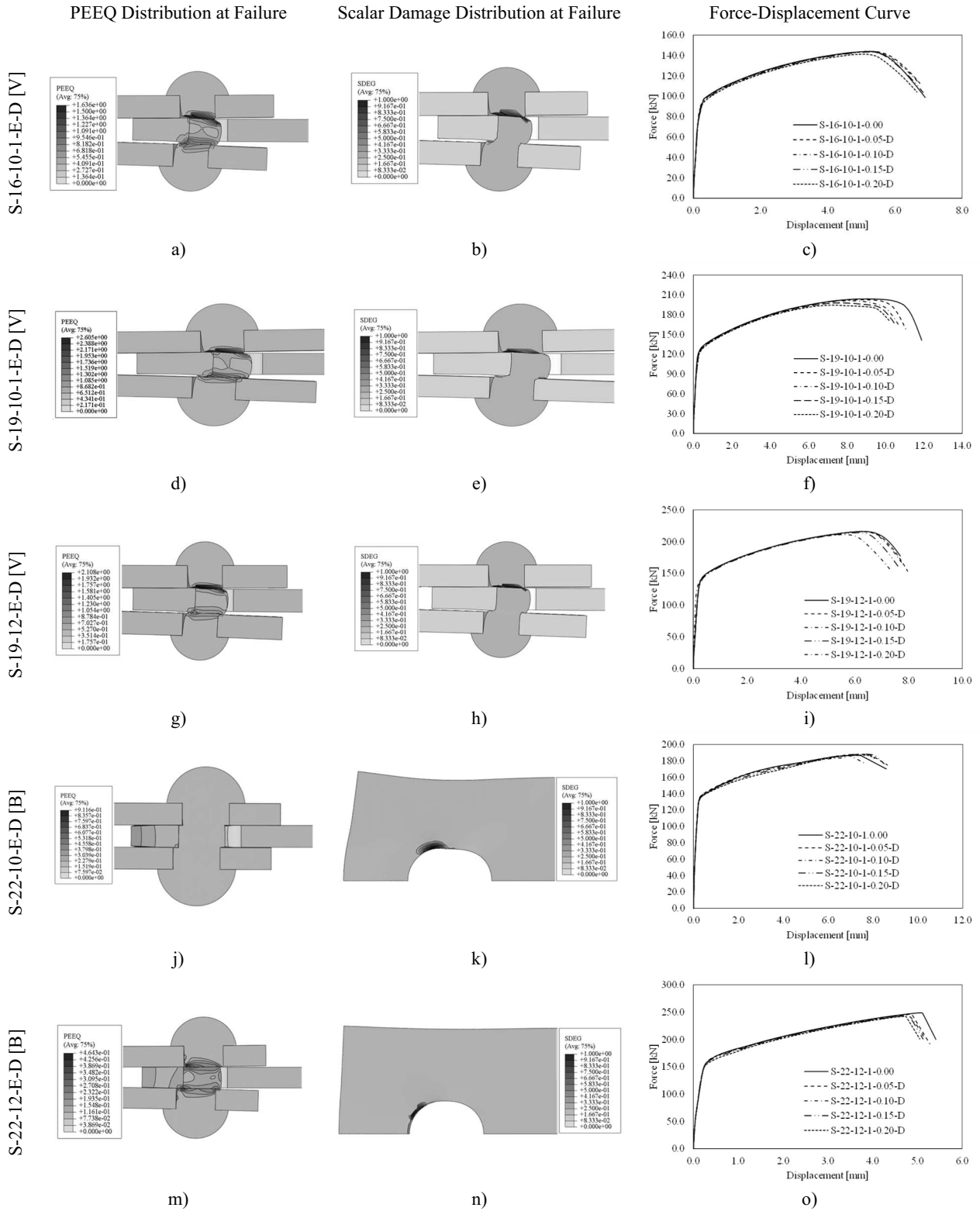
Figure 5.12 Ultimate behaviour of single rivet symmetric distorted connections in terms of PEEQ and scalar damage distributions at failure (for e/d = 0.20) and force-displacement curves.

Moreover, the camming defect also induces asymmetric transverse displacements between the connected plates (i.e., "*plate opening*"), although this effect has minor importance for the investigated values of e/d.

The ultimate displacement is significantly affected by the shank imperfections.

S-19-10-2-E-D [V]

a) PEEQ Distribution at Failure

b) Scalar Damage Distribution at Failure

c) Force-Displacement Curve

S-22-12-2-E-D [T]

d) PEEQ Distribution at Failure

e) Scalar Damage Distribution at Failure

f) Force-Displacement Curve
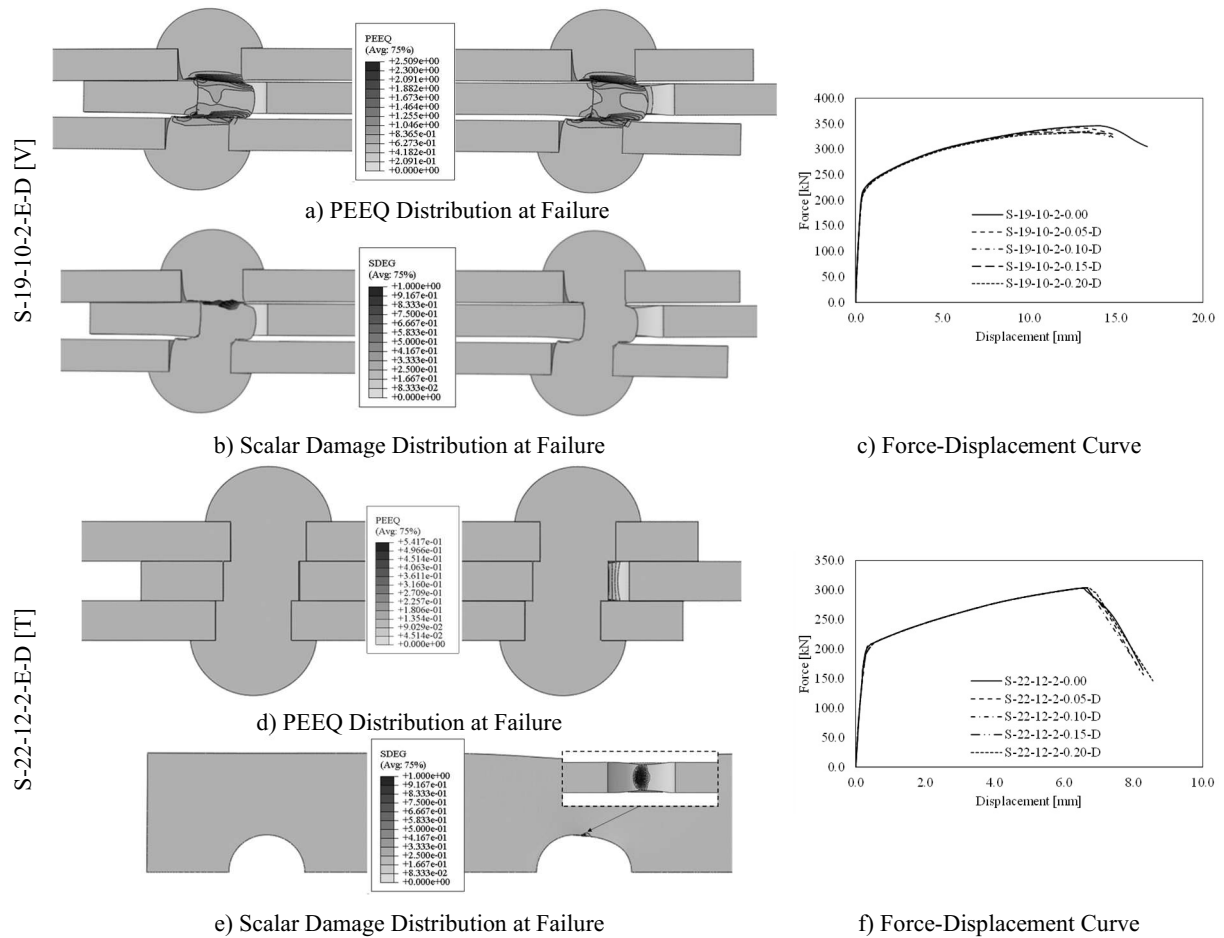
Figure 5.13 Ultimate behaviour of double rivet symmetric distorted connections in terms of PEEQ and scalar damage distributions at failure (for $e/d = 0.20$) and force-displacement curves.

For instance, the maximum reduction in terms of ultimate displacement, which is exhibited by S-19-12-1-0.20-D/R, is about 10% with respect to the relative undistorted connection (see Figure 5.12i). For the sake of clarity, in the present work ultimate displacements Δ_u were measured in correspondence with a reaction force equal to 0.80 F_u on the degrading branch of the force-displacement curves, being F_u the peak resistance of the connection.

This outcome may be important for the assessment of riveted structures under exceptional events, in which the ductility of the connections is a fundamental requirement to prevent the overall collapse. It is worth remarking that similar criticalities were already highlighted for bolted connections (*Tartaglia et al., 2017*). Nevertheless, the reduction of both ultimate capacity and ultimate displacement of symmetric connections is the most severe for the higher values of e/d.

This result is consistent with the Sustainable Bridge report (*Sustainable Bridge, 2006*) that recommends the repair of riveted connections with $e/d > 0.15$.

It should be also remarked that distorted symmetric connections do not exhibit any sensitivity to distortion orientation, e.g., for the same magnitude of e/d both ultimate resistance and ductility are identical in the case of "direct" and "reverse" eccentricity. Indeed, owing to their peculiar geometrical features, symmetric "direct" connections can be transformed in their equivalent "reverse" configurations by means of a rigid reflection along the longitudinal plane. Therefore, in the present Section only results for connections with "direct" eccentricity are presented.

Table 5.5 Behaviour of distorted symmetric connections in terms of ultimate resistance and ultimate displacement for increasing values of *e*/*d*.

Ultimate Resistance F$_u$ [kN]					
Label [-]	E (*e*/*d*)				
	0.00	*0.05*	*0.1*	*0.15*	*0.2*
S-16-10-1-E-D/R	143.9	143.9	144	143.3	141.2
S-19-10-1-E-D/R	203.8	202.7	201.1	197.8	194.5
S-19-12-1-E-D/R	215.8	215.4	215.9	213.9	210.9
S-22-10-1-E-D/R	186.8	188	186.2	188.2	187.1
S-22-12-1-E-D/R	248.7	246.1	241.8	244.5	242.3
S-19-10-2-E-D/R	346	342.9	337.9	333.2	335.5
S-22-12-2-E-D/R	303.3	303.7	303.4	303.5	304
Ultimate Displacement Δ$_u$ [mm]					
Label [-]	E (*e*/*d*)				
	0	*0.05*	*0.1*	*0.15*	*0.2*
S-16-10-1-E-D/R	6.4	6.5	6.4	6.4	6.3
S-19-10-1-E-D/R	11.6	11	10.8	10.7	10.5
S-19-12-1-E-D/R	7.9	7.9	7.8	7.5	7.1
S-22-10-1-E-D/R	10.3	10.2	10.2	10.2	10.2
S-22-12-1-E-D/R	5.4	5.3	5.2	5	5
S-19-10-2-E-D/R	17.1	16.9	16.9	16.8	16.7
S-22-12-2-E-D/R	7.7	7.7	7.6	7.6	7.6

On the other hand, symmetric connections exhibiting plate bearing ("B", i.e. S-22-10-1-[0.05÷0.20]-[D/R] and S-22-12-1-[0.05÷0.20]-[D/R], see Figure 5.12j-o) or tearing in the net-area ("T" i.e. S-22-12-2-[0.05÷0.20]-[D/R], see Figure 5.13d-f) are almost insensitive to the effects of shank distortion, since no appreciable variations of ultimate resistance and/or ultimate ductility can be observed (-3% and -0%, respectively). Moreover, the presence of camming defects within the tolerability ranges provided by the Sustainable Bridge report (*Sustainable Bridge, 2006*) does not modify the type of failure mode, as confirmed by the distribution of scalar damage at failure for the aforementioned connections (see Figures 5.12k, 13n and 14e).

5.5.2 Ultimate Behaviour of Distorted Unsymmetric Connections

The ultimate behaviour of unsymmetric riveted connections with shank distortion is shown in Figures 5.14-5.17 in terms of force-displacement curves and distribution of PEEQ and scalar damage at failure. Calibrated values of plasticity and damage parameters (see Tables 5.3-5.4) have been used to perform refined FEAs. For the sake of brevity, only the results for the cases with *e*/*d* = 0.20 are reported.

Differently from the symmetric connections, in the case of unsymmetric connections two different models were analysed to investigate both "direct" and "reverse" eccentricity due to the absence of longitudinal symmetry that also causes a significant sensitivity to distortion orientation.

The ultimate response of unsymmetric connections with "direct" eccentricity is basically comparable to the behaviour of symmetric ones. Indeed, it can be noticed that no significant reduction in terms of ultimate capacity (≤ 4%) is shown by any of the investigated connections (see Figures 5.14-5.15 and Table 5.6), which exhibited the shear failure of rivets.
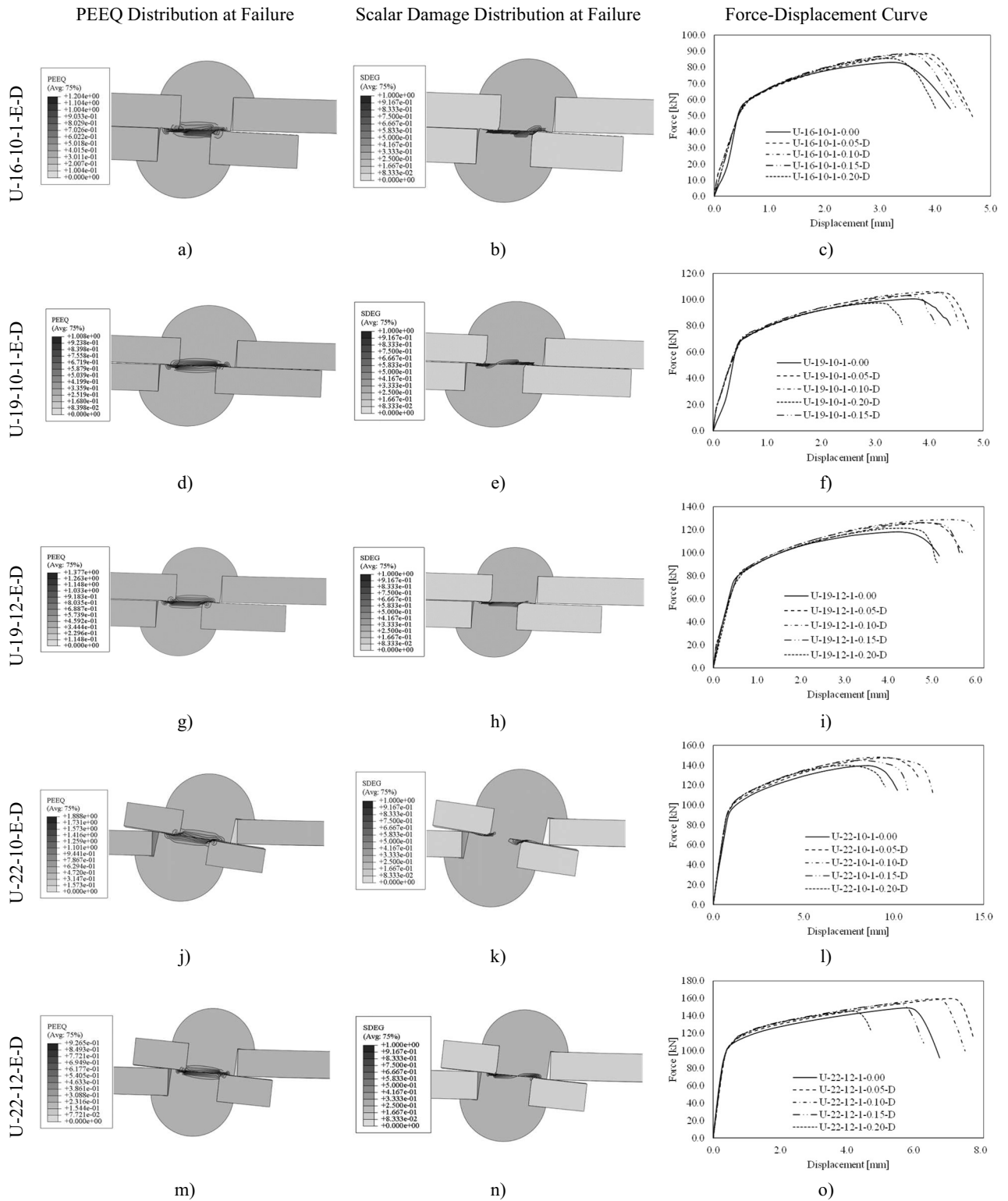
Figure 5.14 Ultimate behaviour of single rivet unsymmetric distorted connections with "direct eccentricity" in terms of PEEQ and scalar damage distributions at failure (for $e/d = 0.20$) and of force-displacements curves.

Nevertheless, some small differences in terms of elastic stiffness ($10 \div 16\%$) can be observed due to the influence of shank distortion on the joint rotation caused by

secondary bending. This effect is more pronounced in the case of highly deformable connections (i.e., U-16-10-1-[0.05÷0.20]-D, see Figure 5.14c).

a) PEEQ Distribution at Failure

b) Scalar Damage Distribution at Failure

c) Force-Displacement Curve

d) PEEQ Distribution at Failure

e) Scalar Damage Distribution at Failure

f) Force-Displacement Curve

g) PEEQ Distribution at Failure

h) Scalar Damage Distribution at Failure

i) Force-Displacement Curve
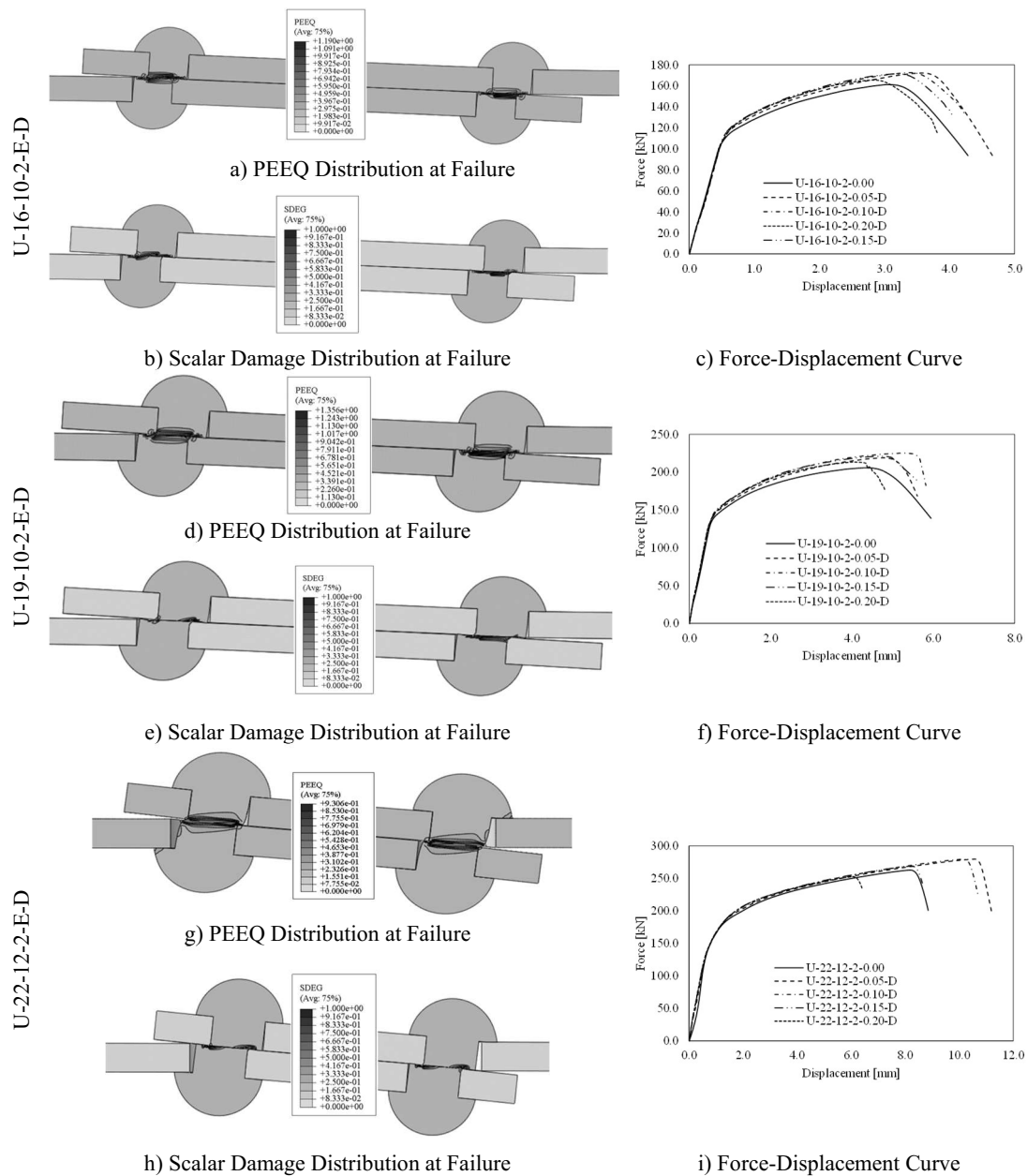
Figure 5.15 Ultimate behaviour of double rivet unsymmetric distorted connections with "direct eccentricity" in terms of PEEQ and scalar damage distributions at failure (for e/d = 0.20) and of force-displacements curves.

Table 5.6 Behaviour of distorted unsymmetric "direct" connections in terms of ultimate resistance and ultimate displacement for increasing values of e/d.

	Ultimate Resistance F_u [kN]				
Label [-]	E (e/d)				
	0	*0.05*	*0.1*	*0.15*	*0.2*
U-16-10-1-E-D	83.1	88.5	88.5	88.5	85.6
U-19-10-1-E-D	100.5	105.4	106	103	97.3
U-19-12-1-E-D	118.2	126	128.8	126.2	121.3
U-22-10-1-E-D	139.5	147.3	148.1	144.7	139.8
U-22-12-1-E-D	149.2	159.8	159.6	154	145.4

Label [-]	E (e/d) 0	0.05	0.1	0.15	0.2
U-16-10-2-E-D	161.2	172.2	172.5	171.4	165.5
U-19-10-2-E-D	205.7	219	225.1	220.9	213.2
U-22-12-2-E-D	262.8	279.8	279.6	269	252.7

Ultimate Displacement Δ_u [mm]					
Label [-]	**E (e/d)**				
	0	*0.05*	*0.1*	*0.15*	*0.2*
U-16-10-1-E-D	3.8	4.4	4.3	4.1	3.8
U-19-10-1-E-D	4.5	4.7	4.5	4.1	3.7
U-19-12-1-E-D	5.2	5.7	6	5.6	5.3
U-22-10-1-E-D	10.3	11.4	11.8	10.9	9.8
U-22-12-1-E-D	6.6	7.8	7.5	6.3	4.9
U-16-10-2-E-D	4	4.5	4.3	4.1	3.9
U-19-10-2-E-D	5.4	5.7	5.8	5.6	4.9
U-22-12-2-E-D	8.7	11.1	10.7	8.7	6.6

Moreover, the ultimate displacement of unsymmetric connections with "direct" eccentricity displays a recurring and peculiar trend, with connections with small eccentricity (i.e., $e/d \leq 0.10$) having higher ultimate displacement than one of the corresponding undistorted ones (up to +18%).

Contrariwise, the connections with greater values of e/d show a reduction of ultimate ductility. This effect is considerable in the connections with the bigger rivets (i.e., $d =$ 22mm). For instance, U-22-12-0.20-1-D and U-22-12-2-0.20-D exhibit a reduction in terms of Δ_u equal to -31% and -24% with respect to the corresponding undistorted connections, respectively (see Figures 5.14o-5.15i).

This effect depends on the alteration of the damage pattern at failure, which is highly influenced by the presence of the camming defect. In fact, the shank misalignment modifies the stress distribution induced both by clamping and secondary bending, thus resulting in an alteration of stress triaxiality T which in turns influences the critical PEEQ at the onset of damage (*Kanvinde et al., 2006; Yang et al., 2019*).

Interestingly, the ultimate behaviour of unsymmetric connections with "reverse" eccentricity is systematically affected by a significant reduction of both ultimate capacity and ductility with increasing values of e/d (see Figures 5.16-5.17 and Table 5.7).

PEEQ Distribution at Failure	Scalar Damage Distribution at Failure	Force-Displacement Curve
a)	b)	c)
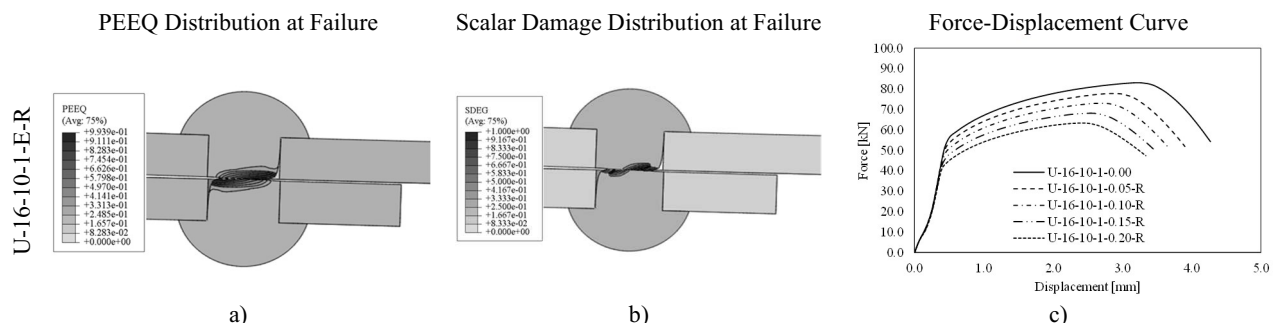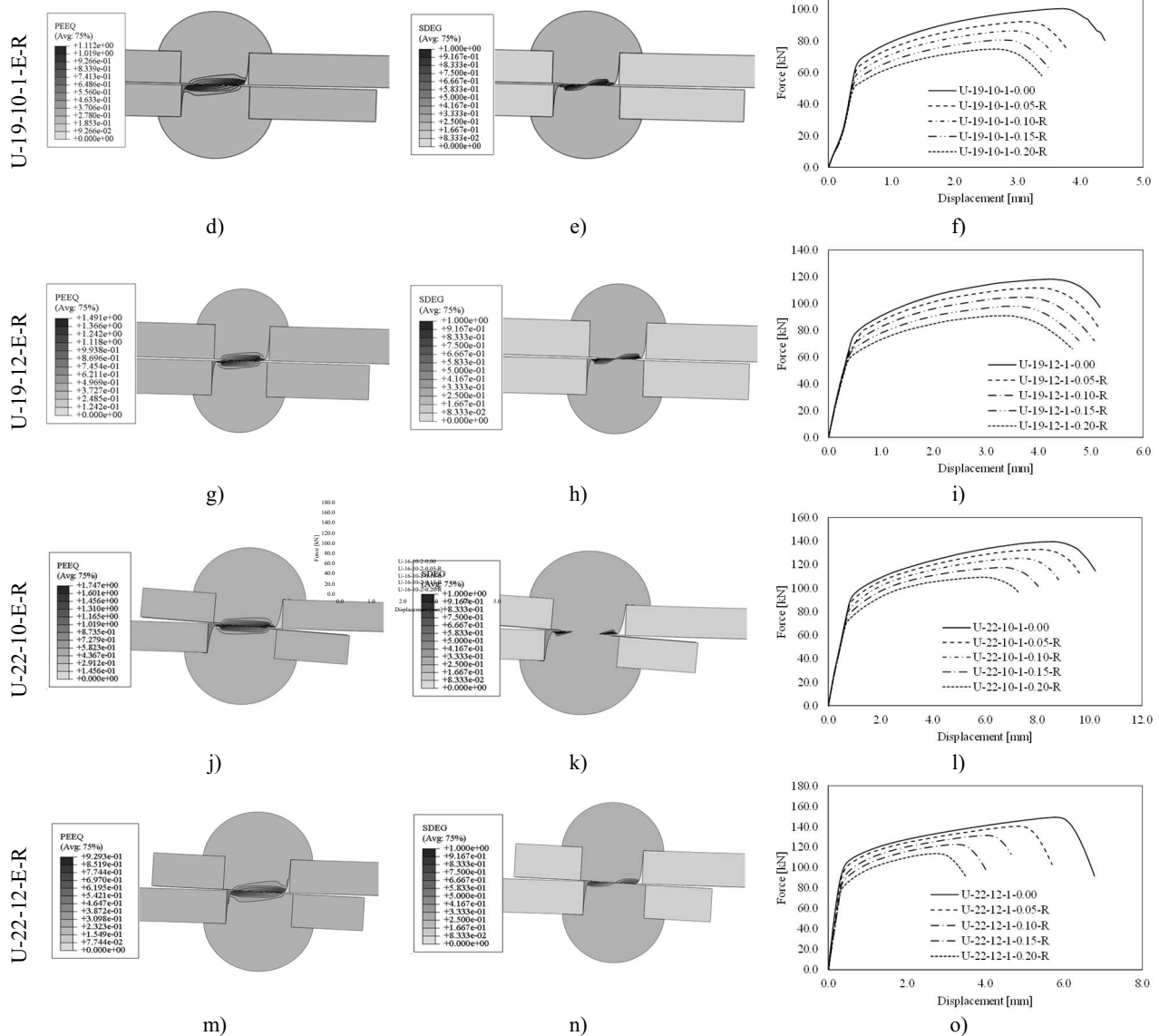
Figure 5.16 Ultimate behaviour of single rivet unsymmetric distorted connections with "reverse eccentricity" in terms of PEEQ and scalar damage distributions at failure (for e/d = 0.20) and of force-displacements curves.

a) PEEQ Distribution at Failure

b) Scalar Damage Distribution at Failure

c) Force-Displacement Curve

U-19-10-2-E-R

d) PEEQ Distribution at Failure

e) Scalar Damage Distribution at Failure

f) Force-Displacement Curve

U-22-12-2-E-R

g) PEEQ Distribution at Failure

h) Scalar Damage Distribution at Failure

i) Force-Displacement Curve
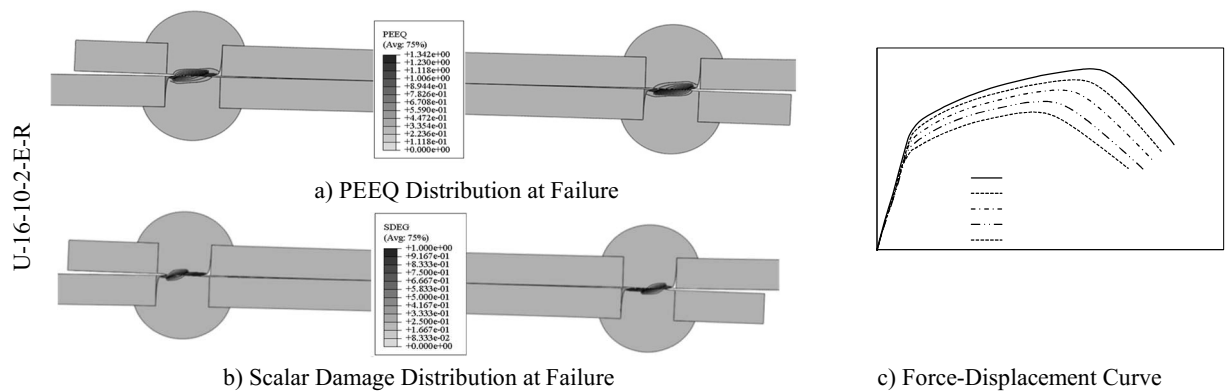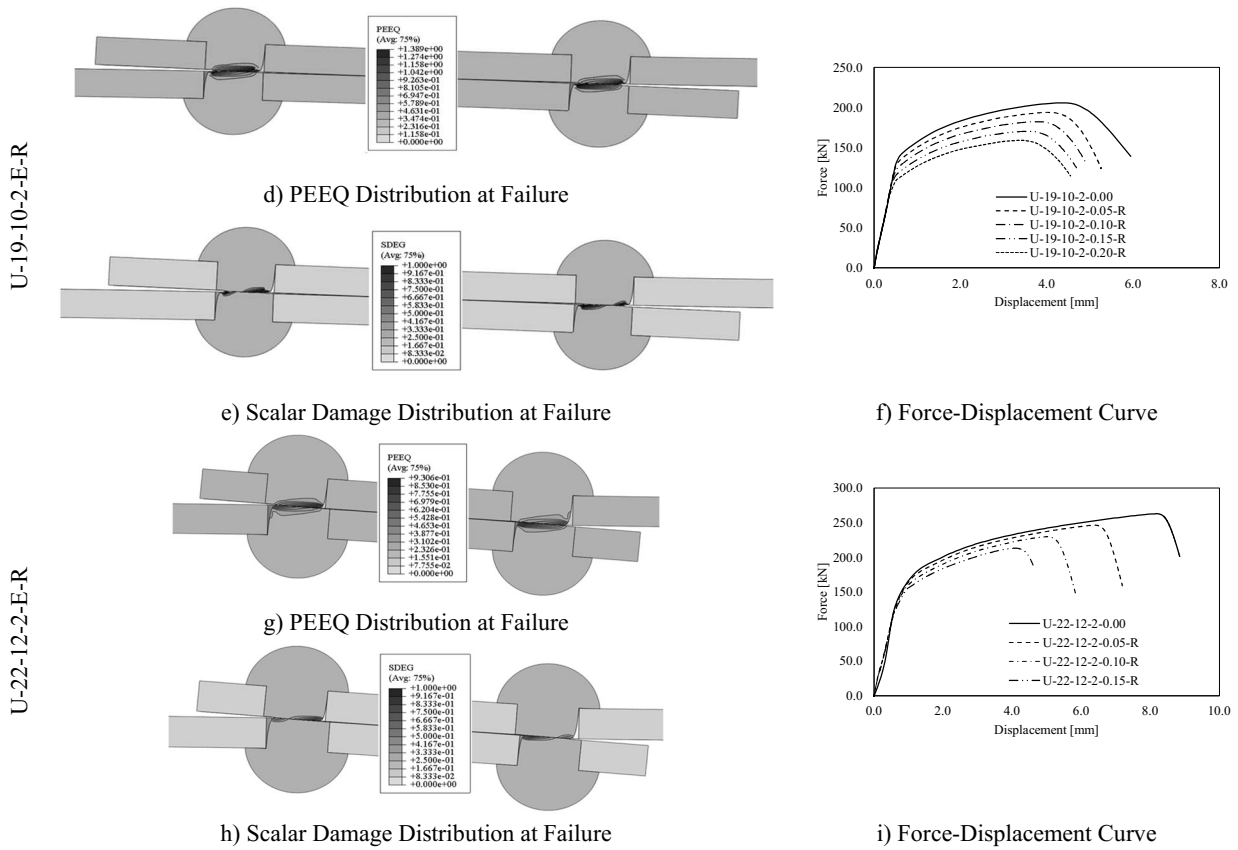
Figure 5.17 Ultimate behaviour of double rivet unsymmetric distorted connections with "reverse eccentricity" in terms of PEEQ and scalar damage distributions at failure (for e/d = 0.20) and of force-displacements curves.

Table 5.7 Behaviour of distorted unsymmetric "reverse" connections in terms of ultimate resistance and ultimate displacement for increasing values of e/d.

Ultimate Resistance F_u [kN]					
Label [-]	E (e/d)				
	0	0.05	0.1	0.15	0.2
U-16-10-1-E-R	83.1	77.9	73.1	68.2	63.4
U-19-10-1-E-R	100.5	92.2	86.4	80.7	74.9
U-19-12-1-E-R	118.2	111.6	104.7	98	90.8
U-22-10-1-E-R	139.5	132.9	125.3	117.5	109.3
U-22-12-1-E-R	149.2	140.3	131.4	122.6	113.7
U-16-10-2-E-R	161.2	151.4	142.3	132.1	122.6
U-19-10-2-E-R	205.7	193.8	182.2	170.2	158.9
U-22-12-2-E-R	262.8	246.3	229.7	213	196.3
Ultimate Displacement Δ_u [mm]					
Label [-]	E (e/d)				
	0	0.05	0.1	0.15	0.2
U-16-10-1-E-R	3.8	3.5	3.3	3.1	3
U-19-10-1-E-R	4.5	3.8	3.6	3.3	3.2
U-19-12-1-E-R	5.2	4.9	4.7	4.5	4.3
U-22-10-1-E-R	10.3	9.6	8.8	8	7.3
U-22-12-1-E-R	6.6	5.7	4.9	4	3.4
U-16-10-2-E-R	4	3.8	3.6	3.4	3.3
U-19-10-2-E-R	5.4	4.9	4.6	4.3	4.2
U-22-12-2-E-R	8.7	7.1	5.6	4.7	4.1

Results for each unsymmetric "reverse" connection are reported in Table 5.7. Notably, the shear resistance decreases almost linearly for all investigated configurations.

The maximum degradation is exhibited by U-19-10-1-0.20-R, with a loss of shear resistance of about 26% with respect to the corresponding undistorted connection (see Figure 5.16d-e-f). It is worth noting that such resistance reduction exceeds the safety limit provided by the adoption of the partial factor γ_{M2} for the calculation of rivet shear capacity according to EN1993-1-8 (that is, $0.74 < 0.80 = 1/\gamma_{M2} - CEN, 2005b$).

The maximum ductility reduction is experienced by U-22-12-2-0.20-R (see Figure 5.17g-h-i), with Δ_u being about half time the value exhibited by U-22-12-2-0.00.

Based on these results, it can be clearly recognized that the ultimate behaviour of distorted unsymmetric riveted connection also depends on the distortion orientation. In the next Section, motivations behind observed discrepancies as respect to the influence of shank camming are widely investigated.

5.5.3 Influence of Camming Defect Orientation

As shown in previous Sections, while symmetric distorted and unsymmetric "direct" connections exhibit a negligible reduction of ultimate resistance due to shank camming, unsymmetric "reverse" connections display an almost linear trend in terms of shear capacity reduction against increasing values of e/d

Nevertheless, as noticeable from Figure 5.17, the post-yield branches of F-Δ curves are almost parallel to each other. Therefore, reasons behind the observed behaviour are to be found in correspondence of the proportionality limit Δ_{el} of connections.

Namely, observed phenomena are mainly caused by the distribution of stresses at the onset of plasticity due to the evolution of axial force and bending moments (see Figure 5.18, where axial force N and bending moment M are normalized against the preload force N_{clamp} and the yielding moment $M_{el,b}$ of the shank) through the shear plane(s) of the rivet shanks. For the sake of brevity, the evolution of axial force and bending moment in the shank is shown solely for U-16-10-1-0.20-D, U-16-10-1-0.20-R and S-16-10-1-0.20-D/R.

Figure 5.18 clearly highlights that the axial force drop is maximum for unsymmetric "reverse" configurations. Moreover, its corresponding secondary bending moment has the opposite sign with respect to the other cases and it is still noticeable under large displacements (i.e., in correspondence of the peak shear resistance), while other configurations exhibit negligible secondary bending for large deformations.

These findings descend from the resisting mechanism of distorted connections. Indeed, for the unsymmetric connections without camming defects the secondary moments due to the offset of the lapped plates are mainly balanced by the bending of both plates and rivets. However, in the connections with distorted rivet shank the flexural equilibrium is also contributed by axial forces developing in the misaligned portions of the shank. Therefore, additional tensile axial forces develop in the shank to balance secondary moments in the case of "direct" eccentricity, while compressive axial forces arise in the case of "reverse" eccentricity (Figure 5.19a-b).

In the case of symmetric connections, the resistance does not decrease because the resulting response of distorted shank is given by the composition of the effects of one coupleof segments with "reverse" local eccentricity (middle and upper segment) and another pair of segments with "direct" eccentricity (middle and lower segment), thus counterbalancing each other (see Figure 5.19c).

As reported in *Section 5.5.1*, this condition does not depend on the direction of the applied load, since a symmetric "direct" connection becomes its corresponding "reverse" configuration by mirroring it against the longitudinal plane. In addition, negligible secondary moments arise in such connections that are simply due to shank distortion (i.e., they are null for $e/d = 0$), therefore the counterbalancing variation of axial forces in the shank are also negligible.

As a consequence of the secondary effects (i.e., axial force and bending moment) in the portions of the distorted shank, the distribution of tensile principal stresses (whose projections of the shear plane are the ones resisting the applied loads – *Irgens, 2008*) is rather different in the cases of "direct" and "reverse" eccentricity.

a)   b)
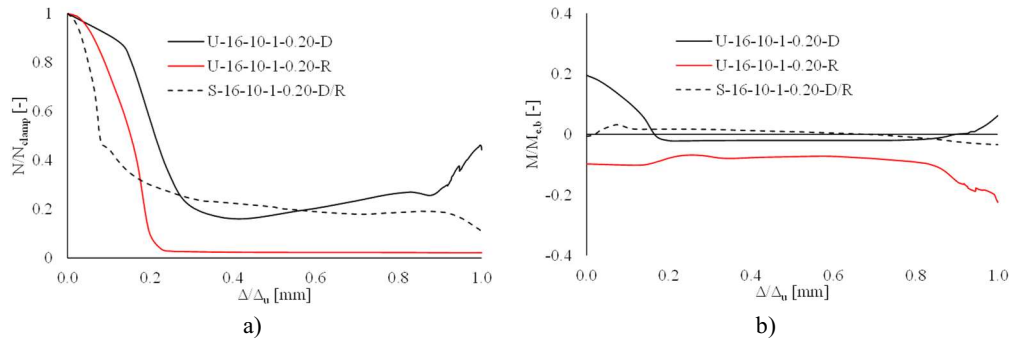
Figure 5.18 Evolution of a) axial force and b) bending moments through the shear plane(s) of the rivet shanks for investigated distorted configurations.
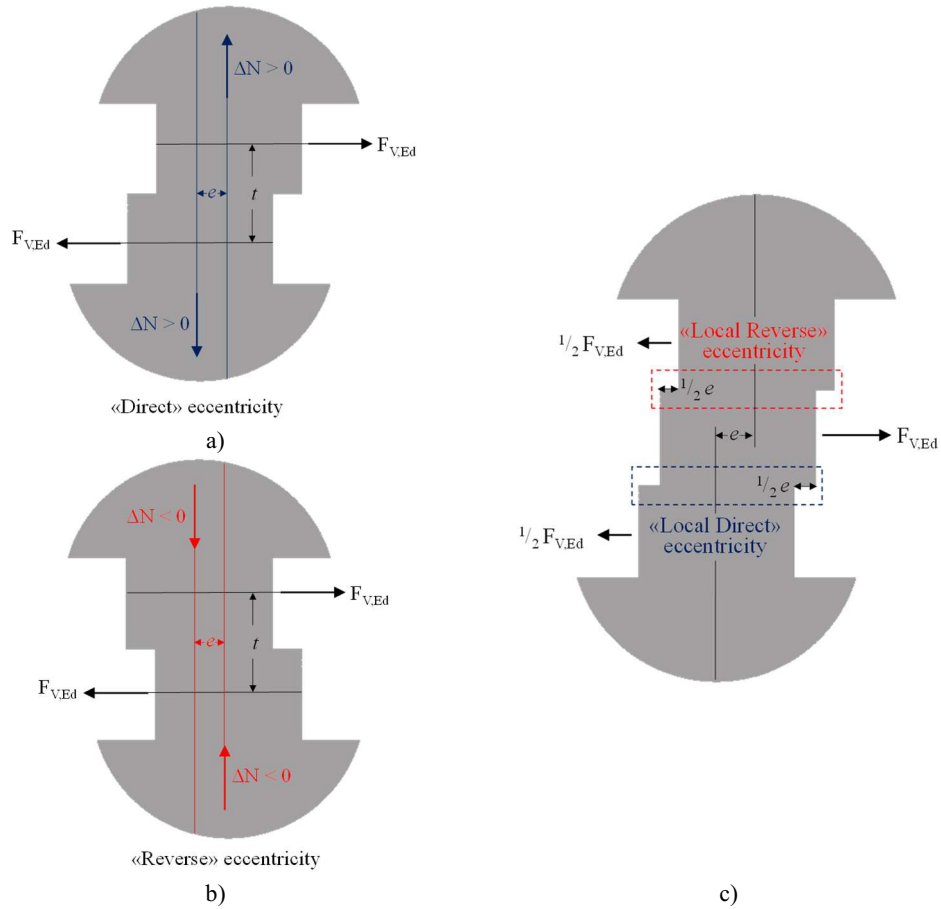
Figure 5.19 Secondary resisting mechanisms in distorted connections: a) unsymmetric "direct" connections, b) unsymmetric "reverse" connections, c) symmetric "direct"/"reverse" connections..

The maximum principal stresses $\sigma_{I,MAX}$ at the onset of plasticity for S-16-10-1-0.20-D/R, U-16-10-1-0.20-D and U-16-10-1-0.20-R are depicted in Figure 5.20a-c-e.

Moreover, the positive values of the third invariant J_3 of the stress tensor are also reported (see Figure 5.20b-d-f) to further identify the portions of the shank subjected to principal tensile stresses (*Irgens, 2008*).

It can be easily noticed that tensile principal stresses are distributed through the entire shear plane in the case of both symmetric and unsymmetric "direct" connections, in spite of the shank discontinuity.

Contrariwise, tensile principal stresses in "reverse" unsymmetric connections are localized into the superposition of misaligned shank segments, i.e., within a smaller resisting zone as the camming defect e/d increases, thus resulting in the observed reduction of the yield force of the connections.
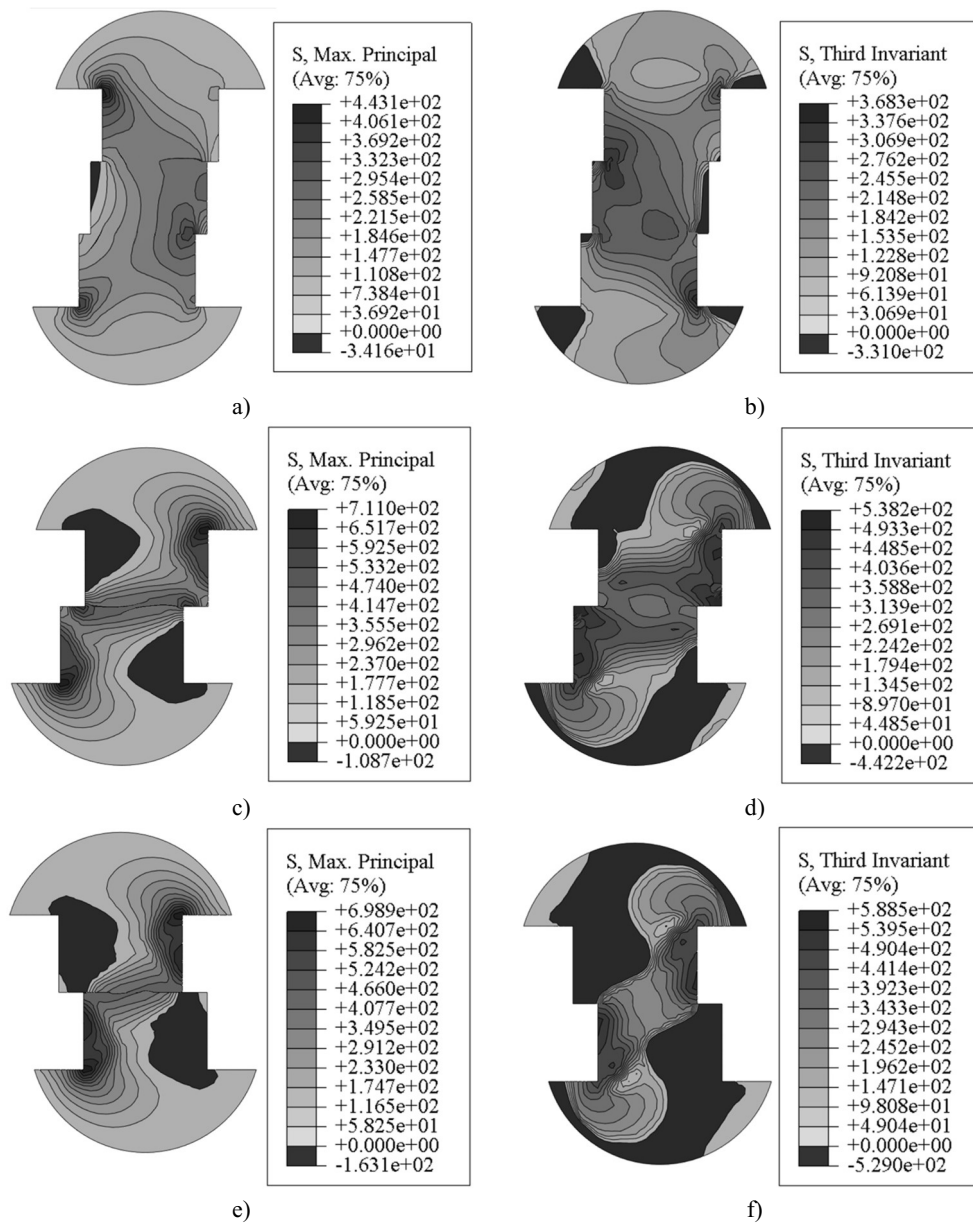
Figure 5.20 Distribution of tensile principal stresses and positive J_3 values for distorted connections at the onset of plasticity: a-b) S-16-10-1-0.20-D/R, c-d) U-16-10-1-0.20-D and e-f) U-16-10-1-0.20-R.

In light of all the above findings related to effects of hot-driving and constructional imperfections, in the next Sections a predictive model for the static resistance of hot-driven riveted connections is proposed and statistically assessed within the framework of EN1990 (*CEN, 2002*) recommendations.

5.6. Predictive model for the static resistance of hot-driven riveted connections

On the basis of the results obtained from FEAs, a formula to evaluate the resistance of riveted connections in presence of constructional imperfections has been derived for unsymmetric connections with "reverse" eccentricity, since all other configurations (see *Section 5.5.1* for symmetric and *Section 5.5.2* for unsymmetric connections with "direct" eccentricity, respectively) are not appreciably affected by camming imperfections.

As shown in *Section 5.5.3*, this outcome derives from the different distributions of tensile principal stresses through the shear planes. However, consistently with the ease-of-use philosophy of the next generation of Eurocodes, resistance predictions are carried out by assuming an equivalent material strength, while the shear-resisting area depends on the superimposition of distorted shank segments.

The proposed formula has been derived by updating the equation given by *D'Aniello et al.* (*2011*), which was originally formulated for undistorted connections (Equation 5.1):

$$F_{V,RdE} = \frac{\Omega_1 \, \Omega_2 \, n_s \, n_r \, \pi \, d^2 f_{ur0}}{4 \, \gamma_{M2}} \left(1 - k \frac{e}{d} \right) \tag{5.1}$$

where:

- f_{ur0} is the ultimate strength of the unheated rivet base material;
- Ω_1 is a statistically significant rivet strength ratio, which accounts for HDP effects variability in a synthetical, yet reliable manner;
- Ω_2 is the shear strength to tensile strength ratio for the rivet material. According to *Schenker et al. (1954)*, and in compliance with *D'Aniello et al.* (*2011*), Ω_2 can be set equal to 0.75;
- n_s is the number of shear planes per rivet;
- n_r is the number of rivets adopted for the considered connection;
- k is a non-dimensional parameter reducing the "effective" shear area of the distorted rivet shank, i.e. accounting for redistribution of principal tensile stresses in an equivalent manner ("*camming sensitivity factor*");
- γ_{M2} is an appropriate partial safety factor for the proposed resistance model (see *Section 5.7* for further details).

For the sake of clarity, while in *D'Aniello et al.,* (*2011*) the selected value for Ω_1 (= 1.20) derived from the comparison of experimental results and the resistance given by EN1993-1-8 (*CEN, 2005b*), in this study the reference value of Ω_1 for Equation 5.1 is selected by statistically assessing the distribution of rivet strength ratios yielded by refined FEAs results.

Namely, the *representative value* of Ω_1 is hence estimated on the basis of a statistical characterization, i.e., addressed by assuming proper probability distributions for the random variable Ω. In particular, two alternative probability distributions can be assumed for Ω, namely a normal distribution (hence also referred as "N") and a lognormal distribution (hence also referred as "LN") according to EN1990, Annex D

(*CEN, 2002*) provisions for new test-based resistance models. On one hand, LN represents a suitable option due to Ω being a non-negative quantity by strict definition, while on the other hand N is expected to yield more conservative results on average.

The statistical characterization of rivet overstrength ratio Ω is reported in Figure 5.21 in terms of both probability density function (PDF_Ω) and cumulative distribution function (CDF_Ω). For the sake of comparison, empirical distribution function (EDF_Ω) of rivet strength ratios is reported as well.

It can be noticed that the two assumed distributions for Ω yield similar statistical indexes of interest (i.e. characteristic value Ω_k and expected value Ω_μ).

Indeed, while $\Omega_{k,N} = 1.06$ and $\Omega_{k,LN} = 1.07$ are basically coincident, only a small difference of $\approx 4\%$ is observed among $\Omega_{\mu,N} = 1.25$ and $\Omega_{\mu,LN} = 1.31$, with N being slightly more conservative as expected.

Nevertheless, while expected values for Ω appear consistent with evidences reported by *Kulak et al.* (*1987*) and *D'Aniello et al.* (*2011*), characteristic values are deemed to be overly conservative, as the beneficial effect of HDP on rivets strength would be almost neglected when adopting $\Omega_{k,N}$ or $\Omega_{k,LN}$ for Equation 5.1.

Moreover, it is worth recalling that EN1993:1-8 (*CEN, 2005a*) recommends the use of the characteristic value of rivets UTS for the estimation of their shear resistance. Therefore, using the characteristic value of rivet strength ratio in Equation 5.1 would result in an exceedance probability $P_S \neq 0.95$, i.e., the target P_S associated to characteristic values (*CEN, 2002*); that is, the characteristic value of the product of two variables is different from the product of the characteristic values of the variables themselves.

In light of the above, the mean N value is assumed for $\Omega_1 = \Omega_{\mu,N} = 1.25$ in Equation 5.1. Regarding *k*, it is worth remarking the geometrical meaning of the "effective" shear resisting area $A_{V,eff}$ (Figure 5.22), which is obtained by the superposition of the cross areas of the discontinuous shank segments as follows (Equation 5.2a-b):

$$A_{V,eff} = \frac{d^2}{4}\left\{2\arccos\left(\frac{e}{d}\right) - \sin\left[2\arccos\left(\frac{e}{d}\right)\right]\right\} \tag{5.2a}$$

$$\rightarrow A_{V,eff} = A_{V,0}\left\{\frac{2}{\pi}\arccos\left(\frac{e}{d}\right) - \frac{1}{\pi}\sin\left[2\arccos\left(\frac{e}{d}\right)\right]\right\} \tag{5.2b}$$
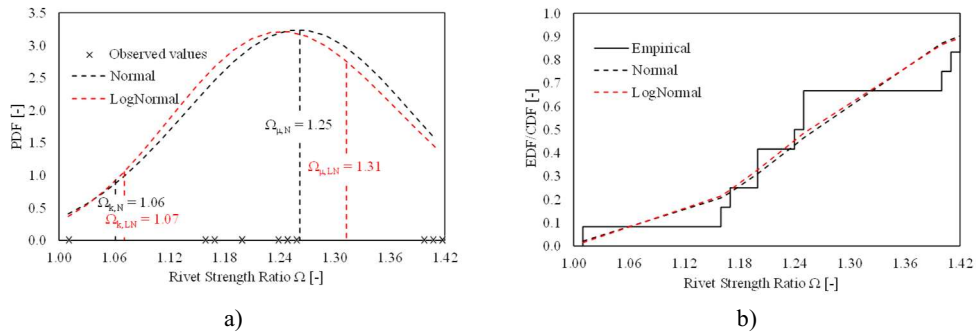
Figure 5.21 Statistical characterization of rivet strength ratio in terms of a) observed values & PDF, and b) EDF normalized to CDF, all derived assuming N and LN distributions for Ω.
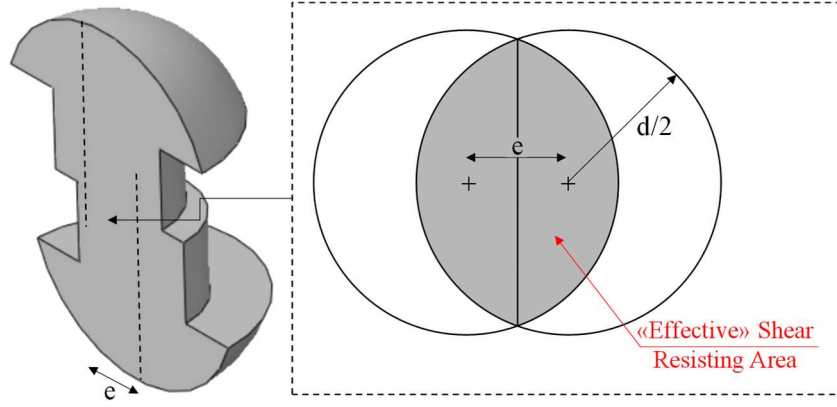
Figure 5.22 Geometry of the assumed "effective" shear resisting area for distorted connections.

with $A_{V,0} = \pi \, d^2/4$ being the area of the entire cross-section of the shank.

In compliance with the investigated values of e/d, the assumption of small relative eccentricity (i.e., $e/d \rightarrow 0$) can be introduced. Therefore, the term into curly brackets from Equation 5.2 can be substituted with the relative McLaurin expansion arrested to the first order, thus yielding the following (Equation 5.3):

$$\frac{e}{d} \rightarrow 0 \ \Rightarrow A_{V,\text{eff}} \approx A_{V,0} \left(1 - k \, \frac{e}{d}\right) \tag{5.3}$$

The parameter k has been derived by minimizing the prediction errors (i.e., via the least squares method, Figure 5.23) on the whole set of unsymmetric connections exhibiting rivet shear failure. For instance, Equations 5.2-5.3 yield the exact value of $k = 4/\pi \approx 1.27$ when $e/d \rightarrow 0$.

However, assuming small eccentricity for highly distorted shank becomes less appropriate, hence the selected value of k requires a further optimization. Accordingly, a slightly more conservative value of $k = 1.40$ was finally selected. It is also worth noting that Equation 5.3 complies with the linear trend observed for the decrease of shear resistance (see *Section 5.5.2*).

Predicted resistances (Equation 5.1) against FEAs results are summarized in Table 5.8 with reference to selected values $\Omega_1 = 1.25$, $k = 1.40$.

The very good agreement among predicted and numerical results is confirmed by the mean ratio of $F_{v,Rd,E}/F_u = 1.00$ and by the rather small COV = 0.07. For the sake of comparison, it is worth reporting that the adoption of $k = 4/\pi$ in Equation 5.1 results in $(F_{v,Rd,E}/F_u)_{\text{mean}} = 1.02$, COV = 0.09.

a)   b)
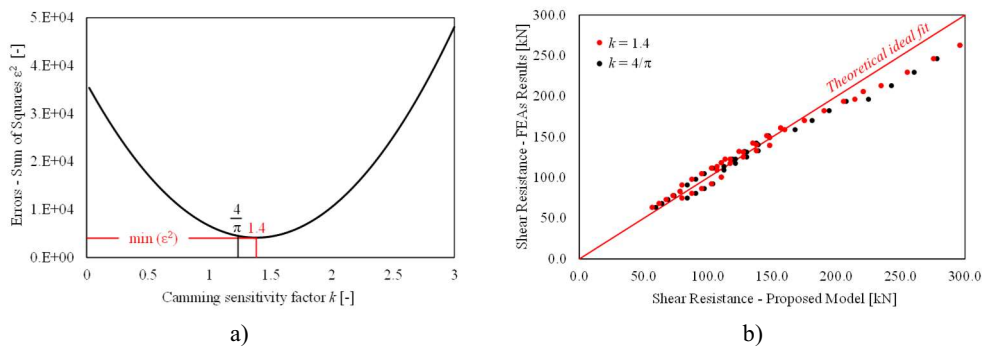
Figure 5.23 Optimization technique for the camming sensitivity factor k: a) least squares method and b) comparison of FEAs vs. resistance model results for $k = 4/\pi$ (theoretical value) $k = 1.40$.

Table 5.8 Comparison against FEAs and predicted resistances according to Equation 5.1 for unsymmetric "reverse" connections failing due to rivet shearing.

Label [-]	Shear Resistance - FEAs [kN]				
	E (*e*/*d*)				
	0.00	*0.05*	*0.10*	*0.15*	*0.20*
U-16-10-1	83.1	77.9	73.1	68.2	63.4
U-19-10-1	100.5	92.2	86.4	80.7	74.9
U-19-12-1	118.2	111.6	104.7	98.0	90.8
U-22-10-1	139.5	132.9	125.3	117.5	109.3
U-22-12-1	149.2	140.3	131.4	122.6	113.7
U-16-10-2	161.2	151.4	142.3	132.1	122.6
U-19-10-2	205.7	193.8	182.2	170.2	158.9
U-22-12-2	262.8	246.3	229.7	213.0	196.3
Label [-]	Shear Resistance - Equation 5.1 [kN]				
	E (*e*/*d*)				
	0.00	*0.05*	*0.10*	*0.15*	*0.20*
U-16-10-1	78.3	72.9	67.5	62.1	56.7
U-19-10-1	110.4	102.8	95.2	87.5	79.9
U-19-12-1	110.4	102.8	95.2	87.5	79.9
U-22-10-1	148.0	137.8	127.6	117.4	107.2
U-22-12-1	148.0	137.8	127.6	117.4	107.2
U-16-10-2	156.6	145.8	135.0	124.2	113.4
U-19-10-2	220.8	205.5	190.3	175.1	159.8
U-22-12-2	296.0	275.6	255.2	234.7	214.3
Label [-]	Eq. 5.1/FEAs [-]				
	E (*e*/*d*)				
	0	*0.05*	*0.1*	*0.15*	*0.2*
U-16-10-1	0.94	0.94	0.92	0.91	0.89
U-19-10-1	1.10	1.11	1.10	1.09	1.07
U-19-12-1	0.93	0.92	0.91	0.89	0.88
U-22-10-1	1.06	1.04	1.02	1.00	0.98
U-22-12-1	0.99	0.98	0.97	0.96	0.94
U-16-10-2	0.97	0.96	0.95	0.94	0.92
U-19-10-2	1.07	1.06	1.04	1.03	1.01
U-22-12-2	1.13	1.12	1.11	1.10	1.09
	Mean	*1.00*			
	COV	*0.07*			

5.7. Statistical assessment of proposed formulations according to EN1990 recommendations

The reliability of Equation 5.1 was finally tested by means of the procedure reported in EN1990, Annex D (*CEN, 2002*). The appropriate value of the partial safety factor γ_M for the assumed resistance model was derived as well. According to EN1990, γ_M is defined as the ratio between the design R_d and the characteristic value R_k of the investigated parameter, e.g. the shear resistance of connections.

The method recommended by EN1990, Annex D is based on the following assumptions (*CEN, 2002*):

- The resistance is expressed as a function of a finite number of variables X_i;
- There is no correlation among the variables concurring to the resistance function (i.e., statistical independence holds for all X_i);
- All variables X_i follow either a normal or log-normal distribution;
- The investigated sample is statistically valid (i.e., a sufficient number of specimens is considered, and all the relevant geometrical and mechanical parameters have been properly measured).

The statistical validity of the proposed equation was ensured by the size of the considered sample. Indeed, 40 specimens were considered, namely 8 unsymmetric configurations × 5 degrees of eccentricity, with *e/d* ranging between 0.00 ÷ 0.20. The procedure was articulated as follows:

- Theoretical evaluation of the resistance for all the specimens by means of the proposed resistance function, using the measured relevant parameters as input data;
- Comparison between theoretical and numerically derived values of the shear resistance;
- Estimation of the mean value of the correction factor *b*;
- Estimation of the coefficient of variation $V_{\delta i}$ related to the errors δ_i;
- Estimation of the coefficient of variation V_{Xi} related to the basic geometrical and mechanical variables X_i;
- Determination of the characteristic and design value of resistance;
- Evaluation of the required partial safety factor γ_M for the assumed resistance model.

Figure 5.24 depicts the comparison between the mean predictive accuracy (black dashed line, i.e. based on linear regression) and the theoretical ideal fit (red solid curve, i.e. $F_u/F_{v,Rd,E}$ bisector), namely showing the good agreement between the results of FEAs and predictions made with the proposed resistance model. Nevertheless, moderate overestimations are obtained for the connections with higher shear resistance. This outcome is mainly due to the scatter of the rivet strength ratio Ω, which is intrinsically characterized by a large variability ($COV_\Omega = 0.10$, see *Section 5.4*).

From the comparison of numerical and theoretical predictions, the mean value of the so-called *correction factor b* can be derived by means of the least squares method as follows (Equation 5.4 – *CEN, 2002*):

$$b = \frac{\sum_{i=1}^{N} R_{ni}\, R_{ti}}{\sum_{i=1}^{N} R_{ti}^2} \tag{5.4}$$

where N is the total number of specimens in the sample, R_{ni} is the resistance of the *i*-th connection derived from the results of FEAs and R_{ni} is the resistance of the same connection obtained by means of the proposed theoretical model. It is also worth noting that, for the relevant case, the estimation of *b* through the least squares method reduces to the estimation of the average value of R_{ni}/R_{ti} ratios.

Hence, the estimated error δ_i for each couple of results (numerical/theoretical) can be derived as follows (Equation 5.5 – *CEN, 2002*):

$$\delta_i = \frac{R_{ni}}{b\, R_{ti}} \tag{5.5}$$

Thus, assuming a log-normal distribution of errors as suggested by EN1990, the related coefficient of variation V_δ can be estimated as follows (Equation 5.6 – *CEN, 2002*):

$$V_\delta = \sqrt{\exp(s_\Delta^2) - 1} \tag{5.6}$$

where $s_\Delta{}^2$ is the sample variance of the errors expressed in a logarithmic scale, which can be derived from the sample mean Δ_{mean} according to Equations 5.7-5.9 (*CEN, 2002*):
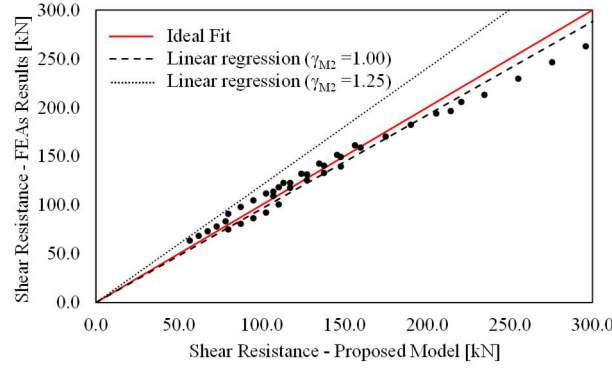
Figure 5.24 Comparison among results of FEAs and predictions from the proposed resistance model in terms of ultimate shear resistance for all considered unsymmetric "reverse" specimens.

$$\Delta_i = \ln(\delta_i) \tag{5.7}$$

$$\Delta_{mean} = \frac{1}{N}\sum_{i=1}^{N}\Delta_i \tag{5.8}$$

$$s_\Delta^2 = \frac{1}{N-1}\sum_{i=1}^{N}(\Delta_i - \Delta_{mean})^2 \tag{5.9}$$

In addition to the scatter associated to the proposed resistance model, the coefficient of variation V_{xi} related to the basic variables X_i in the resistance function, i.e., the base material ultimate strength f_{ur}, the rivet diameter d and the shank eccentricity e, needs to be considered.

In absence of experimental data, EN1990 allows assuming proper values for V_{xi} on the basis of prior knowledge but penalizing the design value of resistance (CEN, 2002). Adopted values of basic coefficients of variation, which were assumed according to *Sneijder et al.* (*1988*), are reported in Table 5.9.

It should be remarked that the same uncertainty has been assumed for both diameter and eccentricity measures since these two parameters are usually evaluated by means of the same on-field techniques (*Sustainable Bridge, 2006*).

Therefore, the total coefficient of variation of shear resistance V_r can be obtained with a simplified expression, since both V_δ, $V_{Xi} \ll 1$ (Equation 5.10 – *CEN, 2002*):

$$V_r^2 = V_\delta^2 + \sum_{i=1}^{M}V_{Xi}^2 \tag{5.10}$$

with $M = 3$ being the total number of basic variables in the proposed resistance function. Once coefficients of variation have been determined, standard deviations (Q_δ, Q_{rt}, Q_r) and non-dimensional coefficients (α_δ, α_{rt}) can be derived as follows (Equations 5.11-5.12 – *CEN, 2002*):

$$Q_\delta = \sqrt{\ln(V_\delta^2 + 1)} \tag{5.11a}$$

$$Q_{rt} = \sqrt{\ln\left(\sum_{i=1}^{M}V_{Xi}^2 + 1\right)} \tag{5.11b}$$

$$Q_r = \sqrt{\ln(V_r^2 + 1)} \tag{5.11c}$$

$$\alpha_\delta = \frac{Q_\delta}{Q_r} \tag{5.12a}$$

$$\alpha_{rt} = \frac{Q_{rt}}{Q_r} \tag{5.12b}$$

Finally, the required partial safety factor γ_M for the proposed model has been derived as the ratio among the characteristic and design values of resistance according to the following Equation 5.13 (*CEN, 2002*):

$$\gamma_M = \frac{R_k}{R_d} = \frac{\exp\left(-k_n \, \alpha_\delta \, Q_\delta - k_\infty \, \alpha_{rt} \, Q_{rt} - 0.5 \, Q_r^2\right)}{\exp\left(-k_{d,n} \, \alpha_\delta \, Q_\delta - k_{d,\infty} \, \alpha_{rt} \, Q_{rt} - 0.5 Q_r^2\right)} \tag{5.13}$$

with (k_n, k_∞) and $(k_{d,n}, k_{d,\infty})$ being the fractiles associated to the characteristic and design values of resistance, respectively. Results of the statistical validation for the proposed resistance function are summarized in Table 5.9.

Table 5.9 Relevant parameters for the statistical validation of the proposed resistance model in compliance with EN1990 (*CEN, 2002*).

b	V_δ	V_{fr}	V_d	V_e	V_r	k_n	k_∞	$k_{d,n}$	$k_{d,\infty}$	γ_M
[-]	[-]	[-]	[-]	[-]	[-]	[-]	[-]	[-]	[-]	[-]
0.973	0.079	0.079	0.005	0.005	0.079	1.730	1.640	3.440	3.040	1.248

It can be recognized that the proposed model can satisfactorily predict the shear resistance of hot-driven riveted connections with camming imperfections. In fact, the correction factor *b*, which is the slope of the regression line interpolating all couples of numerical/predicted values (see the black dashed line in Figure 5.24), is rather close to 1 and a relatively small scatter is observed, although a little overestimation is still obtained for connections with the higher shear resistance.

Nevertheless, when the required partial safety factor γ_M is used, the predicted shear resistance is conservative, as outlined by the relevant regression line which envelopes FEAs results (see the black dotted line in Figure 5.24). Moreover, it is worth remarking that the derived value of γ_M basically coincides with the partial factor adopted in EN1993:1-8 (*CEN, 2005b*) for the capacity of connections in the case of fracture mechanisms (that is, $\gamma_{M2} = 1.25$).

Besides, it is worth highlighting that the eccentricity orientation is not a geometrical feature of the connections per se, but it rather depends on the direction of the applied loads. The same unsymmetric connection may be regarded as "direct" or "reverse" for different load combinations (e.g., as it may occur to the connections of bridges). Therefore, when assessing the static performance of existing unsymmetric lap-shear connections, the shear resistance should be conservatively estimated by always accounting for the reduction of the "effective" shear resisting area (Equation 5.1).

5.8. Comparison among proposed formulation and current EN1993-1-8 recommendations

Finally, it is worth comparing the accuracy of the proposed resistance model against current EN1993:1-8 provisions (*CEN, 2005b*) for hot-driven riveted connections failing due to rivet shearing. To this end, the following assumptions are considered, namely:

i) the comparison is carried out with reference to the sole undistorted connections, as EN1993:1-8 does not address the influence of shank camming. Therefore, *e/d* is identically set equal to 0 in Equation 5.1;

ii) as tensile coupon tests on rivets are available (see *Section 4.3*), mean values of material parameters ($f_{ur0,mean} = 412$ N/mm^2 – *D'Aniello et al., 2011*) are used in place of characteristic ones for both Eurocode-compliant and proposed resistance estimations;

iii) as static tests on connections are available (see *Section 4.3*), actual shear resistances of investigated assemblies are known. Therefore, following calculations are performed by assuming an unitary partial safety factor $\gamma_{M2} = 1.00$.

Accordingly, the following expressions are used to calculate rivet shearing resistance (Equation 5.14):

$$\text{EN1993:1-8: } F_{V,Rd,EC3} = 0.6 \, \frac{\pi \, d^2}{4} \frac{f_{ur0,mean}}{1.00} \tag{5.14a}$$

$$\text{Proposed formulation: } F_{V,Rd,Eq5.1} = 0.75 \, \frac{\pi \, d^2}{4} \frac{1.25 \, f_{ur0,mean}}{1.00} \tag{5.14b}$$

Comparisons among current normative provisions and the proposed formulation are reported in Figure 5.25 and Table 5.10.

It can be easily noticed how EN1993:1-8 predictions are exceedingly conservative, with a mean ratio $F_{u,exp,mean}/F_{V,Rd,EC3}$ equal to 1.46. This overestimation is one-sided and basically constant, as the relative coefficient of variation is rather small instead ($COV_{Exp/EC3} = 0.08$).

Contrariwise, the proposed resistance model estimates more reliably the rivet shearing resistance of connections, as $(F_{u,exp,mean}/F_{V,Rd,EC3})_{mean} = 1.08$.

As both EN1993:1-8 and proposed formulations share the same form, with the only exception of non-dimensional and constant quantities ($\alpha_v = 0.6$ against $\Omega_1 = 1.25 \times \Omega_2 = 0.75$, respectively), the same COV = 0.08 is obtained with reference to Equation 5.14b calculations.

Equation 5.14b effectively captures shear resistance of connections, with prediction errors always lower than 10%, i.e., with the only notable exceptions of S-19-10-1 and U-19-10-1, for which an error higher than 20% is obtained. Nevertheless, it is worth remarking that, for such connections, Equation 5.14b predictions are still on the safe side ($F_{u,exp,mean} > F_{V,Rd,Eq5.1}$).

Table 5.10 Hot-driven riveted connections failing due to rivet shearing: comparison among experimental results, EN1993:1-8 predictions (CEN, 2005b) and predictions according to Equation 5.14b.

Label	$F_{u,exp,mean}$	$F_{V,Rd,EC3}$	$F_{V,Rd,Eq5.1}$	$F_{u,exp,mean}/F_{V,Rd,EC3}$	$F_{u,exp,mean}/F_{V,Rd,Eq5.1}$
[-]	[kN]	[kN]	[kN]	[-]	[-]
S-16-10-1	146.1	99.4	155.3	1.47	1.06
U-16-10-1	80.0	49.7	77.7	1.61	0.97
S-19-10-1	180.5	140.2	219.0	1.29	1.21
U-19-10-1	87.0	70.1	109.5	1.24	1.26
S-19-12-1	225.2	140.2	219.0	1.61	0.97
U-19-12-1	100.6	70.1	109.5	1.44	1.09
U-22-10-1	143.1	94.0	146.8	1.52	1.03
U-22-12-1	143.4	94.0	146.8	1.53	1.02
U-16-10-2	141.9	99.4	155.3	1.43	1.09
U-19-10-2	201.6	140.2	219.0	1.44	1.09
U-22-12-2	279.1	187.9	293.7	1.48	1.05
			Mean	1.46	1.08
			COV	0.08	0.08
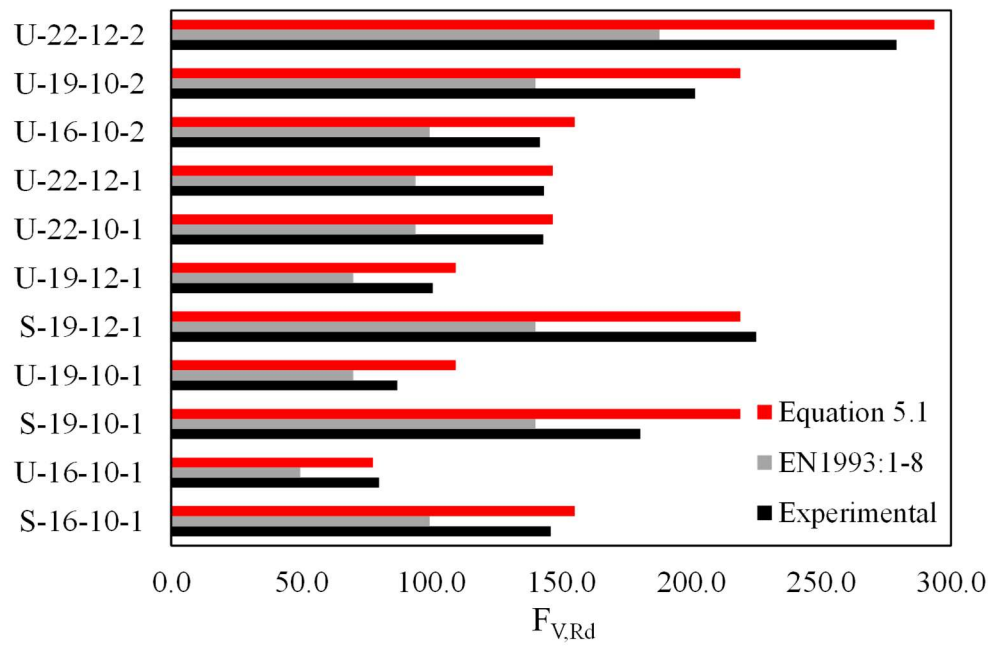
Figure 5.25 Hot-driven riveted connections failing due to rivet shearing: comparison among experimental results (black bars), EN1993:1-8 predictions (grey bars – CEN, 2005b) and predictions according to Equation 5.14b (red bars).

Chapter 6

Fatigue Performance of Mild Steel Components

In the present Chapter, the fatigue performance of notched mild steel components is assessed by means of standard and advanced techniques for fatigue analysis. To this end, parametrical FEAs are performed with the aim to:

- Investigate the stress and strain fields nearby potential fracture spots in components, thus retrieving useful insights on parameters influencing their fatigue performance. Namely, a peculiar focus is given to the distribution of circumferential stresses in round notched coupons, as they can affect the fatigue performance (*Filippi & Lazzarin, 2004; Lazzarin & Filippi, 2006*);
- Numerically estimate the average strain energy density in the relevant control volume, thus enabling the assessment of the fatigue performance of notched and smooth components.

Therefore, in the present Chapter, the following key topics are addressed, namely: *i*) refined numerical analyses of mild steel blunt V-notched cylinders (*Section 6.1*), *ii*) interpretation of results through standard fatigue analysis techniques for structural components (*Section 6.2*) and *iii*) interpretation of results through advanced fatigue analysis techniques, namely with the SED method (*Section 6.3*).

6.1. Refined numerical analyses of mild steel blunt V-notched specimens

6.1.1 Generality

This Section summarizes the parametric numerical study carried out against experimental tests on mild steel blunt-V notched cylinder described in *Section 4.1*.

Namely, the performed wide FEA study was aimed at *i*) estimating stress fields at notch tip (either axial, radial and circumferential) to derive insights on the fatigue performance of specimens and *ii*) estimating relevant material parameters for the fatigue analyses through the SED method.

On one hand, with reference to local notch stresses, a peculiar focus was given to the magnitude of circumferential stresses in the bisector plane of the notch (*hoop stresses*), in order to:

- Preliminarily investigate if these stresses can have an influence on the fatigue response of axisymmetric components, that is, if they could configure a multiaxial fatigue condition for round notched specimens;
- Investigate whether these stresses are significantly different from those derivable with the usual formulations from elasticity theory (*Irgens, 2008*). Namely, notched cylinders are usually addressed under the simplifying assumption of plain strain conditions (*Filippi & Lazzarin, 2004; Lazzarin & Filippi, 2006*), that is, a condition ideally achieved at any given diametral plane across the cylindrical specimen.

This hypothesis, which derives from the *axi-symmetry* constraints of the specimens, is indeed usually adopted for the study of axisymmetric components in order to reduce computational effort (*Cook, 1995*);

- Preliminarily understand, which are the geometric parameters most affecting the distribution of hoop stresses and their discrepancy with respect to plain strains conditions.

One the other hand, with reference to the application of the SED method, a numerical iterative procedure was performed to properly identify the control volume radius based on achieved experimental results.

Estimated value of R_0 was hence compared against theoretical models and suitably used to interpretate experimental fatigue results with a reliable and unified approach.

6.1.2 Modelling Assumptions

Parametrical finite element models (PFEMs) were developed using ABAQUS v. 6.14 software (*Dassault, 2014*). The parametric definition of numerical models was achieved by means of the Python/ABAQUS Scripting language (*Dassault, 2014*; *Python Software Foundation, 2022*). Namely, ABAQUS v. 6.14 fully supports Python 2.8 language, enabling the use of all built-in object-oriented Python features (e.g., tuples, lists, functions, etc…) and further including dedicated modules for each phase of FE modelling (e.g., model definition, attribution of material properties and BCs, meshing, analysis performance and interpretation/manipulation of results – *Dassault, 2014*).

To this end, both investigated geometries of blunt V-notched specimens were redefined in a unique, purely parametric way (Figure 6.1). The developed Python/ABAQUS Script is reported in the *Appendix*.

Specimens were discretized using dedicated axisymmetric quad elements (CAX8, i.e. 8-node *quad axisymmetric element, quadratic geometry, standard integration*). CAX8 elements enabled accounting for axisymmetric BCs while defining only a half diametral cross-section of the specimen. Quadratic elements were adopted for meshing as suggested by *Foti et al.* (*2020*) to ensure the accuracy of the free mesh SED method (*see Section 3.5*).

$$x_A = y_A = 0$$

$$x_B = \frac{D}{2}; \; y_B = 0$$

$$x_C = \frac{D}{2}; \; y_C = L_g$$

$$x_D = \frac{d}{2} + \rho \, (1 - \cos\beta); \; y_D = L_g + \frac{D - d - 2\rho}{2}\cot\beta + \rho \, \frac{\cos^2\beta}{\sin\beta}$$

$$x_E = \frac{d}{2}; \; y_E = L_g + \frac{D - d - 2\rho}{2}\cot\beta + \frac{\rho}{\sin\beta}$$

$$x_F = 0; \; y_F = L_g + \frac{D - d - 2\rho}{2}\cot\beta + \frac{\rho}{\sin\beta}$$

D: Outer cylinder diameter at grip;
d: Minimum inner diameter at notch bisector;
L_g: Grip length;
ρ: Notch radius;
$\beta = (\pi - 2\alpha)/2$: Notch slope, with 2α being the notch opening angle.
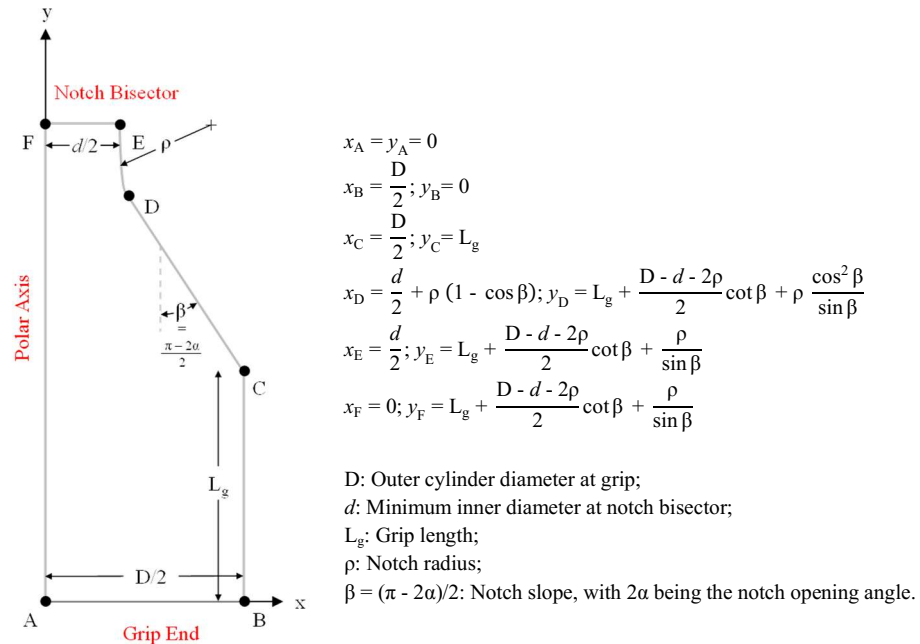
Figure 6.1 Geometrical features of parametrical FEMs.

Specimens were modelled as purely isotropic elastic elements, in compliance with SED method assumptions (*Lazzarin & Zambardi, 2001; Lazzarin et al., 2010, Berto & Lazzarin, 2014*). Accordingly, typical values of Young Modulus $E_s = 210000$ N/mm^2 and Poisson's coefficient $\nu = 0.3$ were assumed for all FEAs.

Fatigue behaviour of notched cylinders was investigated by applying an unitary tensile pressure at the end of the grip, i.e., in order to mimic the test conditions reported in *Section 4.1*. This simplified assumption was allowed by the FEM linearity deriving from assumed material properties. Accordingly, actual fatigue protocols were investigated by scaling results derived as respect to the "reference" model having $\sigma = 1$ (see *Section 6.3* for further details).

In order to further balance predictions accuracy with computational effort deriving from the large number of parametric FEAs performed, specimens symmetry with respect to the notch bisector plane was also explicitly accounted for. Resulting BCs related to test conditions and inherent model symmetries are depicted in Figure 6.2.

Preliminary sensitivity analyses were carried out to select the appropriate mesh density, with element size defined in function of the blunt V-notch radius ρ as suggested by *Lazzarin et al., 2010* and *Foti et al., 2020*. (see *Section 6.1.4* for further details).

Accordingly, at least 40 elements where adopted for the (half) notch radius, while a maximum mesh size equal to D/8 was adopted for portions away from the notch. In order to avoid significant border effects, $L_g = 2$ D was adopted for all parametric FEAs.
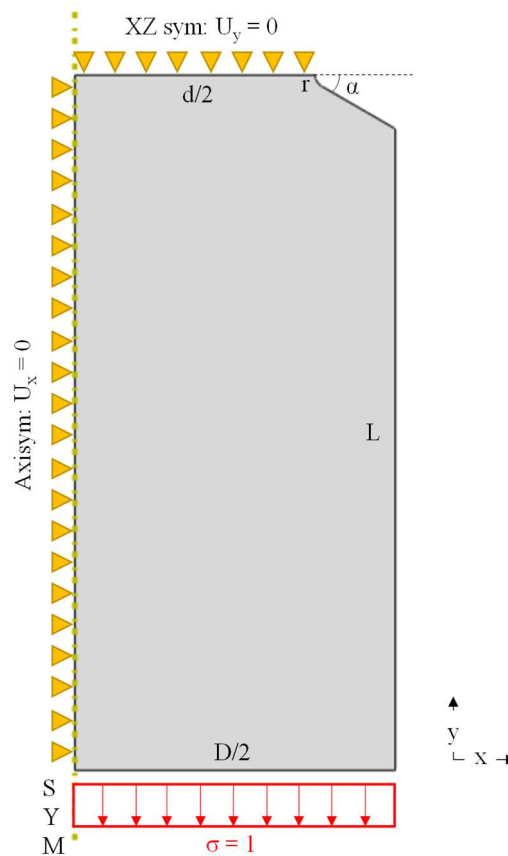
Figure 6.2 Adopted geometry and BCs for the parametric FEAs.

6.1.3 Range of Variability for Relevant Parameters

The performed parametric numerical study accounted for a wide variability of geometrical features defined in Figures 6.1-6.2. Assumed ranges of variability for relevant quantities are summarized in Table 6.1.

In order to investigate the potential influence of size effects, outer diameter D was varied up to 2 times its value for experimental specimens with the ratio d/D being kept constant. Extreme values were assumed on the basis of geometric plausibility of FEMs (that is, in order to avoid notches discontinuity deriving from incompatible values of ρ and d).

Table 6.1 Assumed ranges of variation for parametric FEAs on blunt V-notched cylinders.

	Investigated parameters			
	Diameter ratio d/D [-]	Outer diameter D [mm]	Notch opening angle 2α [mm]	Notch radius ρ [mm]
Assumed range of variation	0.5	10	15	0.1
	0.55	12	30	0.2
	0.6	14	45	0.3
	0.65	16	60	0.4
	0.7	18	75	0.5
	0.75	20	90	0.6
			105	0.7
			120	0.8
				0.9
				1

Reference values of geometrical parameters for experimentally tested specimens are highlighted in red in Table 6.1 for the sake of clarity.

In order to uniquely identify each of the analyzed FEMs, an appropriate labelling summarizing mechanical and geometrical features of interest was introduced, namely:

Labelling "C45-D-N-A-R" with:
C45 with reference to the specimens steel grade;
D = 10 ÷ 20 with reference to the outer cylinder diameter D;
N = 5 ÷ 15 with reference to minimum diameter at notch d;
A = 15 ÷ 120 with reference to the notch opening angle 2α;
R = 0.1 ÷ 1.0 with reference to the notch radius ρ;

A large total of $6 \times 6 \times 8 \times 10 = 2880$ FEAs were carried out accordingly.

In compliance with the above nomenclature, experimental tests reported in *Section 4.1* are hence relabelled as follows:
T50CC, F50BBCC → C45-10-5-60-0.1
T75CC, F75BBCC → C45-10-7.5-60-0.1

Examples of parametric FEMs developed with reference to extreme values of assumed ranges of variability are depicted in Figure 6.3, in conjunction with FEMs resembling experimental tests (Figure 6.3i-j).

a) C45-10-5-15-0.1   b) C45-10-5-15-1   c) C45-10-5-120-0.1   d) C45-10-5-120-1

e) C45-10-7.5-15-0.1   f) C45-10-7.5-15-1   g) C45-10-7.5-120-0.1   h) C45-10-7.5-120-1

i) C-45-10-5-60-0.1   j) C45-10-7.5-60-1
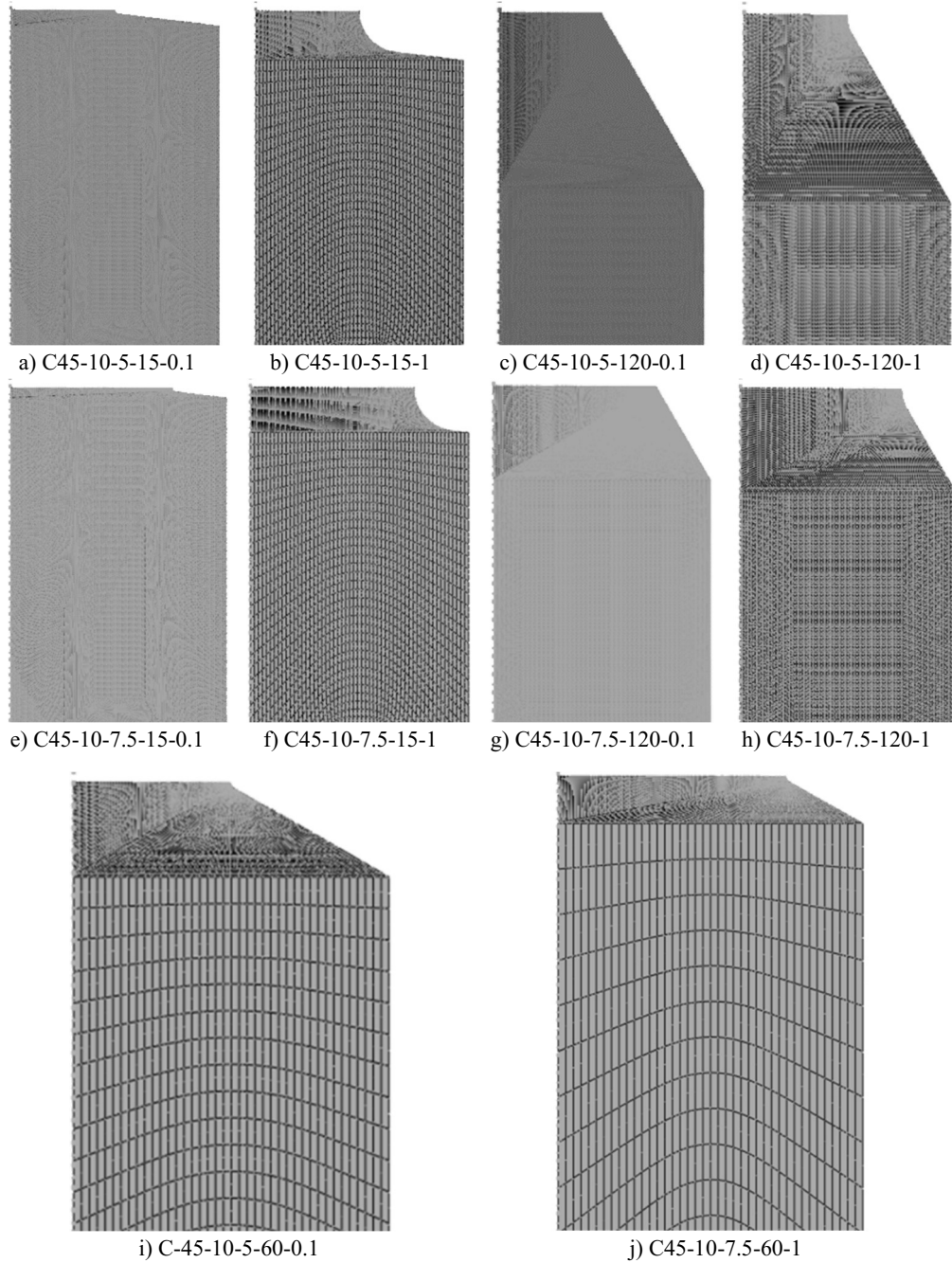
Figure 6.3 Examples of PFEMs: a-h) "extreme" models, i) C45-10-5-60-0.1, j) C45-10-7.5-0.1.

6.1.4 Mesh Sensitivity Analyses

As stated in *Section 3.5*, FEAs accuracy in terms of stresses and strains is strongly related to mesh size, especially in presence of stress raising sources such as sharp or blunt notches. Contrariwise, ASED calculations require a less refined mesh to yield reliable results (*Lazzarin et al., 2010*).

Nevertheless, it is worth remarking that, when average strain energy density is estimated through free mesh FEMs, some degree of mesh refinement is still required in order to properly define the control volume, thus avoiding jagged borders for Ω_{SED} that would result in inaccurate SED calculations (*Foti et al., 2020*)

Therefore, preliminary sensitivity analyses concerning (Figure 6.4) both stresses and SED calculations were carried out for C45-10-5-60-0.1 and C45-10-7.5-60-0.1.

Namely, mesh density was defined based on a single parameter k_R, that is, the number of elements adopted for meshing the (half) notch radius.

Accordingly, the mesh size was kept constant and equal to the minimum value $s_{min} = \pi \rho / 2 \, k_R$ in a neighbourhood of the notch radius having size $2\rho \times 2\rho$, i.e., the zone in which significant stress amplifications were expected, while mesh was gradually enlarged towards the notch end up to a maximum value $s_{max} = 10 \, s_{min}$. As for the grip segment, a maximum mesh size $s_{grip} = D/8$ to balance accuracy and computational effort.

a)

b)

c)
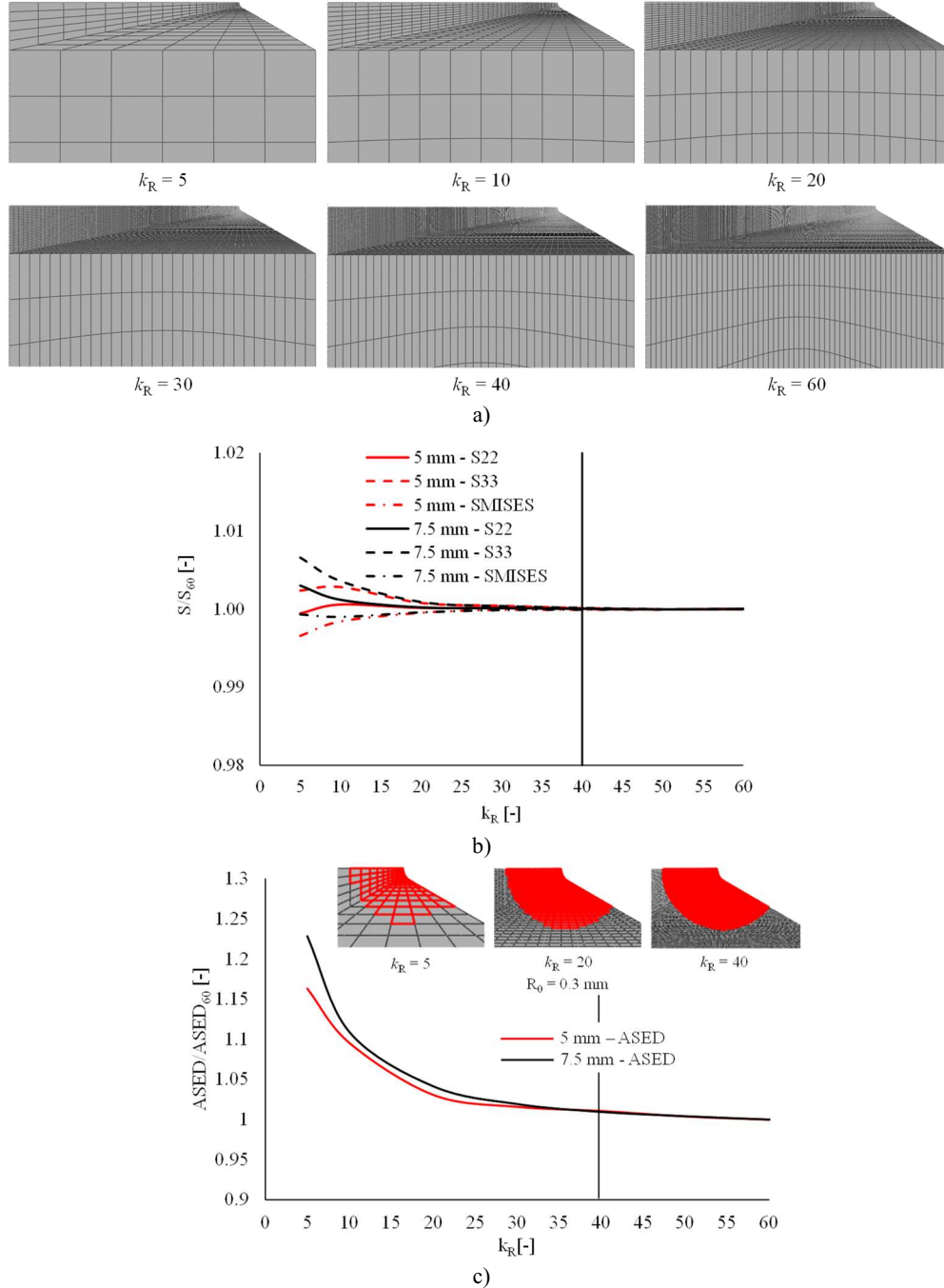
Figure 6.4 Results of preliminary mesh sensitivity analyses: a) adopted meshes for C45-10-5-60-0.1, b) stresses at notch tip, c) average strain energy density over the control volume.

Figure 6.4 depicts results of mesh sensitivity analyses in terms of S22 (normal stress perpendicular to the notch bisector), S33 (hoop stress), SMISES (equivalent Hencky-

Von Mises stress), with each one being estimated at the notch tip, and ASED over the control volume. Values in the range $5 \div 60$ were assumed for the mesh governing parameter k_R.

With regard to SED related sensitivity analyses, a conventional value of $R_0 = 0.3$ mm was initially adopted on the basis of what reported in *Radaj & Vormwald* (*2013*).

As it can be noticed, S22, S33 and SMISES are only moderately sensitive to variations of k_R ($\pm$ 1%), mainly in light of the absence of a stress singularity for $\rho \neq 0$ (*Berto & Lazzarin, 2014*). Nevertheless, a final value of $k_R = 40$ was selected because *i*) no significant increase in computational times was observed and *ii*) to avoid severe errors in the definition of Ω_{SED} on a free mesh PFEM.

Indeed, as shown by Figure 6.4c, estimated ASED values decrease for increasing values of k_R. At first glance, this result may appear counterintuitive in light of remarks reported by *Lazzarin et al.* (*2010*). However, it should be remarked that the Authors referred to a control volume-based FEM application of SED method, and hence Ω_{SED} was always defined accurately by means of a dedicated partition.

For the relevant case of a free mesh application, the use of a lower value of k_R resulted, on one hand, in a strong underestimation of Ω_{SED}, as many elements were not picked, i.e., since them were not fully enclosed in the selection cylinder with radius $R_1 = r + R_0$. On the other hand, the strain energy integrated over the picked volume (see Equation 3.65) did not significantly decrease in case of jagged selections, as maximum values of $W(x)$ were all contained in a small neighbourhood of the notch tip (*Berto & Lazzarin, 2014*). This inconsistency resulted in the observed, improper increase of ASED for overly coarse free meshes and led to the adoption of the final value of $k_R = 40$ for all subsequent analyses.

6.1.5 Estimation of the Control Volume Radius in Cyclic Conditions

As reported in *Radaj & Vormwald* (*2013*), the control volume radius R_0 for the application of the SED method in cyclic conditions can be conveniently estimated based on a numerical interpretation of experimental results (Figure 6.5).
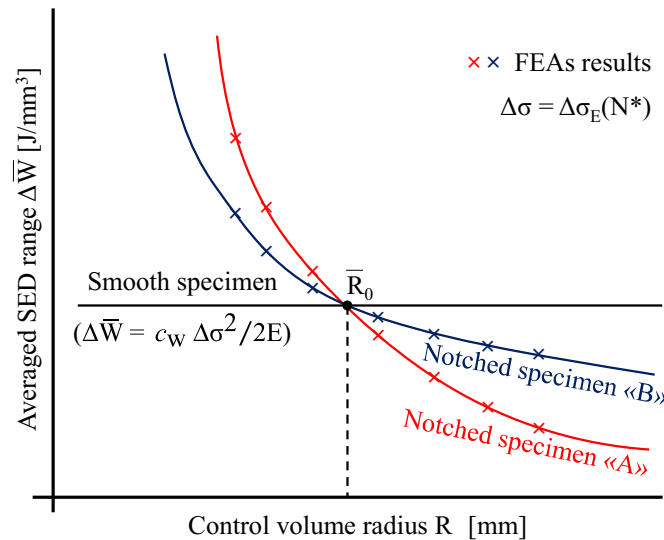
Figure 6.5 Numerical technique for the estimation of the control volume radius for SED calculations.

The main idea behind this technique is related to the independence of R_0 from the actual specimen geometry, as it is rather intended as a base material parameter (*Berto & Lazzarin, 2014*).

Therefore, by considering at least two different specimen configurations (e.g., blunt notches with two different d/D ratios, although a single series of tests on smooth specimens could be also used), a suitable value of R_0 can be estimated through parametrical FEAs (*Radaj & Vormwald, 2013*).

Namely, if the endurance limit $\Delta\sigma_E$ is estimated for different geometries, yet for the same number of cycles at failure N* (e.g., 10^6 or $2 \cdot 10^6$), R_0 can be estimated by imposing the occurrence of failure for all geometries for the same value of ASED range (*Livieri & Lazzarin, 2005*; *Radaj & Vormwald, 2013*).

Indeed, while for smooth specimens $\Delta\overline{W} = c_w \Delta\sigma^2/2E$ independently from R_0, for notched specimens $\Delta\overline{W}$ decreases as R_0 increases (*Berto & Lazzarin, 2014*).

Hence, the actual value of R_0 can be estimated at the intersection of $\Delta\overline{W} - R_0$ curves for the investigated geometries (*Radaj & Vormwald, 2013*). Reliability of derived values can be hence conveniently assessed by comparing them with analytical expressions reported in *Section 3.4* (Equation 3.56a-b – *Yoshibash, 2004*).

Accordingly, a first value of R_0 for investigated C45 steel was derived based on material properties provided by the specimen manufacturer (that is, $f_u = 779.1$ N/mm^2 for smooth round coupons and $K_{IC} = 1932.4$ N/mm$^{3/2}$). The approximation of plain strain conditions, i.e., commonly adopted for axisymmetric specimens, yielded the following upper bound for R_0 (Equation 6.1 – *Yoshibash, 2004*):

$$R_0 \approx \frac{(1 + 0.3)\,(5 - 8 \cdot 0.3)}{4\pi}\,\left(\frac{1932.4}{779.1}\right)^2 \approx 1.66\text{ mm} \tag{6.1}$$

It is worth remarking that such value is quite elevated for mild steels, as for them usually $R_0 < 1$ mm (*Radaj & Vormwald, 2013*). Therefore, the numerical technique aimed at suitably find a lower and more reliable value for the control volume radius.

As for the selection of the endurance limit, a number of cycles N* = $N_C = 2 \cdot 10^6$ was selected in accordance with the runout threshold assumed in experimental activities (see *Section 4.1*). Accordingly, $\Delta\sigma_{E,5} = 97.0$ N/mm^2 and $\Delta\sigma_{E,7.5} = 206.6$ N/mm^2 for specimens T50BBCC (i.e., C45-10-5-60-0.1) and T75BBCC (i.e., C45-10-7.5-60-0.1) were assumed respectively.

For the sake of clarity *i*) endurance limits were referred to gross cross-sections of cylinders $\pi D^2/4$ in both cases and *ii*) nominal stress ranges were corrected through the square root of the prestress coefficient $c_w^{1/2}$ to account for different values of R = 0.7 ÷ 0.9 adopted in experimental tests.

For instance, $c_w^{1/2}$ was assumed as an equivalent, SED-based SMF, as the following expression holds (Equation 6.2 – *Berto & Lazzarin, 2014*):

$$\Delta\overline{W} \propto c_w\,\Delta\sigma^2 = \left(c_w^{1/2}\Delta\sigma\right)^2 \tag{6.2}$$

In other words, adopting $c_w^{1/2}$ as a stress magnification factor ensured that the correct value of ASED range could be estimated through refined FEAs. This operation is allowed as c_w clearly does not depend on R_0 (see Equation 3.60).

Results of the numerical technique are depicted in Figure 6.6.

It can be easily noticed how the most plausible value of $R_0 = 0.20$ mm is sensibly lower than its first approximation yielded by Equation 6.1.
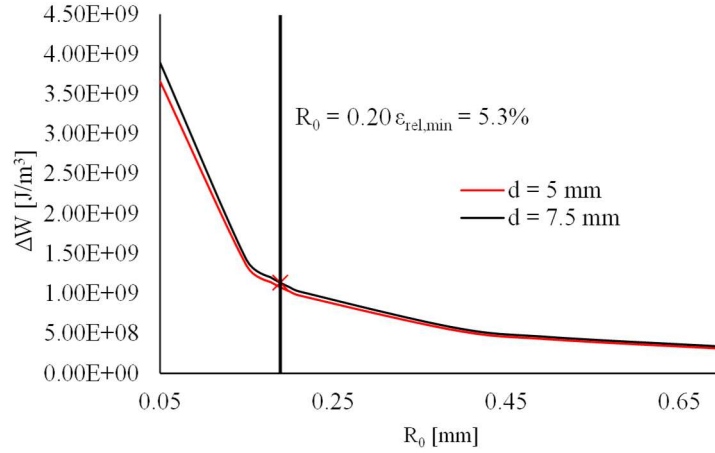
Figure 6.6 Numerical estimation of R_0 for C45 notched specimens in cyclic conditions.

Remarkably, such value complies with typical values of R_0 for mild steels reported in *Radaj & Vormwald* (*2013*). It is worth remarking that this value is deemed as "most plausible" rather than "exact" as the two $\Delta\overline{W} - R_0$ curves do not intersect, but rather the relative error in terms of $\Delta\overline{W}$ minimizes for $R_0 = 0.20$ mm. This outcome is in fact quite common when numerically assessing the performance of notched specimens (*Radaj & Vormwald*, *2013*).

The obtained value of R_0 was hence adopted to interpretate experimental results for blunt V-notched cylinders with the aid of the SED method. Further details are reported in *Section 6.3*.

6.1.6 Preliminary Investigation on Circumferential Stresses in Notched Cylinders

Results of parametrical FEAs for specimens having an experimental counterpart (i.e., C45-10-5-60-0.1 and C45-10-7.5-60-0.1) are reported in Figures 6.7-6.9 in terms of *i*) distribution of Von Mises equivalent stresses, *ii*) evolution of stress components of concern (S22, S33$_{HOOP}$, S33$_{PS}$, SMISES) along the notch bisector and *iii*) percentage differences $\varepsilon_\%$ between the circumferential stresses estimated under the assumption of axisymmetric (S33$_{HOOP}$) and plain strain (S33$_{PS}$) conditions.

For instance, while S33$_{HOOP}$ = S33 were directly derived from FEAs, S33$_{PS}$ were estimated based on notch radial stresses S11 and normal notch stresses S22 according to the well-known formula from elasticity theory (Equation 6.3 – *Irgens, 2008*):

$$S33_{PS} = \nu \, (S11 + S22) \qquad (6.3)$$

As for percentage deviations among S33$_{HOOP}$ and S33$_{PS}$, $\varepsilon_\%$ is assessed by means of Equation 6.4:

$$\varepsilon_\% = \frac{S33_{HOOP} - S33_{PS}}{avg \, (S33_{HOOP}; S33_{PS})} \, [\%] \qquad (6.3)$$

Accordingly, $\varepsilon_\% > 0$ for larger hoop stresses than theoretical plain strain calculations.

For the sake of comparability, numerical results for the two depicted geometries are represented against the normalized notch abscissa $2x/d$, i.e., the ratio among the coordinate of a given point x on the notch bisector and the minimum cross-section radius $d/2$, e.g., $2x/d = 0$ in correspondence of the polar axis and $2x/d = 1$ at the notch tip.
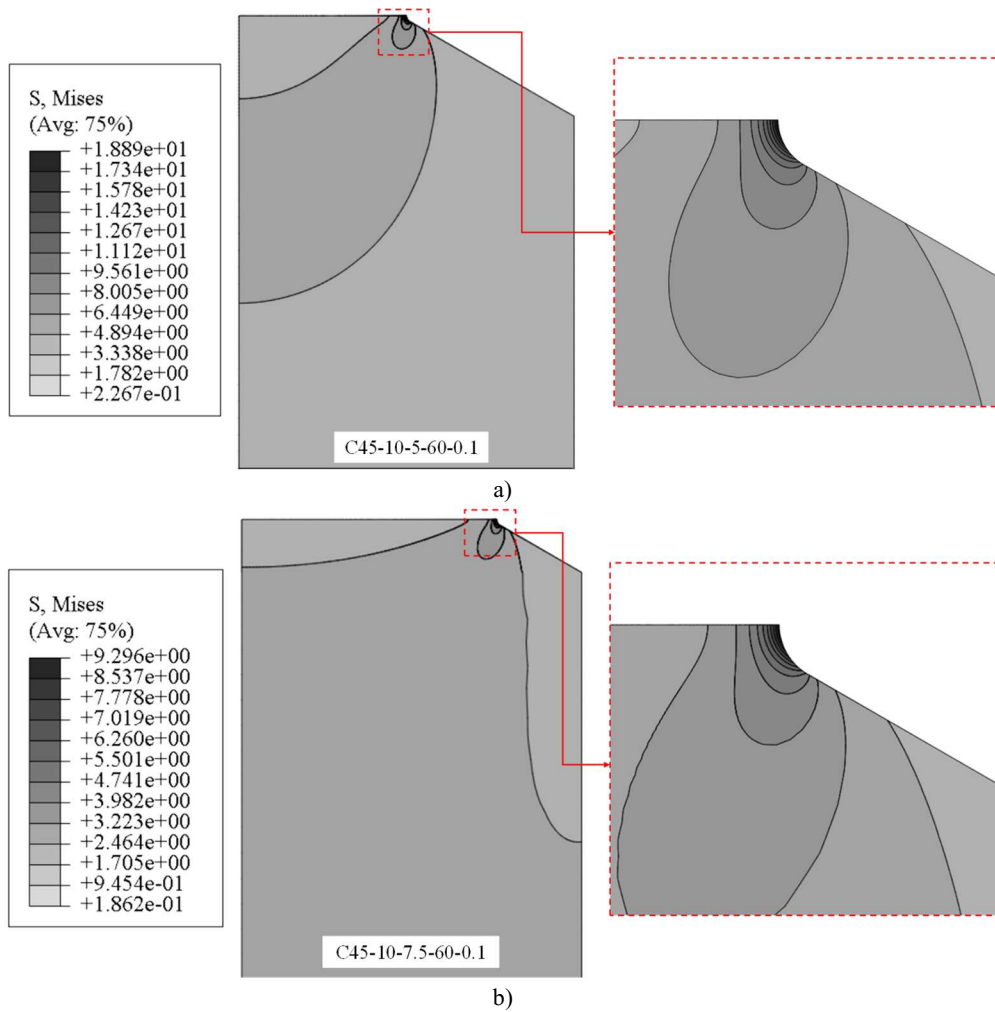
Figure 6.7 Results of numerical analyses: Von Mises stress distributions for a) C45-10.0-5.0-60-0.1 and b) C45-10.0-7.5-60-0.1.

Notably, the adoption of unitary stresses on the grip ends implies that maximum stresses on the model actually represent the stress magnification factor referred to the gross cross-section ($K_{t,gross}$) associated to the considered geometry.

a)

b)
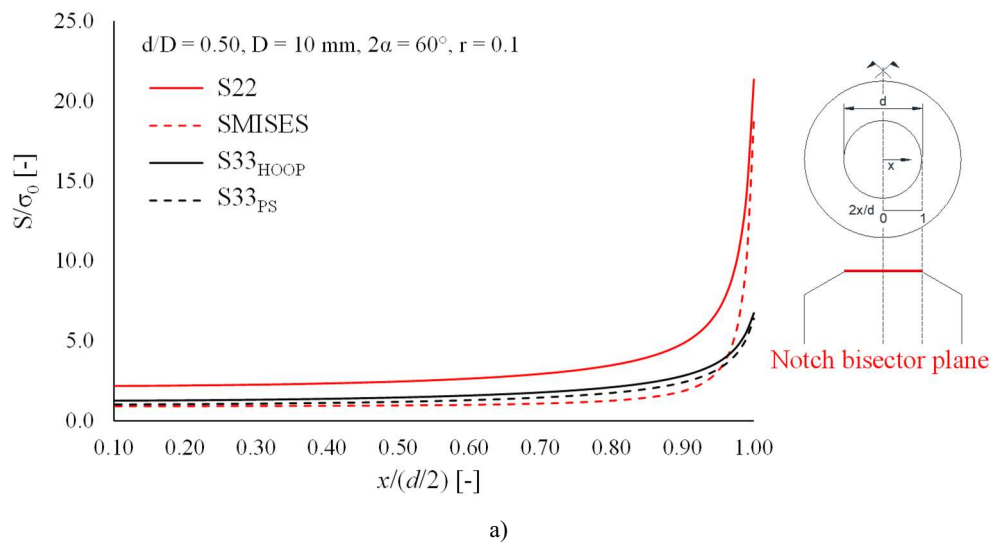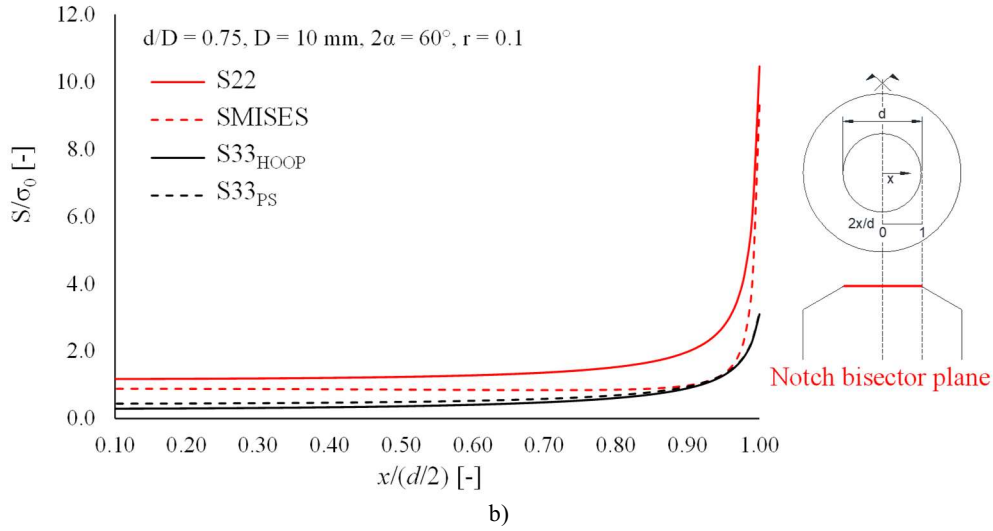
Figure 6.8 Results of numerical analyses: distribution of S22, SMISES, S33$_{HOOP}$ and S33$_{PS}$ along the notch bisector for specimens C45-10.0-5.0-60-0.1 and C45-10.0-7.5-60-0.1.
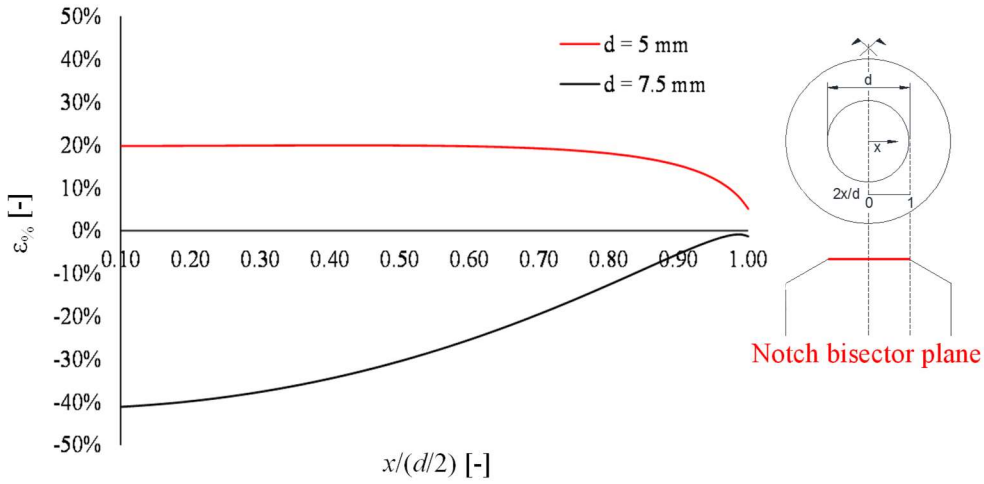
Figure 6.9 Results of numerical analyses: percentage gap among S33$_{HOOP}$ and S33$_{PS}$ along the notch bisector for specimens C45-10.0-5.0-60-0.1 and C45-10.0-7.5-60-0.1.

As expected, the value of $K_{t,gross}$ expressed in terms of equivalent Von Mises stresses (Figure 6.7), is significantly higher for the deeper notch ($K_{t,gross,5mm}$ = 18.90 and $K_{t,gross,7.5mm}$ = 9.30 for C45-10-5-60-0.1 and C45-10-7.5-60-0.1, respectively, relative difference $\Delta_{Kt,gross}$ = +103%).

As it can be noticed from Figure 6.8, trends of circumferential stresses S33$_{HOOP}$ (black solid curves) and ideal plain strain stresses S33$_{PS}$ (black dashed curves) differ throughout the entire notch bisector. The percentage deviation, represented in Figure 6.9 for specimens C45-10-5-60-0.1 (red curve) and C45-10-7.5-60-0.1 (black curve) also shows that the maximum deviation occurs towards the polar axis, while the two formulations tend to the same value at the notch tip.

It is also very interesting to note that, in the case of a deeper notch (d/D = 0.5) S33$_{HOOP}$ are always greater than the corresponding S33$_{PS}$ values, while the opposite condition (S33$_{HOOP}$ < S33$_{PS}$ ∀ $2x/d$ = 0 ÷ 1) occurs for d/D = 0.75.

This outcome suggests that discrepancy between hoop stresses and ideal circumferential stresses derived for plain strain conditions is a nonlinear function of the geometric parameters describing of notched specimens.

This deviation was therefore determined for all the investigated PFEMs. In order to synthetically represent the magnitude of such difference, results were referred both to the notch tip (Figure 6.10, $\varepsilon_{\%,notch}$) and averaged over the entire notch bisector (Figure 6.11, $\varepsilon_{\%,avg}$) as follows (Equation 6.4):

$$\varepsilon_{\%,avg} = \frac{\frac{1}{d/2}\int_0^{d/2} S33_{HOOP}\,dx - \frac{1}{d/2}\int_0^{d/2} S33_{PS}\,dx}{\mathrm{avg}\left(\frac{1}{d/2}\int_0^{d/2} S33_{HOOP}\,dx\,;\frac{1}{d/2}\int_0^{d/2} S33_{PS}\,dx\right)}\ [\%] \qquad (6.4)$$

Accordingly, $\varepsilon_{\%,avg} > 0$ if $S33_{HOOP}$ are averagely higher than corresponding $S33_{PS}$ along the entire notch bisector.

For the sake of clarity, numerical results are summarized in two 6×6 matrices of graphs arranged as follows:

- on the abscissas of matrices: diameter ratio d/D ↑ increases;
- on the ordinates of matrices: outer diameter D ↑ increases;
- on the abscissas of each graph: the notch radius ρ ↑ increases;
- Individual curves in each graph are defined for ranging values of 2α.

For the sake of brevity, only results for D = 10 mm are reported in Figures 6.10-6.11. The full version of the two graphs matrices is reported in the *Appendix*.

Accordingly, results of parametrical FEAs can be summarized as follows:

- The difference between the hoop stresses in axisymmetric regime $S33_{HOOP}$ and simplified plain strain calculations $S33_{PS}$ is often significant, with deviations at the notch radius among -25% ÷ +10%, while averaged deviation on the entire bisector are in the range -40% ÷ +25%;
- The maximum deviation is observed nearby the polar axis ($x/2d \rightarrow 0$), while the relative gap minimizes at the notch tip (that is, $\varepsilon_{\%,avg} > \varepsilon_{\%,notch}$ for each investigated configuration);
- A moderate size effect is observed. Indeed, for increasing values of outer diameter D, the deviation curves tend to flatten for the same value of d/D ratio;
- As the opening angle of 2α increases, a relative reduction in $S33_{HOOP}$ stresses is always observed compared to the corresponding $S33_{PS}$ stresses.
  Although further studies are needed, this outcome suggests that the magnitude of $S33_{HOOP}$ could depend on the generalized N-SIF in case of blunt notches, and possibly on the degree of stress singularity in case of sharp V-notches.
- As the notch radius ρ increases, a relative reduction in terms of $S33_{HOOP}$ is always observed as respect the corresponding values of $S33_{PS}$, although generally speaking, this effect appears less significant as respect to the sensitivity to the notch opening angle 2α;
- In case of "deep" notches (i.e., for lower values of $d/D \leq 0.6$) there are configurations for which $S33_{HOOP}$ stresses are higher than the corresponding values of $S33_{PS}$. Notably, these configurations are all characterized by rather small opening angles (2α ≤ 60°);
- In all other cases, the $S33_{HOOP}$ stresses are always lower than the corresponding $S33_{PS}$ stresses; the deviation increases significantly with increasing d/D ratio, although at the same time the influence of 2α on $\varepsilon_{\%,notch}$ and $\varepsilon_{\%,avg}$ reduces when d/D is high.

It is worth remarking that hoop stresses are always present in case of round elements, as they intrinsically descend from the peculiar specimens geometry (*Irgens, 2008*).

a)

b)

c)

d)

e)

f)
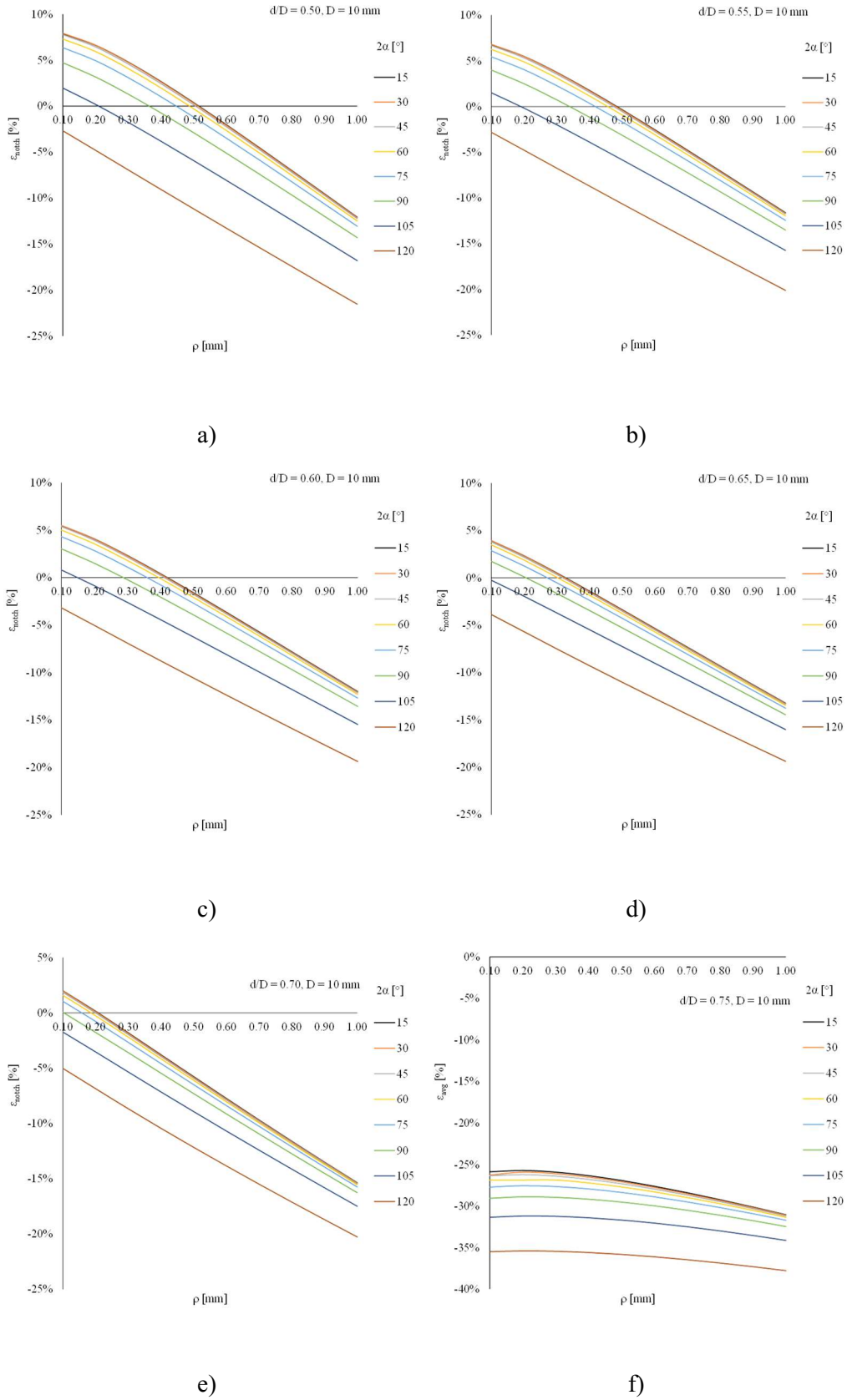
Figure 6.10 Deviation curves estimated at the notch tip ($\varepsilon_{\%,notch}$) for all developed PFEMs with D = 10 mm.

a)

b)

c)

d)

e)

f)
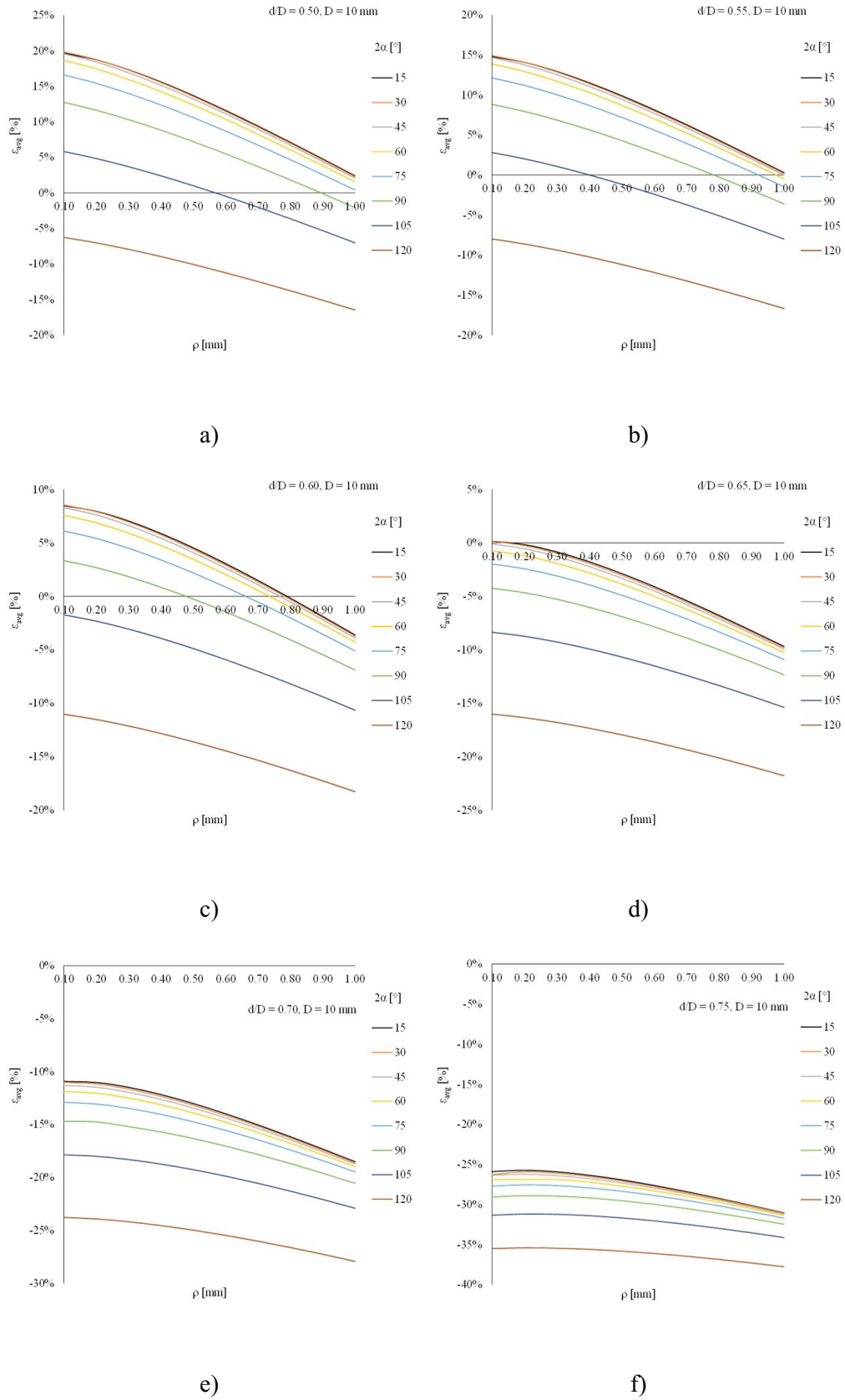
Figure 6.11 Deviation curves averaged over the notch bisector ($\varepsilon_{\%,avg}$) for all developed PFEMs with D = 10 mm.

Therefore, with regard to cyclic condition, S33$_{HOOP}$ can be regarded as a superimposed stress field which is always *in phase* with applied tensile loads (*Filippi & Lazzarin, 2004; Lazzarin & Filippi, 2006*).

Considering that:

i) on principle, for both flat and round specimens S33 detrimentally affect fatigue performance, as they are tensile stresses which locally increase stress triaxiality T (*Kanvinde et al., 2007*);

ii) both $\varepsilon_{\%,notch} > 0$ and $\varepsilon_{\%,avg} > 0$ in most cases, hence hoop stresses are lower than corresponding S33 stresses in plain strain conditions

it can be inferred that fatigue performance of round components is plausibly superior as respect to flat components subjected to nominally identical stress ranges. This outcome can be significant for the case of both riveted and bolted connections, namely for assemblies subjected to nominal tensile loads such as T-stub joints.

Nevertheless, it is worth remarking that the above parametrical investigation reported in the present Thesis work has only a preliminary nature. Thus, further numerical and experimental studies are certainly needed to support the observations that were pointed out.

6.2. Interpretation of results through traditional fatigue verification techniques

As shown in Section 4.1, experimental outcomes for blunt V-notches arranged on multiple scatter bands depending on the relevant stress ratio R = 0.7 ÷ 0.9. Moreover, inverse (log-)slopes of curves increase as R increases.

A first attempt to infer these results in a unified way was hence made considering two mean-stress effect corrections for stress-life methods, namely the *Goodman* (*1899*) and the SWT (*Smith, Watson & Topper, 1970*) formulations (Equation 6.5):

$$\text{Goodman:} \quad \Delta\sigma_{Eq,G} = \Delta\sigma \frac{1}{1 - \dfrac{\sigma_m}{f_u}} = \Delta\sigma \frac{1}{1 - \dfrac{(1+R)}{2(1-R)} \dfrac{\Delta\sigma}{f_u}} \tag{6.5a}$$

$$\text{SWT:} \quad \Delta\sigma_{Eq,SWT} = \Delta\sigma \sqrt{\frac{2}{1-R}} \tag{6.5b}$$

with σ_m being conventionally referred to the minimum section $\pi\, d^2/4$.

Consistently, the UTS values for Goodman's formulation have been assumed equal to the average of nominal f_u test values referred to the minimum cross-section, hence accounting for the notch effect on a flat-rate basis ($f_{u,5}$ = 1298.1 N/mm^2 and $f_{u,7.5}$ 1087.9 N/mm^2, respectively). Results of Goodman and SWT methods are reported in Figures 6.12-6.13 and Tables 6.2-6.3.
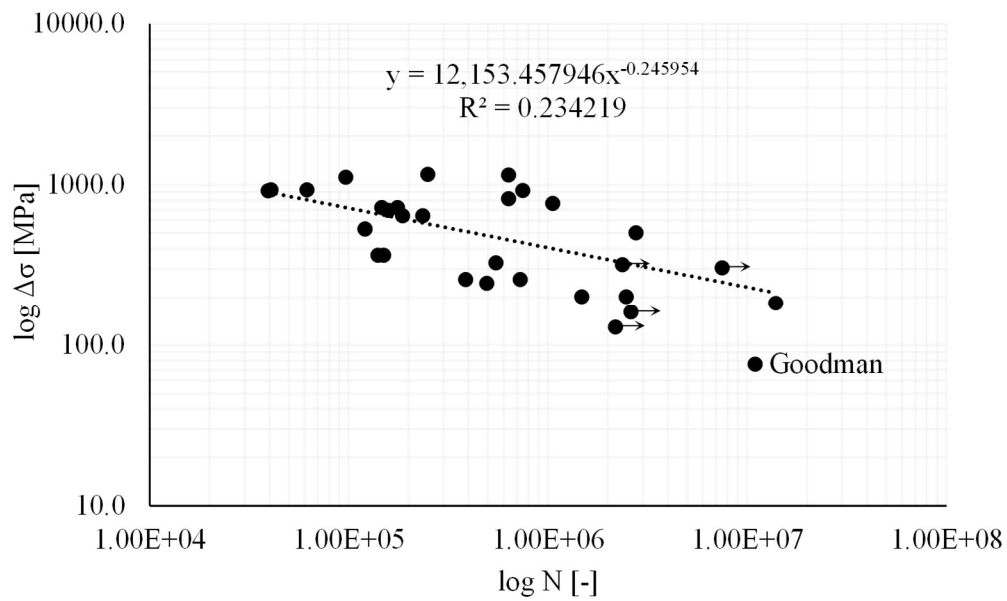
Figure 6.12 Application of the Goodman method to account for mean-stress effect for blunt V-notched specimens.
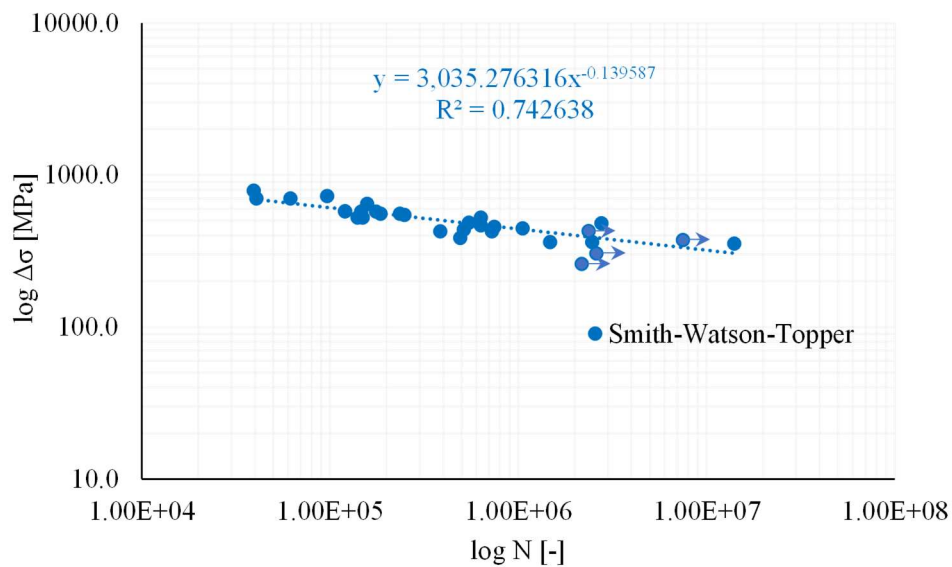
Figure 6.13 Application of the SWT method to account for mean-stress effect for blunt V-notched specimens.

Table 6.2 Mean-stress corrected fatigue results.

Label	R	$\Delta\sigma$	σ_m	$\Delta\sigma_{eq,G}$	$\Delta\sigma_{eq,SWT}$	N	Remarks
[-]	[-]	[N/mm^2]	[N/mm^2]	[N/mm^2]	[N/mm^2]	[-]	[-]
F500701	0.7	305.6	865.8	917.6	789.1	39311	
F500702	0.7	203.2	575.8	365.2	524.7	149099	
F500703	0.7	100.8	285.7	129.3	260.3	2174000	Runout
F500704	0.7	140	396.5	201.5	361.5	2467119	
F500705	0.7	165	467.4	257.8	426.0	724228	
F500706	0.7	203.2	575.8	365.2	524.7	139981	
F500707	0.7	140	396.5	201.5	361.5	1475944	
F500708	0.7	165	467.5	257.9	426.0	385254	

F500801	0.8	203.7	916.7	693.4	644.2	157354	
F500802	0.8	229.2	1031.3	1115.2	724.8	96466	
F500803	0.8	112	504.2	183.2	354.2	1.40E+07	
F500804	0.8	153.3	689.8	327.2	484.8	546636	
F500901	0.9	107.5	1020.9	503.2	480.8	2761807	
F500902	0.9	117.1	1112.8	820.6	523.7	632017	
F500903	0.9	122.2	1161.2	1159	546.5	248212	
F500904	0.9	95.6	908.6	318.8	427.5	2358780	Runout
F750701	0.7	271.6	769.6	928.4	701.3	61511	
F750702	0.7	223	631.8	531.9	575.8	120135	
F750703	0.7	149.4	423.3	244.5	385.7	492223	
F750704	0.7	271.6	769.6	928.4	701.3	40583	
F750705	0.7	223	631.8	531.9	575.8	120185	
F750801	0.8	175.7	790.4	642.4	555.6	234940	
F750802	0.8	181.1	814.9	721.5	572.7	175440	
F750803	0.8	96.4	433.9	160.4	304.8	2600000	Runout
F750804	0.8	181.1	814.9	721.5	572.7	146227	
F750805	0.8	175.7	790.4	642.4	555.6	185495	
F750806	0.8	138.5	623.4	324.4	438.0	514254	
F750901	0.9	99.6	946.2	764.4	445.4	1053000	
F750902	0.9	83.3	791.3	305.6	372.5	7470000	Runout
F750903	0.9	104.1	989.2	1147.3	465.6	632581	
F750904	0.9	101.9	967.7	921.6	455.7	744442	

Table 6.3 Statistical characterization of mean-stress corrected fatigue results.

Criterion [-]	Upper v. $\Delta\sigma_{C,10}$ [N/mm^2]	Mean v. $\Delta\sigma_{C,50}$ [N/mm^2]	Lower v. $\Delta\sigma_{C,10}$ [N/mm^2]	Inv. Slope m [-]	Coeff. of Det. R^2 [-]	Scatter Ratio T_σ [-]
Goodman	655.0	135.7	28.1	4.07	0.23	> 20
SWT	465.5	369.9	293.8	7.19	0.74	1.58

It can be immediately noticed how Goodman's method is not able to infer the results in a univocal way, as a significant scatter of corrected experimental points is observed (see Figure 6.12, $R^2 = 0.23$, $T_\sigma > 20$). This result descends from the assumed high values of stress ratios R, which invalidate the applicability of Goodman's method as observed by *Dowling* (*2004*). Contrariwise, the application of SWT correction yields more condensed results (see Figure 6.12, $R^2 = 0.74$, $T_\sigma = 1.58$).

In the next Section, an attempt to further improve the interpretation of results is carried out by means of the SED method, the theoretical background of which has been introduced in *Section 3.4*. Starting from results of refined parametrical FEAs, average strain energy densities are estimated for the two specimens geometries and results are hence assessed within the framework of an energetic approach. Further details are reported in the following.

6.3. Validation of energetic approaches for the fatigue assessment of blunt notched components

As observed in the previous Section, the application of traditional fatigue analysis techniques did not provide a definitive, univocal interpretation of results related to blunt notched specimens. Namely, while the SWT criterion (*Smith, Watson & Topper, 1970*) yielded more condensed results, the *Goodman* (*1899*) criterion did not suitably capture all experimental results.

Therefore, in the present Section, an attempt to investigate results within the framework of an energetic approach such as the SED method (*Lazzarin & Zambardi, 2001; Berto & Lazzarin, 2014*) is carried out.

The relevant numerical part for a SED-based fatigue assessment of cylindrical blunt V-notched specimens has been widely described in *Section 6.1*. Accordingly, a plausible value of the control volume radius $R_0 = 0.2$ mm is assumed for energetic calculations. Notably, this value complies with usual ranges of variation for R_0 in mild steels reported in *Radaj & Vormwald* (*2013*).

Owing to the linearity of both PFEMs describing experimental specimens, results from FEAs can be simply scaled in compliance with *i*) the quadratic dependence of $\Delta\overline{W}$ from applied stress range $\Delta\sigma$ and *ii*) the direct proportionality between $\Delta\overline{W}(R \neq 0)$ and $\Delta\overline{W}(R = 0)$ expressed by means of the prestress coefficient c_w (*Lazzarin et al., 2004*).

Accordingly, the following expression is used to estimate ASED for each experimental test based on numerical results (Equation 6.6):

$$\Delta\overline{W}(d, \Delta\sigma, R) = \overline{W}_{1,FEA}(d)\, c_w\, (\Delta\sigma)^2 \tag{6.6}$$

with $\overline{W}_{1,FEA}(d)$ being the "unitary" ASED [L^2 / F] according to FEAs, i.e. the average strain energy density over the control volume for reference conditions $\sigma = 1$ N/mm² and $R = 0$, which only depends on the specimen geometry.

For the relevant case of C45-10-5-60-0.1 and C45-10-7.5-60-0.1, the only difference is ascribable to the notch depth, hence $\overline{W}_{1,FEA}$ only depends on the minimum diameter d.

Unitary ASED values for the two different geometries are reported in Table 6.4, in conjunction with prestress coefficient values for $R = 0.7 \div 0.9$.

Table 6.4 Numerical values of unitary ASEDs for the two configurations of notched cylinders.

Label [-]	d [mm]	$\overline{W}_{1,FEA}$ [mm²/N]	R [-]	c_w [-]	$c_w\,\overline{W}_{1,FEA}$ [mm²/N]
C45-10-5-60-0.1	5	$1.151 \cdot 10^{-4}$	0.7	5.7	$6.561 \cdot 10^{-4}$
			0.8	9.0	$1.036 \cdot 10^{-3}$
			0.9	19.0	$2.187 \cdot 10^{-3}$
C45-10-7.5-60-0.1	7.5	$2.674 \cdot 10^{-5}$	0.7	5.7	$1.524 \cdot 10^{-4}$
			0.8	9.0	$2.407 \cdot 10^{-4}$
			0.9	19.0	$5.810 \cdot 10^{-4}$

As expected, values of unitary ASED are smaller for the shallower notch (C45-10-7.5-60-0.1, $d = 7.5$ mm, $\overline{W}_{1,FEA} = 2.674 \cdot 10^{-5}$ mm²/N, while $\overline{W}_{1,FEA} = 1.151 \cdot 10^{-4}$ mm²/N for C-45-10-5-60-0.1) as stress raising effects are less pronounced.

It is also worth noting that the increase of unitary ASED as respect to the notch depth (D - d)/2 is more than linear (i.e., an almost quadratic dependence is observed).

As for the prestress coefficient c_w, it can be noticed that the higher stress ratios R may severely penalize fatigue performance of notched components, as the ASED for a specimen enduring cycles with R = 0.9 is almost 19 times higher as respect to a zero-to-tension cycle having same range $\Delta\sigma$, and almost 38 times higher as respect to a fully-reversal load protocol, as c_w (R = -1) = 0.5 (*Lazzarin et al., 2004*).

Interpretation of fatigue results through the SED method is reported in Figure 6.14 and Table 6.5.
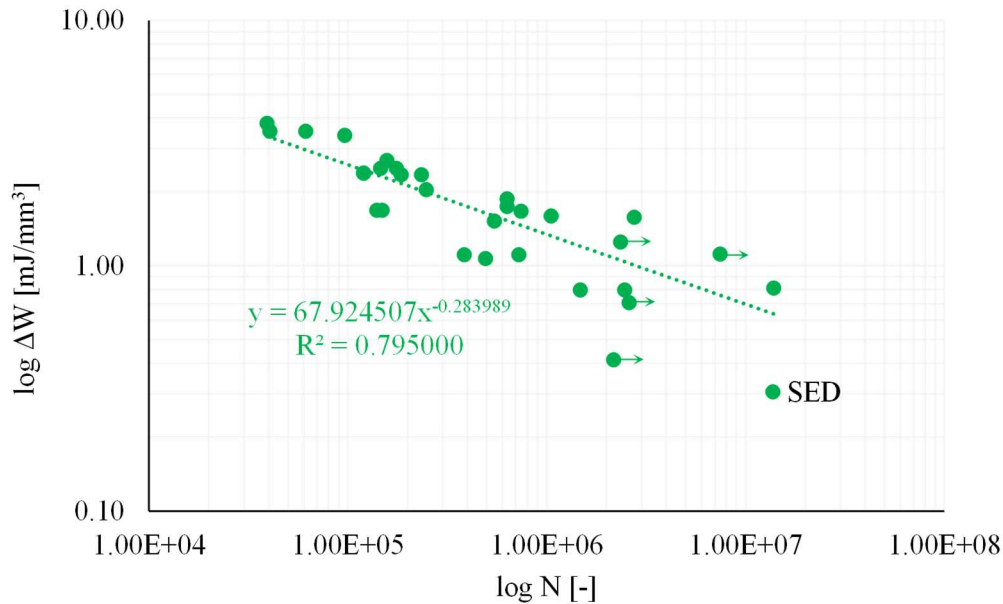
Figure 6.14 Interpretation of fatigue results through the SED method.

Table 6.5 Interpretation of fatigue results through the SED method.

Label	R	$\Delta\sigma$	c_w	$\Delta\overline{W}$	N	Remarks
[-]	[-]	[N/mm²]	[-]	[mJ/mm³]	[-]	[-]
F500701	0.7	305.6	5.7	3.81	39311	
F500702	0.7	203.2	5.7	1.68	149099	
F500703	0.7	100.8	5.7	0.41	2174000	Runout
F500704	0.7	140.0	5.7	0.80	2467119	
F500705	0.7	165.0	5.7	1.11	724228	
F500706	0.7	203.2	5.7	1.68	139981	
F500707	0.7	140.0	5.7	0.80	1475944	
F500708	0.7	165.0	5.7	1.11	385254	
F500801	0.8	203.7	9.0	2.69	157354	
F500802	0.8	229.2	9.0	3.40	96466	
F500803	0.8	112.0	9.0	0.81	1.4E+07	
F500804	0.8	153.3	9.0	1.52	546636	
F500901	0.9	107.5	19.0	1.58	2761807	
F500902	0.9	117.1	19.0	1.88	632017	
F500903	0.9	122.2	19.0	2.04	248212	
F500904	0.9	95.6	19.0	1.25	2358780	Runout

F750701	0.7	271.6	5.7	3.54	61511	
F750702	0.7	223.0	5.7	2.38	120135	
F750703	0.7	149.4	5.7	1.07	492223	
F750704	0.7	271.6	5.7	3.54	40583	
F750705	0.7	223.0	5.7	2.38	120185	
F750801	0.8	175.7	9.0	2.35	234940	
F750802	0.8	181.1	9.0	2.50	175440	
F750803	0.8	96.4	9.0	0.71	2600000	Runout
F750804	0.8	181.1	9.0	2.50	146227	
F750805	0.8	175.7	9.0	2.35	185495	
F750806	0.8	138.5	9.0	1.46	514254	
F750901	0.9	99.6	19.0	1.59	1053000	
F750902	0.9	83.3	19.0	1.12	7470000	Runout
F750903	0.9	104.1	19.0	1.74	632581	
F750904	0.9	101.9	19.0	1.67	744442	

It can be clearly observed that fatigue results interpretated through the SED method are definitely less scattered as respect to the Goodman model (*Goodman, 1899*), namely with a very good fit of the experimental results ($R^2 = 0.80$, $T_w = 2.95$). Likewise, a slightly better fit is obtained also as respect to the SWT model (*Smith, Watson & Topper, 1970*)

It is worth noting that the value of $T_w = 2.95$ is intrinsically higher as respect to a standard fatigue analysis in terms of stress ranges, i.e. by virtue of the quadratic dependence of $\Delta\overline{W}$ on $\Delta\sigma$ (Equation 6.6).

For the sake of comparison, recalling properties of the loglinear regression model (*Wakefield, 2013*) and considering the dependence of the scatter ratio T_i on the data standard deviation *s*, an equivalent value of $T_{\sigma,eq} = 2.95^{1/2} = 1.70$ is obtained by equivalently expressing results in terms of stress ranges (Figure 6.15).
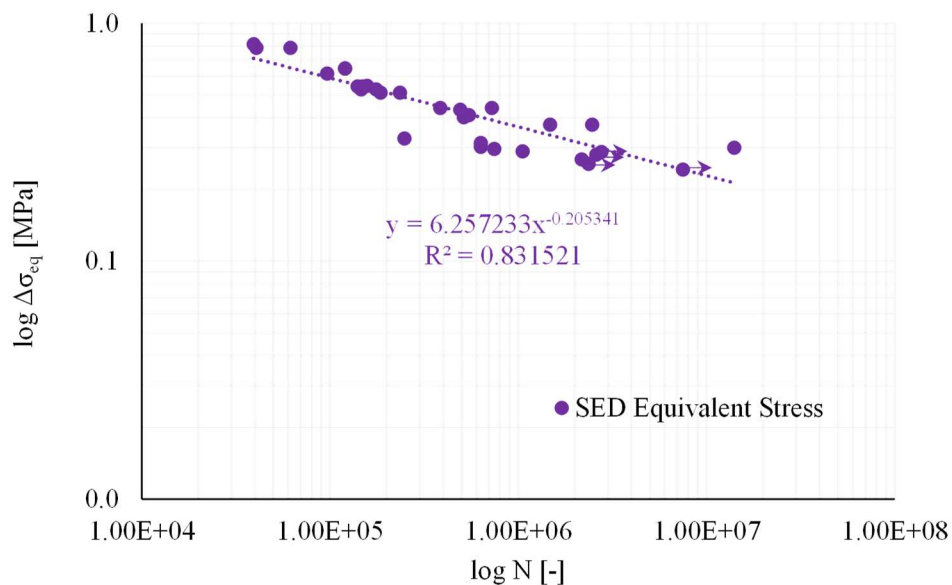
Figure 6.15 Interpretation of fatigue results through SED equivalent stress ranges.

Notably, the same conclusion could be derived by inverting Equation 6.6 and reassessing the reliability of the regression model.

It is worth remarking that under no circumstances SED equivalent stresses $\Delta\sigma_{eq}$ for each specimens coincide with stresses applied at the notch tip, as it can be noticed from the small values depicted in Figure 6.15. More properly, they should be rather intended as an equivalent quantities governing the fatigue performance of notched components having the physical dimensions of a stress.

It is therefore possible to define an ASED detail class T_{wc} associated with a number of cycles at failure $N^* = N_C = 2 \cdot 10^6$ as suggested by EN1993:1-9 (*CEN, 2005a*).

Moreover, assuming a confidence interval CI bounded by usual exceeding probabilities $P_S = 10\% - 50\% - 90\%$, the same statistical characterization usually performed for stress-life methods (see *Section 3.3.9*) can be conveniently extended to a SED fatigue analysis (*Radaj & Vormwald, 2013*).

The statistical characterization of the results obtained by the SED method is given in Table 6.6. Moreover, for the sake of thoroughness, scatter bands for $\Delta\overline{W} - N^*$ results are reported in Figure 6.16.

In light of the above, the application of the SED method to blunt notched components made of mild steel can be considered preliminarily validated.

It is worth remarking that similar results were obtained by *Livieri & Lazzarin* (*2005*) as respect to steel cruciform welded joints. Nevertheless, for such details failing at the weld toe, a brittle fracture was observed in almost all cases, as expected. Moreover, relatively low values of stress ratios R (≈ 0) were investigated.

Table 6.6 Statistical characterization of fatigue results assessed through the SED method.

Upper v. $\Delta\overline{W}_{C,10}$ [mJ/mm^3]	Mean v. $\Delta\overline{W}_{C,50}$ [mJ/mm^3]	Lower v. $\Delta\overline{W}_{C,90}$ [mJ/mm^3]	Inv. Slope m [-]	Coeff. of Det. R^2 [-]	Scatter Ratio T_W [-]
1.55	0.90	0.53	3.52	0.80	2.95
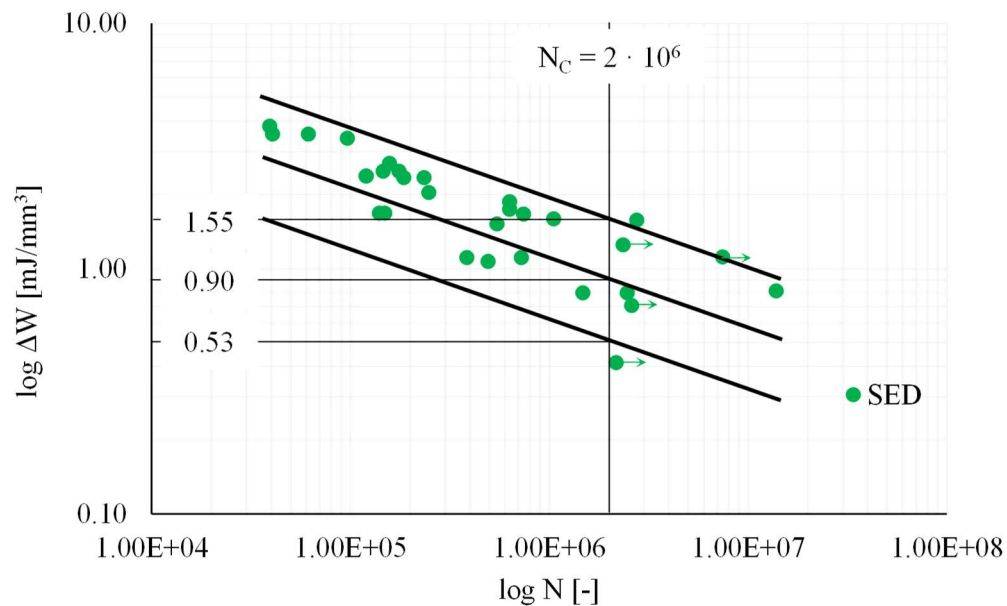
Figure 6.16 Scatter bands for fatigue results assessed through the SED method.

Contrariwise, in the present experimental study, several specimens were tested beyond their proportionality limit, mainly due to stringent conditions imposed by stress ratios, i.e., way higher that the ones inspected for welded joints (see *Section 4.1.3*).

From this perspective, the reported experimental and numerical study can represent a slight extension of the range of validity for the SED method in fatigue conditions for mild steel structural components, although further studies are certainly needed.

Therefore, in the next Chapter, the application of SED method to historical hot-driven connections is addressed based on experimental results reported in *Section 4.3* and refined, dedicated numerical analyses.

Chapter 7

Fatigue Performance of Hot-Driven Riveted Connections

In the present Chapter, the fatigue performance of hot-driven riveted connections is preliminarily assessed by means of standard and advanced techniques for fatigue analysis. To this end, parametrical FEAs are performed with the aim to:

- Investigate stress fields nearby plate holes, both induced by applied loads and by clamping actions. In particular, the influence of pre-loading in terms of stresses transferred to the plies and relevant strain energy is parametrically assessed in detail owing to the well-known clamping variability (*Leonetti et al., 2020*);
- Numerically estimate the average strain energy density in the relevant control volume, thus enabling the energetic assessment of the fatigue performance of hot-driven riveted connections.

The interpretation of results is hence transposed in a easy-of-use form compliant with the philosophy of the next generation of Eurocodes, in order to preliminarily provide some reliable design tools for the fatigue assessment of existing hot-driven riveted connections.

Therefore, in the present Chapter, the following key topics are addressed, namely: *i*) refined numerical analyses of hot-driven riveted connections in fatigue conditions (*Section 7.1*), *ii*) derivation of a predictive model for the fatigue performance of hot-driven riveted connections, namely based on results from the SED method (*Section 7.2*) and *iii*) comparison with literature and EN1993:1-9 (*CEN, 2005a*) recommendations, i.e. both as respect to the current 2005 version and to the prEN1993:1-9-2020 draft (*CEN, 2020*) under revision (*Section 7.3*).

7.1.   Refined numerical analyses of hot-driven riveted connections in fatigue conditions

7.1.1 Modelling Assumptions

FEMs resembling fatigue tests performed at the StrEngTH lab (UNISA) on hot-driven riveted specimens were developed using ABAQUS 6.14 software (*Dassault, 2014*).

In order to balance the accuracy and computational effort, the investigated riveted connections were modelled accounting for their geometrical and mechanical symmetry. Accordingly, a quarter of specimens having symmetric configuration (S19-12-1-115, S22-12-1-60, S22-12-2-160) was modelled, while a half was modelled in case of unsymmetric configurations (U-19-10-2-100, U-22-12-2-160, U-22-12-2-144).

The fatigue response of connections was investigated by applying relevant pressures at one end of the lap-shear riveted connections, with the other one(s) being fixed, in order to mimic experimental test conditions.

Relevant boundary conditions accounting for both symmetry and test conditions are depicted in Figure 7.1a-b.

All elements were discretized using solid C3D20 elements (i.e., 20-node quadratic bricks) as suggested by *Foti et al.* (*2020*) with reference to free mesh SED fatigue analysis of structural components. Consistently with method assumptions (*Lazzarin et al., 2010*), materials were modelled as purely elastic. Therefore, $E_s = 210000$ N/mm^2 and $\nu = 0.3$ were assumed for all the elements.

Clamping was simulated by means of the "Bolt Load" command. After a dedicated study on the influence of rivet preloading on stresses around the rivet hole (see *Section 7.1.3* for further details), a mean value of $\sigma_{clamp} = 0.5\,f_{yr0}$ was adopted for all the specimens in compliance with *D'Aniello et al. (2011)* and *Leonetti et al. (2020)*.

a)

b)
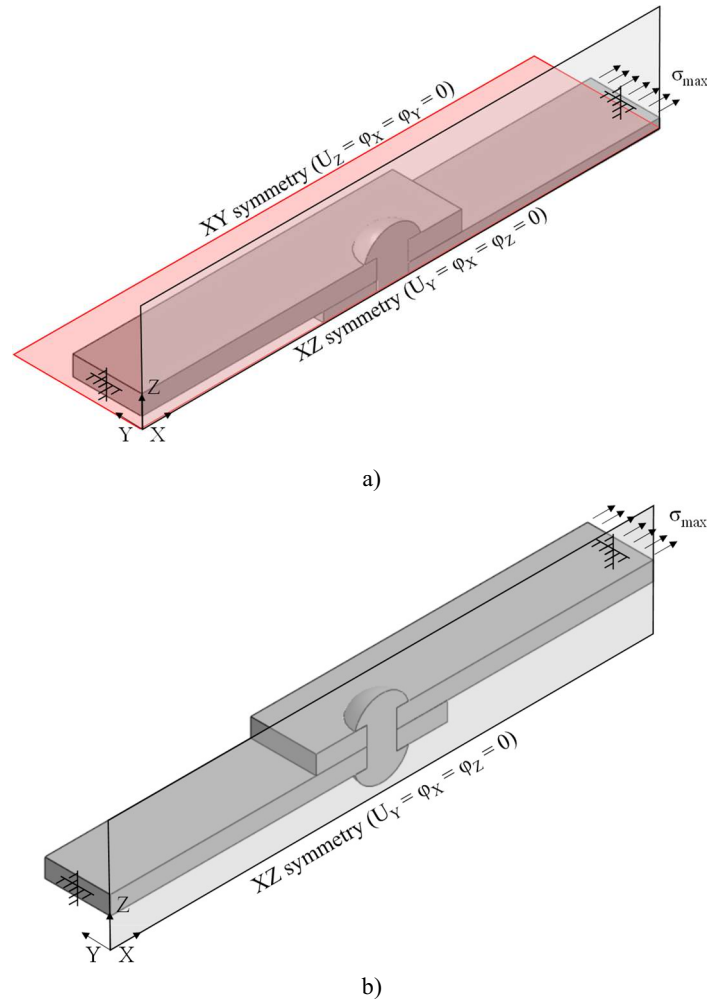
Figure 7.1 Refined fatigue FEAs on hot-driven riveted connections: adopted boundary conditions for connections with a) two planes and b) one plane of symmetry.

7.1.2 Definition of the Control Volume for SED Analyses

In compliance with advanced fatigue analyses of blunt V-notched cylinders, energetic fatigue assessment of hot-driven riveted connections was performed by means of a free mesh application of the SED method (*Berto & Lazzarin, 2014*; *Foti et al., 2020*).

Accordingly, a proper mesh density was selected in order to avoid jagged borders for the control volume. In order to balance computational effort with analyses accuracy, the following constraints on the mesh size were accounted for, namely:

i) results from static FEAs, which yielded a maximum mesh size of 1 mm for rivets and connection zones of plies;

ii) results on blunt V-notched cylinders, which highlighted the necessity of at least 40 × 2 elements on the notch radius, i.e., half the circumference of the rivet hole in case of perforated plates treated as U-notches;

iii) recommendations reported by *Foti et al.* (*2020*), in which a minimum mesh size equal to $R_0/4$ is recommended nearby the notch tip for a free mesh numerical application of SED method.

In light of the above, a first estimation of R_0 was determined as suggested by *Yoshibash* (*2004*) in plain strain conditions. For instance, the calibrated true UTS for plates is equal to $f_{u,true} = 620$ N/mm^2 (see *Section 5.1*), while an approximate value of fracture toughness for undriven historical mild steel can be retrieved in *Da Silva* (*2015*), i.e., $K_{IC} = 1434$ N/mm$^{3/2}$.

Accordingly, the following approximate value of R_0 is obtained (Equation 7.1):

$$R_0 \approx \frac{(1+0.3)\ (5\text{-}8\ 0.3)}{4\ \pi} \left(\frac{1434}{620}\right)^2 \approx 1.42 \text{ mm} \qquad (7.1)$$

In analogy with observations related to blunt V-notched cylinders, an overly high value of R_0 is obtained by using the plain strain approximation for undriven plates. Nevertheless, it is worth recalling that, as reported in *D'Aniello et al.* (*2011*), connected plates undergo a significant reduction of ductility without a corresponding appreciable reduction of UTS. This condition occurs in the immediate proximity of the rivet hole, that is, where Ω_{SED} should be located (see *Section 3.5*).

Therefore, an approximate, yet more reliable value of R_0 can be recalculated by reducing the fracture toughness for driven plates without modifying UTS.

As reported in Table 5.4, for connections experiencing plate fracture the linear DEC should penalized, on average, by assuming a non-dimensional coefficient $\Pi = 0.83$.

By approximately applying such penalization to the fracture toughness of undriven plates, the following approximation for R_0 is derived (Equation 7.2):

$$R_0 \approx \frac{(1+0.3)\ (5\text{-}8\ 0.3)}{4\ \pi} \left(\frac{0.83\ 1434}{620}\right)^2 \approx 1.00 \text{ mm} \qquad (7.2)$$

In compliance with results for notched coupons, this value was conveniently assumed as an upper bound for R_0 for HPD affected plates.

Nevertheless, as usual values of R_0 for mild steels can reduce up to 0.2 mm (*Radaj and Vormwald, 2013*), as also noticed in case of C45 steel grade, in the present Thesis work R_0 was assumed to parametrically vary in the range $0.2 \div 1.0$ mm (with increments of 0.05 mm, for a total of 17 different values). A total of $6 \times 17 = 102$ free mesh SED calculations were hence performed.

Control volumes for ASED calculations were selected by means of the Python/ABAQUS script reported in the *Appendix*.

To uniquely identify each performed FEAs, a nomenclature compliant with experimental fatigue activities was adopted, namely:

Labelling "C-D-T-N-FR" with:

C = S or U with reference to the specimen configuration, i.e., symmetric or unsymmetric;
D = 16, 19 or 22 with reference to the rivet(s) diameter *d*;

T = 10 or 12 with reference to the plies thickness t;
N = 1 or 2 with reference to the number of rivets n_r;
SR = var. with reference to the applied force range ΔF on connected plies.

The adoption of a parametrically varying control volume radius also aimed at providing further insights for different historical mild steels adopted for other railway steel bridges, i.e., for which rather different values of R_0 could be derived.

Accordingly, a minimum mesh size $s_{min} = R_{0,min}/4 = 0.05$ mm (Figure 7.2) was adopted
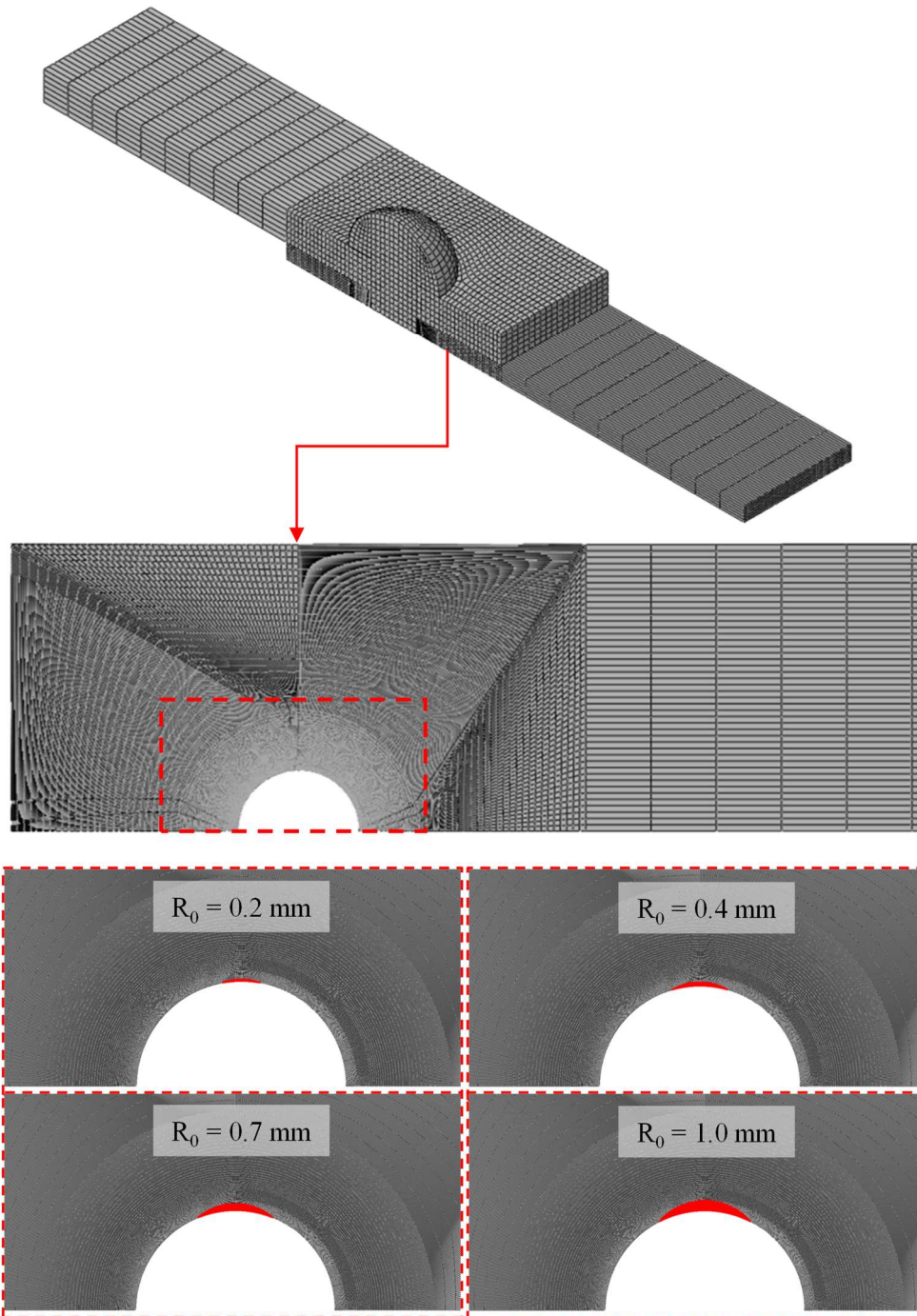
Figure 7.2 Adopted mesh for refined fatigue FEAs and examples of free mesh control volumes for different values of R_0.

for plates in proximity of the rivet hole, while a maximum mesh size of 1 mm was adopted for the rest of the connection zone and for rivets.

In compliance with static analyses, a coarser mesh having size equal to 20 mm was adopted for plates ends.

7.1.3 Influence of Clamping Actions on the Fatigue Performance of Hot-Driven Riveted Connections

As highlighted by *Al-Bahkali (2011)*, *Kafie-Martinez et al. (2017)* and *Leonetti et al. (2020)*, the magnitude of clamping actions in hot-driven rivets is rather variable, with potential values up to the undriven rivet yield strength for short rivets as the ones inspected ($h_s/d \leq 2$). Moreover, the actual value of clamping stress can have a significant effect on the fatigue performance of connections, as preloading induces a compressive prestress in plates that can retard fatigue cracking.

Therefore, a parametrical study on the effect of clamping in terms of *i*) transferred stresses to connected plies and *ii*) corresponding average SED over the control volume has been priorly carried out with reference to all possible combinations of:

i) connections configuration (i.e., symmetric or unsymmetric):

ii) rivets diameter (i.e., $d = 16$, 19 or 22 mm);

iii) connected plates thickness (i.e., $t = 10$ or 12 mm).

iv) magnitude of clamping action (i.e. in the range $0.0 \div 0.8 \, f_{yr0}$ according to *D'Aniello et al., 2011*).

In light of the highly localized nature of clamping stresses, only configuration with a single rivet were parametrically investigated for the sake of brevity. Indeed, all specimens with two rivets are all characterized by a pitch $p_1 \geq 90$ mm, with p_1/t ratio always larger or equal than 7.5. Therefore, null interference among clamping-induced stresses for each rivet hole could be assumed.

A peculiar focus was given to circumferential stresses S11 at the hole quadrant, as they govern the ASED for an ideal U-notch under Mode I loading (Equation 3.61 – *Berto & Lazzarin, 2014*).

Results of clamping sensitivity analyses are reported in Figures 7.3-7.6 and Tables 7.1-7.3 in terms of *i*) distribution of normal and circumferential stresses nearby the rivet hole, *ii*) trends of normal and circumferential stresses in plates for increasing values of σ_{clamp} and for each considered configuration and *iii*) trend of ASED (over Ω_{SED}) against σ_{clamp} each considered configuration.

For the sake of brevity, only results for S-16-10 and U-16-10 are reported in Figure 7.3, namely for a clamping stress $\sigma_{clamp} = 0.8 \, f_{yr}$.

a)

Symmetric – $d = 16$ mm, $t = 10$ mm, $d/t = 1.60$

Normal Stresses S22

Circumferential Stresses S11

b)
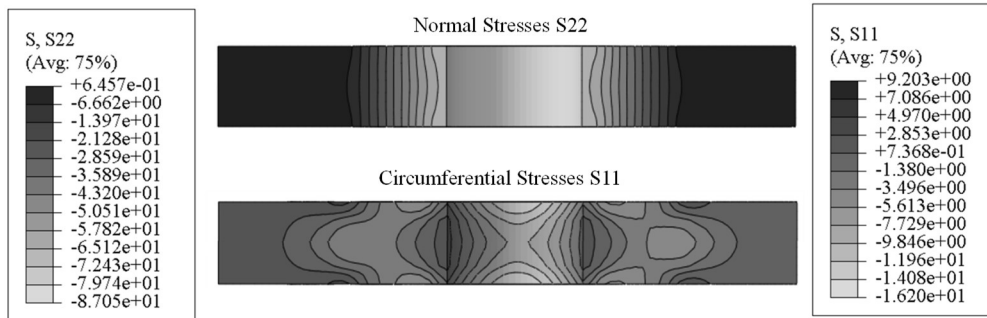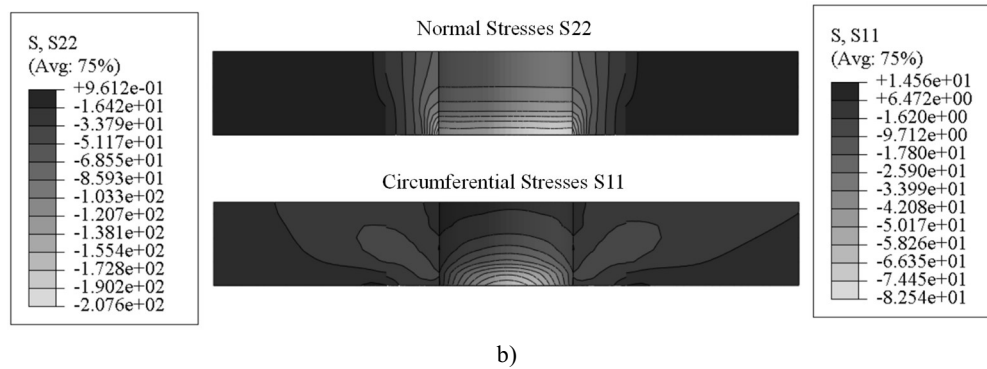
Unsymmetric – d = 16 mm, t = 10 mm, d/t = 1.60

Figure 7.3 Distribution of normal (S22) and circumferential (S11) stresses nearby rivet holes through thickness for a) symmetric (S-16-10) and b) unsymmetric (U-16-10) specimens.

It is worth remarking that stress distributions are referred to plates being pulled by external loads, that is, the middle plate for the symmetric connection and the upper one for the unsymmetric connection.

It can be immediately noticed how, while stresses in symmetric specimens are almost constant through the thickness, with only small variations with reference to circumferential stresses, in case of unsymmetric specimens a significant through-thickness gradient is observed for both normal and circumferential stresses.

Indeed, while in symmetrical specimens clamping action is transferred to the middle plate through contact and friction against external plates, in unsymmetrical specimens both plies are directly in contact with rivets heads, thus resulting in quite different trends of S11 and S22 trough the thickness.

Nevertheless, along the bisector plane of both symmetric and unsymmetric connections the distributions of normal and circumferential stresses are very similar (maximum difference of $\approx$ 5% and $\approx$ 7% for S11 and S22, respectively). This outcome plausibly descends from the achieved condition of plain strains in both cases, as plates are thick (d/t = 1.33 ÷ 2.20) and laterally restrained by rivet heads and/or adjacent plates.

Therefore, in Figure 7.4, where normal and circumferential stresses for all possible combinations of d and t are reported, only results referred to the bisector plane of symmetric specimens are reported for the sake of brevity (namely, for σ_{clamp} = 0.8 f_{yr}).

It can be noticed how normal stresses are systematically higher than corresponding circumferential stresses, compliantly with the direction of clamping forces.

Namely, the ratio S11/S22 ranges among 0.13 ÷ 0.18, with specimens with thinner plates (t = 10 mm) showing the higher values of circumferential stresses normalized as respect to relevant S22.

Normal stresses (S22)

Circumferential stresses (S11)

a)

b)

d = 16 mm, t = 10 mm, d/t = 1.60

c)   d)

$d = 19$ mm, $t = 10$ mm, $d/t = 1.90$

d)   e)

$d = 22$ mm, $t = 10$ mm, $d/t = 2.20$

e)   f)

$d = 16$ mm, $t = 12$ mm, $d/t = 1.33$

g)   h)

$d = 19$ mm, $t = 12$ mm, $d/t = 1.58$

i)   j)

$d = 22$ mm, $t = 12$ mm, $d/t = 1.83$
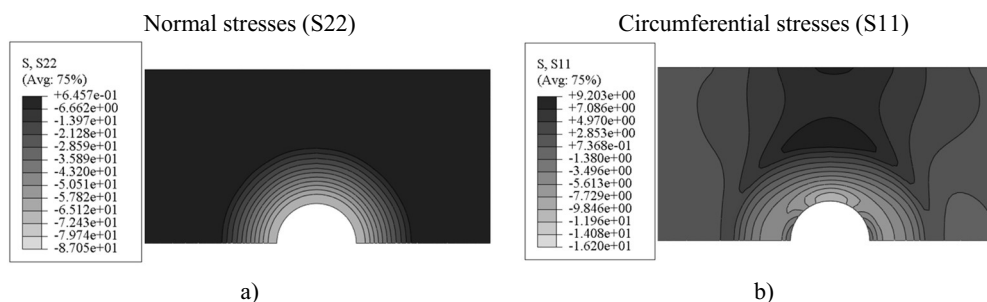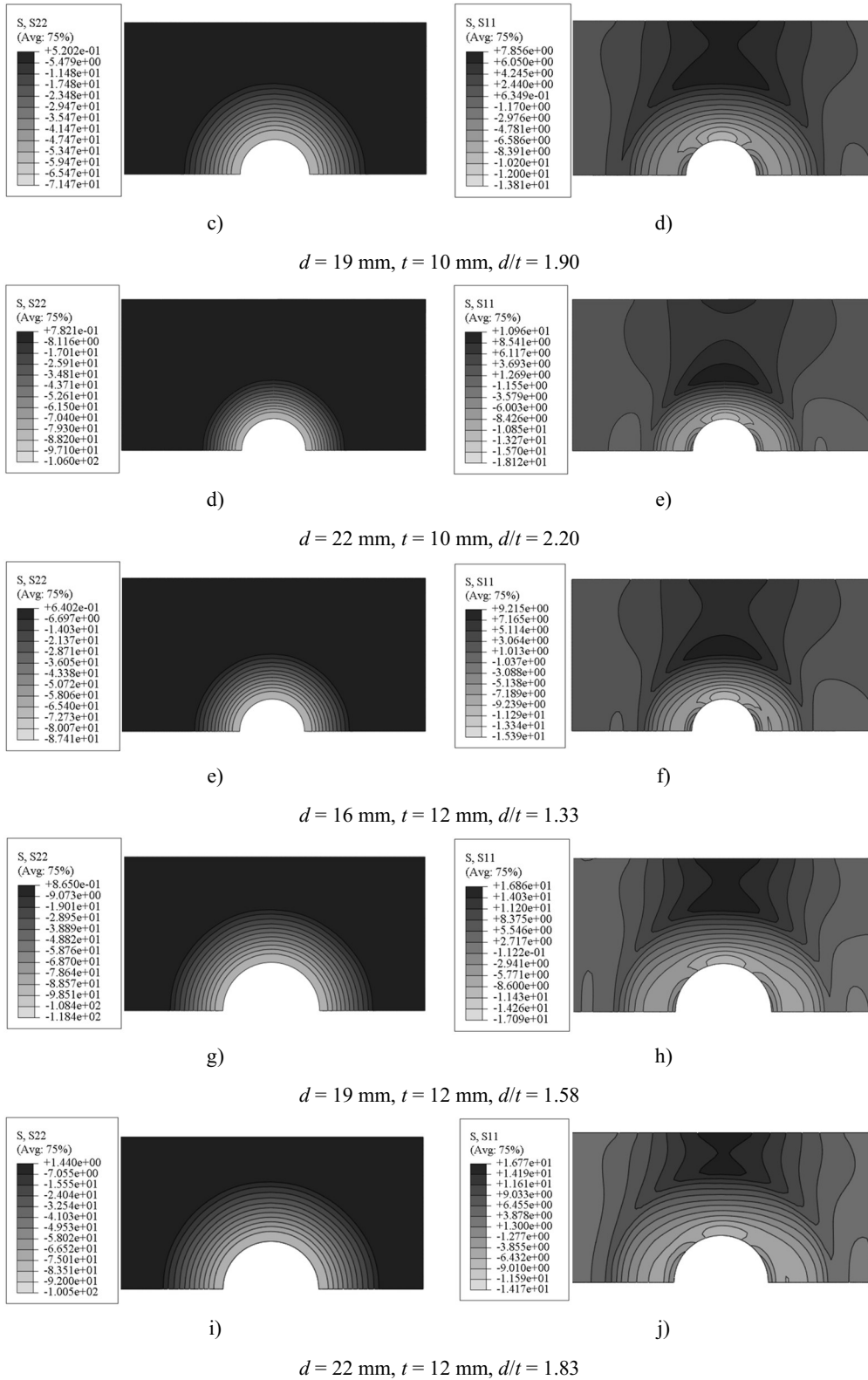
Figure 7.4 Distribution of normal (S22) and circumferential (S11) stresses nearby rivet holes for all considered geometries (longitudinal bisector planes of the plates, $\sigma_{clamp} = 0.8\, f_{yr0}$).

This outcome is confirmed by Figure 7.5, which depicts the trend of circumferential stress at the hole quadrant (that is, at the tip of the equivalent U notch) for increasing values of rivets prestress σ_{clamp}.

It can be noticed that *i*) for both symmetric and unsymmetric specimens, thicker plates are characterized by smaller values of S11 for any given value of σ_{clamp} and that *ii*) for all configurations inspected the functional link between σ_{clamp} and S11 is less than linear. These outcome suggests that increasing values of clamping stress in rivets may induce a less than proportional enhancement of fatigue performance, with specimens featuring thicker plies being further penalized.

For instance, the maximum deviation in terms of S11 for varying *d* and *t* values are obtained for the highest values of $\sigma_{clamp} = 0.8\, f_{yr0}$ (that is, 31% and 27% for symmetric and unsymmetric specimens, respectively). Moreover, in both cases, lowest circumferential stresses are achieved for *d* = 16 mm and *t* = 12 mm, while highest values are attained for *d* = 19 mm and *t* = 12 mm.

The relative values of ASED over the control volume due to clamping stresses ($\overline{W}_{clamp}$) are reported in Figure 7.6. For the sake of brevity, only results related to $R_0 = 0.2$ mm and 1 mm are depicted. Interestingly, results for extreme values within the range of variation for R_0 are almost identical, with only negligible differences ($\leq 3\%$ in case of unsymmetric specimens).

This outcome descends from the peculiar stress field induced by clamping actions.

a)

b)
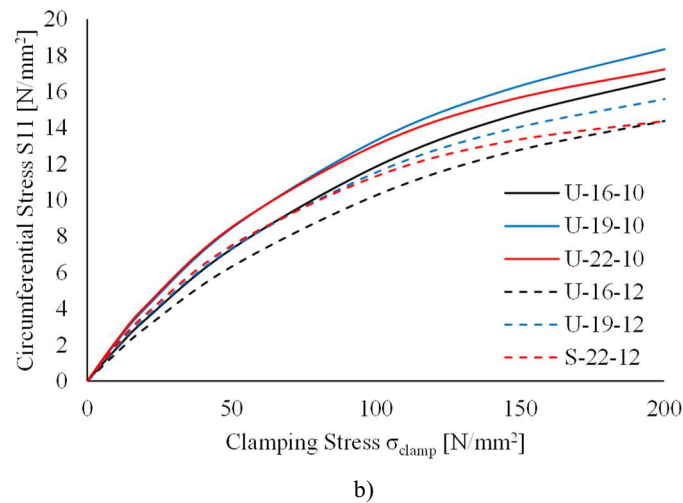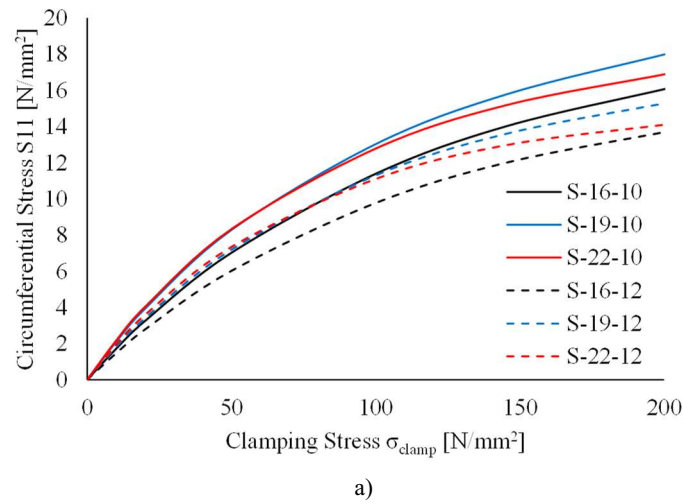
Figure 7.5 Distribution of circumferential stresses at the hole quadrant (U-notch tip) for increasing values of the applied clamping stress: a) symmetric specimens, b) unsymmetric specimens (values referred to the longitudinal bisector plane of plates).
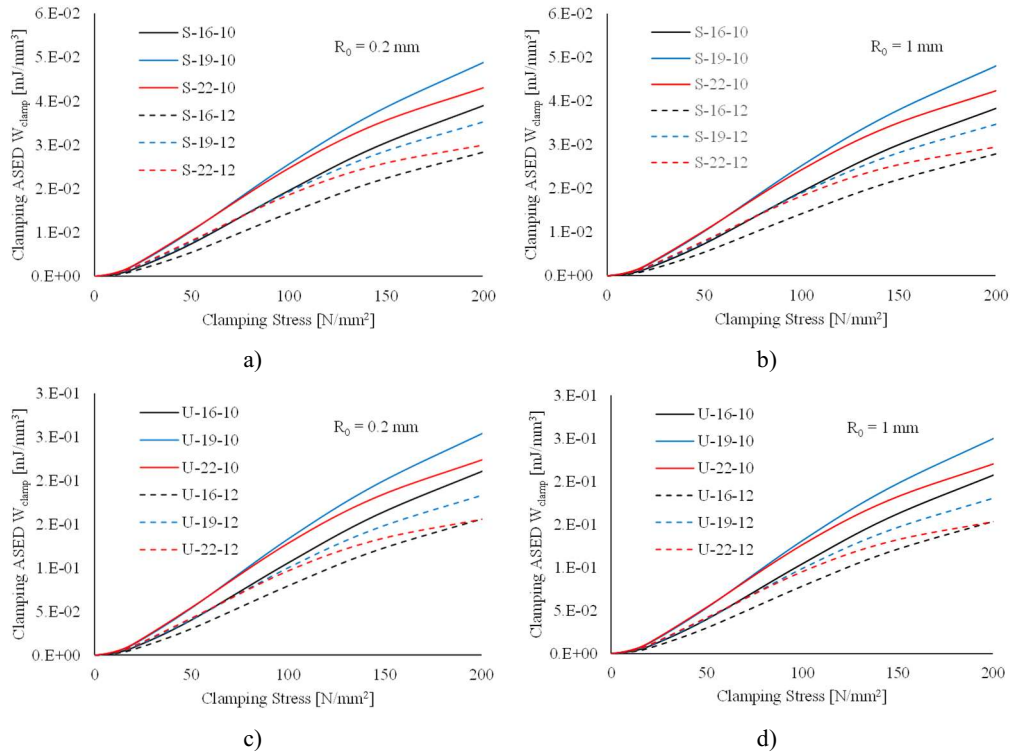
Figure 7.6 Average strain energy density values over the control volume for increasing values of applied clamping stresses: a) symmetric connections, $R_0 = 0.2$ mm, b) symmetric connections, $R_0 = 1$ mm, c) unsymmetric connections, $R_0 = 0.2$ mm and d) unsymmetric connections, $R_0 = 1$ mm.

Indeed, as rivet preloading acts perpendicularly to the plates, the resulting distribution of strain energy density $W(x)$ in plates is almost constant within the projection of the rivet heads. Therefore, calculations of $\overline{W}_{clamp}$ according to Equation 3.65 result in substantial independence from the assumed value of R_0.

Table 7.1 Circumferential stresses measured at the hole quadrant (onto the longitudinal bisector plane of plates) for all considered configurations and for increasing value of rivets clamping stresses.

	$S11_{clamp}$ (Hole Quadrant – Longitudinal [N/mm^2])						
Label [-] σ_{clamp} [N/mm^2]	S-16-10	S-19-10	S-22-10	S-16-12	S-19-12	S-22-12	AVG
0	0.0	0.0	0.0	0.0	0.0	0.0	0.0
1	0.2	0.2	0.2	0.2	0.2	0.2	0.2
10	1.7	2.1	2.2	1.5	1.8	1.9	1.9
20	3.2	3.9	4.0	2.8	3.4	3.6	3.5
50	7.0	8.3	8.3	6.0	7.2	7.3	7.4
100	11.4	13.0	12.8	9.8	11.3	11.1	11.6
150	14.0	15.8	15.2	12.0	13.6	13.0	13.9
200	16.2	18.1	17.0	13.8	15.4	14.2	15.8
Label [-] σ_{clamp} [N/mm^2]	U-16-10	U-19-10	U-22-10	U-16-12	U-19-12	U-22-12	AVG
0	0.0	0.0	0.0	0.0	0.0	0.0	0.0
1	0.2	0.2	0.2	0.2	0.2	0.2	0.2
10	1.8	2.1	2.2	1.5	1.8	2.0	1.9
20	3.4	4.0	4.1	2.9	3.5	3.7	3.6
50	7.3	8.4	8.5	6.3	7.3	7.5	7.6
100	11.8	13.3	13.0	10.3	11.5	11.3	11.9
150	14.6	16.1	15.5	12.6	13.9	13.2	14.3
200	16.8	18.5	17.3	14.5	15.7	14.4	16.2

Table 7.2 Average strain energy density values $\overline{W}_{clamp}$ over the control volume ($R_0 = 0.2$ mm) for increasing values of applied clamping stresses.

	$R_0 = 0.2$ mm						
	$\overline{W}_{clamp}$ [mJ/mm^3]						
Label [-] / σ_{clamp} [N/mm^2]	S-16-10	S-19-10	S-22-10	S-16-12	S-19-12	S-22-12	AVG
0	0.00E+00	0.00E+00	0.00E+00	0.00E+00	0.00E+00	0.00E+00	0.00E+00
1	4.85E-06	7.36E-06	7.97E-06	3.53E-06	5.53E-06	6.29E-06	5.92E-06
10	4.41E-04	6.57E-04	7.05E-04	3.23E-04	4.94E-04	5.61E-04	5.30E-04
20	1.59E-03	2.32E-03	2.45E-03	1.17E-03	1.75E-03	1.94E-03	1.87E-03
50	7.43E-03	1.03E-02	1.05E-02	5.47E-03	7.80E-03	8.13E-03	8.27E-03
100	1.95E-02	2.56E-02	2.46E-02	1.44E-02	1.92E-02	1.85E-02	2.03E-02
150	2.96E-02	3.75E-02	3.48E-02	2.17E-02	2.79E-02	2.54E-02	2.95E-02
200	3.95E-02	4.95E-02	4.35E-02	2.87E-02	3.57E-02	3.02E-02	3.79E-02
Label [-] / σ_{clamp} [N/mm^2]	U-16-10	U-19-10	U-22-10	U-16-12	U-19-12	U-22-12	AVG
0	0.00E+00	0.00E+00	0.00E+00	0.00E+00	0.00E+00	0.00E+00	0.00E+00
1	2.62E-05	3.83E-05	4.14E-05	1.94E-05	2.88E-05	3.27E-05	3.12E-05
10	2.39E-03	3.42E-03	3.67E-03	1.78E-03	2.57E-03	2.92E-03	2.79E-03
20	8.60E-03	1.21E-02	1.27E-02	6.42E-03	9.09E-03	1.01E-02	9.83E-03
50	4.02E-02	5.37E-02	5.44E-02	3.02E-02	4.06E-02	4.23E-02	4.36E-02
100	1.06E-01	1.33E-01	1.28E-01	7.94E-02	1.00E-01	9.65E-02	1.07E-01
150	1.60E-01	1.95E-01	1.81E-01	1.20E-01	1.45E-01	1.32E-01	1.56E-01
200	2.14E-01	2.57E-01	2.26E-01	1.58E-01	1.86E-01	1.57E-01	2.00E-01

Table 7.3 Average strain energy density values $\overline{W}_{clamp}$ over the control volume ($R_0 = 1$ mm) for increasing values of applied clamping stresses.

	$R_0 = 1$ mm						
	$\overline{W}_{clamp}$ [mJ/mm^3]						
Label [-] / σ_{clamp} [N/mm^2]	S-16-10	S-19-10	S-22-10	S-16-12	S-19-12	S-22-12	AVG
0	0.00E+00	0.00E+00	0.00E+00	0.00E+00	0.00E+00	0.00E+00	0.00E+00
1	4.77E-06	7.25E-06	7.84E-06	3.47E-06	5.44E-06	6.19E-06	5.83E-06
10	4.34E-04	6.46E-04	6.93E-04	3.17E-04	4.86E-04	5.52E-04	5.21E-04
20	1.56E-03	2.28E-03	2.41E-03	1.15E-03	1.72E-03	1.90E-03	1.84E-03
50	7.31E-03	1.02E-02	1.03E-02	5.38E-03	7.68E-03	7.99E-03	8.14E-03
100	1.92E-02	2.51E-02	2.42E-02	1.42E-02	1.89E-02	1.82E-02	2.00E-02
150	2.91E-02	3.69E-02	3.42E-02	2.14E-02	2.74E-02	2.49E-02	2.90E-02
200	3.89E-02	4.87E-02	4.28E-02	2.83E-02	3.51E-02	2.97E-02	3.73E-02
Label [-] / σ_{clamp} [N/mm^2]	U-16-10	U-19-10	U-22-10	U-16-12	U-19-12	U-22-12	AVG
0	0.00E+00	0.00E+00	0.00E+00	0.00E+00	0.00E+00	0.00E+00	0.00E+00
1	2.58E-05	3.77E-05	4.08E-05	1.91E-05	2.83E-05	3.22E-05	3.06E-05
10	2.35E-03	3.36E-03	3.61E-03	1.75E-03	2.53E-03	2.87E-03	2.74E-03
20	8.46E-03	1.19E-02	1.25E-02	6.32E-03	8.94E-03	9.91E-03	9.67E-03
50	3.95E-02	5.29E-02	5.36E-02	2.97E-02	3.99E-02	4.16E-02	4.29E-02
100	1.04E-01	1.31E-01	1.26E-01	7.81E-02	9.85E-02	9.49E-02	1.05E-01
150	1.58E-01	1.92E-01	1.78E-01	1.18E-01	1.43E-01	1.30E-01	1.53E-01
200	2.10E-01	2.53E-01	2.23E-01	1.56E-01	1.83E-01	1.55E-01	1.97E-01

It is worth remarking that this outcome is clearly not expected for ASED induced by applied loads, that is, for shear forces on connections, perforated plates are subjected to Mode I loading (*Berto & Lazzarin, 2014*).

Contrariwise, a significant difference in terms of $\overline{W}_{clamp}$ is achieved among symmetric and unsymmetric specimens. For instance, average SED values due to clamping stresses in connections with two plates is ≈ 5 times higher as respect to connections with three plies (on average). This outcome clearly descends from the different distribution of normal and circumferential stresses through the thickness in case of symmetric and unsymmetric specimens (see Figure 7.3).

Derived values of $\overline{W}_{clamp}$ provide a preliminary insight about the fatigue performance enhancement of connected plates, as they counterbalance the ASED deriving from applied loads.

According to the above results, the following preliminary remarks on the influence of clamping action on the fatigue performance of hot-driven riveted connections can be pointed out:

- For the same given value of applied clamping stress, the beneficial effect of preloading is less pronounced in symmetric connections as respect to unsymmetric ones, namely because of the distribution of stresses through the thickness is less favourable;

- Nevertheless, the more beneficial effect of clamping in unsymmetric connections is limited to rather small stress ranges, as $\overline{W}_{clamp}$ will quickly become negligible for higher values of $\Delta\sigma$ due to additional stresses induced by secondary bending;

- For increasing values of applied clamping stresses, specimens with thicker plates are less affected by the beneficial effect of preloading, as smaller compressive stresses are transferred to connected plies;

- Apparently, increases in clamping stresses do not result in proportional enhancements of fatigue performance for the investigated hot-driven connections, as both S11 and $\overline{W}_{clamp}$ trends against σ_{clamp} are less than linear.

7.1.4 Strain Energy Density Calculations for Hot-Driven Riveted Connections

ASED calculations for FEMs resembling experimental tests on hot-driven riveted connections (*Section 4.3*) are summarized in Figure 7.7 and Tables 7.4-7.9 in terms of *i*) magnitude of the control volume Ω_{SED} for increasing values of R_0 and *ii*) ASED trends against R_0 due to clamping (blue curves), external loads (red curves) and corresponding ASED ranges (black curves). For thoroughness, distributions of equivalent Von Mises stresses (SMISES) under the combined action of clamping and maximum stresses are depicted as well.

Equivalent Von-Mises stresses   ASED calculations

a)   b)
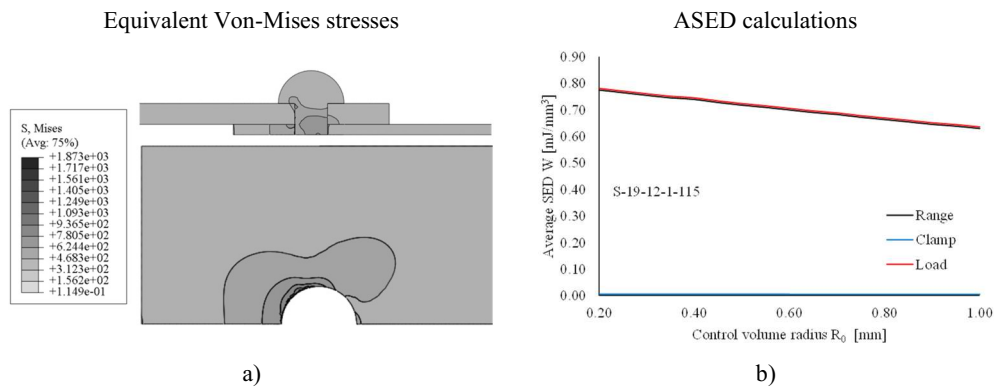
S-19-12-1-115, N* = 602770
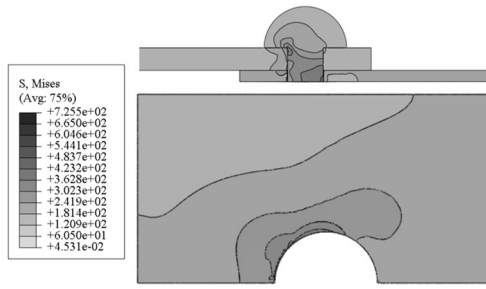
c)
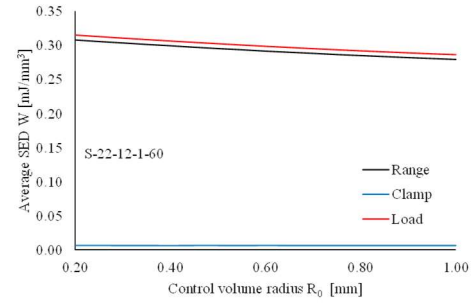
d)

S-22-12-1-60, N* = 774056
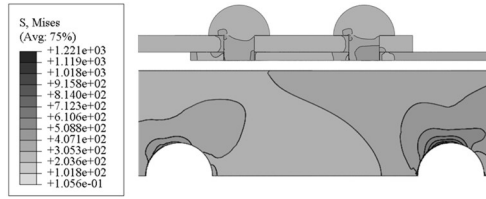
e)
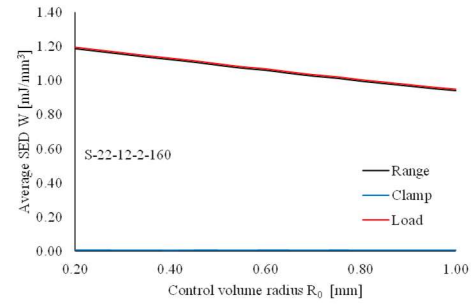
f)

S-22-12-2-160, N* = 497964
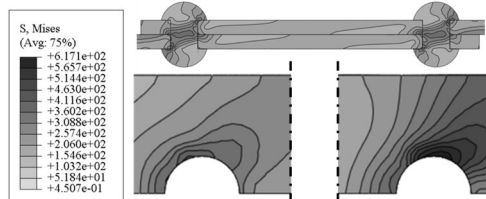
g)
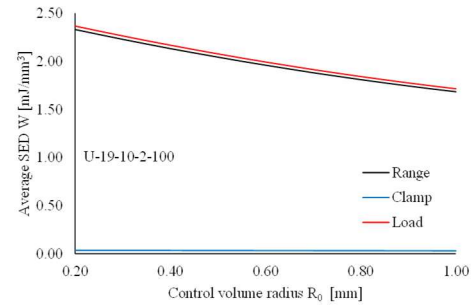
h)

d) U-19-10-2-100, N* = 42963
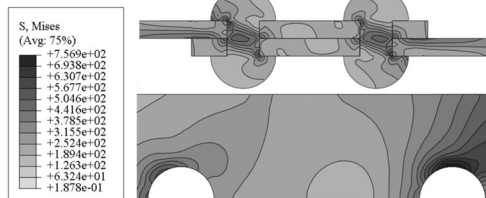
i)
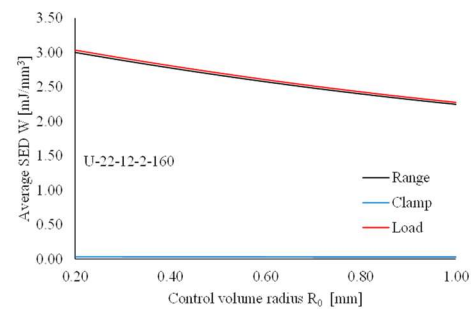
j)

e) U-22-12-2-160, N* = 17436

k)   l)

e) U-22-12-2-144, N* = 26357
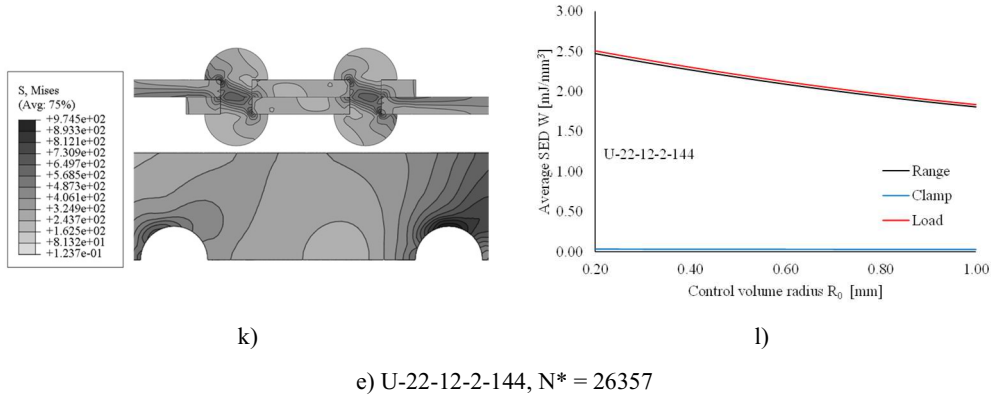
Figure 7.7 FEAs developed for ASED calculations in hot-driven riveted connections: a-b) S-19-12-1-115, c-d) S-22-12-1-60, e-f) S-22-12-2-160, g-h) U-19-10-2-100, i-j) U-22-12-2-160, k-l) U-22-12-2-144.

For the sake of clarity, Ω_{SED} values and integrated strain energies for symmetric specimens (i.e., S-19-12-1-115, S-22-12-1-60 and S-22-12-2-160) are referred to an half of the control volume, that is, due to longitudinal symmetry of such connections. Nevertheless, ASED values are clearly insensitive to this simplifying assumption.

Indeed, in the spirit of a numerical, free mesh application of the SED method, $\overline{W}_{clamp}$, $\overline{W}_{load}$ and $\Delta\overline{W}$ were estimated as the ratio among the total elastic strain energy $E_{TOT,\Omega}$ in the *picked* (half-)control volume and the (half-)control volume itself (that is, the numerical outputs returned by FEAs).

As expected, ASED values monotonically decrease with increasing values of R_0, with a maximum decrease of -29% among $\Delta\overline{W}_{0.2\,mm}$ and $\Delta\overline{W}_{1\,mm}$ for U-19-10-2-100 (see Figure 7.7h).

Moreover, in all cases $\overline{W}_{clamp}$ has a negligible influence on the final value of ASED range. This outcome descends from the rather high values of applied stress range as respect to clamping stresses in rivets.

Most notably, ASED ranges for unsymmetric specimens are sensibly higher as respect to the ones calculated for symmetric connections. For instance, ASED ranges equal to $\Delta\overline{W}_{max,S} = 1.186$ mJ/mm^3 and $\Delta\overline{W}_{max,U} = 3.094$ mJ/mm^3 are obtained for S-22-12-2-160 and U-22-12-2-160, respectively (+161%), i.e., by assuming a control volume radius $R_0 = 0.2$ mm. Conversely, a difference of +138% is obtained in case of $R_0 = 1$ mm for the same two connections (Tables 7.6-7.8).

This evidence becomes even more significant if one considers that both specimens are subjected to the same nominal stress range $\Delta\sigma = 190.1$ N/mm^2.

As expected, the lowest ASED range is achieved for S-22-12-1-60 (see Figure 7.7d, $\Delta\overline{W} = 0.262 \div 0.308$ mJ/mm^3 for $R_0 = 1 \div 0.2$ mm), namely due to the rather low stress range $\Delta\sigma = 71.4$ N/mm^2 and in light of its symmetric configuration.

The distributions of SMISES for all investigated connections (see Figure 7.7, left column) highlight the strong stress concentrations nearby the rivet holes, i.e. identifying plates' net sections as most likely fracture spots for all the specimens.

Moreover, in case of double rivets specimens (i.e., S-22-12-2-160, U-19-10-2-100, U-22-12-2-160 and U-22-12-2-144), the most stressed portion of the plate is always represented by a neighbourhood of the rivet hole closest to the applied tensile loads.

To this end, it is worth remarking that, according to the SED method assumptions, indefinite elastic behaviour were assumed in FEAs for both plates and rivets (*Berto &*

Lazzarin, 2014; Foti et al., 2020), hence equivalent stresses in connected elements are higher than base materials yield strength.

In the next Section, estimated values of ASED ranges for all considered connections are used to interpretate the fatigue performance of specimens.

Table 7.4 ASED calculations for specimen S-19-12-1-115.

S-19-12-1-115						
$\Delta\sigma = 106.5$ N/mm^2, R = 0, N* = 602770						
R_0	Ω_{SED}	$E_{e,clamp}$	$E_{e,load}$	W_{clamp}	W_{load}	ΔW
[mm]	[mm^3]	[mJ]	[mJ]	[mJ/mm^3]	[mJ/mm^3]	[mJ/mm^3]
0.20	2.55	0.02	1.99	0.006	0.781	0.775
0.25	3.80	0.02	2.93	0.006	0.771	0.765
0.30	5.12	0.03	3.90	0.006	0.761	0.755
0.35	6.65	0.04	5.00	0.006	0.751	0.745
0.40	8.02	0.05	5.98	0.006	0.745	0.739
0.45	9.89	0.06	7.25	0.006	0.734	0.728
0.50	11.80	0.07	8.54	0.006	0.724	0.718
0.55	13.65	0.08	9.76	0.006	0.715	0.709
0.60	15.76	0.10	11.12	0.006	0.706	0.700
0.65	17.99	0.11	12.52	0.006	0.696	0.690
0.70	20.06	0.12	13.81	0.006	0.688	0.682
0.75	22.65	0.14	15.36	0.006	0.678	0.672
0.80	25.10	0.15	16.80	0.006	0.669	0.663
0.85	27.69	0.17	18.29	0.006	0.661	0.655
0.90	30.48	0.18	19.85	0.006	0.651	0.645
0.95	33.15	0.20	21.36	0.006	0.644	0.638
1.00	36.12	0.22	22.97	0.006	0.636	0.630

Table 7.5 ASED calculations for specimen S-22-12-1-60.

S-22-12-1-60						
$\Delta\sigma = 71.4$ N/mm^2, R = 0, N* = 774056						
R_0	Ω_{SED}	$E_{e,clamp}$	$E_{e,load}$	W_{clamp}	W_{load}	ΔW
[mm]	[mm^3]	[mJ]	[mJ]	[mJ/mm^3]	[mJ/mm^3]	[mJ/mm^3]
0.20	2.75	0.02	0.54	0.007	0.315	0.308
0.25	4.07	0.03	0.79	0.007	0.314	0.307
0.30	5.56	0.04	1.05	0.007	0.306	0.298
0.35	7.21	0.05	1.35	0.007	0.303	0.296
0.40	8.84	0.06	1.61	0.007	0.294	0.287
0.45	10.61	0.08	1.97	0.007	0.299	0.292
0.50	12.68	0.09	2.32	0.007	0.295	0.288
0.55	14.88	0.10	2.66	0.007	0.288	0.281
0.60	16.72	0.12	3.04	0.007	0.293	0.286
0.65	19.30	0.14	3.43	0.007	0.286	0.279
0.70	21.85	0.15	3.78	0.007	0.279	0.272
0.75	24.05	0.17	4.23	0.007	0.284	0.276
0.80	27.02	0.19	4.63	0.007	0.276	0.269
0.85	29.76	0.21	5.05	0.007	0.274	0.267
0.90	32.52	0.23	5.50	0.007	0.273	0.266

| 0.95 | 35.60 | 0.25 | 5.92 | 0.007 | 0.268 | 0.261 |
| 1.00 | 38.29 | 0.27 | 6.39 | 0.007 | 0.269 | 0.262 |

Table 7.6 ASED calculations for specimen S-22-12-2-160.

S-22-12-1-160						
$\Delta\sigma = 190.1$ N/mm^2, R = 0, N* = 497964						
R_0	Ω_{SED}	$E_{e,clamp}$	$E_{e,load}$	W_{clamp}	W_{load}	ΔW
[mm]	[mm^3]	[mJ]	[mJ]	[mJ/mm^3]	[mJ/mm^3]	[mJ/mm^3]
0.20	2.75	0.02	3.28	0.008	1.194	1.186
0.25	4.07	0.03	4.79	0.008	1.178	1.170
0.30	5.56	0.05	6.46	0.008	1.162	1.153
0.35	7.21	0.06	8.25	0.008	1.145	1.137
0.40	8.84	0.07	10.00	0.008	1.130	1.122
0.45	10.61	0.09	11.83	0.008	1.115	1.107
0.50	12.68	0.11	13.92	0.008	1.097	1.089
0.55	14.88	0.12	16.07	0.008	1.080	1.072
0.60	16.72	0.14	17.85	0.008	1.068	1.059
0.65	19.30	0.16	20.26	0.008	1.050	1.041
0.70	21.85	0.18	22.58	0.008	1.033	1.025
0.75	24.05	0.20	24.56	0.008	1.021	1.013
0.80	27.02	0.22	27.12	0.008	1.004	0.995
0.85	29.76	0.24	29.44	0.008	0.990	0.981
0.90	32.52	0.27	31.72	0.008	0.975	0.967
0.95	35.60	0.29	34.19	0.008	0.961	0.952
1.00	38.29	0.31	36.32	0.008	0.948	0.940

Table 7.7 ASED calculations for specimen U-19-10-2-100.

U-19-10-2-100						
$\Delta\sigma = 166.7$ N/mm^2, R = 0, N* = 42963						
R_0	Ω_{SED}	$E_{e,clamp}$	$E_{e,load}$	W_{clamp}	W_{load}	ΔW
[mm]	[mm^3]	[mJ]	[mJ]	[mJ/mm^3]	[mJ/mm^3]	[mJ/mm^3]
0.20	5.11	0.19	12.09	0.037	2.367	2.330
0.25	7.59	0.27	17.42	0.036	2.293	2.257
0.30	10.25	0.37	23.02	0.036	2.247	2.210
0.35	13.31	0.48	28.91	0.036	2.173	2.137
0.40	16.04	0.58	34.60	0.036	2.158	2.121
0.45	19.77	0.69	40.50	0.035	2.048	2.014
0.50	23.59	0.81	48.42	0.034	2.052	2.018
0.55	27.30	0.94	56.09	0.035	2.055	2.021
0.60	31.51	1.05	61.79	0.033	1.961	1.927
0.65	35.98	1.20	69.77	0.033	1.939	1.905
0.70	40.13	1.34	77.32	0.034	1.927	1.893
0.75	45.30	1.47	83.58	0.032	1.845	1.812
0.80	50.20	1.63	91.85	0.032	1.830	1.797
0.85	55.37	1.78	99.27	0.032	1.793	1.761
0.90	60.96	1.93	106.48	0.032	1.747	1.715
0.95	35.60	0.29	34.19	0.008	0.961	0.952
1.00	38.29	0.31	36.32	0.008	0.948	0.940

Table 7.8 ASED calculations for specimen U-22-12-2-160.

U-22-12-2-160						
$\Delta\sigma$ = 190.1 N/mm², R = 0, N* = 17436						
R_0	Ω_{SED}	$E_{e,clamp}$	$E_{e,load}$	W_{clamp}	W_{load}	ΔW
[mm]	[mm³]	[mJ]	[mJ]	[mJ/mm³]	[mJ/mm³]	[mJ/mm³]
0.20	5.49	0.19	17.19	0.034	3.128	3.094
0.25	8.13	0.27	24.76	0.034	3.044	3.010
0.30	11.13	0.37	32.73	0.033	2.941	2.908
0.35	14.42	0.48	41.11	0.033	2.852	2.819
0.40	17.69	0.58	49.19	0.033	2.781	2.748
0.45	21.23	0.69	57.58	0.032	2.713	2.680
0.50	25.37	0.81	68.84	0.032	2.714	2.682
0.55	29.75	0.94	79.75	0.032	2.680	2.649
0.60	33.44	1.05	87.85	0.031	2.627	2.596
0.65	38.60	1.20	99.19	0.031	2.570	2.539
0.70	43.70	1.34	109.92	0.031	2.515	2.484
0.75	48.11	1.47	118.82	0.031	2.470	2.439
0.80	54.04	1.63	130.58	0.030	2.416	2.386
0.85	59.51	1.78	141.13	0.030	2.371	2.342
0.90	65.03	1.93	151.39	0.030	2.328	2.298
0.95	71.19	2.09	162.68	0.029	2.285	2.256
1.00	76.59	2.23	173.32	0.029	2.263	2.234

Table 7.9 ASED calculations for specimen U-22-12-2-144.

U-22-12-2-144						
$\Delta\sigma$ = 171.4 N/mm², R = 0, N* = 17436						
R_0	Ω_{SED}	$E_{e,clamp}$	$E_{e,load}$	W_{clamp}	W_{load}	ΔW
[mm]	[mm³]	[mJ]	[mJ]	[mJ/mm³]	[mJ/mm³]	[mJ/mm³]
0.20	5.49	0.19	14.18	0.034	2.581	2.546
0.25	8.13	0.27	20.43	0.034	2.511	2.477
0.30	11.13	0.37	27.00	0.033	2.427	2.393
0.35	14.42	0.48	33.91	0.033	2.353	2.320
0.40	17.69	0.58	40.58	0.033	2.294	2.261
0.45	21.23	0.69	47.51	0.032	2.238	2.206
0.50	25.37	0.81	56.79	0.032	2.239	2.207
0.55	29.75	0.94	65.79	0.032	2.211	2.180
0.60	33.44	1.05	72.48	0.031	2.168	2.136
0.65	38.60	1.20	81.83	0.031	2.120	2.089
0.70	43.70	1.34	90.68	0.031	2.075	2.044
0.75	48.11	1.47	98.03	0.031	2.038	2.007
0.80	54.04	1.63	107.73	0.030	1.993	1.963
0.85	59.51	1.78	116.43	0.030	1.956	1.927
0.90	65.03	1.93	124.90	0.030	1.921	1.891
0.95	71.19	2.09	134.21	0.029	1.885	1.856
1.00	76.59	2.23	142.99	0.029	1.867	1.838

7.2. Predictive model for the fatigue resistance of hot-driven riveted connections

Based on performed ASED calculations, a predictive model for the fatigue resistance of hot-driven riveted connections is hence derived. Namely, the SED-based form of Basquin's formula is initially adopted to interpretate experimental results (Equation 7.1 – *Lazzarin & Zambardi, 2001*; *Livieri & Lazzarin, 2005*):

$$N^* = N_C \left(\frac{\Delta \overline{W}_C}{\Delta \overline{W}^*} \right)^{-m} \tag{7.1}$$

Therefore, calibrated values of the ASED detail class $\Delta \overline{W}_C$ and of the reciprocal logarithmic slope m can be suitably derived by using a logarithmic regression model (*Wakefield, 2013*).

Interpretation of experimental fatigues failure through Equation 7.1 is summarized in Figure 7.8 and Table 7.10.
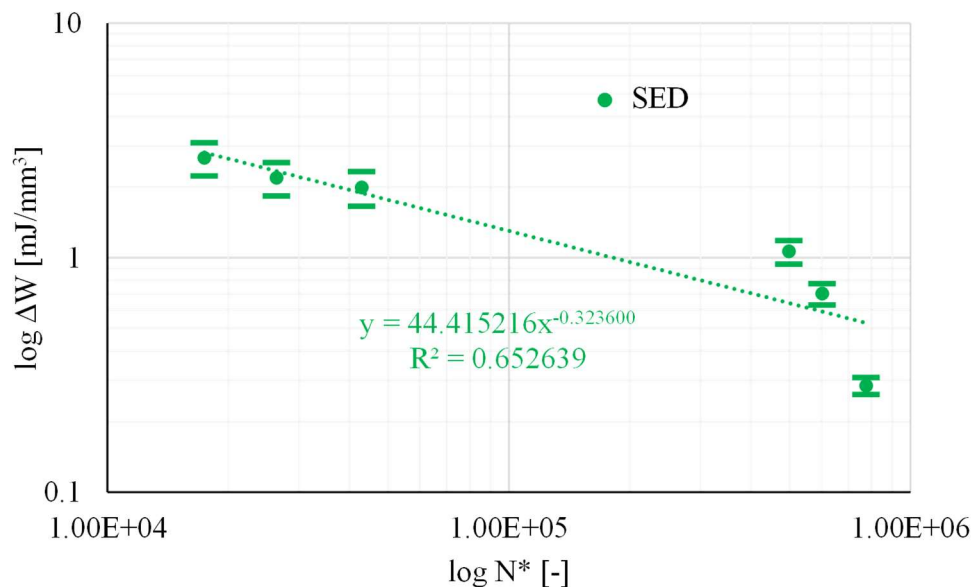
Figure 7.8 Interpretation of fatigue results through the SED-based form of Basquin's formula.

Table 7.10 Interpretation of fatigue results through the SED-based form of Basquin's formula.

Label	N*	Δσ	ΔW_{max}	ΔW_{min}	ΔW_{mean}
[-]	[-]	[N/mm²]	[mJ/mm³]	[mJ/mm³]	[mJ/mm³]
S-19-12-1-115	602270	106.5	0.775	0.630	0.702
S-22-12-1-60	774056	71.4	0.308	0.261	0.285
S-22-12-2-160	497964	190.1	1.186	0.940	1.063
U-19-10-2-100	42963	166.7	2.330	1.657	1.993
U-22-12-2-160	17436	190.1	3.094	2.234	2.664
U-22-12-2-144	26357	170.1	2.546	1.838	2.192

As proved by the obtained coefficient of determination $R^2 = 0.65$, the adoption of a SED-based form of Basquin's formula allows a more consistent interpretation of experimental outcomes. As a comparison, a rather low value of $R^2 = 0.11$ was obtained by adopting

the stress range-based Basquin's formula (see *Section 4.3*), e.g., also owing to a significant flattening of the mean regression $\Delta\sigma - N^*$ curve.

Based on mean regression coefficients ($C = 44.41$, $b = -1/m = -0.3236$), the following values of $\Delta\overline{W}_C = 1.02$ mJ/mm^3 and $m = 3.09$ are derived for the investigated hot-driven riveted connections.

In compliance with observations reported in *Radaj & Vormwald* (*2013*), it can be noticed how changes in terms of R_0 within the assumed range of variability have only a minor influence on the interpretation of results. This outcome plausibly descends from the absence of any stress singularity for the perforated plates, which leads to a less strain energy density gradient as respect to sharp notches.

An equivalent, stress-based formulation for fatigue assessment of hot-driven riveted connections can be derived by manipulating the expression for average SED in case of U-notches (Equation 7.2 – *Berto & Lazzarin, 2014*):

$$\Delta\overline{W} = c_{\mathrm{w}}\,\mathrm{H}\left(\frac{R_0}{\rho},\nu\right)\frac{(\Delta\sigma_{\mathrm{tip}})^2}{2E} \tag{7.2}$$

with c_{w} being the prestress coefficient accounting for the mean-stress effect, H being a non dimensional coefficient depending on both geometrical and mechanical parameters and $\Delta\sigma_{\mathrm{tip}}$ being the local stress range achieved at the notch tip.

Recalling the well-known result from elasticity theory, for an isolated hole in a large plate $\sigma_{\mathrm{tip}} = 3\,\sigma_0$, and hence $\Delta\sigma_{\mathrm{tip}} = 3\,\Delta\sigma$ (*Anderson, 2017*). Therefore, a SED-equivalent stress range for investigated connections can be derived by inverting Equation 7.2 as follows (Equation 7.3):

$$\Delta\overline{W} = c_{\mathrm{w}}\,\mathrm{H}\left(\frac{R_0}{\rho},\nu\right)\frac{(3\,\Delta\sigma)^2}{2E} \stackrel{\mathrm{def}}{=} \frac{9}{2}\frac{c_{\mathrm{w}}}{E}(\mathrm{SMF}_{\mathrm{SED}}\,\Delta\sigma)^2 \tag{7.3}$$

with $\mathrm{SMF}_{\mathrm{SED}}$ being a SED-equivalent stress magnification factor that synthetically accounts for *i*) geometrical features, *ii*) material properties and *iii*) stress raising sources for hot-driven riveted connections.

Vales of $\mathrm{SMF}_{\mathrm{SED}}$ for each connection can be immediately derived based on results of refined FEAs according to Equation 7.4:

$$\mathrm{SMF}_{\mathrm{SED}} = \left(\frac{2E\,\Delta\overline{W}}{9\,c_{\mathrm{w}}}\right)^{1/2}\frac{1}{\Delta\sigma} \tag{7.4}$$

Trends of $\mathrm{SMF}_{\mathrm{SED}}$ against R_0 for each investigated connection, e.g., based on refined FEAs described in *Section 7.1.4,* are summarized in Figure 7.9 and Tables 7.11-7.12.

Table 7.11 SED-based SMFs for symmetric specimens.

	Label					
	[-]					
	S-19-12-1-115		S-22-12-1-60		S-22-12-2-160	
$\Delta\sigma$ [N/mm^2]	106.5		71.4		109.1	
c_{w} [-]	1.0		1.0		1.0	
R_0	ΔW	$\mathrm{SMF}_{\mathrm{SED}}$	ΔW	$\mathrm{SMF}_{\mathrm{SED}}$	ΔW	$\mathrm{SMF}_{\mathrm{SED}}$
[mm]	[mJ/mm^3]	[-]	[mJ/mm^3]	[-]	[mJ/mm^3]	[-]
0.20	0.775	1.26	0.308	1.19	1.186	0.87
0.25	0.765	1.25	0.307	1.19	1.170	0.87
0.30	0.755	1.25	0.298	1.18	1.153	0.86
0.35	0.745	1.24	0.296	1.17	1.137	0.86
0.40	0.739	1.23	0.287	1.15	1.122	0.85

0.45	0.728	1.22	0.292	1.16	1.107	0.85
0.50	0.718	1.22	0.288	1.15	1.089	0.84
0.55	0.709	1.21	0.281	1.14	1.072	0.83
0.60	0.700	1.20	0.286	1.15	1.059	0.83
0.65	0.690	1.19	0.279	1.14	1.041	0.82
0.70	0.682	1.18	0.272	1.12	1.025	0.81
0.75	0.672	1.18	0.276	1.13	1.013	0.81
0.80	0.663	1.17	0.269	1.12	0.995	0.80
0.85	0.655	1.16	0.267	1.11	0.981	0.80
0.90	0.645	1.15	0.266	1.11	0.967	0.79
0.95	0.638	1.15	0.261	1.10	0.952	0.78
1.00	0.630	1.14	0.262	1.10	0.940	0.78
$SMF_{SED,S}$ *Mean*:					1.03	
COV:					0.16	

Table 7.12 SED-based SMFs for unsymmetric specimens.

	Label					
	[-]					
	U-19-10-2-100		U-22-12-2-160		U-22-12-2-144	
$\Delta\sigma$ [N/mm^2]	166.7		190.1		171.4	
c_w [-]	1.0		1.0		1.0	
R_0	ΔW	SMF_{SED}	ΔW	SMF_{SED}	ΔW	SMF_{SED}
[mm]	[mJ/mm^3]	[-]	[mJ/mm^3]	[-]	[mJ/mm^3]	[-]
0.20	2.330	1.40	3.094	1.42	2.546	1.42
0.25	2.257	1.38	3.010	1.39	2.477	1.40
0.30	2.210	1.36	2.908	1.37	2.393	1.38
0.35	2.137	1.34	2.819	1.35	2.320	1.36
0.40	2.121	1.33	2.748	1.33	2.261	1.34
0.45	2.014	1.30	2.680	1.32	2.206	1.32
0.50	2.018	1.30	2.682	1.32	2.207	1.32
0.55	2.021	1.30	2.649	1.31	2.180	1.32
0.60	1.927	1.27	2.596	1.29	2.136	1.30
0.65	1.905	1.26	2.539	1.28	2.089	1.29
0.70	1.893	1.26	2.484	1.27	2.044	1.27
0.75	1.812	1.23	2.439	1.25	2.007	1.26
0.80	1.797	1.23	2.386	1.24	1.963	1.25
0.85	1.761	1.22	2.342	1.23	1.927	1.24
0.90	1.715	1.20	2.298	1.22	1.891	1.23
0.95	1.695	1.19	2.256	1.21	1.856	1.21
1.00	1.657	1.18	2.234	1.21	1.838	1.21
$SMF_{SED,U}$ *Mean*:					1.29	
COV:					0.05	
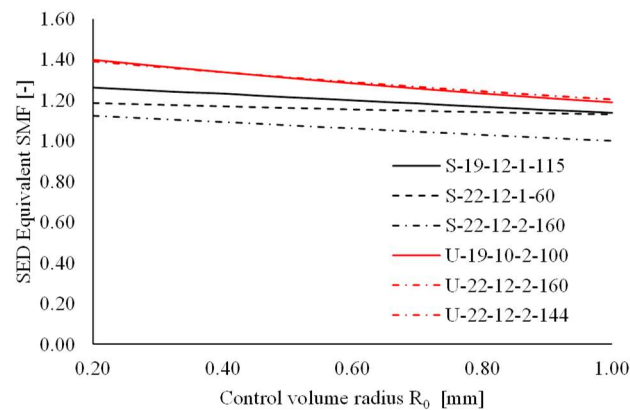
Figure 7.9 Trends of SED-equivalent stress magnification factor against increasing values of R_0 for each considered hot-driven riveted connection.

Consistently, it can be noticed how, for all investigated configuration, values of SMF$_{SED}$ are decreasing for increasing values of R$_0$. Namely, the highest values are achieved for U-22-12-2-144/160 (i.e., SMF$_{SED}$ = 1.21 ÷ 1.42 for R$_0$ = 0.2 ÷ 1 mm, see Table 7.12). Contrariwise, SMF$_{SED}$ is actually smaller than unity for S-22-12-2-160 (i.e., SMF$_{SED}$ = 0.87 ÷ 0.78 for R$_0$ = 0.2 ÷ 1 mm, see Table 7.11). As stated previously, S-22-12-2-160 and U-22-12-2-160 are nominally identical in terms of plates geometry and applied stress range, with the only difference being represented by connections configurations (e.g., symmetric or unsymmetric, respectively).

Therefore, for such relevant case, the detrimental effect of secondary bending moments can be regarded as an equivalent penalization of ≈ 1.6 times in terms of nominal stress range (that is, 1.21/0.78 = 1.55 ÷ 1.63 =1.42/0.87).

Moreover, it is interesting to note that the equivalent stress magnification factor for S-22-12-2-160 is slightly lower as respect to other symmetric connections, for which in fact SMF$_{SED}$ ranges among 1.10 ÷ 1.26.

This outcome potentially derives from the presence of two rivet holes. Indeed, as reported in *Peterson & Pilkey* (*1997*), for a plate in tension featuring two holes with "finite" pitch ($p_1/d \leq 10$, see Figure 3.22), the corresponding SMF at the first hole quadrant is smaller than 3. Therefore, in case of double rivet specimens, smaller values of equivalent SMF are yielded by Equation 7.4 (e.g., where $\Delta\sigma_{tip}$ = 3 $\Delta\sigma$ is always conventionally assumed).

This condition possibly suggests that fatigue performance of hot-driven riveted connections with multiple rivets is enhanced as respect to single rivet specimens subjected to the same stress range, although further investigations are needed to this end owing to the small sample of experimental results.

Therefore, a predictive expression for fatigue performance of hot-driven riveted connections can be preliminarily derived by assuming two separate SMFs, e.g. for the cases of symmetric and unsymmetric connections.

As only 3 × 2 outcomes are available, mean values of SMF$_{SED}$ for each connection configuration are hence assumed to correct nominal stress ranges, that is, in absence of a more significant bulk of data (Equation 7.5):

$$\text{N}^* = \text{N}_\text{C} \left(\frac{\Delta\sigma_{C,eq}}{k_{eq} \, \Delta\sigma} \right)^{-m} \begin{cases} k_{eq} = 1.00 \text{ "S" connections} \\ k_{eq} = 1.30 \text{ "U" connections} \end{cases} \qquad (7.5)$$

with k_{eq} = mean(SMF$_{SED}$) being the equivalent stress magnification factor accounting for the connection configuration.

It is worth remarking that, as a constant nominal stress ratio R = 0 was adopted for all tests, no insights are currently provided by Equation 7.5 about the mean-stress effect. Nevertheless, consistently with the theoretical background of the SED method (*Berto & Lazzarin, 2014*), and in line with results for blunt V-notched cylinders (see *Chapter 6*), an equivalent stress magnification factor equal to $c_w^{1/2}$ may be used to account for the mean-stress effect.

For the sake of simplicity, mean values reported in Tables 7.11-7.12 have been conveniently approximated as k_{eq} = 1.00 and k_{eq} = 1.30, e.g., for symmetric and unsymmetric connections, respectively.

According to Equation 7.5, a logarithmic regression model can be suitably used to derive $\Delta\sigma_{C,eq}$ and *m* (*Wakefield, 2013*).

Interpretation of experimental fatigue failures through Equation 7.5 is summarized in Figure 7.10a and Table 7.13.

It can be noticed how the mean regression line is in good agreement with experimental results, as proved by the acceptable coefficient of determination $R^2 = 0.74$.

Based on mean regression coefficients $C = 2528.4$ and $b = -1/m = -0.234$, an equivalent detail class $\Delta\sigma_{C,eq} = 84$ N/mm^2 is obtained, with a reciprocal logarithmic slope equal to $m = 4.27$.

Finally, it is worth remarking that a certain degree of accuracy is lost in Equation 7.5 owing to the necessity of selecting a reference value for k_{eq}, namely in line with the ease-of use philosophy of the next generation of Eurocodes.
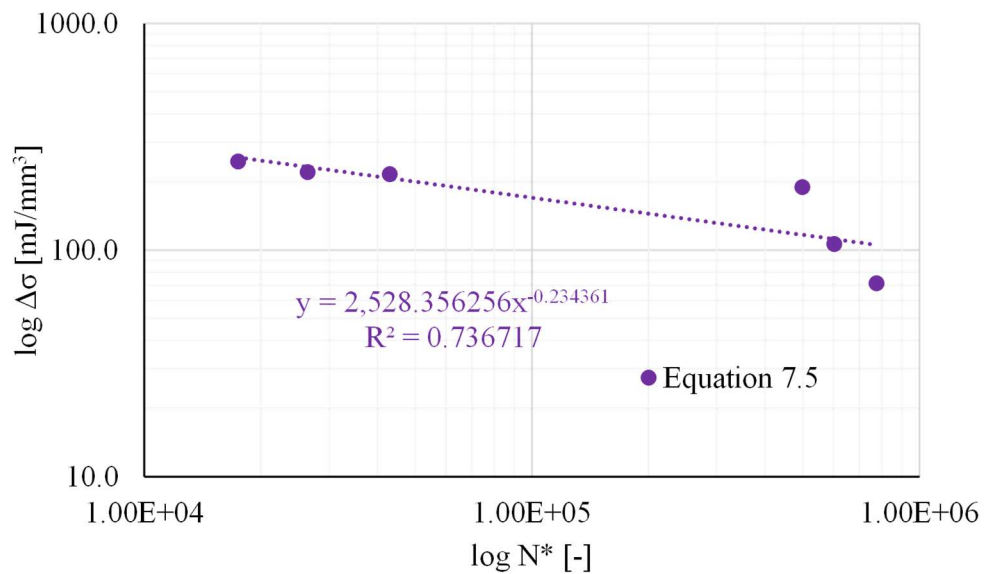
a) $N^* = N_C \left(\dfrac{\Delta\sigma_{C,eq}}{k_{eq} \, \Delta\sigma} \right)^{-m}$
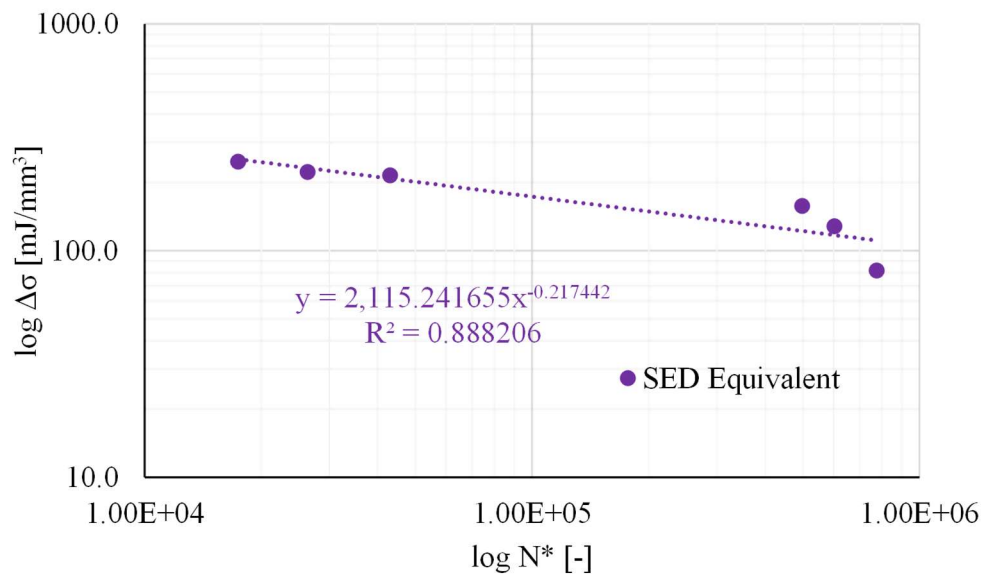
b) $N^* = N_C \left(\dfrac{\Delta\sigma_{C,eq}}{SMF_{SED,mean} \, \Delta\sigma} \right)^{-m}$

Figure 7.10 Interpretation of fatigue results according to Equations 7.4-7.5.

Table 7.13 Interpretation of fatigue results according to Equation 7.5.

Label	N*	$\Delta\sigma$	k_{eq}	$\Delta\sigma_{eq,E7.5}$	SMF$_{SED,mean}$	$\Delta\sigma_{eq,E7.4}$
[-]	[-]	[N/mm^2]	[-]	[N/mm^2]	[-]	[N/mm^2]
S-19-12-1-115	602270	106.5	1.00	106.5	1.20	127.8
S-22-12-1-60	774056	71.4	1.00	71.4	1.14	81.5
S-22-12-2-160	497964	190.1	1.00	190.1	0.83	157.1
U-19-10-2-100	42963	166.7	1.30	216.3	1.29	214.5
U-22-12-2-160	17436	190.1	1.30	246.7	1.30	247.0
U-22-12-2-144	26357	170.1	1.30	220.7	1.31	222.4

Indeed, if relevant mean values of SMF$_{SED}$ are used for each connection (Equation 7.4), a further improved accuracy is achieved (Figure 7.10b and Table 7.13, $R^2 = 0.89$).

7.3. Comparison among proposed formulations and current literature and EN1993:1-9 recommendations

In this Section, the proposed formulation is finally compared against current literature and normative fatigue provisions. For instance, the same two mean-stress effect corrections adopted for notched cylinders, namely the *Goodman* (*1899*) and the SWT (*Smith, Watson & Topper, 1970*) formulations, are used (Equation 7.6):

$$\text{Goodman:} \quad \Delta\sigma_{Eq,G} = \Delta\sigma \, \frac{1}{1 - \dfrac{\sigma_m}{f_u}} = \Delta\sigma \, \frac{1}{1 - \dfrac{(1+R)}{2\,(1-R)}\,\dfrac{\Delta\sigma}{f_u}} \tag{7.6a}$$

$$\text{SWT:} \quad \Delta\sigma_{Eq,SWT} = \Delta\sigma \, \sqrt{\frac{2}{1-R}} \tag{7.6b}$$

with σ_m being conventionally referred to the gross cross-section of plates.

Interpretation of fatigue results through Goodman and SWT models are summarized in Figures 7.11-7.12 and Table 7.14.
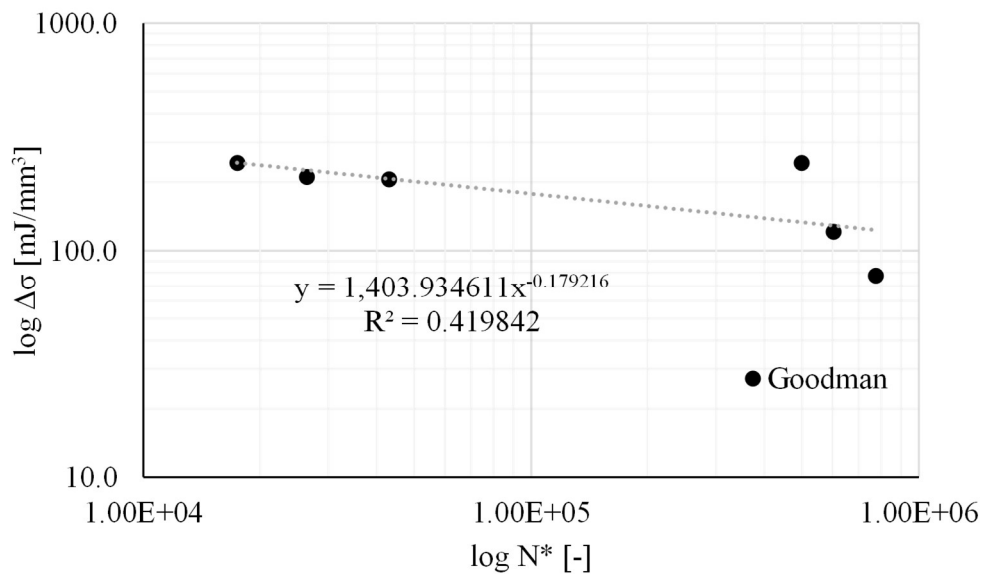
Figure 7.11 Application of the Goodman model for investigated hot-driven riveted connections.
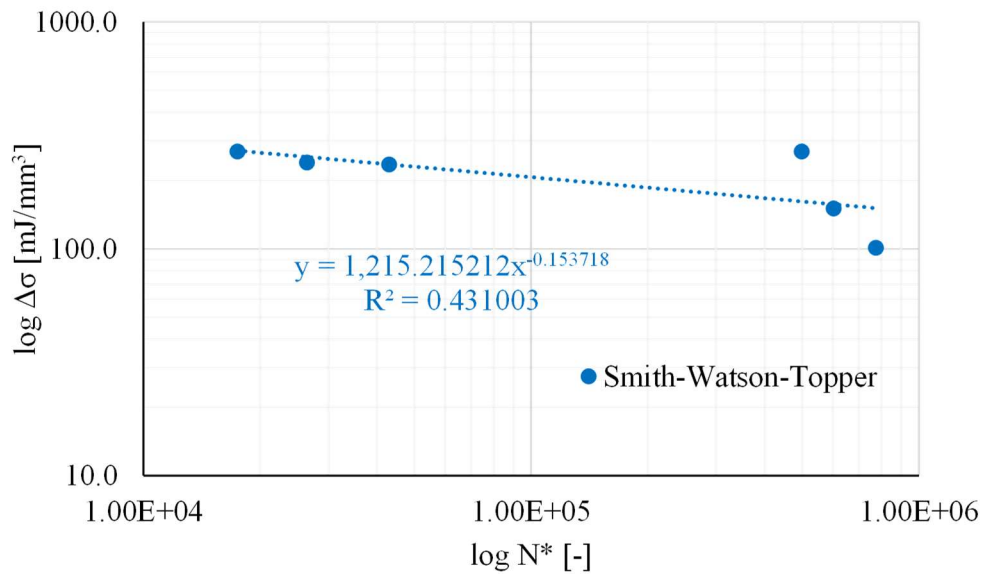
Figure 7.12 Application of the SWT model for investigated hot-driven riveted connections.

Table 7.14 Corrected fatigue results according to Goodman and SWT models.

Label	N*	$\Delta\sigma$	R	σ_m	$\Delta\sigma_{eq,G}$	$\Delta\sigma_{eq,SWT}$
[-]	[-]	[N/mm²]	[-]	[-]	[N/mm²]	[N/mm²]
S-19-12-1-115	602270	106.5	0	53.3	121.4	150.6
S-22-12-1-60	774056	71.4	0	35.7	77.8	101.0
S-22-12-2-160	497964	190.1	0	95.1	243.6	268.8
U-19-10-2-100	42963	166.7	0	83.4	206.4	235.7
U-22-12-2-160	17436	190.1	0	95.1	243.6	268.8
U-22-12-2-144	26357	170.1	0	85.1	211.7	240.6

The plates UTS value for Goodman's formulation was assumed according to experimental outcomes reported in *D'Aniello et al. (2011)*, that is, f_u = 433 N/mm².

It can be immediately noticed how Goodman's method is not able to infer the results in a univocal way, as a significant scatter of corrected experimental points is observed (see Figure 7.11, R^2 = 0.42). Likewise, the application of SWT correction yields equally scattered results (see Figure 7.12, R^2 = 0.43).

Indeed, neither of the above formulations is able to capture the different stress distribution induced by connections configuration.

As for relevant normative fatigue provisions, it is worth recalling that neither the present nor the future version of EN1993:1-9 (*CEN, 2005a, 2020*) provide a dedicated detail category for hot-driven riveted connections.

Nevertheless, as reported in *Section 2.4.3*, earlier drafts of EN1993:1-9 featured two detail categories for riveted joints, namely $\Delta\sigma_C$ = 71 N/mm² for unsymmetric lap-shear joints and $\Delta\sigma_C$ = 90 N/mm² for any type of symmetric joints. In both cases, a constant slope of S-N curves (*m* = 5) is assumed (Equation 7.7 – *CEN, 2005a*).

Fatigue life estimations according to the above detail classes are compared with the proposed formulation in Figure 7.13 and Table 7.15.

It can be noticed that both formulations yield similar results, although the proposed Equation 7.5 is slightly more accurate (e.g., COV = 0.06 for experimental outcomes over prediction ratios, while COV = 0.12 for the EN1993:1-9 formula).

Table 7.15 Fatigue in hot-driven riveted connections: comparison among experimental results, EN1993:1-9 predictions (*CEN, 2005a*) and predictions according to Equation 7.5 (red bars).

Label	$\Delta\sigma$	log N^*_{Exp}	log N^*_{EC3}	log $N^*_{E7.5}$	log N^*_{Exp}/ log N^*_{EC3}	log N^*_{Exp}/ log $N^*_{E7.5}$
[-]	[N/mm^2]	[-]	[-]	[-]	[-]	[-]
S-19-12-1-115	106.5	5.78	5.94*	5.61[+]	0.97	0.97
S-22-12-1-60	71.4	5.89	6.80*	6.50[+]	0.87	1.10
S-22-12-2-160	190.1	5.70	4.68*	5.19[+]	1.22	0.91
U-19-10-2-100	166.7	4.63	4.66**	4.57[++]	0.99	0.99
U-22-12-2-160	190.1	4.24	4.16**	4.29[++]	1.02	1.01
U-22-12-2-144	170.1	4.42	4.60**	4.50[++]	0.96	1.02
				Mean	1.01	1.00
				COV	0.12	0.06

*Detail category 90 N/mm^2
** Detail category 71 N/mm^2
[+]Detail category 84 N/mm^2, k_{eq} = 1.00
[++]Detail category 84 N/mm^2, k_{eq} = 1.30
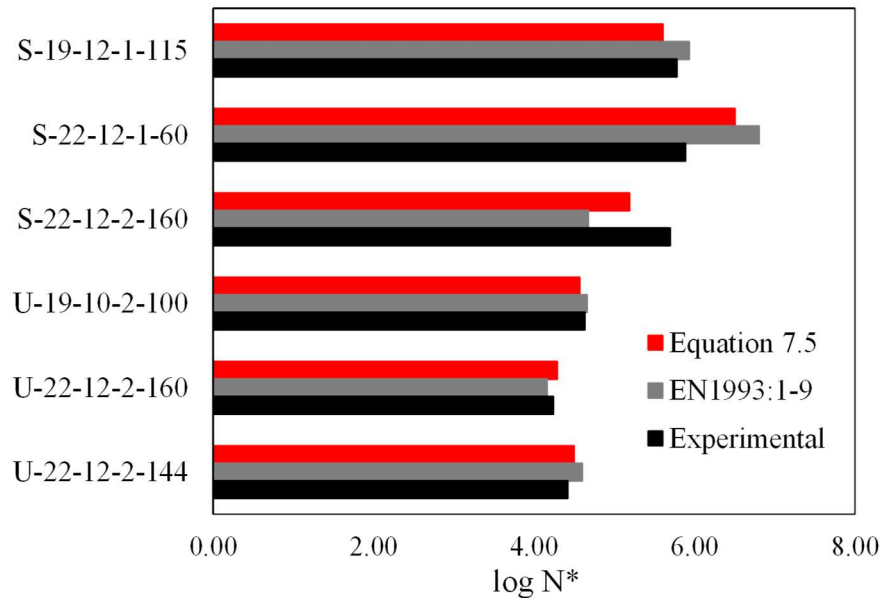
Figure 7.13 Fatigue in hot-driven riveted connections: comparison among experimental results (black bars), EN1993:1-9 predictions (grey bars – CEN, 2005a) and predictions according to Equation 7.5 (red bars).

Interestingly, earlier EN1993:1-9 recommendations accounted in a similar way for connections configurations as respect to the proposed formulation. Indeed, if the ratio among detail categories for symmetric and unsymmetric specimens is extracted, a value of 90/71 = 1.26 is obtained, i.e. rather similar to the proposed value of k_{eq} for unsymmetric connections.

To this end, the two formulations appear equivalent to some extent, although the proposed formulation is slightly more accurate.

Finally, it is interesting to compare the proposed formulation against the stress range correction proposed by *Maljaars & Euler* (*2021*). Indeed, as earlier stated in *Section 3.5*, this formulation will be featured in the next version of EN1993:1-9, which is currently under review (prEN1993:1-9-2020 – *CEN, 2020*).

According to the Authors, $\Delta\sigma_{mod}$ should be estimated as follows (Equation 7.7):

$$\Delta\sigma_{\mathrm{mod}} = k_{\mathrm{mod}}\,\Delta\sigma_{\mathrm{net}} = k_{\mathrm{mod}}\frac{w}{w - d_0}\Delta\sigma \qquad (7.7a)$$

$$k_{\mathrm{mod}} = a + \left(b - c\frac{d_0}{w}\right)^3 \qquad (7.7b)$$

with *a*, *b*, *c* depending on the number of fasters rows (Table 7.16).

Table 7.16 Suggested values of *a*, *b*, *c* for fatigue assessment of non-preloaded fitted bolted connections (*CEN, 2020*; *Maljiars & Euler, 2021*).

Number of rivet rows	*a* [-]	*b* [-]	*c* [-]
1	1.0	1.6	2.7
2	1.0	1.3	2.2
≥ 3	1.0	1.1	1.8

As stated in *Section 3.5*, Equation 7.7 was not intended by *Maljaars & Euler* (*2021*) for hot-driven riveted connections.

Indeed, the above formulation is related to *non-preloaded fitted bolts*, namely with a detail class $\Delta\sigma_C = 71$ N/mm^2. Nevertheless, due to geometrical and mechanical similarities highlighted in *Section 3.5* (e.g., low or negligible clamping stresses and absence of fastener-hole gaps), Equation 7.7 appears a suitable choice for hot-driven lap-shear specimens.

Estimation of fatigue life according to the above formulation is summarized in Figure 7.14 and Table 7.17, where comparisons with Equation 7.5 are also reported.

It can be noticed that prEN1993:1-9-2020 recommendations always yield conservative results, with a mean ratio log N^*_{exp}/log $N^*_{\mathrm{M\&E}} = 1.13$ (COV = 0.13).

Nevertheless, it interesting to notice that *Maljaars & Euler* (*2021*) propose less penalizing coefficients for specimens with multiple rivet rows (Table 7.16).

This outcome complies with preliminary findings for symmetric riveted specimens remarked in *Section 7.2*.
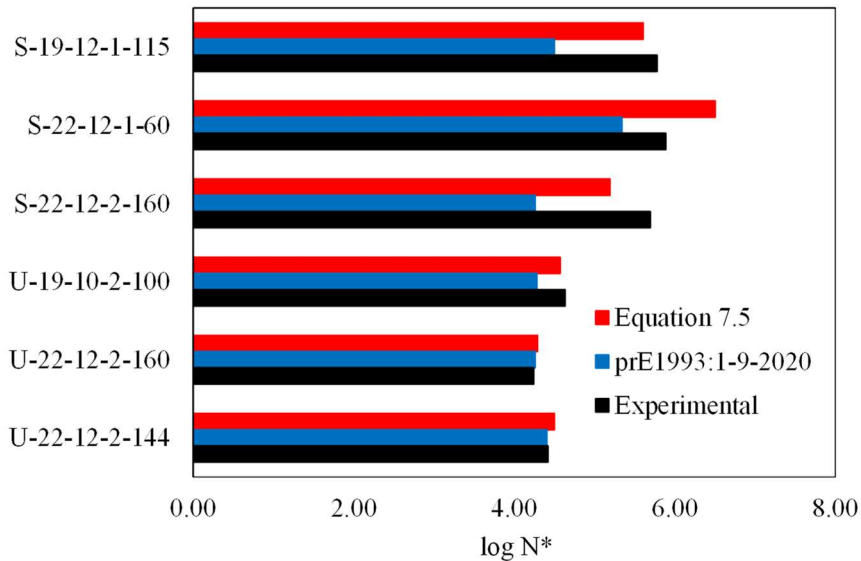
Figure 7.14 Fatigue in hot-driven riveted connections: comparison among experimental results (black bars), prEN1993:1-9-2020 predictions (blue bars – CEN, 2020; Maljaars & Euler, 2021) and predictions according to Equation 7.5 (red bars).

Table 7.17 Fatigue in hot-driven riveted connections: comparison among experimental results, prEN1993:1-9-2020 predictions (CEN, 2020; Maljaars & Euler, 2021 and predictions according to Equation 7.5 (red bars).

Label	$\Delta\sigma$	log N^*_{Exp}	k_{mod}	log $N^*_{M\&E}$	log $N^*_{E7.5}$	log N^*_{Exp}/ log $N^*_{M\&E}$	log N^*_{Exp}/ log $N^*_{E7.5}$
[-]	[N/mm^2]	[-]	[-]	[-]	[-]	[-]	[-]
S-19-12-1-115	106.5	5.78	2.09	4.50	5.61	1.28	0.97
S-22-12-1-60	71.4	5.89	1.42	5.34	6.50	1.10	1.10
S-22-12-2-160	190.1	5.70	1.23	4.26	5.19	1.34	0.91
U-19-10-2-100	166.7	4.63	1.58	4.28	4.57	1.08	0.99
U-22-12-2-160	190.1	4.24	1.23	4.26	4.29	1.00	1.01
U-22-12-2-144	170.1	4.42	1.23	4.41	4.50	1.00	1.02
					Mean	1.13	1.00
					COV	0.13	0.06

Chapter 8

Conclusions and Further Developments

8.1. Main conclusions of the work

In the present Thesis work, the influence of relevant geometrical and mechanical parameters on the static and fatigue performance of lap-shear riveted connections was deeply investigated.

For this purpose, three different sets of experimental activities were accounted for.

The first experimental campaign, which was previously carried out by the Candidate's Research group, aimed at investigating the static performance of hot-driven riveted connections accounting for their geometrical and mechanical peculiarities (*D'Aniello et al., 2011*).

A second set of experimental tests was performed with the aid of the Candidate during his visiting period at the Norwegian University of Science and Technology (NTNU, Trondheim, Norway). Namely, notched coupons made of mild steel were cyclically tested under high stress ratios, thus simulating potential service conditions for fasteners adopted in structural joints.

A successful interpretation of results was hence carried out by means of advanced energetic approaches (SED method – *Lazzarin & Zambardi, 2001; Berto & Lazzarin, 2014*) in spite of the problem complexity (e.g., due to strong mean-stress effect and/or some amount of plasticity).

Therefore, such fatigue analysis techniques were extended to the relevant case of cyclic behaviour of hot-driven riveted connections, namely based on an ongoing experimental campaign performed in collaboration with University of Salerno (UNISA).

In light of *i*) the illustrated theoretical background, *ii*) the assessment of experimental results and *iii*) the proposed formulations, the following concluding remarks can be pointed out:

- In *Chapter 2*, a comprehensive state-of-the-art review about hot-driven riveted connections was presented. The relevance of such structural detail for historical constructions such as bridges, domes or monumental structures was highlighted by means of significative examples.

  Peculiar issues of hot-driven connections were also emphasized, namely with reference to *i*) alteration of base material properties due to hot-driving, *ii*) variability of clamping actions due to shank cooling and *iii*) constructional imperfections such as the camming defect (*Vermes, 2007*).

- In *Chapter 3*, damage and fatigue modelling of hot-driven riveted connections was extensively addressed based on a careful literature review. On one hand, formulations for post-necking plasticity, damage initiation and

evolution were introduced for mild steels (*Hillerborg et al., 1976*, *Tu et al., 2019*, *Yang et al., 2019*). Hence, a two-stage procedure was proposed to quantitatively estimate the effects of hot-driving in investigated connections, e.g., based on comparison of material properties for both undriven and driven components.

On the other hand, most suitable standard and advanced fatigue analysis techniques for hot-driven assemblies were explored. In particular, stress- and strain-life methods were addressed, with a peculiar focus on the influence of mean-stress effect, e.g., relevant for riveted bridge structures (*Dowling, 2004*). Moreover, starting from basic findings from fracture mechanics (*Anderson, 2017*), the theoretical background of the SED method was introduced (*Lazzarin & Zambardi, 2001*; *Berto & Lazzarin, 2014*).
Hot-driven riveted connections proved to be a suitable field of application for such energetic approach due to strong analogies with blunt notched components (U-notches). Namely, free-mesh numerical approaches were deemed suitable for SED calculations (*Foti et al., 2020*) required for fatigue analyses.

- In *Chapter 4*, a detailed description of the three aforementioned test campaigns on mild steel components and aged hot-driven riveted connections was presented. Several key aspects were addressed within the framework of experimental activities, namely: *i*) the influence of geometrical features, *ii*) the impact of hot-driving process (HDP) and *iii*) the effect of stress raisers and elevated stress ratios.
  With regard to static performance of hot-driven riveted connections, a sensible increase of shear resistance was observed in connections failing due to rivet shearing (up to 50% increase as respect to EN1993:1-8 provisions – *CEN,2005b*), while no significant increment was noticed in case of plate failure.
  Contrariwise, a detrimental decrease of ultimate displacements as respect to expected material properties was noticed for all the specimens.
  This outcome suggested that HDP may alter the performance of both rivets and connected plies, although to a different extent (*D'Aniello et al., 2011*).

  As for the cyclic fatigue performance of blunt notched mild steel components, a significant influence of the mean-stress effect was noticed. Namely, a significant flattening of mean S-N curves was observed while ranging from R = 0.7 ÷ 0.9.
  Simultaneously, two parallel, yet separate scatter bands were observed for specimens with different geometry.
  This outcome suggested that a univocal and reliable fatigue analysis for such specimens would have required a careful addressment of both mean-stress and notch effects (*Berto & Lazzarin, 2014*).

  Finally, with respect to the fatigue performance of hot-driven riveted assemblies, a strong sensitivity to connections configuration (i.e., symmetric or unsymmetric) was noticed. For instance, with applied nominal stress ranges being equal, unsymmetric connections exhibited a fatigue life of about one order of magnitude smaller as respect to symmetric ones.

This outcome was plausibly ascribed to the effects of secondary bending moments (*Kulak et al., 1987*).

- In *Chapter 5*, the static performance of hot-driven riveted connections was carefully addressed by means of refined Finite Element Analyses developed in ABAQUS v. 6.14 software (*Dassault, 2014*).
  Numerical analyses enabled to quantify the impact of HDP in terms of alteration of base material properties and the influence of clamping action and geometrical features on the static performance of connections.
  FEAs showed that the ratio between the yield strength of base and hot-driven material ranges between $1.00 \div 1.42$, with a mean value of 1.26 and a significant scatter. Additionally, HDP also induces a significant reduction of the base material ductility. Indeed, the damage initiation strain (*Yang et al., 2019*) of the altered material is 0.56 times lower on average with respect to the base material.

  Based on calibrated FEMs, the effect of one of the most common constructional imperfections found in existing hot-driven riveted constructions ("camming" defects) was also preliminarily discussed with reference to the sole static performance of connections.

  As for the case of symmetric connections, which failed due to different mechanisms (i.e., rivet shearing, plate bearing or tearing in the net-area of the plates), no appreciable reduction of the ultimate capacity due to shank distortion was observed (e.g., the maximum resistance loss was equal to 4%). Contrariwise, significant reductions of ultimate ductility were detected (e.g., the maximum observed reduction was about 10%), namely proportional to the relative shank eccentricity *e/d*.

  Interestingly, the response of unsymmetric connections was found to be sensitive to the orientation of shank distortion. Indeed, connections with "direct" eccentricity (i.e., those having all camming defects in the direction of the applied external force) behaved similarly to symmetric connections, while those with "reverse" eccentricity (i.e., those having all camming defects in the opposite direction of the applied force) exhibited a significant reduction of resistance.
  The results of FEAs showed that loss of shear resistance was mainly caused by an alteration of principal stresses distribution at the onset of plasticity, while post yielding branches of force-displacement curves appeared as almost parallel to each other.
  In line with the ease-of-use philosophy of next generation of Eurocodes, a simple equation was proposed to predict the shear resistance of rivets of connections with camming imperfections. Accordingly, shear resistance linearly decreases with relative shank eccentricity *e/d*.
  The predicted values were in good agreement with numerical results, as testified by a statistic assessment of the proposed formula within the framework of EN1990 (*CEN, 2002*).

- In *Chapter 6*, the fatigue performance of mild steel notched components was investigated based on a numerical interpretation of experimental results.

  For this purpose, a second set of refined FEMs was properly developed within ABAQUS v. 6.14 software (*Dassault, 2014*).

  Fatigue assessment of notched cylinders made of C45 steel grade was preliminarily assessed by means of standard fatigue analysis techniques, namely with the aid of *Goodman* (*1899*) and *Smith, Watson & Topper* (*1970*) models.

  However, both methods did not provide an univocal interpretation of experimental results. Therefore, based on numerical results, an application of energetic fatigue techniques was developed for such specimens.

  Namely, the use of the aforementioned SED method (*Lazzarin & Zambardi, 2001*; *Berto & Lazzarin, 2014*) resulted in a successful interpretation of experimental results, namely accounting for both mean-stress and notch effects. As a result, energetic fatigue approaches has been deemed validated for mild steels, allowing the following extension of such methods to hot-driven riveted splices.

  In order to further investigate the reasons behind the observed fatigue behaviour of notched specimen, a total of 6 × 6 × 8 × 10 = 2880 parametrical FEAs was performed to investigate the influence of circumferential stresses, which are an intrinsic feature distinguishing round notched specimens from flat ones (*Filippi & Lazzarin, 2004; Lazzarin & Filippi, 2006*).

  Accordingly, the difference between axisymmetric circumferential stresses and equivalent plain strain calculations, which are usually adopted for polarly symmetric specimens, was deeply investigated.

  Deviations found were often significant, with differences at the notch radius among -25% ÷ +10% depending on geometrical features (inner to outer diameter ratio d/D, notch opening angle 2α, notch radius ρ).

  Interestingly, averaged deviations on the entire bisector were in the range -40% ÷ +25%, suggesting that highest discrepancies are observed nearby the polar axis. A moderate size effect was also observed.

  For lower values of d/D and 2α (i.e., ≤ 0.6 and $\leq 60°$, respectively) some configurations exhibited higher hoop stresses as respect to simplified plain strain calculations according to elasticity theory.

  In all other cases, hoop stresses are always lower than the corresponding plain strain stresses. This outcome preliminarily suggests an enhanced fatigue performance for round specimens with respect to flat ones and may have useful implications while assessing the fatigue performance of cylindrical fasteners such as rivets or bolts.

- In *Chapter 7*, the fatigue performance of full-scale hot-driven riveted connections was finally investigated by extending the same approaches adopted for mild steel components.

  Namely, the SED method was employed to derive a fatigue design formulation for hot-driven splices accounting for geometrical and mechanical peculiarities.

  To this end, a preliminary numerical study on the influence of clamping actions in terms of stresses and strain energies nearby rivet holes was carried out.

Accordingly, unsymmetric specimen may benefit more significantly from the influence of clamping action, mainly because of the different through thickness distribution of principal stresses induced by preloading.

For instance, strain energy density values at the hole quadrant due to clamping are of one order of magnitude higher as respect to symmetric connections with same preloading.

Nevertheless, this effect was deemed to be of minor importance owing to *i*) the randomness and low entity of clamping in hot-driven rivets (*Leonetti et al., 2020*) and *ii*) the detrimental effect of secondary bending moments.

ASED calculations for hot-driven connections resembling experimental trials provided a good interpretation of tests results, in spite of the small size of the sample (3 × 2 specimens).

Accordingly, a first SED-based fatigue curve was derived for considered specimens. Nevertheless, in line with the ease-of-use philosophy of next generation of Eurocodes, a preliminary stress-based correction was developed for hot-driven assemblies.

Namely, on the basis of theoretical background for U-notches (*Berto & Lazzarin, 2014*), equivalent stress magnification factors (SMFs) were derived for each configuration. Remarkably, such SMFs proved to be higher for unsymmetric specimens (1.18 ÷ 1.42) as respect to symmetric ones (0.78 ÷ 1.26), e.g., suggesting that the detrimental influence of secondary bending overcome the beneficial effect of clamping for such configurations.

Accordingly, a stress based S-N curve was provided, i.e., having equivalent detail class $\Delta\sigma_{C,eq} = 84$ N/mm^2 and (log-)slope $m = 4.3$.

The mean value of the above SMFs was assumed as non-dimensional parameter accounting for the influence of connections configurations. Accordingly, $k_{eq} = 1.00$ and $k_{eq} = 1.30$ were assumed to correct nominal stress ranges referred the gross plates cross-sections.

The validity of the proposed formulation was assessed against literature and normative provisions, highlighting similar remarks as respect to earlier drafts of EN1993:1-9 (i.e., ≈ 1.3 ÷ 1.0 ratio in terms of fatigue strength for symmetric and unsymmetric details – *CEN, 2005a*).

Moreover, similarities were also found as respect to the prEN1993:1-9-2020 draft recommendations for non-preloaded fitted bolts (*CEN, 2020*), which can be approximately assimilated to hot-driven rivets owing to *i*) small magnitude of clamping stress and *ii*) absence of rivet-hole gaps.

Accordingly, a more favorable performance for specimens with multiple bolts is assumed. This outcome complied with SMFs values for symmetric specimens with two rivets, as they are lower than corresponding factors for single rivet connections (-26% on average).

Nevertheless, in light of the small size of the experimental sample, no definitive conclusions can be drawn to this end, and hence further investigations are needed.

8.2. Possible further research developments

8.2.1 Fatigue tests on historical mild steel coupons

As stated in *Section 3.4*, a more accurate approach to the stress- or strain-life fatigue assessment of hot-driven riveted connections can be addressed by properly calibrating Baquins' (*1910*) and BMC (*Manson, 1953*; *Coffin, 1954*) parameters for base plates and rivets material.

To this end, a further extension of the experimental campaign on hot-driven connections has been designed and it is currently ongoing.

In the present Section, experimental activities being carried out for the characterization of the fatigue behaviour of historic mild steels are summarized.

Experimental tests are being performed at SOLOGEA LAB test laboratory (Caserta, Italy) under the supervision of the Candidate.

In particular, the extension of the present experimental campaign aims at *i*) investigating the stress- and strain-life behaviour of historical mild steel, that is, calibrating Basquin and BMC parameters and *ii*) estimating the actual value of control volume radius R_0 in cyclic conditions for a more rational application of the SED method.

Namely, smooth and pierced specimens have been designed and were derived from the same pristine plates adopted for hot-driven riveted assemblies (*Section 4.3*)

2×2 different configurations of flat specimens are being used for the fatigue characterization of historical mild steel, for a total of 22 (15 + 7) specimens.

In particular, the four geometries differ in terms of plate thickness t and presence or absence of a 4 mm drilled hole (Table 8.1).

Geometrical features for specimens being tested are depicted in Figure 8.1.
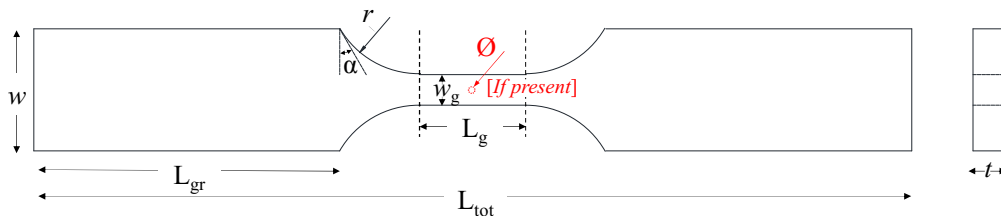
Figure 8.1 Geometrical features of flat smooth/pierced specimens of historical mild steel.

Table 8.1 Geometrical features of flat smooth/pierced specimens of historical mild steel.

	Configurations I/II	Configurations III/IV
Grip width w [mm]	40	50
Grip length L_{gr} [mm]	100	120
Transition radius r [mm]	30	38
Transition angle α [°]	30	30
Gauge width w_g [mm]	10	12
Gauge length L_g [mm]	35	42
Thickness t [mm]	10	12
Total length L_{tot} [mm]	287	348
Hole diameter Ø [mm]	Not present (I) – 4 (II)	Not present (III) – 4 (IV)

Adopted smooth configurations are compliant with *ASTM E606* (*2012*) recommendations. All relevant geometrical features have been designed in function of

the specimen thickness *t*, which was consistently set equal to the thickness of plates adopted for hot-driven riveted connections (i.e., *t* = 10 or 12 mm, respectively).

Moreover, 4 mm holes were drilled in pierced specimens to introduce a stress raising source, which can be regarded as an equivalent U-notch (*Radaj & Vormwald, 2013*).

The specimens characterized by the same geometry are all nominally identical and made of the same historical mild steel adopted for plates.

In the next Sections, the following key aspects related to performed experimental activities are addressed, namely:

Compatibly with the characteristics of the base material, a constant test frequency f_{test} = 5 Hz is assumed for all fatigue tests.

The plan for the experimental campaign was defined in order to provide a sufficient number of stress/strain range levels to calibrate Basquin and BMC model parameters.

In order to avoid cyclic buckling of specimens during fatigue tests, zero-to-tension load cycles (R = 0) were adopted as allowed by *ASTM E606* (*2012*).

The stress/strain ranges $\Delta\sigma/\Delta\varepsilon$ of concern were determined based on the characterization of the static properties reported in *D'Aniello et al.* (*2011*) as respect to the same historical mild steel. Accordingly, subsequent fatigue tests are being performed assuming aliquots of the ultimate load compliant with the desired number of points in Wohler and strain-life diagrams.

An appropriate labelling was also defined for each of the ongoing experimental tests. As all specimens are compliant with *ASTM E606* (*2012*) provisions, plate thickness and hole diameter (if present) can be used to univocally describe their geometry. Moreover, encoding relevant load parameters the following nomenclature was adopted, namely:

Labelling "FAABCCDD" with:

F = Fatigue test (i.e., load-controlled, composed by an initial ramp up to the mean stress σ_m and by a superimposed constant-amplitude, sinusoidal wave with range $\Delta\sigma$);

AA = 10 or 12 in reference to the plate thickness *t*;

B = S or P with reference to smooth or pierced specimens, respectively;

CC = 01, 02, ..., 05 with reference to the selected stress/strain range, i.e., increasing with increasing values of $\Delta\sigma/\Delta\varepsilon$;

DD = 01, 02, etc... with reference to order of performed tests, i.e., increasing for multiple tests having the same stress/strain range.

Table 8.2 summarizes the tests carried out according to the above indications. Load protocols are expressed in terms of forces, stress and strain ranges.

It is worth noting that stress and strain ranges are intended as nominal quantities referred to the gauge segment. In case of pierced specimens, $\Delta\sigma$ were conventionally calculated for the minimum notched cross section.

Table 8.2 Summary of fatigue tests on historic mild steel flat specimens.

Label	Test #	*t*	Hole	$F_{max} = \Delta F$	$\Delta\sigma$	$\Delta\varepsilon$
[-]	[-]	[mm]	[mm]	[kN]	[N/mm²]	[-]
F10S0101	1	10.0	NO	20.0	200.0	0.0011
F10S0102	2	10.0	NO	20.0	200.0	0.0011
F10S0103	3	10.0	NO	20.0	200.0	0.0011
F10S0201	1	10.0	NO	25.0	250.0	0.0023

F10S0202	2	10.0	NO	25.0	250.0	0.0023
F10S0203	3	10.0	NO	25.0	250.0	0.0023
F10S0301	1	10.0	NO	30.0	300.0	0.0060
F10S0302	2	10.0	NO	30.0	300.0	0.0060
F10S0303	3	10.0	NO	30.0	300.0	0.0060
F10S0401	1	10.0	NO	35.0	350.0	0.0168
F10S0402	2	10.0	NO	35.0	350.0	0.0168
F10S0403	3	10.0	NO	35.0	350.0	0.0168
F10S0501	1	10.0	NO	40.0	400.0	0.0449
F10S0502	2	10.0	NO	40.0	400.0	0.0449
F10S0503	3	10.0	NO	40.0	400.0	0.0449
F10P0101	1	10.0	4.0	12.0	200.0	-
F10P0102	2	10.0	4.0	12.0	200.0	-
F12P0101	1	12.0	4.0	14.0	210.0	-
F12P0202	2	12.0	4.0	17.0	255.0	-
F12P0301	1	12.0	4.0	17.0	255.0	-
F12P0302	2	12.0	4.0	20.0	300.0	-
F12P0303	3	12.0	4.0	20.0	300.0	-

8.2.2 Influence of constructional imperfections on the fatigue performance of hot-driven riveted connections

In *Section 5.5*, the influence of constructional imperfections on the static performance of hot-driven riveted connections was thoroughly investigated by means of refined FEAs. As highlighted by numerical results, stress distributions in connected elements are strongly influenced by distortions such as camming defects.

Therefore, a further extension concerning the influence of constructional imperfection on the fatigue performance of hot-driven riveted connections has been planned.

For instance, preliminary studies on the cyclic performance of hot-driven riveted connections belonging to an existing riveted bridge located in Italy (*Milone, 2022a*) highlighted how camming defect can create new potential fracture spots nearby shank discontinuities (Figure 8.2).

a)

b)
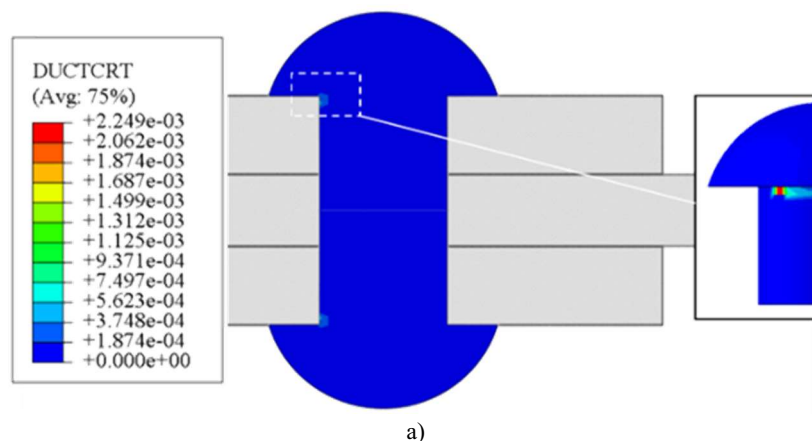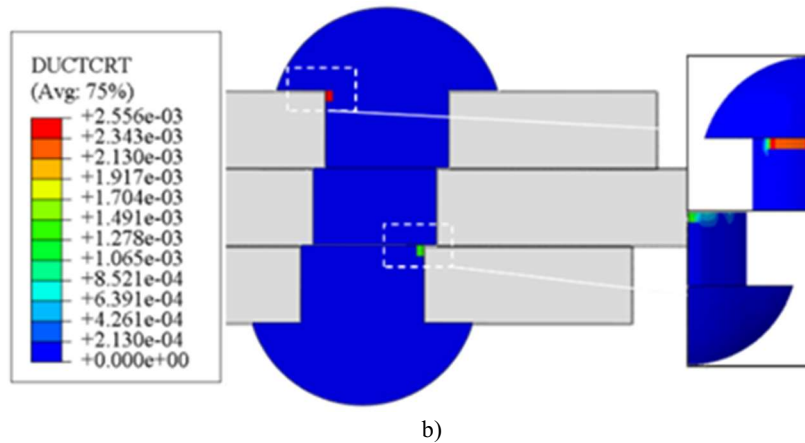
Figure 8.2 Preliminary study on the influence of camming defect on the fatigue behaviour of hot-driven splices: damage initiation due to cyclic loads in a) pristine specimen (S-16-10-1-0.00) and b) distorted specimen (S-16-10-1-0.20-D) (*Milone, 2022a*).

Namely, the following preliminary remarks were pointed out:

- The fatigue behaviour of hot-driven riveted joints is significantly influenced from shank eccentricity in terms of stress alteration in connected elements;
- Higher values of *e*/*d* lead to higher damages and potential development of new fracture locations nearby shank discontinuities;
- A low rivet slenderness *t*/*d* may play a role in penalizing fatigue performance of specimens.

Therefore, further numerical studies will be carried out, plausibly within the framework of the SED method.

Appendix

Python/ABAQUS Scripts

Parametrical FEAs on blunt V-notched components

```python
# Importing ABAQUS Programming language
# -*- coding: utf-8 -*-

from part import *
from material import *
from section import *
from assembly import *
from step import *
from interaction import *
from load import *
from mesh import *
from optimization import *
from job import *
from sketch import *
from visualization import *
from connectorBehavior import *
from odbAccess import *
#import os
#import sys

# Defining Function for Parametrical Analysis (Mesh Sensitivity)

def Create_Model_Run_Analysis(D,d,Two_alfa,r,k_R):

    L = D # L Length of the Grip
    # D Outer Diameter
    # d Inner Diameter
    # Two_alfa Opening Angle
    # r Notch radius
    # k_R Mesh Size Parameter
    # Importing Abaqus Modules in Python

    # Defining Parameters for Analysis
    # Lenghts in mm, Angles in deg, Forces in N

    import numpy as np # Importing Numpy Library

    E_s=210000.0 # Young Modulus
    ni=0.3 # Poisson's constant

    alfa=np.radians(90.0-Two_alfa/2)

    # Name of the Model/Instance/Job...

    import math

    # Splitting D for Labelling

    if int(D) == D:
        mant_D = 0
    else:
        digit_D = int(math.log10(D))+1
        tot_D = len(str(D))
        m_D = 10**(tot_D-digit_D-1)
        n_D = str(int(D*m_D))
        end_D = len(n_D)
        mant_D = n_D[digit_D:end_D]

    # Splitting d for Labelling
```

```
if int(d) == d:
    mant_d = 0
else:
    digit_d = int(math.log10(d))+1
    tot_d = len(str(d))
    m_d = 10**(tot_d-digit_d-1)
    n_d = str(int(d*m_d))
    end_d = len(n_d)
    mant_d = n_d[digit_d:end_d]

# Splitting r for Labelling

n_r = str(r)
end_r = len(n_r)
mant_r = n_r[2:end_r]

MyName = 'C45-'+str(int(D))+','+str(mant_D)+'-'+str(int(d))+','+str(mant_d)+'-'+str(int(Two_alfa))+'-
'+str(int(r))+','+str(mant_r)+'-'+str(int(k_R))
MyNameMod = 'Model-'+MyName
MyNameSkt = 'Sketch-'+MyName
MyNamePar = 'Part-'+MyName
MyNameIns = MyName
MyNameJob = MyName
MyNamePrt = 'P'+MyName

# Sketching Part -> First Parametric Input

x_a = 0.0
y_a = 0.0

x_b = D/2
y_b = y_a

x_c = x_b
y_c = L

x_d = d/2+r*(1-np.cos(alfa))
y_d = (D-d-2*r)/(2*np.tan(alfa))+L+r*np.cos(alfa)/np.tan(alfa)

x_e = d/2
y_e = (D-d-2*r)/(2*np.tan(alfa))+L+r/np.sin(alfa)

x_d2 = x_e + r*(1-np.cos(alfa/2))
y_d2 = y_e - r*np.sin(alfa/2)

x_f = x_a
y_f = y_e


mdb.Model(modelType=STANDARD_EXPLICIT, name=MyNameMod)
mdb.models[MyNameMod].ConstrainedSketch(name=MyNameSkt, sheetSize=200.0)
mdb.models[MyNameMod].sketches[MyNameSkt].sketchOptions.setValues(viewStyle=AXISYM) #Visualization
Option for Axisymmetric Models
mdb.models[MyNameMod].sketches[MyNameSkt].ConstructionLine(point1=(0.0,-100.0), point2=(0.0,100.0)) #
Axis of Symmetry
mdb.models[MyNameMod].sketches[MyNameSkt].Line(point1=(x_a, y_a), point2=(x_b,y_b)) # First H Segment
(Outer Diameter)
mdb.models[MyNameMod].sketches[MyNameSkt].Line(point1=(x_b,y_b), point2=(x_c,y_c)) # First V Segment
(Outer Grip)
mdb.models[MyNameMod].sketches[MyNameSkt].Line(point1=(x_c,y_c), point2=(x_d,y_d)) # Sloped Segment
mdb.models[MyNameMod].sketches[MyNameSkt].Arc3Points(point1=(x_d,y_d), point2=(x_e, y_e),
point3=(x_d2,y_d2)) # Circle for Blunt Notch
mdb.models[MyNameMod].sketches[MyNameSkt].Line(point1=(x_e, y_e), point2=(x_f, y_f)) # Last H Segment
(Inner Diameter)
mdb.models[MyNameMod].sketches[MyNameSkt].Line(point1=(x_f, y_f), point2=(x_a, y_a)) # Closing the Sketch

# Part Creation
mdb.models[MyNameMod].Part(dimensionality=AXISYMMETRIC, name=MyNamePar, type=
    DEFORMABLE_BODY)
mdb.models[MyNameMod].parts[MyNamePar].BaseShell(sketch=
    mdb.models[MyNameMod].sketches[MyNameSkt])
del mdb.models[MyNameMod].sketches[MyNameSkt]

# Materials Definition and Section
```

```
mdb.models[MyNameMod].Material(name='Elastic Steel')
mdb.models[MyNameMod].materials['Elastic Steel'].Elastic(table=((E_s, ni), ))

#mdb.models[MyNameMod].materials['Material-1'].Plastic(hardening=COMBINED,     ->
ISOTROPIC/KINEMATIC...
    #table=((sigma_true, eps_plastic_true), (..., ...), (..., ...)))   # Plasticity (if Needed)

mdb.models[MyNameMod].HomogeneousSolidSection(material='Elastic Steel', name='C45', thickness=None)
mdb.models[MyNameMod].parts[MyNamePar].SectionAssignment(offset=0.0, offsetField='',
offsetType=MIDDLE_SURFACE,
region=Region(faces=mdb.models[MyNameMod].parts[MyNamePar].faces.getByBoundingBox(-0.1,-0.1,-
0.1,D/2+0.1,(D-d-2*r)/(2*np.tan(alfa))+L+r/np.sin(alfa)+0.1,0.1)), sectionName='C45',
thicknessAssignment=FROM_SECTION)
    # Assigning Section Properties # Selection was made by
getByBoundingBox(x_min,y_min,z_min,x_max,y_max,z_max) command

    # Instance Creation
    mdb.models[MyNameMod].rootAssembly.DatumCsysByThreePoints(coordSysType=
        CYLINDRICAL, origin=(0.0, 0.0, 0.0), point1=(1.0, 0.0, 0.0), point2=(0.0,
        0.0, -1.0))
    mdb.models[MyNameMod].rootAssembly.Instance(dependent=OFF, name=MyNameIns,
        part=mdb.models[MyNameMod].parts[MyNamePar])

    # Creating Sets for Boundary Conditions

    mdb.models[MyNameMod].rootAssembly.Set(edges=
        mdb.models[MyNameMod].rootAssembly.instances[MyNameIns].edges.findAt(((0.0,L/2,0),)), name='Left') #
Left Edge # Selection was made by findAt(((x,y,z),))
    mdb.models[MyNameMod].rootAssembly.Set(edges=
        mdb.models[MyNameMod].rootAssembly.instances[MyNameIns].edges.findAt(((D/4,0,0),)), name='Bottom') #
Bottom Edge # ""
    mdb.models[MyNameMod].rootAssembly.Set(edges=
        mdb.models[MyNameMod].rootAssembly.instances[MyNameIns].edges.findAt(((d/4,(D-d-
2*r)/(2*np.tan(alfa))+L+r/np.sin(alfa),0),)), name='Up') # Upper Edge # ""
    mdb.models[MyNameMod].rootAssembly.Set(edges=
        mdb.models[MyNameMod].rootAssembly.instances[MyNameIns].edges.findAt(((D/2,L/2,0),)), name='Right') #
Right Edge # ""
    mdb.models[MyNameMod].rootAssembly.Set(edges=
        mdb.models[MyNameMod].rootAssembly.instances[MyNameIns].edges.findAt((((x_c+x_d)/2,(y_c+y_d)/2,0),)),
name='Sloped') # Sloped Edge # ""
    mdb.models[MyNameMod].rootAssembly.Set(edges=
        mdb.models[MyNameMod].rootAssembly.instances[MyNameIns].edges.findAt(((x_d2,y_d2,0),)), name='Round')
# Round Edge # ""

    # Creating Surfaces for Boundary Conditions

    mdb.models[MyNameMod].rootAssembly.Surface(name='LowSurf', side1Edges=
        mdb.models[MyNameMod].rootAssembly.instances[MyNameIns].edges.findAt(((D/4,0,0),))) # Lower Surface for
Applied Loads # Detected using findAt(((x,y,z),))

    # Assigning FE Type

mdb.models[MyNameMod].rootAssembly.setElementType(elemTypes=(ElemType(elemCode=CAX8,
elemLibrary=STANDARD),),
    regions=(mdb.models[MyNameMod].rootAssembly.instances[MyNameIns].faces.getByBoundingBox(-0.1,-0.1,-
0.1,x_b+0.1,y_e+0.1,0.1), )) # Detected using getByBoundingBox
    # CAX8: ABQ Standard Library, Axisymmetric Quad Element, Quadratic Geometry, Standard Integration

    # Assigning Global & Local Seeds

    L_R = r*alfa # Length of the Half-Notch for Proportion

    L_up = L_R - r*(1-np.cos(alfa)) # Length of Upper Square Side
    L_down = L_R # Length of Lower Square Side
    L_sx = y_e - y_d # Length of Left Square Side
    L_H = x_e - L_R # Length of the Upper H Segment
    L_grip = D # Lenght of the H Grip Zone

    rat_SV = 15 # Ratio for Bias Seeding of Edges (20 -> /7; 15 -> /5; 10 -> /4)

    k_S = max(min(int(k_R*L_H/L_R/5),10000),100-k_R) # Number of Elements for Other Segments
    k_up = int(k_R*L_up/L_R) # Number of Elements for USS
    k_sx = int(k_R*L_sx/L_R) # Number of Elements for LSS
    k_grip = int(k_R*L_grip/L_R) # NUmber of Elements for HGZ
```

```
#L_S = ((x_c-x_d)**2+(y_c-y_d)**2)**(0.5) # Length of Sloped Segments
#L_V = y_f - y_d # Length of the Vertical Segment

# Central Point Abscissa

x_p = x_d - L_R

# Seeding Global Instance

mdb.models[MyNameMod].rootAssembly.seedPartInstance(deviationFactor=0.1,
    minSizeFactor=0.1, regions=(
    mdb.models[MyNameMod].rootAssembly.instances[MyNameIns], ), size=L_grip/k_grip*8)

# Sketching Partition for Mesh

mdb.models[MyNameMod].ConstrainedSketch(name=MyNamePrt, sheetSize=200.0)
mdb.models[MyNameMod].sketches[MyNamePrt].Line(point1=(d/2+r*(1-np.cos(alfa)),(D-d-
2*r)/(2*np.tan(alfa))+L+r*np.cos(alfa)/np.tan(alfa)),
    point2=(d/2-L_R+r*(1-np.cos(alfa)),(D-d-2*r)/(2*np.tan(alfa))+L+r*np.cos(alfa)/np.tan(alfa))) # Sketch: First H
Segment from Notch End
mdb.models[MyNameMod].sketches[MyNamePrt].Line(point1=(d/2-L_R+r*(1-np.cos(alfa)),(D-d-
2*r)/(2*np.tan(alfa))+L+r*np.cos(alfa)/np.tan(alfa)),
    point2=(d/2-L_R+r*(1-np.cos(alfa)),(D-d-2*r)/(2*np.tan(alfa))+L+r/np.sin(alfa))) # Sketch: First V Segment from
Middle
mdb.models[MyNameMod].sketches[MyNamePrt].Line(point1=(d/2-L_R+r*(1-np.cos(alfa)),(D-d-
2*r)/(2*np.tan(alfa))+L+r*np.cos(alfa)/np.tan(alfa)),
    point2=(0.0,L)) # Sketch: Connecting Segment
mdb.models[MyNameMod].sketches[MyNamePrt].Line(point1=(0.0,L),
    point2=(D/2,L)) # Sketch: Last H Segment from Grip to Axis

# Partitioning From Sketch

mdb.models[MyNameMod].rootAssembly.PartitionFaceBySketch(faces=
mdb.models[MyNameMod].rootAssembly.instances[MyNameIns].faces.getByBoundingBox(-0.1,-0.1,-
0.1,x_b+0.1,y_e+0.1,0.1),
    sketch=mdb.models[MyNameMod].sketches[MyNamePrt])

# Seeding Edges
# If the V/H ratio of the second region exceeds 77, seeds on H and I segments should be released

V_H_ratio = (y_d-y_c)/(x_d-x_p)
V_H_limit = 77.0

if V_H_ratio < V_H_limit:
    k_grip_corr = k_grip/8
else:
    k_grip_corr = k_grip/20

mdb.models[MyNameMod].rootAssembly.seedEdgeByBias(biasMethod=SINGLE,
    constraint=FINER,
end1Edges=mdb.models[MyNameMod].rootAssembly.instances[MyNameIns].edges.findAt(((x_p/2,y_e,0),)),
number=k_S, ratio=rat_SV) # Segment A
mdb.models[MyNameMod].rootAssembly.seedEdgeByNumber(constraint=FINER,
    edges=mdb.models[MyNameMod].rootAssembly.instances[MyNameIns].edges.findAt((((x_e+x_p)/2,y_e,0),)),
number=k_up) # Segment B
mdb.models[MyNameMod].rootAssembly.seedEdgeByNumber(constraint=FINER,
    edges=mdb.models[MyNameMod].rootAssembly.instances[MyNameIns].edges.findAt(((x_p,(y_d+y_e)/2,0),)),
number=k_sx) # Segment C
mdb.models[MyNameMod].rootAssembly.seedEdgeByNumber(constraint=FINER,
    edges=mdb.models[MyNameMod].rootAssembly.instances[MyNameIns].edges.findAt(((x_d2, y_d2,0),)),
number=k_R) # Segment D
mdb.models[MyNameMod].rootAssembly.seedEdgeByNumber(constraint=FINER,
    edges=mdb.models[MyNameMod].rootAssembly.instances[MyNameIns].edges.findAt(((x_d-L_down/2,y_d,0),)),
number=k_R) # Segment E
mdb.models[MyNameMod].rootAssembly.seedEdgeByBias(biasMethod=SINGLE,
    constraint=FINER,
end1Edges=mdb.models[MyNameMod].rootAssembly.instances[MyNameIns].edges.findAt(((x_p/2,(y_c+y_d)/2, 0),)),
number=k_S, ratio=rat_SV) # Segment F
mdb.models[MyNameMod].rootAssembly.seedEdgeByBias(biasMethod=SINGLE,
    constraint=FINER,
end2Edges=mdb.models[MyNameMod].rootAssembly.instances[MyNameIns].edges.findAt((((x_c+x_d)/2,(y_c+y_d)/2
,0),)), number=k_S, ratio=rat_SV) # Segment G
mdb.models[MyNameMod].rootAssembly.seedEdgeByNumber(constraint=FREE,
```

```
        edges=mdb.models[MyNameMod].rootAssembly.instances[MyNameIns].edges.findAt((((x_c)/2,y_c,0),)),
number=k_grip_corr)  # Segment H (Grip Up)
    mdb.models[MyNameMod].rootAssembly.seedEdgeByNumber(constraint=FREE,
        edges=mdb.models[MyNameMod].rootAssembly.instances[MyNameIns].edges.findAt((((x_a+x_b)/2,y_a,0),)),
number=k_grip_corr/4)  # Segment I (Grip Down)

    # Assigning Structured Mesh to All Elements

    mdb.models[MyNameMod].rootAssembly.setMeshControls(regions=
        mdb.models[MyNameMod].rootAssembly.instances[MyNameIns].faces.getByBoundingBox(-0.1,-0.1,-
0.1,x_b+0.1,y_e+0.1,0.1), technique=STRUCTURED)

    # Introducing Sweep Method where needed
    # If one of the i-th angles is below 10.44 degrees, the i-th Region should be meshed with FREE - MEDIAL AXIS
algorithm

    beta2 = np.arctan((y_d-y_c)/x_p) # Left H Angle
    beta1 = np.pi/2 - beta2 # Left V Angle
    beta3 = np.pi/2 - alfa # Right H Angle

    beta_lim = np.deg2rad(10.44) # Limit (Empirical...)

    if beta1 < beta_lim:
        mdb.models[MyNameMod].rootAssembly.setMeshControls(regions=
            mdb.models[MyNameMod].rootAssembly.instances[MyNameIns].faces.findAt(((x_p/2,y_d,0),)),
technique=FREE, algorithm=MEDIAL_AXIS) # STRUCTURED is selected if SWEEP is unavailable
    else:
        mdb.models[MyNameMod].rootAssembly.setMeshControls(regions=
            mdb.models[MyNameMod].rootAssembly.instances[MyNameIns].faces.findAt(((x_p/2,y_d,0),)),
technique=SWEEP) # First Region (CEF)

    if beta2 < beta_lim or beta3 < beta_lim:
        mdb.models[MyNameMod].rootAssembly.setMeshControls(regions=
            mdb.models[MyNameMod].rootAssembly.instances[MyNameIns].faces.findAt(((x_p,(y_c+y_d)/2,0),)),
technique=FREE, algorithm=MEDIAL_AXIS) # STRUCTURED is selected if SWEEP is unavailable
    else:
        mdb.models[MyNameMod].rootAssembly.setMeshControls(regions=
            mdb.models[MyNameMod].rootAssembly.instances[MyNameIns].faces.findAt(((x_p,(y_c+y_d)/2,0),)),
technique=SWEEP) # Second Region (EFC)

    mdb.models[MyNameMod].rootAssembly.setMeshControls(regions=

            mdb.models[MyNameMod].rootAssembly.instances[MyNameIns].faces.findAt((((x_p+x_e)/2,(y_d+y_e)/2,0
),)), technique=SWEEP) # Third Region (Square)

    # Generating Mesh

    mdb.models[MyNameMod].rootAssembly.generateMesh(regions=(
        mdb.models[MyNameMod].rootAssembly.instances[MyNameIns], ))

    # Creating a Step

    mdb.models[MyNameMod].StaticStep(maxNumInc=1000000, name='Load', nlgeom=OFF,
        previous='Initial') # Static Step: Load # Geometric Non-Linearity: OFF # Maximum Number of Increments = 10^6

    # Assigning Boundary Conditions

    mdb.models[MyNameMod].DisplacementBC(amplitude=UNSET, createStepName='Initial',
        distributionType=UNIFORM, fieldName='', fixed=OFF, localCsys=None, name=
        'Up', region=mdb.models[MyNameMod].rootAssembly.sets['Up'], u1=UNSET, u2=
        0.0, ur3=UNSET) # Upper Edge: U2 = 0 (Symmetry Condition)
    mdb.models[MyNameMod].DisplacementBC(amplitude=UNSET, createStepName='Initial',
        distributionType=UNIFORM, fieldName='', fixed=OFF, localCsys=None, name=
        'Left', region=mdb.models[MyNameMod].rootAssembly.sets['Left'], u1=0.0,
        u2=UNSET, ur3=UNSET) # Left Edge: U1 = 0 (Symmetry Condition)
    mdb.models[MyNameMod].Pressure(amplitude=UNSET, createStepName='Load',
        distributionType=UNIFORM, field='', magnitude=-1.0, name='LowLoad', region=
        mdb.models[MyNameMod].rootAssembly.surfaces['LowSurf']) # Lower Edge: Tensile Pressure

    # Applying SED Method for Blunt V Notch

    R_0 = 0.39 # Radius of the Control Volume for Sharp Notch, L in mm
    r_0 = r*(np.pi - np.radians(Two_alfa))/(2*np.pi - np.radians(Two_alfa)) # Distance from the Notch Tip
    R_1 = R_0 + r_0 # Radius of Cylinder
```

```
    mdb.models[MyNameMod].rootAssembly.Set(elements=

mdb.models[MyNameMod].rootAssembly.instances[MyNameIns].elements.getByBoundingCylinder(center1=(x_e +
r_0, y_e, -0.1),center2=(x_e + r_0, y_e, +0.1),radius=R_1), name='SED') # Creating SET for Strain Energy Density
Measure
    mdb.models[MyNameMod].HistoryOutputRequest(createStepName='Load', name='SED', rebar=EXCLUDE,
region=
        mdb.models[MyNameMod].rootAssembly.sets['SED'], sectionPoints=DEFAULT,
        variables=('ALLSE', 'VOL')) # Tracking Strain Energy (Non Averaged) and Volume for SED

    # Defining the Job and Submitting

    mdb.Job(atTime=None, contactPrint=OFF, description='', echoPrint=OFF,
        explicitPrecision=SINGLE, getMemoryFromAnalysis=True, historyPrint=OFF,
        memory=80, memoryUnits=PERCENTAGE, model=MyNameMod, modelPrint=OFF,
        multiprocessingMode=DEFAULT, name=MyNameJob, nodalOutputPrecision=SINGLE,
        numCpus=4, numDomains=4, numGPUs=0, queue=None, resultsFormat=ODB, scratch=
        '', type=ANALYSIS, userSubroutine='', waitHours=0, waitMinutes=0)
    mdb.jobs[MyNameJob].submit(consistencyChecking=OFF)
    mdb.jobs[MyNameJob].waitForCompletion()

def Open_ODB_and_Write_To_Text(D,d,Two_alfa,r,k_R):

    import math
    import numpy as np

    E_s=210000.0 # Young Modulus
    ni=0.3 # Poisson's constant

    L = D # Setting L as a f(D)

    # Splitting D for Labelling

    if int(D) == D:
        mant_D = 0
    else:
        digit_D = int(math.log10(D))+1
        tot_D = len(str(D))
        m_D = 10**(tot_D-digit_D-1)
        n_D = str(int(D*m_D))
        end_D = len(n_D)
        mant_D = n_D[digit_D:end_D]

    # Splitting d for Labelling

    if int(d) == d:
        mant_d = 0
    else:
        digit_d = int(math.log10(d))+1
        tot_d = len(str(d))
        m_d = 10**(tot_d-digit_d-1)
        n_d = str(int(d*m_d))
        end_d = len(n_d)
        mant_d = n_d[digit_d:end_d]

    # Splitting r for Labelling

    n_r = str(r)
    end_r = len(n_r)
    mant_r = n_r[2:end_r]

    # Labelling Job and Defining Notch Ordinate

    MyNameJob = 'C45-'+str(int(D))+','+str(mant_D)+'-'+str(int(d))+','+str(mant_d)+'-'+str(int(Two_alfa))+'-
'+str(int(r))+','+str(mant_r)+'-'+str(int(k_R))
    alfa=np.radians(90.0-Two_alfa/2)
    y_e = (D-d-2*r)/(2*np.tan(alfa))+L+r/np.sin(alfa)

    # Opening ODB file and Viewport

    odb1 = session.openOdb(str(MyNameJob)+'.odb')
    session.Viewport(name='Viewport: 1', origin=(0.0, 0.0), width=300.0,
    height=150.0)
    session.viewports['Viewport: 1'].makeCurrent()
    session.viewports['Viewport: 1'].maximize()
```

```
session.viewports['Viewport: 1'].setValues(displayedObject=odb1)

# Introducing Path along Notch Bisector

MyPath = 'Path-'+MyNameJob
#n_points = 99

#b = [(0,y_e,0)]

#for i in range(1,n_points+1):
    #b.append((i/n_points*d/2, y_e, 0))

#MyExpression = tuple(b)
MyExpression = ((0,y_e,0),(d/2,y_e,0))
session.Path(name=MyPath, type=POINT_LIST, expression=MyExpression)

lastStep = odb1.steps['Load']
last_fr = len(lastStep.frames)-1
lastFrame = lastStep.frames[last_fr]
pth = session.paths[MyPath]


session.XYDataFromPath(name='S_22', path=pth, includeIntersections=False,
    projectOntoMesh=False, pathStyle=UNIFORM_SPACING, numIntervals=100,
    projectionTolerance=0, shape=UNDEFORMED, labelType=TRUE_DISTANCE_X, step=0, frame = last_fr,
    variable= ('S',INTEGRATION_POINT, (
    (COMPONENT, 'S22' ), ), )) # Getting S22 from Notch Bisector (100 intervals, evenly spaced)

session.XYDataFromPath(name='S_MISES', path=pth, includeIntersections=False,
    projectOntoMesh=False, pathStyle=UNIFORM_SPACING, numIntervals=100,
    projectionTolerance=0, shape=UNDEFORMED, labelType=TRUE_DISTANCE_X, step=0, frame = last_fr,
    variable= ('S',INTEGRATION_POINT, (
    (INVARIANT, 'Mises' ), ), )) # Getting Mises from Notch Bisector ""

session.XYDataFromPath(name='S_33_Hoop', path=pth, includeIntersections=False,
    projectOntoMesh=False, pathStyle=UNIFORM_SPACING, numIntervals=100,
    projectionTolerance=0, shape=UNDEFORMED, labelType=TRUE_DISTANCE_X, step=0, frame = last_fr,
    variable= ('S',INTEGRATION_POINT, (
    (COMPONENT, 'S33' ), ), )) # Getting S33 from Notch Bisector ""

session.XYDataFromPath(name='S_11', path=pth, includeIntersections=False,
    projectOntoMesh=False, pathStyle=UNIFORM_SPACING, numIntervals=100,
    projectionTolerance=0, shape=UNDEFORMED, labelType=TRUE_DISTANCE_X, step=0, frame = last_fr,
    variable= ('S',INTEGRATION_POINT, (
    (COMPONENT, 'S11' ), ), )) # Getting S11 from Notch Bisector ""

session.XYDataFromHistory(name='SE', odb=odb1,
outputVariableName='Strain energy: ALLSE in ELSET SED', steps=('Load', ), ) # Getting Strain Energy from
Control Volume

session.XYDataFromHistory(name='VOLUME', odb=odb1,
outputVariableName='Current volume of an element set or entire model: VOL in ELSET SED', steps=('Load', ), ) #
Getting Strain Energy from Control Volume

S_11_Path = list(session.xyDataObjects['S_11']) # Obtaining S11 Data as a LIST
S_22_Path = list(session.xyDataObjects['S_22']) # Obtaining S22 Data as a LIST
S_33_Path = list(session.xyDataObjects['S_33_Hoop']) # Obtaining S33 Data as a LIST
S_Mises_Path = list(session.xyDataObjects['S_MISES']) # Obtaining Mises Data as a LIST
SED_Time = list(session.xyDataObjects['SE']/session.xyDataObjects['VOLUME'])  # Obtaining SED vs Time Data
as a LoL
SED_Data = SED_Time[1]  # Obtaining SED Data as a LIST
SED = SED_Data[1]*10**9 # Extracting SED (IN N/MQ!!)
Data = (S_22_Path,S_33_Path,S_Mises_Path) # Collecting Data
txt_file = str(MyNameJob)+'.txt'

row_x = [q[0] for q in S_22_Path] # Abscissas
row_S_11 = [u[1] for u in S_11_Path] #S_11
row_S_22 = [w[1] for w in S_22_Path] #S_22
row_S_33 = [z[1] for z in S_33_Path] #S_33
row_Mises = [t[1] for t in S_Mises_Path] #Mises

row_S_33_len = int(min(len(row_S_11),len(row_S_22))) # Setting the length of list for Elasticity Theory
row_S_33_el = [0]*row_S_33_len
for n in range(row_S_33_len):
    row_S_33_el[n] = ni*(row_S_11[n]+row_S_22[n])
```

```
    model_data = list(zip(row_x,row_S_11,row_S_22,row_S_33,row_S_33_el,row_Mises)) # Ordering Rows -> Path
Data
    header_model = ['D [mm]'+'\t','d [mm]'+'\t','2 Alfa [deg]'+'\t','r [mm]'+'\t','k_R [-]'+'\t','SED [N/mq]'+'\n'] # Header for
Model Label
    model_name = [str(D)+'\t',str(d)+'\t',str(Two_alfa)+'\t',str(r)+'\t',str(k_R)+'\t',str(SED)+'\n'] # Model Parameters and
SED Value
    header_data =['x [mm]'+'\t','S11 [MPa]'+'\t','S22 [MPa]'+'\t','S33_Hoop [MPa]'+'\t','S33_Plane [MPa]'+'\t','Mises
[MPa]'+'\n'] #Header for Path Data

    writing = open(str(MyNameJob)+'.txt','a') # Opening New File in Append Mode
    np.savetxt(writing, header_model, newline='', delimiter='\t', fmt='%s') # Writing Model Header
    np.savetxt(writing, model_name, newline='', delimiter='\t',fmt='%s') # Writing Model Parameters and SED
    np.savetxt(writing, header_data, newline='', delimiter='\t',fmt='%s') # Writing Data Header
    np.savetxt(writing, model_data, newline='\n', delimiter='\t', fmt='%.6f') # Writing Data
    writing.close() # Closing .txt file

    session.odbs[str(MyNameJob)+'.odb'].close() # Closing .odb file

def Delete_Stuff(D,d,Two_alfa,r,k_R):

    # Name of the Model & Job...

    import math

    # Splitting D for Labelling

    if int(D) == D:
        mant_D = 0
    else:
        digit_D = int(math.log10(D))+1
        tot_D = len(str(D))
        m_D = 10**(tot_D-digit_D-1)
        n_D = str(int(D*m_D))
        end_D = len(n_D)
        mant_D = n_D[digit_D:end_D]

    # Splitting d for Labelling

    if int(d) == d:
        mant_d = 0
    else:
        digit_d = int(math.log10(d))+1
        tot_d = len(str(d))
        m_d = 10**(tot_d-digit_d-1)
        n_d = str(int(d*m_d))
        end_d = len(n_d)
        mant_d = n_d[digit_d:end_d]

    # Splitting r for Labelling

    n_r = str(r)
    end_r = len(n_r)
    mant_r = n_r[2:end_r]

    MyName = 'C45-'+str(int(D))+','+str(mant_D)+'-'+str(int(d))+','+str(mant_d)+'-'+str(int(Two_alfa))+'-
'+str(int(r))+','+str(mant_r)+'-'+str(int(k_R))
    MyNameMod = 'Model-'+MyName
    MyNameJob = MyName
    MyPath = 'Path-'+MyNameJob
    com = MyName+'.com'
    dat = MyName+'.dat'
    inp = MyName+'.inp'
    ipm = MyName+'.ipm'
    log = MyName+'.log'
    msg = MyName+'.msg'
    odb = MyName+'.odb'
    prt = MyName+'.prt'
    sim = MyName+'.sim'
    sta = MyName+'.sta'
    lck = MyName+'.lck'
    gen_files = [com,dat,inp,ipm,log,msg,odb,prt,sim,sta,lck]

    del mdb.models[MyNameMod] # Deleting Model
    del mdb.jobs[MyNameJob] # Deleting Job
```

```
        del session.paths[MyPath]
        del session.xyDataObjects['SE']
        del session.xyDataObjects['S_11']
        del session.xyDataObjects['S_22']
        del session.xyDataObjects['S_33_Hoop']
        del session.xyDataObjects['S_MISES']
        del session.xyDataObjects['VOLUME']
        del session.xyDataObjects['_temp_1']

        import os
        for i in gen_files:
            if os.path.exists(i):
                os.remove(i)

def Run_Analysis(D,d,Two_alfa,r,k_R):

    L = D # L Length of the Grip
    # D Outer Diameter
    # d Inner Diameter
    # Two_alfa Opening Angle
    # r Notch radius
    # k_R Mesh Size Parameter
    # Importing Abaqus Modules in Python


    # Defining Parameters for Analysis
    # Lenghts in mm, Angles in deg, Forces in N

    import numpy as np # Importing Numpy Library

    E_s=210000.0 # Young Modulus
    ni=0.3 # Poisson's constant

    alfa=np.radians(90.0-Two_alfa/2)

    # Name of the Model/Instance/Job...

    import math

    # Splitting D for Labelling

    if int(D) == D:
        mant_D = 0
    else:
        digit_D = int(math.log10(D))+1
        tot_D = len(str(D))
        m_D = 10**(tot_D-digit_D-1)
        n_D = str(int(D*m_D))
        end_D = len(n_D)
        mant_D = n_D[digit_D:end_D]

    # Splitting d for Labelling

    if int(d) == d:
        mant_d = 0
    else:
        digit_d = int(math.log10(d))+1
        tot_d = len(str(d))
        m_d = 10**(tot_d-digit_d-1)
        n_d = str(int(d*m_d))
        end_d = len(n_d)
        mant_d = n_d[digit_d:end_d]

    # Splitting r for Labelling

    n_r = str(r)
    end_r = len(n_r)
    mant_r = n_r[2:end_r]

    MyName = 'C45-'+str(int(D))+','+str(mant_D)+'-'+str(int(d))+','+str(mant_d)+'-'+str(int(Two_alfa))+'-
'+str(int(r))+','+str(mant_r)+'-'+str(int(k_R))
    MyNameJob = MyName

    mdb.Job(atTime=None, contactPrint=OFF, description='', echoPrint=OFF,
        explicitPrecision=SINGLE, getMemoryFromAnalysis=True, historyPrint=OFF,
```

```
            memory=80, memoryUnits=PERCENTAGE, model=MyNameMod, modelPrint=OFF,
            multiprocessingMode=DEFAULT, name=MyNameJob, nodalOutputPrecision=SINGLE,
            numCpus=4, numDomains=4, numGPUs=0, queue=None, resultsFormat=ODB, scratch=
            ", type=ANALYSIS, userSubroutine=", waitHours=0, waitMinutes=0)
    mdb.jobs[MyNameJob].submit(consistencyChecking=OFF)
    mdb.jobs[MyNameJob].waitForCompletion()

def Parametrical(Parameters):
    D = Parameters[0] # Extracting Outer Diameter
    d = Parameters[1]*Parameters[0] # Extracting d/D and calculating Inner Diameter
    Two_alfa = Parameters[2] # Extracting Opening Angle
    r = Parameters[3] # Extracting Notch Radius
    k_R = 40 # Shape Parameter, fixed
    Create_Model_Run_Analysis(D,d,Two_alfa,r,k_R) # Model + Analysis
    #Run_Analysis(D,d,Two_alfa,r,k_R) # Only Analysis
    Open_ODB_and_Write_To_Text(D,d,Two_alfa,r,k_R) # Post-Processing
    Delete_Stuff(D,d,Two_alfa,r,k_R) # Deleting


# Parametrical Analyses

D_range = [10.0, 12.0, 14.0, 16.0, 18.0, 20.0] # Range of possible Outer Diameters
d_D_range = [0.50,0.55,0.60,0.65,0.70,0.75] # Range of possible d/D ratios
Two_Alfa_range = [15.0,30.0,45.0,60.0,75.0,90.0,105.0,120.0] # Range of possible Opening Angles
r_range = [0.1,0.2,0.3,0.4,0.5,0.6,0.7,0.8,0.9,1.0] # Range of possible Notch Radiuses

Cartesian_Product = [[p1,p2,p3,p4] for p1 in D_range for p2 in d_D_range for p3 in Two_Alfa_range for p4 in r_range]
# Defining Cartesian Product
for i in range(2810,len(Cartesian_Product)):
    Combo = Cartesian_Product[i]
    Parametrical(Cartesian_Product[i])
```

Definition of Control Volume for SED calculations in Hot-Driven Riveted Connections

```
# Importing ABAQUS programming language
# -*- coding: utf-8 -*-

from part import *
from material import *
from section import *
from assembly import *
from step import *
from interaction import *
from load import *
from mesh import *
from optimization import *
from job import *
from sketch import *
from visualization import *
from connectorBehavior import *
from odbAccess import *
import numpy as np

def SED_Connections(Geom,R0_min,R0_max,Step):

    # geometrical features
    D = Geom[0]
    w = Geom[1]
    t = Geom[2]
    L = Geom[3]
    e1 = Geom[4]
    Config = Geom[5]
    n_r = Geom[6]
    label = Geom[7]

    x_p = L - e1
    y_pa = 0.1
    y_pb = -3*t - 0.1
    z_p = w/4 - D/2
    r = D/2

    MyNameMod = str(Config)+'-'+str(int(D))+'-'+str(int(t))+'-'+str(int(n_r))+str(label)
    MyNameIns = 'Lower plate'
```

```python
    Num = int((R0_max-R0_min)/Step)+1
    R_0_range = np.linspace(R0_min,R0_max, num=Num)

    for i in R_0_range:

        R_0 = i # Radius of the Control Volume for Sharp Notch, L in mm
        r_0 = r*(np.pi - np.radians(0.0))/(2*np.pi - np.radians(0.0)) # Distance from the Notch Tip
        R_1 = R_0 + r_0 # Radius of Cylinder
        R_0_str = 'SED_'+str(R_0)
        R_0_str = R_0_str.replace('.',',')

        mdb.models[MyNameMod].rootAssembly.Set(elements=

mdb.models[MyNameMod].rootAssembly.instances[MyNameIns].elements.getByBoundingCylinder(center1=(x_p,
y_pa, z_p+r_0),center2=(x_p, y_pb, z_p+r_0),radius=R_1*1.001), name=R_0_str) # Creating SET for Strain Energy
Density Measure
        mdb.models[MyNameMod].HistoryOutputRequest(createStepName='Loading', name=R_0_str, frequency=1,
rebar=EXCLUDE, region=
            mdb.models[MyNameMod].rootAssembly.sets[R_0_str], sectionPoints=DEFAULT,
            variables=('ALLSE', 'VOL')) # Tracking Strain Energy (Non Averaged) and Volume for SED

Models = [[16.0,70.0,10.0,245.0,35.0,'S',1,''],[19.0,90.0,10.0,255.0,45.0,'S',1,''],[19.0,90.0,10.0,345.0,45.0,'S',2,''],
        [19.0,90.0,12.0,195.0,45.0,'S',1,'-A'],[19.0,90.0,12.0,195.0,45.0,'S',1,'-B'],[22.0,70.0,10.0,245.0,35.0,'S',1,'-A'],
        [22.0,70.0,10.0,245.0,35.0,'S',1,'-B'],[22.0,70.0,12.0,185.0,35.0,'S',1,'-A'],[22.0,70.0,12.0,185.0,35.0,'S',1,'-B'],
        [22.0,70.0,12.0,185.0,35.0,'S',1,'-B'],[22.0,70.0,12.0,280.0,35.0,'S',2,'-A'],[22.0,70.0,12.0,280.0,35.0,'S',2,'-B'],
[19.0,90.0,10.0,255.0,45.0,'U',1,''],[19.0,60.0,10.0,345.0,45.0,'U',2,''],[19.0,60.0,10.0,355.0,30.0,'U',2,'G'],
        [19.0,90.0,12.0,195.0,45.0,'U',1,''],[22.0,70.0,12.0,280.0,35.0,'U',2,'-A'],[22.0,70.0,12.0,280.0,35.0,'U',2,'-B']]

for i in Models:
    Geometry = i
    R0_min = 0.20
    R0_max = 1.00
    Step = 0.05
    SED_Connections(Geometry,R0_min,R0_max,Step)
```
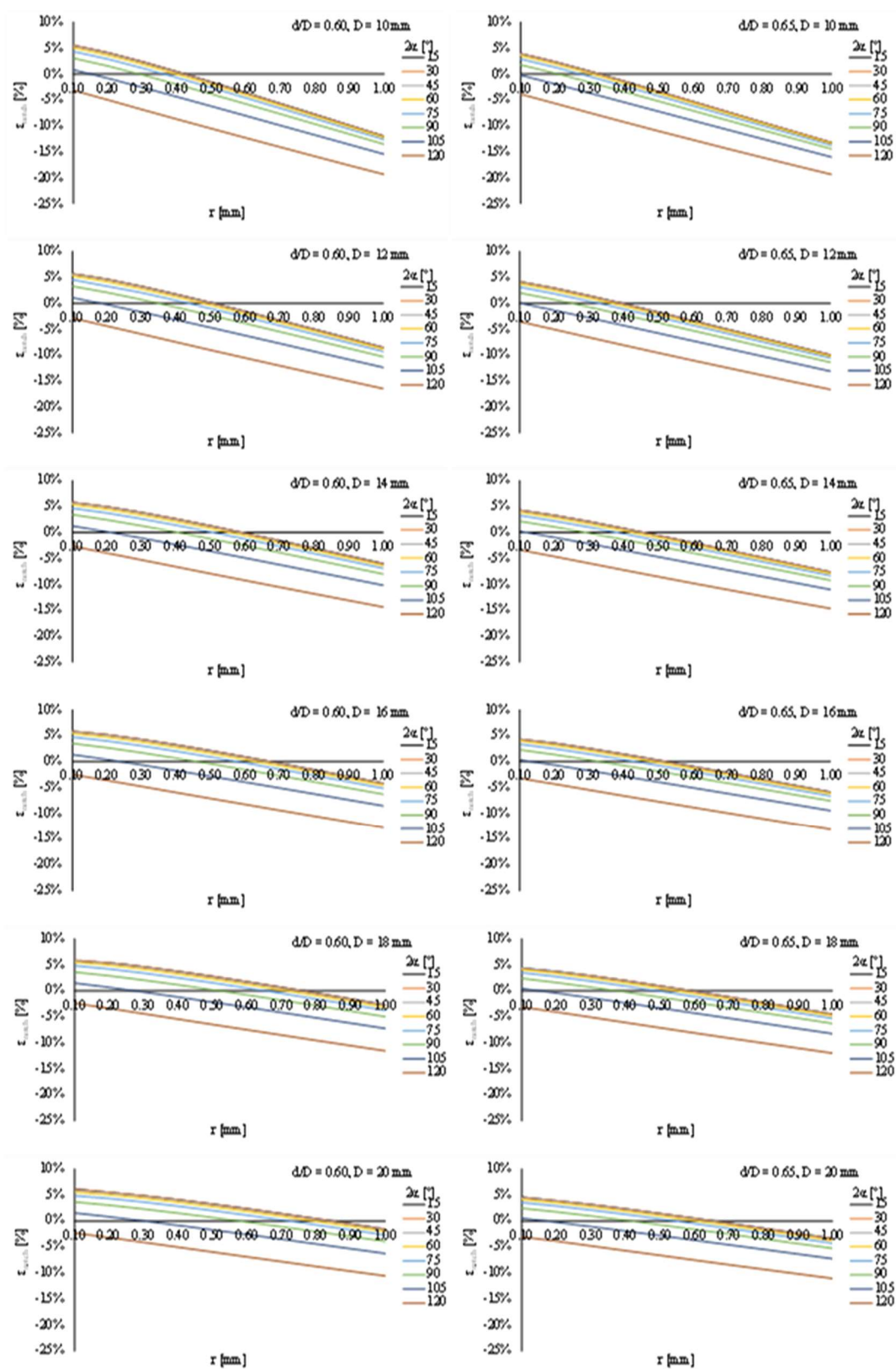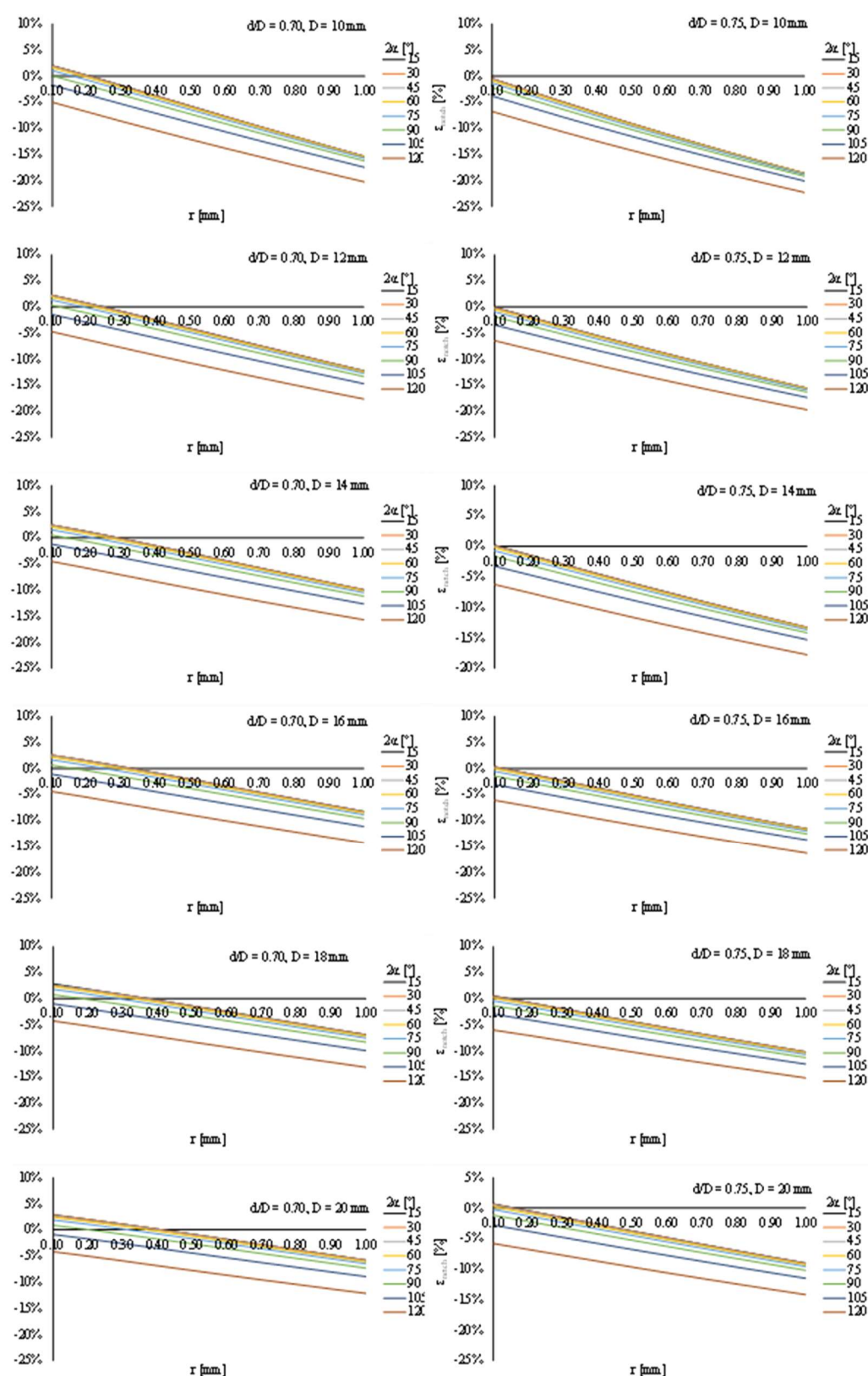
ccli

Stress analysis of blunt V-notched cylinders of mild steel
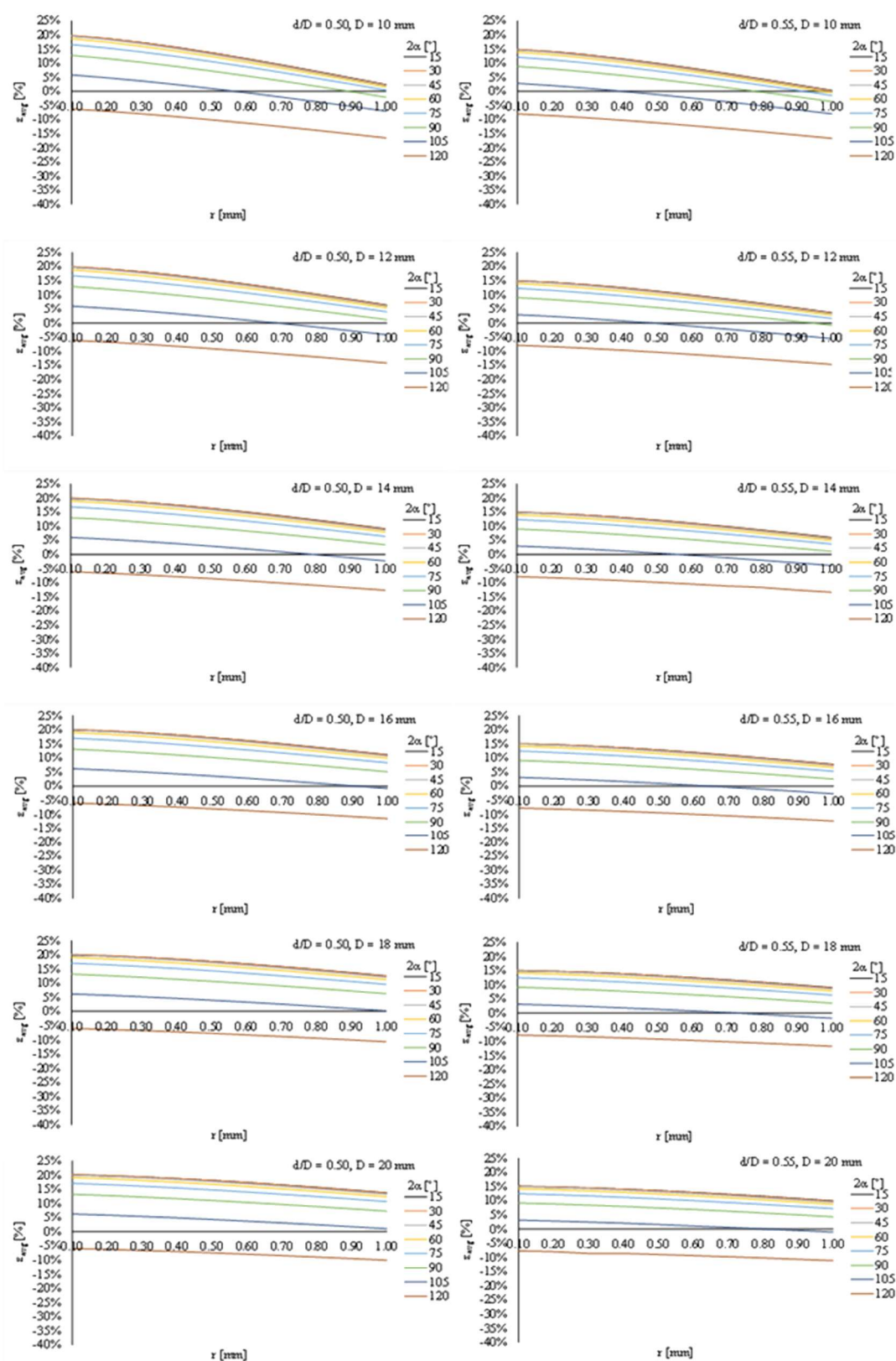
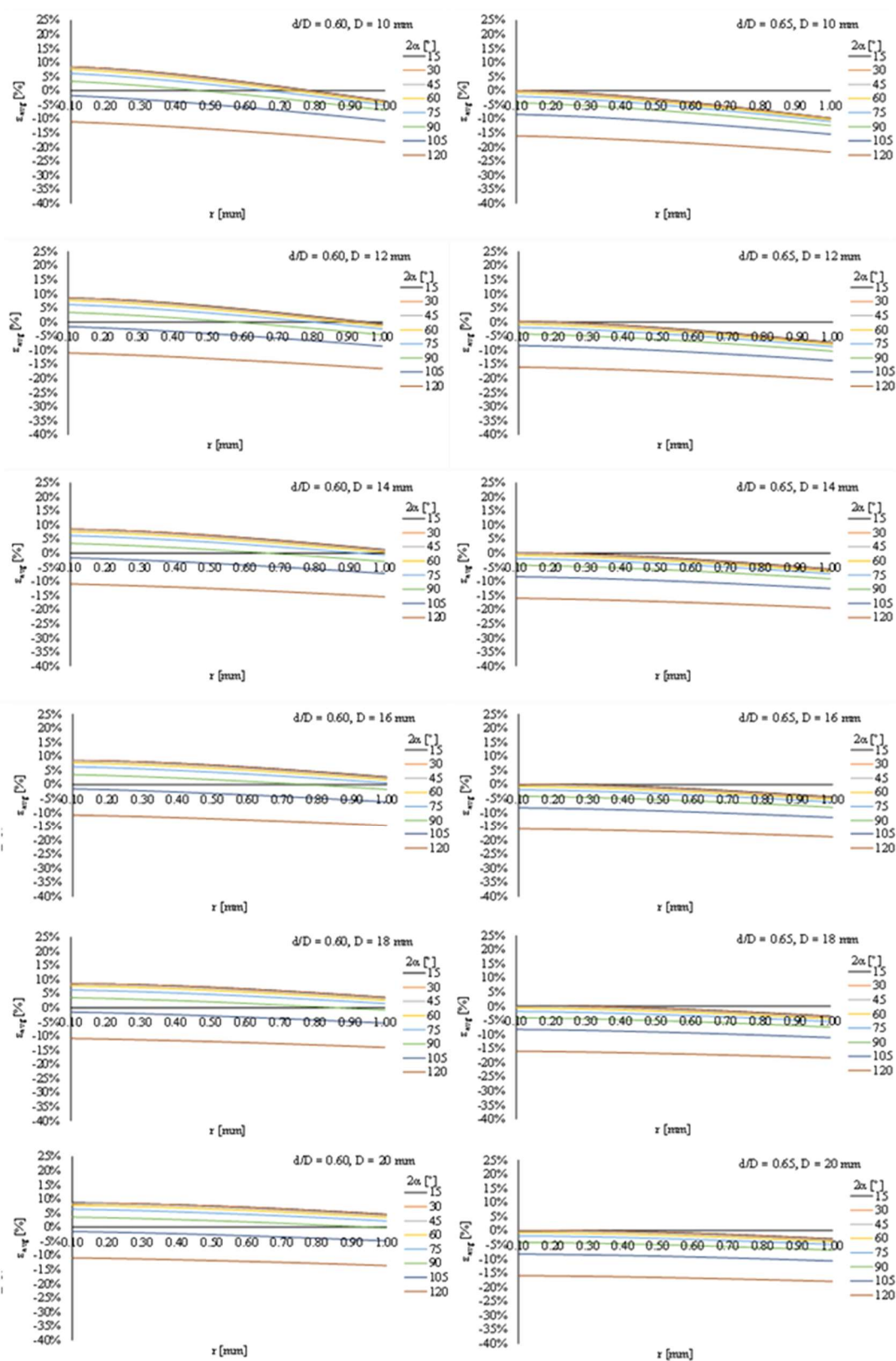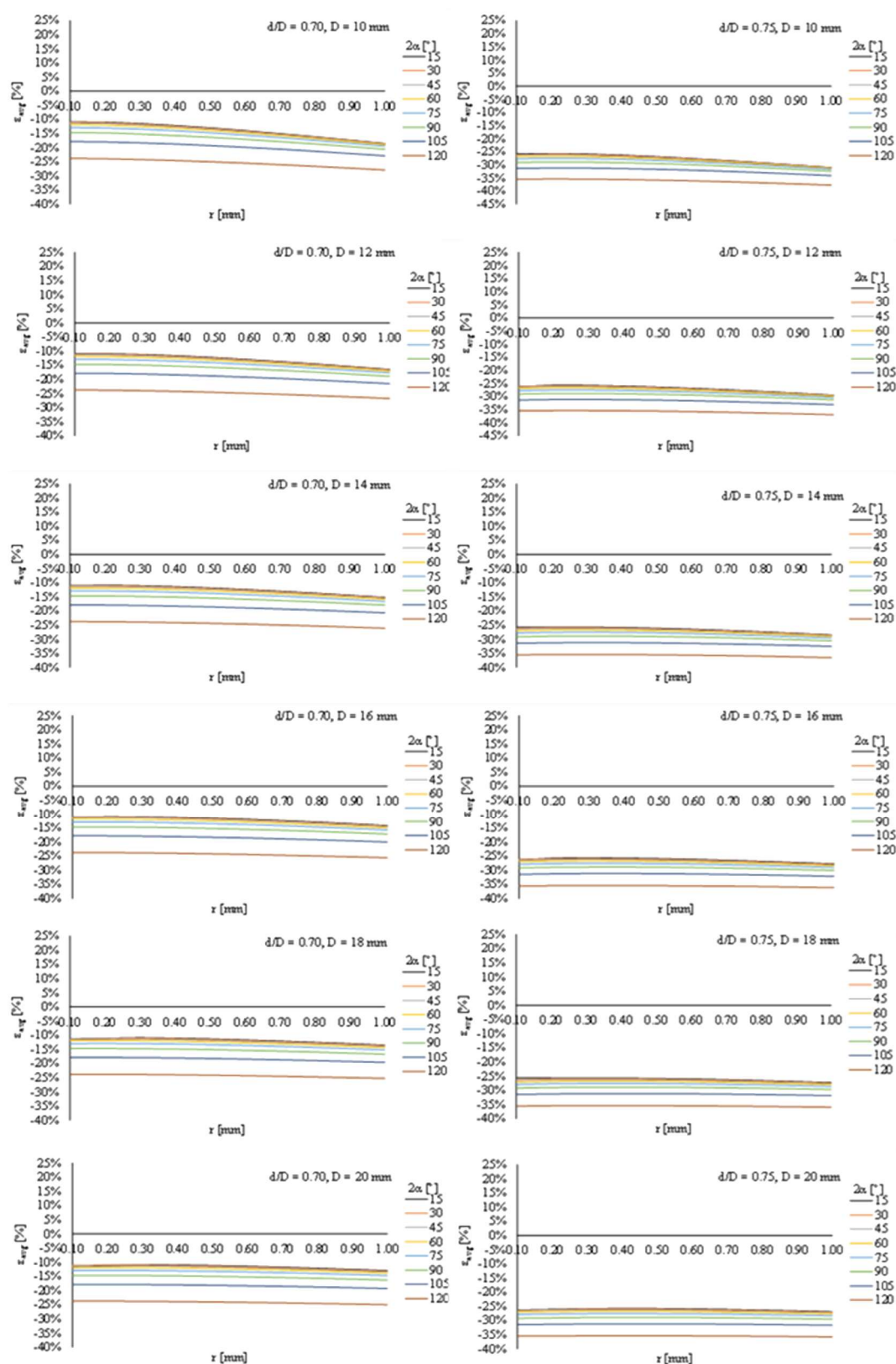Deviation among hoop stresses and equivalent plain strain conditions at the notch tip
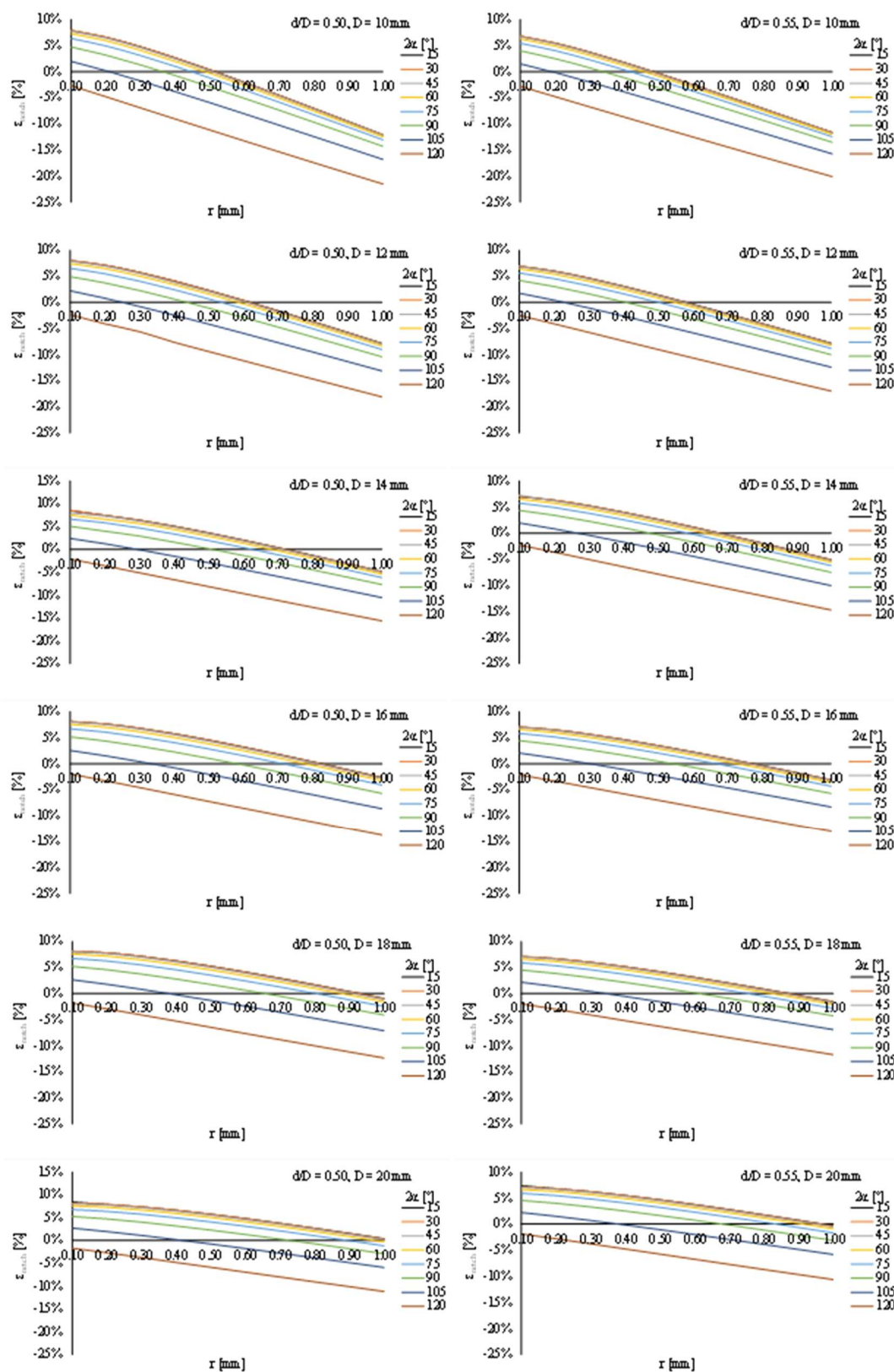
Average deviation among hoop stresses and equivalent plain strain
conditions over the notch bisector

References

Al-Bahkali E.A. (2011). Finite Element Modelling for Thermal Stresses Developed in Riveted and Rivet Bonded Joints. *International Journal of Engineering & Technology*. 11(6), 86-92.

American Society of Civil Engineers (2010). Civil engineers create wonders of the world. *Civil Engineering.*

Ammar M.M.A., Shirinzadeh B, Elgamal H. Nasr M.N.A. (2022). On the Role of Damage Evolution in Finite Element Modeling of the Cutting Process and Sensing Residual Stresses. *Sensors,* 22, 8547.

Anderson T.L. (2017). Fracture Mechanics: Fundamentals and Applications, 4th Edition. CRC Press, Taylor & Francis Group.

ASTM (2010). ASTM E8 – Standard Test Methods for Tension Testing of Metallic Materials.

ASTM (2012). ASTM E606 – Standard Test Method for Strain-Controlled Fatigue Testing.

ASTM (2016). ASTM E647 – Standard Test Method for Measurement of Fatigue Crack Growth.

ASTM (2018). ASTM E1820 – Standard Test Method for Measurement of Fracture Toughness.

Ballio G., Mazzolani F.M., Bernuzzi C., Landolfo R. (2020). Strutture di Acciaio: Teoria e Progetto. Hoepli, Milano. ISBN 978-8820391805 [In Italian].

Basquin O.H. (1910). The Exponential Law of Endurance Tests. *American Society for Testing and Materials Proceedings*, 10, 625-630.

Batho C., Bateman E.H. (1934). Investigations on bolts and bolted joints. *Second report of the steel structures research committee*. London.

Berto F., Lazzarin P. (2009). A review of the volume-based strain energy density approach applied to V-notches and welded structures. *Theoretical and Applied Fracture Mechanics.* 52, 183–194.

Berto F., Lazzarin P. (2014). Recent developments in brittle and quasi-brittle failure assessment of engineering materials by means of local approaches. *Materials Science and Engineering R.* 75(1), 183–194.

Bresler B., Lyn T. Y. (1960). Design of Steel Structures. John Wiley & Sons, Inc., New York.

BSI (2008). UK National Annex to Eurocode 3: Design of steel structures - Part 1-8: Design of joints.

BSI (2014). BS 7608 - Guide to fatigue design and assessment of steel product.

BSI (2019). BS 7910 - Guide to methods for assessing the acceptability of flaws in metallic structures.

Billington D.P. (1983). The tower and the bridge, Princeton University press.

Boller C., Seeger T. (1987). Materials Data for Cyclic Loading – Low Alloy Steels. Elsevier.

Bonora N. (1997). A nonlinear CDM model for ductile failure. *Engineering Fracture Mechanics*, 58(1),11-28.

Callister, Jr. W.D. (2005). Fundamentals of Materials Science and Engineering - 2nd Edition. John Furkan & Sons, ISBN 978-0-471-47014-4.

Carughi U. (1996). La galleria Umberto I. Architettura del ferro a Napoli. Di Mauro Franco Libri, Napoli [In Italian].

CEN (2002). EN1990 Eurocode 0 Basis of structural design. Brussels: CEN.

CEN (2005a). EN1993:1-9 Eurocode 3 design of steel structures part 1.9: Fatigue. Brussels: CEN.

CEN (2005b). EN1993:1-8 Eurocode 3 design of steel structures part 1.8: Design of joints. Brussels: CEN.

CEN (2006). EN1993:1-11 Eurocode 3 design of steel structures part 1.11: Design of structures with tension components. Brussels: CEN.

CEN (2007). EN1999:1-3 Eurocode 9 design of aluminium structures part 1.3: Structures susceptible to fatigue. Brussels: CEN.

CEN (2020). prEN1993:1-9-2020 Eurocode 3 design of steel structures part 1.9: Fatigue (2020 Draft). Brussels: CEN.

CIDECT (2001). Design guide for circular and rectangular hollow section joints under fatigue loading.

Coffin L.F. (1954). A Study of the Effects of Cyclic Thermal Stresses on a Ductile Metal. *Trans. ASME*, 76, 931–950.

Collette Q. (2014). Riveted Connections in Historical Metal Structures (1840-1940). Hot-driven Rivets: Technology, Design and Experiments [PhD Thesis].

Collette Q., Wouters I., Lariks L. (2011). Evolution of Historical Riveted Connections: Joining Typologies, Installation Techniques and Calculation Methods, *Structural Repairs and Maintenance of Heritage Architecture XII*, WIT Press, 118, 295-306.

Cook R.D. (1995) Finite element modelling for stress analysis. J Wiley, New York.

Considère A. (1885). *Annales des Ponts et Chaussées*, 9, 574

Correia J.A.F.O., De Jesus A.M.P., Da Silva A.L.L., Pedrosa B., Rebelo C., Calcada R.A.B. (2017). FE simulation of S-N curves for a riveted connection using two-stage fatigue models. *Advances in Computational Design*, 2(4), 333-349.

Cossons N., Trinder B.S. (2002). The Iron Bridge: Symbol of the Industrial Revolution. History Pr Ltd., London.

D'Aniello M., Portioli F., Fiorino L., Landolfo R. (2010). Experimental investigation on shear behaviour of riveted connections in steel structures. *Engineering Structures.* 33, 516–531.

Da Silva A.L.L. (2015). Advanced Methodologies for the Fatigue Analysis of Representative Details of Metallic Bridges [PhD Thesis].

Da Silva A.L.L., Correia J.A.F.O., De Jesus A.M.P., Figueiredo M.A.V., Pedrosa B., Fernandes A.A., Rebelo C., Berto F. (2019). Fatigue characterization of a beam-to-column riveted joint. *Engineering Failure Analysis*, 103, 95-123.

Dassault (2014), Abaqus 6.14 User's Manual, Dassault Systèmes Simulia Corp.

Deng X., Hutchinson J.W. (1998). The Clamping Stress in a Cold Driven Rivet. *International Journal of Mechanical Sciences*, 40(7), 683-694.

Di Lorenzo G., Formisano A., Terracciano G., Landolfo R. (2021). Iron alloys and structural steels from XIX century until today: Evolution of mechanical properties and proposal of a rapid identification method. *Construction and Building Materials*. 302, 124132.

DiBattista J.D., Adamson D.E.J., Kulak G.L. (1998). Fatigue Strength of Riveted Connections. *Journal of Structural Engineering*, 124(7), 792-797.

DNV (2010). DNV-RP-C203 - Fatigue design of offshore steel structures: recommended practice, Det Norske Veritas, Norway.

Donahue R.J., Clark H.M., Atanmo P., Kumble R., McEvily A.J. (1972). Crack opening displacement and the rate of fatigue crack growth. International Journal of Fracture Mechanics, 8, 209–219.

Dowling N.E.. (2004). Mean Stress Effects in Stress-Life and Strain-Life Fatigue. SAE Technical Paper 2004-01-2227.

Duggal S.K. (2000). *Design of steel structures*. Tata McGraw-Hill, ISBN 0-07463095-4.

Dutta A., Dhar S., Acharyya S.K. (2010). Material characterization of SS 316 in low cycle fatigue loading, *Journal of Material Science*, 45, 1782-1789.

ECCS (1985). Recommendations for the Fatigue Design of Steel Structures, P043, European Convention for Constructional Steelwork, Brussels.

ECCS (2018). Fatigue Design of Steel and Composite Structures – 2nd Edition. Ernst & Sohn, Berlin, Germany.

Erice B., Galvez F. (2014). A coupled elastoplastic-damage constitutive model with Lode angle dependent failure criterion. *International Journal of Solids and Structures*, 51, 93-110.

Filippi S., Lazzarin P. (2004). Distributions of the elastic principal stress due to notches in finite size plates and rounded bars uniaxially loaded. *International Journal of Fatigue*, 26, 377-391

Fisher J.W., Yoshida N. (1969). Large bolted and riveted shingle splices. *Journal of Structural Division, ASCE*; 96(ST9).

Forman R.G., Mettu S.R. (1992), Behavior of Surface and Corner Cracks Subjected to Tensile and Bending Loads in Ti–6Al–4 V Alloy. ASTM STP 1131, American Society for Testing and Materials, Philadelphia, 519–546.

Foti P., Razavi S.M.J., Marsavina L., Berto F. (2020). Volume free strain energy density method for applications to blunt V-notches, *Procedia Structural Integrity*, 28, 734-742.

Freitag, JK. 1904. Architectural Engineering: with Especial Reference to High Building Construction, Including Many Examples of Prominent Office Buildings – 2nd Edition. New York: John Wiley & Sons.

Frémont, C. (1906). Etude Expérimentale du Rivetage. Paris: Société d'encouragement pour l'industrie nationale [In French].

Gerber W.Z. (1874). Bestimmung der zulässigen Spannungen in Eisen-Konstruktionen (Calculation of the Allowable Stresses in Iron Structures). *Ztg. Bayer Archit.*, 6, 101–110. [In German]

Gimsing N.J., Georgakis C.T. (2012) Cable Stayed Bridges – Concept and Design, 3rd Edition. John Wiley & Sons: New York, NY, USA.

Goodman J. (1899). Mechanics Applied to Engineering. Longman, Green & Company: London, UK.

Griffith A.A. (1920). The Phenomena of Rupture and Flow in Solids. *Philosophical Transactions*, Royal Society, London, Series A, 221, 163-198.

Gross B., Mendelson A. (1972). Plane elastostatic analysis of V-notched plates, *International Journal of Fracture Mechanics*, 8, 267–276.

Guerrieri M.R., Di Lorenzo G., Landolfo R. (2005). Influence of atmospheric corrosion on the XIX century iron structures: assessment of damage for Umberto I Gallery in Naples. *Proc. Of XX CTA Conference*, Ischia (Italy) 26-28 September.

Haibach E. (1970). Modified linear damage accumulation hypothesis accounting for a decreasing fatigue strength during increasing fatigue damage. Report TM Nr. 50. Darmstadt: Laboratorium für Betriebsfestigkeit, LBF [In German].

Hancock J.W., Mackenzie A.C. (1976). On the mechanisms of ductile failure in high-strength steels subjected to multi-axial stress-states. *Journal of the Mechanics and Physics of Solids*, 24(2-3), 147-160.

Hanser D.A. (2006). Architecture of France. Greenwood Publishing Group, Westport, CT.

Hechtman R.A. (1948). A study of the effects of heating and driving conditions on hot driven structural steel rivets. *Off. Of nav. Res. Project. University of Illinois.*

Hencky H. (1924). Zur Theorie plastischer Deformationen und der hierdurch im Material hervorgerufenen Nachspannngen. *Z. Angew. Math. Mech*, 4(4), 323–334 [In German].

Hertz H. (1881) Über die berührung fester elastischer Körper. *Journal für die reine und angewandte Mathematik*, 92, 156-171 [In German].

Hillerborg A., Modeer M., Petersson P.E. (1976). Analysis of crack formation and crack growth in concrete by means of fracture mechanics and finite elements. *Cement and Concrete Research*, 6(6), 773-781.

Hollomom (1945). Tensile Deformation. *Transactions of the Metallurgical Society of AIME*, 162, 268-290.

Hooputra H., Gese H., Dell H. Werner H. (2004). A comprehensive failure model for crashworthiness simulation of aluminium extrusions. *International Journal of Crashwortiness*, 9(5), 449-464.

Hrennikoff A. (1934). Work of rivets in riveted joints. *Trans ASCE*;99:437–49.

IIW (2000). Fatigue design procedure for welded hollow section joints, Doc. XIII-1804-99, XV-1035-99, IIW, Cambridge, Abington.

Irgens F. (2008). Continuum Mechanics, Springer Berlin, Heidelberg.

Irwin G.R. (1956). Fracture dynamics. Fracturing of Metals. American Society for Metals, Cleveland, 147–166.

ISO (2016). ISO 683-1 - Heat-treatable steels, alloy steels and free-cutting steels - Part 1: Non-alloy steels for quenching and tempering.

Iwankiw N., Sghlafly T. (1982). Effect of hole-making on the strength of double lap joints. *Engineering Journal*, AISC, III–IV, 170–178.

Jia L.J., Kuwamura H. (2014). Ductile Fracture Simulation of Structural Steels under Monotonic Tension. *Journal of Structural Engineering*, 04013115.

Jiang C., Wu C., Jiang X. (2018). Experimental study on fatigue performance of corroded high-strength steel wires used in bridges. *Construction and Building Materials*, 187, 681–690.

Johnson G.R., Cook W.H. (1985). Fracture characteristics of three metals subjected to various strains, strain rates, temperatures and pressures. *Engineering Fracture Mechanics,* 21(1) 31-48.

Kafie-Martinez J., Keating P.B. (2017). Finite Element Modeling for Clamping Stresses Developed in Hot-Driven Steel Structural Riveted Connections. *Proc. Of 19th International Conference on Structural Engineering*, London, United Kingdom.

Kanvinde A.M., Deierlein G.G. (2006). The Void Growth Model and the Stress Modified Critical Strain Model to Predict Ductile Fracture in Structural Steels, *Journal of Structural Engineering*, 132, 1-52.

Kanvinde A.M., Deierlein G.G. (2007). Cyclic Void Growth Model to Assess Ductile Fracture Initiation in Structural Steels due to Ultra Low Cycle Fatigue. *Journal of Engineering Mechanics*, 133(6), 701-712.

Klesnil M., Lukas P. (1972). Influence of strength and stress history on growth and stabilisation of fatigue cracks. *Engineering Fracture Mechanics*, 4, 77–92.

Koegler R.K., Schnitt A. (1943). Effects of yielding on perforations on a wing tension surface. *Journal of Aeronautic Science*,10, 273–84.

Korgesaar M. (2019). The effect of low stress triaxialities and deformation paths on ductile fracture simulations of large shell structure. *Marine Structures*, 63, 45-64.

Kulak G.L. (2002). Fatigue strength of riveted shear splices. *Progress in Structural Engineering and Materials*, 2, 110–119.

Kulak G.L., Fisher J.W., Struik J.H.A. (1987). *Guide to design criteria for bolted and riveted joints*. 2nd ed. New York: John Wiley & Sons; 1987.

Landolfo R., Cascini L., D'Aniello M., Portioli F. (2011). Gli effetti del degrado da fatica e corrosione sui ponti ferroviari in carpenteria metallica: un approccio integrato per la valutazione della vulnerabilità. *Rivista Italiana della Saldatura*, 63, 3, 367-377 [In Italian].

Landolfo R., Shakeel S., Fiorino L. (2022). Lightweight steel systems: Proposal and validation of seismic design rules for second generation of Eurocode 8. *Thin-Walled Structures*, 172, 108826.

Lazzarin P., Tovo R. (1998). A Notch Intensity Factor Approach to The Stress Analysis of Welds, *Fatigue & Fracture of Engineering Materials & Structures*, 21(9), 1089-1103.

Lazzarin P, Zambardi R (2001) A finite volume energy based approach to predict the static and fatigue behaviour of components with sharp V-shaped notches. *International Journal of Fracture*, 112, 275–298.

Lazzarin P, Sonsino CM, Zambardi R (2004) A notch stress intensity approach to assess the multiaxial fatigue strength of welded tube-to-flange joints subjected to combined loadings. *Fatigue & Fracture of Engineering Materials & Structures,* 27, 127–140.

Lazzarin P, Filippi S (2006) A generalized stress intensity factor to be applied to rounded V-shaped notches. *Int J Solids Struct* 43:2461–2478.

Lazzarin P, Berto F, Zappalorto M (2010) Rapid calculations of notch stress intensity factors based on averaged strain energy density from coarse meshes: Theoretical bases and applications. *Int J Fatigue* 32:1559–1567.

Leahey T.F., Munse W.H. (1954). Static and Fatigue Tests of Rivets and High-Strength Bolts in Direct Tension. University of Illinois Engineering Experiment Station. Urbana, Illinois.

Leonetti D., Maljaars J., Pasquarelli G., Brando G. (2020). Rivet Clamping Force of As-Built Hot-Riveted Connections in Steel Bridges, *Journal of Constructional Steel Research*, 167, 105955.

Lesiuk G., Kucharski P., Correia J.A.F.O., De Jesus A.M.P., Rebelo C., Simoes Da Silva L. (2017). Mixed mode (I+II) fatigue crack growth in puddle iron. *Engineering Fracture Mechanics,* 185, 175-192.

Liebermann G.J. (1957). Tables for One-Sided Statistical Tolerance Limits. Technical rept. No. 34, Stanford University, CA, USA.

Ling Y. (1996) Uniaxial true stress-strain after necking. *AMP Journal of Technology*, 5(1), 37-48.

Livieri P, Lazzarin P (2005). Fatigue strength of steel and aluminium welded joints based on generalised stress intensity factors and local strain energy values. *International Journal of Fracture*, 133, 247–276.

Lode W. (1926). Versuche über den Einfuss der mittleren Hauptspannung auf das Fliessen der Metalle Eisen Kupfer und Nickel. *Zeitung Phys.*, 36, 913–939 [In German].

Maarschalkerwaart, H.M.C.M. (1982). Fatigue Behaviour of Riveted Joints. *IABSE Reports*, 37.

Mackaness C. (2006). Bridging Sydney, Historic Houses Trust of New South Wales.

Malcher L., Andrade Pires F.M., César de Sá J.M.A. (2014). An extended GTN model for ductile fracture under high and low stress triaxiality. *International Journal of Plasticity*, 54, 193-228.

Maljaars J., Euler M. (2021). Fatigue S-N curves of bolts and bolted connections for application in civil engineering structures. *International Journal of Fatigue*, 151, 106355.

Manson S.S. (1953). Behavior of Materials Under Conditions of Thermal Stress. *Heat Transfer Symposium*, University of Michigan, June 27–28, 1952, University of Michigan Press.

Manson S.S., Halford G.R. (1981). Practical implementation of the double linear damage rule and damage curve approach for treating cumulative fatigue damage. *International Journal of Fracture,* 17, 35–42.

Marmo R., D'Aniello M., Portioli F., Landolfo R. (2010). Finite element modelling of lap shear riveted connections in fire. *Proc. Of International Conference on Urban Habitat Constructions Under Catastrophic events Final Conference*, COST Action C26, Napoli, 16-18 September.

Marmo R. (2011). Numerical and Experimental Investigation on Shear Behaviour of Riveted Connections [PhD Thesis].

Masi F. (1996). Costruire in acciaio. Hoepli, Milano [In Italian].

Matsuishi M., Endo T. (1968). Fatigue of metals subjected to varying stress. Presented to the Japan Society of Mechanical Engineers, Fukuoka, Japan.

Mazzolani F.M. (2009): The PROHITECH Project – Earthquake protection of historical buildings by reversible mixed technologies. http://www.prohitech.com/.

McClintock F.A. (1968). A Criterion for Ductile Fracture by the Growth of Holes. *Journal of Applied Mechanics*, 35(2), 363-371.

Milone A. (2022a). Behaviour of Lap Shear Riveted Connections with Constructional Imperfections. *Proc. Of 8th International Conference on Computational Methods in Structural Dynamics and Earthquake Engineering,* COMPDYN 2021, 28-30 June, Athens, Greece.

Milone A., Landolfo R. (2022b). A Simplified Approach for the Corrosion Fatigue Assessment of Steel Structures in Aggressive Environments. *Materials,* 15(6), 2210.

Milone A., Landolfo R., Berto F. (2022c). Methodologies for the fatigue assessment of corroded wire ropes: A state-of-the-art review. *Structures*, 37, 787-794.

Milone A., D'Aniello M., Landolfo R. (2023). Influence of camming imperfections on the resistance of lap shear riveted connections. *Journal of Constructional Steel Research*, 203, 107833.

Miner M.A. (1945). Cumulative Damage in Fatigue. *Journal of Applied Mechanics*, 3, 159-164.

Mirone G., Barbagallo R., Corallo D. (2016) A new yield criteria including the effect of lode angle and stress triaxiality. *Procedia Structural Integrity*, 2, 3684-3696.

Moes N.J.D., Belytschko T. (1999). A finite element method for crack growth without remeshing. *International Journal for Numerical Methods in Engineering,* 46(1), 131-150.

Morrow J. (1968) Fatigue properties of metals, Section 3.2. Fatigue Design Handbook, Pub. No. AE-4. SAE, Warrendale, PA, USA.

Munse W.H. (1970). Final report on riveted and bolted structural joints project IHR-5. *Illinois cooperative highway research program*. Urbana: University of Illinois.

Munse WH, Cox HC. (1956). The static strength of rivets subjected to combined tension and shear. *Engineering experiment station bulletin*, *437*. Urbana: University of Illinois.

New South Wales Government (2017). Sydney Harbour Bridge Precinct. Road & Maritime Services.

Niemi E., Fricke W., Maddox S.J. (2006). Fatigue Analysis of Welded Components - Designer's Guide to the Structural Hot-Spot Stress Approach, Woodhead Publ., Cambridge.

Osgood C.C. (1982). Fatigue Design – 2nd Edition. Pergamon Press.

Out J.M.M., Fisher J.W., Yen B.T. (1984). Fatigue strength of weathered and deteriorated riveted members. *Fritz Laboratory Reports*, 2282.

Paris P.C., Gomez M.P., Anderson W.E. (1961). A rational analytic theory of fatigue. *The Trend in Engineering*. 13, 9–14.

Paris P.C., Erdogan F. (1963). A Critical Analysis of Crack Propagation Laws. *Journal of Basic Engineering*, 85, 528-533.

Parola J.F., Chesson Jr. E., Munse W.H. (1964). Effect of Bearing Pressure on Fatigue Strength of Riveted Connections. *Engineering experiment station bulletin*, *481*. Urbana: University of Illinois.

Pascual M.A., Kareiva P. (1996). Predicting the Outcome of Competition Using Experimental Data: Maximum Likelihood and Bayesian Approaches. *Ecology*, 77(2), 337-349.

Pedrosa B., Raposo P., Correia J.A.F.O., Rebelo C., Gervasio H., De Jesus A.M.P., Calcada R., Samoes Da Silva L. (2017a). Fatigue resistance of reinforced and unreinforced steel connections. *Proc. Of XI Congresso de Construção Metálica e Mista*, Coimbra, Portugal.

Pedrosa B., Correia J., Rebelo C., De Jesus A., Simões da Silva L. (2017b) Experimental Fatigue tests of resin-injected and standard single bolted connections combining S355 mild steel and old steel from Eiffel Bridge. *Proc. Of International Conference of Structural Integrity*. Funchal, Madeira, Portugal.

Peterson C., Pilkey W.H. (1997). Peterson's Stress Concentration Factors – 3rd Edition, Wiley.

Pipinato A., Pellegrino C., Bursi O.S., Modena C. (2009). High-cycle fatigue behavior of riveted connections for railway metal bridges, *Journal of Constructional Steel Research*, 65(12), 2167-2175.

Python Software Foundation (2022). Python 3 Language Manual.

Qu R.T., Zhang Z. J., Zhang P., Liu Z. Q., Zhang Z. F. (2016). Generalized energy failure criterion. *Scientific Reports*, 6, 23359.

Radaj D., Vormwald M. (2013). Advanced Methods of Fatigue Assessment, Springer, Berlin, Germany.

Ramberg W., Osgood W.R. (1943). Description of Stress-Strain Curves by Three Parameters. Technical Note No. 902, National Advisory Committee for Aeronautics, Washington DC.

Rice J.R., Tracey D.M. (1969). On the Ductile Enlargement of Voids in Triaxial Stress Fields. *Journal of the Mechanics and Physics of Solids*, 17, 201-217.

Rychlik I. (1987). A new definition of the rainflow cycle counting method. *International Journal of Fatigue*, 9(2), 119-121.

Schenker L., Salmon C.G., Johnston B.G. (1954). Structural steel connections. *AFSWP Report 352. Ann Arbor:* Department of Civil Engineering. University of Michigan.

Schijve J. (2009). Fatigue of structures and materials, Kluwer Academic Publ., The Netherlands.

Schumacher A (2003). Fatigue behavior of welded circular hollow section joints [PhD Thesis].

Schutz F.W. (1952). The efficiency of riveted structural joints [PhD Thesis].

Schwedler, JW. (1867). "Ueber Nietverbindungen." *Wochenblatt Herausgegeben von Mitgliedern des Architekten – Vereins zu Berlin*, 48 [In German].

Smith K.N., Watson P., Topper T.H. (1970). A stress-strain function for the fatigue of materials. *Journal of Materials* 5, 767–778.

Snijder HH, Ungermann D, Stark JWB, Sedlacek G, Bijlaard FSK, Hemmert-Halswick A. (1988). Evaluation of test results on bolted connections in order to obtain strength functions and suitable model factors—part A: results. Eurocode no. 3 — part 1 background documentation. *Document 6.01. Brussels: Commission of the European Communities*; [Chapter 6].

Soderberg C.R. (1930). Factor of Safety and Working Stress. *ASME Trans*, 52, 13–28.

Spearritt P. (2011). The Sydney Harbour Bridge: A Life. University of New South Wales Press. ISBN 978-0868409252.

Sustainable bridges. (2006). Guideline for load and resistance assessment of existing european railway bridges—advices on the use of advanced methods. *European research project under the EU 6th framework programme*. http://www.sustainablebridges.net/.

Taras A., Greiner R. (2009). Development and Application of a Fatigue Class Catalogue for Riveted Bridge Components. *Structural Engineering International: Journal of the International Association for Bridge and Structural Engineering (IABSE)*, 20(1), 91-103.

Tartaglia R., D'Aniello M. (2017). Nonlinear performance of extended stiffened end plate bolted beam-to-column joints subjected to column removal. *Open Civil Engineering Journal*, 11(1), 369-383.

Tartaglia R., D'Aniello M., Zimbru M. (2020). Experimental and numerical study on the T-Stub behaviour with preloaded bolts under large deformations. *Structures*, 27, 2137-2155.

Tartaglia R., Milone A., D'Aniello M., Landolfo R. (2022). Retrofit of non-code conforming moment resisting beam-to-column joints: A case study. *Journal of Constructional Steel Research*, 189, 107095.

Tu S., Ren X., He J., Zhang Z. (2019). Stress–strain curves of metallic materials and post-necking strain hardening characterization: A review. *Fatigue & Fracture of Engineering Materials & Structures*, 43, 3–19.

Twelvetrees WN (1900). Structural Iron and Steel. A Text Book for Architects, Engineers, Builders, and Science Students. The Builder Student's Series, London - NY: Whittaker & Co.

Van der Zee, J. (2000). The Gate: The True Story of the Design and Construction of the Golden Gate Bridge, Backprint.

Vermes W. (2007). Designing and Performance of rivetd bridge connections. *In: Proc. of Ohio Transportation Engineering Conference,* 24 October.

Von Mises R. (1913). Mechanik der festen Körper im plastisch-deformablen Zustand. *Nachrichten von der Gesellschaft der Wissenschaften zu Göttingen. Mathematisch-Physikalische Klasse*, 1, 582–592 [In German].

Voyiadjis G.Z., Kattan P.I. (1992). A Plasticity-Damage Theory for Large Deformation of Solids - I. Theoretical Formulation. *International Journal of Engineering Science*, 30(9), 1089-1108.

Walker K. (1970). The effect of stress ratio during crack propagation and fatigue for 2024-T3 and 7075-T6 aluminium. Effects of Environment and Complex Load History on Fatigue Life, ASTM STP 462, 1–14.

Wakefield J. (2013). Bayesian and Frequentist Regression Methods. Springer.

Wang Y., Xu S., Ren S., Wang H. (2016). An Experimental-Numerical Combined Method to Determine the True Constitutive Relation of Tensile Specimens after Necking. *Advances in Civil Engineering*, 6015752.

Williams M.L. (1952) Stress singularities resulting from various boundary conditions in angular corners of plates in tension. *Journal of Applied Mechanichs,* 19, 526–528.

Wirsching P.H., Ortiz K., Chen Y.N. (1987). Fracture mechanics fatigue model in a reliability format. *Proc. Of the 6th International Symposium on Offshore Mechanics and Arctic Engineering*, ASME, New York.

Wöhler A. (1860). Versuche zur Ermittlung der auf die Eisenbahnwagenachsen einwirkenden Kräfte und die Widerstandsfähigkeit des Wagen-Achsen. *Zeitschrift für Bauwesen*, 10, 583-616 [in German].

Xin H., Veljkovic M., Correia J.A.F.O., Berto F. (2021). Ductile Fracture Locus Identification Using Mesoscale Critical Equivalent Plastic Strain. *Fatigue & Fracture of Engineering Materials & Structures*, 10.1111/ffe.13429.

Yang F., Veljkovic M. (2019). DAMAGE MODEL CALIBRATION FOR S275 AND S690 STEELS, *ce/papers,* 3, 5-6, 262-271.

Yosibash Z, Bussiba AR, Gilad I (2004) Failure criteria for brittle elastic materials. *Int J Fract* 125:307–333.